

Published Quarterly by The American Society of Mechanical Engineers

VOLUME 109 • NUMBER 4 • OCTOBER 1987

Technical Editor  
**ARTHUR J. WENNERSTROM**  
Senior Associate Editor  
**G. K. SEROVY**  
Associate Editors  
Advanced Energy Systems  
**S. I. FREEDMAN**  
Environmental Control  
**H. E. HESKETH**  
Fuels and Combustion Technologies  
**R. E. BARRÉTT**  
Gas Turbine  
**S. KUO**  
Internal Combustion Engine  
**K. J. SPRINGER**  
Nuclear Engineering  
**S. M. CHO**  
Power  
**R. W. PORTER**

**BOARD ON  
COMMUNICATIONS**  
Chairman and Vice-President  
**K. N. REID, JR.**

Members-at-Large  
**J. T. COKONIS**  
**M. FRANKE**  
**M. KUTZ**  
**F. LANDIS**  
**J. R. LLOYD**  
**T. C. MIN**  
**R. E. NICKELL**  
**R. E. REDER**  
**R. ROCKE**  
**F. W. SCHMIDT**  
**W. O. WINER**

President, **R. ROSENBERG**  
Executive Director,  
**D. L. BELDEN**  
Treasurer, **ROBERT A. BENNETT**

**PUBLISHING STAFF**  
Mng. Dir., Publ., **J. J. FREY**  
Dep. Mng. Dir., Pub.,  
**JOS. SANSONE**  
Managing Editor,  
**CORNELIA MONAHAN**  
Sr. Production Editor,  
**VALERIE WINTERS**  
Editorial Prod. Asst.  
**MARISOL ANDINO**

Transactions of the ASME, Journal of Engineering for Gas Turbines and Power (ISSN 0022-0825) is published quarterly (Jan., Apr., July, Oct.) for \$95 per year by The American Society of Mechanical Engineers, 345 East 47th Street, New York, NY 10017. Second class postage paid at New York, NY and additional mailing offices. POSTMASTER: Send address change to The Journal of Engineering for Gas Turbines and Power, c/o The AMERICAN SOCIETY OF MECHANICAL ENGINEERS, 22 Law Drive, Box 2300, Fairfield, NJ 07007-2300. CHANGES OF ADDRESS must be received at Society headquarters seven weeks before they are to be effective. Please send old label and new address.

PRICES: To members, \$27.00, annually, to nonmembers, \$95.00.  
Add \$12.00 for postage to countries outside the United States and Canada.

STATEMENT from By-Laws. The Society shall not be responsible for statements or opinions advanced in papers or ... printed in its publications (B 7.1, para. 3).

COPYRIGHT © 1987 by the American Society of Mechanical Engineers. Reprints from this publication may be made on condition that full credit be given the TRANSACTIONS OF THE ASME—JOURNAL OF ENGINEERING FOR GAS TURBINES AND POWER, and the author, and date of publication be stated.  
INDEXED by Engineering Information

## TECHNICAL PAPERS

- 355 Engine Valves—Design and Material Evolution  
J. M. Larson, L. F. Jenkins, S. L. Narasimhan, and J. E. Belmore
- 362 Caterpillar's 3600 PEEC Locomotive Governor (Programmable Electronic Engine Control)  
S. R. Burns and R. G. Evans
- 367 Partially Stabilized Zirconia Piston Bowl Reliability  
D. L. Hartsock
- 374 New Cement-Based Materials for Engine Construction  
M. Love
- 380 Materials and Surface Finish Effects in the Breaking-in Process of Engines  
G. C. Barber, J. C. Lee, and K. C. Ludema
- 388 Development of the B2400 Engine  
R. M. Dunton, L. Propetto, and G. E. Murray
- 396 Comparing Expanders for Direct Recovery of Exhaust Energy From a Low-Heat-Rejection Diesel (87-ICE-26)  
C. A. Amann
- 402 Application of Several Variable-Valve-Timing Concepts to an LHR Engine (87-ICE-29)  
T. Morel, R. Keribar, M. Sawlivala, and N. Hakim
- 410 Tests of Thick Flame Combustion Estimates in a Single-Cylinder Engine (87-ICE-22)  
J. Boisvert and P. G. Hill
- 419 Combustion Characteristics of a Single-Cylinder Open-Chamber Diesel Engine (87-ICE-35)  
A. C. Alkidas
- 426 Reduction of NO<sub>x</sub> and Particulate Emissions in the Diesel Combustion Process (87-ICE-37)  
W. R. Wade, C. E. Hunter, F. H. Trinker, and H. A. Cikanek
- 435 Dual Fuel Engine Control Systems for Transportation Applications (87-ICE-12)  
L. E. Gettel, G. C. Perry, J. Boisvert, and P. J. O'Sullivan
- 439 A Correlation for the Burning Velocity of Methane-Air Mixtures at High Pressures and Temperatures (87-ICE-6)  
T. J. Al-Himyary and G. A. Karim
- 443 Operation of a Caterpillar 3516 Spark-Ignited Engine on Low-Btu Fuel (87-ICE-13)  
N. C. Macari and R. D. Richardson
- 448 Progress Toward Life Modeling of Thermal Barrier Coatings for Aircraft Gas Turbine Engines (87-ICE-18)  
R. A. Miller
- 452 Study of the Flow Pattern in Compact Manifold Type Junctions by LDA (87-ICE-25)  
R. Sierens and P. Snauwaert
- 459 An Analysis of the Engine Blowdown Process Using Multidimensional Computations (87-ICE-17)  
T. Uzkan
- 465 Continued Development of a Coal/Water Slurry-Fired Slow-Speed Diesel Engine: a Review of Recent Test Results (87-ICE-10)  
S. E. Nydick, F. Porchet, and H. A. Steiger
- 477 Calculation of Integral Compressor Misalignments From Measured Web Deflections (87-ICE-3)  
R. W. James and L. E. Bishop, Jr.
- 481 Reciprocating Compressor Frame Distortion During a Cold Start (87-ICE-4)  
A. J. Smalley
- 487 Maintaining Low Exhaust Emissions With Turbocharged Gas Engines Using a Feedback Air-Fuel Ratio Control System (87-ICE-2)  
D. W. Eckard and J. W. Servé
- 491 Induction System Effects on Small-Scale Turbulence in a High-Speed Diesel Engine (87-ICE-38)  
A. E. Catania and A. Mittica

## DISCUSSION

- 503 Discussion of a previously published paper by  
T. Uzkan and N. J. Lipstein

## ANNOUNCEMENTS

- 401 Change of address form for subscribers  
504 Reference citation format

Inside back cover Information for authors

**J. M. Larson**  
Chief Engineer of Materials.

**L. F. Jenkins**  
Chief Engineer of Valves.

**S. L. Narasimhan**  
Materials R. & D. Supervisor.

**J. E. Belmore**  
Division Manager—Engineering Services.  
Eaton ECD—Engineering Center,  
Marshall, MI

# Engine Valves—Design and Material Evolution

*This paper reviews the design and material evolution of poppet valves used in reciprocating internal combustion engines in the United States. Driving forces which led to the current state-of-the-art technology, such as needs for improved durability and cost effectiveness, are described. This paper also endeavors to predict how valve materials, design, and construction will change over the next two decades in response to continual engine performance improvement demands in a worldwide competitive environment. As a basis for understanding the past evolution and future trends in valve design, the key operating parameters that affect valve function are detailed.*

## Exhaust Valve Operating Environment

The selection of base materials and heat treatments used for exhaust valves depends upon the operating environment in each specific engine application. Key factors of this environment are the operating temperature, the imposed stress levels, and the corrosive nature of the products of combustion to which the valve is exposed [1–3].

**Operating Temperature.** The operating temperature of the exhaust valve is a function of the specific output of the engine, the relative efficiency of the combustion process, and the effectiveness of the engine cooling system. The temperature profile is particularly dependent upon the temperature of the exhaust gases. The higher exhaust gas temperatures typical of spark ignition (gasoline) engines result in significantly higher heat input into the port side of the exhaust valve, producing higher valve temperatures in this area than are seen in compression ignition engines, as shown in Fig. 1.

**Imposed Stress Levels.** Every combustion event imposes high pressures on the combustion chamber side of the valve head, generating cyclic tensile stresses on the port side of the valve head, as shown in Fig. 2. The magnitude of these stresses is a function of the peak combustion pressure of the engine and is considerably higher for compression ignition than spark ignition engines.

The valve seating event imposes cyclic tensile stresses at the junction of the stem and fillet on the port side of the head. Valve seating initiates at a single contact point due to the inherent thermal distortion of the cylinder seat at high output conditions, as shown in Fig. 3. Bending stresses created by this initial single-point contact of the valve and cylinder seat increase the magnitude of these valve seating stresses.

**Corrosive Environment.** The exhaust valve head is exposed to products of combustion which often contain highly

corrosive constituents [4]. The potential severity of corrosive attack is a function of the chemical composition of the valve alloy, its metallurgical characteristics such as grain size and microconstituent phases, and the valve operating environment.

There are several problems related to corrosive attack of valve materials. An obvious concern is the prevention of proper sealing of the valve seat–cylinder seat interface. An additional problem is overall material loss in highly stressed areas of the valve which could lead to breakage. A less recognized concern is the effect of the corrosive medium on the basic fatigue life of valve materials. This phenomenon can play a significant role in not only alloy selection but also in the choice of heat treatments to be applied to the materials.

Figure 4 illustrates the effect of a leaded fuel environment on the fatigue strength of Nimonic 80A, a nickel base superalloy, at an operating temperature of 815°C (1500°F). (Refer to Table 1 for all alloy compositions discussed in this paper.) A fine-grain microstructure achieved without solution treatment optimizes the fatigue resistance of Nimonic 80A in an air environment. In the presence of a leaded fuel environment the situation is reversed. A coarse-grained, solution-treated structure offers the best fatigue strength, thus resisting corrosion fatigue more effectively [5].

## Intake Valve Operating Environment

Selection of the materials and their associated heat treatments for intake valves must take into account the same environmental operating factors as the exhaust valve.

**Operating Temperature.** The operating temperature of the intake valve is generally a function of the intake charge temperature and the effectiveness of the engine cooling system. Primarily due to the cooling effect of the incoming charge, the operating temperature is significantly lower than that of the exhaust valve.

**Imposed Stress Levels.** The intake valve is subjected to the

Contributed by the Internal Combustion Engine Division and presented at the Internal Combustion Engine Division Technical Conference, Oakbrook, Illinois, October 5–7, 1986. Manuscript received at ASME Headquarters July 9, 1986.

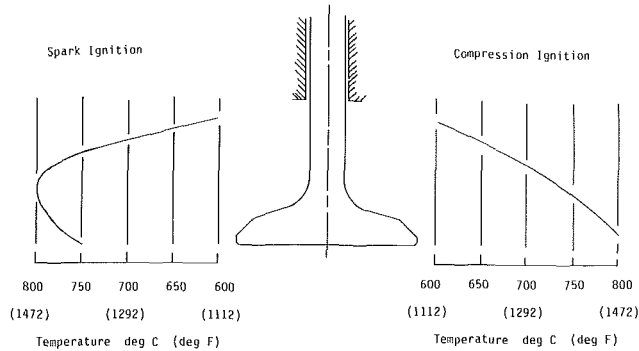


Fig. 1 Comparison of typical exhaust valve temperature profiles for spark and compression ignition engines; temperatures are along axis of a valve head section

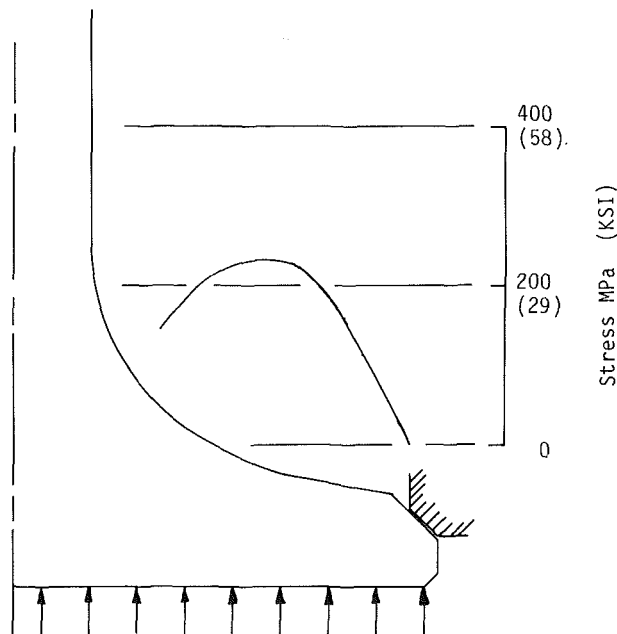


Fig. 2 Tensile stresses on the surface of the port side of the valve head from combustion loading

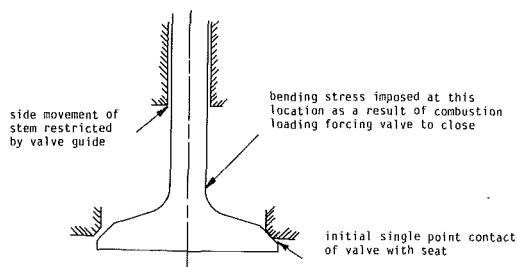


Fig. 3 Bending stress imposed at the junction of the head and fillet surfaces

same imposed stresses from the combustion event and valve seating as the exhaust valve.

**Corrosive Environment.** While the combustion chamber side of the intake valve head is exposed to the same products of combustion as the exhaust valve, its relatively low operating temperature generally precludes concern for detrimental corrosive attack [6].

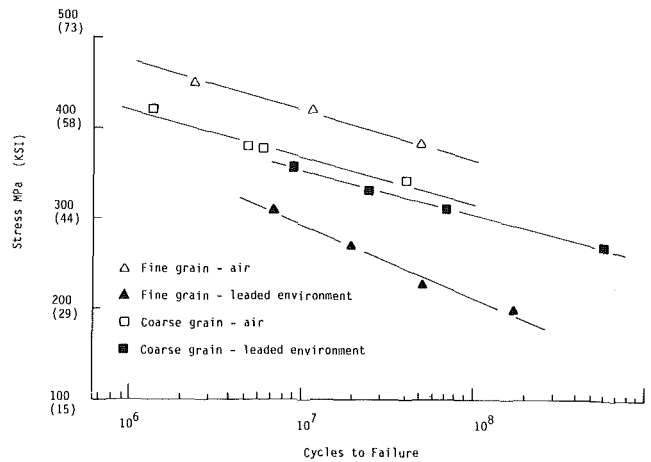


Fig. 4 Effect of corrosive environment on the fatigue life of Nimonic 80A at 815°C (1500°F)

### Exhaust Valve Construction

The use of iron and nickel base austenitic alloys for exhaust valves is primarily dictated by the elevated temperature fatigue strength requirements in the head portion of the valve [5, 7]. Depending on other performance and cost objectives, the final construction of the valve can be one of several designs.

**One-Piece Design.** A one-piece valve represents the most cost-effective design when an iron base austenitic alloy is used. This design is widely employed in passenger car applications (Fig. 5a).

**Wafer or Tip Welded Design.** There are several valve gear configurations in use where one-piece austenitic valves may experience an unacceptable level of tip wear or scuffing. To minimize or eliminate this concern, a hardenable martensitic steel may be welded to the tip of the valve and heat treated to maximum hardness. This design has seen extensive usage in passenger car engines and limited application in heavy-duty engines (Fig. 5b).

**Two-Piece Design.** In a two-piece design, the austenitic alloy head is welded to a hardenable martensitic stem. In contrast to the use of a tip weld, this design enables one to extend the selective full hardening of the tip end through the keeper groove area to maximize low-temperature fatigue strength. The balance of the martensitic stem, used in the hardened and tempered condition, enhances valve stem scuffing resistance. This design has increasingly penetrated the passenger car market and is predominant in the heavy-duty sector (Fig. 5c).

**Seat Welded Design.** Iron base austenitic alloys used in heavy-duty applications often lack adequate wear and/or corrosion resistance to withstand the operating environment at the seat face. In these cases, hard facing alloys with superior wear and/or corrosion resistance may be applied to the seating face by gas or shielded arc techniques [8] (Fig. 5d).

**Internally Cooled Design.** An internally cooled valve contains a cavity partially filled with a coolant, typically sodium or sodium potassium. The coolant transports heat from the valve head to the valve stem for dissipation through the valve guide to the cylinder head cooling medium. This significantly reduces the valve head temperature, which minimizes or eliminates detrimental corrosive attack by the products of combustion (Fig. 5e).

### Intake Valve Construction

The use of carbon steel, low alloy steel, or corrosion-resistant martensitic stainless steel is primarily dictated by

**Table 1 Compositions of valve materials**

<i>Nominal Compositions of Martensitic Valve Materials</i>									
Material designation	C	Composition (weight percent)							
		Mn	Si	Cr	Ni	Mo	Fe	Other	
SAE 1541	0.40	1.50	0.23	-	-	-	Bal.		
SAE 1547	0.47	1.50	0.23	-	-	-	Bal.		
SAE 3140	0.40	0.80	0.28	0.65	1.25	-	Bal.		
SAE 4140	0.40	0.88	0.28	0.95	-	0.20	Bal.		
SAE 8645	0.45	0.88	0.25	0.50	0.55	0.20	Bal.		
Silchrome 1	0.45	0.80 max	3.25	8.50	0.50 max	-	Bal.		
Sil XB	0.80	0.80 max	2.12	20.00	1.35	-	Bal.		
422 SS	0.22	0.75	0.50 max	11.75	0.75	1.08	Bal.	W 1.08 V 0.25	
T1 (610)	0.75	0.30	0.30	4.00	-	0.70	Bal.	W 18.00 V 1.00	

<i>Nominal Compositions of Austenitic Valve Steel Materials</i>									
Material designation	C	Composition (weight percent)							
		Mn	Si	Cr	Ni	N	Fe	Other	
21-2N	0.55	8.25	0.25 max	20.38	2.12	0.30	Bal.		
21-4N	0.53	9.00	0.25 max	21.00	3.88	0.46	Bal.		
21-12	0.20	1.50	1.00	21.25	11.50	-	Bal.		
23-8N	0.33	2.50	0.75	23.00	8.00	0.32	Bal.		
Silchrome 10	0.38	1.05	3.00	19.00	8.00	-	Bal.		
Gaman H	0.52	12.25	2.65	21.25	-	0.45	Bal.		
XCR	0.45	0.50	0.50	23.50	4.80	-	Bal.	Mo 2.80	
TXCR	0.40	4.30	0.80	24.00	3.80	-	Bal.	Mo 1.40	
TPA	0.45	0.50	0.60	14.00	14.00	-	Bal.	W 2.40 Mo 0.35	

<i>Nominal Compositions of Superalloy Valve Materials</i>									
Material designation	C	Composition (weight percent)					Fe	Other	
		Mn	Si	Cr	Ni				
N-155	0.12	1.50	1.00 max	21.25	19.50	Bal.	Co Al W Nb	19.75 3.50 2.50 1.00	
TPM	0.04	2.25	0.08	16.0	Bal.	6.50	Ti	3.05	
Inconel 751	0.06	0.50 max	0.50 max	15.50	Bal.	7.00	Ti Al Nb + Ta	2.30 1.22 0.95	
Nimonic 80A	0.10 max	1.00 max	1.00 max	19.50	Bal.	3.0 max	Ti Al	2.25 1.40	
Pyromet 31	0.04	0.20 max	0.20 max	22.60	56.50	Bal.	Ti Al Mo Nb	2.25 1.25 2.00 0.85	

<i>Nominal Composition of Typical Valve Seat Facing Materials</i>									
Material designation	C	Composition (weight percent)							
		Mn	Si	Cr	Ni	Co	W	Mo	Fe
Stellite 6	1.20	0.50	1.20	28.00	3.00	Bal.	4.50	0.50	3.00
Stellite F	1.75	0.30	1.00	25.00	22.00	Bal.	12.00	-	3.00
Stellite 1	2.50	0.50	1.30	30.00	1.50	Bal.	13.00	0.50	3.00
Eatonite	2.40	0.50	1.00	29.00	Bal.	10.00	15.00	-	8.00
Eatonite 3	2.00	0.50	1.20	29.00	Bal.	-	-	5.50	8.00
Eatonite 6	1.75	0.75	1.30	28.00	16.50	-	*	4.50	Bal.
VMS 585	2.25	-	1.00	24.00	11.00	-	-	5.50	Bal.

\*May substitute W for Mo according to formula  $Mo = W/2$ .

moderate to low temperature strength requirements. Since these families of alloys can be selectively hardened to address the durability concerns of the tip and keeper groove, the final construction of the valve is usually the one-piece design shown in Fig. 5(a). In applications such as high peak pressure compression ignition engines and dry fuel (e.g., natural gas) spark ignition engines where seat face wear resistance is inadequate, a seat welded design, shown in Fig. 5(d), is used.

## US Spark Ignited Engine Valve Design and Materials Evolution

**Exhaust Valves.** The evolution of the material content for exhaust valves used in spark ignition engines is chronologically illustrated in Fig. 6. For each material type the date of introduction and the span of usage is depicted. The associated

progression of events related to valve configuration and manufacturing processes is shown in Table 2.

The first US gasoline fueled automobile was produced by the Duryea brothers in 1892 [9]. This vehicle was powered by a spark ignited engine containing wrought iron or carbon steel valves made by a blacksmith. A two-piece valve with a cast iron head screwed or riveted onto a steel stem was soon developed to improve corrosion and seat face wear resistance [10]. This design was used in the Wright brothers' first successful flight. In 1906, Thompson formed a company, now part of TRW, and introduced the mass produced alloy steel head, resistance welded to a carbon steel stem [11].

The Great War, and its associated rapid aircraft engine

developments, imposed ever-increasing demands on exhaust valve needs. By 1919, there were 23 different aircraft exhaust valve alloys [12, 13]. Cutlery type stainless steels, similar to the SAE 440 series, found their way into valves. These martensitic materials, later termed Silchrome 1 and Silchrome XB, were the most prominent exhaust valve materials used through the 1920s [14]. These materials were extremely hard, corrosion resistant, and strong up to about 590°C (1100°F), but tempered rather quickly at higher operating temperatures. Austenitic stainless steels, produced by Krupp, were used in several German aircraft engines. However, these materials were only used on a very limited basis in the United States.

During the Great War, refractory elements such as tungsten, molybdenum, and vanadium were added to these materials to improve their hot strength and seat wear resistance [15]. By the mid-1930s, austenitic stainless steels, such as 21-12 and Silchrome 10, were widely used in automotive engines. These materials had reasonable strength, creep, and fatigue resistance up to 820°C (1500°F), although they exhibited considerably lower strength at low to moderate temperatures than earlier Silchrome martensitic alloys.

The Rich Company, now part of Eaton Corporation, began manufacturing tool steel valves during World War I [16]. As a tool maker, Rich recognized that 18W-4Cr-1V tool steels had excellent hot strength. Unfortunately, these materials had extremely poor corrosion resistance and poor weldability. The corrosion problem was further exacerbated by the demands of high-performance aircraft engines developed during this period. Ethyl Corporation's 1919 introduction of tetraethyl lead to gasoline further increased corrosion susceptibility [12].

These corrosion problems were circumvented by several novel approaches. Bright Ray (Ni-20%Cr) coatings were applied to the seat and combustion face of the valve for corrosion resistance. By 1940 Bright Ray had been supplanted by Stellite (cobalt based) seat facing, providing both wear and corrosion resistance. Facings were eventually utilized on most heavy-duty exhaust valves.

In the mid-1920s, Heron, of Ethyl Corporation, invented the sodium-cooled valve [13]. This not only decreased temperatures and, thus, corrosion, but also decreased the likelihood of preignition, commonly called "knock." Without the internally cooled valves, advances in aircraft engine performance and application would have been considerably curtailed in the 1920s and 1930s, and the history of World War II

**Table 2 Poppet engine valve design chronology**

Valve Design	Decade of Introduction
Riveted or threaded martensitic stem	1890
Hardened tip end of stem	1900
Resistance welded martensitic stem	1900
Seat faced with Ni-20 percent Cr	1920
Combustion faced with Ni-20 percent Cr	1920
Internally cooled	1920
Seat faced with Co based alloys	1930
Tip faced with Co base alloys	1930
Chromium-plated stem	1930
Oxalate stem coating	1930
Nitrided stem	1940
Seat faced with nickel base alloys	1940
Aluminized head	1940
Wafer welded tip	1950
Friction welded martensitic stem	1960
Nickel-plated head	1970
Seat faced with Fe base alloys	1980

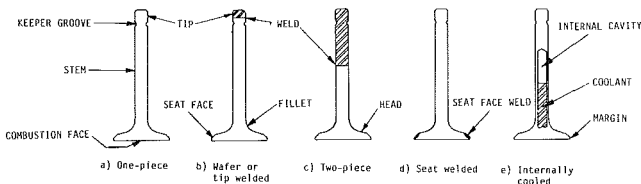


**Fig. 5 Cross-sectional view of typical exhaust valve constructions**

**U.S. SPARK IGNITED ENGINE POPPET EXHAUST VALVE MATERIAL & DESIGN EVOLUTION**

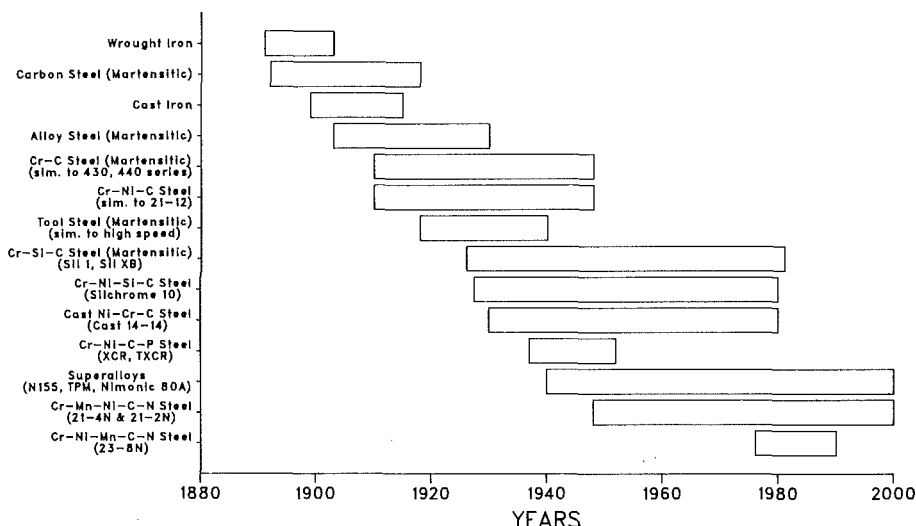


**Fig. 6 Family listed in austenitic unless specified martensitic; all are wrought alloys except where stated as cast; alloy listed is typical example of family**

might have been totally different. A typical internally cooled valve design is illustrated in Fig. 5(e).

Wear on the tip of the austenitic valve stem was avoided by welding the stem with Stellite alloys. This approach has been replaced by resistance welding a martensitic alloy to the valve tip, commonly referred to as the wafer welded design.

In the early 1930s, Ford introduced the Cast 14-14 austenitic exhaust valve material. Most US engines were using wrought austenitic alloys at this time. However, Ford used stainless steel radiator shells and wanted to utilize their own internally created stamping scrap better to make the cast austenitic valves.

In the late 1930s, the XCR and TXCR austenitic exhaust valves were commercialized in passenger car engines. These alloys were similar to Silchrome 10 and 21-12 and hardened by sigma phase formation. The precipitation of sigma phase increased the volume fraction of hard phases, improving wear resistance. However, these alloys were difficult to weld and had a brittleness which tended to increase during service, causing a degradation of ductility and corrosion resistance [17].

Aircraft applications continued to be more demanding and World War II greatly expedited the use of a new group of materials known as superalloys [18]. The first superalloy used was called N-155. N-155 was followed by Inconel M (TPM) and Nimonic 80A. Although most of these alloys were developed for gas turbines, they have served well in heavy-duty exhaust valve applications and Nimonic 80A is still the material of choice for reciprocating aircraft engines.

Prior to World War II, nitrogen had been added to Silchrome 10 and 21-12 as an austenite stabilizer. Later, Jennings [19] at Armco discovered that if over 0.2 percent nitrogen was added to austenitic steels with sufficient carbon, a precipitation hardenable grade would result. His work culminated in the development of 21-4N alloy that virtually replaced all other passenger car engine exhaust valve alloys in the 1950s. This material was especially attractive economically because of its lower nickel content. Its strength properties were substantially improved over prior alloys by the combination of carbon and nitrogen, resulting in carbonitride precipitation. The low silicon content made it much less susceptible to lead oxide corrosion than the other available austenitic alloys.

A relatively slight modification of 21-4N (decreasing the nickel content by 2 percent) led to the more cost-effective 21-2N austenitic valve steel in the early 1960s. This alloy dominates the passenger car exhaust valve material market today and is expected to do so in the foreseeable future. Friction welding replaced resistance welding in the 1960s as a cost saving measure and a quality improvement. The low-cost, reliable exhaust valve design currently used for passenger cars incorporates 21-2N head material friction welded to a carbon steel stem.

The most recently commercialized valve alloy in spark ignited engines is referred to as 23-8N. This alloy was developed by Tanzan, also of Armco, for heavy-duty diesel applications [7]. It has also found limited application in sodium cooled valves used in heavy-duty gasoline engines, e.g., delivery truck engines.

**Intake Valves.** Until World War I, the intake valve for spark ignited engines was the same in design and materials as the exhaust valve. Cutlery steels found intake valve application during that period, and their predecessors, Silchrome 1 and Silchrome XB, are still used in heavy-duty and aircraft applications.

The environmental demands are much less for the intake valve than for the exhaust valve. As a result, the main factor affecting its evolution has been cost reduction. Current spark ignited passenger car engines use low alloy steels such as SAE 1541 or 1547 for intake valve applications. Considerable effort

is being expended to improve the quality and heat treat response of these materials, but it will be difficult to find a less expensive material with properties that are comparable to these medium carbon steels.

### Future Evolution of Spark Ignited Engine Valve Design

The spark ignited engine is expected to remain the dominant power plant for passenger car applications in the United States. By contrast, in commercial truck and aircraft applications, diesel and turbine engines are replacing the gasoline engines. As such, the vast majority of new valve-related engine design activity will be concentrated in the passenger car section. The most significant driving forces for the future evolution of the passenger car spark ignited engine will be improved fuel economy and reduced initial engine costs.

**Exhaust Valves.** Any fuel economy gains made as a result of improvements in the basic combustion process are expected to be manifested in reduced exhaust gas temperature, and thus lower valve operating temperatures. Also, the exclusive use of lead-free fuels virtually eliminates any detrimental corrosive environment. It is conceivable that the combination of these two factors may permit substitution of a lower cost austenitic or martensitic alloy for the austenitic valve steel (21-2N) presently in use.

Reduced valve gear friction has also successfully demonstrated fuel economy gains [20]. This has resulted in widespread usage of roller cam followers. For those valve gear configurations where roller cam followers are not practical or cost effective, reduced valve weight can accomplish the same objective. Reduced valve weight permits the use of lighter valve spring loads, which results in a significant reduction in friction between the flat cam follower and the cam shaft. This reduced weight can be achieved through substantial reduction of the cross-sectional thickness of the valve head and stem. Alternative means include a hollow stem steel configuration or use of low-density materials such as titanium [3]. Considerable material and process development effort will be required to make these latter alternatives cost effective.

Fuel economy gains may also be achieved through favorable adjustment of parameters such as compression ratio and spark advance. Unfortunately, preignition occurs during certain transient modes of engine operation which preclude these adjustments. Industry discussion has centered on the hot exhaust valve as a cause of the preignition. If this could be demonstrated, internal cooling would provide yet another means to reduce fuel consumption. Again, a large development effort in material and processing would be required to produce a cost-effective product. However, there would be an additional benefit; internal cooling would permit use of simpler alloys with a significant reduction in strategic alloy content, e.g., chromium, manganese, nickel.

There is also a large industry effort to reduce oil consumption in evolving passenger car engines. One approach to this is to reduce significantly the amount of oil reaching the valve stem/valve guide interface. In the present environment, chromium plating applied to the valve stem has been an effective means of adhesive wear prevention. With reduced lubrication, however, there is the potential need for the development of improved antiscuff coatings.

**Intake Valves.** Alloy changes from the presently used SAE 1541 and 1547 are not anticipated due to improvements made to the basic combustion system. The identified benefits for weight reduction in exhaust valves apply to the intake valves, as do concerns for reduction in lubrication to the valve stem/valve guide interface.

## U.S. COMPRESSION IGNITED ENGINE POPPET EXHAUST VALVE MATERIAL & DESIGN EVOLUTION

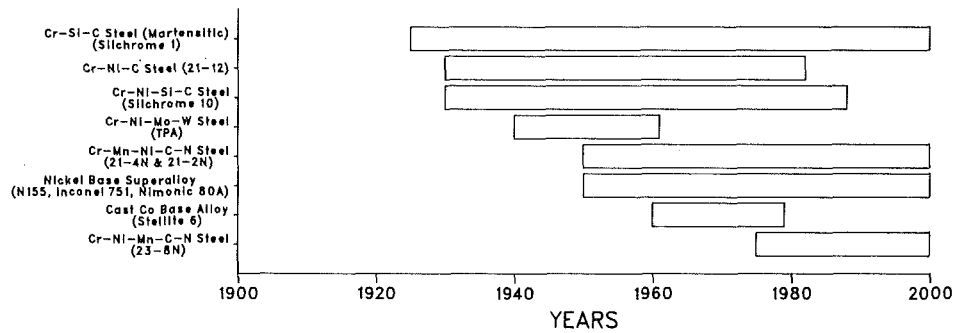


Fig. 7 Family listed is austenitic unless specified martensitic; all are wrought alloys except where stated as cast; alloy listed is typical example of family

### US Compression Ignited Engine Valve Design and Material Evolution

**Exhaust Valves.** R. Diesel conceived the first compression ignited engine in 1892, but World War I propelled the development of the first high-speed Diesel engines in Germany and the United Kingdom [9]. By the late 1930s the high-speed normally aspirated Diesel engine was firmly established in the truck, bus, and heavy-duty construction equipment industries. The first valve materials used were identical to those for spark ignited engines, but the more severe environmental conditions forced a considerably different course of evolution as shown in Fig. 7.

The first US Diesel exhaust valves were of the cutlery steel type, i.e., Silchrome 1. However, their poor high-temperature strength necessitated the use of 21-12 and Silchrome 10 materials. The much higher peak combustion pressures associated with Diesel engine operation created high contact stresses and considerable adhesive wear at the valve seat interface. The wear problem was addressed by hard facing the valve seats with Stellite type cobalt base alloys.

As was the case for the Great War, World War II greatly expedited the development of the Diesel engine. Molybdenum and tungsten were added to alloys similar to 21-12 in order to improve strength and seat wear resistance. An alloy known as TPA proved to be the leader using this approach.

Superalloys soon found their way into Diesel engines. N-155 was the first superalloy and TPM (Inconel M) came soon thereafter. These alloys were followed by Inconel 751, Nimonic 80A and Nimonic 90 in the late 1950s and early 1960s [21].

Although developed for spark-ignited engines, 21-4N and its later variant 21-2N found applications in the 1950s and 1960s vintage Diesel engines as well as in recent passenger car Diesel engines. A high nitrogen version of these alloys, Gaman H, had even better seat face wear resistance, and also found application in two-cycle Diesel engines [22]. In the 1960s, one engine manufacturer used cast Stellite heads in order to use high-sulfur fuels. These changes also supplemented the development of turbocharged Diesels to improve efficiency.

Although virtually no new passenger car valve materials were introduced in the 1970s or 1980s, substantial changes occurred in the Diesel exhaust valve alloy applications. Armco developed an alloy called 23-8N [7] which was based on 21-4N but was more carefully balanced to improve long term stability and seat facing weldability. Because of these improvements, it has virtually replaced Silchrome 10 and 21-12N.

In the late 1970s, Pyromet 31 alloy was also introduced. Because of its improved sulfidation resistance, higher strength, and better seat face wear resistance, it proved to be a better substitute for several superalloys.

The 1970s also saw the development of nickel and iron base seat facing alloys such as Eatonite 3, 5, and 6 [23]. In 1978, political instabilities in Zaire resulted in a "cobalt crisis" which necessitated and greatly expedited the substitution of these alloys for the cobalt based Stellite alloys. Very little Stellite is expected to be used in Diesel engines by the late 1980s. It should also be noted that the use of these materials was in part made possible by the development of the plasma transferred arc seat facing technology [8]. Plasma transferred arc welding is replacing the oxy-acetylene process used since the introduction of the first Stellite faced valve.

**Intake Valves.** Diesel intake valve material has actually changed very little since the introduction of Silchrome 1, Cr-Si-C martensitic steel. The exceptions are those Diesel engine manufacturers who wish to use the same material in their intake valves as in the exhaust valves. Both a 12 percent super Cr steel (similar to 422 SS) and 21-2N have found limited use in those instances where Sil 1 has failed to meet the service requirements.

### Future Evolution of US Compression Ignited Valves and Materials

The heavy-duty exhaust valve offers the greatest opportunity for future development. As multistage turbocharging and adiabatic approaches increase peak pressures and temperatures, current designs and materials will not meet the strength, wear resistance, and corrosion resistance requirements. More wear resistant, metallic, and ceramic coatings will find application, particularly in Diesel engines converted to natural gas and those powered with residual fuels. To meet the consequent high seating loads and adhesive wear resistance requirements, ceramic monolithic or composite components offer many advantages over their metallic counterparts [24]. These materials, as well as aluminides, offer much higher temperature capability (2000° to 2200°F versus 1700°F) making them extremely attractive for adiabatic Diesel engines.

### Summary

Exhaust valves have evolved in response to changing application needs: higher temperatures, more severe corrosives, higher imposed stresses. The carbon steel and cutlery grades used in early engines have been superseded by specially alloyed, precipitation hardened austenitic materials. One-piece valves have been replaced by two-piece, internally cooled designs with welded seat hardfacings.

Intake valves have also evolved with less significant changes in materials, although cost has played a more important role than for exhaust valves. Today's intake valve materials offer

many alternatives for different engine applications with better durability and at very low cost.

Yet, today's valves are not the ultimate in valve technology. Tomorrow's intake and exhaust valves will be lighter weight, have lower strategic alloy content, and provide longer durability, higher fuel efficiency, and better dynamic performance. Exhaust valves will retain high strength at very high operating temperatures. Costs will remain low. In conclusion, poppet valves will continue their long tradition of evolution to meet engine needs.

### Acknowledgments

The authors of this paper wish to acknowledge all those who provided input to this paper. Particular credit should be extended to L. Danis for his contribution in tracing the history of valve evolution. We also wish to thank D. Saxton, S. Schaefer, P. Crisenbery, and R. Martin for their effort in preparing this paper.

### References

- 1 Tunnecliffe, T. N., and Jenkins, L. F., "Why Valves Succeed," SAE Publication 249B, 1960.
- 2 Larson, J. M., and Jenkins, L. F., "The Development of a New Austenitic Stainless Steel Exhaust Valve Material," ASTM Special Technical Publication 612, 1979.
- 3 Narasimhan, S. L., and Larson, J. M., "Valve Gear Wear and Materials," SAE Publication 851497, 1985.
- 4 Umland, F., and Ritzkopf, M., *MTZ Magazine*, No. 36, 1975, pp. 191-195.
- 5 Caird, S. B., and Trela, D. M., "High Temperature Corrosion Test Method for Exhaust Valve Alloys," SAE Publication 810033, 1981.
- 6 Zinner, K., "Investigations Concerning Wear of Inlet Valve Seats in Diesel Engines," ASME Paper No. 63-OGP-1, 1963.
- 7 Jenkins, L. F., and Larson, J. M., "The Development of a New Austenitic Exhaust Valve Material," SAE Publication 780245, 1978.
- 8 Milligan, J., and Narasimhan, S., "A Powder Fed Plasma Transferred Arc Process for Hardfacing Internal Combustion Engine Valves," SAE Publication 800317, 1980.
- 9 Rogers, W. L., "Automobile," *Encyclopedia International*, Vol. 2, Grolier Inc., New York, 1969, pp. 243-257.
- 10 *Symposium on Internal Combustion Engine Valves*, reprinted technical articles, Thompson Products, 1956.
- 11 Aitchison, L., *Institute of Automobile Engineers Journal*, Vol. 14, 1919, p. 31.
- 12 Henshaw, P. B., "Valve Steels," *Journal of the Royal Aeronautical Society*, Vol. 31, 1927, pp. 187-217.
- 13 Heron, S. D., "Exhaust Valves and Guides for Aircraft Engines," *Journal of the Society of Automotive Engineers*, Vol. XV, No. 2, 1924, pp. 122-132.
- 14 Handforth, J. R., "Metallurgical Problems Arising From Internal Combustion Engine Valves," *Journal of the Iron and Steel Institute*, No. 74, 1932, pp. 93-157.
- 15 Hatfield, W., *Journal of the Iron and Steel Institute*, No. 1, 1928, p. 573.
- 16 "Exhaust Valve Steels," *Automobile Engineering*, Mar. 1962, pp. 93-97.
- 17 Cowley, W. E., Robinson, P. J., and Flock J., *Proceedings of the Institute of Metallurgical Engineers*, Vol. 179, No. 5, 1964-1965, pp. 145-180.
- 18 Pilling, N. B., and Merica, P. D., U.S. Patent No. 2048-163.
- 19 Jennings, P. A., U.S. Patent No. 2495731, 1950.
- 20 Armstrong, W. B., and Buuck, B., "Valve Gear Energy Consumption," SAE Paper 810787, 1981.
- 21 Betteridge, W., and Heslop, J., *The Nimonic Alloys*, Crane Russak and Co., Inc., New York, 1974.
- 22 Dulis, E., Kasak, A., and Stasko, W., "Low Nickel Valve Steel," U.S. Patent No. 3,681,058.
- 23 Narasimhan, S., Larson, J., and Whelan, E., "Wear Characterization of New Nickel Base Alloys for Internal Combustion Engine Valve Applications," *Wear Journal*, Vol. 74, 1982, p. 213.
- 24 Asnani, M., and Kuonen, F., "Ceramic Valve and Seat Insert Performance in a Diesel Engine," SAE Publication 850358, 1985.



# Caterpillar's 3600 PEEC Locomotive Governor (Programmable Electronic Engine Control)

**S. R. Burns**

Senior Design Engineer.

**R. G. Evans**

Project Engineer.

Caterpillar, Inc.,  
Peoria, IL

*Caterpillar Inc. recently introduced the 3600 Series medium speed, 280 kW/cylinder diesel engine to its product line. Offered in 6 and 8 cylinder inline and 12 and 16 cylinder vee configurations, the 3600 Series engines will be used for marine, electrical power generation, industrial, and locomotive applications. Caterpillar has also developed a microprocessor-based digital electronic control to meet the applications of these engines. The control system can be tailored for many applications; however, this system was developed primarily for locomotive use. The PEEC (Programmable Electronic Engine Control) locomotive speed and load control governor provides minimum fuel consumption and increases productivity of locomotives in both mainline and switch yard service. This paper describes the PEEC locomotive system as applicable to 3600 Series engines.*

## Introduction

For the past decade, Caterpillar has been developing a 3600 Series engine for addition to its engine product line and to compete in a world of increasing demand for low fuel consumption and good performance/productivity. This engine is well suited in size and power for locomotive applications (Fig. 1). In order to meet the goals of this engine the PEEC locomotive governor has been developed and is currently in use.

## Objectives

Early in the 3600 Series engine development program locomotive governing strategy was evaluated. Two types of governors were identified:

- Simple mechanical governor.
- Advanced electronic governor.

Caterpillar chose to pursue an advanced technology electronic governor for the prime development path for the 3600 engine. The reasons for this choice were better economy (fuel consumption) and greater performance for increased productivity, both of which tend to minimize overall operating costs for the railroad. Different commercially available electronic governors were evaluated for overall performance and reliability and were deemed unacceptable for meeting Caterpillar's performance criteria. Caterpillar decided to develop and market their own electronic control to satisfy all the requirements.

Contributed by the Internal Combustion Engine Division and presented at the Internal Combustion Engine Division Technical Conference, Oakbrook, Illinois, October 5-7, 1986. Manuscript received at ASME Headquarters July 9, 1986.

Serviceability, reliability, and cost were also considered when designing the PEEC locomotive system. The primary objectives were:

- Fuel consumption—lowest possible at all operating conditions.
- Performance—smooth transition of power when accelerating or decelerating.
- Cost—lower than conventional locomotive controls.

## 3600 ENGINE SPECIFICATIONS

COMBUSTION SYSTEM	4 STROKE
CYLINDER ARRANGEMENT	6-8 INLINE 12-16 VEE
BORE	280 mm
STROKE	300 mm
DISPLACEMENT	18.5 L/cyl
MAX RATED SPEED	1000 RPM
MAX BMEP	1880 kPa
LOW IDLE SPEED	350 RPM
POWER RANGE	1300-4500 KW
COMPRESSION RATIO	13/1

Fig. 1

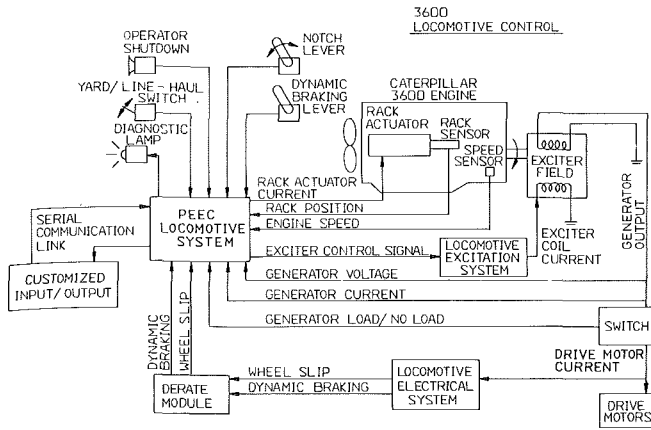


Fig. 2 Block diagram of 3600 locomotive control system

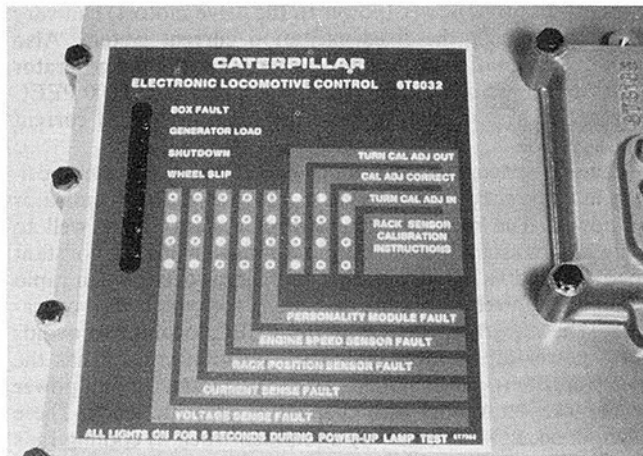


Fig. 3 Caterpillar PEEC locomotive diagnostic panel

- Digital electronics—good electrical noise immunity.
- Minimum field adjustments—only those necessary to interface with the existing locomotive controls.
- Serviceability—self diagnostics included.
- Reliability—equal to or better than existing locomotive controls.

### System Description

A block diagram of the 3600 PEEC locomotive system is shown (Fig. 2). The PEEC system is integrated with the locomotive system to provide total system power output control. The primary operator input to the system is the notch lever setting. The notch signal is encoded onto four digital input channels to the PEEC system by the locomotive's electrical system. The control can be configured to handle up to 16 notch settings, each of which corresponds to a particular output power level specified by the customer. The typical US application has eight power notch settings plus an idle setting. The control can also be configured with an analog power demand signal as used on many European applications. The ramp rate of the generator output power, under transient conditions between notches, is controlled by the yard/main switch which selects one of two customer defined rates. This expands the versatility of the locomotive by providing optimum power ramp rates for both yard operation and main line operation. For maximum productivity on a yard operation such as "kicking cars," the power ramp rate should be steep and consistent with the available traction on the locomotive. On main line operation, good controllability is required to minimize stress in the rolling stock draft gear and also to minimize the shock

imposed on the occupants. A much lower ramp rate is therefore required for line operation. The second most commonly used operator input to the system is the dynamic brake input. In the dynamic brake mode the traction motors are used as generators and their output is dissipated through resistor grids. In this mode the engine is used to provide power for the auxiliary equipment and also excitation power for the traction motor field windings. The dynamic brake input signal from the locomotive electrical system is interfaced with the PEEC system by an external derate module. The derate module also interfaces the wheel slip signal generated by the locomotive's electrical system. Both these signals are 0–50 V analog signals which are digitally encoded by the derate module to provide good electrical noise immunity.

Other functional inputs to the control system are:

- Rack position sensor signal.
- Magnetic speed sensor signal.
- Generator output current signal.
- Generator output voltage signal.
- Generator load/no load signal.

The rack position is measured at the rack actuator with a linear transducer. The analog signal is digitally encoded at the sensor for improved electrical noise immunity. The speed sensor is externally powered to provide measurable signal strength at low speeds during starting. The generator current and voltage signals are 0–50 V analog signals generated by the locomotive electrical system. They have a low source impedance and are fed directly into the PEEC system. The generator load/unload signal is generated by the locomotive electrical system and is fed directly into a PEEC digital input channel.

The main functional outputs from the control system are:

- Rack actuator drive signal.
- Generator exciter control signal.

The rack actuator drive signal is a 0–200 mA current signal that drives an electrohydraulic actuator. This output is used to control engine speed. The generator exciter control signal is a 0–50 V signal used by the locomotive generator excitation system to determine the main generator excitation current and is used to control the engine output power.

A cab-mounted warning lamp is provided to indicate that a fault has been detected by the PEEC diagnostic system. There is an LED display (Fig. 3) on the front face of the PEEC unit that provides a breakdown of the faults; these include:

- personality module
- engine speed sensor
- rack position sensor
- generator current signal
- generator voltage signal.

The 3600 PEEC locomotive system also has a serial communication link. More detailed, customer-defined diagnostic information can be provided through this serial communication link.

The main PEEC circuitry is contained in a sealed metal housing for environmental protection. A plug-in personality module (Fig. 4) is bolted to this housing. The circuitry for this personality module is also packaged in a metal housing and is sealed to the surface of the main PEEC housing. The personality module contains:

- Customized software
- Serial communication link information
- Low idle engine speed adjustment
- Operating parameters specific to the application.

The main PEEC unit memory contains all the basic software required to handle a standard locomotive installation. The

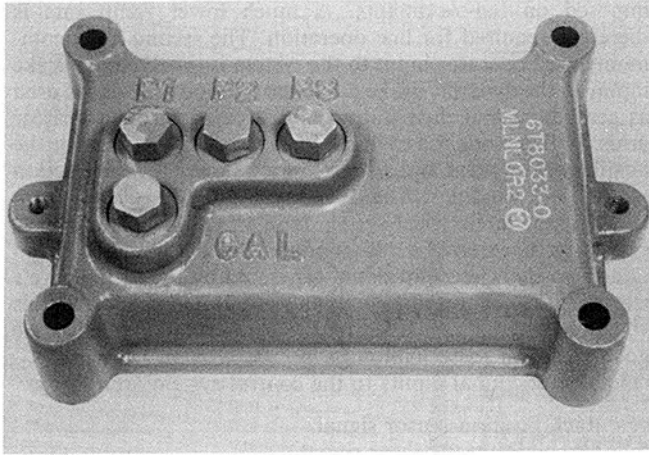


Fig. 4 Caterpillar PEEC locomotive personality module

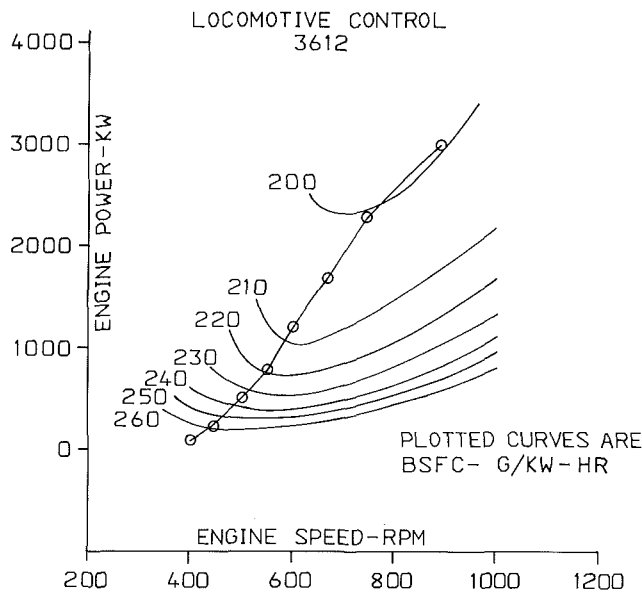


Fig. 5 3612 locomotive fuel consumption operating curves

personality module contains additional software for custom operating parameters. The serial communication link was included to expand the input/output capacity to meet customer requirements beyond a standard application. Another item on the personality module is an adjustment for the low idle engine speed. Access is gained to this by removing a sealed plug. The personality module also contains a list of operating parameters that are specific to a particular application. These are:

- Desired engine speed for each notch.
- Desired rack position for each notch.
- Desired traction motor power for each notch.
- Generator voltage limit for each notch.
- Generator current limit for each notch.
- Excitation control signal limit for each notch.
- Engine speed governing loop gain constants.
- Generator excitation control loop gain constants.
- Yard/main switch power ramp rates.
- Dynamic brake settings.

### Control Strategy

Each notch position corresponds to a preset power output which is specified by the customer. Since power output and

not speed is the critical parameter the engine load and speed at each notch setting can be set at the lowest fuel consumption condition. A 3612 fuel consumption map (Fig. 5) illustrates how the engine operating conditions can be tailored for optimum fuel consumption conditions. Also a certain amount of speed variation between notches is desirable to the operator and to provide sufficient power to drive all the auxiliary equipment.

The capability of programming the engine operating curve allows the engine operating conditions to be tailored to avoid other undesirable operating conditions related to items such as smoke, emissions, noise, exhaust temperature, cylinder pressure, or any parameter for which data are available.

Three types of load control strategies are available for locomotive controls:

- Fixed excitation current for each notch.
- Rack position control to indicate power for each notch.
- Constant kilowatt load control for each notch.

Generator output power (power to the drive motors) can vary significantly with the fixed excitation current system. Also with fixed excitation current the power output of the generator varies as a function of generator temperature. The 3600 PEEC locomotive system does not use the fixed excitation current strategy.

Control systems have been developed which use rack position in conjunction with engine speed as a feedback indicator of power. The rack position control systems work well to maintain constant power output of the engine at constant speed operation but power dips and surges occur when rapid changes in power output are demanded for switch yard operation. The integrated design of the PEEC locomotive avoids these power dips and surges. Rack position control has the disadvantage in lower notches of significantly varying power to the traction motors with changes in parasitic loads. These changes occur when auxiliary equipment such as cooling fans or air compressors is turned on and off. In lower notch settings the parasitic loads can nearly equal the desired traction power resulting in little or no power to the traction wheels.

The constant kilowatt load control system uses the actual generator voltage and current signals as input to assure that the drive motors receive the desired amount of power.

The 3600 PEEC locomotive system uses the constant kilowatt load control in lower notch lever settings. This method minimizes the variations in traction power due to variations in parasitic loading. The rack position control strategy is used in higher notch lever settings so that the maximum engine power available can be delivered to the traction motors when parasitic loads are low.

The speed and the load of the engine are controlled independently with the PEEC locomotive system. Engine speed control has priority over load control. Conventional rack position control systems tend to increase excitation current when the proper rack feedback signal is not achieved. This can lead to a problem that the engine is not able to support the load and could possibly cause the engine to stall. The PEEC locomotive system reduces the excitation current to the generator to maintain engine speed. Thus the engine is not lugged back or overloaded to an undesirable operating condition if the rack position sensor is faulty or not calibrated correctly, or if the generator current and/or voltage signals are faulty.

The PEEC locomotive system uses preset speed and load ramp rates when increasing or decreasing notch settings. The preset speed ramp rate provides a smooth and continuous rate of power change when changing notches because the power output is determined as a function of engine speed rather than notch position.

The PEEC locomotive system also ramps power down when a wheel slip condition occurs. The wheel slip signal is provided

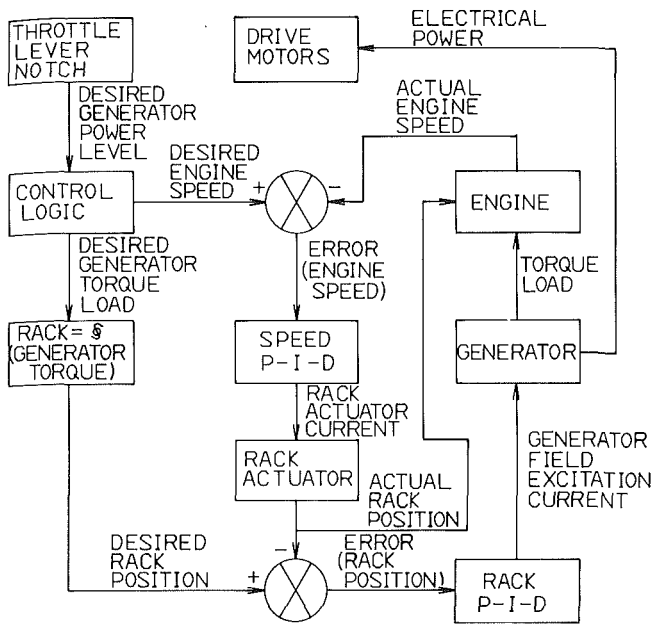


Fig. 6 Logistics diagram of 3600 PEEC locomotive system

by the locomotive system and is interfaced to the PEEC system through a derate module. The control ramps power down until the wheel slip condition clears. The power is then ramped to the desired level specified by the notch setting. Vehicle response is improved since engine speed is unchanged from the level selected through the notch lever setting. Only the power output is reduced when a wheel slip condition occurs.

A dynamic braking function is also provided by the locomotive system. Typically eight levels of dynamic braking are provided by the locomotive drive motors (same as the number of notch lever settings). When dynamic braking is required, the operator deactivates the notch lever and activates the dynamic braking lever to the level of braking desired. During dynamic braking the exciter control signal is a function of the dynamic brake notch setting rather than engine power. In low levels of dynamic braking the engine speed is normally at or near low idle speed. At higher levels of dynamic braking the engine speed is increased to provide more cooling air flow to the traction motors.

Generator voltage and current signals are provided to the governor by the locomotive system. These limits are required for both the rack position control and constant kilowatt load control systems to prevent generator or traction motor damage. Generator voltage and current limits can be specified for each notch lever setting. This capability allows the locomotive designer more flexibility to provide the desired type of voltage and current limiting functions. The voltage and current limiting functions can be specified based on one individual drive motor, the highest of all drive motors, the average of all drive motors, or the total output of all drive motors. The generator voltage and current limiting is a step function with notch lever setting and is not ramped as is the power output.

The PEEC locomotive system continuously performs internal diagnostics to insure that the control system is functioning properly and that the sensors are sending proper signals to the control. When faulty sensor signals are detected, the control system either substitutes a calculated value for the signal or switches to another mode of operation for which valid signals

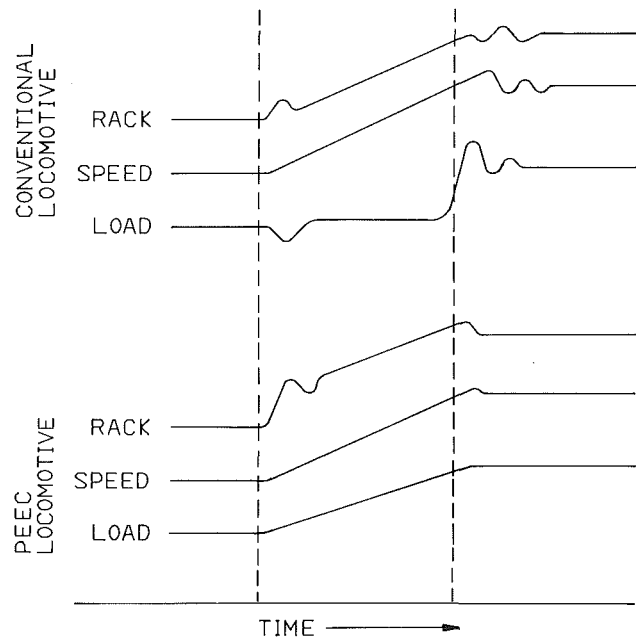


Fig. 7 Performance of PEEC versus conventional locomotive control

are provided. As an example, current to the rack actuator is used to infer rack position during engine operation when the rack position sensor is sending a valid signal. If an error in rack position occurs then the inferred value is used for the control.

### System Development/Modeling

Extensive computer simulation was utilized during the control development process to evaluate various control strategies and hardware designs. Numerous designs were simulated prior to actually implementing them into control hardware. Once a particular strategy was selected simulations guided the software engineers to establish control system constants and allowed minimized development time and dollars due to fewer iterations in the lab.

A dynamic model was used in the simulation of the control system. The model was developed using available engine and generator data. Sensor and actuator characteristics are also based on actual data.

The control system characteristics are expressed in terms of two interdependent Proportional Integrator Derivative (PID) equations (Fig. 6) which are the same PID's used for the actual control system logic. The first PID loop is an engine speed control loop. The control senses the notch lever position and converts it into a corresponding desired engine speed. A speed sensor is used to sense the actual engine speed and the current to the rack actuator is modulated to maintain a zero speed error. The second PID loop is a generator load control loop. The control converts the notch setting into a desired rack position. This control loop modulates the generator field excitation current to maintain rack position at the desired level.

A problem in the early development of the control on the engine was speed instability. It was found that rack actuator response was slower than that which had been simulated. When the actual actuator response was simulated, the same engine speed instability was demonstrated. The PID gains were tuned using the simulation. It was discovered that by increasing PID gains, stability was obtained. When these gains

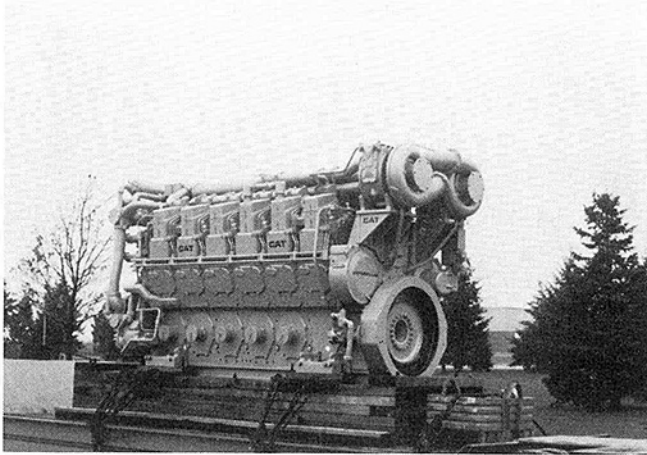


Fig. 8 Caterpillar 3612 locomotive engine



Fig. 9 Chicago-Northwestern 3612 repower of an EMD SD45 locomotive

were used with the actual control engine speed stability was demonstrated.

A traditional problem with locomotive controls that use rack position as an indicator of load is that power instability occurs when the notch lever is changed. This is due to transient errors that occur when engine torque is transmitted into engine acceleration/deceleration, thus resulting in an erroneous rack/load relationship within the control system. The modeling was used to define notch up and down ramp rates and transient rack position correction factors which allow smooth load transition between notch settings (Fig. 7).

The simulation was also used to develop an overload protection strategy for the PEEC system. When the engine is lugged too much due to a fault in the system that causes excessive generator load and the speed drops by more than 50 rpm below the desired speed, the control will back the load off until the correct speed is obtained.

### Installation/Applications

The first 3600 PEEC locomotive system was installed with a 3612 engine (Fig. 8) at Chicago-Northwestern. This engine in-

stallation is a repower of an EMD SD45. The engine is rated 3120 kW at 900 rpm. This engine installation has demonstrated reliable, economical service in this line haul application (Fig. 9).

Several other 3600 locomotive engines which will use the PEEC system have been sold.

The PEEC locomotive control system has also been used in installations with Caterpillar 3500 and D Series engines for lighter line haul and switch yard applications.

### Additional Applications/Potential

Marine applications can benefit greatly from the use of the PEEC locomotive system. Marine applications that use a variable pitch prop have a prop demand curve which is very similar to the locomotive notch lever curve. The electronic control can be programmed to control the prop pitch for minimum fuel consumption and to maintain maximum thrust conditions. High smoke conditions can also be avoided. The PEEC system can also be used for fixed prop marine applications to avoid undesirable operating conditions. The control can be programmed to maintain optimum power output and fuel consumption conditions to maintain lowest possible vessel operating costs. The control system can also interface with other control systems such as the prop pitch control, marine gear control, generator set control, energy management systems, dredge engine controls, and tandem engine and prop controls.

Electrical power generation (EPG) systems can also benefit from the use of the PEEC system. The control can be programmed for isochronous governing and the load acceptance rate can be tailored to give the best possible response while avoiding high smoke regions and to avoid excessive overshoot and undershoot conditions. The control can also compensate for seasonal changes so that year round constant power can be maintained.

### Summary

Caterpillar has designed and developed an electronic control governing system for use with the new 3600 engine series in locomotive applications. The PEEC locomotive system meets the design goals for performance, improved fuel economy, reliability, serviceability, and low cost. The system has standard self diagnostics. Reliability has been demonstrated in the field. Optional features and various control strategies are easily incorporated into the control system.

### References

- 1 Moncelle, M. E., and Earleson, W. E., "Caterpillar's Electronic Speed and Load Governor for Locomotive Applications" presented at the ASME Diesel and Gas Engine Division Technical Conference, Boulder, CO, Oct. 7-9, 1984.
- 2 Harrell, B. W., and Duchnowski, L. J., "The Role of Computer Simulations in the Development of Electronic Engine Controls," presented at the Joint International Computers in Engineering Conference and Exhibition, Chicago, IL, July 20-24, 1986.
- 3 Kieser, R. D., "Development of the Caterpillar 3600 Series Diesel Engines," presented at the ASME Internal Combustion Engine Division Technical Conference, West Middlesex, PA, Oct. 6-8, 1985.

# Partially Stabilized Zirconia Piston Bowl Reliability

D. L. Hartsock

Research Staff,  
Ford Motor Company,  
Dearborn, MI

The Weibull based "Simplified Structural Ceramic Design Technique" [1] was used to calculate the reliability of a partially stabilized zirconia (PSZ) piston bowl design. The details of the method and a set of sample calculations are presented. Test results of the piston bowl showed cracks in regions which had a high calculated probability of failure. In addition cracks developed in a region of high compressive/shear stress. Since Weibull reliability analysis only uses tensile stresses this area did not have a high calculated probability of failure. Several hypotheses are presented for the mode of failure in this region. The simplified technique was used to predict what the necessary material properties would have to be for successful PSZ insert of the design shown.

## Introduction

There is much interest in low heat rejection diesel engines for increased thermal efficiency, improved packaging, and reduced maintenance by eliminating the cooling system and possibly the lubrication system. One method being investigated to insulate the combustion chamber is to use a ceramic insulating material inserted into a metallic shell. The prime ceramic material choice for this inserted-type engine is partially stabilized zirconia because of its low thermal conductivity, high strength, and a thermal expansion close to that of metals for ease of attachment.

In order to design ceramic components successfully, such as piston bowl inserts, thermal, stress, and reliability analyses of the components must be completed. The thermal and stress analyses are the same as those which have been done for years for metal structures with the exception that more accurate results may be required. The use of Weibull theory to predict the reliability of a component is well established. A modified Weibull based method, the "Simplified Structural Ceramic Design Technique" [1], has been developed to aid in reliability calculations. This method was used to analyze a partially stabilized zirconia (PSZ) piston bowl design and to determine what the material properties would have to be to make this design work.

## Engine Configuration

The engine used in this study was a single-cylinder 80 mm bore  $\times$  80 mm stroke high-speed direct injection diesel engine (Fig. 1). The AVL-type high-speed, direct injection combustion system was used in the engine and consisted of a medium-swirl, helical intake port, a valve covered orifice multihole injector, and a re-entrant combustion bowl in the piston. The engine had no cooling water but did have two oil jets squirting

directly onto the bottom of the piston in addition to the normal oil flow in the sump and valve train. The engine was analyzed using finite element analysis by Analysis and Design Application Co. Ltd. (Adapco). For analysis the speed was set at 4500 rpm with an air-fuel ratio of 21.2, and a peak cylinder pressure of 8.28 MPa (1200 psi). The thermal boundary conditions were iterated with a cycle simulation model until good agreement was obtained. Details of this analysis are given in [2, 3].

In the three-piece piston model (Fig. 2), the skirt area has been detached from the top portion of the piston and is coupled at the wrist pin. The top portion of the piston has an insert 6.22 cm (2.45 in.) in diameter by 2.03 cm (0.8 in.) thick which is interference fit into the stainless steel base. The model incorporated compression only gap elements at the ceramic-to-metal interfaces to allow the parts to move in and out of

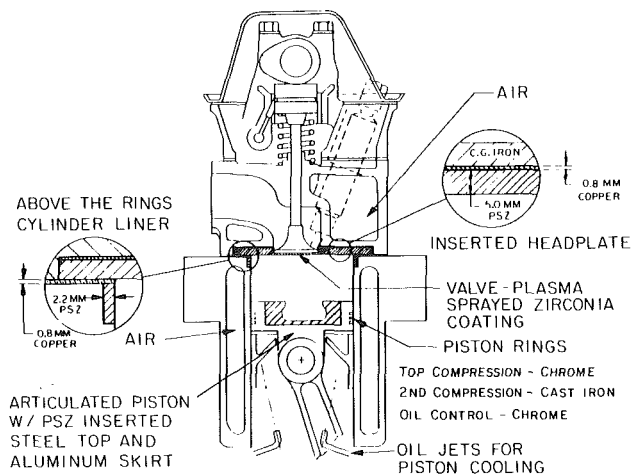


Fig. 1 Design of insulated single-cylinder engine with a PSZ piston bowl insert

Contributed by the Internal Combustion Engine Division and presented at the Internal Combustion Engine Division Technical Conference, Oakbrook, Illinois, October 5-7, 1986. Manuscript received at ASME Headquarters July 9, 1986.

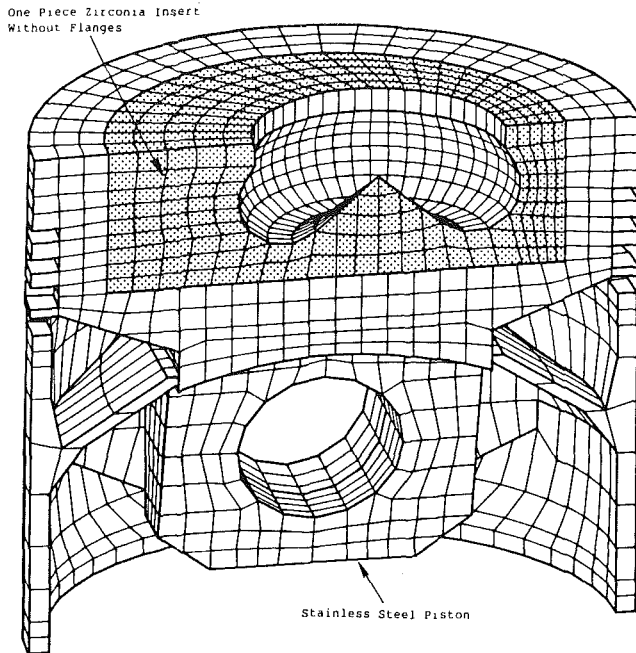


Fig. 2 Stainless steel piston with PSZ piston bowl insert

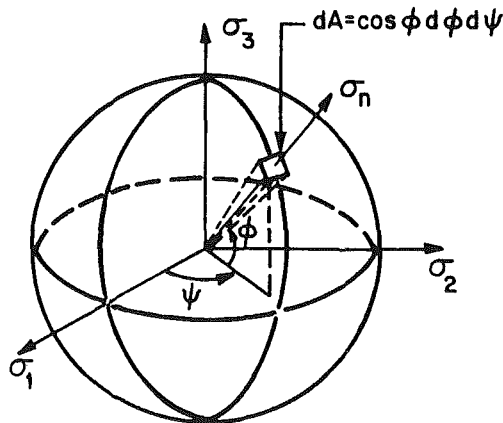


Fig. 3 Integration of normal stress around the unit radius sphere

contact depending on the thermal deformation of the components. Thus the final stress solution was iterated until convergence was obtained.

### Reliability

After determination of the temperatures and stresses, the

reliability is calculated to determine whether the component will survive. Because ceramics have small randomly distributed flaws, the strength of the material is somewhat variable. Because of this there is some finite probability that any local stress may exceed the local strength of the material causing failure. To account for this, ceramic design is based on probability theory. The method used to calculate the reliability of ceramics is Weibull's weakest link theory [4, 5]. This theory says that a part is like a chain. If any link in the chain fails then the chain has failed. Similarly if any small element in a ceramic component fails the crack will propagate through the ceramic and the component will fail. Weibull's probability of failure equation for the case of uniaxial tensile stress is

$$P_f = 1 - \exp \left[ - \int \left( \frac{\sigma - \sigma_u}{\sigma_0} \right)^m dV \right] \quad (1)$$

The reliability  $R$  is defined as

$$R = 1 - P_f \quad (2)$$

Weibull extended equation (1) to the multiaxial stress case by integrating the normal stress  $\sigma_n$  around the unit radius sphere (Fig. 3) [6]. By forcing the multiaxial equation to reduce to the uniaxial stress case, equation (1), when  $\sigma_2$  and  $\sigma_3$  are zero, the following equation was obtained:

$$\sigma_n = \cos^2 \phi [\sigma_1 \cos^2 \Psi + \sigma_2 \sin^2 \Psi] + \sigma_3 \sin^2 \phi$$

$$P_f = 1 - \exp \left[ - \int_V \left[ \frac{2m+1}{2\pi\sigma_0^m} \int_0^{2\pi} \int_0^{\pi/2} \sigma_n^m \cos \phi d\phi d\Psi \right] dV \right] \quad (3)$$

This is the base equation used for prediction of probability of failure and, when coupled with equation (2), the reliability.

By expressing the second and third principal stresses as ratios to the first principal stress,  $C$  and  $D$  respectively, equation (3) can be rewritten as shown below [7]:

$$P_f = 1 - \exp[-B]$$

$$B = \int_V k_0 \left( \frac{\sigma_1}{\sigma_0} \right)^m dV \quad (4)$$

$$k_0 = \frac{2m+1}{2\pi} \int_0^{2\pi} \int_0^{\pi/2} \{ \cos^2 \phi [\cos^2 \Psi + C \sin^2 \Psi] + D \sin^2 \phi \}^m \cos \phi d\phi d\Psi$$

where  $C = \sigma_2/\sigma_1$  and  $D = \sigma_3/\sigma_1$ .

Weibull chose to call  $B$  in the above equation the Risk of Rupture. The risk of rupture is nearly equal to the probability of failure for values less than 0.1. The value of  $k_0$  in the above equation is the effective volume multiplier and indicates the degree to which an element is in a state of multiaxial stress. Figure 4 shows  $k_0$  as a function of  $\sigma_2/\sigma_1$  for various values of the Weibull modulus.

### Nomenclature

$A$ = area	volume gives the effective volume	$\sigma_2$ = intermediate principal stress
$B$ = risk of rupture	$m$ = Weibull modulus	$\sigma_3$ = minimum principal stress
$C$ = ratio of the second principal stress to the maximum principal stress	MOR = modulus of rupture of test bars	$\sigma_n$ = normal stress to unit radius sphere
$D$ = ratio of the third principal stress to the maximum principal stress	MOR <sub>0</sub> = characteristic modulus of rupture = stress at which 63.2 percent of test bars will fail	$\sigma_0$ = unit volume characteristic strength
exp = exponential function	$P_f$ = probability of failure	$\sigma_u$ = minimum material strength, usually taken as zero
$k_0$ = a constant determined by the state of stress and the Weibull modulus which when multiplied by the	$V$ = volume	$\Psi$ = angle used in integration of unit radius sphere
	$\sigma$ = stress	$\phi$ = angle used in integration of unit radius sphere
	$\sigma_1$ = maximum principal stress	

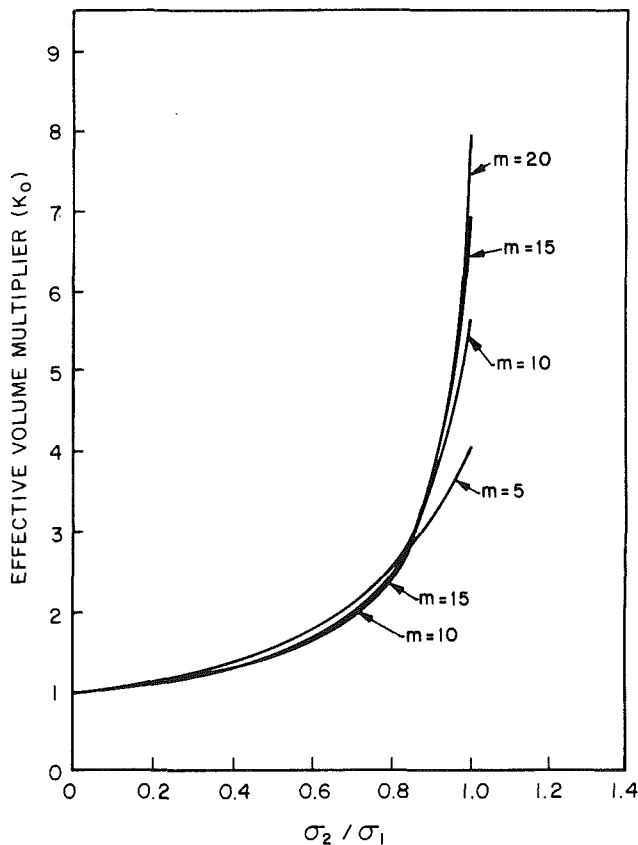


Fig. 4 Effective volume multiplier  $k_0$  versus the ratio of the second to the first principal stress

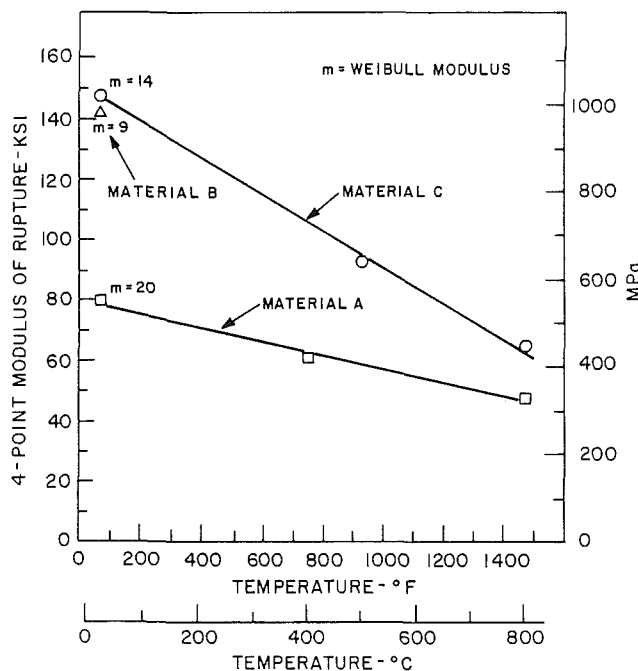


Fig. 5 Weibull material strength data for PSZ (load spans =  $1.905 \times 9.525$  cm, test bar size =  $0.3175 \times 0.635 \times 3.175$  cm)

Based on the above Weibull theory an approximate technique has been developed for calculating reliability of ceramic structures. This "Simplified Structural Ceramic Design Technique" [1] was used to calculate the reliability of the PSZ

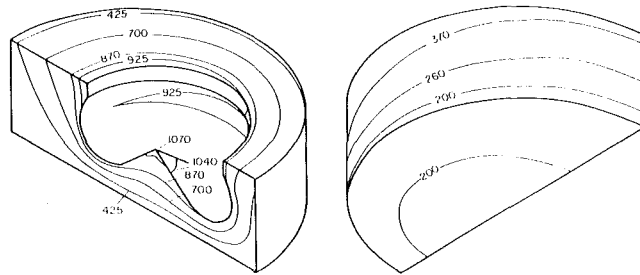


Fig. 6 Calculated temperatures ( $^{\circ}\text{C}$ ) for the PSZ piston bowl insert

piston bowl insert. This method approximates the more precise full Weibull analysis technique and has been shown to give good results. The steps in the analysis are as follows:

- 1 Estimate the maximum stresses in the part.
- 2 Estimate the volume of the component which is subjected to a tensile stress equal to or greater than 80 percent of the maximum tensile stress.
- 3 Estimate the range of temperatures through which the tensile region of the part will pass and the temperature of the part at the point of maximum stress.
- 4 From the material property data determine whether the material strength and/or Weibull modulus drops off significantly in the temperature range of Step 3. If so use the minimum values and go to Step 6. (For this case this procedure will tend to give very conservative reliabilities.)
- 5 From the material property data get the  $\text{MOR}_0$  and  $m$  value corresponding to the temperature at the maximum stress.
- 6 Determine the unit volume characteristic strength  $\sigma_0$  from the  $\text{MOR}$  data and the Weibull modulus.
- 7 Determine if the component is likely to be in a state of equal or nearly equal biaxial or triaxial tension. If so determine the appropriate effective volume multiplier  $k_0$  [4]. If the stress is nearly uniaxial tension then use  $k_0$  equal to 1.
- 8 Using the above information substitute into the following equations to estimate the reliability:

$$B = \left( k_0 \left( \frac{\sigma_1}{\sigma_0} \right)^m V \right)_{\text{volume 1}} + \left( k_0 \left( \frac{\sigma_1}{\sigma_0} \right)^m V \right)_{\text{volume 2} + \dots} \quad (5)$$

$$R = \exp[-B]$$

### Material Properties

The strength data for the three materials used for reliability analysis are shown in Fig. 5. Material A is a magnesia stabilized zirconia. Since only room temperature strength data were available for material B (yttria stabilized zirconia) and these were close to material C's (yttria stabilized zirconia), it was assumed that material B's high-temperature strength was the same as material C's. For later work on determining material requirements, material C is considered as the baseline material.

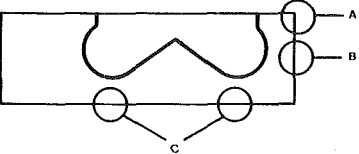
### FEA Results

The design of the piston bowl being analyzed is shown in Fig. 2. The thermal analysis results for this design (Fig. 6) show that there is more than a  $670^{\circ}\text{C}$  ( $1200^{\circ}\text{F}$ ) gradient from the bottom of the bowl to the bottom of the insert. Also there is a radial gradient from the bowl to the outer diameter of over  $500^{\circ}\text{C}$  ( $900^{\circ}\text{F}$ ).

The stress contours (Figs. 7 and 8) show that the tensile stress in the bottom of the bowl is 660 MPa (96 Ksi). The stress



**Table 1 Reliability of PSZ piston bowl insert using material C**



Location	Stress ( $\sigma_1$ ) (MPa)	Effective volume multiplier ( $k_0$ )	Temperature ( $T$ ) ( $^{\circ}$ C)	Volume ( $V$ ) (cu. cm)	Unit volume characteristic strength ( $\sigma_0$ ) (MPa cm $^{3/m}$ )	Weibull modulus (m)	Probability of failure ( $P_f$ )	Reliability ( $R$ )
A	410	6.6	425	0.392	493	14	0.18	0.82
B	550	6.6	370	0.084	525	14	0.65	0.35
C	660	6.6	260	0.062	594	14	0.83	0.17

Total component reliability = 0.05

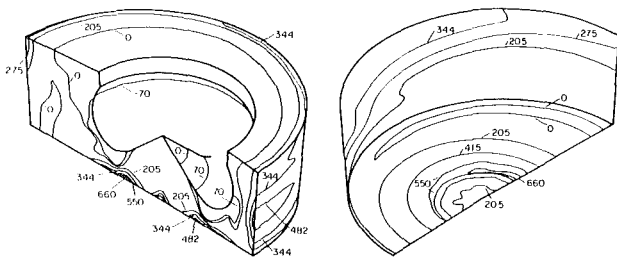


**Fig. 7** Calculated maximum principal tensile stresses ( $\sigma_1$ ) for the PSZ piston bowl insert (MPa)

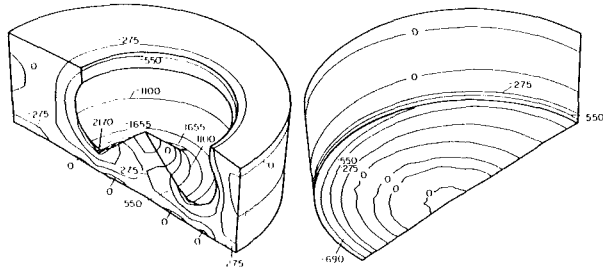


**Fig. 8** Calculated maximum principal compressive stresses  $\sigma_3$  for the PSZ piston bowl insert (MPa)

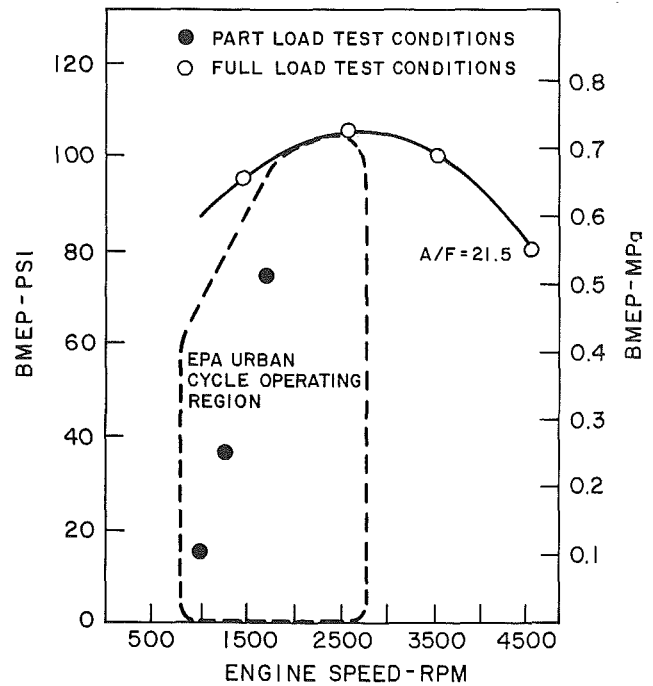


**Fig. 9** Test conditions used to evaluate the ceramic components shown on a BMEP versus RPM map of the engine

in the outer diameter region is 550 MPa (80 Ksi). Both of these stresses are primarily thermally induced and are slightly modified due to the interference fit.

**Reliability Results**

Using the “Simplified Structural Ceramic Design Technique,” the reliability was calculated for the three highly stressed sections giving the results shown in Table 1; see Appendix for details. All three sections had unacceptably high probabilities of failure, which produced an overall component reliability of only 0.05. The reliability of this design was analyzed for material A also, and as expected the probability of failure for this material was even higher than for material C, indicating almost certain failure.

**Test Results**

Parallel to the design work, a fabrication and test effort was undertaken [2]. This hardware evaluation would provide important feedback to the analyses. Although the reliability analysis indicated a high probability of failure, engine testing of the PSZ bowls proceeded since previous experience in-

dicated that excessive stress in PSZ produces cracks and not catastrophic failure. One component each from materials A and B was fabricated and tested for approximately 10 h with the severity of the conditions increasing with time. Tests were steady state at the speed and load points shown in Fig. 9, and movement between points was done gradually to minimize transient stresses. Both parts failed before completing one pass through the test sequence. The part of material A was undamaged at the 1700 rpm 0.517 MPa (75 psi) point but was cracked while attempting to run the full load test conditions at the 4500 rpm point. The insert of material B was cracked after running the 1700 rpm 0.517 MPa (75 psi) point. As expected both components developed cracks as shown in Fig. 10. Radial cracks developed at the top outer edge (location A, Table 1), circumferential cracks developed on the outer diameter (location B, Table 1), and a circular crack developed on the bottom following the thinnest cross section under the bowl (location C, Table 1). These cracks all occurred in locations predicted by the analysis and helped verify that the analysis was giving valid results.

There was also a set of cracks (Fig. 11) that was not predicted by the analysis. This set consisted of both radial and

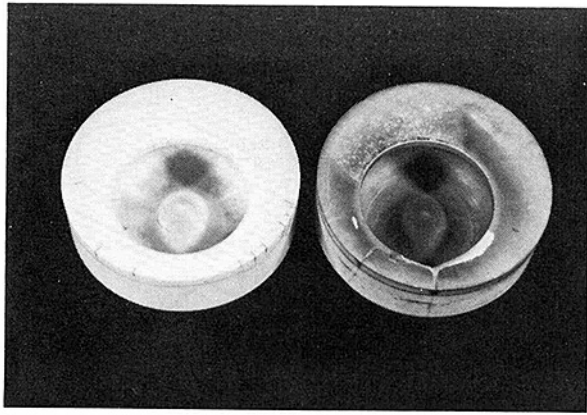


Fig. 10 PSZ piston bowls after 10 h of operation in the engine

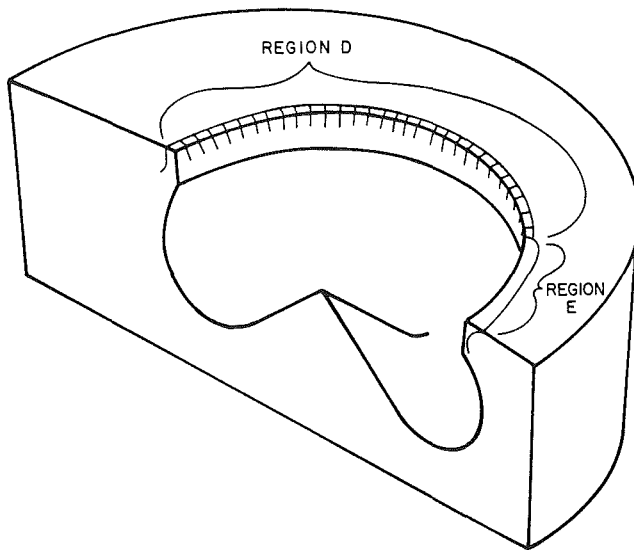


Fig. 11 Compressive stress cracks in the PSZ piston bowl insert

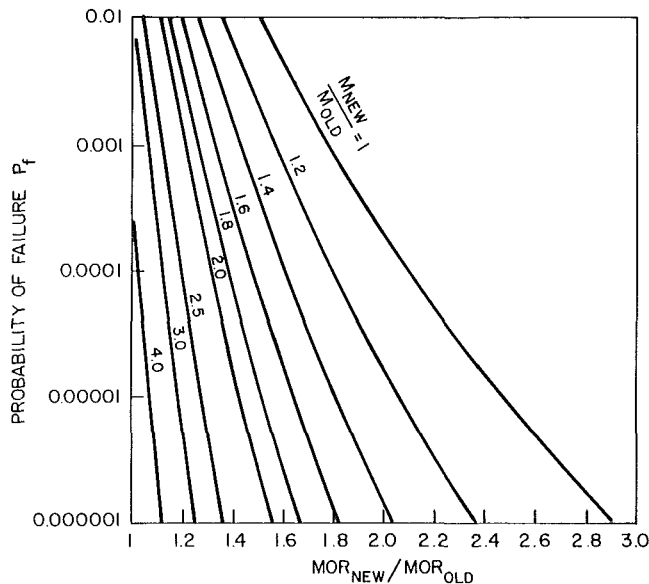


Fig. 12 Probability of failure of the PSZ piston bowl insert as a function of increases in the modulus of rupture and the Weibull modulus

circumferential cracks around the top of the bowl lip. The analysis shows this area to be in compression and at temperatures greater than 925°C (1700°F). Failure theory for ceramics assumes the material will fail in tension since ceramics are generally much stronger in compression than ten-

sion. Consequently, the Weibull reliability analysis does not show these areas as having a high probability of failure. PSZ does have some unusual characteristics for ceramics which may have caused these cracks. As shown by Lankford [8, 9], PSZ exhibits compressive yield at relatively low temperatures and low compressive stresses. One hypothesis for these “compressive” failures is that the hot section underwent some creep in compression, and then on cooldown the area that had exhibited creep went into tension and failed. This hypothesis is supported by Lankford’s observations and points out a potential problem in the use of PSZ. PSZ can also exhibit microstructural change and phase transformations at high temperature. The steady-state level of temperatures coupled with the transient surface temperature fluctuations may have been sufficient to cause these material changes inducing high localized stresses in the lip area. Either of these hypotheses could explain the cracks in region “D” of Fig. 11 where the cracks are perpendicular to the surface. Because of the high stress gradient, shear stress may be the cause of failure in region “E” where the cracks are at a 45-deg angle to the surface, plane of maximum shear stress. All of these possible modes of failure are aggravated by the cyclic nature of the temperature on the piston bowl. During each firing cycle the surface temperature of the PSZ may rise significantly, >100°C (180°F) [10], above the steady-state temperature shown. The relatively sharp edge of the top bowl lip will cause this region to be very responsive to the gas temperature fluctuations, causing the bowl lip temperature and stresses to be significantly higher than those shown in the curves. Thus there are several possible sources for the bowl lip cracks, but which of these problems caused the failure is still under investigation.

### Material Requirements

In order to determine the future likelihood of success with the full PSZ piston bowl like the one analyzed and tested, an analysis, again using the “Simplified Structural Ceramic Design Technique,” was conducted to see what the required material improvements would have to be to make this design successful. For high volume mass production of this part, a calculated reliability of 0.999999 was estimated to be required. It was assumed that the temperatures and stresses would remain the same and only the material strength and/or Weibull modulus would be improved. It was also assumed that the compressive-type failures could be eliminated by material modifications, but this is yet to be demonstrated.

The analysis was conducted by doing a series of calculations on percentage improvements on the baseline PSZ material (Fig. 5, material C). It assumes that the percentage improvement in material strength is constant regardless of temperature. Therefore, because of the dropoff in strength with temperature, the absolute value of a percentage increase at high temperatures is less than that at lower temperatures. The analysis is conducted by calculating the probability of failure for fixed increments in Weibull modulus and modulus of rupture. These values were then plotted as shown in Fig. 12. From this curve the incremental improvement in Weibull modulus and modulus of rupture for a fixed probability of failure were determined and used to generate Fig. 13. The results of the analyses (Fig. 13) show that if only the strength is increased, Weibull modulus equal to 14, then the required strength, to have a 0.999999 reliable part, is 2958 MPa (429 ksi), which is a 190 percent increase in the baseline data. If only the Weibull modulus is improved, MOR strength equal to 1020 MPa (148 ksi), then a Weibull modulus greater than 56 is required, which is more than a 300 percent improvement over the baseline. If strength and Weibull modulus are both improved by equal percentages, then the required strength is

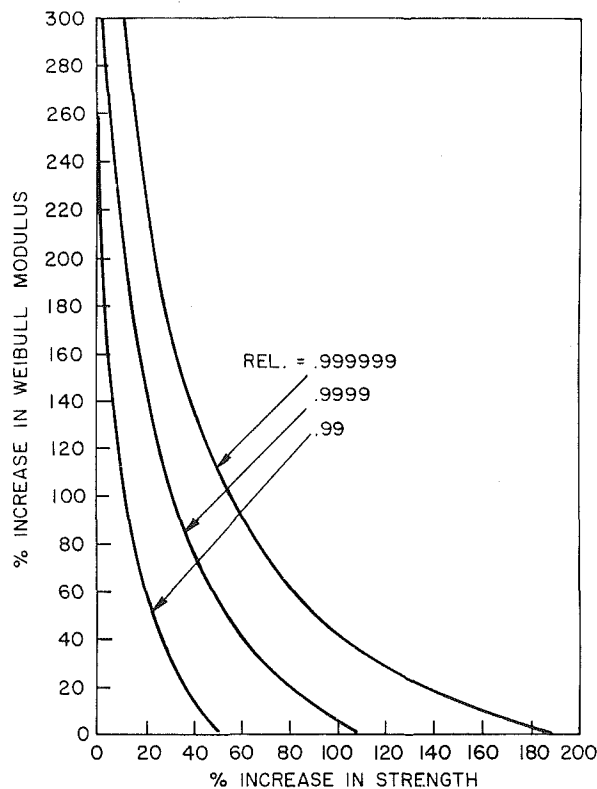


Fig. 13 Reliability of the PSZ piston bowl insert versus increases in Weibull modulus and MOR for PSZ

1754 MPa (254 ksi) (72 percent increase) and the required Weibull modulus is 24 (also 72 percent increase). The curve of required material strength for this case is shown in Fig. 14. From this analysis it is obvious that sufficient material improvements cannot be made in either the strength or Weibull modulus, if taken independently, to make the piston bowl successful. Also even if improvements were made in both, the amount of increase required (72 percent) in either property is still very large and therefore unlikely. This indicates that further design improvements must be made before the PSZ piston bowl concept can be successful. It is expected that improvements in both the design and the material will be necessary before a successful PSZ piston bowl will be produced.

### Conclusion

The "Simplified Structural Ceramic Design Technique" has been successfully demonstrated as a useful tool in the design of a ceramic piston bowl. This method was used for analytical prediction of reliability and to predict what material properties were necessary to make the proposed design work.

Design and test of a PSZ piston bowl have shown several problem areas. The thermally induced tensile stresses are sufficiently high that the current design will not work unless dramatic improvements in the material properties are made. Thermally induced compressive stresses in the PSZ piston bowl lip have caused failure in this region not predicted by the Weibull analysis. Although several hypotheses have been suggested for these bowl lip failures, none have yet been verified.

### Acknowledgments

The author acknowledges the many individuals and activities that contributed to the ceramic inserted piston design and evaluation effort. Special acknowledgments are given to

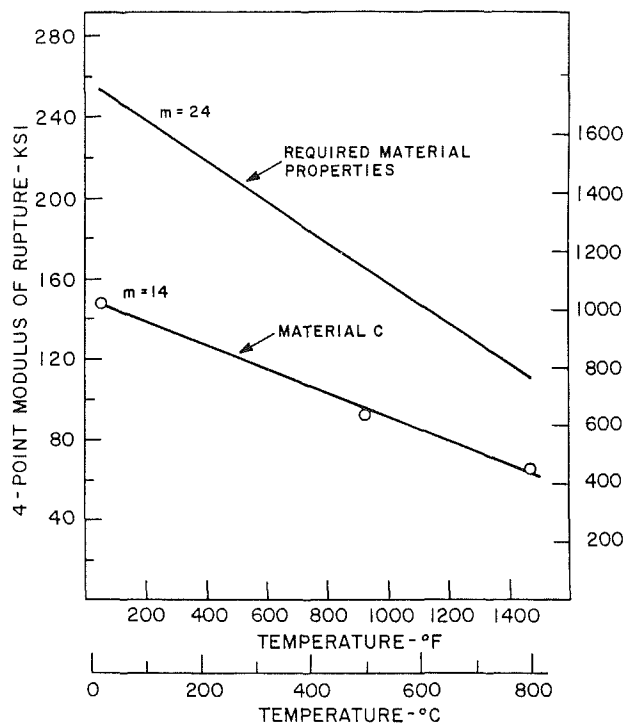


Fig. 14 Calculated Weibull material properties necessary to make the calculated reliability of the PSZ piston bowl insert equal to 0.999999

Mr. W. R. Wade who directed the diesel engine activity, Mr. P. H. Havstad who coordinated the insulated engine design and evaluation, Mr. E. J. Ounsted who assisted in the design of experimental engines, Mr. I. J. Garwin who conducted the engine evaluation, and Messrs. G. C. DeBell, R. L. Allor, D. J. Cassidy, and S. A. Zyck who provided the guidance on ceramic material technology, fabrication, and furnished the machined ceramic components. The excellent assistance provided by Mr. P. S. MacDonald of the Analysis and Design Application Co. Ltd. (Adapco) in conducting the finite element analyses is also acknowledged.

### References

- Hartscock, D. L., "A Simplified Structural Ceramic Design Technique," ASME Paper No. 85-GT-100, 1985.
- Havstad, P. H., Garwin, I. J., and Wade, W. R., "A Ceramic Insert Uncooled Diesel Engine," SAE Paper No. 860447, 1986.
- Wade, W. R., Havstad, P. H., Ounsted, E. J., Trinker, F. H., and Garwin, I. J., "Fuel Economy Opportunities With an Uncooled D. I. Diesel Engine," SAE Paper No. 841286, IMechE Paper No. C432/84, 1984.
- Weibull, W., "A Statistical Theory of the Strength of Materials," *Ing. Ventenstape Akad.*, No. 151, 1939, pp. 1-45.
- Paluszny, A., and Wu, W., "Probabilistic Aspects of Designing With Ceramics," ASME JOURNAL OF ENGINEERING FOR POWER, Vol. 99, No. 4, 1977, pp. 617-730.
- Vardar, O., and Finnic, I., "An Analysis of the Brazilian Disk Fracture Test Using the Weibull Probabilistic Treatment of Brittle Strength," *International Journal of Fracture*, Vol. 11, No. 3, 1975.
- Dukes, W. H., "Handbook of Brittle Material Design Technology," NTIS, AD-719-712, Feb. 1971, pp. 16-24.
- Lankford, J., Jr., "Compressive Strength and Damage Mechanisms in Partially Stabilized Zirconia," Interim Technical Report, 1 Aug. 1982-31 Dec. 1983, ONR Contract No. N00014-75-C0668, Dec. 1983.
- Lankford, J., Jr., "Characterization of Mechanical Damage Mechanisms in Ceramic Composite Materials," Interim Report, 24 May 1984-23 May 1985, ONR Contract No. N00014-84-C-0213, June 1985.
- Morel, T., Keribar, R., and Blumberg, P. N., "Cyclical Thermal Phenomena in Engine Combustion Chamber Surfaces," SAE Paper No. 850360, 1985.

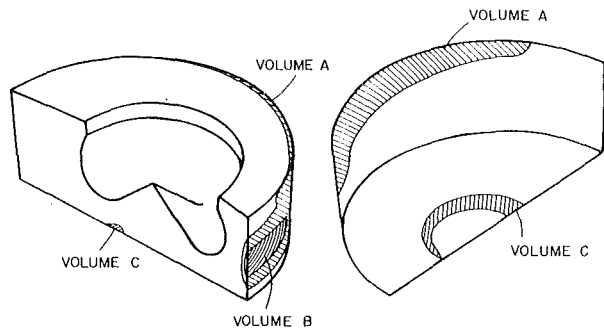


Fig. A1 Location of high stressed volumes used in the reliability calculations

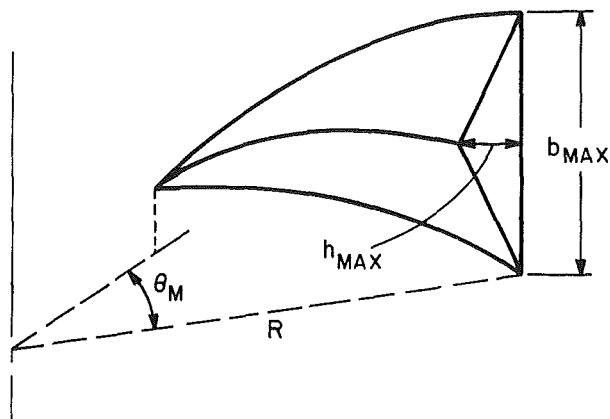


Fig. A2 Decreasing triangular prism section of high stress in region B

## APPENDIX

The reliability of the piston bowl was calculated using equation (5), and the eight steps preceding it.

*Step 1.* The maximum tensile stresses in the part were determined using finite element analysis and are given in Fig. 7.

*Step 2.* From this analysis three regions, A, B, and C in Table 1, were chosen for inclusion in the reliability calculations. The locations of the three regions are shown in Fig. A1. Region B will be used as an example. Eighty percent of the

peak stress (550 MPa) in region B is 440 MPa, so the volume of material in region B at a stress level greater than 440 MPa is included in the analysis. This volume is approximated by a decreasing triangular section moving around the circumference of the insert (Fig. A2).

The volume of this section is approximated by the following equation (note this equation gives only half the volume and thus must be multiplied by two to account for symmetry):

$$V = (1/6) R \theta_m h_{\max} b_{\max}$$

The volume for region B is 0.084 cm<sup>3</sup>. The volumes of sections A and C would be calculated in a similar manner, and are given in Table 1, column 5.

*Step 3.* The maximum temperatures for the three regions are determined from Fig. 6. For region B the maximum temperature is 370°C.

*Step 4.* The material properties of PSZ change significantly with temperature (Fig. 5), so the properties corresponding to the maximum temperature in each region will be used for the analysis.

*Step 5.* From Fig. 5 for a temperature of 370°C the modulus of rupture is 750 MPa and the Weibull modulus is 14.

*Step 6.* The unit volume characteristic strength is calculated from the modulus of rupture and Weibull modulus from the following equation for test bars in four-point bending:

$$\sigma_0 = \text{MOR}_0 (V_{\text{eff}})^{1/m} \text{ where } V_{\text{eff}} = \frac{bh}{2} \left( \frac{L_1 + mL_2}{(m+1)^2} \right)$$

In this case  $b$  and  $h$  are the test bar cross-sectional dimensions of 0.635 cm and 0.3175 cm. The load spans  $L_1$  and  $L_2$  are 1.905 cm and 0.9525 cm, respectively. From this the unit volume characteristic strength  $\sigma_0$  for material C at 370°C is 525 MPa cm<sup>3/m</sup>.

*Step 7.* Because the stresses induced in region B are primarily caused by a thermal gradient, the stresses will be nearly equal in the axial and tangential directions. Thus the condition of equal biaxial stresses will be used in the reliability calculation ( $\sigma_2/\sigma_1 = 1$ ). From Fig. 4 the  $K_0$  factor is interpolated to be 6.6 for a Weibull modulus of 14.

*Step 8.* We have now determined values for  $K_0$ ,  $\sigma_1$ ,  $\sigma_0$ ,  $V$ , and  $m$  for region B. After determining these values for regions A and C in a similar manner, the risk of rupture B in equation (5) could be calculated which would then give the reliability  $R$ .

# New Cement-Based Materials for Engine Construction

M. Love

Ricardo Consulting Engineers,  
Bridge Works,  
Shoreham by Sea, West Sussex, England

*A study of new and unconventional materials for use in engine construction highlighted several interesting developments. One which stood out as providing useful physical properties at low cost was the cement-based material known as NIMS. A design study for a cylinder block molded from this material was undertaken and a novel construction method devised. In order to gain practical experience with the material, a valve cover for a four-cylinder gasoline engine has been designed and manufactured. The cover is being developed on an engine in a test vehicle and shows potential for noise reduction with little or no increase in cost or weight.*

## 1 Introduction

The increase in specific engine power of naturally aspirated automotive engines in volume production over the last 20 yr has been substantial. In Fig. 1 it can be seen that specific power output has been improving at an increasing rate. This is partly due to increased efficiency and partly due to reduced engine weight. Figure 2 shows the rate of decrease of engine weight per unit displacement for the same sample of engines and it is interesting to note that this change has been considerably less significant. These weight reductions are partly due to reductions in component wall thickness facilitated by more precise analytical techniques; apart from the increased use of aluminum, there have not been any major advances in the use of new materials.

Ricardo has carried out a study of new or unconventional materials for engine construction. This covered the work being undertaken on fiber-reinforced aluminum both in random chopped fiber form for piston reinforcement and as continuous aligned bundles for connecting rods. Another area of interest was the development of the high-performance polymers reinforced with carbon fibers which have been used for many engine components on an experimental level.

The benefits of using these materials for engine components, however, have to be weighed against significant increases in cost. One material that stood out as being an exception to this was the Imperial Chemical Industries (ICI) product NIMS (New Inorganic Materials). This fundamentally cheap material, which has not previously been applied to engine components, offers noise reduction and weight advantages in some applications with little or no cost penalty.

A further research project has now been undertaken aimed at applying this material to specific engine components.

## 2 NIMS (New Inorganic Materials)

**2.1 General Description.** ICI have carried out a program of research aimed at the development of a new group of materials based on naturally occurring chemicals which would

compete with polymers, metals, and ceramics in engineering applications. The cement-based materials known as NIMS, which have a unique set of properties (summarized in Table 1), are the result of this research.

The strength of a brittle material such as cement is influenced mainly by the size of the largest flaws within it and not by the overall porosity. It has been shown that if these flaws are removed the tensile strength of the material can increase by an order of magnitude. The research carried out by ICI was based on the principle of preventing the formation of flaws in cement by adding a water-soluble polymer as a rheological aid

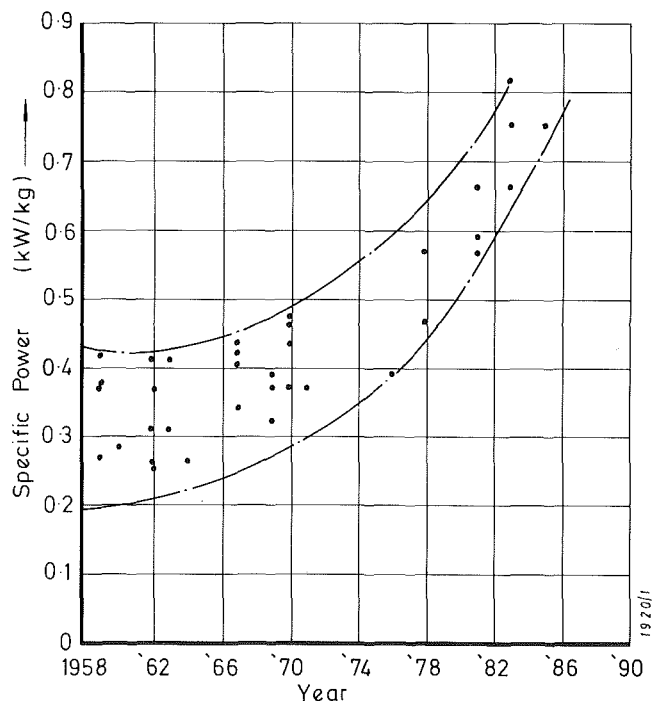


Fig. 1 Trends in specific power for naturally aspirated four-cylinder gasoline engines

Contributed by the Internal Combustion Engine Division and presented at the Internal Combustion Engine Division Technical Conference, Oakbrook, Illinois, October 5-7, 1986. Manuscript received at ASME Headquarters July 9, 1986.

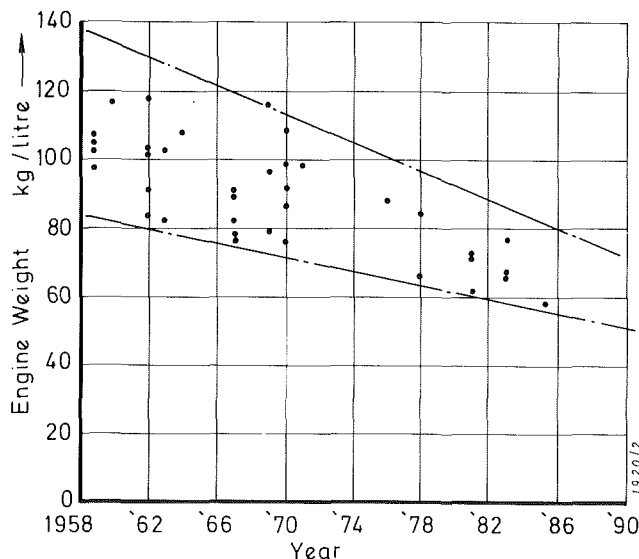


Fig. 2 Trends in weight per unit displacement for naturally aspirated four-cylinder gasoline engines

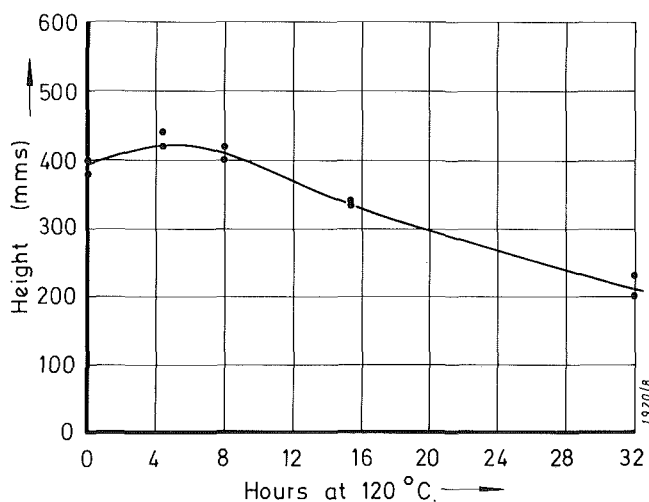


Fig. 3 Results of impact tests on NIMS samples heated to 120°C

during the mixing stage. The polymer did not originally contribute significantly to the strength of the material after curing but following further research, different material combinations were found in which the polymer acted both as a rheological aid and as a functional component in the material structure. The earlier materials of this type were called Macro-Defect-Free cements, but they have more recently become known as New Inorganic Materials.

**2.2 Material Properties.** The important effects of the addition of the polymer to the cement are dramatically to increase its toughness and tensile strength. The strain to failure of brittle materials such as ceramics is almost invariably less than 0.2 percent and often much lower, whereas the figure for NIMS is 0.4 percent. This degree of toughness allows the material to be readily machined by most conventional processes such as turning, milling, drilling, and sawing. NIMS also have a significantly higher impact toughness than other ceramics and this can be further improved by the addition of one or more layers of nylon mesh reinforcement to the material.

Another important property of NIMS is the high level of internal damping which is similar to that of some plastics,

Table 1 Properties of NIMS (from Alford and Birchall, 1985)

Density	2500	kgm <sup>-3</sup>
Tensile strength	100	MPa
Compressive strength	300	MPa
Unnotched charpy (including 15 percent volume nylon fiber)	120	kJm <sup>-2</sup>
Thermal expansion	$9.7 \times 10^{-6}$	/K
Young's Modulus	50	GPa

although NIMS has a significantly higher Young's Modulus. It also has the advantage of being based on fundamentally cheap materials. The raw material cost is around £400/tonne which is less than 20 percent of the cost of glass-reinforced nylon.

NIMS is processed by thoroughly mixing accurately measured proportions of cement, polymer, and water. This produces a dough which can either be rolled into a sheet and compression molded, injection molded, or extruded. The molding operation takes place under pressure at about 80°C and takes several minutes. The molding is then cured after removal from the mold and 2-3 percent shrinkage occurs during this operation. The curing is accelerated by heating and would take typically 16 h at 80°C.

Due to the contribution made by the polymer toward the overall strength of the material, its physical properties are affected by temperature. The flexural strength falls reversibly by up to 50 percent at 100°C compared to the figure at room temperature. At temperatures higher than about 110°C there is an irreversible deterioration in strength due to degradation of the polymer. A reduction of up to 50 percent in the flexural strength can occur after 3 days at 120°C.

Further tests on the resistance of the material to impact after heating have been carried out at Ricardo.

A steel ball weighing 66 g was dropped onto simply supported flat NIMS plates at room temperature (plate dimensions were 98 mm × 50 mm × 2.5 mm thick), from increasing heights until fracture occurred. The plates had been reinforced with one internal layer of nylon mesh and they were heated to 120°C for varying lengths of time. Figure 3 shows the results and it can be seen that there is a progressive reduction in impact strength after heating until a 40 percent reduction occurs after about 30 h.

Similar tests were also carried out in order to determine whether the position of the nylon mesh reinforcement within the material would affect the impact strength. Sample plates were tested with a single layer of 1-mm nylon mesh reinforcement incorporated either in the top surface or the bottom surface and these were compared to unreinforced plates. It was found that at room temperature compared to an unreinforced plate, top surface reinforcement gave a 30 percent improvement in impact strength and bottom surface reinforcement gave a 40 percent reduction. It is believed that this result is due to the effective introduction of stress raisers in the tensile strength, this being more significant than the toughening effect of the nylon.

NIMS has a tendency to absorb water although at a considerably slower rate than for the plastics. A 3-mm-thick NIMS plate, for example, would take 40 days to reach saturation (4 percent by weight) after immersion in water. This can cause a deterioration in the properties of the material and about 1 percent linear expansion but the material recovers completely on drying. NIMS is, however, impervious to organic solvents and lubricants.

### 3 Potential Applications of NIMS in Engine Manufacture

In order to consider reducing the weight of an engine com-

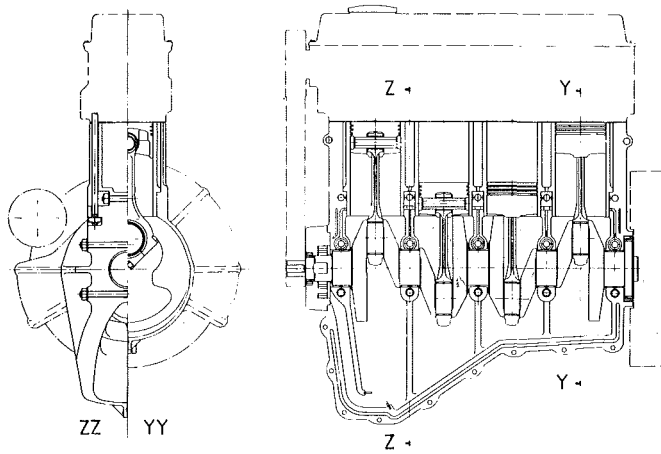


Fig. 4 Arrangement of NIMS cylinder block assembly

ponent by using a different material it is necessary to establish whether it is a strength or stiffness-limited application. It is often the case that one of these is dominant, such as for valve train components which are generally stiffness limited. It is important to establish the types of loading to which the component is subjected so that materials of different specific strength or stiffness may be compared for the application.

For a stiffness-limited component in pure axial loading, the mass of material for equal stiffness is proportional to  $\rho/E$  (where  $E$  = Young's Modulus and  $\rho$  = density). If this quantity is calculated for different materials it can be used as a basis for comparison for applications where axial stiffness is dominant.

Analysis of this type has shown that NIMS does not give any potential for weight saving over metals for axial loading applications. However, for applications which are predominantly in bending, NIMS could make weight savings, for both stiffness and strength-limited design, over ferrous metals but not over aluminum. However, when an allowance is made for a 50 percent reduction in tensile strength of NIMS after high-temperature use this analysis indicates that for equal bending strength the weight of a NIMS molding would be approximately 27 percent greater than a steel component. In many applications however, where a NIMS molding is being compared with a steel pressing, for example, the molding has the advantage of the inclusion of different material thicknesses, webs, fillet radii, etc., which can give an overall weight reduction for equal strength.

These considerations lead to the conclusion that NIMS has some potential for cylinder block manufacture. Considerable noise reduction could be made over a cast iron block possibly for similar weight and cost.

Other components which are worthy of investigation for production in NIMS are the inlet manifold and the engine covers. Here the high internal damping of the material would be particularly beneficial from the point of view of noise emission.

It was decided to carry out a design study on a NIMS cylinder block in order to gain experience in design in this material. The type of unit considered for this design exercise is a four-cylinder in-line gasoline engine of 1300 cc capacity. It was decided that the small car market would be most appropriate for a material aimed at low cost and reduced noise emission.

#### 4 NIMS Cylinder Block Design Study

The most likely method of production of a NIMS cylinder block would be to produce two compression moldings which could be bolted together. Injection molding is also possible but a wetter mix is required, which is likely to produce inferior material properties in the finished component. Since the

NIMS dough cannot be poured, the molding would be produced from a rolled or extruded sheet placed in the mold cavity. Each molding should therefore be designed to have a minimum draw depth and a relatively uniform distribution of material across the area of the mold. These requirements are best met by a vertical split line in the plane of the cylinder centerlines and a block design of this type is shown in Fig. 4.

The two halves of the cylinder block are held together with three sets of horizontal bolts running through the bulkheads and a ring of smaller bolts around the sealing flange. The top set of bolts runs through the location area for the bottom-located wet liners and the other two sets form the main bearing bolts. The lower bolts also house ring dowels for accurate block location.

The shear and tensile strength of NIMS are not adequate to allow cylinder head bolts to be tapped directly into the cylinder block. It is therefore preferable to secure the cylinder head bolts by means of nuts which bear on a flange in the cylinder block. The cylinder head bolts pass below the level of the liner seat so that the load is taken by NIMS predominantly in compression.

The stiffness of the cylinder block has been improved by connecting the bulkheads through to the bottom of the sump. This is possible due to the vertical split line which allows the sump to be included in the molding. A useful side effect of this would be to reduce oil surge in the sump.

Another effect of the vertical split line is that oilways can be molded into the joint face including the suction pipe from the sump. With this arrangement a crescent type oil pump runs directly off the crankshaft. It is intended that the body of the pump would also be a NIMS molding.

While a detailed stress analysis of the NIMS cylinder block design has not been carried out it is estimated that the weight and material cost would lie between those of equivalent cast iron and aluminum components. The most significant anticipated difference would be the airborne noise emission which, due to the stiff structure and highly damped material, should be dramatically lower in the case of the NIMS block.

### 5 NIMS Valve Cover

**5.1 Introduction.** The cylinder block design needed to be supported by more relevant practical experience before such a molding could be produced. A complete design and prototype production program was therefore instigated, aimed at producing a NIMS valve cover to be fitted to a Ricardo research engine. The unit chosen was a four-cylinder in-line 1500-cc gasoline engine which is installed in a Volkswagen Jetta.

**5.2 Design Considerations.** The functions of the valve cover are:

- 1 provide a seal to prevent oil from escaping;
- 2 protect the valve gear;
- 3 reduce noise emission from the valve gear;
- 4 house other components such as filler cap and breather.

The main loadings to which the cover is subjected are due to light impacts, vibration of the engine, fixing bolt loads, and differential thermal expansion.

The strength of NIMS has been shown to deteriorate significantly with prolonged exposure to temperatures in excess of about 110°C. The requirements of the design will therefore be influenced by the temperatures which will be experienced in service.

A test was carried out on a chassis dynamometer using the same test vehicle to which the NIMS cover would be fitted. Thermocouples were attached to the standard steel cover and insulated from the surrounding air. The vehicle was run with varying speed load conditions and cooling air at 25°C was blown through the radiator using an external fan. Finally the

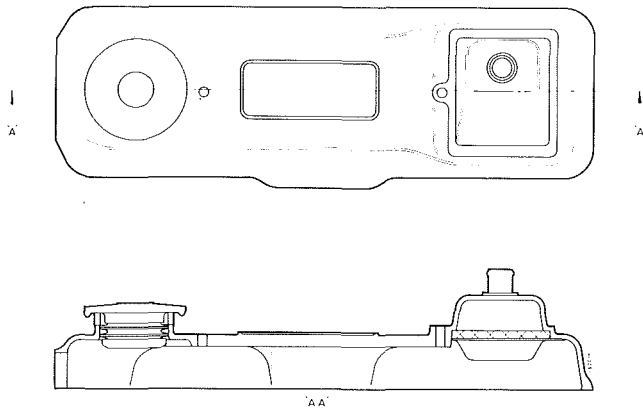


Fig. 5 First generation valve cover design

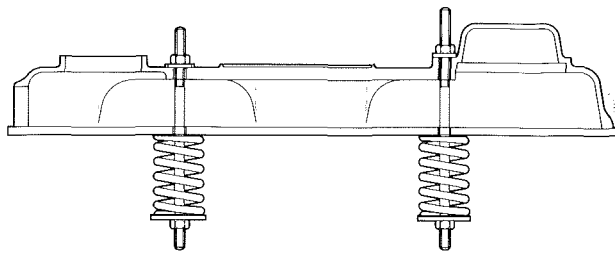


Fig. 6 Method of testing the load to failure for the first generation valve cover

engine was stopped and the external fan switched off so that the effect of heat soak could be measured. However, the internal thermostatically controlled fan was left connected.

Under running conditions the temperature of the cover reached a maximum of 91°C and after the engine and external fan were switched off the temperature rose to 104°C for about 1 min.

**5.3 First Generation Cover Design.** It was decided at an early stage that lack of experience with the material would necessitate the production of a preliminary molding so that test work could be carried out. A definitive design would then be produced in light of the results obtained.

The existing head was fitted with a pressed steel cover containing a breather and filter assembly and a bayonet-type oil filler cap. Although this cover was mounted using eight studs on an external flange, the option of using studs positioned on the cover center line existed because they could be mounted on the camshaft bearing caps. This latter option was adopted for the first cover design because of the benefits of a more even sealing pressure along the flange. It was felt that the flange-bolted NIMS cover would not be sufficiently stiff to seal successfully in between the stud centers before causing excessive deflection at the stud. (Subsequent test results, however, have proved this assumption to be incorrect.)

The design is shown in Fig. 5 and the webs necessary to give sufficient stiffness and strength can be seen. A material thickness of 3 mm was specified, which gives a cover of similar weight to the standard pressed steel cover. A simple press-in oil filler cap was specified and the breather oil separator assembly was designed to be bonded to the inside of the cover. For this cover no attempt was made to mold the holes for the breather tube or the bolts, although this could be incorporated with the penalty of additional mold cost.

The mold was constructed from epoxy resin impregnated with aluminum spheres to improve the thermal conductivity. This form of construction is suitable for small production

quantities (fewer than 20 components) and is considerably cheaper to produce than a steel mold. It is possible, however, that slightly inferior material properties are obtained with this type of construction since it cannot tolerate such high molding pressures as a steel mold.

Nylon mesh reinforcement was incorporated in some of the moldings, either in the form of a single layer positioned at midthickness or layers incorporated at one or both surfaces of the NIMS.

**5.4 Results of First Generation Moldings.** The general appearance and finish of the moldings were of very high quality with the exception of those where reinforcement was incorporated in the surface. Some damage to sealing surfaces had, however, been caused where material flashes had been removed before the covers were cured.

A shrinkage allowance of 2.3 percent was incorporated in the mold manufacture and it was found that this produced some components that were within 1 mm of the correct length. There was, however, some variation in the finished size of the covers, which may be attributable to differences in molding and curing conditions.

The sealing flange was found to be warped by up to 1.5 mm initially, although extra care in removal of the cover from the mold later improved this feature by about 50 percent. Some distortion of the moldings had also occurred during the curing process, which tended to cause the top to sag and the sides to bow outward. This was again improved by supporting the moldings during curing.

The covers were tested for sealing ability and strength by bolting them to a 6-mm-thick flat steel plate. The bolts acted through springs of known rate to give a measure of the applied loads (see Fig. 6). With no gasket, the load to failure was 500 N on each bolt, which caused a single crack about 30 mm long to develop from one bolt boss on the underside of the cover.

Further tests with different gasket materials showed that effective sealing could not be achieved with cork or with dry silicone rubber. However, soft rubber could be made to seal with a load of 370 N per bolt. Liquid silicone rubber gasket could be made to seal with a load of 200 N per bolt provided that the cover was fitted while the sealant was wet. In this case the sealant also contributed to the holding force on the cover once it had set.

Impact tests were carried out by dropping a 66-g steel ball onto rigidly supported covers from known heights. It was found that unreinforced moldings were undamaged, if the ball was dropped from heights of up to 1.5 m. The cover with reinforcement on the top surface survived when the ball was dropped from 2.6 m and the center-reinforced cover was undamaged if the ball was dropped from heights of up to 1.8 m. The cover with reinforcement on the underside was damaged when the ball was dropped from 1.4 m and was therefore weaker than the unreinforced cover. This result is consistent with the tests, previously described, which were carried out using flat plates.

A cover with reinforcement incorporated in the top surface was fitted to the engine of a test vehicle. Acoustic intensity measurements were made with the standard pressed steel cover and compared to the NIMS molding. The results are shown in Fig. 7 for engine speeds of 16 rev/s and 38 rev/s. Reductions in sound power of between 5 and 7 dB over the frequency spectra were recorded, which represents a significant improvement.

The cover fitted to the research vehicle completed a total of 2000 miles of testing over a period of 6 weeks but after about 1500 mi some cracking started to occur. The cover had been loaded to about 30 percent of the load to failure measured on other test covers when it was fitted to the engine. However, the deterioration in tensile strength due to high-temperature use



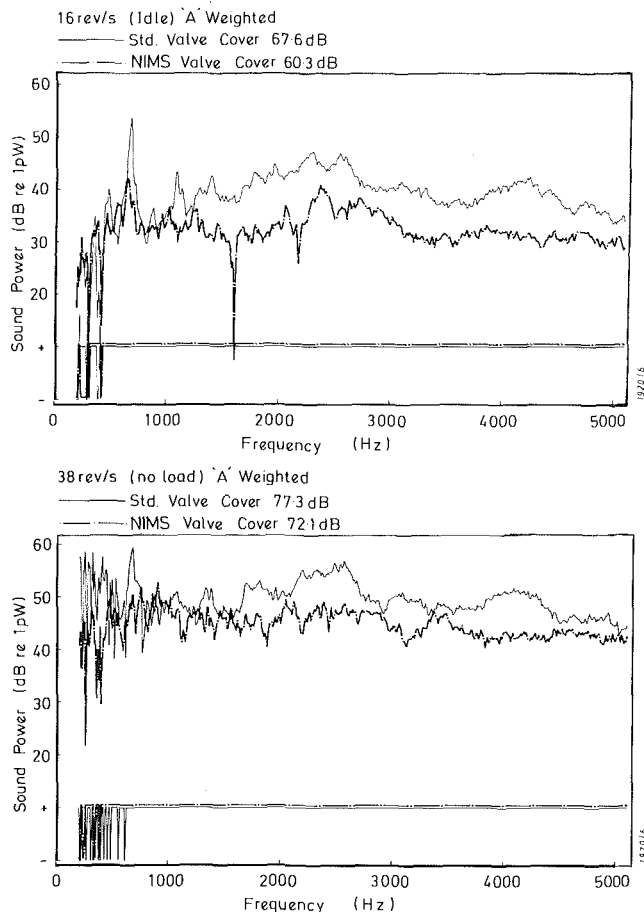


Fig. 7 Comparisons of the power of emitted sound from steel and NIMS valve covers at 16 rev/s and 38 rev/s

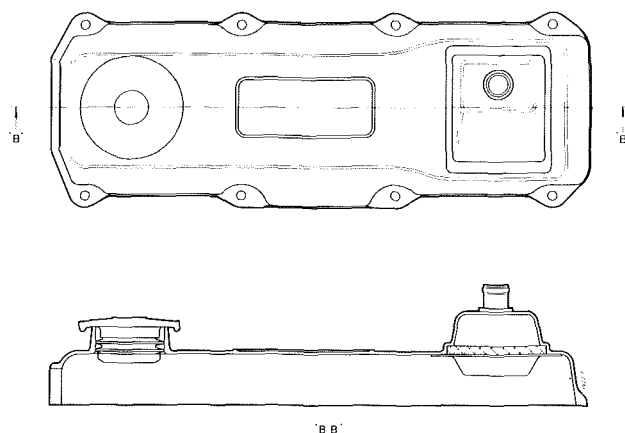


Fig. 8 Second generation valve cover design

could have been around 50 percent and additional stresses due to engine vibration and thermal expansion of the aluminum head would then have been enough to cause failure.

**5.5 Second Generation Cover Design.** The poor sealing performance and ultimate failure of the first cover moldings were attributed to the low sealing pressure achieved at the flange. Since the load was applied in an overhung position away from the sealing face it was limited by bending stresses in

the material. It was felt that much higher sealing pressures could be achieved by using flange bolts so that the stresses in the material would be predominantly compressive. Since the stiffness of the covers was much greater than had been expected, it was felt that the previous fears of poor sealing performance due to uneven pressure with flange bolting were unfounded.

The second generation cover design was produced, which uses the flange attachment with eight studs in the same positions as for the standard cover. Since less strength was required in the central section of the cover, the material thickness was reduced from 3 to 2.5 mm and the ribs were removed (see Fig. 8). The height of the oil filler cap sealing lip was also increased as some difficulty had been experienced with the first generation cover in locating the cap correctly.

The mold construction was similar to the first generation except that ejector pins were fitted. It was hoped that this would enable the molding to be removed without distortion of the sealing flange.

**5.6 Results of Second Generation Moldings.** The general quality of the moldings was good except that some cracking of the mold surface had occurred causing low ridges in the surface of the NIMS. The ejector pins had facilitated removal of the molding with less distortion and some of the cover flanges were flat to within 0.5 mm. The worst flange distortion measured was 1.5 mm.

The improved flatness and higher load capability due to the flange bolting arrangement were found to improve the sealing performance of these covers considerably. For this design a thin bead of silicone rubber sealant was adequate to produce an oil-tight seal.

A cover was successfully fitted to the engine using a setting silicone rubber sealant and a load of 200 N per stud. However, at the time of writing, durability testing has not been completed.

## 6 Conclusions

The ICI material NIMS has been identified as having potential for use in engine construction and a NIMS cylinder block design for a four-cylinder gasoline engine has been produced.

In order to gain practical experience with using the material, a valve cover for a similar engine has been designed and manufactured. This has been successfully fitted to a Ricardo research engine in a test vehicle and acoustic intensity measurements have shown that there is a significant reduction in sound level. The weight of the NIMS molding was 10 percent less than that of the pressed steel cover previously fitted to the same engine. The material has been found to be readily moldable and machinable giving an acceptable appearance and surface finish. Its inherent low cost and density make it particularly attractive for exterior engine applications where noise emission is currently a problem.

It has been shown, however, that the strength of NIMS is significantly affected by the temperature to which it has been subjected. The material deteriorates irreversibly at temperatures above about 110°C although this process takes a significant amount of time. It is therefore important that maximum and normal running temperatures are carefully surveyed for the particular component to be considered for this material.

Tests have shown that the temperature of the valve cover is unlikely to exceed 110°C for significant lengths of time, for the Volkswagen Jetta used in this project.

The experience gained in producing the valve cover indicates that the NIMS cylinder block is still a possibility, for light-duty applications, particularly if future material development were to produce any increase in its high-temperature capability.

Another component which should be considered as an application for NIMS is the inlet manifold. This component has the advantage of being cooled by the incoming air and is likely to remain at a lower temperature than the engine covers under high load conditions.

The hostile environment associated with the internal combustion engine makes the application of new materials extremely difficult. However, NIMS has now been used for the first time to produce an engine component which has been successfully run in a vehicle, giving significant noise reduction. This demonstration project indicates that the material should, therefore, be given serious consideration by the engine designer, as an alternative to metals and polymers.

### **Acknowledgments**

The authors wish to acknowledge the valuable assistance of Mr. J. C. Crane and Mr. A. R. Heath, of Ricardo Consulting Engineers, in this project.

### **References**

Alford, N. McN., and Birchall, J. D., 1985, "The Properties and Potential Applications of Macro-Defect-Free Cement," Materials Research Society, United Kingdom.

# Materials and Surface Finish Effects in the Breaking-in Process of Engines

**G. C. Barber**

Graduate Student.

**J. C. Lee**

Graduate Student.

**K. C. Ludema**

Professor.

Mechanical Engineering Department,  
University of Michigan,  
Ann Arbor, MI

*In this investigation, three materials and several surface finishes on cylinder walls were compared in laboratory tests that simulate the running-in behavior of fired engines. The three materials were the conventional cast gray iron, a sintered graphite-iron powder, and a cast aluminum-silicon alloy. The surface finishes were formed by various types of polishing and honing, including "plateau honing." The run-in behavior of these materials was indicated by a laboratory simulator that is known to correlate with the early wear seen in fired engines. Two test sequences were used. One is a scuff test, in which a quick succession of increasing contact pressure is applied between a piston ring and a cylinder wall until surface failure occurs. The other is a "normal" wear test in which a lower contact pressure is applied, for a longer term study of surface change and coefficient of friction. Scuff load and midstroke friction were found to be dependent on roughness but independent of the amount of plateauing, as measured by skewness of the height distribution in the surface roughness trace. Plateau-honed cylinders were found to run in no more quickly than uniform-honed cylinders. Graphite-iron powder and aluminum-silicon cylinder walls had lower scuff resistance than did gray iron, but their "normal" wear behavior and midstroke friction performance were about the same as gray iron.*

## Introduction

The most widely advocated finish for automobile engine cylinder walls is a plateau-honed surface. The goal in plateau honing is to produce relatively smooth plateaus between the deepest scratches or valleys of the previous rough honing or fine boring operation. Most often this finish is applied to cylinder walls of pearlitic gray cast iron in gasoline engines.

Modern production honing of gray iron produces reasonably satisfactory engine performance, but it could be improved and the cost could be reduced. However, when the function of cylinder walls is studied, it is not obvious how the chemistry of combustion, the chemistry of the engine lubricant, the piston ring materials and contact pressure, and several other variables contribute to the present success. Some of these variables are studied in isolation, but rarely as a system. This paper compares the performance of three materials used as cylinder wall materials, finished in several different ways.

Two alternatives to gray iron were studied in this paper: an aluminum-silicon alloy and sintered graphite-iron powder. Aluminum is attractive because it reduces the weight of engines. In some cases aluminum engines may have iron or steel cylinder sleeves but the maximum weight savings can be achieved by dispensing with the iron [1]. The first automobile

to use an aluminum cylinder block without liners was the Chevrolet Vega in 1970. Early problems with this engine cast doubts on the effectiveness of using aluminum but most of the problems have now been solved [1, 2]. The Vega engine block was cast in an Al-Si alloy (now known as aluminum 390) that contained a uniform distribution of primary silicon particles (16-18 percent by weight) of approximately 0.025 mm diameter. After conventional boring and honing, the cylinder bores were etched by an electrochemical process. This etching process removes some of the aluminum from the bore surface, leaving raised facets of hard silicon in the surface. A properly etched surface provides good resistance to scuffing and other modes of wear [3-9]. Unetched cylinder bores scuffed during cold starting and warm-up operation; overetched cylinder bores caused high wear of piston and rings.

Recently, sintered powdered irons have been studied as a material to replace cast iron in cylinder liners [10, 11]. Powdered metal technology can be used to make parts more accurately than can casting for simple shapes like cylinders, and this has the potential for reducing manufacturing costs. No conclusions on the effectiveness of sintered powdered iron are available at this time.

Cylinder wall finishing has been discussed for many years but there are few papers that specifically discuss the influence of surface finish on engine performance [12, 13]. The surface finish on cylinder walls is usually produced by first boring the cylinders and then honing. The honing process can consist of

Contributed by the Internal Combustion Engine Division and presented at the Internal Combustion Engine Division Technical Conference, Oakbrook, Illinois, October 5-7, 1986. Manuscript received at ASME Headquarters July 9, 1986.

between one and three operations with each operation using increasingly finer honing stones. This boring and honing sequence seems to have been developed by trial and error over many years. Thus, when an engine manufacturer attempts to change any aspect of surface processing it is again necessary to resort to a trial and error testing procedure.

Honing is usually performed in order to form a spiral crosshatch of grooves in the cylinder wall surface. Several explanations for this practice are given in the literature:

- 1 The grooves "store" oil to prevent scuffing during startup and at times of overloading [14, 15].
- 2 The grooves act as a repository for wear particles, thereby removing them from the contact region between the rings and cylinder wall [16].
- 3 A hydrodynamic effect arises from thermal expansion of the oil in the grooves [17].

Plateau honing emphasizes the formation of deep grooves, which is thought to enhance the function of grooves. Another claim for the deep grooves (or perhaps for the plateaus) is that they reduce break-in time of cylinder walls [18-21].

Most of the above statements concerning honing are hypotheses based upon experience rather than the result of scientific investigations. For example, there are few comments in the literature regarding the mounds and flakes of loosely attached metal that are built up along the grooves formed by honing. These mounds and flakes can be expected to influence cylinder wall performance.

The nearest confirmation of the effectiveness of plateau honing in the literature is some work done with motorcycle engines [22, 23]. Some cylinders were conventionally honed and then run for 10,000 km (considered to be run-in). The surface topography of worn cylinders was found to consist of valleys and plateaus, and the measured surface roughness was  $0.5 \mu\text{m } R_a$ . The authors reasoned that the plateau topography is the "natural" run-in condition and thus an engine would run-in in a very short time if the production finish were nearer the natural finish. The authors claim that experiments confirmed this hypothesis, provided the plateau surfaces were not too smooth. However, the unworn conventionally honed

cylinders were much rougher ( $R_a = 2.0 \mu\text{m}$ ) than the unworn plateau-honed cylinders ( $R_a = 0.5 \mu\text{m}$ .) It was therefore unclear whether the improved engine performance should have been attributed to a plateau surface finish rather than to a smoother surface finish.

In summary, there is no model available that describes the role of surface finish on any material in the successful performance of engines. The problem is too large and complicated to expect a model to cover all aspects of engine operation. Thus this investigation is a restricted study of the influence of three materials and several surface finishes on the surfaces changes that take place early in engine operation. This early stage of change is often referred to as the running-in or break-in stage.

## Experiments

**Materials.** The three materials used in these experiments are the conventional gray cast iron (GI), a sintered graphite-iron powder (PM), and a cast aluminum-silicon alloy referred to as 390Al. The compositions and some properties of the tested materials are shown in Table 1. The GI and PM test materials were cut from Cadillac cylinder liners (88 mm bore diameter) and the 390Al test materials were cut from a prototype engine block (75 mm bore diameter) intended for use in the GM Saturn project.

The microstructures of these three materials are shown in Fig. 1. These metallographic specimens were polished and then etched for 10 s in picral before examination. The GI and the PM materials both have matrices that are almost 100 percent pearlitic. The graphite in the GI is in the form of flakes (ASTM type A, size 4) and some of the carbon in the graphite-iron powder is present in irregularly shaped nodules. The silicon particles in the 390Al are approximately 0.040 mm in diameter, which is slightly larger than that specified for the Vega engine block.

A molybdenum-coated piston ring was used with the iron cylinder specimens. This type of ring was not available for the 75 mm bore diameter of the 390Al cylinder, so a chrome-plated piston ring was substituted, with no detrimental effect on the experiment.

**Table 1 Composition and properties of cylinder liner materials studied in the simulator**

Element (percent)	Gray iron	Graphite-iron powder	Aluminum-silicon
C	3.1-3.4	1.32	
Mn	0.50-0.70	0.23	<0.20
P	0.15 max	0.21	
S	0.15 max	0.012	
Si	2.1-2.4	0.21	16.0-18.0
Cr	0.20-0.40	0.082	
Ni	0.06	0.096	
Mo	0.02	0.026	
Cu	0.15	0.28	4.0-5.0
Ti	0.04	0.009	<0.20
Mg			0.45-0.65
Fe	Balance	Balance	<0.70
Zn			<0.20
Rockwell b	85	88	54
Tensile strength	241 MPa	399 MPa	216 MPa
Percent elongation	0.1	0.76	1.0
	Graphite is ASTM type A size 4	Graphite is irregular and nodular	Silicon particles are 0.040 mm on average



Fig. 1(a) Microstructure of gray iron, 550x

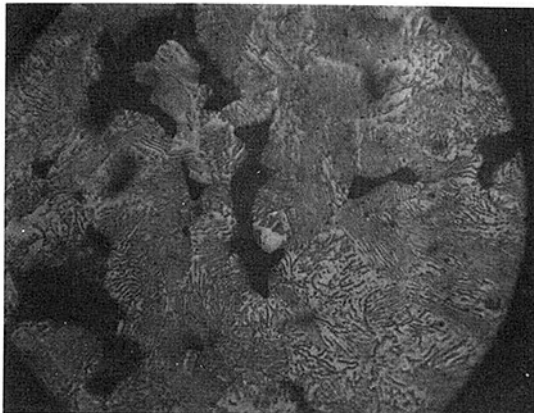


Fig. 1(b) Microstructure of graphite-iron powder, 550x

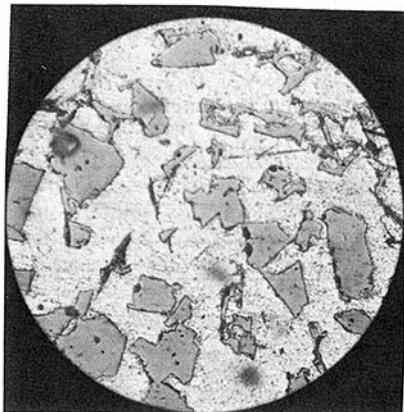


Fig. 1(c) Microstructure of aluminum-silicon alloy, 250x

**Surface Finishes.** Traditionally, the only surface roughness parameter used to characterize surface finish is the arithmetic average  $R_a$ . In recent years it has been recognized that to characterize surface finish more completely, a parameter to describe the shape of asperities should be used in addition to  $R_a$  [24]. The additional parameter selected for use in this investigation is skew  $R_{sk}$ . As a surface becomes more valley-biased, the skew becomes more negative. The surface finish on a cylinder wall becomes increasingly valley-biased during its run-in period due to the wearing away of plowed mounds. Also, the goal of plateau honing is to produce a valley-biased surface finish; hence, skew is an appropriate in-

**Table 2** Surface tracer parameter values obtained on cylinder liners in normal wear tests (GI = gray cast iron, PM = sintered graphite-iron powder, 390 AI = aluminum-silicon)

Liner ID	Roughness, $R_a$ ( $\mu\text{m}$ )		Skewness, $R_{sk}$	
	before test	after test	before test	after test
GI-1	0.21	0.14	-0.85	-1.64
GI-2	0.25	0.19	-1.6	-2.7
GI-3	0.53		-0.4	
GI-4	0.45		-1.1	
GI-5	0.70	0.54	-1.0	-1.7
GI-6	0.56	0.40	-1.9	-2.3
GI-7	1.20	0.67	-1.5	-1.8
GI-8	0.35	0.27	-2.9	-3.61
GI-9	0.38		-0.61	
GI-polished	0.08		-1.0	
PM-A	0.42	0.23	-1.8	-3.57
PM-B	0.20	0.08	0.0	-1.38
PM-C	0.22	0.15	-2.1	-4.02
PM-D	0.45	0.28	+0.10	-1.51
PM-E	0.62		-0.40	
PM-F	0.29		-0.44	
PM-polished	0.09		-1.4	
390AI	0.12		-0.4	

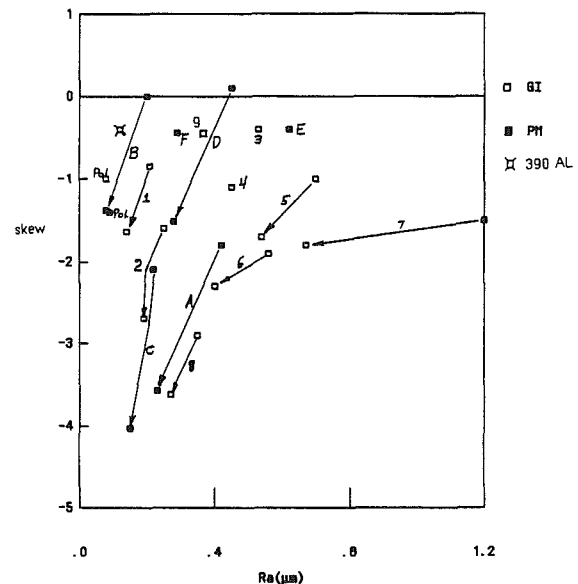


Fig. 2  $R_a$ -skew map, showing the changes during break-in

dicator to describe the shape of asperities on engine cylinder walls.

Nine types of honed GI specimens and six honed PM specimens were used with  $R_a$  ranging from 0.2  $\mu\text{m}$  to 1.20  $\mu\text{m}$  and skews ranging from 0.0 to -2.9. In addition, several GI and PM specimens were hand polished using 600 grit abrasive paper to remove the honing grooves completely and produce relatively smooth specimens. The 390AI specimens were honed and electrochemically etched to produce an  $R_a$  value of 0.12  $\mu\text{m}$  and a skew value of -0.4. The list of all the materials and surface parameter values used in this investigation is given in Table 2, and the data are also given graphically on a roughness-skew plot in Fig. 2.

**Table 3 Honing conditions and surface roughness for gray iron cylinder liners**

Liner ID	GI-1	GI-2	GI-3	GI-4	GI-5	GI-6	GI-7	GI-8, 9
Honing time (s)	60 <sup>1</sup>	60	60	60		20	30	15
	60	60	29	27				7
Pressure (kPa)	410	410	410	410	620	410	410	570
rpm	180	180	180	180	195	195	195	220
Stroke/min	31	20	31	31	29	31	30	60
Stones <sup>2</sup>	C-100L	C-100L	C-100L	C-100L				D-200
	C-240L	C-240L	C-240L	C-240L	C-100L	C-100L	C-100L	D-150
								D-30
Honing oil	Water Sol.	Water Sol.	Water Sol.	Water Sol.	Water Sol.	Water Sol.	Water Sol.	Water Sol.
Roughness $R_a$ ( $\mu\text{m}$ )	0.21	0.25	0.53	0.45	0.70	0.56	1.20	0.35

<sup>1</sup>Multiple entries denote a honing sequence using different stones in each step.

<sup>2</sup>The code for the stones: C = SiC, D = diamond, 100 (e.g.) = grit size.

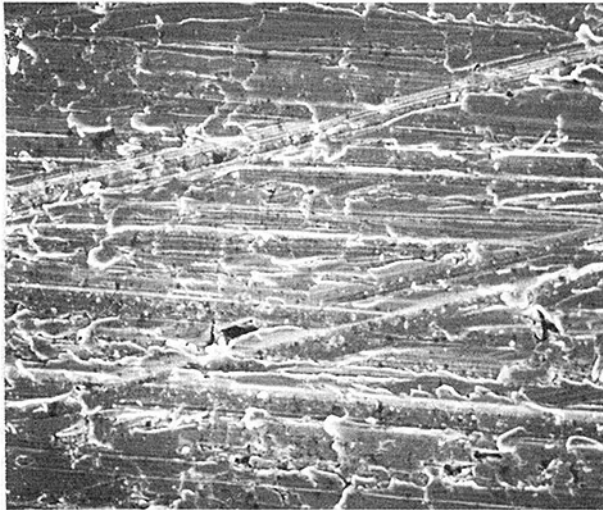


Fig. 3(a) Specimen GI-4, unworn, 500x

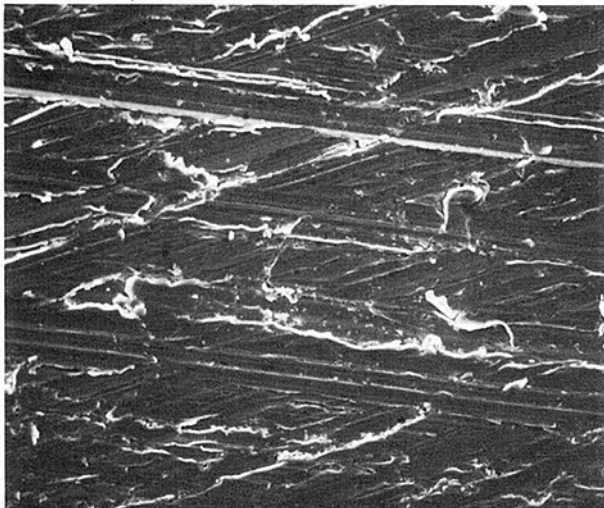


Fig. 3(b) Specimen GI-8, unworn, 500x

The honing variables used to produce the surface finishes on the GI specimens are given in Table 3. The gray iron specimens GI-1 through GI-7 were honed using silicon carbide honing stones. A micrograph of specimen GI-4 is given in Fig. 3(a). Note the large amount of plowed-up wear debris along the honing grooves. This large amount of wear debris is typical of specimens GI-1 to GI-7.

Specimens GI-8 and GI-9 were honed using diamond honing stones. Diamond honing stones are often thought to produce more plowed-up wear debris than do silicon carbide honing stones. However, Fig. 3(b) shows that one of the specimens produced by diamond honing (GI-8) has less plowed-up debris than specimens GI-1 to GI-7. Apparently, the fine D-30 honing stones used in the last honing operation remove much of the plowed-up debris. The honing conditions for the PM and 390Al specimens were not available.

**Laboratory Simulator.** A perspective should be given on the methods available for studying cylinder wall finishing. As mentioned above, several variables interact to allow sliding of piston rings along cylinder walls without dire consequence, and each of them is complicated. The effect of any one or two of the variables can be readily examined in the laboratory, and is the subject of very many papers under the heading of Tribology. Unfortunately, the results of such studies are not readily applicable to real engines. The use of real engines, on the other hand, is very costly and time-consuming. A compromise is sometimes sought in the development of laboratory devices that simulate the performance of some particular engine part. Again, in the literature a number of simulators are described, but it appears that no simulator absolutely reproduces the wear behavior of cylinder walls from fired engines. In the work reported below, a simple simulator was used that was found in previous work [25] to correlate with the run-in wear of fired engines. Because of the great care taken in finding the proper operating conditions for simulation, this simulator can be used with confidence as an initial screening device for new cylinder wall materials.

The simulator is an oscillating test machine, a drawing of which is shown in Fig. 4. It moves a segment of actual cylinder wall in an oscillatory cycle against a commercial piston ring. The machine has a stroke of 19 mm, a maximum nominal contact pressure of 120 MPa between the piston ring and cylinder wall segment, and a maximum reciprocation rate of 15 cps.

Previous work with this device [25] included a comparison

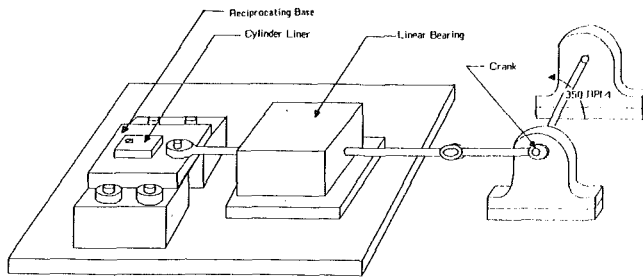


Fig. 4(a) Mechanisms used to oscillate the cylinder liner specimen

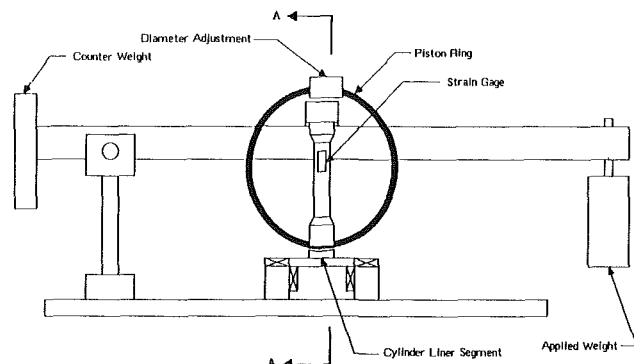


Fig. 4(b) End view of Fig. 4(a) showing piston ring support and load application system

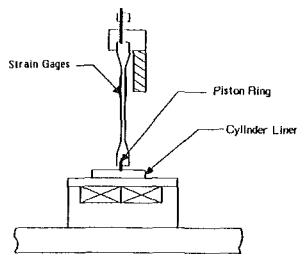


Fig. 4(c) Cross section A-A showing piston ring support

of the specimens from the simulator with worn cylinder walls from fired engines made of gray iron. The criterion used to determine the validity of simulation was the appearance of the same progression of surface change in the test machine as in fired engines, with time of running. The previous study concentrated on the upper part of the cylinder wall where the contact pressures between the piston rings and cylinder walls are the highest and lubrication is poor. In the upper 10 mm of travel of the top compression ring in engines there was loss of material and the formation of an oxide layer. The operating conditions in the simulator that duplicated these events on GI were an oscillatory speed of 350 cycles per minute and a nominal contact pressure of 4.9 MPa (700 psi), using mineral oil as lubricant. These same operating conditions were used in the present work to test the PM and 390Al materials even though it is not confirmed that engines made of these materials will be expected to operate under the same conditions as engines made of GI.

As shown on Fig. 4(b), two strain gages on the test machine made it possible to measure the friction force between the piston ring and cylinder liner segment. The strain gage output was amplified, then displayed on a strip chart recorder.

**Tests.** Two types of test were done with the simulator. A

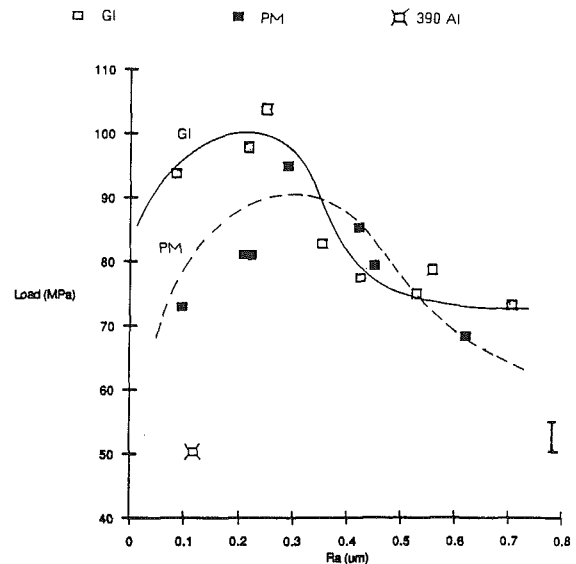


Fig. 5 Scuff load versus original roughness; note: The standard error of estimate for this class of experiment is +2.1 MPa

severe test, referred to as the scuff test, imposed a step load, beginning with a nominal contact pressure of 2.8 MPa and increasing it every 2 min by 2.8 MPa to failure. Mineral oil was dripped onto the cylinder wall segment during the test. Failure was indicated by increased vibration of the simulator, and the load at which this first occurred was taken as the scuff load. The scuff tests were done to determine the influence of surface topography on failure load for all three materials. The rationale for using a step-load test arises from its successful use in previous work. It might be more realistic to apply a succession of higher starting loads on new specimens until a load is found that causes immediate failure of a surface. Unfortunately, this is a tedious process. Where such tests have been done it has also been found that a step-load test will rank materials in the same order as will a sequence of increasing starting loads.

The second type of test is referred to as the normal wear test. In this test a contact pressure of 4.9 MPa was applied and held constant for 2 h. Again mineral oil was dripped on the cylinder segment during the test. For all three materials the normal wear tests were done to measure the change in surface topography and coefficient of friction with time of sliding.

## Results

**Scuff Tests.** Two tests were run for each type of material and surface finish. The average nominal contact pressure required to cause failure by scuffing in the two tests is plotted versus initial  $R_a$  in Fig. 5. The standard error of estimate  $S_m$  [26] was used to obtain the error in determining the nominal contact pressure to produce scuffing. This is given by

$$S_m = \frac{S}{\sqrt{n}}$$

where  $n$  = the number of measurements and  $S$  = the standard deviation of an infinite number of measurements. An approximation for  $S$  was determined by measuring the load required to cause scuffing on five different PM-E specimens and was found to be 2.9 MPa. Since  $n=2$ , the standard error is 2.1 MPa. It should be noted that  $S_m$  is a property or characteristic of the test and is thus applicable to all data taken from the simulator.

The scuff behavior was similar for the PM and the GI specimens. For both materials the scuff load is seen to increase to a maximum as the initial  $R_a$  is increased in the range from

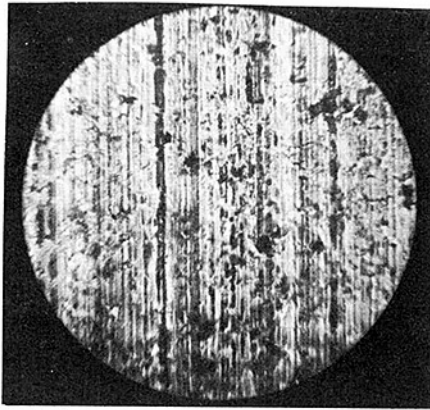


Fig. 6 Scuffed graphite-iron powder specimen, 40 x



Fig. 7(a) Unworn 390Al specimen, 175x

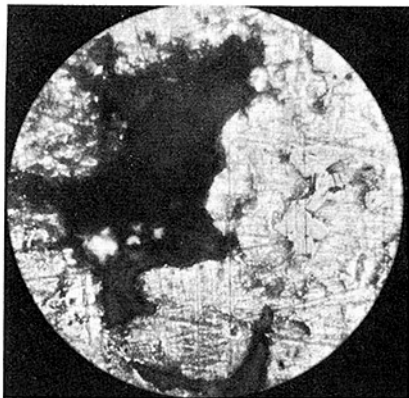


Fig. 7(b) Same location as shown on Fig. 7(a), photo taken after 8.4 MPa step during a scuff test, 175x

0.1  $\mu\text{m}$  to 0.3  $\mu\text{m}$ . On specimens rougher than 0.3  $\mu\text{m}$  the scuff load decreases with increasing  $R_a$ . Differences in initial skew did not affect the scuff load, i.e., specimens with approximately the same roughness but different skew values scuffed at the same load. At low  $R_a$  values the PM is less scuff resistant than is GI, and the two 390Al specimens failed at considerably lower loads than the others.

Examination of the failed surfaces revealed scratches in the dark film, as shown in Fig. 6. It is likely that these scratches were caused by metallic and oxide particles that developed by accumulation of fine wear debris. The particles accumulated

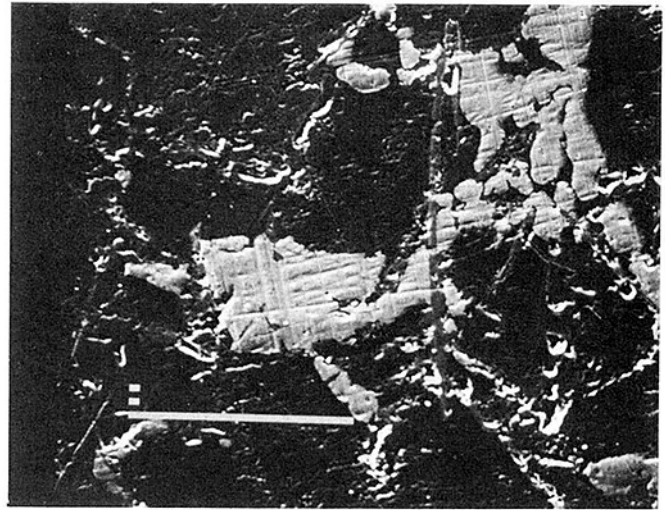


Fig. 8(a) Worn 390Al specimen, 400x

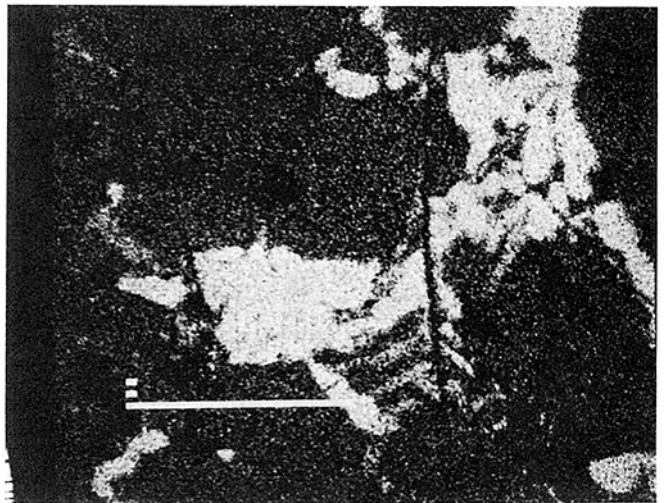


Fig. 8(b) Copper map of location shown in Fig. 8(a), 400x

at the piston ring cylinder wall interface, and they plowed grooves in the surface of the cylinder wall.

A possible source of this wear debris in the 390Al specimens is shown in Fig. 7. A small unworn area of surface is shown in Fig. 7(a), and the exact same location after a scuff test is shown on Fig. 7(b). It can be seen that a large fragment was removed from the surface by friction forces. This condition was seen frequently.

Another interesting phenomenon is seen by x-ray mapping the 390Al specimens. Figure 8 is a scan for copper, showing large "patches" as well as a finer distribution of particles. The patches were uniformly distributed on the surface of both worn and unworn specimens, appearing to constitute more than the 4 to 5 percent given in the composition for this material. The copper on the surface may be another reason this material failed at such low loads in the scuff tests.

**Normal Wear Test.** Figure 9 shows typical surface profile graphs, both in the unworn state and after 2 h of running in the simulator. All of the worn specimens showed considerable smoothing and change toward larger negative skewness, indicating that peaks are worn off, leaving a valley-biased surface. The data are given in Table 2.

Figure 10(a) shows the specimen PM-E in the unworn state and Fig. 10(b) shows the same specimen after the 2-h test. It can be seen that in the worn state the surface was covered with



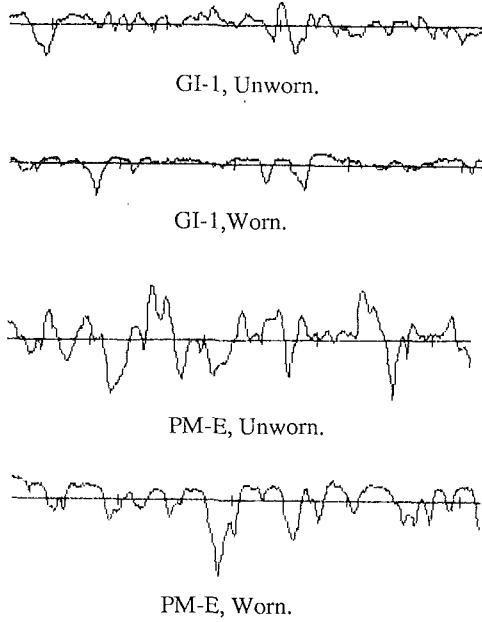


Fig. 9 Surface profile graphs of specimens run in a normal wear test for two hours; horizontal magnification 200x, vertical magnification 5000x

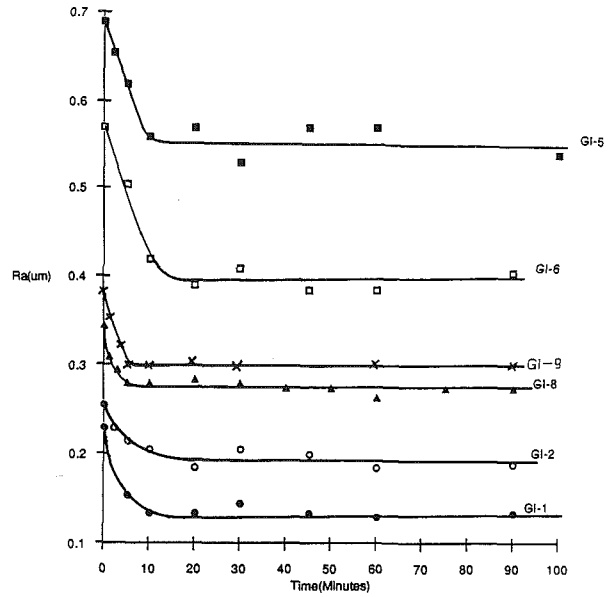


Fig. 11  $R_a$  versus time of running in "normal" wear tests for GI specimens

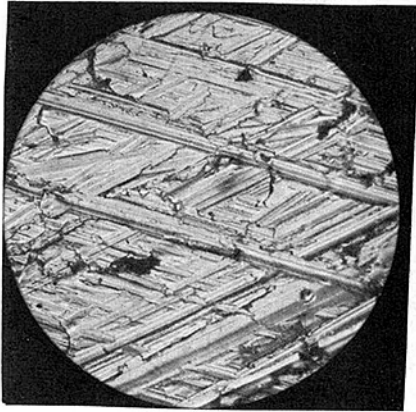


Fig. 10(a) Unworn PM-E specimen, 250x

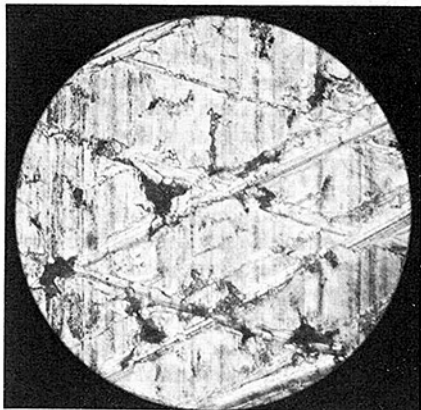


Fig. 10(b) PM-E specimen run in a normal wear test for two hours, 250x

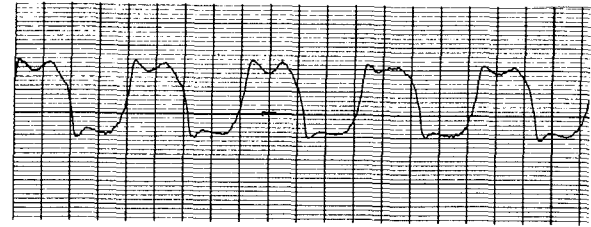


Fig. 12 Strain gage output, aluminum-silicon specimen

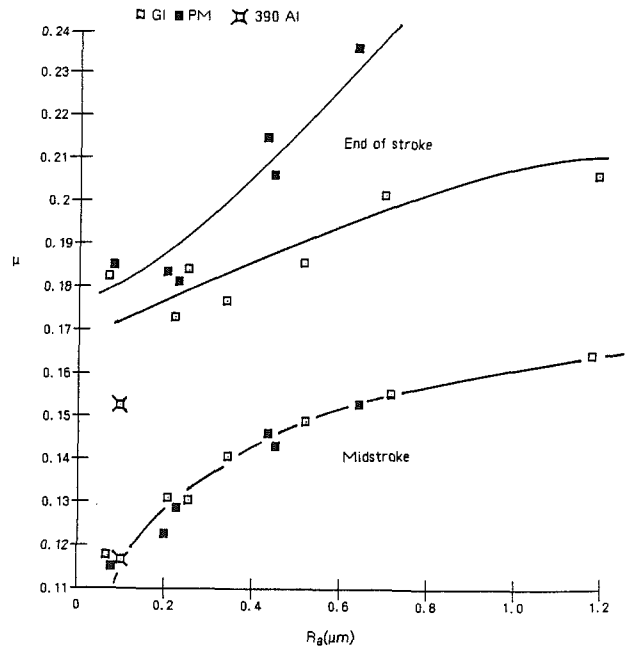


Fig. 13 Coefficient of friction versus initial  $R_a$

a dark film, which from previous work was identified as  $Fe_3O_4$  [27]. Also, only the deepest honing grooves were left on the specimen, indicating that considerable wear took place. This same behavior was seen with the GI and 390Al specimens. However, it was not possible to rank the specimens according to their normal wear resistance because they were

very similar. An observation of the wear debris as well as the surfaces indicated that the primary wear mechanism in all three materials was oxidative; the secondary mechanism was mild scratching. Scratches were found to be far more likely to form on the smoother surfaces. This is probably because

rougher surfaces provide large grooves into which wear debris may migrate and avoid scratching the cylinder wall surface.

Figure 11 shows how  $R_a$  of GI specimens changes with running time. It can be seen that the  $R_a$  of most of the specimens stabilizes after approximately 10 min. Some authors define this as being run-in. Specimens GI-8 and GI-9 stabilize after only 5 min running. Both of these specimens were honed with diamond hones, which must produce surfaces that "wear" more readily than others. The reason for the shorter run-in time is not due to differences in skew. GI-8 has the highest of all and GI-9 has the lowest of all.

Figure 12 shows a typical frictional measurement in the oscillatory test. The friction was higher at the points of sliding reversal than in midstroke. This is because boundary or inadequate fluid film lubrication occurs as the velocity approaches zero. The coefficient of friction,  $\mu$ , was determined from tests of all three materials and various initial surface finishes. In the first few minutes of running,  $\mu$  steadily decreased until it stabilized after 5–15 min for all materials. During this time  $\mu$  decreased between 5 and 20 percent.

Figure 13 shows the stabilized values of  $\mu$ , both at the end of stroke and at midstroke, over a range of  $R_a$ . All values of  $\mu$  increased as  $R_a$  increased. No effect of skew was seen in these tests. It may be seen that there is a difference due to materials at the end of stroke but not in midstroke. The lowest values of  $\mu$  were obtained with the specimens that were hand polished to completely remove the grooves produced by honing. This suggests that, to lower frictional power losses, cylinder walls should be finished as smoothly as possible without sacrificing some other aspect of engine performance.

## Conclusions

In this study, gray cast iron, sintered graphite-iron powder, and 390 aluminum-silicon alloy exhibited similar wear behavior when run under the load conditions that simulate conditions near TDC of the top compression ring.

Break-in times for the diamond-honed GI specimens were found to be less than for the other GI specimens. Photomicrographs of one diamond-honed surface showed the presence of less plowed-up material due to honing than with SiC hones.

At low  $R_a$  values the GI has greater scuff resistance than does the PM, and the 0.12  $\mu\text{m}$  Ra 390Al specimen was considerably less scuff-resistant than are the GI and PM specimens. The ease with which particles are worn from the 390Al surface, perhaps due to casting defects, may contribute to the relatively poor scuffing resistance of this particular material.

The value of  $\mu$  at the end of the stroke was found to increase with increasing roughness and was also dependent upon the material used. The value of  $\mu$  in midstroke also increased with increasing roughness but showed no dependence on the type of material used. The type of material in an engine in the midstroke region would be of less concern than at the top dead center location. The measured values of  $\mu$  at midstroke in the simulator were characteristic of mixed lubrication, which would confirm that lubrication at midstroke in fired engines is primarily hydrodynamic since piston speeds in engines are ten times or more greater than that in the simulator [28].

Plateau-honed specimens performed no better than normal-ly or simply honed cylinder materials in the reported laboratory tests. It remains to be seen if the practice of plateau honing can be proven to be of some value in full-scale engine tests. One difficulty in showing the value of plateau honing is that engine cylinders are not actually honed to "plateaued"

specifications. Rather, surfaces are badly torn in an attempt to follow an orderly procedure of honing.

## Acknowledgments

We are grateful to: General Motors Manufacturing Development Section and Dr. Chi-hung Shen for financial support, test materials and helpful advice in the course of our research; Mr. Mike Bingham of Sheffield Instruments (Dayton, OH) who allowed us to use one of their surface tracer systems, the Sheffield Proficorder Spectre; Mr. Ken Sheir and Mr. Gary Blair of Cadillac Division of General Motors, who aided our investigation with engine test results and many cylinder specimens.

## References

- 1 Jacobsen, E. G., "General Motors 390 Aluminum Alloy 60 V6 Engine," SAE Paper 830006, 1983.
- 2 Renninger, G., Abendroth, D., and Bolien, M., "Casting Engine Blocks in GK Al Si 17 Cu 4 Mg," SAE Paper 830003, 1983.
- 3 Kneisler, F. J., Martens, D. A., and Midgley, R. W., "The Vega 2300 Engine," SAE Paper 710147, 1971.
- 4 Jorstad, J. L., "Reynolds 390 Engine Technology," SAE Paper 830010, 1983.
- 5 Andrews, J. B., Seneviratne, M. V., Zier, K. P., and Jett, T. R., "The Influence of Silicon Content on the Wear Characteristics of Hypoeutectic Al-Si Alloys," *Proceedings of Conference on Wear of Materials*, ASME, 1985.
- 6 Clarke, J., and Sarkar, A. D., "Wear Characteristics of As-Cast Binary Al Si Alloys," *Wear*, Vol. 54, 1979, p. 7.
- 7 Sarkar, A. D., "Wear of Aluminum Silicon Alloys," *Wear*, Vol. 31, 1975, p. 331.
- 8 Razavizadeh, K., and Eyre, T. S., "Oxidative Wear of Aluminum Alloys," *Wear*, Vol. 79, 1982, p. 325.
- 9 Shivanath, R., Sengupta, P. K., and Eyre, T. S., "Wear of Aluminum Silicon Alloys," *Proceedings of Conference on Wear of Materials*, ASME, 1977.
- 10 Kaufman, S. M., and Mocarski, S., "What Automotive Design Engineers Require From the P/M Industry," SAE Paper 831032, 1983.
- 11 Hall, D. W., and Mocarski, S., "Powder Metal Parts for Automotive Applications," SAE Paper 850458, 1985.
- 12 Conner, K. W., "Surface and Shape Characteristics of Cylinder Bores," *SAE Transactions*, Vol. 36, No. 3, 1935, p. 95.
- 13 Conner, K. W., "Surface Finish Related to Wear in Internal Combustion Engines," *SAE Transactions*, Vol. 43, No. 2, 1938, p. 305.
- 14 Munro, R., and Hughes, G. H., "Current Piston and Ring Practice and the Problem of Scuffing in Diesel Engines," Diesel Engineers and Users Association, Publication 335, 1970, p. 1.
- 15 Kragelsky, I. V., and Alisin, V. V., "Friction, Wear and Lubrication," *Tribology Handbook*, Vol. 3, Pergamon Press, Oxford, 1979, p. 57.
- 16 Hesling, D. M., "A Study of Typical Bore Finishes and Their Effect on Engine Performance," *Lubrication Engineering*, Oct. 1963, p. 414.
- 17 Neale, M. J., "Piston Ring Scuffing—A Broad Survey of Problems and Practice," *Proc. Instn. Mech. Engrs.*, Vol. 185, No. 2, 1970–1971, p. 21.
- 18 Santochi, M., and Tantussi, G., "Surface Parametrical Microgeometry and Functional Models: A New Approach," *Precision Engineering*, Vol. 6, No. 4, 1984, p. 201.
- 19 Grigor'ev, M. A., et al., "Study of Kamaz Engine Cylinder Liner Working Surface Microgeometry," *Soviet Journal of Friction and Wear*, Vol. 2, No. 1, 1981, p. 110.
- 20 Fischer, H., "Honing," SME Paper MR 82-939, Honing Technology Clinic, Los Angeles, CA, June 8, 1982.
- 21 Kauten, W. R., "Diesel Engine Cylinder Liner Honing," SME Paper MR 82-938, Honing Technology Clinic, Los Angeles, CA, June 8, 1982.
- 22 Santochi, M., and Vignale, M., "Study on the Functional Properties of a Machined Surface," CIRP General Assembly, Toronto, 1981.
- 23 Santochi, M., and Vignale, M., "A Study on the Functional Properties of a Honed Surface," *Annals of the CIRP*, Vol. 31, No. 1, 1982, p. 431.
- 24 Stout, K. J., and Davis, E. J., "Surface Topography of Cylinder Bores—The Relationship Between Manufacture, Characterization and Function," *Wear*, Vol. 95, 1984, p. 111.
- 25 Barber, G. C., and Ludema, K. C., "The Break-in Stage of Cylinder-Ring Wear," *Wear*, Vol. 118, 1987, p. 57.
- 26 Lyon, J. A., *Dealing With Data*, Pergamon Press, Oxford, 1970.
- 27 Kang, S. C., and Ludema, K. C., "The Breaking-in of Lubricated Surfaces," *Proceedings of the International Conference on Wear of Materials—1985*, ASME, Vancouver, B. C., p. 280.
- 28 Uras, H. M., and Patterson, D. J., "A Study of Piston-Ring Assembly Friction," Technical Report for DRDA Projects #320934 and #388147, University of Michigan, Apr. 1984.

**R. M. Dunton**

Vice President,  
Engineering Research and Development.

**L. Propetto**

Manager,  
Engine Development.

Bombardier, Inc.,  
Montreal, Canada

**G. E. Murray**

Section Leader,  
Ricardo Consulting Engineers,  
West Sussex, England

## Development of the B2400 Engine

*A new engine has been designed to meet future requirements for heavy-duty locomotive applications as found in North America and developing countries. After a thorough analysis of future market requirements, a detailed specification was prepared to serve as guideline throughout the evaluation of the design. Objectives were established for many fundamental parameters including efficiency, introductory and growth power ratings, weight and package size, durability, and maintainability. The paper describes the engine configuration, detail design, and the significant use of computer analytical techniques, to provide increased levels of performance in the integrity of the crankshaft, cylinder block, and other key components. In addition, reference to many years' experience with an existing locomotive engine design has provided assurance of the reliability of many of the new components. Design details are included for many components, with descriptions of the rationale behind those designs.*

### Introduction

Market research surveys at Bombardier during the late 1970s indicated a long-term demand for locomotives and engines with high power-to-weight ratios for heavy freight haulage duties, for railways in developing countries, and for rebuilding existing locomotives.

Bombardier policy dictated that features had to be incorporated into the basic design to permit use of the engine in stationary, marine propulsion, and auxiliary generating applications.

The 251 range of engines was assessed for its suitability to satisfy the new engine specification, particularly an ultimate increase in the rating to 250 kW/cyl. A design assessment indicated that modifications to many major components would ultimately be required involving major changes to production facilities. After examining alternative strategies, a new engine range, designated the B2400 series (Fig. 1), was proposed and studies commenced. Fundamental design parameters were examined and their effect on installation limitations reviewed. Emphasis was placed on improved reliability, durability, ease of maintenance, and low fuel consumption.

This paper describes the advancement of an existing design philosophy by one generation from concept studies to detail design using today's extensive prediction techniques.

### Concept Study

**Approach.** At the commencement of the design of a new engine all the factors which affect that design have to be examined. The marketing and technical decisions taken during the initial stage are critical to the concept of the engine and determine the basic parameters for the whole of its commercial life. The new engine, which starts from a clean sheet of paper, will be an integration of all the tasks that go to make it—marketing, design, development, production, servicing—and must be optimized for its prime application.

Contributed by the Internal Combustion Engine Division and presented at the International Combustion Division Technical Conference, Oakbrook, Illinois, October 5-7, 1986. Manuscript received at ASME Headquarters July 9, 1986.

Engine manufacturing cost, fuel consumption, servicing, and maintenance were factors that had to be carefully weighed and compared for the design of the Bombardier engine, to obtain low total life cycle costs within the constraints of the application. Stricter competition and increasing legislation are always increasing the number and complexity of factors that have to be taken into account. To convert these factors into an engine design, complex optimization procedures were used [1],

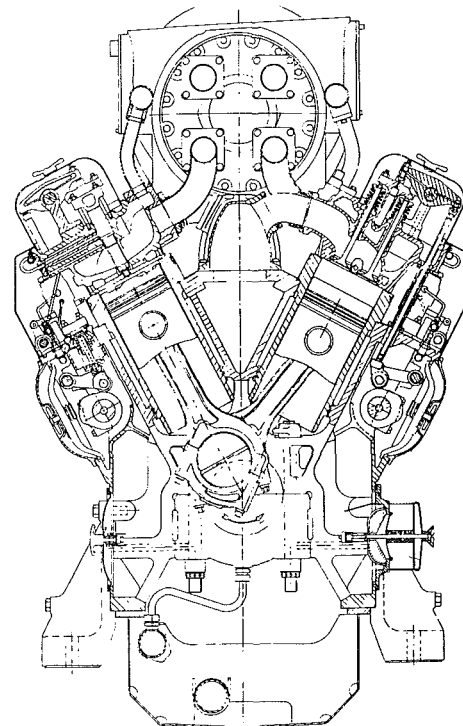


Fig. 1 Transverse sectional arrangement

such as computer performance simulation prediction and finite element programs, together with expert knowledge of engine design, operation, and marketing to establish the basic engine parameters.

Some of the basic thinking to resolve these factors is set out in the next section.

**Optimization of Fundamental Design Parameters.** To establish what the engine has to achieve, a specification was drawn up covering its operating environment:

Prime application	— locomotive
Target rating	— 205 kW/cyl.
Growth rating	— 250 kW/cyl.
Power curve	— propeller law (speed) <sup>3</sup>
Maximum overspeed without component failure	— 130 percent rated speed
Maximum altitude	— 5000 m
Air temperature	— 45°C to +55°C
Cold start unaided	— 5°C at sea level
Fuel	— locomotive ASTM No. 2 with allowance for lower grades
Lubricating oil	— SAE 30
Overhaul—major	— 1 million km or 6 yr 0.5 million km or 3 yr

The engine had to meet the following demands:

- (i) Low fuel consumption.
- (ii) Ability to burn lower fuel grades than in current locomotive use.
- (iii) High levels of reliability and durability.
- (iv) Ease of maintenance.
- (v) Use existing production facilities where possible.
- (vi) Ability to meet foreseeable environmental pollution limits.
- (vii) Dimensions and weight not to exceed present engine package.

The engine would be complimentary to the range of the Bombardier/Alco 251 engine, and production would continue simultaneously.

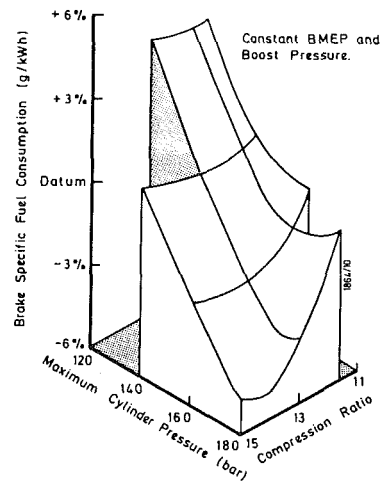
The design philosophy adopted was to avoid incorporating unproven ideas and concepts, but to use features requiring minimum development, thus avoiding unnecessary delays to the development program.

The locomotive engine has severe restraints on weight and size. Very high specific powers and lightweight designs of quick-running engines were ruled out. Although offering advantages in engine size and weight, the high load factors required would undoubtedly have introduced problems in achieving the levels of durability and reliability required together with increased development, maintenance, and fuel consumption. Alternatively, larger bore engines would exceed the present engine package limitations, and with correspondingly lower BMEP's, would not be competitive at the introductory power rating.

A four-stroke cycle for locomotive application was selected as offering:

- (i) Lower combined mechanical and thermal stresses [2].
- (ii) Better full and part-load fuel consumption [3].
- (iii) Less development for a company already experienced in four-stroke manufacture and operation.
- (iv) Acceleration as good, if not better, than two-stroke engines [3].

BMEP and piston speed are independent of, but influence, engine weight and size. The BMEP has to be set at a level which is technically achievable and commercially viable for the duty concerned, while considering limitations set by turbocharger performance flexibility, altitude, and derating, without employing two-stage turbocharging with its added complexity and size.



Medium Speed Diesel Performance Simulation. Predicted Effect of Maximum Cylinder Pressure and Compression Ratio on Specific Fuel Consumption.

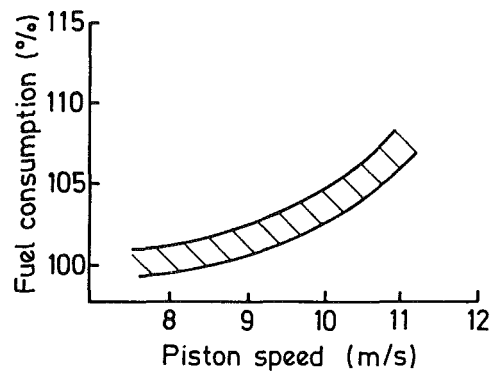


Fig. 2 Review of fundamental parameters

Continued development of the Bombardier turbocharger to match growth rating performance resulted in a target of 22 bar being set, which allowed some turbocharger flexibility for altitude derating. This gave an introductory rating of 18–19 bar BMEP, a competitive rating within the capability of current turbocharger builds. High maximum cylinder pressures, which can be designed [4], assist good fuel consumption and allow high power outputs, but component weights, material costs, complexity and friction losses increase. The compression ratio had to be set to allow ease of starting and to limit the mechanical loading.

Figure 2 shows results of a performance simulation, typical of this engine class, which considers the effect of compression ratio and firing pressures on fuel consumption. This indicates optimum fuel consumptions to be obtained with high compression ratios and correspondingly high firing pressures. However, higher firing pressures require correspondingly heavier and larger components and at the optimum condition of all parameters considered, resulted in a maximum design firing pressure of 145 bar with a nominal compression ratio of 12.5:1.

The packaging and weight limitations on locomotive engines generally result in piston speeds between 9.5 and 10.75 m/s.

High piston speeds, which reduce engine breathing ability and increase SFC, assist in keeping engine size and weight down, but may require increased development effort to achieve equal durability targets. To minimize SFC and weight without sacrificing durability, a mean piston speed of 10 m/s was selected.

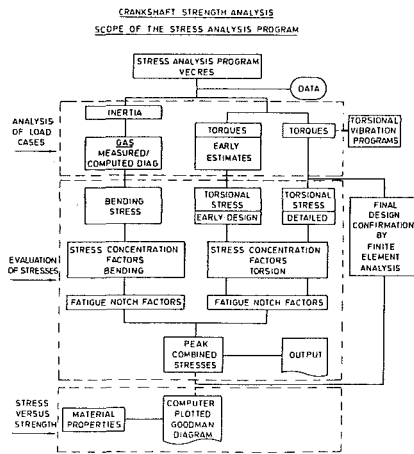


Fig. 3 Scope of crankshaft stress analysis program

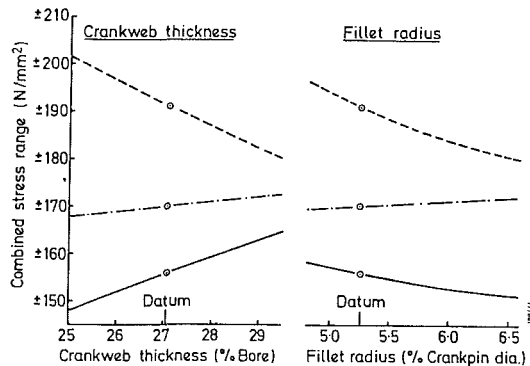
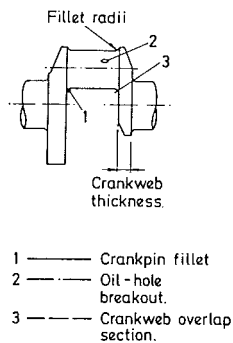


Fig. 4 Evolution of crankthrow design

**Basic Engine Design Specification.** The power growth from 205 to 250 kW/cyl. had a strong influence on the final selection of bore, stroke, and other major engine dimensions. For practical and economical considerations these should not undergo changes during the engine's commercial life.

Having selected parameters of BMEP and piston speed for the growth rating, the cylinder bore became 240 mm.

The locomotive engine is not restrained by industrial generator synchronous speeds. Of the available locomotive generators capable of absorbing the design powers, the most suitable were between 1000 and 1100 rev/min. To minimize engine weight and size the highest speed of 1100 rev/min was chosen. Keeping within the set limits of piston speed, a stroke of 270 mm was chosen for a piston speed of 9.9 mm/s, which satisfied stroke/bore ratio criteria and packaging restraints.

The power requirements are covered by a range of engines of 6, V8, V12, V16, and V18 cylinders. Alternative L6 and V6 engines will be considered.

A range of vee angles was schemed.

An acceptable strong fabricated design for the cylinder block could not be achieved at 45 deg due to the close proximity of liner skirts. The V8 firing interval and performance, air chest, manifold arrangements, and cylinder block strength were all improved at 60 deg Vee. However, that design exceeded the existing package width and early crankshaft stress analysis on the V16 engine showed high fourth-order torsional stresses.

The angle was reduced to 55 deg, which satisfied all packaging requirements and crankshaft stress limits.

Optional turbocharger and aftercooling arrangements at the free end and centrally in the vee were considered. For the 55 vee, packaging size and installation costs were higher with the turbocharger and aftercooler placed centrally, and a simpler installation at the free end was chosen. Although it gives a relatively longer installation the turbine exhaust position was similar to existing locomotives and total installed length was approximately 300 mm less than the 251 engine package.

Lubricating oil and water pumps were located at the free end with a gear drive from crankshaft, and were placed to connect to pipes from the locomotive filter and cooling modules. To improve engine design integrity and overhaul, hydraulic fasteners have been adopted where possible.

A summary of basic engine data is presented:

Bore	240 mm
Stroke	270 mm
Rated speed	1100 rev/min
Overspeed	1430 rev/min
Compression ratio	12.5:1
Target rating	(18.33 bar BMEP)
Growth rating	(22 bar BMEP)
Maximum firing pressure	145 bar

## Component Design

**Crankshaft and Main Bearings.** Rigorous analysis was carried out during the crankshaft design optimization process and took many interactive parameters into consideration: firing sequence, bearing length and width, fillet radius size and design, counterweight size web proportions, cylinder centers, bank stagger, and maximum number of cylinders in engine range.

Features established as desirable early in the concept design stage included nitrided surface treatment, plain fillet radii, and welded balance weights. These set the pattern for the ultimate design and had a large effect on the ultimate cylinder centers of 425 mm for all vee engines.

Using a number of computer programs, originated and developed in-house for crankshaft analysis, the peak bending and torsional stresses were calculated across the engine operating envelopes. Figure 3 shows the program structures and interaction. The use of a proprietary bearing program enabled bearing pressures and oil film thicknesses also to be analyzed and formed part of the crankshaft optimization program. Figure 4 demonstrates typical results of two of the parameters optimized.

Over the 720 deg cycle, the combined peak bending stresses and cyclic torsional stresses resulting from combustion, inertia, and applied cyclic torques were evaluated for the critical sections at fillet radii and crankpin oil holes where most fatigue failures occur. Three-dimensional finite element models of 1/2 crankthrow and 1/8 crankpin with an oil hole were analyzed to assist in validation of stress concentration effects and fatigue notch factors at these two points. Figure 5 shows the crankthrow loading and crankpin models. The results of the F. E. analysis were compared with crankshaft program predictions and were found to agree within 10 percent.

The combined results of the stress analysis in terms of mean and alternating stress components were compared with design limiting stresses of selected materials, the limiting stress being

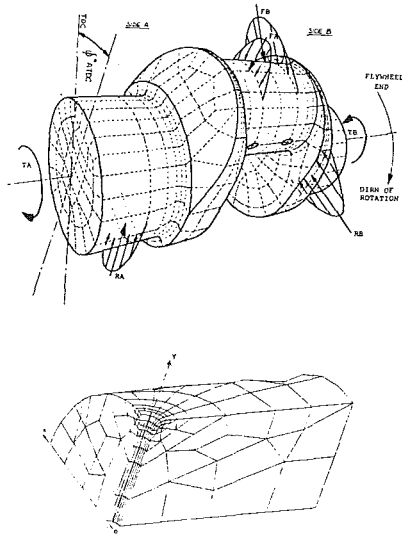
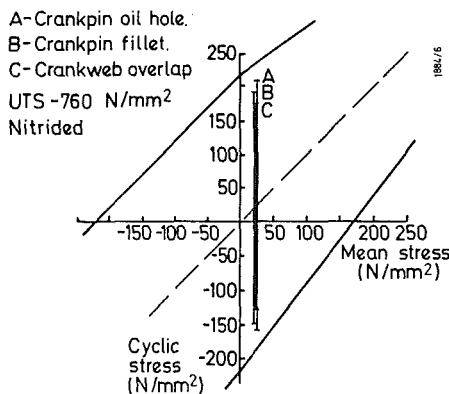
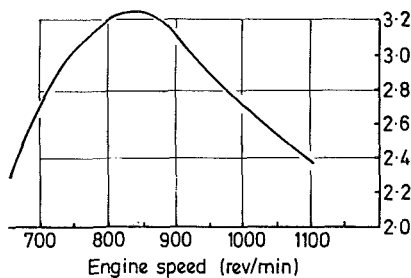


Fig. 5 Finite element mesh models of crankthrow and crankpin oil hole



V16 comparison of strength and stress 250 kW/cyl



V18 safety factor across speed range

Fig. 6 Crankshaft safety factors

obtained from a combination of endurance limit, size, surface finish and treatment, and safety factor required. Figure 6 shows the comparison of strength and stress for the V16 at 250 kW/cyl. at 1100 min<sup>-1</sup>. A minimum safety factor of 2.3 was obtained. The design criteria demanded a minimum safety factor of 2, which was determined by correlation between actual test data and design analysis of many engines. Analysis of all crankshafts showed the V18 to have the highest stress values. Safety factors through its speed range are shown in Fig. 6.

Maximum bearing pressures were 368 bar for the large-end bearing and 285 bar for No. 9 main bearing on the V18 engine. Minimum oil film thicknesses satisfactorily exceed minimum

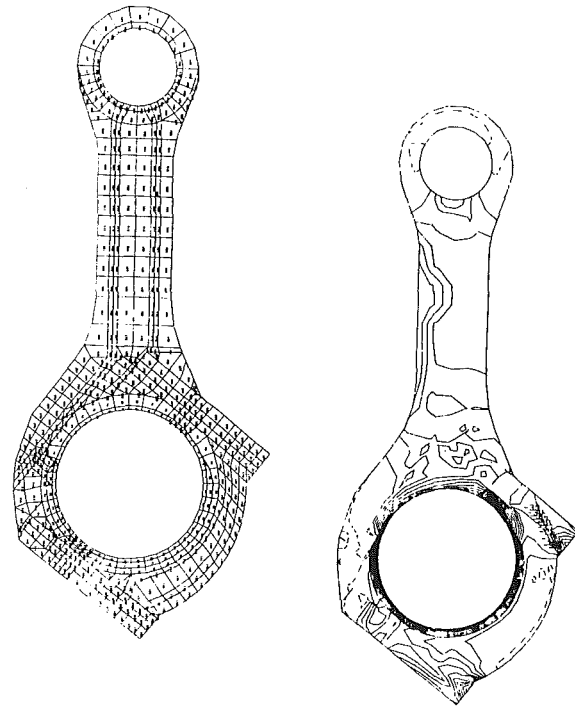


Fig. 7 Finite element model and maximum principle stress distribution

design criteria by 10 percent. Satisfactory rotating load conditions on main bearings at high-speed idle have been obtained by adjustment to balance weight systems.

Within the requirements of the functional specification there are no barred speed or load conditions throughout the engine range.

**Connecting Rod.** A side-by-side configuration of connecting rods was selected. This offered advantages of simple forging, machining, and large-end bearing arrangement. The disadvantage of the design is the small increase in engine length due to cylinder bank offset.

The connecting rod has an angle split large end optimized to provide adequate abutment faces while being able to be assembled through the cylinder bore. The thin-wall bearing shell and cap are fastened by four set bolts.

An F. E. analysis was used as a guide in optimizing the correct geometric configurations. The analysis was divided into two phases.

In phase 1, a static linear analysis was designed primarily to assess the con-rod forging design. The two-dimensional finite element model consisted of 617 quadrilateral shell elements as shown in Fig. 7 and solved for stresses and displacements by using ANSYS general purpose finite element program. The main objectives of this analysis were to calculate mean and alternating stresses, evaluate bore distortion, and gain a better understanding of the stiffness distribution throughout the connecting rod.

Three load cases were considered:

- (i) Assembly load (shell interference and bolt preload).
- (ii) Assembly load plus maximum firing load.
- (iii) Assembly load plus maximum inertia load; results combined for total stress ranges.

Bolt preloads, bearing shell interferences, firing, and inertia loads were suitably applied to the model to simulate operating conditions. To prevent rigid body motion, vertical and lateral soft springs properly grounded were used at the shank of the con-rod.

The F. E. results indicate that stresses throughout the con-

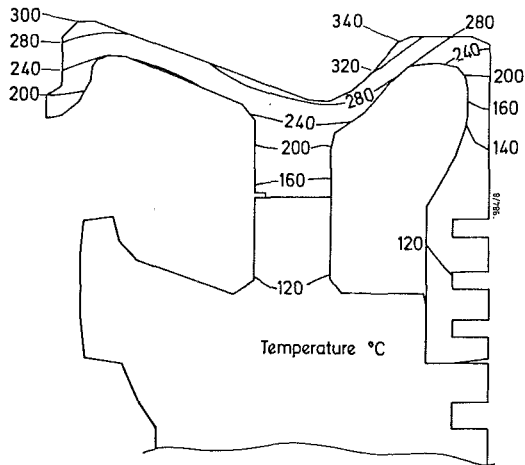


Fig. 8 Piston calculated temperature distribution

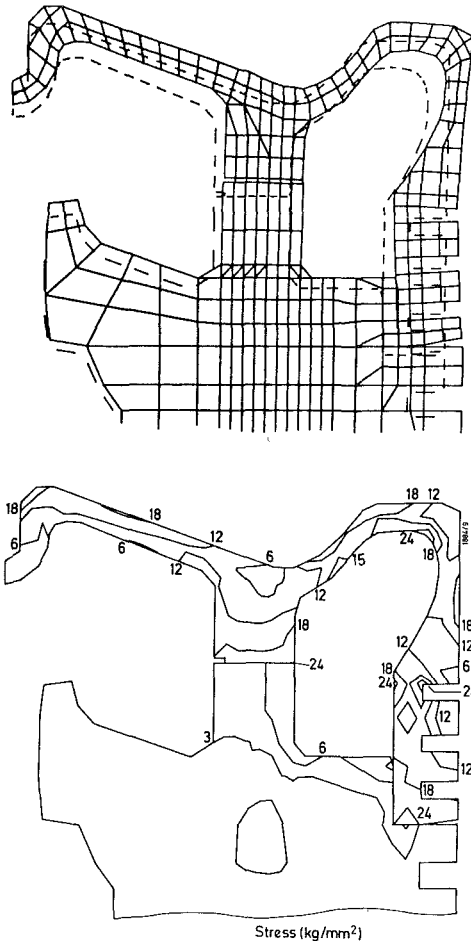


Fig. 9 Piston deformed shape and combined loading stress pattern

necting rod are within the safe operating limits when plotted on a Goodman diagram, and that the maximum bore distortions are acceptable. A typical stress contour is shown in Fig. 7 where the maximum principal stress distribution is plotted.

In phase II a static nonlinear analysis was performed. The objective of this analysis was designated primarily to assess the strength/stress state of the serrated joint and to study the dynamic behavior under operating conditions of the connecting rod and cap, such that relative movement within the joint could be eliminated.

To accomplish this purpose, the F. E. model generated in

phase I was modified to include a detailed mesh at the joint. The final model consisted of 895 elements of which 129 were two-dimensional interface elements at the joints and at the crankpin/bearing interface.

The forces applied were the same as phase I. The boundary conditions were slightly modified to meet the purpose of this study. The results indicate that stresses and deformations within the joint are within acceptable limits and that during the various loading conditions, gapping and/or sliding is not likely to occur.

**Piston.** To contain thermal stresses and control cooling oil at 22 bar BMEP, a two-piece design with forged steel crown and forged aluminum body was necessary for the specific rating of 0.55 kW/cm<sup>2</sup> and is a logical development of the piston used in the 251 engine.

Piston proportions are generous to allow combustion bowl, ring pack, and skirt profiles to be developed for alternative fuels, lubricating oils, and higher firing pressures and maintain durability levels.

Initially, compression ratio is 12.5:1, appropriate to meet cold starting, fuel consumption, and part-load running requirements.

The crown is retained by four internal bolts and supplemented by a flexible collar to improve joint resilience against thermal expansion and contraction of the aluminum body.

Piston pin bosses and con-rod small end are stepped to minimize pin bending. Mean bearing pressures are 540 bar in the piston body and 630 bar in the connecting rod.

During the piston design particular attention was given to the design aspects which affect the performance characteristics (low fuel consumption and clear exhaust), as well as the thermal and mechanical loading behavior for both the piston cap and piston body.

The conflicting requirements of low piston thermal loading and linear protection have been balanced to achieve the best compromise possible during the piston design. The torus has been adjusted to protect the liner from fuel spray cone impingement and to avoid excessive thermal loading. A finite element representation of the calculated temperature distribution of the two-piece piston is shown in Fig. 8.

Particular attention was devoted to the study of the joint behavior between the piston body and cap to minimize fretting and to ensure continuous contact throughout the full cycle of the engine. For a better study of this effect nonlinear elements at the joint were added to the two-dimensional axisymmetric F. E. model of the piston body and cap so that any variation in bolt loading and/or slight modifications of the piston geometry during the design could be properly assessed in influence studies at the body-cap joint.

Deflection and stresses throughout the piston body and cap due to the individual and the combined assembly, thermal, and mechanical loading were optimized to ensure safe piston operation.

The deformed shape and Von Mises stress pattern distribution throughout the piston for the combined loading are shown in Fig. 9.

**Cylinder Liner.** The centrifugally cast iron liner has a deep bore cooled flange to avoid excessive mechanical and thermal stresses at 22 bar BMEP. The inherent stiffness of the flange provides an even distribution of clamping load around the cylinder head joint and the flange fillet radius is positioned low down and away from high mechanical and thermal loads. Coolant at the bottom of the liner passes along the block, which has no diaphragms, a feature successfully used on the 251 engine. Cooling in the higher critical area is now controlled by the drillings in the thick flange. The F. E. analysis

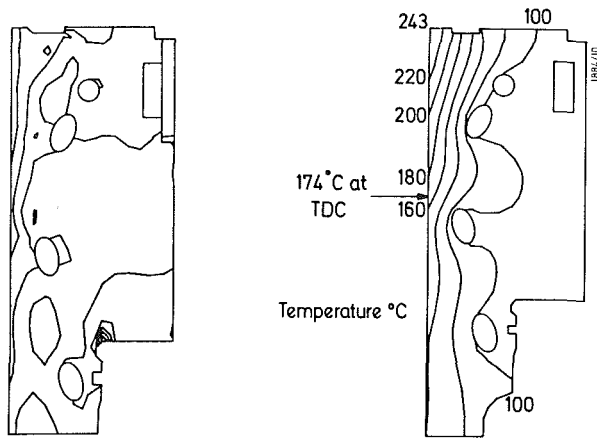


Fig. 10 Cylinder liner stress and temperature pattern

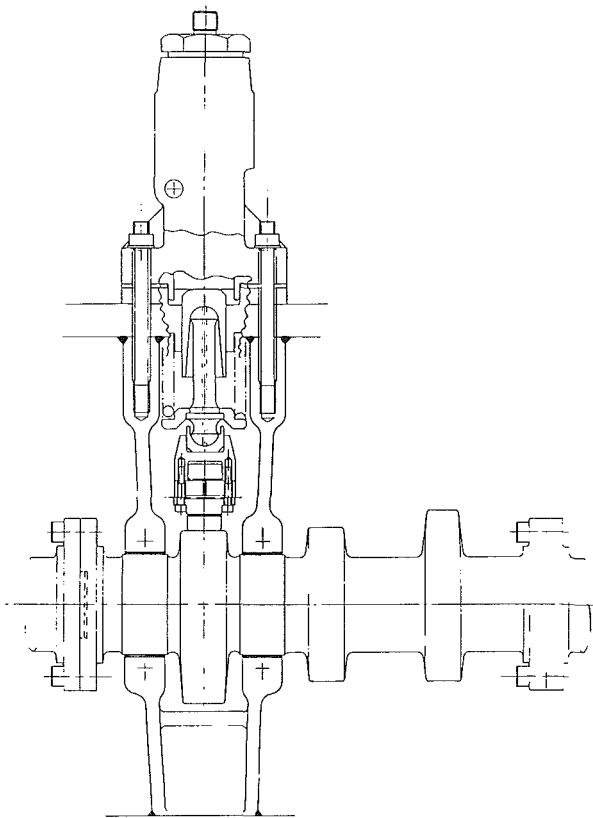


Fig. 11 Arrangement of fuel pump drive

has assisted in positioning the drillings to obtain correct cooling and minimize hot bore distortion.

The cast-iron sleeve insert is retained as on the 251 engine to provide a suitable replaceable sealing face against the cylinder block.

Although the basic geometry of the liner was finalized in the early design stages, particular attention was devoted to the selection of the size and orientation of the coolant drillings and the thermal characteristics through the liner. This was of particular interest since distortions of the cylinder liner had to be predicted fairly accurately so that sufficient running clearance was allowed between the cylinder liner and piston body in order to minimize any incident of seizure during development.

Based on heat flux, and heat transfer coefficients already established from previous analysis, or calculated using empirical equations, thermal boundary conditions throughout

the cylinder liner were found. These were then applied to a two-dimensional axisymmetric F. E. model to study the thermal behavior of the liner range as shown in Fig. 10.

The resulting temperature data were then used to assess and optimize the cooling conditions and hot bore distortion and study the fit between the crankcase and liner. The above parameters combined with the mechanical loading were then used to assess and minimize the deflection and stresses throughout the cylinder liner.

**Cylinder Block.** With the successful and long experience gained from previous Bombardier cylinder blocks, and a requirement to use present production facilities, the design and method of construction for the B2400 engine have been tailored toward a block fabricated from steel plate. Complexity of the block and welds in high-stress areas was minimized by the use of steel forgings and castings. Although more expensive than a similar iron design, the benefits of steel for locomotive duty are lighter weight and increased stiffness.

An underslung crankcase has been designed with a deep skirt for torsional rigidity. Long vertical studs and cross bolts for the main bearing provide high structural rigidity around the crankshaft. During design optimization, reference was made to the influence of installation height and mounting feet positions.

The essential features of the engine structure can be seen in Fig. 1. The main bearing saddles are welded to an extruded Vee section spline. Longitudinal sheets running the length of the engine are welded to the spline at the center of the Vee and to webs on the bearing saddles. These sheets form the side of the water jacket and transmit the firing loads down to the main bearings. The load bearing structure is completed by a thick plate welded onto the top of the side sheets forming the top deck. The cylinder head studs are threaded into this plate which also supports the liner flange. A top plate ties the two banks together and forms an air chest in the Vee. The top plate also ties the two cylinder banks of the Vee together, reducing noise and improving structural rigidity.

A steel casting welded to the cast saddle and top deck supports the camshaft bearings, one on either side of the fuel pump cam. The fuel pump is placed over the fuel cam and the pump stud loads pass completely through the top deck into the casting, eliminating pulsating tensile loads in the welded joint (see Fig. 11).

To make sure that stresses and deflections of the crankcase are within tolerable and admissible limits, a finite element stress analysis was performed on the engine block. Calculations of varying complexity were carried out on the prototype frame, starting with a simple two-dimensional F. E. model used to optimize the position and the size of the main bearing studs, and cross bolts required to prevent the sideways movement of the main bearing caps. A partial three-dimensional F. E. model was used to assess the bending and torsional effects of the inertia, gas loading, and various crankcase loadings on the engine frame. Figure 12 shows the three-dimensional finite element model used to analyze the prototype engine block.

The analysis was done using the NASTRAN F. E. package with a total of 1300 plate elements and 64 solid elements.

Although the three-dimensional model represents only a typical section of the total engine block, its boundaries were chosen such that planes of symmetry and antisymmetry could be used to assess the effect of the transmitted deflections and loadings on the model boundary conditions due to the adjacent cylinder loadings.

The basic criteria used to determine acceptable geometry and the cross-sectional properties for the crankcase plates, forgings, and welds were:

(i) Maintain fatigue stress levels for full penetration welded



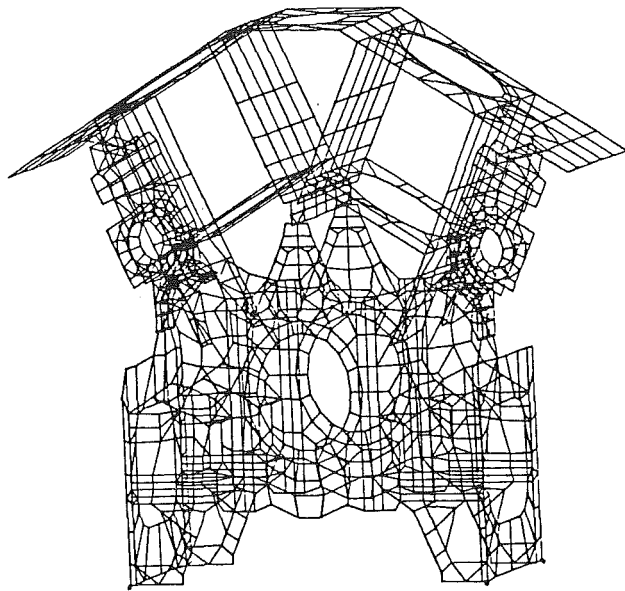
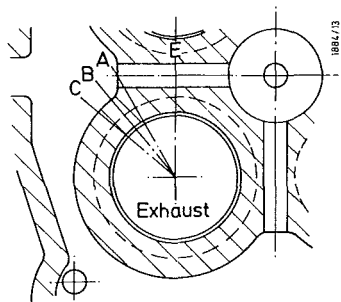
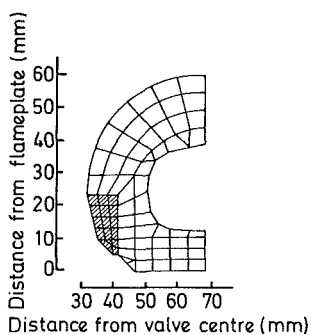


Fig. 12 Cylinder block three-dimensional finite element model



Sections for 2D F.E. analysis



Mesh model of section B

Fig. 13 Cylinder head thermal analysis

joints below  $34 \text{ N/mm}^2$  to ensure a fatigue life with a variable load factor of 108 cycles [5-7].

(ii) Control and maintain the relative deflection between an adjacent pair of main bearings within  $0.0005 \text{ mm/mm}$  of horizontal distance between them. This will allow a longer main bearing life [5].

(iii) Determine the basic form of the structure to ensure adequate bending and torsional stiffness within the crankcase. The low fatigue strength is the main disadvantage of welded joints compared to steel plate or forging and is the reason for limiting weld stresses to  $34 \text{ N/mm}^2$ .

**Cylinder Head and Valve Gear.** The cylinder head is an iron casting of unit design with four valves and a central injector. Valve operating gear and side entry injector pipe are easily accessible on the outside of the vee.

Alternative cylinder head stud arrangements with four to eight studs were investigated; four studs required deep countersunk holes into the water jacket to distribute the clamping load under the liner flange. To suit the philosophy of the fabricated block design, crankshaft and cylinder head studs were eventually fastened into the thick top deck, distributing firing and stud loads into the water jacket welded sheets and liner flange.

The outer walls of the cylinder head casting are conical in order to concentrate the stud load around the cylinder head joint. A double-decked head design has been adopted to accommodate the high thermal and mechanical loads. The lower flame deck is thin enough to limit gas face temperatures to acceptable values and minimize thermal distortion and stresses while the upper conical deck is designed to rigidly carry the firing loads. Coolant from the liner is delivered from the liner by four transfer ports into a lower water jacket formed between the two decks. It is then directed through drillings in each of the four valve bridges to the annular space around the injector sleeve.

Valve sizes were selected to give a nominal gas velocity of  $57 \text{ m/s}$ , at  $1100 \text{ rev/min}$ , below the limiting design figures set at  $60$  and  $70 \text{ m/s}$  for inlet and exhaust valves, respectively, to assist low fuel consumption. Port blowing tests will be carried out on prototype castings with the aim of improving port shape to improve fuel consumption.

A conventional roller-lever cam follower, push rod, rocker arm, and bridge piece actuate the valves, all bearings and surfaces being oil pressure fed for durability.

To assess the thermal loading and temperature distribution on the cylinder head fire deck region, two and three-dimensional finite element analyses were carried out using the commercially available computer programs NASTRAN and ANSYS. Two flame plate designs were analyzed: bore cooled flame deck and conventional cored and drilled design. Methods of predicting heat flow into the flame deck and exhaust valve were established from heat flow measurements of many similar engines. These predictions allowed the heat flow conditions in the B2400 engine to be calculated. Thermal and mechanical characteristics of steel and flake, nodular and vermicular irons were examined.

In conjunction with the above analysis, to assess the heat distribution between the cylinder head and the exhaust valves, the exhaust valve bridge was modeled together with the exhaust valve. This resulted in a better understanding of the heat transfer conditions and the thermal contact resistance effect that would arise when using differing valve seat materials.

Particular attention was taken in assessing the temperature distribution and thermal characteristics around the cored twin deck region which was finally selected. The positions of the two-dimensional finite element sections chosen to study these characteristics are shown in Fig. 13. These are vertical sections in the area between the two exhaust valves, spaced radially about the valve centerline, and were modeled axisymmetrically about the valve center. Each section was terminated at the centerline of the relevant water passage.

A typical metal section, complete with finite element mesh, is shown in Fig. 13, and the calculated temperature variation through the section is shown in the form of isotherm plots in Fig. 14. Metal surface temperatures measured radially along the valve seat and flame deck are shown in Fig. 14. The maximum temperature occurring at the valve seat is shown as  $450^\circ\text{C}$ . When account has been taken of heat flow in the third dimension and valve rotation, true maximum temperatures are likely to be 10-15 percent lower at  $410^\circ\text{C}$ . Based on previous

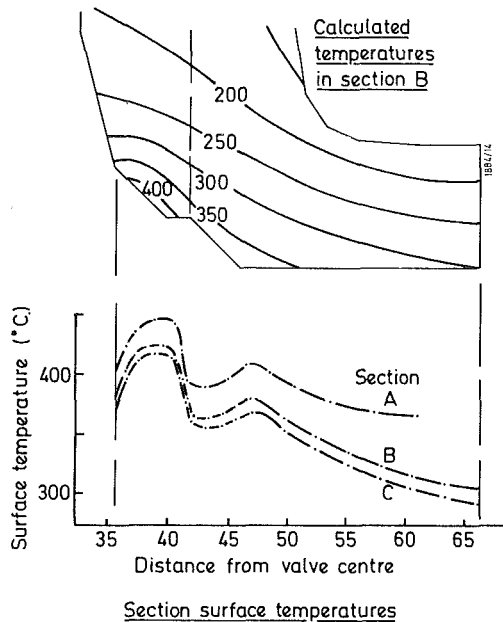


Fig. 14 Cylinder head thermal analysis

experience of heat flow and temperature differences between the exhaust valve and cylinder head and the effect of seat contact resistance, the seat of the valve is expected to be around 450°C, which is a very acceptable value for an engine running on distillate fuel.

Flake alloy cast iron was selected. Several variations of the alloy content on the chemical composition and its effect on the mechanical properties were studied. Consideration was given to parameters such as modulus, elongation, thermal conductivity, thermal expansion, and microstructural characteristics in order to achieve mechanical properties which will ensure safe operation in operating conditions.

**Camshaft, Fuel Pump, and Gear Drive.** The camshafts are mounted in outboard bearings in the cylinder block. For a locomotive duty with restricted accessibility under the hood, single-cylinder forged camshaft elements with flange bolted joints are preferred for ease of servicing.

Alternatives to tunnel bearings and split bearings were studied. Split bearings were preferred to facilitate initial camshaft assembly, ease of servicing, and replacement of single elements and minimize bearing friction loss. Calculations showed a nominal reduction of 6 kW (0.5 gram of fuel consumption) between split and larger tunnel bearings.

Each flanged camshaft element is supported by two split bearings, one on either side of the fuel pump cam, to minimize bending deflection and provide a rigid fuel pump drive. One element covers the complete range of vee engines except the V18 which has one additional element with different bolt phasing.

The fuel pump drive (Fig. 11) has a roller lever cam follower

with a short pushrod and spring, and a high stiffness factor is obtained between camshaft and fuel pump.

A conventional pump, pipe, and injector system has been selected. Of the alternative systems investigated, it was the most attractive system for locomotive servicing and development. With the development of fuel injection systems for 2000 bar underway, the camshaft and gear drive were sized to allow use of these pressures should this be found to be beneficial during the life of the engine.

A compound gear train at the drive end is used to minimize gear diameters and cylinder block apertures providing maximum support between engine and generator. This is driven by a split crankshaft gear. All gears, camshaft, and thrust bearings can be removed with the engine and generator in situ. V8 balancer shafts can be fitted without changes to the gear train.

## Conclusions

The basic objectives—to design a long-lived family of heavy-duty locomotive engines and establish the basic parameters that they will retain during their life—have been met. Unproven ideas have not been incorporated into the basic design.

The first prototype engine has been built and is now under developmental testing.

During its life, engine design and performance improvements and adherence to stricter environmental legislation will be required. These may have a significant effect on component details but it is expected that the generous design features will enable alternative engine specifications to be built from the basic structure.

Tools and equipment for engine servicing and maintenance have been reviewed and simplified.

## Acknowledgments

The authors would like to thank their colleagues for their assistance, and the Management of both Bombardier and Ricardo for permission to publish this paper.

## References

- 1 Taylor, D. H. C., "Diesel Engine Development and Design: A View to the Future," North East Coast Institution of Engineers and Shipbuilders, May 1984.
- 2 Steiger, H. A., "2 Stroke Versus 4 Stroke Cycle. A Report About Tests With Two Otherwise Absolutely Similar Experimental Trunk Piston Diesel Engines of 320 mm Bore," Paper No. A3. CIMAC, 1968.
- 3 Schur, T., "Developing a High Powered Diesel Engine for Railway Traction," ASME Paper, Apr. 1967.
- 4 French, C. C. J., and Taylor, D. H. C., "An Investigation Into Diesel Engine Operation at Very High Ratings," CIMAC, Vol. 1, 1975.
- 5 Moreland, G. W., and Flear, B. S., "Design of a Space Frame Crankcase for Large Medium Speed Diesel Engine," Symposium of Mechanical Design and Diesel Engines, Mar. 1967.
- 6 Briner, M. J., and Boregeand, P., "Analysis of Diesel Engine Structures With Special Reference to Traction Applications," *Sulzer Technical Review*, Research Number, 1968.
- 7 Howe, A. G., and Watson, H., "Design Methods of Development of Medium Speed and High Speed Oil Engines," *Institute of Marine Engineers Transactions*, Nov. 1967.

# Comparing Expanders for Direct Recovery of Exhaust Energy From a Low-Heat-Rejection Diesel

C. A. Amann

General Motors Research Laboratories,  
Warren, MI 48090-9057

*Part-load performance of a compound low-heat-rejection (LHR) engine is estimated at constant speed. The engine consists of an LHR diesel reciprocator geared to a supercharging compressor and an exhaust expander. Two classes of expander differing substantially in both flow characteristics and energy-extraction principles are ranked: aerodynamic (reaction turbine) and positive-displacement (internal expansion). To focus the comparison on differences in fundamental expander characteristics rather than differences in efficiency levels among specific samples of each type of expander, each is assigned an efficiency of 100 percent at its best-efficiency point. Although differences in fundamental characteristics between the expanders were sufficient to rank them on a performance basis, these differences were largely overshadowed by the magnitude of the indicated work developed in the reciprocator relative to the work developed by the expander.*

## Introduction

Heat conservation in diesel engines has recently enjoyed increasing interest. The concept most often advanced involves elimination of the conventional liquid cooling system, with the resulting increase in operating temperatures of the engine structure being accommodated by the use of high-temperature ceramics. The idea behind such a low-heat-rejection (LHR) diesel is to convert heat formerly rejected to the coolant into useful brake output power.

A previous study showed that most of the heat saved through elimination of the cooling system appears in the exhaust stream in the form of increased gas temperature rather than as increased power on the engine crankshaft [1]. This makes an effective exhaust-energy recovery system an essential part of any successful LHR diesel. Such a recovery system can be of either the direct or the indirect type.

In the direct recovery system, energy is extracted directly from the exhaust stream, e.g., by a turbine. Turbocharged and turbocompound engines typify direct recovery systems. These particular approaches fulfill another requirement of the successful LHR diesel. The increased wall temperatures of an uncooled cylinder heat the fresh incoming charge, decreasing engine volumetric efficiency. Unless the density of the trapped fresh charge is increased by supercharging, lower engine brake thermal efficiency can actually result from conserving heat rejected to the coolant in the LHR engine [1]. Both turbocharging and turbocompounding make use of supercharging compressors.

In the indirect recovery system, heat energy is extracted from the exhaust stream across a heat exchanger to operate an

auxiliary "bottoming-cycle" engine. The Rankine (both steam [2] and organic working fluid [3]), Brayton [4], and Stirling [5] cycles have all been studied for this purpose in the heavy-duty truck application. Thus far, the capital and maintenance costs of such bottoming-cycle engines have been judged non-competitive on an economic payback basis in that application [6].

Direct energy recovery is the focus of the present study. Specifically, the compound engine arrangement of Fig. 1 is considered as it might be applied to the light-duty application, e.g., the passenger car, pickup truck, or van. Two of the characteristics that distinguish these uses from the heavy-duty truck are the importance of rapid engine response to a sudden increase in demanded engine power and the greater significance of fuel economy at light loads. With respect to the first of these, an often-cited shortcoming of the turbocharger has been the delay in boost pressure with which it responds to a sudden depression of the accelerator pedal. This delay arises from the lag displayed by the turbocharger in reaching its new equilibrium operating speed when the reciprocator is ac-

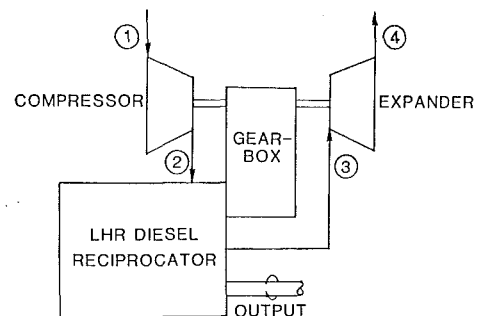


Fig. 1 Component arrangement for compound engine

Contributed by the Internal Combustion Engine Division and presented at the Energy-Sources Technology Conference and Exhibition, Dallas, Texas, February 15-20, 1987. Manuscript received at ASME Headquarters December 5, 1986. Paper No. 87-ICE-26.

celerated. The arrangement of Fig. 1 avoids this criticism by gearing the supercharging compressor to the engine crankshaft. With respect to the second characteristic of light-duty application, in this study brake thermal efficiency trends are considered at a selected speed over the full range of engine load.

There are two basic types of compressor and expander that can be selected to complete the block diagram of Fig. 1. One is the aerodynamic type, as typified by the centrifugal compressor and the axial-flow turbine expander. The other is the positive-displacement type, as typified by the helical-screw compressor advanced by Lysholm [7] and its expander counterpart. In this study, a positive-displacement helical-screw compressor is chosen for supercharging. The primary purpose of the study is to compare aerodynamic and positive-displacement expanders as they affect part-load trends in brake thermal efficiency.

### Basic Relationships

The brake output of the compound engine of Fig. 1 can be divided into five components. Using mean effective pressure (mep) as a displacement-normalized indicator of power at the specified speed

$$\bar{p}_b = \bar{p}_i + \bar{p}_f + \bar{p}_c + \bar{p}_p + \eta_e \bar{p}_e \quad (1)$$

where  $\bar{p}_b$  = engine brake mep;  $\bar{p}_i$  = indicated mep developed in the cylinders;  $\bar{p}_f$  = friction mep of the diesel reciprocator;  $\bar{p}_c$  = mep of supercharging compressor;  $\bar{p}_p$  = pumping mep of reciprocator;  $\bar{p}_e$  = mep of 100 percent efficient expander;  $\eta_e$  = expander efficiency.

To evaluate the terms in equation (1), the components of Fig. 1 must be matched so that at all steady-state operating conditions, the following equations are satisfied (station numbers defined in Fig. 1):

$$(1 + F)\dot{m}_1 = (1 + F)\dot{m}_2 = \dot{m}_3 = \dot{m}_4 \quad (2)$$

$$(p_2/p_1)(p_3/p_2)(p_4/p_3)(p_1/p_4) = 1 \quad (3)$$

where  $F$  = fuel-air ratio;  $\dot{m}$  = mass flow rate;  $p$  = absolute pressure.

The four-stroke direct-injection LHR diesel reciprocator on which this study is based has a displacement of 3.2 L. It has a compression ratio of 17, a bore/stroke ratio of 0.9, a deep re-entrant combustion bowl fueled by a multi-spray injector, and two valves per cylinder. The small squish height necessitates a modest valve overlap in order for the valves to clear the piston crown near top dead center. The cylinders are joined to the supercharging compressor by an adiabatic intake manifold and to the expander by an adiabatic exhaust manifold. For present purposes the reciprocator is assigned a fixed intermediate speed of 2500 rpm. An air-fuel ratio of 24 is specified for maximum load and then varied through the com-

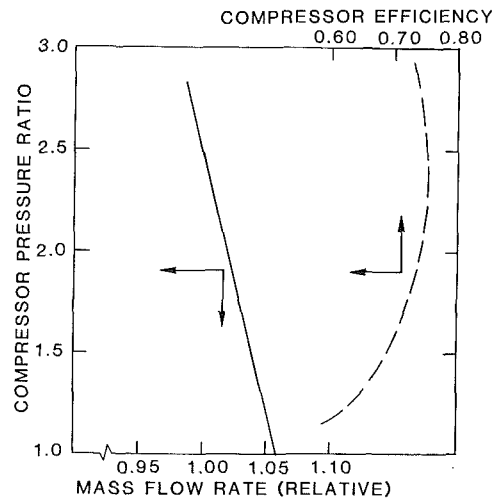


Fig. 2 Constant-speed characteristic of supercharger

plete part-load range. Injection timing is set for best economy, which occurs for these conditions at a nominal injection advance of 6 deg BTDC. Reciprocator indicated mep in equation (1), as developed during the compression and expansion strokes, is calculated as a function of fuel rate, intake pressure and temperature, and exhaust back pressure using a computer model. This model includes a burning submodel patterned after that of Whitehouse and Way [8] and a heat transfer submodel modified from that of Woschni [9]. The thermal resistance of the cylinder head, piston and liner is lowered to effect a 75 percent reduction in full-load heat rejection relative to a conventional liquid-cooled version of the same engine and held constant over the load range. Radiational heat loss is not treated.

Assignment of a friction mep in equation (1) for the four strokes of the LHR reciprocator is problematic. At the cylinder-wall temperatures of the LHR diesel, a suitable liquid lubricant with satisfactory life has yet to be identified. Gas leaking from the combustion chamber has been used as a cylinder lubricant in a laboratory setting [10], but it remains to be established that this approach is reasonable for vehicular application at acceptable leakage rates when the extreme range of ambient temperatures and the uncontrolled startup and shutdown procedures practiced in light-duty vehicles are encountered. The use of solid lubricants has been suggested, but the merit of that approach awaits demonstration. In the absence of better data, a friction mep of 187 kPa is assigned. This value, assumed invariant with load, is typical of current diesel engines of this size operated at 2500 rpm with petroleum-based lubricant.

The constant-speed characteristic of the screw compressor is

### Nomenclature

$C_{is}$  = velocity equivalent of isentropic enthalpy drop  
 $D$  = reciprocator displacement  
 $F$  = gravimetric fuel-air ratio  
 $g$  = gravitational constant  
 $k$  = ratio of specific heats for air  
 $\dot{m}$  = mass flow rate  
 $N$  = rotational speed  
 $p$  = absolute pressure  
 $\bar{p}$  = mean effective pressure

$P$  = power  
 $R$  = gas constant  
 $T$  = absolute temperature  
 $U$  = tangential blade speed  
 $Y = (p_2/p_1)^{(k-1)/k} - 1$   
 $Z = 1 - (p_4/p_3)^{(\gamma-1)/\gamma}$   
 $\gamma$  = ratio of specific heats in exhaust gas  
 $\eta$  = adiabatic efficiency  
 $\Pi$  = built-in pressure ratio

### Subscripts

$b$  = brake  
 $c$  = compressor  
 $e$  = expander  
 $f$  = friction  
 $i$  = indicated  
 $p$  = pumping  
 $1$  = compressor inlet (= ambient)  
 $2$  = compressor discharge = reciprocator inlet  
 $3$  = reciprocator discharge = expander inlet  
 $4$  = expander discharge (= ambient)

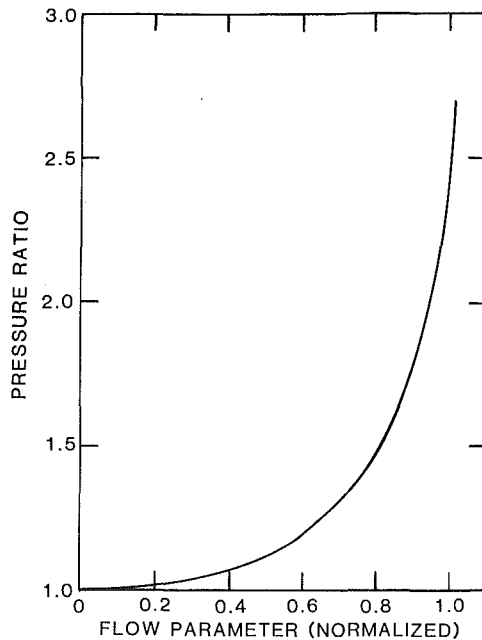


Fig. 3 Flow characteristic of reaction turbine

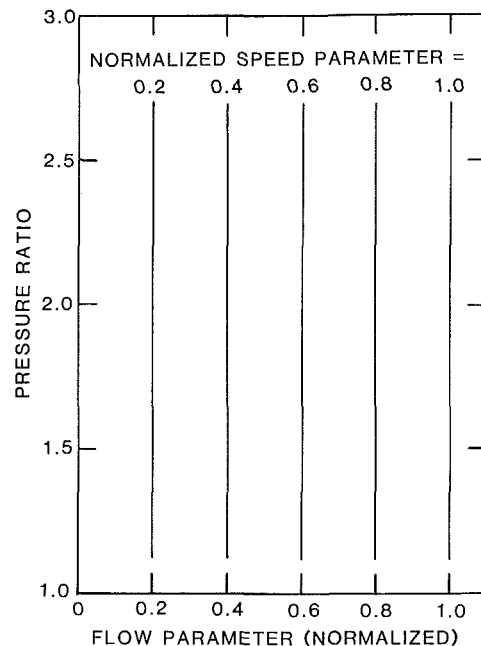


Fig. 4 Flow characteristic of positive-displacement expander

shown in Fig. 2. The full-load design point for the compound engine of this study is selected at a compressor ratio of 2.5. The power  $P_c$  required to drive the compressor is given by

$$P_c = \frac{\dot{m}_1}{\eta_c} \frac{RkT_1 Y}{(k-1)} \quad (4)$$

where  $\dot{m}_1$  = compressor mass flow rate;  $R$  = gas constant;  $k$  = ratio of specific heats for air;  $T_1$  = compressor inlet absolute temperature;  $Y = (p_2/p_1)^{(k-1)/k} - 1$ ;  $\eta_c$  = compressor efficiency.

The compressor power is converted to mep by

$$\bar{p}_c = \frac{2P_c}{DN} \quad (5)$$

where  $D$  = reciprocator piston displacement;  $N$  = reciprocator speed.

Pumping mep in equation (1) reflects the energy expended in passing the airflow through the cylinders during the gas-exchange process (intake and exhaust strokes) of the reciprocator. This component is always negative in a naturally aspirated engine, but in a supercharged engine like that portrayed in Fig. 1, it can assume positive values when the compressor discharge pressure exceeds the exhaust back pressure. In this study the pumping mep is determined by the same reciprocator model that provides indicated mep.

The power output from the expander is given by

$$P_e = \frac{\dot{m}_3 \eta_e R \gamma T_3 Z}{\gamma - 1} \quad (6)$$

where  $\dot{m}_3$  = expander mass flow rate;  $\gamma$  = ratio of specific heats for exhaust gas;  $T_3$  = expander inlet absolute temperature;  $Z = 1 - (p_4/p_3)^{(\gamma-1)/\gamma}$

This power is converted to mep by the approach of equation (5). To illustrate the differences between aerodynamic and positive-displacement expanders, results are presented in turn for both the case of a perfect expander (i. e., 100 percent efficient) and the case with representative expander-efficiency trends.

### Expander Flow Characteristics

In matching the components according to equations (2) and (3), it is necessary to define the flow characteristics of the ex-

pananders considered as well as those of the compressor. In Figs. 3 and 4, expander pressure ratio is plotted against a flow parameter,  $\dot{m}_3 \sqrt{T_3}/p_3$ , for the aerodynamic expander and the positive-displacement expander, respectively.

The flow parameter on the abscissa has been normalized to the value for each expander at a pressure ratio of 2.5, which is the expander full-load design point chosen in this study. Given that the chosen compressor design-point ratio is also 2.5, it follows that when the reciprocator is running at full load, its intake and exhaust pressures are equal. Full load for the reciprocator is defined by an air-fuel ratio of 24.

The aerodynamic-expander characteristic of Fig. 3 is for a reaction turbine that follows the Stodola ellipse law. For a fixed inlet-gas state, its flow capacity is independent of turbine speed. The flow characteristics of Fig. 4 are for a generic constant-displacement expander. In contrast, for a fixed inlet state, its flow rate is directly proportional to speed but is independent of pressure ratio at a given value of speed parameter  $N_e/\sqrt{T_3}$ . It is reasonable to wonder whether these radical differences in flow characteristics could produce part-load thermal efficiency differences in the compound LHR engine of Fig. 1. Investigating that question is the objective of this study.

The positive-displacement expander most often suggested for use with the LHR diesel is one of the helical-screw type. It should be recognized that at a fixed value of the speed parameter the value of the flow parameter for such an expander is not strictly independent of pressure ratio because of leakage through the rotor clearance space. It is this leakage that is primarily responsible for the slight inclination from vertical of the compressor speed line in Fig. 2. Because the speed-line slope of a real machine depends of the details of its design, the general class of positive-displacement expanders is approximated generically here by vertical speed lines. This approximation is in keeping with that made for the turbine that its flow parameter is independent of speed. In both cases the resulting expander characteristics adequately capture their significant features for this study.

### Results of Flow Matching

The flow rates and pressure ratios for the arrangement of Fig. 1 were matched according to equations (2) and (3) by

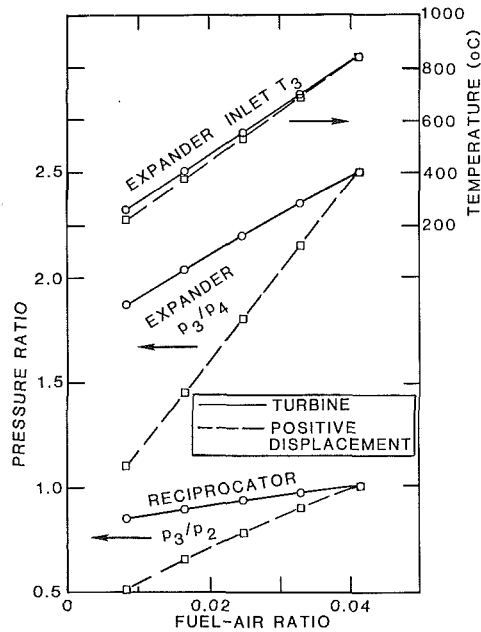


Fig. 5 Pressure ratios and temperatures versus load at constant speed

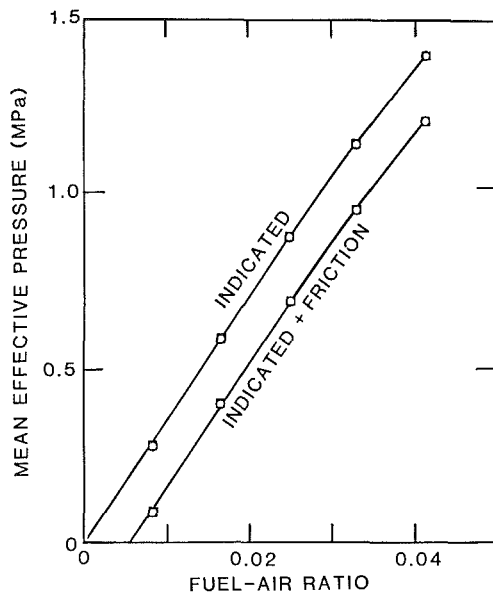


Fig. 6 Reciprocator mean effective pressure at constant speed

employing Figs. 2, 3, and 4, and the computer model of the reciprocator. The resulting reciprocator pressure ratios ( $p_3/p_2$ ) and expander pressure ratios ( $p_3/p_4$ ) are plotted against fuel-air ratio in Fig. 5 for the two expander types, along with expander inlet temperature. Because mass airflow rate is nearly constant at the fixed 2500 rpm reciprocator speed of this analysis, as constrained by the positive-displacement supercharging compressor (see the flow characteristic of Fig. 2), fuel rate is essentially proportional to fuel-air ratio in this study. Thus the fuel-air ratio points plotted in Fig. 5 and subsequent figures correspond nominally to 20, 40, 60, 80, and 100 percent of full-load fuel flow.

Since this analysis excludes pressure losses in the intake and exhaust systems, the pressure ratio of the supercharging compressor can be obtained from Fig. 5 by dividing the expander pressure ratio by the reciprocator pressure ratio. With both expanders, the pressure ratio of the supercharging compressor falls slightly as engine load (fuel-air ratio) is reduced, from 2.5

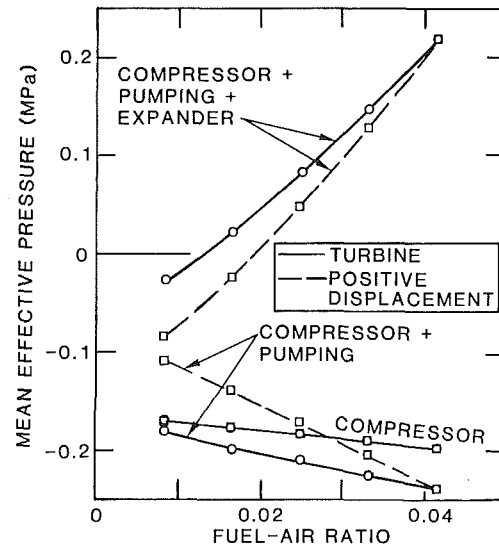


Fig. 7 Contribution to mean effective pressure from compounding, 100 percent expander efficiency

at full load to around 2.2 when the fuel rate is decreased to 20 percent of full load.

The curves for both expanders in Fig. 5 converge at the full-load fuel-air ratio, as specified by the design point. What is particularly noteworthy in the fact that as load (fuel-air ratio) is decreased, expander pressure ratio falls much more quickly for the positive-displacement machine than for the turbine. This results in a greater pressure drop across the reciprocator for the positive-displacement expander, as reflected by the lower pair of curves, and consequently a somewhat lower expander inlet temperatures for the positive-displacement expander at part load. These differences arise in reconciling the radically different flow characteristics of Figs. 3 and 4 for the two expander types with equations (2) and (3).

In Fig. 6, both the indicated mep and indicated plus friction mep for the reciprocator alone are plotted against fuel-air ratio when it is operated with each of the two expanders. The upper curve represents the first term on the right side of equation (1), and the lower curve is the sum of the first two terms in this equation. Although it was seen in Fig. 5 that expander selection had a significant effect on reciprocator exhaust back pressure, reciprocator indicated performance is clearly insensitive to expander selection in this engine because of its modest valve overlap.

The last three terms on the right side of equation (1) are the subject of Fig. 7. Beginning with the compressor mep, the two expanders share a common curve. Compressor mep is negative, of course, denoting work expended by the engine to drive the supercharging compressor.

When the pumping mep generated by the reciprocator during its exhaust and intake strokes is added on, the more favorable pumping mep of the positive-displacement expander is evident in Fig. 7, but that comes at the expense of a lower pressure ratio for the expander. As a result, when the work output of a perfect expander (efficiency = 100 percent) is added in, the turbine emerges superior, as shown in by the uppermost pair of curves. This reversal is due to the fact that for a given available pressure ratio across a device, the perfect turbine is more effective in extracting work than is the piston of the reciprocator [1]. Thus the reaction turbine comes out ahead at a given fuel-air ratio because it distributes more of the pressure drop available on the exhaust side of the reciprocator to the turbine and less to the gas exchange process in the reciprocator.

These upper curves illustrate a problem associated with

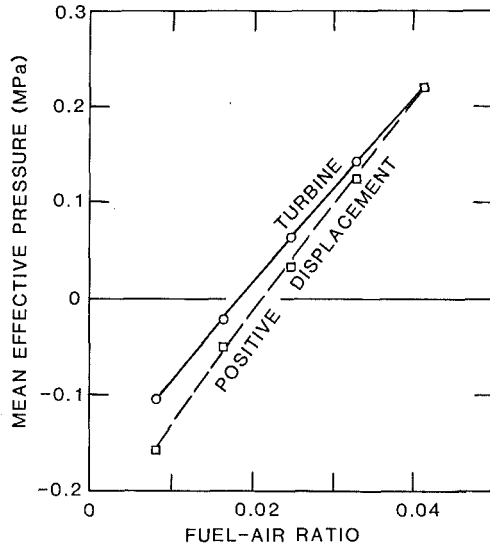


Fig. 8 Contribution to mean effective pressure from compounding, including expander inefficiency

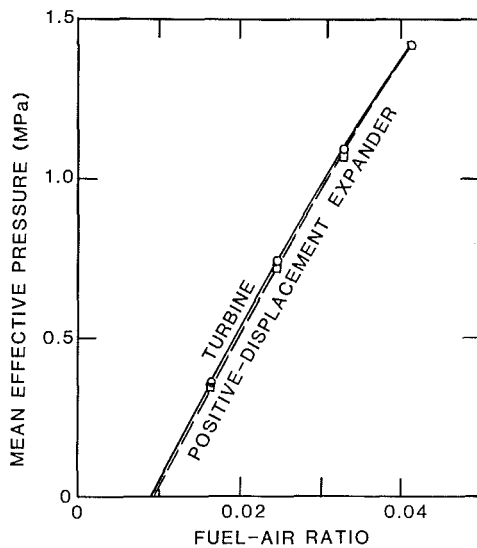


Fig. 9 Mean effective pressure of compound engine at constant speed

compounding a light-duty diesel. Although the additional output work generated can be substantial at heavy loads, compounding may actually reduce net output at a given fuel rate.

### Expander Efficiency

While Fig. 7 shows the effect of expander characteristics on the compound engine fitted with a perfect (100 percent efficiency) expander, ultimately the inefficiency of the expander must be considered. Efficiency levels vary in a given type of expander from one design to the next, but beyond that, there are fundamental differences in the way various expander types respond to operating conditions. Those fundamental differences are of primary concern in this study. Therefore each expander is assigned an efficiency of 100 percent at its optimum operating condition, and the comparisons are based on how the efficiency of each expander deteriorates when operated at nonoptimum conditions.

The efficiency of the turbine is taken to be a function only of its velocity ratio  $U/C$ , where  $U$  is the tangential velocity of the rotor blade (proportional to reciprocator speed in the ar-

angement of Fig. 1) and  $C_{is}$  is the velocity equivalent of the isentropic enthalpy drop across the turbine, given by

$$C_{is} = \sqrt{\frac{2g\gamma RT_3 Z}{\gamma - 1}} \quad (7)$$

The trend in efficiency of the turbine expander follows the following parabolic relationship:

$$\eta_e = 4 \left[ \frac{U}{C_{is}} \right] \left[ 1 - \frac{U}{C_{is}} \right] \quad (8)$$

In this study the design-point  $U/C_{is}$  is chosen such that the turbine has an efficiency ratio of 1.0 at 2500 reciprocator rpm full load.

The positive displacement expander is assigned the efficiency characteristics of an ideal (zero leakage) helical-screw expander. Such a machine features internal compression, the rotors being designed with a built-in pressure ratio  $p_3/p_4 = \Pi$ . As indicated above, in this comparison of trends in expander influence, when the positive-displacement expander is operated at its built-in pressure ratio, it is assigned an efficiency ratio of unity. When the operating pressure ratio  $p_3/p_4$  is less than  $\Pi$ , the gas may be thought of as overexpanding isentropically through the built-in pressure ratio internal to the expander. It then undergoes an inefficient recompression at the expander outlet to  $p_4$ . The efficiency of such an internal-expansion machine is given [11] by

$$\eta_e = \frac{(\gamma - 1) \left[ 1 - \frac{\Pi^{1/\gamma}}{p_3/p_4} \right] + [1 - \Pi^{(1-\gamma)/\gamma}]}{\gamma [1 - \Pi^{(1-\gamma)/\gamma}]} \quad (9)$$

The built in pressure ratio of the positive-displacement expander was chosen to be 2.5, giving an efficiency ratio of unity at 2500 reciprocator rpm, full load, to match that of the turbine.

### Effects of Expander Efficiency

In Fig. 8 the sum of compressor, pumping, and expander mep, this time including the effects of expander efficiency, is plotted against fuel-air ratio. The previously shown inferiority of the internal-expansion positive-displacement machine relative to the turbine prior to factoring in expander efficiency is seen to be retained when expander efficiency is considered. Again it is noted that at light loads, the plotted mep summation for the expander, reciprocator gas-exchange process, and supercharging compressor is negative, indicating that even with the significant decrease in coolant heat loss achieved in this LHR diesel reciprocator, the positive work developed in this powerplant outside of the reciprocator expansion and compression strokes is insufficient to compensate for the negative work of the supercharging compressor.

In Fig. 9 the sum of reciprocator indicated mep and friction mep from Fig. 6 is added to the results of Fig. 8 to provide the brake mep for the entire powerplant, as expressed by equation (1). This is the performance indicator of ultimate importance to the engine user. Now the mep differences between expanders in Fig. 8 are almost obscured by the comparative magnitude of the reciprocator indicated mep, although the relative ranking of the expanders remains unchanged from Fig. 8. Within the restrictions of this study, the differences in effects on overall engine performance characteristics between the two options considered are not considered large enough to identify a clearly superior expander choice despite substantial differences in flow characteristics and energy-extraction principles between the aerodynamic and positive-displacement expanders.

It seems appropriate to point out once again that this com-

parison has been based on expanders with matched efficiencies (100 percent) at their best operating point. If large differences in efficiency levels exist between real machines of the types studied here, then the comparison must be modified accordingly and a superior choice might emerge. The final selection must also comprehend such additional factors as performance effects over the remainder of the engine operating range, and expander operating speed, mass, size, noise, and cost.

## Conclusions

For a compound LHR diesel with both a helical-screw supercharging compressor and either a reaction turbine or an internal-expansion positive-displacement expander geared to the crankshaft for direct recovery of exhaust energy:

1 At the selected constant reciprocator speed, the turbine gave better part-load performance trends than the positive-displacement expander when both had the same adiabatic efficiency at full load.

2 A significant factor contributing to the superiority of the reaction turbine in this study was the greater flow restriction it imposed at part load. This shifts available pressure drop away from the reciprocator pumping process and toward the expander. Fundamentally, the expander is able to extract work from the exhaust more efficiently than the reciprocator pistons can during gas exchange.

3 With both types of expander, for the operating conditions of this study, the sum of the positive work outputs from the reciprocator gas-exchange process and the expander was insufficient to drive the supercharging compressor at light loads.

4 Reciprocator indicated output (compression plus expansion strokes) is so large compared to the contributions from the exhaust-energy recovery system that when total engine brake output is considered, differences between the expanders of this study are judged small enough that the ultimate choice

of expander type must also take into account such factors as operating speed, mass, size, noise, cost, reliability, and actual performance effects over the complete operating range of the engine.

## Acknowledgments

The author is grateful to D. C. Siegla for providing the necessary reciprocator data through application of the cycle simulation, and to R. M. Carlson for his help in data management.

## References

- 1 Siegla, D. C., and Amann, C. A., "Exploratory Study of the Low-Heat-Rejection Diesel for Passenger-Car Application," *SAE Transactions*, Vol. 93, 1984, pp. 259-283.
- 2 Poulin, E., Demler, R., Krepchin, I., and Walker, D., "Steam Bottoming Cycle for an Adiabatic Diesel Engine," NASA CR-168255, Mar. 1984.
- 3 DiNanno, L. R., DiBella, F. A., and Koplou, M. D., "An RC-1 Organic Rankine Bottoming Cycle for an Adiabatic Diesel Engine," NASA CR-168256, Dec. 1983.
- 4 Khalifa, H. E., "Waste Heat Recovery From Adiabatic Diesel Engines by Exhaust-Driven Brayton Cycles," NASA CR-168257, Dec. 1983.
- 5 Carlqvist, S. G., and Kamo, R., "Combined Cycle Diesel-Stirling Heat Engine," SAE Paper No. 851521, 1985.
- 6 Baily, M. M., "Comparative Evaluation of Three Alternative Power Cycles for Waste Heat Recovery From the Exhaust of Adiabatic Diesel Engines," NASA TM-86953, July 1985.
- 7 Lysholm, A. J. R., "A New Rotary Compressor," *I. Mech. E. Proceedings*, Vol. 150, 1943, pp. 11-16.
- 8 Whitehouse, N., and Way, R., "A Simple Method for the Calculations of Heat Release Rates in Diesel Engines Based on the Fuel Injection Rate," SAE Paper No. 710134, 1971.
- 9 Woschni, G., "A Universally Applicable Equation for the Instantaneous Heat Transfer Coefficient in the Internal Combustion Engine," SAE Paper No. 670931, 1967.
- 10 Timoney, S., and Flynn, G., "A Low Friction, Unlubricated SiC Diesel Engine," SAE Paper No. 830313.
- 11 Tatushi, K., and Hirayama, N., "Study on Fundamental Performance of Helical Screw Expander," *Bulletin of JSME*, Vol. 28, 1985, pp. 1970-1977.



# Application of Several Variable-Valve-Timing Concepts to an LHR Engine

T. Morel

R. Keribar

Integral Technologies Incorporated,  
Westmont, IL 60559

M. Sawlivala

N. Hakim

Detroit Diesel Allison—GM,  
Romulus, MI 48174

*An analytical study was made of advantages provided by electronically controlled hydraulically activated valves when applied to a low heat rejection engine with and without exhaust heat recovery devices. The valves, which could be designed to operate with variable timings and variable rates of opening and closing, would allow the use of certain sophisticated valve strategies not possible with conventional systems. Three individual investigations were carried out. The first concerned the optimization of the timing and rate of valve opening at several speeds and loads, to obtain maximum volumetric efficiency and lowest BSFC. A second investigated early intake valve closing (IVC before BDC), coupled with increased boost, a concept that had been suggested previously in the literature. The present results showed much lower benefits than those predicted by the earlier study. The final study addressed the use of an organic Rankine cycle bottomer (ORCB) to extract energy from the exhaust stream and directing the ORCB output power to the engine air compressor shaft rather than to the engine output shaft. At rated engine conditions, when not employing a power turbine, this concept was found to produce higher BSFC compared to the more standard configuration where the ORCB was directly coupled to the engine shaft. When a power turbine was used between the engine and the ORCB, nearly the same BSFC was achieved with the two configurations.*

## Introduction

The use of high-temperature thermal barrier materials and coatings in low heat rejection diesel engines presents major long-term opportunities for improved thermal efficiency, reduced package size and weight, due to the elimination of the cooling system, and ultimately longer life and lower cost. In developing an advanced technology low heat rejection engine, it is desirable to evaluate a variety of additional concepts that have the potential to provide synergistic improvements in the areas mentioned above.

One such area concerns the potential use of electronically controlled, hydraulically activated valves (ECV), which would offer total flexibility with respect to timing and considerable flexibility in opening and closing rates. In this paper we describe the results of three studies, in which promising advanced concepts based on such a valve system were evaluated for their potential implementation in low heat rejection diesel engines. One of these was an extensive study of the advantages provided by the ECVs in volumetric efficiency and fuel consumption. Such a concept would provide added flexibility for optimal engine control, by allowing a dynamic adjustment of valve timing and of rate of opening or closing based on instantaneous engine operating conditions. The second study con-

cerned itself with early valve closing (IVC more than 180 crank angle deg before firing TDC), coupled with increased boost, a concept that has been suggested in the literature (Miller, 1946; Chute, 1985). A study was undertaken to evaluate the Miller concept for a turbocharged engine without exhaust heat recovery, in both insulated and cooled configurations. The final study concerned the use of an organic Rankine cycle bottomer (ORCB) to extract energy from the exhaust stream and to use the output power to drive the engine compressor, rather than applying that power directly to the engine shaft. This study also addressed the use of this concept in conjunction with the early intake valve closing, with the ORCB providing additional power to accomplish the requisite high boost.

The evaluation of these three concepts was carried out for the Adiabatic Diesel Reference Engine (ADRE), which is being designed by Detroit Diesel Allison as a part of a DOE/NASA sponsored program (Bennethum and Hakim, 1985).

The primary tool employed in this study was the engine system design analysis code IRIS, described, for example, in Morel et al. (1986). A central feature of this code is a system representation of a turbocharged multicylinder engine, with full transient capability. Among its unique capabilities are highly detailed heat transfer models including convection and radiation from gases to structure, and fully integrated finite element heat conduction, temperature, and stress calculations. All of the models are capable of tracking heat transfer and performance transients during engine speed and load changes.

Contributed by the Internal Combustion Engine Division and presented at the Energy-Sources Technology Conference and Exhibition, Dallas, Texas, February 15–20, 1987. Manuscript received at ASME Headquarters December 5, 1986. Paper No. 87-ICE-29.

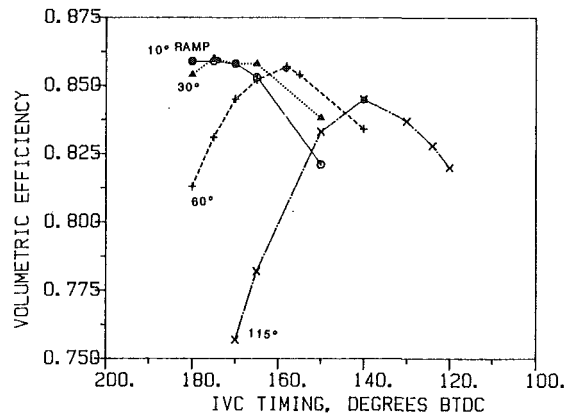


Fig. 1 Variation of volumetric efficiency with intake valve closing angle at various ramp durations; 1800 rpm, fixed plenum conditions

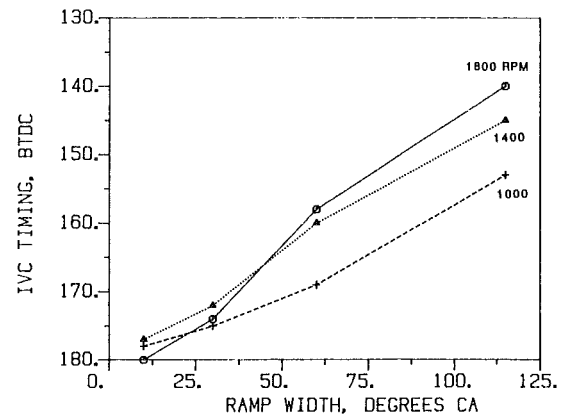


Fig. 2 IVC timing for maximum volumetric efficiency as a function of ramp duration and engine speed (data of Fig. 1)

### Electronically Controlled Valve Concept

The electronically controlled valve concept provides additional engine control flexibility by allowing for a variable valve timing as a function of speed and load, or for a given transient condition. The valves, of unit design, would be actuated individually by a camless hydraulic system, which, in addition to variable timing, can also produce a faster rate of valve opening and closing than achievable with conventional cam systems.

A study was carried out to assess the benefits that this flexibility can offer in the following areas: BSFC; pumping losses; volumetric efficiency; power; emissions; cold start; peak pressure control.

The engine analyzed in this study was insulated on the piston top, head, valves, and top of the liner with plasma-sprayed zirconia coating to provide a 62 percent reduction of in-cylinder heat transfer.

The work involved studies of the sensitivity of the engine performance to:

- shape of the opening and closing ramps; these were simulated by sinusoidal curves with variable durations extending from an abrupt 10 deg CA ramp to a gradual 115 deg CA ramp (typical of production cam-driven systems);
- timing of valve opening and closing; searching for the optimum for a particular ramp duration and for a particular engine operating condition.

The engine operating conditions considered were 300 hp and 200 hp power levels at the 1800 rpm rated speed, and 250 hp at the 1200 rpm peak torque speed. The engine was turbocharged with an advanced turbocharger with overall efficiency of 64 percent.

The study was organized in a sequence of steps which constitute analyses of the effects of the individual valve events, and also the interactions between them:

- 1 intake valve closing;
- 2 exhaust valve opening;
- 3 overlap period;
- 4 interaction of all events at rated conditions, and reoptimization of opening and closing timings at off-rated conditions.

**Intake Valve Closing.** The evaluation of the intake valve closing event was done with the intake and exhaust plenum conditions and structure temperatures fixed at those levels calculated for the rated conditions with standard valves. The engine was simulated under motoring conditions, and a search was made for the optimum IVC timing for the maximum volumetric efficiency at three engine speeds 1800, 1400, and 1000 rpm. The results for 1800 rpm are shown in Fig. 1. The volumetric efficiency showed a strong sensitivity to timing at

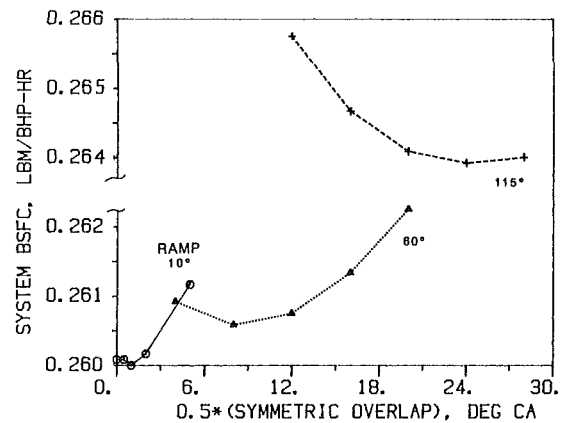


Fig. 3(a) Variations of system BSFC with valve overlap duration at various ramp durations (1800 rpm; full turbocharger simulation)

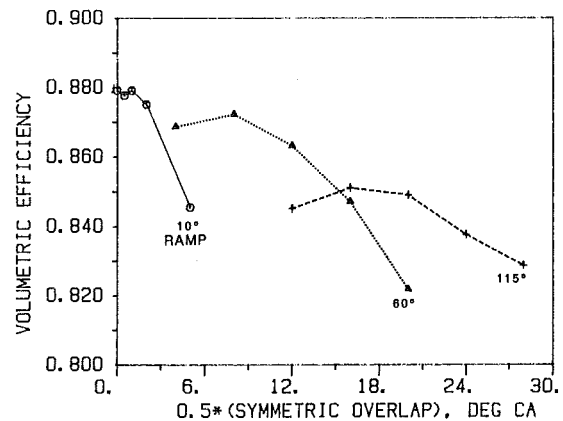


Fig. 3(b) Variation of volumetric efficiency with valve overlap duration at various ramp durations (1800 rpm; full turbocharger simulation)

any fixed ramp duration. By contrast, the maximum values of volumetric efficiency at the various ramp angles varied much less strongly. In fact, there was almost no loss in going from 10 to 60 deg. Increasing the ramp angle beyond 60 deg produced a more substantial loss in  $\eta_v$ , amounting to one percentage point drop at a ramp angle of 115 deg. Plotting the optimum timing angle with respect to ramp duration produces the result shown in Fig. 2. The optimum timing for a valve ramp of short duration is just after BDC, which indicates that the intake valve areas are large enough and that the engine is free-breathing even at the rated speed. This timing is retarded roughly linearly with ramp duration, reaching 30-40 deg CA

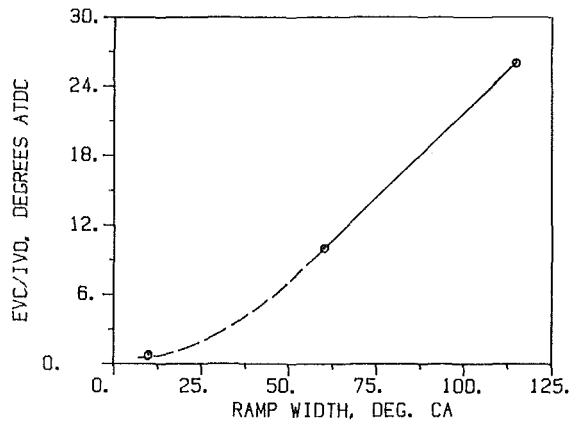


Fig. 4 Half overlap duration for best BSFC versus valve event ramp duration (data of Fig. 3a)

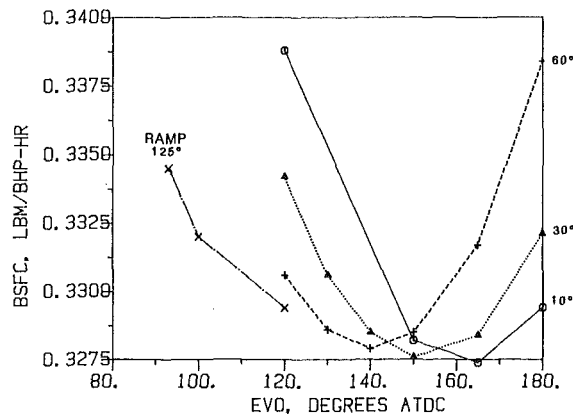


Fig. 5 Reciprocator BSFC versus exhaust valve opening angle at various ramp durations (1800 rpm; fixed plenum conditions)

after BDC (depending on engine speed) at a ramp angle of 115 deg. The figure also shows that the optimum timing depends on engine speed. This means that optimizing the valve timing for rated speed compromises engine breathing somewhat at lower rpm. This is a problem with conventional valves, but it can be eliminated by electronically controlled systems.

**I/O/EVC Overlap Period.** The I/O/EVC period was studied by simultaneous variation of IVO and of EVC symmetrically about TDC, i.e., in each run the ramp angles of both were equal and the overlap extent was symmetric with respect to TDC. A full turbocharger and exhaust plenum dynamics simulation was used. The monitored parameters were reciprocator BSFC and  $\eta_v$ . The BSFC results showed that best performance is obtained with abrupt valve opening/closing at TDC. However, the degradation with increasing ramp angle was quite small until durations of 60-80 deg, beyond which it became more significant. A similar trend was seen in the volumetric efficiency trends. A series of runs was carried out to determine the optimum overlap for 10, 60 and 115 degree ramps (Fig. 3a, b). These showed again a relatively small change in BSFC and  $\eta_v$  from 10 to 60 deg ramps, but a significant rise in BSFC beyond that point. The trends of optimum overlap with ramp duration are shown in Fig. 4.

**Exhaust Valve Opening.** The study of EVO was first carried out with fixed plenum conditions. Again the ramp duration and timing were varied to determine the optimum points. This had almost no effect on volumetric efficiency, and so only BSFC was monitored (Fig. 5). The results showed that at the optimum timing, the reciprocator BSFC was quite independent of ramp duration, with only small degradation with in-

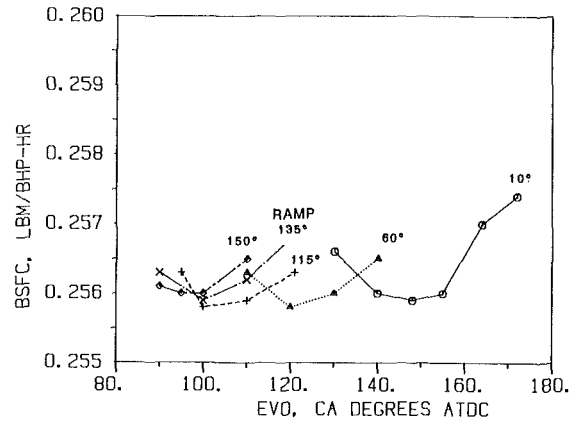


Fig. 6 System BSFC versus exhaust valve opening angle at various ramp durations (1800 rpm; full turbocharger simulation)

creasing duration. As expected, a large sensitivity of BSFC to EVO at a given ramp duration was observed. To confirm this result for a turbocharged engine, the study was rerun with a full turbocharger simulation and exhaust plenum dynamics. The results showed (Fig. 6) that when the whole system is considered (with exhaust plenum dynamics, turbocharger, power turbine and Rankine cycle bottoming), the sensitivity to ramp duration is even lower; the BSFC at best timing for each ramp was essentially independent of the ramp duration. It also indicated that for conventional valve schedules the EVO timing must be well advanced before the BDC, and that even for a sharp 10 deg ramp it still had to be advanced some 32 deg. This was an interesting result worth further investigation to identify the processes governing the location of the optimum EVO timing. At first glance it would appear that the optimum EVO event should be a sharp ramp with opening at BDC, allowing the full expansion of the combustion gases and thus producing the maximum piston work. Since the optimum timing is not at BDC, this indicates that there is a counteracting effect during the exhaust period which increases as EVO is delayed, eventually more than offsetting the benefits of the additional piston expansion work.

Examination of the detailed plots of exhaust mass flows versus crank angle for the EVO retarded from optimum shows that some of the blowdown takes place after BDC, implying that the piston moves against an elevated pressure on the exhaust stroke. This generates additional pumping work, which increasingly offsets the rapidly diminishing extra piston work obtained by the late EVO timing. It thus appears that the optimum timing is the one which permits the blowdown to be completed within a few degrees after BDC, before the piston starts moving rapidly upward. Since the intensity of the blowdown decreases with decreasing load, and depends also on engine speed, the optimum timing may be expected to vary with these parameters. This variation could be accounted for in an electronically controlled valve system, resulting in a slightly increased engine efficiency.

**Interaction of All Valve Events and Comparison to Conventional Valves.** In this part of the study, the engine was equipped with power turbine and ORCB, both directly coupled to the engine shaft. Comparisons were made of conventional versus electronically controlled valves. The electronically controlled valves were set to open and close with ramps of 60 deg in duration. This duration was found to be near optimum in the studies of the individual events discussed above. A final optimization was performed by simultaneous variation of all four timings for the 60 deg ramp duration at rated conditions. This optimization resulted in slightly different timings than those detailed in the decoupled studies above, i.e., IVC = -168, EVO = 118, IVO = 352, and EVC = 368. The

**Table 1 Engine performance with conventional and electronically controlled valves; engine equipped with power turbine and Rankine cycle bottom**

	Rated		Peak torque		Part Load		best 60R*	
	Orig	best 60	Orig	best 60	Orig	best 60	Orig	best 60R*
Valve timing IVC	standard	-168	standard	-168	standard	-168	standard	-168
EVO	-	118	-	118	-	118	-	126
IVO	-	368	-	368	-	368	-	368
EVC	-	352	-	352	-	352	-	352
BHP	293.7	297.5	247.2	246.9	247.6	187.3	190.3	190.4
Pumping (psi)	16.2	14.8	1.1	0.4	1.8	14.0	13.2	13.7
Friction (psi)	21.3	20.8	20.3	20.3	20.4	17.4	17.1	17.1
BSFC	0.2586	0.2553	0.2561	0.2563	0.2556	0.2706	0.2663	0.2660
Air-fuel ratio	29.0	29.1	24.5	24.1	24.2	35.2	35.7	35.8
IVC	0.807	0.871	0.861	0.893	0.893	0.803	0.869	0.869
Peak pressure (psi)	2220	2151	2412	2396	2404	1704	1658	1660
Ign. delay (CA)	2.3	2.5	1.6	1.6	1.6	3.0	3.2	3.2
Compressor PR	2.55	2.37	2.47	2.34	2.34	2.04	1.91	1.91
Turbine PR	1.76	1.68	1.64	1.56	1.56	1.60	1.53	1.53
Power turbine PR	1.65	1.56	1.34	1.33	1.33	1.49	1.49	1.49
T <sub>exhaust man.</sub> (K)	913	904	951	959	954	809	799	798
NOx (ppm)	1634	1640	2372	2371	2373	1106	1116	1114
BSNOx (g/hp-hr)	6.0	5.9	7.1	7.0	6.5	5.1	5.1	5.1
Soot (g/m <sup>3</sup> )	0.023	0.023	0.013	0.014	0.013	0.019	0.019	0.018
T <sub>avg</sub> (K)	1735	1732	1901	1911	1909	1592	1583	1582
T <sub>max burned</sub> (K)	2855	2857	2890	2890	2890	2793	2802	2802

\* Best 60° ramp as determined under peak torque and part load, respectively.

resulting profiles of effective ECV valve areas are shown in Fig. 7(a), as compared to the standard valve effective areas shown in Fig. 7(b).

The results are summarized in Table 1, which shows comparisons for the three engine operating conditions described above. In all comparisons at a given engine operating condition the fuel flow rate was kept the same. The turbocharger characteristics were adjusted at the rated conditions to produce a desired air fuel ratio for both the original valves and the electronically controlled valves (ECVs). This required compressor pressure ratios of 2.55 and 2.37, respectively. The ECVs produced a higher volumetric efficiency and lower peak firing pressures, while the BSFC was 1.3 percent lower and the predicted emissions were unchanged.

The differences produced by the standard and ECV systems were also observed by comparing the valve mass flow profiles, which displayed increased rate of flow through the electronically controlled exhaust valve during the initial blowdown due to the faster rate of valve opening. They also showed a decrease in the extent of backflows across both the intake and exhaust valves in the ECV system.

For peak torque and part load conditions, Table 1 shows comparison for three cases: standard valves, ECVs with the same timings as at rated conditions, and ECVs with timing schedule reoptimized (but the same ramp duration) for these two engine operating conditions. The turbocharger maps used were the same as used at the rated conditions for the standard valves and ECVs, respectively. Similar results were found as for the rated conditions: The ECVs produced a higher volumetric efficiency, lower peak firing pressures, slightly lower BSFC, and about the same emissions levels.

It was found in this study that it is not necessary to require very fast valve ramps, because the point of diminishing return is reached at a ramp angle of about 60 deg for all three events: IVC, EVO and valve overlap IVO/EVC. This is a significant result from the point of view of the practicality of this concept, as decreasing the valve ramp to very short durations rapidly increases the forces and power required for valve operation.

Comparison of the optimum ECVs to the original conventional valves showed that the ECVs can provide modest benefits in BSFC (on the order of 1.5 percent) and peak firing pressures (on the order of 50 psi) over the conventional valves, which were quite well optimized to begin with. Thus one concludes that the direct application, in freely breathing engines, of electronically controlled valves with sharp opening and closing ramps and with timings similar to those used in conventional systems does not produce sufficiently large benefits in volumetric and thermal efficiency to warrant a serious development program in its own right. However, once ECVs

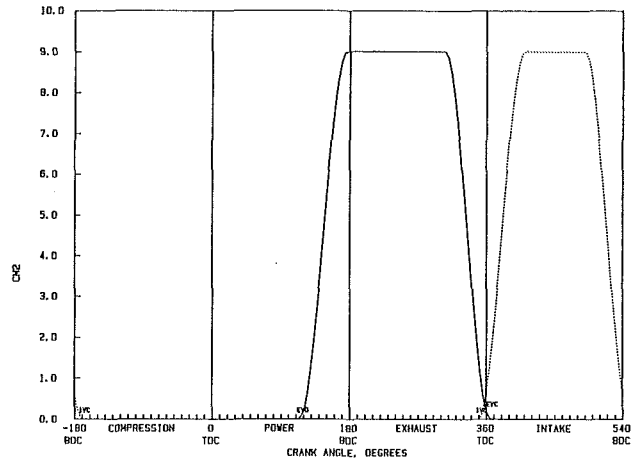


**Fig. 7(a) Effective valve area profiles for ECVs with 60 deg ramp durations, optimized for operation at rated conditions**

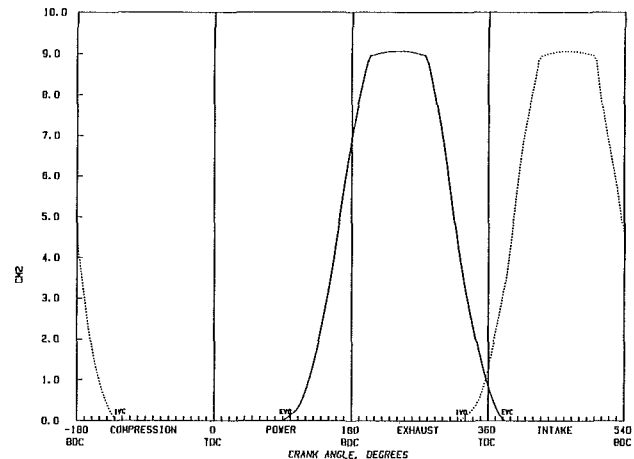


**Fig. 7(b) Effective valve area profiles of a conventional valve system**

are installed on an engine, they permit certain more sophisticated valve timing strategies not possible otherwise:

- reoptimization of valve events with speed and load;
- IVC closing at BDC for cold start and light load operation;
- engine braking by elimination of expansion work, i.e., EVO near TDC.
- selective cylinder cutouts (shutoff valves and injector).

### Early Intake Valve Closing

Early intake valve closing (i.e., IVC more than 180 deg before firing TDC) has been suggested in the literature by Miller (1946) as a means to accomplish a larger degree of intercooling and higher BMEP. More recently, the idea was proposed by Chute (1985) as a method of producing higher engine thermal efficiency. The objective of Chute's work was to demonstrate that the energy allowed to be wasted at the exit of turbocharger turbines in today's engines can be used simultaneously to provide additional compressor boost and reduce the engine compression work by early intake valve closing. Chute analyzed the concept and concluded that with highly insulated engines equipped with high-efficiency turbochargers (64 percent overall efficiency), early intake valve closing can produce over 7 percent improvement in BSFC, whereas a much smaller benefit would be available under noninsulated conditions.

**Turbocharged Engine With No Exhaust Energy Recovery.** In this part of the study the engine studied was

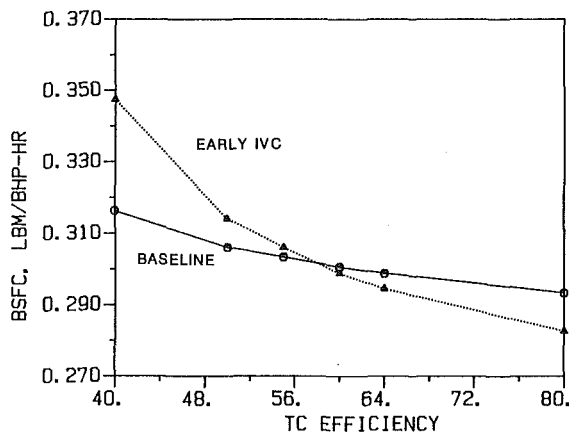


Fig. 8 Fuel consumption as a function of turbocharger efficiency for an ADRE engine: — baseline turbocharged engine, --- same engine with early IVC

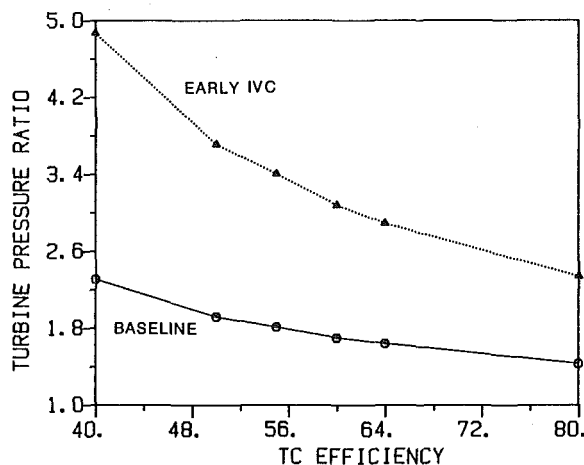


Fig. 9 Turbocharger turbine pressure ratio as a function of turbocharger efficiency for an ADRE engine: — baseline turbocharged engine, --- same engine with early IVC

highly insulated, turbocharged, employed no exhaust energy recovery, and had valve ramp durations of 60 deg, except the intake valve closing ramp which was 30 deg in duration for the early-closing case only. The intake valve closed at 168 deg before firing TDC for the baseline engine and at 255 deg for the early-closing case.

The volumetric efficiency declined by almost a factor of two for the early closing case, which required a greatly increased boost so that the fuel air ratio would be unchanged. The air was intercooled to the same level (311 K) for all cases studied, and the impact of this will be discussed subsequently.

The early-closing case was run first with injection timing set so that the combustion start would be the same as in the baseline engine (-7.8 BTDC). A parametric study was then run with variable turbocharger efficiency (turbine  $\times$  compressor peak efficiencies  $\times$  mechanical efficiency) over a range from 40 to 80 percent. The results are shown in Fig. 8, which shows that for turbocharger efficiencies greater than about 58 percent the early closing produces lower BSFC than the baseline. The dependence of the early closing concept on turbocharger efficiency is much stronger than for the baseline case. BSFC rises sharply with declining turbo efficiency, and at low turbo efficiencies the early closing is clearly inferior. This trend is tied to the sharp variation in engine backpressure, illustrated in Fig. 9 by the turbine pressure ratio. The compressor pressure ratio was 2.32 for the baseline and 4.26 for the early closing case, and it was independent of the turbo efficiency.

Table 2 Comparison of turbocharged insulated engine with no exhaust heat recovery with conventional valves, and with early closing electronically controlled intake valves; the latter concept incorporates increased boost, produced by a higher backpressure turbocharger turbine; engine at rated fuel rate, 1800 rpm

	Baseline	Early IVC Std BOI	Early IVC Advanced BOI
IVC	-168	-255	-255
EVO	126	126	126
BOI	-10.4	-12.0	-19.0
BHP	254.5	258.0	263.9
Pumping (psi)	-1.8	11.4	13.0
Friction (psi)	20.5	19.9	20.2
BSFC	0.2985	0.2945	0.2878
Air-fuel ratio	29.2	29.2	29.1
$\eta_v$	0.896	0.482	0.480
Peak pressure (psi)	2135	1993	2302
Ign. delay (CA)	2.6	4.2	6.3
Comb. start (CA)	-7.8	-7.8	-12.7
T exhaust	864	867	856
T avg. max.	1743	1646	1714
T burned max.	2867	2786	2825
Compressor PR	2.32	4.26	4.26
Turbine PR	1.63	2.89	2.94
NO <sub>x</sub> (ppm)	1776	1208	1706
BSNO <sub>x</sub> (g/hp-hr)	7.2	4.9	7.0
Soot (g/m <sup>3</sup> )	0.025	0.032	0.020

At an overall turbocharger efficiency of 64 percent, a practical level achievable with advanced turbochargers, the improvement in BSFC was only 1.5 percent. Essentially the same trends were obtained with a cooled version of the engine but at higher overall levels of BSFC. Thus, in contrast to the conclusions drawn by Chute, there was no additional advantage generated by engine insulation that would enhance the usefulness of the concept.

One of the very important effects present in the cases studied is the level of intercooling. As already mentioned, in both cases the air exiting the compressor is intercooled to the same level of 311 K, to be accomplished by an air-to-air intercooler. In the baseline case that requires (at compressor efficiency of 80 percent) a reduction of 86 K, equivalent to a heat removal equal to 6 percent of fuel energy. At the same compressor efficiency, the increased compressor pressure ratio and increased compressor outlet temperature of the early IVC closing case lead to the need to reduce the intake air temperature by 174 K, equivalent to a heat removal equal to 12.2 percent of fuel energy. This would place a severe burden on the intercooling system, requiring perhaps an unrealistically large unit. On the positive side, this means that the intake charge starts with the same temperature at IVC, but in the early IVC closing case it is expanded inside the engine cylinder after the valve closes, and so the charge is cooler at the start of compression. As a result the peak pressures are reduced and the lower temperatures lead to lower NO<sub>x</sub> emissions as discussed below.

Since the concept showed a measurable predicted benefit in the BSFC, this prompted a more detailed look at the performance at the target level of 64 percent turbo efficiency. The results are shown in Table 2. The first two columns refer to the previously discussed two cases, in which combustion begins at the same crank angle. It may be seen that the early closing case provides not only a decrease in BSFC, but also a reduction in peak firing pressure (by 140 psi) and in NO<sub>x</sub> emissions, and there is a small increase in the soot level. This provides an opportunity to achieve additional decrease in BSFC by injection advance. Advancing by the timing to 19 deg BTDC increases the peak pressure to about 170 psi above the baseline and the NO<sub>x</sub> emissions are about the same, while the smoke levels are predicted a little lower than the baseline. The BSFC has improved, and is in this case 3.7 percent lower than the baseline.

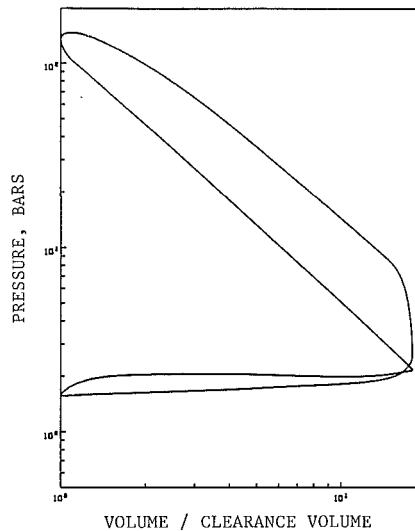


Fig. 10(a) Pressure-volume diagram, ECVs optimized for conventional valve timing schedules

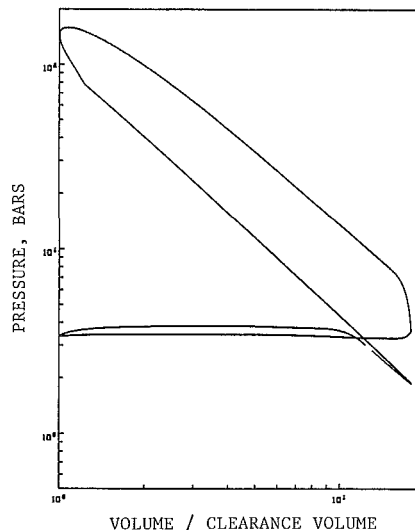


Fig. 10(b) Pressure-volume diagram, ECVs with early intake valve closing

Reducing the injection advance to maintain the same peak pressure, produced a lower BSFC benefit of 3 percent, and also lower  $\text{NO}_x$  than the baseline.

A more detailed look at the differences between the baseline and the early closing cases is provided by Fig. 10, comparing the pressure-volume diagrams of the two cases, showing clearly the difference near BDC of the intake stroke, where in the early closing case the trapped air is expanded and then compressed again, and also showing the much higher levels of intake and exhaust pressures.

The study also examined whether the IVC timing used (chosen based on Chute's results) was indeed the optimum for this engine and turbocharger efficiency. A range of IVC timings was scanned, again subject to constant A/F ratio and  $\text{NO}_x$  levels. The results, displayed in Fig. 11, showed that the originally chosen IVC value was very close to the optimum and that no further improvement in BSFC could be obtained at this turbocharger efficiency.

The results obtained disagree with the findings of Chute (1985) in two areas. First, the benefit in BSFC for 64 percent turbo efficiency (the value used by Chute) was only 1.5 percent compared to 7.5 percent found by Chute. Second, while Chute found that engine insulation increased the viability of the con-

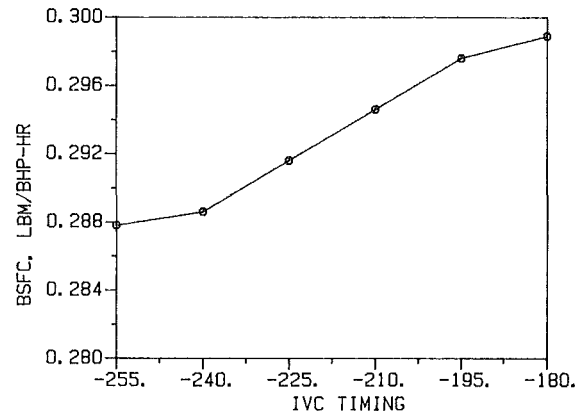


Fig. 11 Fuel consumption for a TC engine with no exhaust heat recovery as a function of IVC timing; timing of BOI adjusted for constant  $\text{NO}_x$  emissions; constant A/F ratio

cept, our results showed no such trends. Another way of looking at this is to note that at 64 percent efficiency both the present results and Chute's results show that the early intake valve closing provides only small improvement in BSFC for the cooled engine, if advantage is not taken of the lower  $\text{NO}_x$  levels by advancing injection. Further, while our calculations show that this result extends to insulated engines, Chute's show a large improvement with insulation. The difference can be traced to the heat transfer model, which greatly affects the predicted exhaust temperatures. Chute's exhaust temperatures for the adiabatic engines (simulated by setting wall temperatures to unrealistically high values) are sharply higher than for the cooled engine, and this exhaust enthalpy is then available to the turbine for generating the required increased boost. By contrast, the ITI model shows a much smaller exhaust temperature increase with insulation than calculated by Chute and this is responsible for the lower observed benefits.

**Turbocharged Engine With Exhaust Heat Recovery Devices.** The above study concerning the early IVC timing was carried out for an engine without heat recovery devices, at conditions similar to those adopted by Chute in his study. With that accomplished, the work was extended to an engine configuration which had both a power turbine and ORCB bottomer. The turbocharger efficiency was fixed at 64 percent and the power turbine efficiency at 78 percent. In all of the runs the valve ramp durations were fixed at 60 deg and the timings were fixed at the optimum values. The injection timing was advanced where appropriate, taking advantage of the lower gas temperature, to a point where peak firing pressures matched those of the baseline case and  $\text{NO}_x$  emissions were lower than for the baseline. The A/F ratio was maintained at a constant value of 29:1.

A parametric study was carried out over a range of IVC timings seeking the optimum timing for minimum BSFC at rated engine conditions. In contrast to the previous investigation of early IVC for an engine without exhaust heat recovery, these results showed a very flat BSFC curve with IVC timing (Fig. 12a), maintaining essentially constant values from -168 to -235 deg before firing TDC. At timings earlier than -235 deg the BSFC started to sharply increase. The compressor pressures required at early IVC timings for maintenance of constant A/F ratio are shown in Fig. 12(b).

An analysis of these somewhat surprising results showed that as the IVC timing was advanced, the power produced by the reciprocator kept increasing up to -235 deg much as it did in the earlier study of the engine with no exhaust energy recovery. However, the power produced by the engine exhaust energy recovery devices kept decreasing at about the same rate, due to the lower energy content of the exhaust

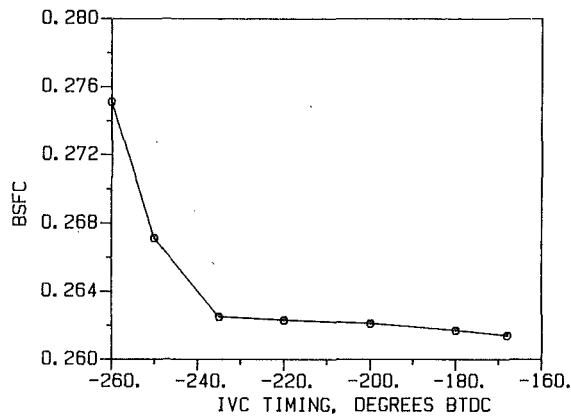


Fig. 12(a) Fuel consumption of the ADRE engine (with power turbine and RCB bottomer) as a function of IVC timing; timing of BOI adjusted for constant peak firing pressure; constant A/F ratio

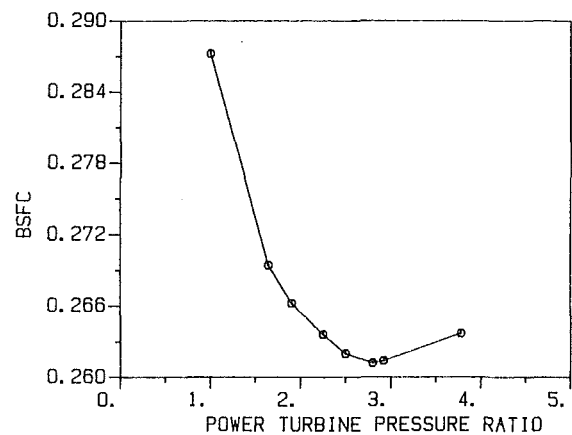


Fig. 13 Effect of power turbine pressure ratio on the fuel consumption of the ADRE engine, with ORCB power used to drive the compressor rather than the engine shaft

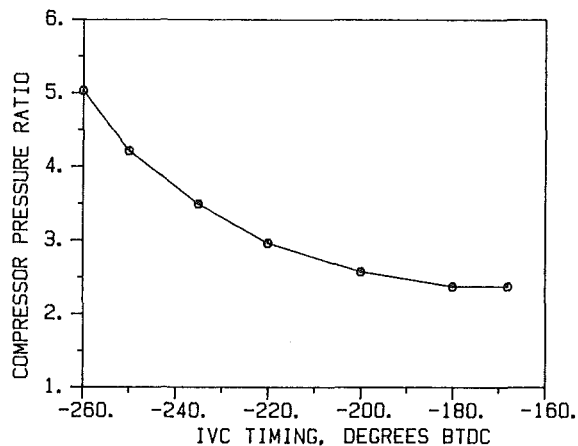


Fig. 12(b) Compressor pressure ratio of the ADRE engine as a function of IVC timing

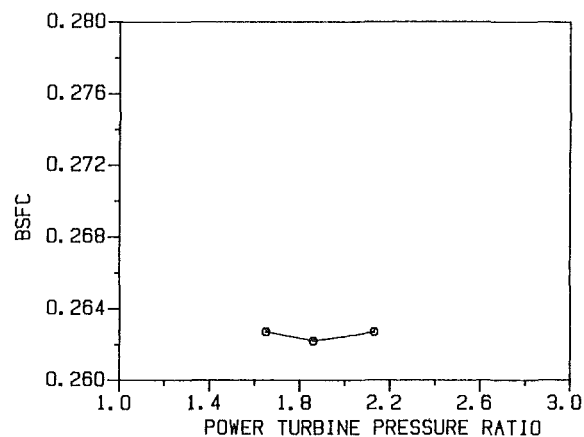


Fig. 14 Effect of power turbine pressure ratio on the fuel consumption of the ADRE with early valve closing (IVC = -235 deg) and ORCB-driven compressor

downstream of the turbocharger turbine. As a result, the early IVC produced no efficiency gain for the engine equipped with an exhaust energy recovery system.

In summary, even with highly efficient turbocharger with 64 percent overall efficiency, and advanced injection timing to take advantage of lower  $\text{NO}_x$  and lower peak pressures, only a modest 3 percent BSFC improvement was obtained for an engine with no exhaust heat recovery. This conclusion was the same for cooled and insulated engines. The addition of exhaust recovery devices tended to eliminate all of the advantages of the concept.

### ORCB-Driven Compressor

One possible concept for insulated engines equipped with ORCB is to use the generated work to compress the air ahead of the turbocharger compressor in an extra stage of compression. This would replace the direct use of the ORCB power to augment the mechanical power produced by the engine (i.e., by gearing it to the engine shaft).

An analysis was carried out employing this idea for an engine equipped with a power turbine placed ahead of the ORCB. This was done both in connection with conventional IVC timing, and in connection with the early intake valve closing concept. The objective was to reduce the power requirement on the turbocharger turbine, thus reducing the backpressure and pumping losses. For the purpose of the simulation, a single-stage turbocharger compressor was used with a common shaft to the turbocharger turbine and the

ORCB. The same boost was generated in each case, but the required turbine pressure ratio was less.

### ORCB-Driven Compressor With Conventional IVC Timing

At rated conditions, the power available from the ORCB was almost equal to that required by the compressor and so the TC turbine had to produce only a small complementary power. As a result, the engine backpressure was quite low and this provided the opportunity for increasing the power turbine pressure ratio and power. A parametric study was run to determine the optimum power turbine pressure ratio (Fig. 13). The optimum was found to be near  $\text{PR} = 2.8$ , as a result of opposing trends in reciprocator and power turbine power.

Analysis of the results showed that in this arrangement a large part of the ORCB power is converted through increased pressure work into increased reciprocator power. This is further compounded by the higher exhaust temperature entering the ORCB (due to small pressure drop across the TC turbine), i.e., by increased ORCB power.

The total power produced by the engine at the optimum was almost exactly equal to that of the baseline engine in which the ORCB drives the engine shaft directly. It should be pointed out that this is a more positive result than would be obtained for an engine without a power turbine, where it would be more advantageous to drive the engine shaft directly, rather than driving the compressor. The reason the concept is more favorable when power turbine is used is that there are further

benefits due to increased power turbine work, produced by higher upstream pressure and temperature.

**Combined Early IVC and ORCB-Driven Compressor.** In this study we combined the two approaches. The calculations were carried out for a single value of IVC timing set at  $-235$  deg, found earlier to be near optimum. It was again necessary to reoptimize the power turbine to take advantage of the reduced TC turbine load. The optimum power turbine pressure ratio was found to lie near 1.86 (Fig. 14). The power produced by the optimum configuration fell slightly short of the power produced by the baseline engine.

In summary, the ORCB-driven compressor, investigated in order to improve the efficiency of the baseline engine, gave at rated conditions results essentially identical to those attainable with the baseline engine with direct coupling of ORCB to the engine shaft. Since there were no advantages in BSFC at steady-state high loads, ORCB-driven compressor would be a favorable alternative only if it could be shown that at low loads or during engine transients there are advantages from BSFC point of view, or for mechanical complexity, or for engine power control reasons. Those aspects were not addressed in this study.

## Conclusions

1 For a typical heavy-duty diesel engine equipped with ECVs, it is not necessary to use very fast valve opening/closing ramps, because the point of diminishing return is reached at a ramp angle of 60 deg. Valve ramps of this duration are quite practical from the point of view of the forces and power required for valve operation.

2 In comparison to conventional valve profiles, ECVs provided only modest benefits in BSFC, volumetric efficiency, and peak firing pressures. These benefits are not large enough to warrant the cost of the system on the basis of BSFC gains alone. However, once installed on the engine, they would permit a whole range of certain more sophisticated variable valve timing strategies not possible otherwise, such as high compression cranking, engine braking, cylinder cutouts, volumetric efficiency timing with engine speed, etc.

3 Early intake valve closing (well before BDC), combined with increased boost, can produce BSFC improvements of up

to 3 percent, with the same peak firing pressures and lower  $\text{NO}_x$ . However, a large intercooler is required, removing twice as much energy than in a conventional engine. These conclusions were the same for a cooled, as well as for an insulated engine. When applied to an engine equipped with exhaust heat recovery devices, the concept produced no improvement in BSFC. This was the result of reduced work produced by the exhaust heat recovery devices, which canceled the increased basic engine power output.

4 The observed effects of early valve closing are in disagreement with previous literature. These differences can be traced to the details of models used in evaluation of the concept. The most significant were the differences in the heat transfer models used, with the present models being more physically based.

5 The use of organic Rankine cycle bottomer (ORCB) to drive the intake air compressor produced higher BSFC than when the ORCB was used to drive the engine shaft directly. When an exhaust power turbine driving the engine output shaft was added to the engine, the BSFC levels were equal for the ORCB power directed to either the compressor or the engine output shaft.

## Acknowledgments

This work has been supported by the DOE Heavy Duty Transport Technology program, contract DEN 3-329, which is technically managed by NASA-LeRC. The authors thank Mr. H. Yacobucci, NASA Project Manager, for his interest and support. Thanks are also due to the management of Detroit Diesel Allison for permission to publish this work, and for their continuous support.

## References

- Bennethum, J. E., and Hakim, N. S., 1985, "The Low Heat Rejection (Adiabatic) Reference Engine Design for On-Highway Applications," *Proceedings of XXIII Automotive Technology Development Contractors' Coordination Meeting*, SAE P-165.
- Chute, R., 1985, "Pressure Compounding a Four Cycle Diesel Engine," SAE Paper No. 851520.
- Miller, R. H., 1946, "Supercharging and Internal Cooling Cycle for High Output," ASME Paper No. 46-OGP-4.
- Morel, T., Keribar, R., Blumberg, P. N., and Fort, E. F., 1986, "Examination of Key Issues in Low Heat Rejection Engines," SAE Paper No. 860316.



# Tests of Thick Flame Combustion Estimates in a Single-Cylinder Engine

J. Boisvert

P. G. Hill

Department of Mechanical Engineering,  
The University of British Columbia,  
Vancouver, British Columbia, Canada

*Estimates of turbulent burning speed, burning zone thickness, and randomness of ignition delay have been incorporated in a model of spark-ignited engine combustion. The estimates have been made on the assumption that turbulence during combustion is homogeneous, isotropic, and has Tennekes' small-scale structure with integral length scale proportional to chamber height. Flame propagation rate has been assumed to depend on turbulence intensity in accord with Chomiak's vortex-bursting hypothesis. The resulting method of calculating combustion has been tested with cylinder pressure data from a Ricardo single-cylinder engine over a wide range of rpm and equivalence ratio and operating with natural gas fuel. Hot-wire measurements of turbulence intensity were made in the motored engine, but window-averaged estimates of intensity were a factor of two lower than ensemble-averaged estimates. Given a factor of two uncertainty in the turbulence intensity measurements it can be said that estimates of combustion duration and pressure agreed well with experimental data over the range of speed and equivalence ratio. The sensitivity of the calculation method to alterations in assumed parameters has been tested. The most important uncertainty appears to be the turbulence intensity.*

## 1 Introduction

In spark-ignition engines without substantial swirl or squish motion it appears that turbulence generated at the inlet valve has enough time to decay to an approximately homogeneous isotropic state before combustion begins. Taking the results of previous turbulence measurements [1-6], typical turbulence intensities at top dead center are in the range 3-10 m/s at, say, 3000-5000 rpm. Measurements of length scales in engines (see, e.g., [7]) suggest that the integral length scale of the turbulence during the combustion period is approximately 1/5 of the chamber height or typically 1-2 mm. This suggests that the turbulence decay time  $L/u'$  is in the range 0.1 to 1 ms so that typically the period between inlet valve closure and spark ignition may be of the order of 10 times the turbulence decay time.

As has been pointed out [8-14], the implication that the engine turbulence is in a relaxed state during combustion is that the well-known scaling rules for decay of isotropic turbulence apply; given the turbulence intensity  $u'$  and an empirically derived relationship between integral length scale and chamber height, one may estimate the Taylor microscale of the turbulence. This in turn means that the model of Tennekes [15] of the small-scale structure of turbulence (whose combustion implications have been emphasized by Tabaczynski) can be quantitatively employed in estimates of flame propagation rate, burning zone thickness, and of random ignition delay.

Daneshyar and Hill [16] have reviewed the combustion implications of the Tennekes hypothesis (that dissipation is con-

centrated in vortex tubes of typical spacing equal to the Taylor microscale) coupled with the notion of Chomiak [17] that rapid flame propagation is caused by vortex bursting. They have shown by approximate calculations that literal application of these ideas is quantitatively compatible with engine performance measurements over a wide range of conditions. Their method, summarized in Section 3, is further tested by the measurements and calculations presented in this paper and given in more detail in [18].

The purpose of the work was to develop an engine combustion model consistent with the Tennekes-Chomiak hypothesis and to assess its quantitative validity over a range of speed and equivalence ratio. Measurements were made of turbulence intensity (in the absence of combustion) using hot-wire anemometry and pressure development in the cylinder of a single cylinder engine, with and without combustion. The uncertainty of the turbulence intensity estimates is high, but within this uncertainty a consistent quantitatively valid description of engine performance has been developed; it includes an estimate of the range of the cyclic variations which can be associated with small-scale turbulent structure.

## 2 Experimental Investigation

**2.1 Engine Description.** Table 1 shows the characteristics of the single-cylinder Ricardo Hydra engine used in the tests. It has a bathtub combustion chamber with overhead camshaft and vertical valves.

**2.2 Pressure Measurement.** The pressure was measured with a Kistler 6121 piezoelectric transducer which was flush mounted in the cylinder head of the Ricardo engine. The

Contributed by the Internal Combustion Engine Division and presented at the Energy-Sources Technology Conference and Exhibition, Dallas, Texas, February 15-20, 1987. Manuscript received at ASME Headquarters December 1, 1986. Paper No. 87-ICE-22.

**Table 1 Ricardo Hydra engine characteristics**

Number of cylinders	1
Bore, mm	80.26
Stroke, mm	88.9
Swept volume, liter	0.45
Maximum speed, rpm	5400
Maximum power, kW	15
Compression ratio	8.93:1
Valve arrangement	Overhead camshaft, vertical valves
Valve lift, mm	9
Intake port diameter, mm	32
Valve events:	
Inlet opens (IVO)	12° BTDC
Inlet closes (IVC)	56° ABDC
Exhaust opens (EVO)	56° BBDC
Exhaust closes (EVC)	12° ATDC

The engine was fueled by natural gas whose composition is given by:

	Vol. percent
Methane	94.0
Ethane	3.3
Propane	1.0
Nitrogen	1.0
Other	0.7
	100.0

resulting charge signal was fed to a Kistler model 5004 charge amplifier to yield a voltage proportional to cylinder pressure. For both part-throttle and wide-open throttle operation, the piezo crystal output was adjusted so that at bottom dead center on the intake stroke

$$P = P_{amb} \eta_v (T_{intake}/T_{amb})$$

in which the subscript amb signifies ambient pressure,  $\eta_v$  is the volumetric efficiency, and the temperature ratio is unity for nonfired tests. One hundred cycles of pressure data were digitized at a rate of 1 sample/deg for each measuring condition. An AVL model 360c/600 optical crank angle pickup was mounted on the engine flywheel. This sensor generated pulses every crank angle degree that were used to trigger the data acquisition, and a single pulse at BDC was used to synchronize the data with the position of the crank shaft. An Isaac 2000 high-speed data acquisition unit was used for data sampling.

Comparison of indicated and brake mean effective pressures showed that the apparent friction mean effective pressure was about 9 percent ( $\pm 2$  percent) of the brake value at 1800 rpm, and 14 percent ( $\pm 2$  percent) at 3000 rpm.

**2.3 Hot-Wire Measurements.** A high-temperature hot-wire probe with a DISA M-10 constant-temperature bridge was used to measure hot-wire voltages. The signal was filtered at 20 kHz with a DISA 55D26 signal conditioner before being digitized every 0.2 deg crank angle. These settings remained unchanged over all engine speeds.

The probe was inserted through the spark plug hole. Figure 1 shows the probe measuring positions. The hot wire (Type TSI P125) was of platinum-iridium alloy, 6.3  $\mu$ m in diameter and 1.5 mm in length. It was calibrated at atmospheric temperature and pressure against a pitot tube in a small wind tunnel. The wire was operated at a constant temperature of 600°C.

The temperature of the air in the nonfiring tests in which turbulence was measured was estimated on the assumption that compression up to the point of inlet valve closure was isentropic. Following valve closure, the temperature was calculated from the ideal gas uniform-state assumption

$$T = T_1 (P/P_1)(V/V_1)$$

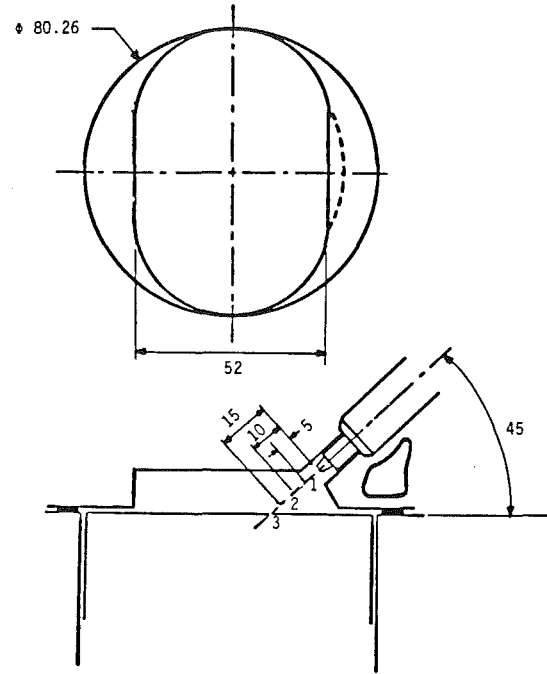


**Fig. 1 Hot-wire anemometer measuring positions**

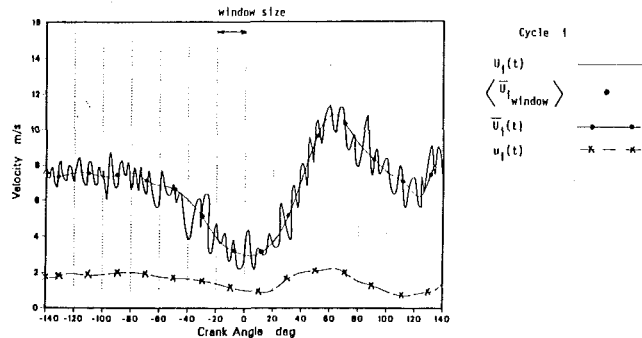


**Fig. 2 Definitions of mean window velocity, fitted true mean velocity, rms window intensity, and true rms intensity**

in which subscript 1 signifies conditions at inlet valve closure,  $V$  is the cylinder volume, and  $P$  the measured pressure.

The method adopted for interpreting the hot-wire signal at a temperature considerably different from the calibration temperature was that of Lancaster [2]. Gas properties were evaluated at the mean gas temperature, as Witze [19] had recommended after critical comparison of hot-wire and laser measurements of velocities in engines. The procedure takes into account thermal conduction to the mounting needles (which are assumed to be at ambient temperature) and involves an iterative solution for the convection coefficient of heat transfer for the wire at each operating point.

To obtain representative values of mean and fluctuating velocities in the cylinder two methods of averaging were used: ensemble and nonstationary cycle-by-cycle analysis. The second of these is based on the method of Catania and Mittica [6] and the following remarks pertain mainly to this method.

The instantaneous velocity  $U_i(t)$  in the engine can be thought of as a "mean" flow  $\bar{U}(t)$  on which are superimposed turbulent fluctuations  $u_i(t)$ . For purposes of analysis, we decompose the instantaneous velocity into two components

$$U_i(t) = \bar{U}_i(t) + u_i(t)$$

This is meaningful as long as the typical frequency content of

**Table 2 Time associated with each window size**

Engine speed rpm	Time (msec)						
	2°	4°	6°	8°	10°	12°	15°
1200	0.278	0.556	0.833	1.111	1.389	1.667	2.083
1800	0.185	0.370	0.556	0.741	0.926	1.111	1.389
2400	0.139	0.278	0.417	0.556	0.694	0.833	1.042
3000	0.111	0.222	0.333	0.444	0.556	0.667	0.833

$\bar{U}_i(t)$  is much lower than that of  $u_i(t)$ . To determine the function  $\bar{U}_i(t)$  for a portion of the  $U(t)$  record for a single cycle, a short crank angle interval (i.e., window) was chosen. The instantaneous velocity  $U_i(t)$  was time-averaged (using a trapezoidal rule) over that interval to yield an average velocity value centered in the window as shown in Fig. 2. This average may be written

$$\langle \bar{U}_i, \text{window} \rangle = \frac{1}{T} \int_0^T U_i(t+\tau) d\tau$$

Next a cubic spline was fitted to these mean values to obtain a mean velocity curve  $\bar{U}_i(t)$  for cycle  $i$ . The resulting mean velocity curves (one per cycle) were ensemble averaged over all cycles to give the "true" mean velocity

$$U_{\text{true}}(t) = \frac{1}{N} \sum_{i=1}^N \bar{U}_i(t)$$

The squared average intensity for each previously defined window was then calculated as follows:

$$\langle u', \text{window}^2 \rangle = \frac{1}{T} \int_0^T [U_i(t+\tau) - \bar{U}_i(t+\tau)]^2 d\tau$$

Next these squared average intensities were ensemble averaged over the  $N$  cycles, and the root extracted

$$\langle u', \text{window} \rangle = \sqrt{\frac{1}{N} \sum_{i=1}^N \langle u', \text{window}^2 \rangle}$$

The choice of the averaging window size establishes a frequency cutoff point between mean velocity and fluctuations. If the window is too small, there is loss of higher frequency information as turbulence is interpreted as mean flow variations and  $u'$  is underestimated. If the window is chosen too large, the mean flow patterns are attributed to turbulent fluctuations and we tend to overestimate  $u'$ .

Catania and Mittica [11] recommend that the choice of an appropriate window size be made by reducing the data over a number of window sizes and selecting the best result. They found that 8 deg at 1600 rpm was the best choice. Table 2 shows the time associated with each window size. The results of ensemble and window-averaging the turbulent signal are given in Section 4.

### 3 Method of Analysis

In the following the method of analysis described by Daneshyar and Hill [16] is summarized and applied to the prediction of performance of the single-cylinder Hydra engine on which measurements were made.

**3.1 Turbulence Intensity and Scales.** With the assumption of homogeneous isotropic turbulence one may write

$$\frac{L}{\lambda} = \frac{1}{\sqrt{15}} \left( \frac{u' L}{\nu} \right)^{1/2} = \frac{1}{15} \left( \frac{u' \lambda}{\nu} \right) \quad (1)$$

in which  $L$  is the integral length scale,  $\lambda$  is the Taylor microscale,  $u'$  is the turbulence intensity, and  $h$  is the chamber height.

Experimentally it has been shown [7] that for engine combustion

$$L \approx 0.2 h \quad (2)$$

Using perhaps the simplest form of rapid-distortion theory (conservation of angular momentum of a large eddy undergoing compression) one may write that

$$u' = u'_s \left( \frac{\rho}{\rho_s} \right)^{1/3} \quad (3)$$

in which  $\rho$  is the gas density and the subscript  $s$  denotes the state at the time of the spark. This would imply

$$L = L_s \left( \frac{\rho}{\rho_s} \right)^{-1/3} \quad (4)$$

With  $u'$  estimated from turbulence data (obtained from motored tests) for the spark ignition crank angle, equation (2) has been used to estimate the integral length scale at the ignition point and equations (1), (3), and (4) have been used to estimate the variation of  $u'$ ,  $L$ , and  $\lambda$  in the unburned gases during the combustion period.

**3.2 Flame Propagation Speed.** Using the Chomiak hypothesis regarding the effect of vortex bursting on flame propagation it has been shown [16] that the speed of propagation, relative to the unburned gas, of the turbulent flame front can be estimated as

$$u_t = u_\ell + \sqrt{\frac{2}{3} \frac{\rho_u}{\rho_b}} u' \quad (5)$$

in which  $u_\ell$  is the laminar burning velocity and  $\rho_u/\rho_b$  is the ratio of densities of unburned and burned gases. This result has been shown to be in good agreement with measurements of turbulent flame speeds outside engines as long as  $u'/u_\ell$  does not exceed 10–15; for greater values Abdel-Gayed et al. [20] have reported departure from a linear dependence of  $u_t$  on  $u'$  and a tendency to flame extinction at very high  $u'$ .

In the calculations whose results are presented in section 4 the dependence of the laminar velocity  $u_\ell$  of the natural gas on pressure, temperature, and equivalence ratio has been estimated from

$$u_\ell = [1 + 1.56(\phi - 1)][0.1 + 3.71 \times 10^{-6} T_u^2] P^{-1/2} \text{ m/s} \quad (6)$$

in which  $P$  is the pressure in atm,  $T_u$  is the unburned gas temperature, K, and  $\phi$  is the equivalence ratio. This formula is consistent with the data of Andrews and Bradley [21] for methane-air mixtures in the range

$$0.6 < \phi < 1.0 \quad (7)$$

**3.3 Thickness of the Burning Zone.** Consistent with the Tennekes structure of small-scale turbulence, there is fast burning along the vortex tubes that model the regions of high vorticity, and slow laminar burning in the  $\lambda$ -sized pockets between them.

With a characteristic burning time of  $\lambda/u_t$ , the burning zone thickness would be

$$\delta = u_t \frac{\lambda}{u_\ell}$$

This result differs little from those of [12, 20], who postulate an exponential rate of decay of unburned mass within the burning zone.

Using the assumption of an exponential burning law, we obtain

$$\delta = 1.15 u_t \frac{\lambda}{u_t} \quad (90 \text{ percent burned})$$

or

$$\delta = 2.3 u_t \frac{\lambda}{u_t} \quad (99 \text{ percent burned}) \quad (8)$$

Equation (8) has been used in these calculations.

To satisfy the conservation equations it is necessary to estimate not only the burning zone thickness but also the average volume fraction  $y_b$  of the burned gas in the burning zone.

Assuming the exponential decrease of unburned mass in the burning zone, it may be shown that the average mass-burned fraction in the burning zone is

$$\bar{x}_b = 1 + \frac{1}{c} (e^{-c} - 1)$$

in which  $c = 1.15$  (90 percent burned) or  $c = 2.3$  (99 percent burned).

Converting to volume fraction we obtain

$$\bar{y}_b = \frac{1}{1 - \frac{\rho_b}{\rho_u} \left(1 - \frac{1}{\bar{x}_b}\right)}$$

For  $1.15 < c < 2.3$  and  $\rho_b/\rho_u = 5$  we obtain

$$0.77 < \bar{y}_b < 0.89$$

An alternative way in which this estimate may be made is to assume approximately spherical pockets whose size is given by

$$r = \frac{\lambda}{2} - u_t t$$

Given the density change from  $\rho_u$  to  $\rho_b$  on burning and one unburned pocket initially of radius  $\lambda/2$  we obtain, for the average volume fraction  $y_b$  of burned gas at a point within the flame

$$y_b = \frac{\left[\left(\frac{\lambda}{2}\right)^3 - \left(\frac{\lambda}{2} - u_t t\right)^3\right]}{\left[\left(\frac{\lambda}{2}\right)^3 - \left(\frac{\lambda}{2} - u_t t\right)^3 + \left(\frac{\lambda}{2} - u_t t\right)^3\right]}$$

Integrating this expression over time, between 0 and  $\lambda/2u_t$ , yields an average value

$$\bar{y}_b = 3/4$$

Since the calculated thickness of the burning zones was in the range 3–10 mm, the calculated pressure development was quite sensitive to the assumed constant value of  $\bar{y}_b$ . It was found that  $\bar{y}_b = 0.82$  was in best accord with the experimental data.

**3.4 Random Time Delay.** The mean random time delay for initiation of fast burning has been taken to be  $\lambda/4u_t$  (the average of 0 and  $\lambda/2u_t$ ). Calculations have been performed for this mean value, and consideration is given later to the effect of varying the mean value in the range  $\pm \lambda/4u_t$  on calculated value of the maximum pressure and the mean effective pressure. The results of comparison of calculated and experimental values are presented in Section 5 of the paper.

**3.5 Gas Properties.** The gas constituents were assumed to be ideal. Spatial variations in pressure were neglected and the

burned gas temperature was taken to be uniform at a value satisfying the mass and energy conservation statements.

Dissociation products CO, O<sub>2</sub>, H<sub>2</sub>, OH, and NO were determined with the assumption of thermodynamic equilibrium and the use of a dissociation calculation method developed by Jones [22].

Since the intake and exhaust strokes were not modeled, a few assumptions had to be made regarding these processes.

For initial pressure and temperature at bottom dead center, the motoring test assumptions were used

$$P_{\text{BDC}} = P_{\text{amb}} \eta_v \frac{T_{\text{intake}}}{T_{\text{amb}}}$$

$$T_{\text{BDC}} = T_{\text{intake}}$$

The total number of moles was calculated from

$$N_{\text{tot}} = \frac{P_{\text{BDC}} V_{\text{BDC}}}{R_{\text{MOL}} T_{\text{BDC}}}$$

The residual fraction  $F_{\text{res}}$  was assumed to be 5 percent in calculating the molar fraction of each specimen. The mass fraction of each residual component was estimated by assuming complete combustion of the fuel.

$$X_{\text{O}_2} = \frac{\lambda \left(C_n + \frac{H_m}{4}\right) [1 - F_{\text{res}}]}{1 + 4.76 \lambda \left(C_n + \frac{H_m}{4}\right)} + F_{\text{res}} X_{\text{resO}_2}$$

in which  $C_n$  and  $H_m$  are the respective numbers of carbon and hydrogen atoms. Here  $\lambda$  is the relative air–fuel ratio. The same type of calculation was performed for each component of the cylinder mixture.

**3.6 Heat Loss.** The rate of heat transfer to that portion of the chamber wall exposed to hot gas was estimated by Annand's formula [23]

$$\Delta Q = A 0.8 \frac{k}{D} (\text{Re})^b (T_b - T_{\text{wall}}) \Delta t \quad (9)$$

in which  $D$  is the cylinder bore,  $\text{Re}$  the Reynolds number,  $V_{mp}$  the mean piston velocity, and  $T_{\text{wall}}$  the wall temperature which was assumed to be 450 K in equation (9). The coefficients used in these calculations were  $A = 0.8$ ,  $B = 0.7$ , as recommended by Annand.

**3.7 Flame and Chamber Geometry.** It was assumed that the inner and outer surfaces of the burning zone were those portions of spherical surfaces centered at the spark location which fell between the intersecting, boundary walls of the chamber.

As functions of crank angle (piston location) and radius of the frontal surface of the burning zone, tables of flame frontal surface area, unburned gas volume, and area of wall exposed to hot gases were generated using a computer program for the Hydra combustion chamber geometry. Details of the geometric calculation procedure are given in [18].

**3.8 Numerical Procedure.** The equations which were solved simultaneously in steps through the firing stroke in 1-deg crank angle increments are given below.

*Conservation of Mass*

$$M_{\text{tot}} = M_u + M_f + M_b$$

*First Law*

$$E_2 = E_1 = p \Delta V + \Delta Q$$

*Entrainment Equation*

$$\frac{dm_e}{dt} = \rho_u A_u u_t$$

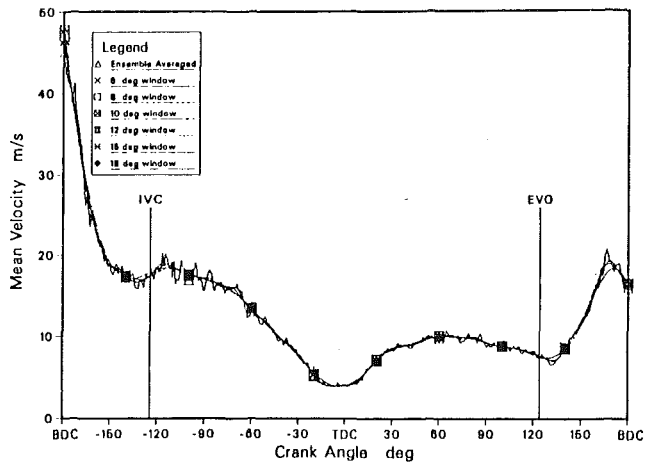


Fig. 3 Comparison of ensemble-averaged mean velocity with mean velocity obtained by nonstationary cycle-by-cycle analysis using various window sizes, 3000 rpm, baseline position

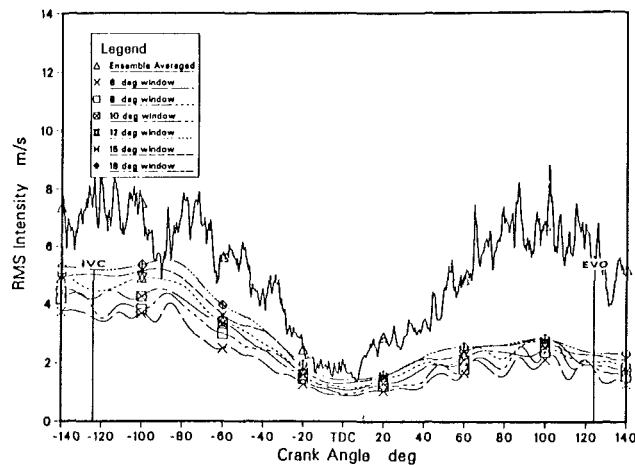


Fig. 4 Comparison of ensemble-averaged turbulence intensity with intensity obtained by nonstationary cycle-by-cycle analysis using various window sizes, 3000 rpm, baseline position

with

$$u_t = u_l + c\sqrt{\rho_u/\rho_b}u'$$

Burning zone thickness equation

$$\delta = \lambda \frac{u_t}{u_l}$$

An approximate equation was needed for the first burning step since no unburned area was available. The initial kernel is small and grows rapidly. It has a negligible mass compared to the charge. For this first step it is assumed that the density inside the kernel is the burned gas density and that density variations are small compared to the growth of the flame.

$$\frac{d(\rho_b V_f)}{dt} = \rho_u A_u u_t$$

in which  $V_f$  is the volume of the burning zone

$$V_f \frac{d\rho_b}{dt} + \rho_u A_u \frac{dR_u}{dt} = \rho_u A_u u_t$$

$$\frac{dR_u}{dt} = \frac{\rho_u}{\rho_b} u_t$$

Alternatively the calculation could be started with an initial

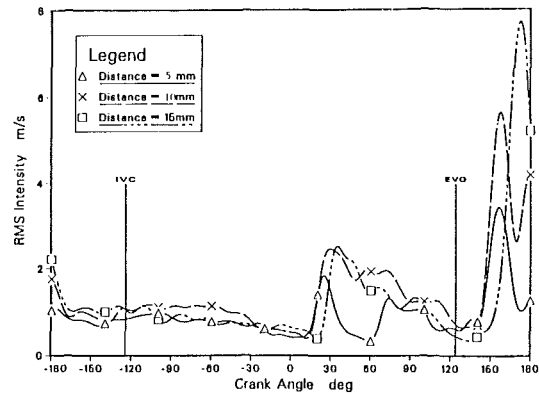


Fig. 5 Effect of position along the spark plug axis on turbulence intensity at 1200 rpm

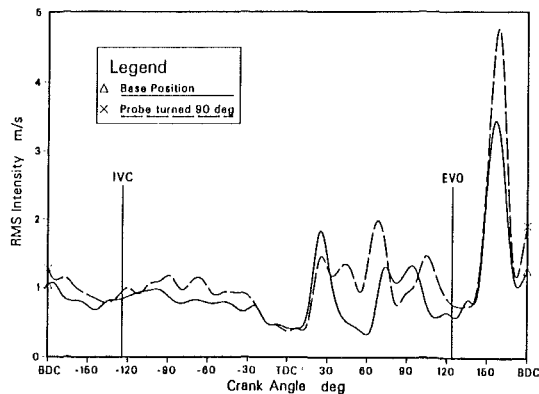


Fig. 6 Effect of wire orientation on turbulence intensity at 1200 rpm

radius equal to  $\lambda/4$ , corresponding to the average ignition delay distance.

**Final Burnup.** Once the outer edge of the flame has engulfed the chamber, the definition of  $\delta$  is no longer feasible. In this case, the simple burning rate equation is used to describe the laminar burnup of the remaining pockets.

According to the exponential burning law, the rate of mass burned is proportional to the amount of unburned gas left in the flame zone.

$$\frac{dm_b}{dt} = \frac{m_u}{\tau_c}$$

$$\Delta m_u = m_{u1} \frac{2u_l}{\lambda} \Delta t$$

in which  $m_{u1}$  is the unburned mass at the end of the previous calculation step. This equation is used up to complete burning of the charge.

#### 4 Measurements of Turbulence Intensity

Figure 3 shows the results of ensemble-averaged mean velocity and also the cycle-by-cycle nonstationary time-averaged mean velocity as a function of crank angle for 3000 rpm. For the crank angle interval around top dead center associated with combustion, it may be seen that the choice of window size has little effect on the computed average mean velocity.

In contrast Fig. 4 shows that for the computed rms-average fluctuation intensity  $u'$ :

(i) that ensemble averaging the velocity traces for all cycles produces substantially higher rms averages (roughly a factor

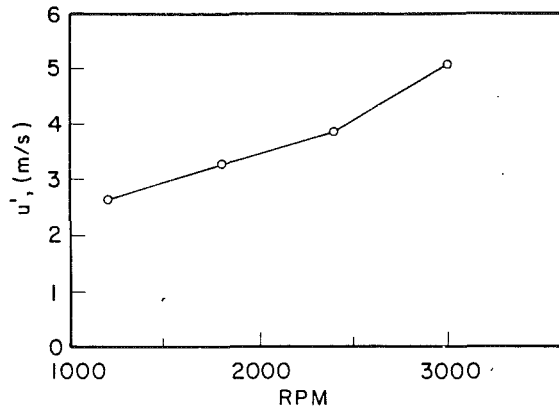


Fig. 7 Mean turbulence intensity estimated from model and pressure data with near-stoichiometric operation

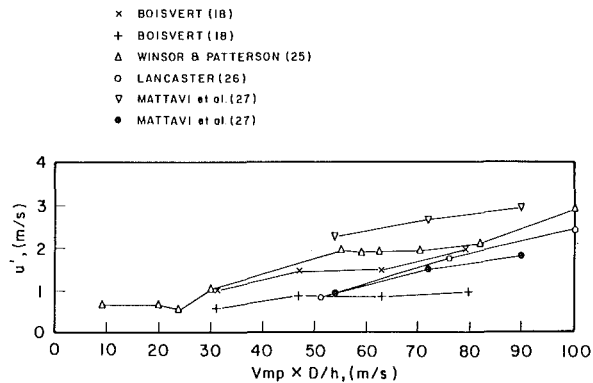


Fig. 8 Comparison of top dead center turbulence intensity with other measurements

of two higher) for a given crank angle, than does the cycle-by-cycle nonstationary time-averaged values for each of the 100 cycles. This indicates that cycle-to-cycle variation of the turbulence is substantial.

(ii) The effect of window size on the cycle-by-cycle nonstationary time-averaged values is large; no window size in the range 6–18° appears to be satisfactory.

Figures 5 and 6 show that the apparent turbulence intensity  $u'$  (computed with an 8° window size) is sensitive to probe location and orientation.

Given also that the result is quite sensitive to window size it appears that the hot-wire data provide indications of spatially averaged turbulence intensity which are uncertain by a factor of 2 or 3.

With this in mind we ask whether the simulation model coupled with the pressure data at a given speed can indicate the effective average  $u'$  at a given engine speed. One test of the validity of this determination is whether for the same rpm and the same  $u'$  the model correctly predicts the changes in performance with equivalence ratio. That this test is satisfied is shown in Section 5. Figure 7 shows the values of  $u'$  at spark, deduced from the model and the pressure data, as a function of rpm. These values are in rough agreement with the ensemble-averaged  $u'$  values presented in Fig. 4.

Figure 8 compares the  $u'$  values presented in Fig. 7 with the results of other investigators. If the average velocity through the valve is taken to be the appropriate scaling velocity for  $u'$  then it is reasonable to plot  $u'$  against  $V_p (D/h) (D/d)$ , in which  $V_p$  is the mean piston velocity,  $D$  the cylinder diameter,  $h$  the valve lift, and  $d$  the inlet valve port diameter. Since  $D/d$  is not always reported and does not vary greatly, the  $x$  axis in Fig. 9 is simply  $V_p (D/h)$ . (Bopp et al. [24] plotted  $u'$  versus

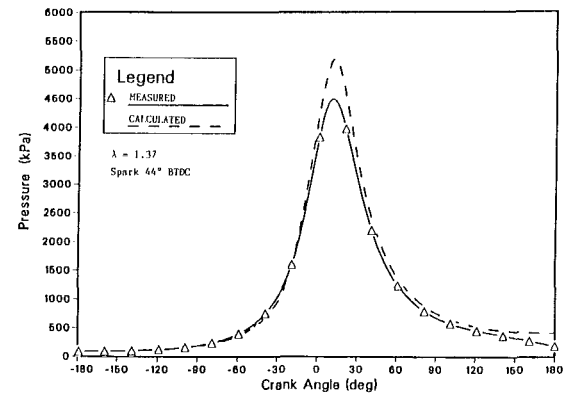
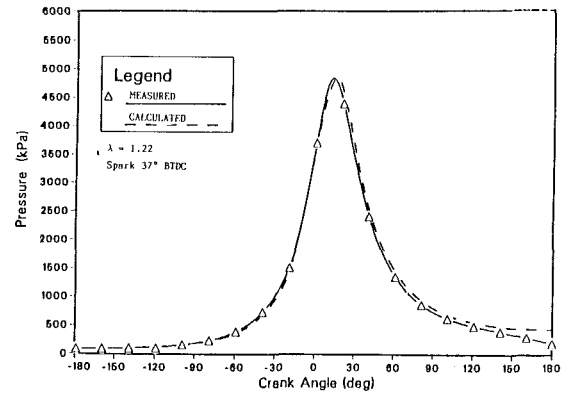
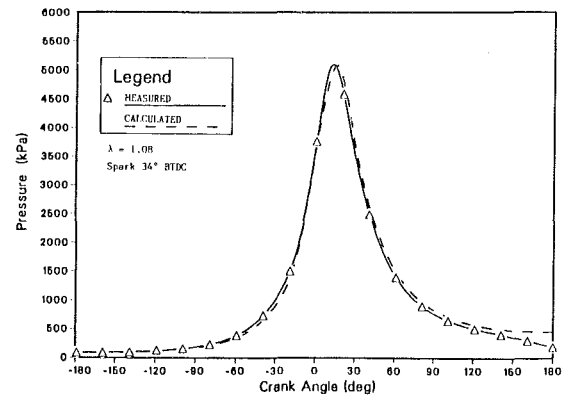


Fig. 9 Comparison of calculated and experimental pressure histories for 3000 rpm

$V_p$  for different experimental results; the scatter was somewhat greater than shown in Fig. 8).

It will be seen that the  $u'$  values deduced from the model and the measured pressures are in quite reasonable agreement with the hot-wire determinations of  $u'$  of other workers, bearing in mind the large uncertainties associated with the use of hot wires to measure turbulence in engines.

## 5 Measurements of Pressure

Figure 9 shows comparisons at 3000 rpm of measured pressure rise for various equivalence ratios; in each case the spark was timed for minimum advance at best torque. Shown also are the model predictions which use the  $u'$  variation with speed specified in Fig. 8. In general the shape of the predicted curves agrees well with the measured values except for overestimation of the peak values. Similar agreement was shown in comparisons for 1800 and 2400 rpm.

**Table 3 Cyclic variations**

rpm	Relative air-fuel ratio	Spark, °BTDC	IMEP, kPa	$\sigma_{IMEP}$ , kPa	$P_{max}$ , kPa	$\sigma_{P_{max}}$ , kPa	$\frac{\lambda}{4u_t}$ , ms	$\sigma_{IMEP}^*$ , kPa	$\sigma_{P_{max}}^*$ , kPa
1800	1.00	29	875	12.5	4830	287	0.19	1.6	315
1800	1.15	29	835	21.9	4430	404	0.28	0.6	326
1800	1.28	35	764	23.4	4074	450	0.37	1.5	353
2400	1.06	35	899	16.7	4904	300	0.21	4.1	268
2400	1.30	37	809	29.7	4509	443	0.28	4.0	357
2400	1.35	42	749	31.8	4058	629	0.35		777
3000	1.08	34	951	28.5	5034	406	0.22	2.4	458
3000	1.25	37	898	34.	4767	485	0.28	2.6	539
3000	1.39	44	780	39.4	4430	637	0.33		973

\*With standard deviation in delay time equal to 0.57 ( $\lambda/4u_t$ ).

The ability of the model to predict changes in pressure development with change in equivalence ratio at the same rpm is shown over a considerable range of interval between spark timing and peak pressure.

Figure 10 shows the mass-burned fractions, for 3000 rpm, deduced from the pressure-crank angle distribution in each case.

The method of calculation consisted of first adjusting the pressure to correspond to constant volume combustion, then using the approximation (for constant-volume combustion)

$$x = \frac{p - p_1}{p_{max} - p_1}$$

in which  $x$  is the burned-mass fraction,  $p_1$  is the pressure at spark angle, and  $p_{max}$  is the value of the maximum adjusted pressure (at the end of the combustion period).

To remove the effect of piston motion, a calculation was made of what the pressure in the cylinder would have been if combustion had taken place entirely at the cylinder volume at spark timing. Starting from the occurrence of spark, for each subsequent crank angle, the pressure was expanded polytropically from its value at the current volume to the value it would have had at the spark volume by using the following equation:

$$P_{rise}(n) = P(n) \left( \frac{V(n)}{V_{spark}} \right)^{1.30} \quad (19)$$

A polytropic index of 1.3 was used as a mean value over the range of temperatures covered. Thus constant-volume combustion was simulated.

It may be noted that the values of  $u'$  of Fig. 7 produce very close agreement in the burning rate for  $\lambda$  close to 1 for most of the burning period, and quite close agreement for other values of  $\lambda$ . Toward the end of the combustion period, the model consistently overpredicts the combustion rate; this is also shown by overprediction of the pressure (Fig. 10).

Table 3 shows the mean and standard deviations of indicated mean effective pressures and maximum pressures for sets of 100 cycles at each rpm and relative air-fuel ratios. The standard deviations increase substantially with both rpm and air-fuel ratio.

Shown also in Table 3 are the changes in the maximum pressure and mean effective pressure values calculated using the simulation model on the assumption that the standard deviation of the ignition delay time is 0.57 times the estimated mean value ( $\lambda/4u_t$ ); this standard deviation is reasonable given a postulated range of ignition delay from 0 to  $\lambda/2u_t$ .

As shown, the measured and calculated standard deviations of the maximum pressures show similar trends and are in fairly good quantitative agreement. This is so even though, as Fig. 9 shows, the mean values of the peak pressures (measured and calculated) are not particularly close. The similarity of the standard deviations does however suggest that the Tennekes

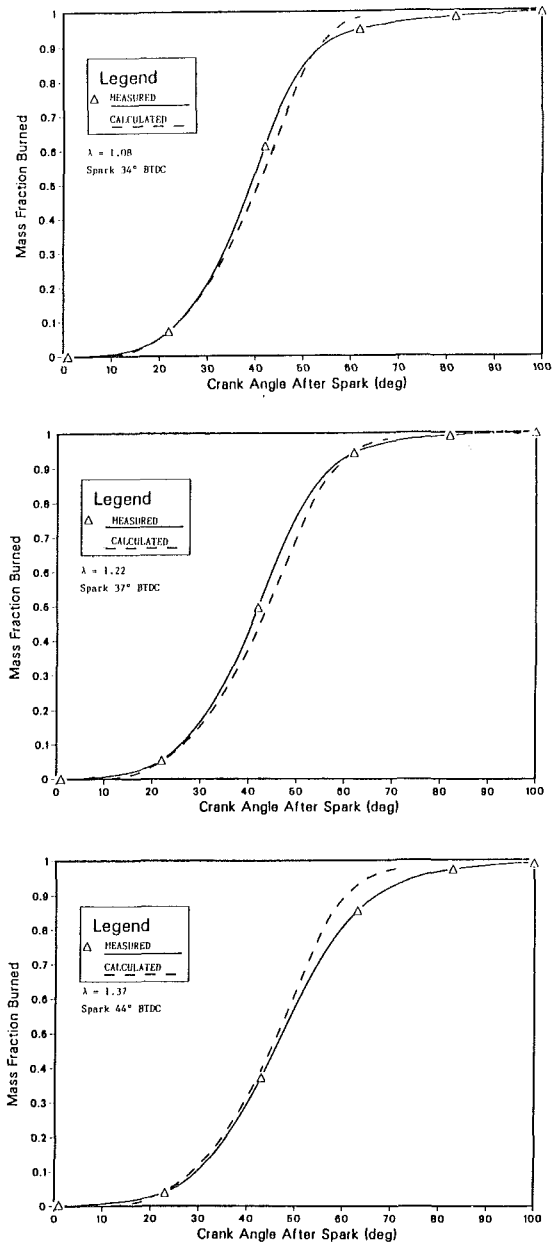


**Fig. 10 Comparison of calculated and experimental mass burned fractions for 3000 rpm**

structure of small-scale turbulence provides an explanation for at least a significant part of the observed cycle-to-cycle variation of combustion.

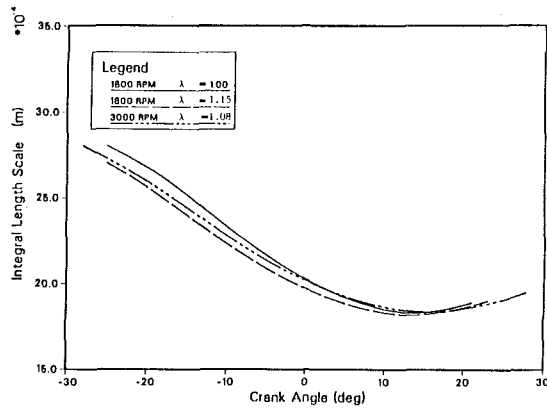


Fig. 11 Estimated integral length scales

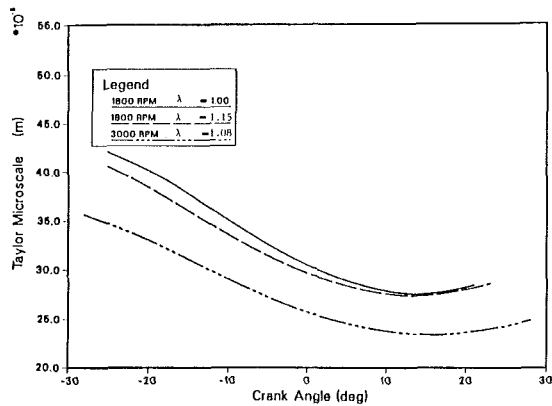


Fig. 12 Estimated Taylor microscales

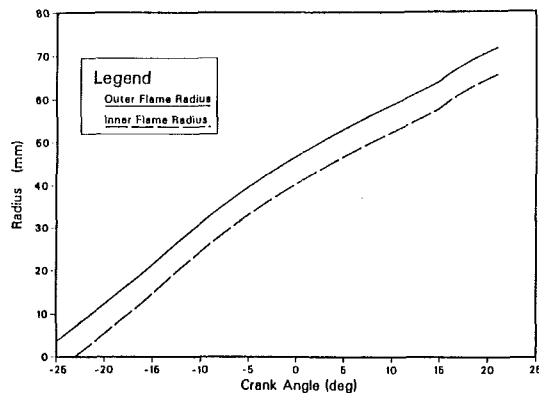


Fig. 13 Predicted inner and outer flame radius for 1800 rpm and  $\lambda = 1.00$

It may be noted that very small standard deviation in indicated mean effective pressure is estimated by using the simulation model. This is not surprising since the experimental data correspond to minimum spark advance for best torque. The standard deviations in the mean effective pressure values are small (1–3 percent) and not much greater than the uncertainty level.

## 6 Typical Turbulence Quantities

Figures 11 and 12 show typical computations of the variation in integral length scale and Taylor microscale during the combustion period.

Figure 13 shows the result of a typical calculation of the variation of flame radius and flame thickness with crank angle.

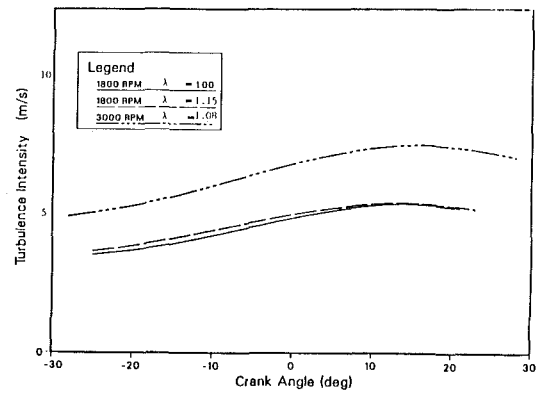


Fig. 14 Estimated turbulence intensity during combustion

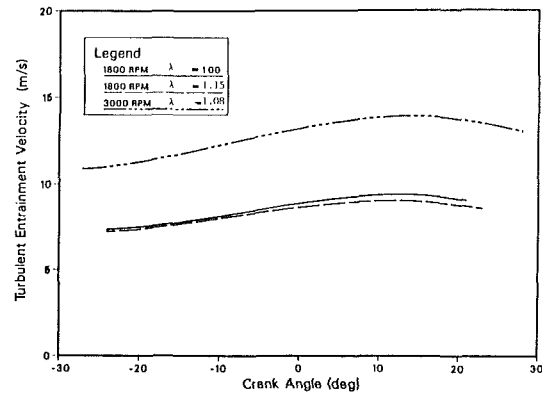


Fig. 15 Estimated turbulent entrainment velocity at 1800 rpm,  $\lambda = 1.00$  and  $\lambda = 1.15$ ; 3000 rpm,  $\lambda = 1.08$

Figure 14 shows the result of a typical calculation of the variation of  $u'$  during the combustion period, at 1800 and 3000 rpm.

Figure 15 shows the result of a typical calculation of the variation of turbulent entrainment velocity  $u_t$  during the combustion period, at 1800 and 3000 rpm.

## 7 Conclusions

1 An engine simulation program was developed incorporating the turbulent entrainment model. This program simulates the firing strokes of the Ricardo Hydra engine operating on a gaseous fuel. The model features ignition delay and turbulent entrainment of a thick reaction front accompanied by slow laminar burning inside the thick flame.

2 The turbulence levels in the motored engine were measured using hot-wire anemometry. Measurements were conducted at four engine speeds and at various positions along the spark plug axis in the chamber. The resulting window-averaged turbulence intensity levels were lower than the ensemble-averaged turbulence quantities by about a factor of 2.

3 Combustion pressure histories were measured over a range of engine speeds and air-fuel ratios. From the pressure data, mass-fraction-burned curves were calculated. Deducing turbulence intensity values from the model experimental pressures gave excellent agreement between calculations and experiments with regard to combustion initiation and mass burn rates over the speed and air-fuel ratio range investigated. Discrepancy toward the end of combustion is believed to be a result of the method used to calculate the experimental mass fraction burned. The model predicted higher peak pressures



by about 10 percent. The correct trend was obtained over the speed and air-fuel ratio range.

4 Considering estimated and measured standard deviations of the peak pressure, it appears that the observed cycle-to-cycle variations in peak pressure are consistent with the combustion implications of the Tennekes model of the small-scale structure of turbulence.

### Acknowledgments

The authors are grateful for financial support from Energy Mines and Resources Canada.

### References

- 1 Lancaster, D. R., Krieger, R. B., Sorensen, S. C., and Hull, W. L., "Effect of Turbulence on Spark-Ignition Engine Combustion," SAE Paper No. 760160, 1976.
- 2 Lancaster, D. R., "Effect of Engine Variables on Turbulence in a S. I. Engine," SAE Paper No. 760159, 1976.
- 3 Lancaster, D. R., Frieiger, R. B., and Lienesch, J. H., "Measurement and Analysis of Engine Pressure Data," SAE Paper No. 750026, 1975.
- 4 Semenov, E. S., "Studies of Turbulent Gas Flow in Piston Engines," NASA Technical Translation F-97, 1963.
- 5 Daneshyar, H., and Fuller, D. E., "Definition and Measurement of Turbulence Parameters in Reciprocating IC Engines," SAE Fuels and Lubricants Meeting, Philadelphia, Oct. 6-9, 1986.
- 6 Catania, A. E., and Mittica, A., "A Contribution to the Definition of Turbulence in a Reciprocating I. C. Engine," ASME Paper No. 85-DGP-12, 1985.
- 7 Fraser, R. A., Felton, P. G., Bracco, F. V., and Santavicca, D. A., "Preliminary Turbulence Length Scale Measurements in a Motored IC Engine," SAE Paper No. 860021, 1986.
- 8 Tabaczynski, R. J., "Turbulence and Turbulent Combustion in Spark-Ignition Engines," *Prog. Energy Combust. Sci.*, Vol. 2, 1976, pp. 143-165.
- 9 Tabaczynski, R. J., "Turbulence Measurement and Modelling in Reciprocating Engines—An Overview," *I Mech. Eng.*, 1983.
- 10 Tabaczynski, R. J., Ferguson, C. R., and Radhakrishnan, K., "A Turbulent Entrainment Model for Spark-Ignition Engine Combustion," *SAE Transactions*, Vol. 86, 1977, pp. 2414-2433.
- 11 Hires, S. D., Tabaczynski, R. J., and Novak, J. M., "The Prediction of Ignition Delay and Combustion Intervals for a Homogeneous Charge Spark-Ignition Engine," SAE Paper No. 780232, 1978.

12 Tabaczynski, R. J., Trinker, F. H., and Shannon, B.A.S., "Further Refinements and Validation of a Turbulent Entrainment Model for Spark-Ignition Engines," *Combustion and Flame*, Vol. 39, 1980, pp. 111-121.

13 Keck, J. C., "Turbulent Flame Structure and Speed in Spark-Ignition Engines," *Nineteenth Symposium (International) on Combustion*, The Combustion Institute, 1982, pp. 1451-1466.

14 Beretta, G. P., Rashidi, M., and Keck, J. C., "Turbulent Flame Propagation in Spark Ignition Engines," *Combustion and Flame*, Vol. 52, 1983, pp. 217-245.

15 Tennekes, H., "Simple Model for the Small-Scale Structure of Turbulence," *The Physics of Fluids*, Vol. 11, No. 3, pp. 669-670.

16 Daneshyar, H., and Hill, P. G., "The Structure of Small Scale Turbulence and Its Effect on Combustion in Spark-Ignition Engines," *Progress in Combustion Science and Technology*, in press.

17 Chomiak, J., "Dissipation Fluctuations and the Structure and Propagation of Turbulent Flames in Premixed Gases at High Reynolds Numbers," *Sixteenth Symposium (International) on Combustion*, The Combustion Institute, 1977, pp. 1665-1673.

18 Boisvert, J., "Turbulent Combustion of Gas-Air Mixtures in Spark-Ignition Engines," M.A.Sc. Thesis, University of British Columbia, June 1986.

19 Witze, P. O., "A Critical Comparison of Hot-Wire Anemometry and Laser Doppler Velocimetry for I. C. Engine Applications," SAE Paper No. 800132, 1980.

20 Abdel-Gayed, R. G., Al-Khishali, K. J., and Bradley, D., "Turbulent Burning Velocities and Flame Straining in Explosions," *Proceedings of the Royal Society, London*, Ser. A., Vol. 391, 1984, pp. 393-414.

21 Andrews, G. E., and Bradley, D., "The Burning Velocity of Methane-Air Mixtures," *Combustion and Flame*, Vol. 19, 1972, pp. 275-288.

22 Jones, A. L., "The Performance of a Turbocharged Spark-Ignition Engine Fuelled With Natural Gas and Gasoline," M.A.Sc. Thesis, University of British Columbia, 1985.

23 Annand, W. J. D., "Heat Transfer in the Cylinder of Reciprocating Internal Combustion Engines," *Proc. I. Mech. E.*, Vol. 177, No. 36, 1983, pp. 973-996.

24 Bopp, S., Vafidis, C., and Whitelaw, J. H., "The Effect of Engine Speed on the TDC Flowfield in a Motored Reciprocating Engine," SAE Paper No. 860023, 1986.

25 Winsor, R. E., and Patterson, D. J., "Mixture Turbulence—A Key to Cyclic Combustion Variations," SAE Paper No. 730086, 1973.

26 Lancaster, D. R., "Effects of Engine Variables on Turbulence in a Spark-Ignition Engine," SAE Paper No. 760159, 1976.

27 Mattavi, J. N., Groff, E. G., and Matekunas, F. A., "Turbulence, Flame Motion and Combustion Chamber Geometry—Their Interactions in a Lean Combustion Engine," General Motors Research Laboratory Report, GMR-2884, 1979.

# Combustion Characteristics of a Single-Cylinder Open-Chamber Diesel Engine

A. C. Alkidas

Engine Research Department,  
General Motors Research Laboratories,  
Warren, MI 48090-9055

*The combustion characteristics of an open-chamber diesel engine were examined by means of heat-release analysis and flame luminosity measurements. Increasing the load was found to decrease premixed burning and correspondingly to increase diffusion burning. During most of the diffusion combustion the burning rate of the fuel appeared to be directly proportional to the amount of unburned fuel present in the cylinder. The duration of heat release in crank-angle degrees increased linearly with load and, in general, increased with decreasing engine speed and retarded injection timing. The measured duration of flame luminosity was significantly longer than the calculated duration of heat release, which suggested that emission of radiation continued long after the heat-release reactions ceased.*

## Introduction

Heat-release analysis has been widely used to study the combustion characteristics of open-chamber [1-3] and divided-chamber [4-6] diesel engines. The heat-release history of the fuel in the combustion chamber is computed from a thermodynamic model that utilizes as input the measured cylinder-pressure history.

A typical heat-release history of an open-chamber engine is shown schematically in Fig. 1. Combustion consists of an initial premixed-combustion stage which has a short duration and a high rate of heat release, followed by the main diffusion-combustion stage. The heat-release history during premixed combustion is strongly dependent on the amount of fuel that mixes with air to form a combustible mixture during the ignition-delay period [7]. The rate of heat release during diffusion combustion is controlled by the air-fuel mixing [8].

This study examined the combustion characteristics of a single-cylinder heavy-duty open-chamber diesel engine. In particular, this study investigated the influence of load and injection timing on the premixed and diffusion peak heat-release rates, on the fraction of fuel which burned in the premixed mode of combustion (premixed-burned fuel), on the duration of heat release, and on the duration of premixed combustion. In addition, from measurements of flame luminosity in the combustion chamber of the engine, the duration of flame luminosity was obtained and compared to the computed duration of heat release.

## Experimental Program

The measurements were made in an experimental water-cooled single-cylinder 2-L open-chamber diesel engine. The

Contributed by the Internal Combustion Engine Division and presented at the Energy-Sources Technology Conference and Exhibition, Dallas, Texas, February 15-20, 1987. Manuscript received at ASME Headquarters December 10, 1986. Paper No. 87-ICE-35.

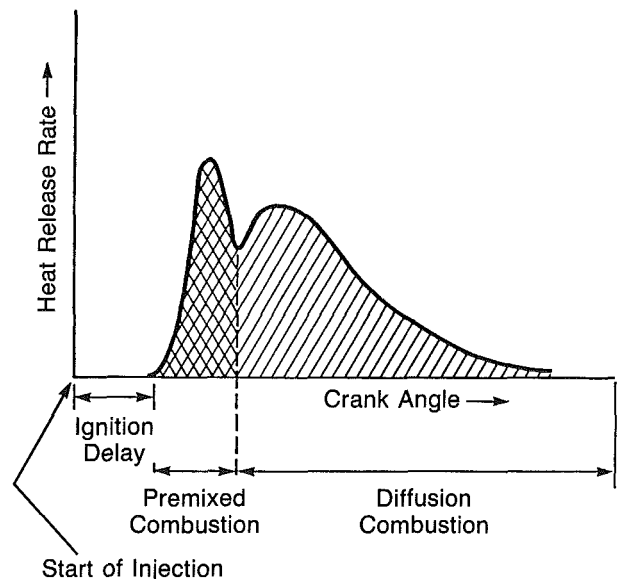


Fig. 1 Schematic of typical heat-release history in an open-chamber diesel engine

Table 1 Engine specifications

Bore, mm	130
Stroke, mm	153
Displacement, L	2.03
Compression ratio	16:1
Unit injector:	
No. of holes	8
Hole diameter, mm	0.25
Included angle, deg	160

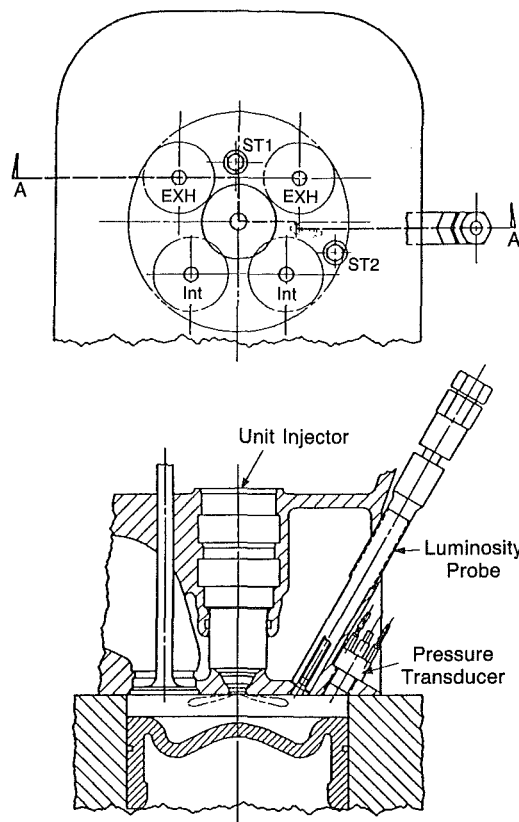


Fig. 2 Combustion-chamber geometry of the test engine

engine specifications are listed in Table 1. The injector is a mechanical unit injector with constant start of injection and variable injection duration. The combustion-chamber geometry is shown schematically in Fig. 2. The cylinder head is designed to allow surface-temperature measurements at two locations (ST1 and ST2), cylinder-pressure measurements, and flame-luminosity measurements. The articulated cast-iron piston has a shallow bowl.

The time-averaged surface temperatures at two locations on the cylinder head were measured with eroding-type chromel-alumel thermocouples [9, 10] having a body manufactured from the same material as the cylinder head. The flame luminosity was detected by a luminosity probe which consisted of a long quartz rod that transmitted flame radiation from the combustion chamber of the engine to a photodiode sensor. From this measurement the start of luminosity, which can be interpreted as a measure of the ignition of the fuel, and the luminosity duration, which may be a measure of the combustion duration of the fuel, could be evaluated. The cylinder pressure was measured using a water-cooled piezoelectric pressure transducer. Because of its importance in heat-release analysis, details of the pressure measurements and signal conditioning are given in a subsequent section.

**Test Conditions.** Tests were performed at two engine speeds, 1200 and 1800 rpm. At each engine speed  $N$ , for constant static injection timing ( $\tau_{inj} = 8$  deg BTDC) the fueling rate  $\dot{m}_F$ , and hence the load, was varied, and for constant fueling rate the injection timing was varied. Details for all the engine conditions examined, including engine inlet pressure  $p_A$ , exhaust pressure  $p_E$ , fuel-air ratio  $F/A$ , and brake mean effective pressure BMEP, are shown in Table 2. These conditions were chosen to simulate operation of a turbocharged, aftercooled engine. For all operating conditions, the intake air, cooling water, and lubricating oil were maintained at about 49°C, 82°C, and 94°C, respectively.

Table 2 Test series

Test No.	$N$ , rpm	$\tau_{inj}$ , deg BTDC	$p_A$ , kPa	$p_E$ , kPa	$\dot{m}_F$ , kg/h	$F/A$	BMEP, kPa
01	1200	8	205	164	6.09	0.0396	1392
02	1200	8	181	153	4.75	0.0350	1083
03	1200	8	157	144	3.41	0.0291	774
04	1200	8	133	135	2.34	0.0238	464
05	1200	8	110	127	1.18	0.0147	155
12	1800	8	240	206	8.29	0.0308	1238
13	1800	8	204	186	6.40	0.0281	928
14	1800	8	169	166	4.53	0.0240	619
15	1800	8	135	149	2.88	0.0195	309
22	1200	12	195	160	5.27	0.0362	1256
17	1200	8	195	160	5.37	0.0368	1238
18	1200	4	194	160	5.37	0.0369	1191
20	1200	0	194	160	5.47	0.0375	1111
23	1800	12	204	186	6.45	0.0283	965
19	1800	4	203	186	6.46	0.0289	888
21	1800	0	203	186	6.35	0.0280	810

**Pressure Measurements.** For each test condition examined, the gas pressure was recorded every 0.5 crank-angle deg for 96 consecutive engine cycles. The time-mark signal was generated by a magnetic pickup sensing the 720 teeth of the flywheel. The output of the piezoelectric pressure transducer was digitized with a 15-bit resolution. From these data the corresponding averaged cylinder-pressure history was calculated and stored for heat-release computations.

The sampling frequency of the pressure data is very important for heat-release analysis in open-chamber diesel engines. Although Pischinger and co-workers [11] contended that the sampling interval should be between 0.1 and 0.2 crank-angle deg (i. e., a data point every 0.1 to 0.2 crank-angle deg) in order to obtain reliable and accurate heat-release histories, others have sampled at intervals up to 1-crank-angle deg.

### Heat-Release Analysis

The heat-release analysis is based on a single-zone thermodynamic model that considers the cylinder contents to be a homogeneous ideal-gas mixture of air and products of combustion in thermodynamic equilibrium. The products of combustion are assumed to be in chemical equilibrium, and their thermodynamic properties are computed based on temperature, pressure, and the overall equivalence ratio of the mixture. For negligible dissociation of the products of combustion, the rate of heat release  $\dot{Q}_{HR}$  is related to the mass rate of burning of the fuel  $\dot{m}_B$  by

$$\dot{Q}_{HR}(\theta) = (\Delta H_o) \dot{m}_B(\theta) \quad (1)$$

where  $\Delta H_o$  is the lower heating value of the fuel and  $\theta$  is the crank angle.

The combustion-chamber-surface heat transfer  $\dot{Q}_w$  is described by

$$\dot{Q}_w(\theta) = h(\theta) \Sigma A_i(\theta) [T_g(\theta) - T_{w,i}] \quad (2)$$

where  $T_g$  and  $h$  are the gas temperature and convective heat-transfer coefficients, respectively, at crank angle  $\theta$ ,  $A_i$  represents the surface areas of cylinder head, piston crown, and liner which are exposed to the gases, and  $T_{w,i}$  represents the corresponding time-averaged surface temperatures. The convective heat transfer coefficient is computed from an empirical equation developed by Woschni [12]. The surface temperatures were estimated from measured cylinder-head surface temperatures whose variation with load is shown in Fig. 3 for engine speeds of 1200 and 1800 rpm. The surface heat transfer is scaled, by using a constant multiplier in equation (2), such that the computed final fuel-burned fraction is equal to a specified value which is estimated from exhaust-emission measurements.

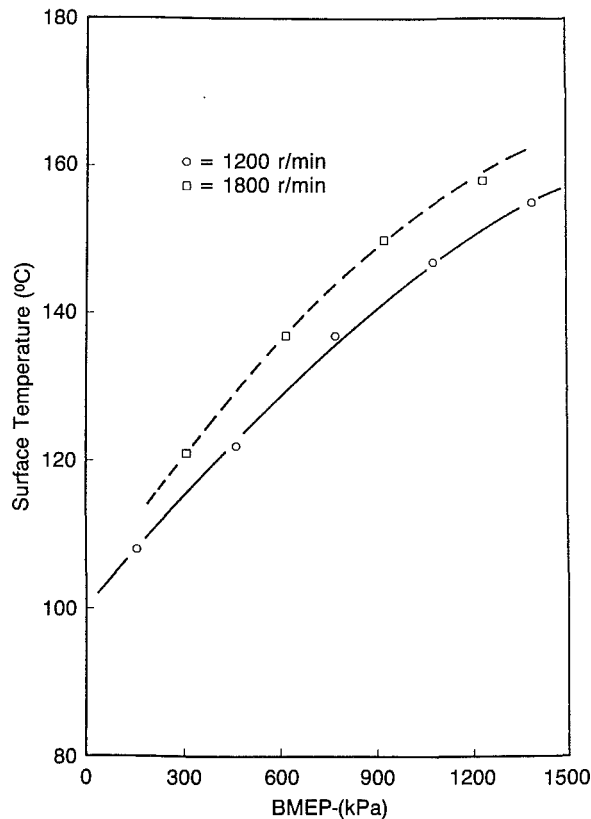


Fig. 3 Cylinder-head surface-temperature measurements versus load

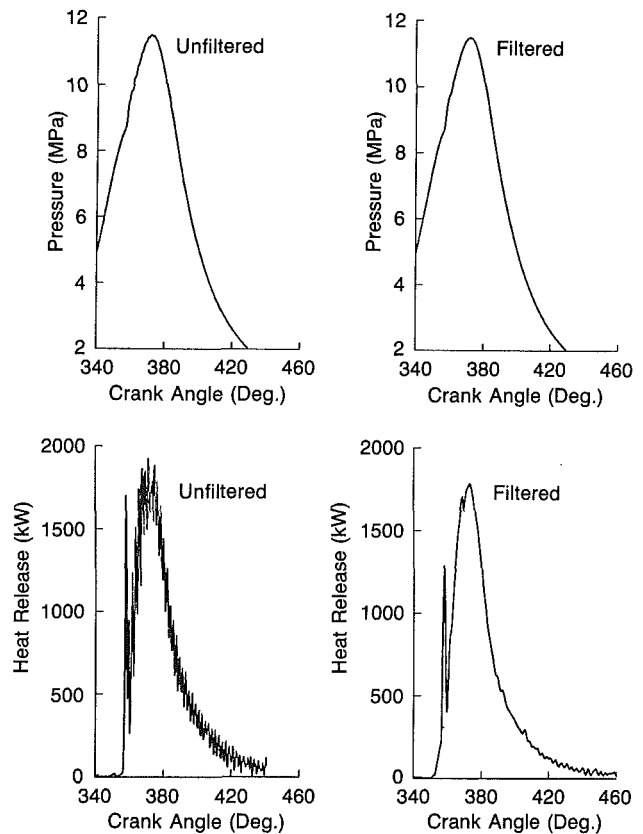


Fig. 4 Comparisons of filtered and unfiltered pressures and their corresponding heat-release histories (BMEP = 1392 kPa, 1200 rpm)

The measured cylinder-pressure histories contained high-frequency ripples which are believed to be generated by the rapid expansion of combustion gases in the engine cylinder [13]. These pressure ripples could cause significant high-amplitude noise in the computed heat-release histories, and in some cases they may render the heat-release histories unusable. To eliminate this high-amplitude noise in the heat-release history, the high-frequency ripples in the pressure data were removed by means of digital filtering. Details on the design of various digital filters may be found in [14].

Comparisons of filtered and unfiltered pressure histories and their corresponding computed heat-release histories are presented in Figs. 4 and 5 for heavy and light loads, respectively. These results show the high-amplitude noise in the heat-release histories produced by the high-frequency ripples in the pressure data and how effectively they were removed by digital filtering. One may also recognize that, for the light-load condition, the computed heat-release history is totally unusable without filtering the pressure data.

To characterize and compare the heat-release history of the fuel at different operating conditions of the engine, the following parameters were evaluated:

- 1 Premixed peak heat-release rate—the value of the peak heat-release rate during the period of premixed combustion.
- 2 Diffusion peak heat-release rate—the value of the peak heat-release rate during the period of diffusion combustion.
- 3 Premixed-burned fraction—the fraction of fuel mass which burns in the premixed mode of combustion.
- 4 Heat-release duration—period between the start of heat release, which is arbitrarily defined as the time (or crank angle) corresponding to a mass-burned fraction of 0.01, and the end of heat release, which is arbitrarily defined as the time corresponding to mass-burned fraction of 0.90.
- 5 Ignition delay period—period between the start of injection and the start of heat release.

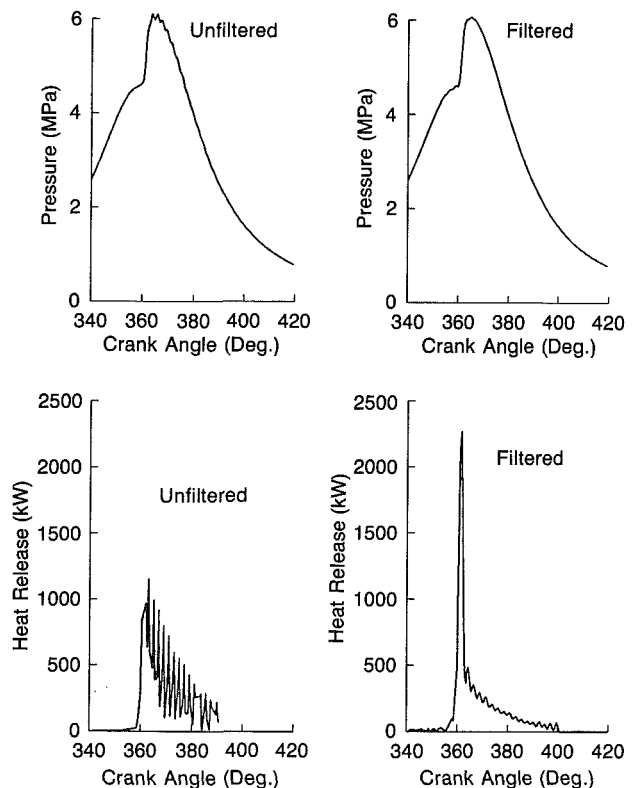


Fig. 5 Comparisons of filtered and unfiltered pressures and their corresponding heat-release histories (BMEP = 155 kPa, 1200 rpm)

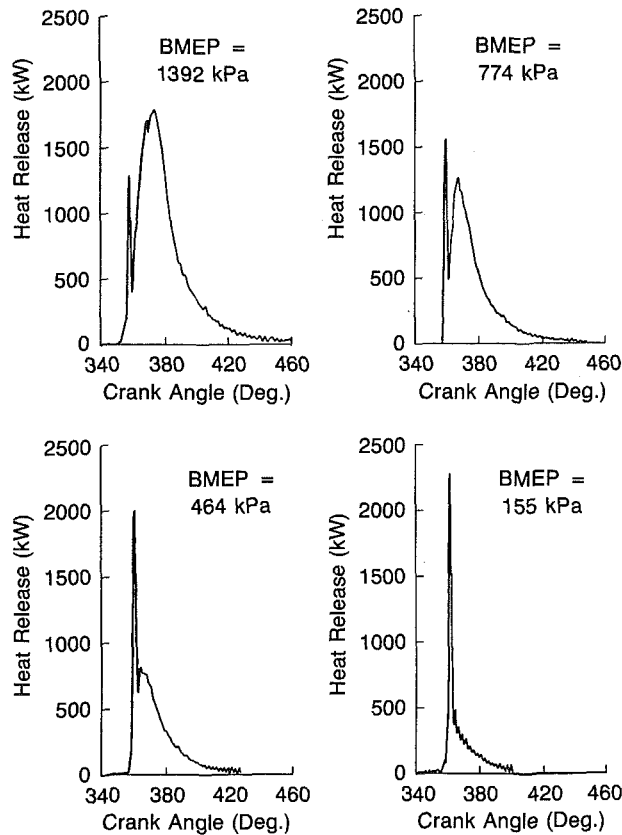


Fig. 6 Heat-release histories for various loads (1200 rpm)

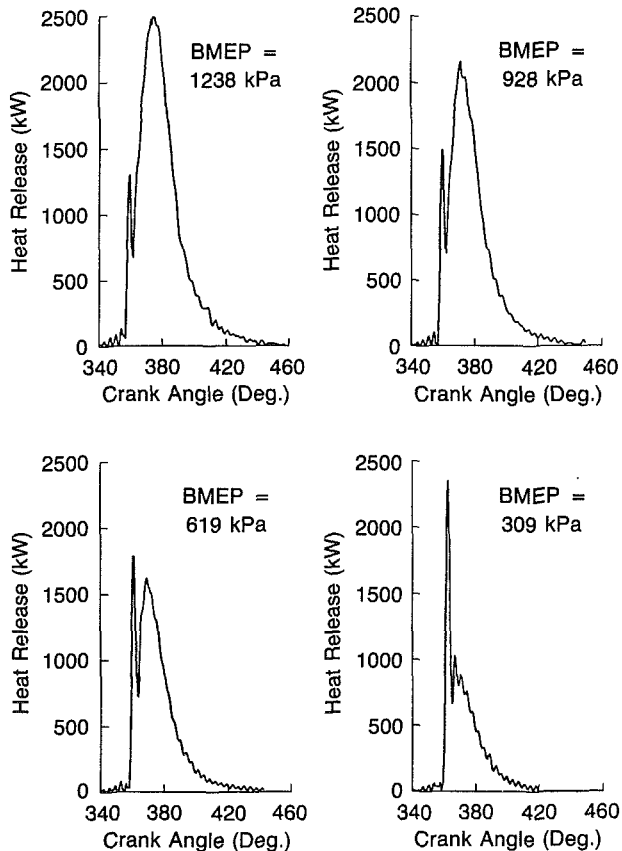


Fig. 7 Heat-release histories for various loads (1800 rpm)

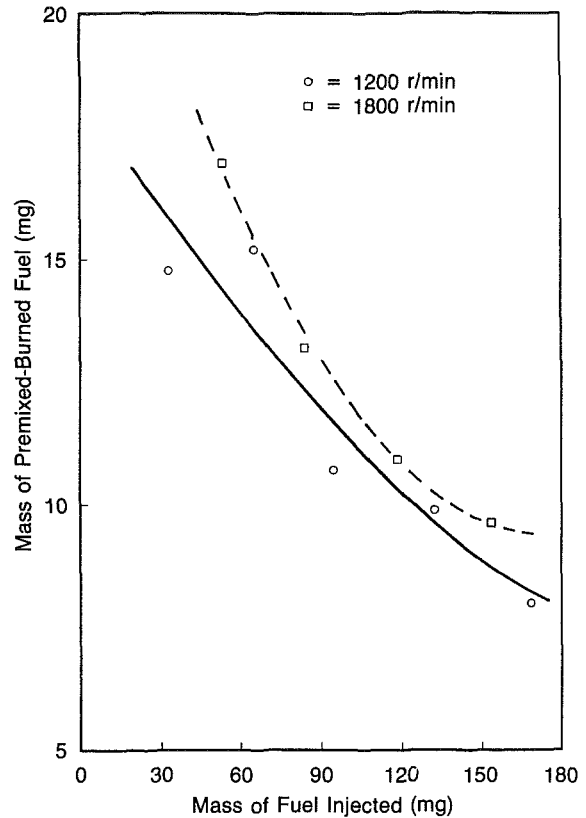


Fig. 8 Mass of premixed-burned fuel as a function of the mass of fuel injected in the cylinder

Similar to the definition of heat-release duration, the definition of premixed-burned fraction or premixed burning is somewhat arbitrary. In the present study the method adopted to define premixed combustion is shown in Fig. 1 and is the same as that used by Van Gerpen et al. [3] and Wade and Hunter [15].

## Results

Figures 6 and 7 show the variation of heat-release histories with load (BMEP) for engine speeds of 1200 and 1800 rpm, respectively. It is apparent from both figures that at high load, diffusion burning is the principal mode of combustion. However, as the load is decreased, the role of premixed burning becomes increasingly important, and at the light-load condition, premixed burning is at least of equal importance to diffusion burning.

The increase in the amount of fuel burned in the premixed mode of combustion with decreasing load shown in Figs. 6 and 7 is demonstrated clearly in Fig. 8, which shows that, for both engine speeds, the mass of premixed-burned fuel increased with decreasing mass of fuel injected in the cylinder.

The increasing importance of premixed burning as the load decreases is demonstrated also in Fig. 9, which shows the relations between the rate of heat release and mass-burned fraction for various loads and for an engine speed of 1800 rpm. Even at the lightest load examined, more than 50 percent of the fuel is burned in the diffusion mode of combustion. An interesting observation is that after the diffusion peak heat-release rate, which occurs when 30 to 50 percent of the fuel is consumed, the rate of heat release appears to vary roughly linearly with the mass-burned fraction of the fuel. The slope of this linear relation is negative and decreases with decreasing load. This may be expressed as follows:

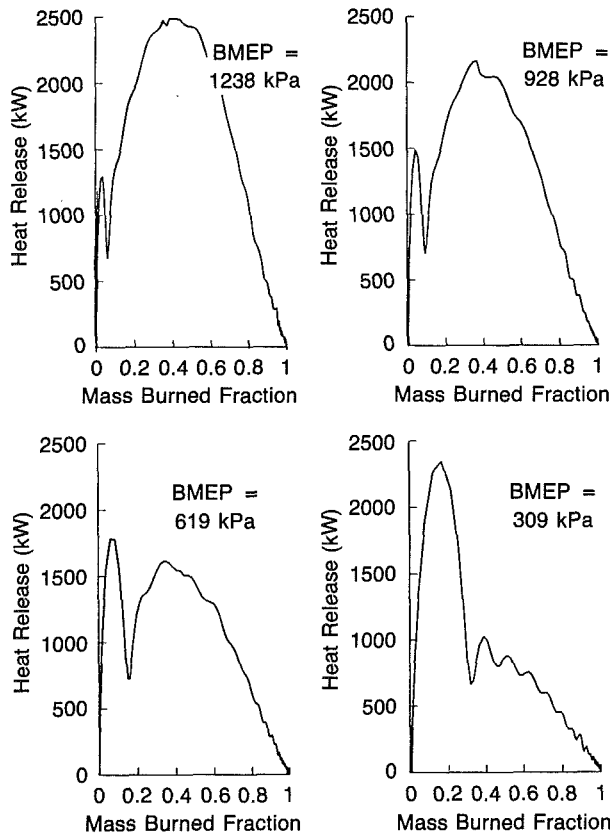


Fig. 9 Rate of heat release as a function of fuel mass-burned fraction for various loads (1800 rpm)

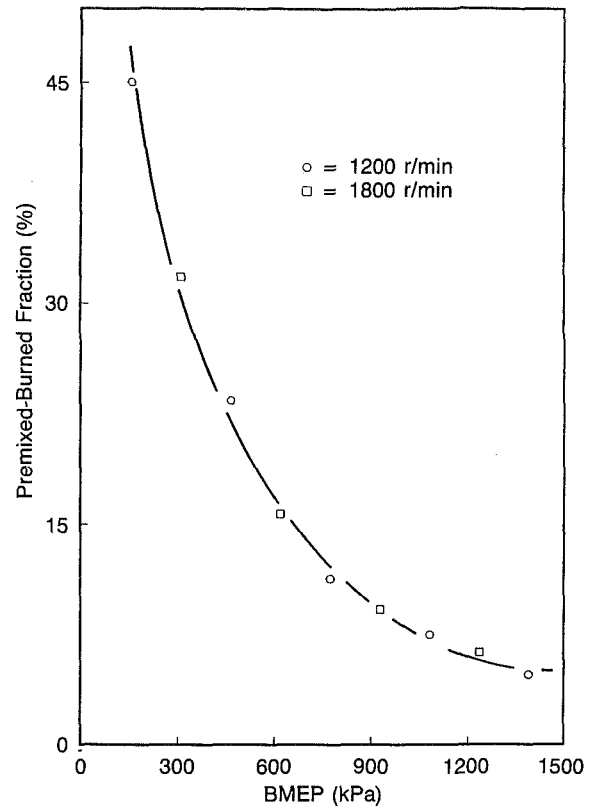


Fig. 11 Premixed-burned fraction versus BMEP

$$\dot{Q}_{HR}(\theta) = K \left( 1 - \frac{m_B(\theta)}{m_F} \right) \quad (3)$$

where  $m_B(\theta)$  is the cumulative mass of fuel burned at crank angle  $\theta$ ,  $m_F$  is the total mass of fuel injected, and  $K$  is a constant of proportionality. A mass balance of the fuel gives

$$m_B(\theta) = m_F - m_u(\theta) \text{ and } \dot{m}_B(\theta) = -\dot{m}_u(\theta) \quad (4)$$

where  $m_u$  is the mass of unburned fuel in the combustion chamber. Combining equations (4), (3), and (1) yields

$$\dot{m}_B(\theta) = -\frac{K}{\Delta H_o} m_u(\theta) \quad (5)$$

Thus the linear relationship between the rate of heat release and the mass-burned fraction implies that the burning rate of the fuel is directly proportional to the amount of unburned fuel present in the combustion chamber.

The effects of load on the peak rates of heat release during premixed and diffusion combustion are shown in Fig. 10 for the two engine speeds examined. As expected from the above heat-release histories, decreasing the load results in a significant increase in the peak rate of heat release in the premixed-combustion stage (premixed peak rate of heat release) and in a significant decrease in the peak rate of heat release in the diffusion-combustion stage (diffusion peak rate of heat release).

Perhaps the best method to quantify the role of premixed burning in diesel-engine combustion is to consider the premixed-burned fraction, i.e., the fraction of fuel which burns in the premixed mode of combustion. Figure 11 shows the computed variations in the premixed-burned fraction with BMEP for the two engine speeds examined. It is seen that the premixed-burned fraction increases dramatically with decreasing load, and for the same BMEP level, it appears to be insensitive to engine speed. As was found in an earlier study [7] which was performed on an automotive-type open-chamber diesel engine, the sensitivity of the premixed-burned fraction

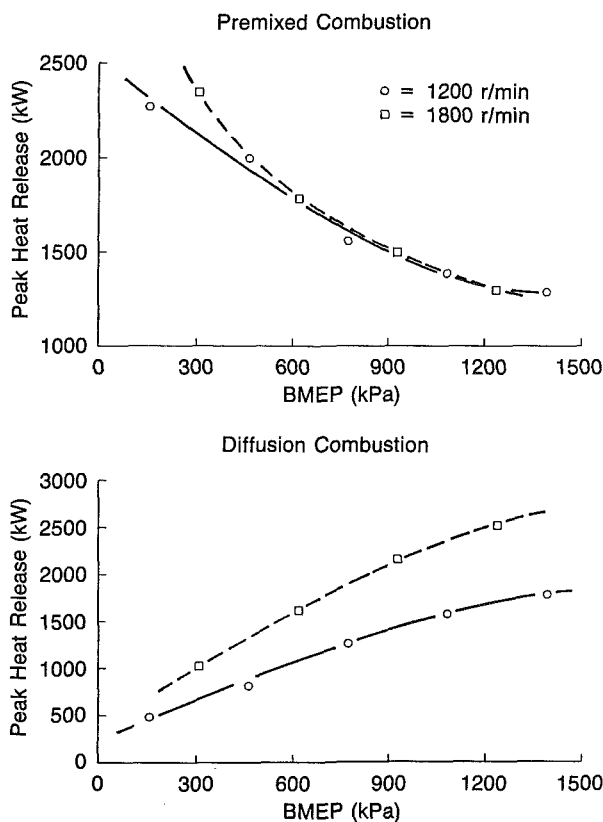


Fig. 10 Premixed and diffusion peak rate of heat release versus BMEP

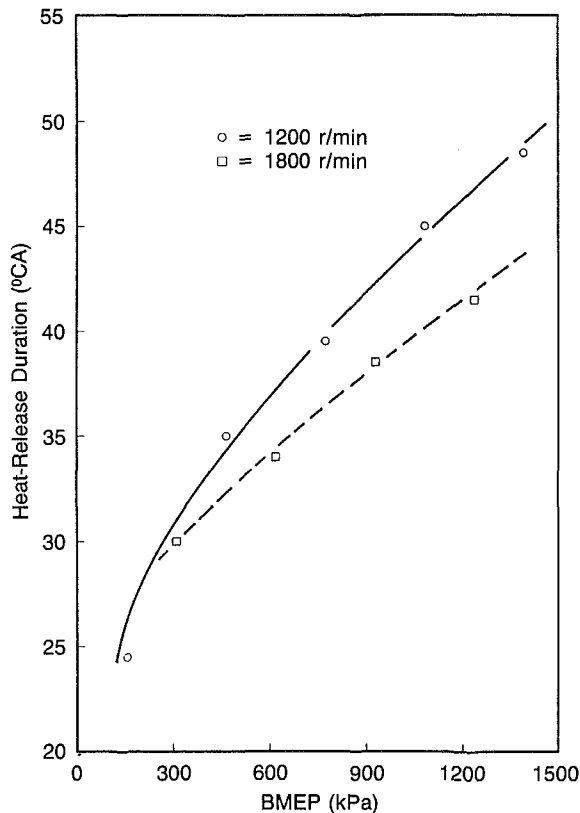


Fig. 12 Duration of heat release as function of BMEP

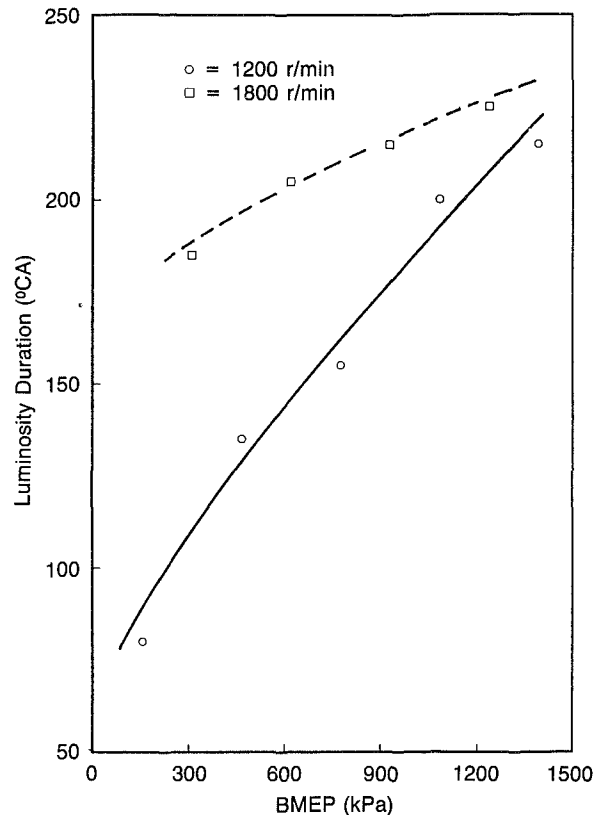


Fig. 13 Flame-luminosity duration as function of BMEP

to load increases with decreasing load. For all the operational conditions of the engine examined, the percent mass of fuel burned in premixed combustion varies from about 5 to 45 percent.

The effect of load on the duration of heat release is shown in Fig. 12 for engine speeds of 1200 and 1800 rpm. As a reminder, the duration of the heat release was defined arbitrarily as the period between the 1 and 90 percent mass-burned fractions. The duration of heat release, which is expressed in crank-angle degrees, increases with increasing load and with decreasing engine speed. With the exception of the light-load condition at 1200 rpm, the duration of heat release appears to vary linearly with load. This may be due partially to the corresponding linear increase of the injection duration with increasing load.

The corresponding durations of luminosity which were obtained from the measured flame-luminosity histories are presented in Fig. 13. Comparing the duration of heat release and the duration of luminosity, it is evident that the products of combustion continue emitting radiation in the visible and near-infrared wavelength range even after significant heat release from combustion ceases. These data were obtained for a start of heat release near TDC. Since the exhaust valve opens at about 121 deg ATDC, it is evident from Fig. 13 that emission of radiation persists well after the opening of the exhaust valves. These results are in agreement with the findings of Hiroyasu and co-workers [16], who attempted to correlate the end of luminosity with the smoke level emitted by their engine. They observed that whenever the end of flame luminosity exceeded the crank angle of exhaust valve opening, the exhaust smoke level was high.

To consider the influence of injection timing on the heat-release characteristics, Fig. 14 shows the variations of heat-release histories with injection timing for an engine speed of 1800 rpm. Unlike the load, the heat-release history of the fuel with injection timing does not appear to change significantly within the range examined. The premixed burned fraction was

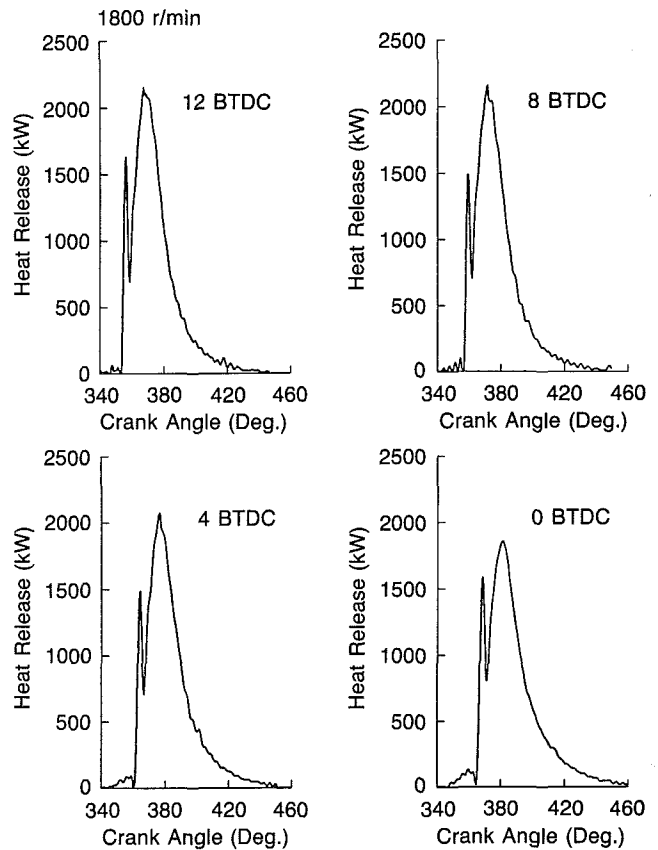


Fig. 14 Heat-release histories for various injection timings (1800 rpm)

found to decrease slightly and then to increase with advancing the injection timing from 12 deg BTDC to TDC.

The effect of injection timing on the duration of heat release

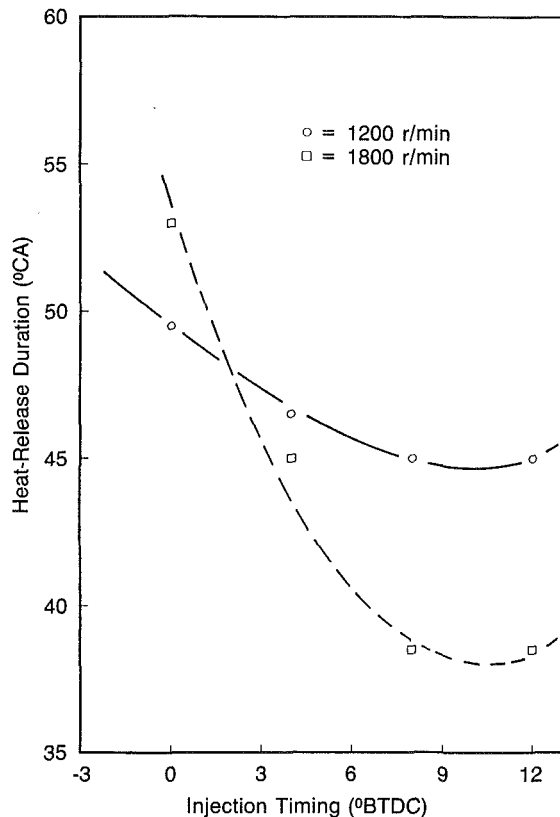


Fig. 15 Duration of heat release as function of injection timing

is shown in Fig. 15 for engine speeds of 1200 and 1800 rpm. As expected, the duration of heat release generally decreases with advancing injection timing. The influence of injection timing on the duration of heat release decreases with advancing injection timing, however.

### Summary and Conclusion

Based on the results of this investigation, the following conclusions were reached:

- 1 Increasing the load decreased the amount of fuel burned in the premixed mode of combustion and correspondingly increased the amount of fuel burned in the diffusion mode of combustion.
- 2 During most of the diffusion combustion, the burning rate of the fuel appeared to vary roughly linearly with the mass-burned fraction of the fuel.
- 3 Retarding the injection timing from 12 to 8 deg BTDC had little effect on the premixed-burned fraction. However, substantially retarding the injection timing resulted in an increase in the premixed-burned fraction and a corresponding decrease in the diffusion-burned fraction.

4 The duration of heat release, defined as the crank-angle interval between 1 and 90 percent mass-burned fractions, increased with increasing load, with decreasing engine speed and generally increased with retarded injection timing. In general, the duration of heat release was found to vary linearly with load.

5 The measured duration of flame luminosity was found to be significantly longer than the calculated duration of heat release. In some cases, emission of radiation persisted well after the opening of the exhaust valves.

### Acknowledgments

The author gratefully acknowledges the contributions of Martin Huber, who provided the main technical support to the experimental program, and Joyce Awad, who wrote the program for analyzing the heat-release results. The author also appreciates the contributions of Robert Talder in the planning of the experimental program.

### References

- 1 Lyn, W. T., "Study of the Burning Rate and Nature of Combustion in Diesel Engines," *Ninth Symposium (International) on Combustion*, Academic Press, New York, 1963, pp. 1069-1082.
- 2 Krieger, R. B., and Borman, G. L., "The Computation of Apparent Heat Release for Internal Combustion Engines," ASME Paper No. 66-WA/DGP-4, 1966.
- 3 Van Gerpen, J. H., Huang, C., and Borman, G. L., "The Effects of Swirl and Injection Parameters on Diesel Combustion and Heat Transfer," SAE Paper No. 850265, 1985.
- 4 Bowden, C. M., Samaga, B. S., and Lyn, W. T., "Rate of Heat Release in High-Speed Indirect Injection Diesel Engines," *Proc. Instn. Mech. Engrs.*, Vol. 184, 1969/70, pp. 122-129.
- 5 Watson, N., and Kamel, M., "Thermodynamic Efficiency Evaluation of an Indirect Injection Diesel," *SAE Transactions*, Vol. 88, 1979, pp. 158-171.
- 6 Alkidas, A. C., "Heat Release Studies in a Divided-Chamber Diesel Engine," ASME JOURNAL OF ENGINEERING FOR GAS TURBINES AND POWER, Vol. 109, 1987, pp. 193-199.
- 7 Alkidas, A. C., "On the Premixed Combustion in a Direct-Injection Diesel Engine," ASME JOURNAL OF ENGINEERING FOR GAS TURBINES AND POWER, Vol. 109, 1987, pp. 187-192.
- 8 Plee, S. L., and Ahmad, T., "Relative Roles of Premixed and Diffusion Burning in Diesel Combustion," *SAE Transactions*, Vol. 92, 1983, pp. 4.892-4.909.
- 9 Alkidas, A. C., "Heat Transfer Characteristics of a Spark-Ignition Engine," *ASME Journal of Heat Transfer*, Vol. 102, 1980, pp. 189-193.
- 10 Alkidas, A. C., "Thermal Loading of the Cylinder Head of a Spark-Ignition Engine," *Heat Transfer Engineering*, Vol. 3, 1982, pp. 66-75.
- 11 Pischinger, R., Krassnig, G., and Taucar, G., "Problems Concerning the Digital Recording of Rapidly Changing Values of Internal Combustion Engines," *ISATA 79*, Vol. 1, 1979, pp. 379-396.
- 12 Woschni, G., "A Universally Applicable Equation for the Instantaneous Heat Transfer Coefficient in the Internal Combustion Engine," *SAE Transactions*, Vol. 76, 1967, pp. 3065-3083.
- 13 Hickling, R., Feldmaier, D. A., Chen, F. H. K., and Morel, J. S., "Cavity Resonances in Engine Combustion Chambers and Some Applications," *J. Acoust. Soc. Am.*, Vol. 73, 1983, pp. 1170-1178.
- 14 Hamming, R. W., *Digital Filters*, Prentice-Hall Inc., Englewood Cliffs, NJ, 1983.
- 15 Wade, W. R., and Hunter, C. E., "Analysis of Combustion Performance of Diesel Fuel," CRC Workshop on Diesel Fuel Combustion Performance, Atlanta, GA, Sept. 14, 1983.
- 16 Hiroyasu, H., Arai, M., and Nakanishi, K., "Soot Formation and Oxidation in Diesel Engines," SAE Paper No. 800252, 1980.



# Reduction of NO<sub>x</sub> and Particulate Emissions in the Diesel Combustion Process

W. R. Wade

C. E. Hunter

F. H. Trinker

H. A. Cikanek

Research Staff,  
Ford Motor Company,  
Dearborn, MI 48121

*A model of the combustion and emission formation processes was formulated to identify modifications to combustion process parameters with potential for reducing NO<sub>x</sub> and particulate emissions in a diesel engine. The model was calibrated using data from an experimental, single-cylinder, direct injection diesel engine. Several combustion system modifications were made to the engine that reduced NO<sub>x</sub> and particulate emissions. The model was used to estimate the changes in the combustion process parameters responsible for the reductions observed. After calibration, the model was used to evaluate the effects of a wide range of modifications to the combustion process parameters on NO<sub>x</sub> and particulate emissions. These results were used to estimate changes in the combustion process parameters required to approach the objectives assumed for the 1991 Federal emission regulations for heavy-duty diesel engines. A reduction in the lubricating oil contribution to the particulate emissions was also projected to be required to approach the 1991 objectives.*

## Introduction

The Federal heavy-duty diesel engine emission regulations for 1991 and 1994 have prompted a comprehensive re-examination of the diesel combustion process [1]. These regulations require major reductions in the NO<sub>x</sub> and particulate emissions of diesel engines used in trucks over 8500 lb GVW (gross vehicle weight). Although particulate traps are being considered as a means for meeting these regulations, controlling the emissions within the engine by modifications to the combustion system is the preferred approach. This paper describes the techniques that were developed to project changes in the combustion process parameters that could be made to approach future emission regulations. Included in the paper is a description of the development of a simplified model of the combustion and emission formation processes in a diesel engine, the calibration of the model with test data from an engine that contained experimental modifications for low emissions, and the application of the model to evaluate modifications required to approach future emission regulations.

Typical NO<sub>x</sub> and particulate emissions from a range of conventional, heavy-duty diesel engines are shown in Fig. 1. Also shown in this figure are the 1991 Federal standards and the low mileage objectives. Two significant features are apparent from this figure. The first observation is that the NO<sub>x</sub> and particulate emissions of conventional diesel engines are significantly higher than the 1991 Federal requirements. The second observation is that, as changes are made to the conventional engine to reduce NO<sub>x</sub> emissions, the particulate emissions tend to increase. This interaction of NO<sub>x</sub> and particulate

emissions makes the simultaneous control of both pollutants a difficult task requiring major changes to the diesel combustion system. The objective of this research program was to identify combustion system modifications with the potential for simultaneously reducing NO<sub>x</sub> and particulate emissions.

A model of the diesel combustion system was considered imperative for defining techniques with the potential for achieving reductions in emissions. Numerous models of the diesel combustion process with the capability of predicting cylinder pressure, power, and fuel consumption have been described in the literature [2]. In a few of these models, at-

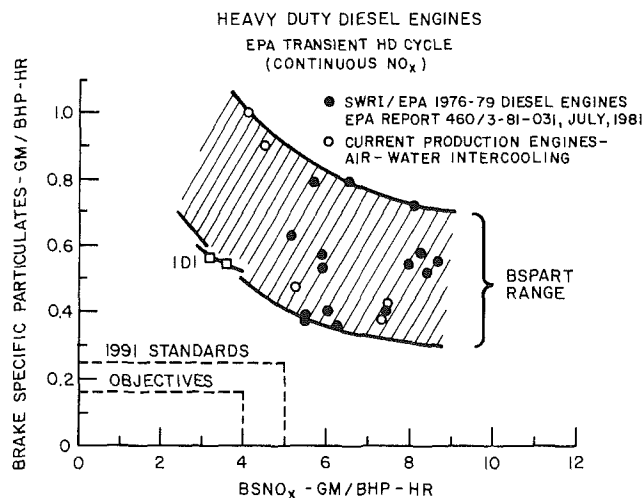


Fig. 1 Particulate versus NO<sub>x</sub> emissions of conventional heavy-duty diesel engines

Contributed by the Internal Combustion Engine Division and presented at the Energy-Sources Technology Conference and Exhibition, Dallas, Texas, February 15-20, 1987. Manuscript received at ASME Headquarters December 10, 1986. Paper No. 87-ICE-37.

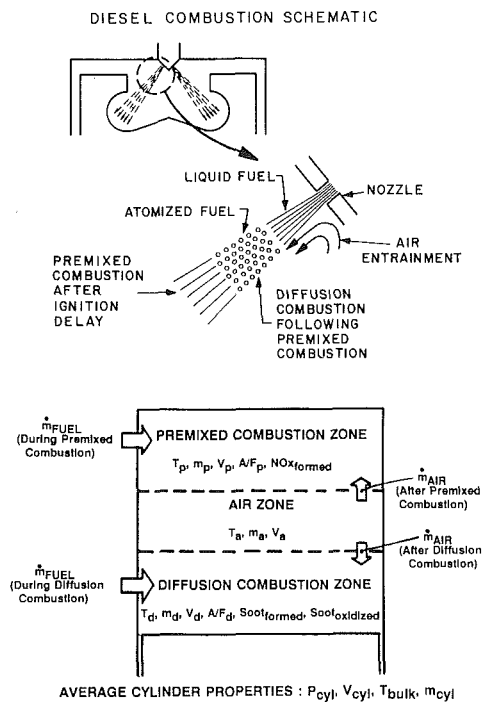


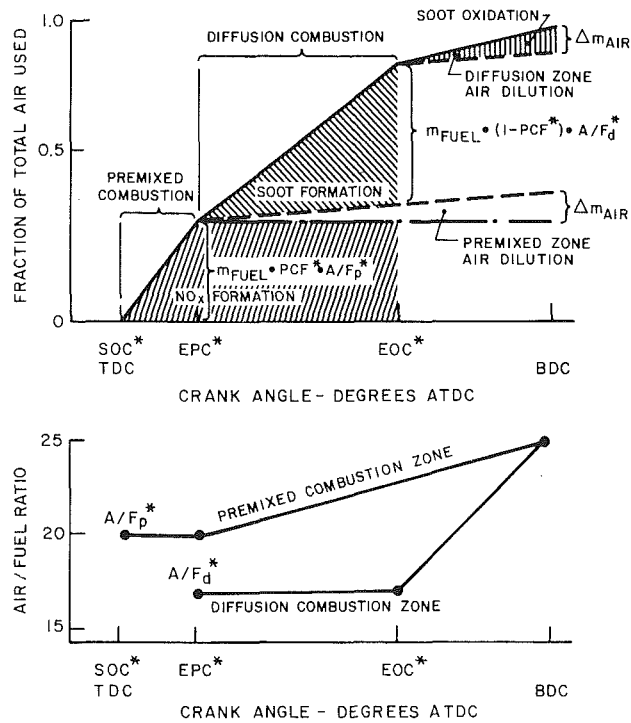
Fig. 2 Schematic of simplified diesel combustion model

tempts were made to predict  $NO_x$  and soot emissions with varying degrees of success [3-5]. For the few models where these attempts were made, a specific combustion system was modeled in detail so that predictions of the emission levels of new or modified combustion systems were beyond the capabilities of the models.

Due to the limitations of existing diesel combustion models, a new approach to modeling the diesel combustion process was developed. Instead of attempting to predict the detailed mechanisms of the diesel fuel-air preparation, mixing, combustion and emission formation processes, a simplified diesel combustion model was developed to provide insight into the changes in the combustion process parameters which have the potential to reduce  $NO_x$  and particulate emissions simultaneously. These parameters, which included the local air-fuel ratios in the cylinder, the mixing rates of air and combustion products, and the combustion rates, were inputs to the model.

Emission test data from a single cylinder research engine with a direct injection combustion system were used to calibrate the model and to evaluate selected experimental techniques for reducing  $NO_x$  and particulate emissions. Generally, engines with cylinder bores ranging from 95 mm to 125 mm are used in the class of trucks applicable to the future Federal heavy-duty diesel engine emission regulations. However, for this research program, a highly instrumented single-cylinder engine with an 80 mm bore and an 88 mm stroke was used. Trendwise effects from this engine were considered valid for the larger bore engines, although the absolute magnitude of the effects would be expected to show some differences.

After the model was calibrated, selected experimental modifications were made to the engine to reduce  $NO_x$  and particulate emissions. The model was used to examine the changes in the combustion process parameters which were responsible for the measured reductions in emissions. The model was then used to evaluate the effects of more generalized modifications to the combustion process parameters on emissions. This information was subsequently used to project the changes in the combustion process parameters that could be made to approach the future emission regulations.



\* - DENOTES MODEL INPUT

Fig. 3 Air utilization and air-fuel ratios during the combustion processes and subsequent air entrainment processes for premixed and diffusion combustion modes

### Simplified Diesel Combustion Model

The simplified diesel combustion model was developed to identify modifications to the combustion process parameters which would be effective in reducing  $NO_x$  and particulate emissions. The combustion process parameters of interest included the start of combustion SOC, the end of premixed combustion EPC, the end of combustion EOC, the local air-fuel ratios in the premixed or diffusion zone  $A/F_p$  or  $A/F_d$ , the mixing rates of air and premixed or diffusion combustion products  $\Delta A/F_p$  or  $\Delta A/F_d$ , the fraction of fuel which burned in the premixed mode PCF, and the overall air-fuel ratio  $A/F_o$  [6]. These parameters, which were inputs to the diesel combustion model, were required in the calculation of instantaneous temperatures and pressures in the premixed and diffusion combustion zones. Empirical chemical kinetic equations were applied to these state conditions to calculate the  $NO_x$  and particulate emissions [5, 7].

**Combustion Submodel.** In the simplified model, the diesel combustion process was assumed to occur in two distinct modes, namely the premixed and the diffusion combustion modes. The premixed combustion mode consisted of combustion of the fuel that was injected during the ignition delay period and was premixed with air. The diffusion combustion mode consisted of the combustion of fuel at the fuel vapor-air interface of the injected fuel droplets. These two modes were modeled separately in two distinct zones, together with a zone containing the excess air, as shown schematically in Fig. 2.

An overview of the combustion processes and subsequent air entrainment processes for each zone are illustrated in Fig. 3. The air utilization in the zones is illustrated in the upper graph and the resulting local air-fuel ratios of each zone are shown in the lower graph. No spatial resolution is inferred by the establishment of separate combustion zones.

Initial properties of the cylinder air charge were assigned at bottom dead center of the compression stroke. Incremental calculations were made every 0.2 degrees through 360 degrees

80mm BORE X 80mm STROKE DI DIESEL ENGINE  
1500 RPM / 87 PSI IMEP  
MODEL PROJECTIONS

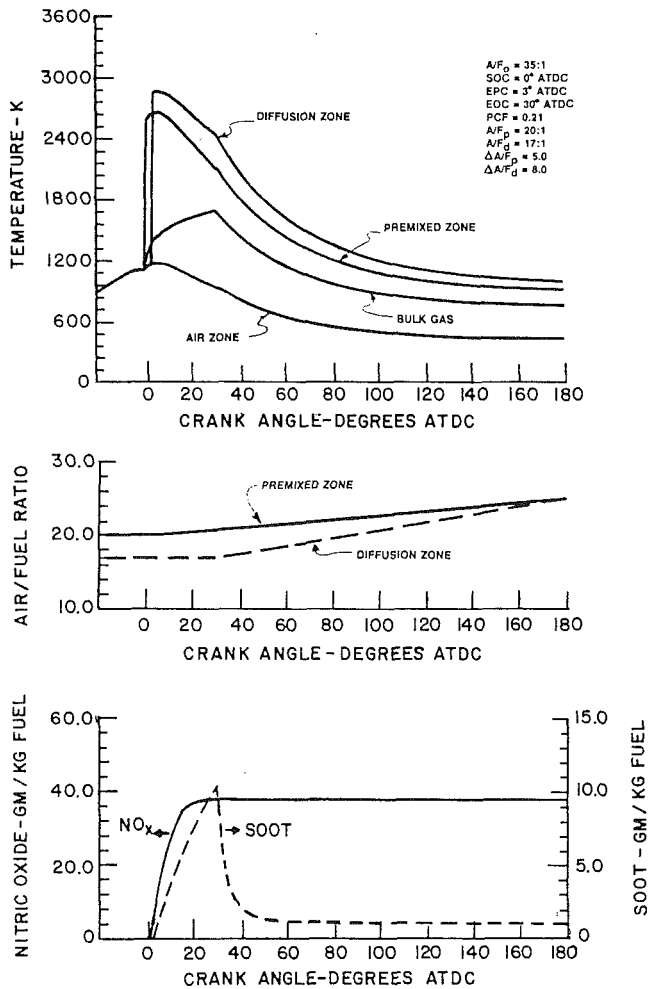


Fig. 4 Calculated zone temperatures, air-fuel ratios, NO<sub>x</sub>, and soot profiles versus crank angle

from bottom dead center of the compression stroke to bottom dead center of the expansion stroke. The gas properties in each zone were calculated at each crank angle increment. Prior to combustion, the premixed and diffusion zones do not exist so that only the change in properties in the air zone were calculated.

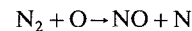
The combustion processes in the premixed and diffusion combustion zones were modeled in three phases. First, the zones followed an adiabatic compression or expansion process due to piston motion. Second, heat was added in a constant volume combustion process. The amount of heat added was determined by the fraction of the total fuel burned in that crank angle increment, the heating value of the fuel, and the heat loss from the combustion chamber. The heat loss was an adjustable parameter but was assumed to be approximately 30 percent of the fuel energy for the baseline single-cylinder engine. The fuel burning rate in each mode was assumed to be constant throughout the respective combustion period. Third, the nonreacting zone or zones were compressed adiabatically due to the increase in cylinder pressure resulting from the combustion process.

After the end of combustion in either the premixed or diffusion zones, the combustion products entrained air from the air zone. The mass of air entrained at each crank angle increment was determined from the model input which specified the incremental increase in the air-fuel ratio of the zone due to mixing. An updated zone temperature was determined by assum-

ing reversible, adiabatic mixing. Entrainment of air into the combustion products from either the premixed or diffusion zone was terminated at the earliest occurrence of one of the following criteria: (1) all of the air in the air zone had been entrained, (2) a specified end of mixing for one or both of the zones was reached, or (3) bottom dead center of the expansion stroke occurred.

**Emissions Submodel.** The temperature, pressure, and air-fuel ratio values in the premixed and diffusion combustion zones were used as inputs for the empirical equations used to calculate the formation of NO<sub>x</sub> and the formation and oxidation of soot.

The formation of NO<sub>x</sub> was assumed to occur in the premixed combustion zone only. The calculation of the rate of formation of NO<sub>x</sub> was based on the following rate controlling step in the NO<sub>x</sub> formation mechanism:



The rate of formation of NO<sub>x</sub> was calculated from the following expression [7]:

$$d(NO)/dt = A_n * (O_2)^{0.5} * (N_2) * \exp(-110/RT + 24.088) \quad (1)$$

where:

- (NO), (O<sub>2</sub>), (N<sub>2</sub>) = partial pressures of NO, O<sub>2</sub>, N<sub>2</sub>, atm
- R = universal gas constant = 1.986 cal/mol/K
- T = premixed zone temperature, K
- t = time, s
- A<sub>n</sub> = calibration constant

The formation of soot was assumed to occur during the diffusion combustion process while the oxidation of soot was assumed to occur during the mixing of air and diffusion combustion products. The equations used to calculate the formation and oxidation of soot were derived by Hiroyasu [5] and are shown below:

(Formation)

$$dM_s/dt = A_f * M_f * P^{0.5} * \exp(-E_f/RT) \quad (2)$$

(Oxidation)

$$dM_s/dt = A_o * M_s * (P_{O_2}/P) * P^{1.8} * \exp(-E_o/RT) \quad (3)$$

where:

- M<sub>f</sub> = mass of fuel, g
- M<sub>s</sub> = mass of soot, g
- E<sub>f</sub> = 1.25 × 10<sup>4</sup> cal/mole
- E<sub>o</sub> = 1.40 × 10<sup>4</sup> cal/mole
- R = universal gas constant = 1.986 cal/mole/K
- T = diffusion zone temperature, K
- P<sub>O<sub>2</sub></sub> = partial pressure of oxygen, MPa
- P = cylinder pressure, MPa
- t = time, s
- A<sub>f</sub>, A<sub>o</sub> = calibration constants for formation and oxidation.

**Detailed Model Calculations.** An example of the detailed model calculations for the temperature profiles, air-fuel ratio profiles, and NO<sub>x</sub> and soot emission profiles in the premixed and diffusion zones is illustrated in Fig. 4. These results were calculated for the following input parameters:

Engine speed	= 1500 rpm
Overall air-fuel ratio	= 35:1
Premixed zone air-fuel ratio	= 20:1
Diffusion zone air-fuel ratio	= 17:1
Premixed zone mixing* air-fuel ratio	= 5.0
Diffusion zone mixing* air-fuel ratio	= 8.0
Start of combustion	= 0 deg ATDC
End of premixed combustion	= 3 deg ATDC
End of combustion	= 30 deg ATDC
Premixed combustion fraction	= 0.21

**Table 1 Single-cylinder DI diesel test engine**

Bore	80 mm
Stroke	88 mm
Displacement	0.44 L
Compression ratio	20.4:1
<i>Fuel injection system (baseline)</i>	
Injection pump	Bosch VE distributor
Plunger diameter	10 mm
Number of nozzle holes	4
Nozzle orifice diameter	0.18 mm
Spray angle	150 deg
<i>Intake port</i>	
Swirl ratio	2.2
Type	Helical
<i>Piston</i>	
Squish area	81.2 percent
Bowl type	Re-entrant
Bowl diameter	37.8 mm
Bowl height	17.5 mm

**Table 2 Relationship between fuel-specific and brake-specific emissions**

Assumed cycle average BSFC = 0.450 lb/bhp-hr

	NO <sub>x</sub>		Particulates	
	1991 Federal standard	Low-mileage objective	1991 Federal standard	Low-mileage objective
Brake specific values, g/bhp-hr	5.0	4.4	0.25	0.18
Fuel specific values, g/kg fuel	24.5	21.6	1.22	0.88

The mixing\* air-fuel ratios refer to the incremental change in air-fuel ratio during the air entrainment period.

### Experimental Test Engine

A well-instrumented, single-cylinder, direct injection diesel engine was used in this study to calibrate the model and to evaluate selected combustion system modifications for reduced emissions. The engine had an 80 mm bore and an 88 mm stroke. Although this engine was smaller than those used in heavy-duty applications where the future emission regulations apply, the trends obtained were considered valid for a large range of bore sizes. Key features of the single-cylinder engine are shown in Table 1.

Combustion analysis parameters, which are described in [6, 8], were calculated to assist in determining the reasons for changes in the measured emissions and to provide input to the diesel combustion model. The calculation of the combustion analysis parameters required combustion pressure, injection pressure, and injector needle lift data. A Kistler Model 6123 pressure transducer was used to obtain cylinder pressure; a Kistler Model 6227 pressure transducer was used to obtain injection pressure; and a Wolff Hall-effect sensor was used to obtain injector needle lift data. A Norland Model 3001A digital oscilloscope was used to record these data every crank angle. A 200 cycle average of the pressure and injector needle lift data was used in the analysis of the combustion parameters.

### Soot Contribution to Total Particulates

Particulate emissions are defined by the Environmental Protection Agency as any exhaust effluent collected on a binderless glass fiber filter at a temperature below 125°F. Therefore, particulates include not only the solid carbon, but also sulfate emissions and the soluble organic fraction con-

80mm BORE X 88mm STROKE DI DIESEL ENGINE

1500 RPM / 87 PSI IMEP

EXPERIMENTAL DATA

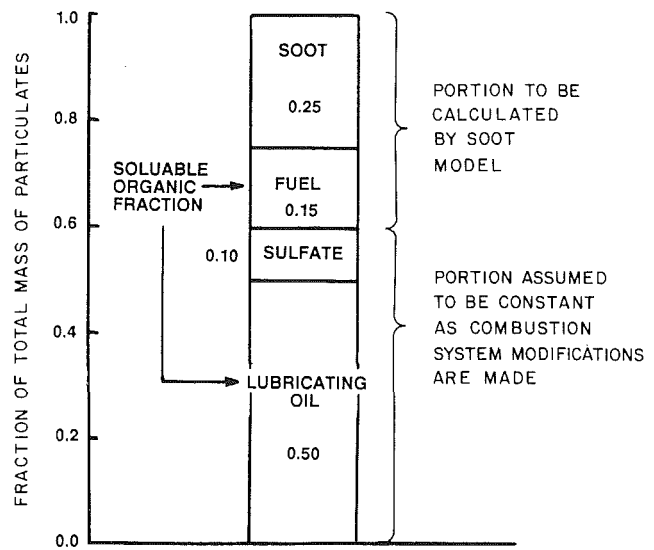


Fig. 5 Detailed composition of the total particulate emission from the baseline single-cylinder DI diesel engine

sisting of unburned and partially burned fuel and lubricating oil absorbed on the soot. The future emission regulations limit total particulate emissions. Since the model only had the capability for estimating soot, which includes the absorbed fuel [9], measured values of the absorbed oil and sulfate emissions were added to the model projections to estimate total particulate emissions.

The detailed composition of the total particulate emissions from the baseline, single-cylinder engine was examined and is shown in Fig. 5. Only 40 percent of the total particulate emissions consisted of soot and absorbed fuel, while the remainder consisted of sulfate emissions and unburned and partially burned oil. For comparisons of measured particulate emissions with calculated values, the measured absorbed oil and sulfate value, equivalent to 1.55 gm/kg fuel, was added to the soot and absorbed fuel emissions projected from the model.

### Model Applications

The overall goal in developing the simplified diesel combustion model was to estimate the changes in the combustion process parameters that would be required to approach the future emission regulations. Several steps were required to accomplish this goal. First, the model was calibrated with emission data from the baseline configuration of the single-cylinder engine. Close agreement was obtained by choosing appropriate values for the combustion process parameters and adjusting the constants in the equations describing the formation of NO<sub>x</sub> and formation and oxidation of soot. Once these constants were selected, they were not changed throughout this study.

After calibration, the combustion process parameters were adjusted to reflect the expected changes that occurred due to modifications in the experimental diesel combustion system and to provide trendwise agreement with measured emission data. The model was then used to provide insights into the effect of each combustion process parameter on NO<sub>x</sub> and particulate emissions. These insights were used to identify techniques for approaching future emission regulations.

The model was used to project emissions on a fuel specific basis, defined as the grams of emissions per kilogram of fuel

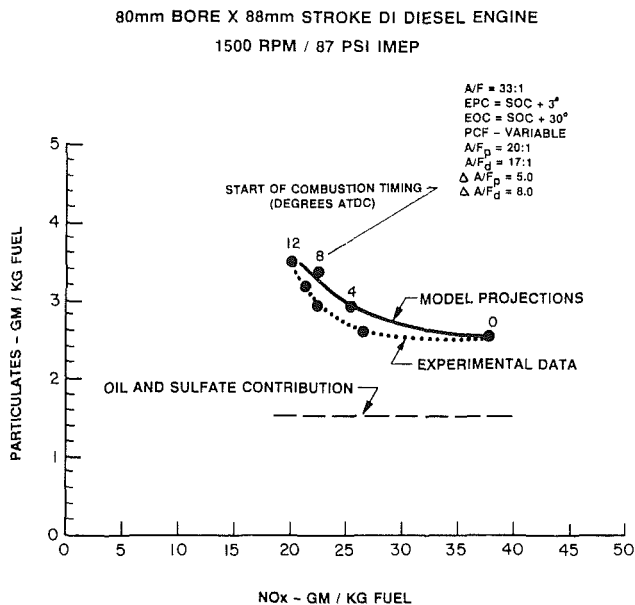


Fig. 6 Comparison of projected and measured particulate and NO<sub>x</sub> emissions for a range of start of combustion timings

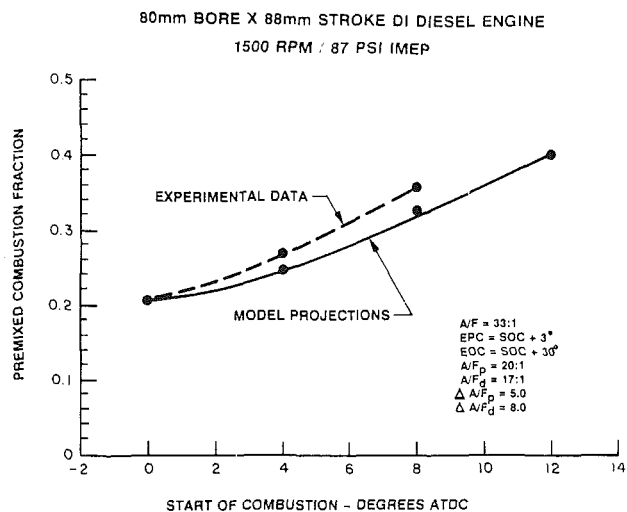


Fig. 7 Projected and measured premixed combustion fraction versus start of combustion timing

consumed. By using an assumed cycle average fuel consumption for an engine operated over the transient heavy-duty cycle, the relationship between fuel specific emissions and brake specific emissions specified by the 1991 Federal regulations was defined and is shown in Table 2. Values for the assumed low-mileage objectives are also shown in the table.

**Start of Combustion Timing.** A comparison of the measured particulate and NO<sub>x</sub> emissions for a range of start of combustion timings with the values projected from the calibrated model is shown in Fig. 6. For this comparison, the engine speed was 1500 rpm and the load was 87 psi IMEP. In the experimental test engine, start of combustion timing was defined as the beginning of the rapid rate of rise of the cylinder pressure. Without modifying the emission calibration constants, the projected increase in particulate emissions associated with a reduction in the NO<sub>x</sub> emissions as the start of combustion timing was retarded agreed closely with the experimental test results.

The close agreement of the emission test results and model projections shown in Fig. 6 was obtained by choosing ap-

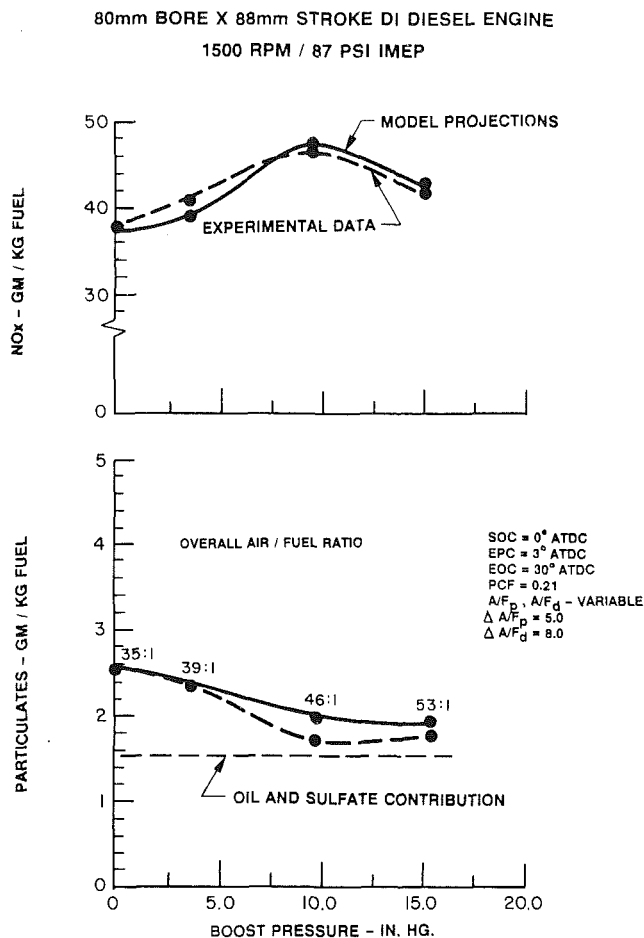


Fig. 8 Comparison of projected and measured NO<sub>x</sub> and particulate emissions versus boost pressure

propriate values for the combustion process parameters, as shown in Fig. 7. The premixed combustion fraction was the only parameter which changed with the start of combustion timing. As the start of combustion timing was retarded, the premixed combustion fraction increased due to the longer ignition delay encountered after top dead center. The values of the premixed combustion fraction used in the model were selected to agree closely with the measured values, as shown in Fig. 7. Although an increase in the premixed combustion fraction alone would increase NO<sub>x</sub> emissions, the late start of combustion timing reduced peak combustion temperature levels to provide an overall reduction in NO<sub>x</sub> emissions.

Likewise, an increase in the premixed combustion fraction alone would decrease particulate emissions. However, the late timing of the diffusion combustion period resulted in a reduction in the oxidation of particulates, yielding an overall increase in particulate emissions.

**Boost Pressure.** By applying boost pressure to the diesel combustion process, a leaner overall air-fuel ratio can be obtained if the turbocharger used to supply the boost pressure has adequate efficiency. In addition, the average air-fuel ratio in the diffusion combustion zone may be leaner.

Tests to evaluate the effects of boost pressure on NO<sub>x</sub> and particulate emissions were conducted on the single-cylinder engine operating at 1500 rpm and 87 psi IMEP. The boost pressure was increased up to a maximum of 16 in. Hg. The exhaust back pressure of the engine was adjusted to maintain a constant negative pressure differential of 1.0 in. Hg from the intake to the exhaust port. Start of combustion timing for these tests was maintained at top dead center. The effects of

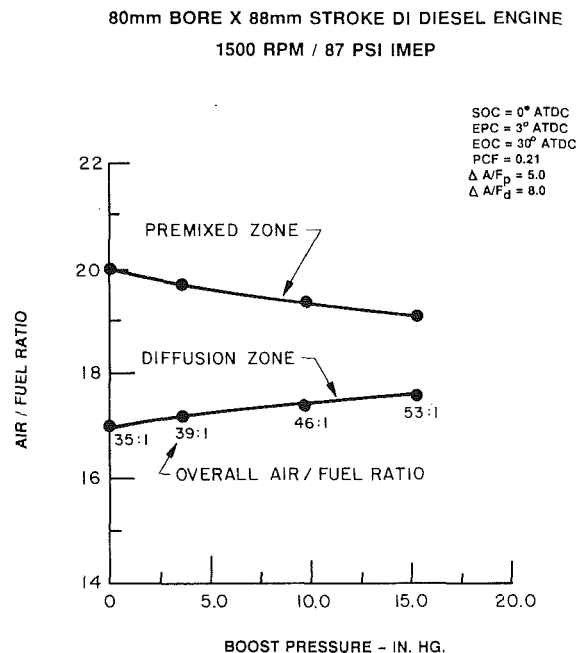


Fig. 9 Effects of boost pressure on combustion process parameters

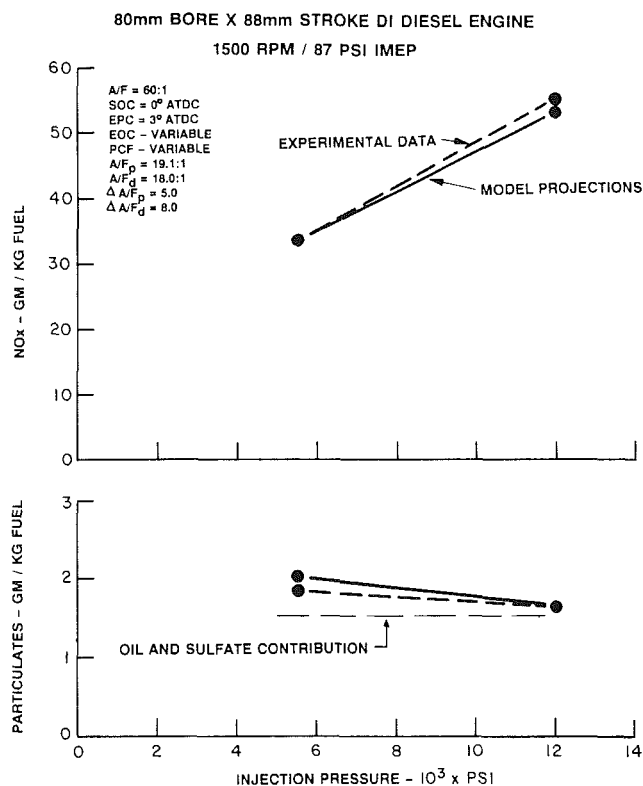


Fig. 10 Comparison of projected and measured NO<sub>x</sub> and particulate emissions versus fuel injection pressure

boost pressure on emissions are illustrated in Fig. 8. NO<sub>x</sub> emissions increased and particulate emissions decreased as the boost pressure was increased. The emissions projected from the model agreed closely with the experimental test results.

To obtain the close agreement of experimental results with values projected from the model, several combustion process parameters were modified to reflect the effects of the boost pressure. The modified parameters are shown in Fig. 9. Due to the increased air density, the fuel penetration was reduced so

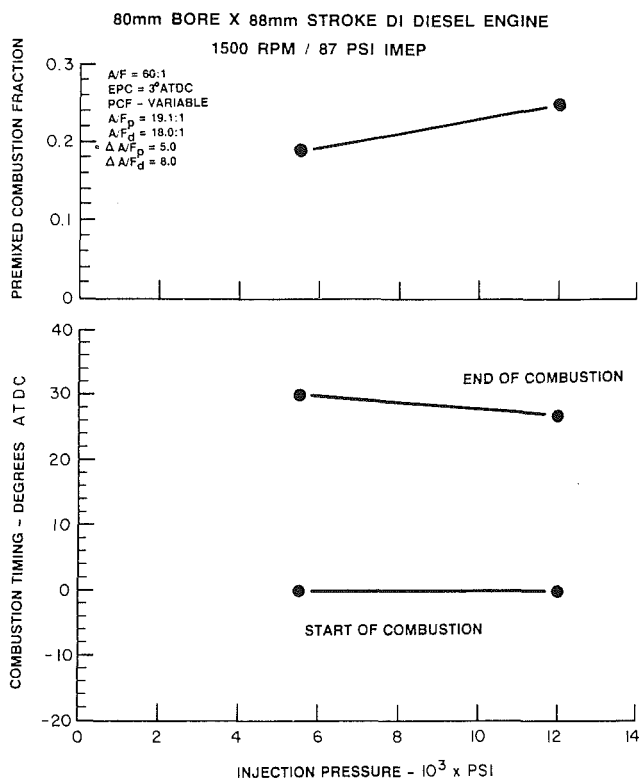


Fig. 11 Effects of fuel injection pressure on combustion process parameters

that the premixed zone air-fuel ratio was decreased. This effect, combined with the higher pressures, was responsible for the increase in NO<sub>x</sub> emissions. The diffusion zone air-fuel ratio was increased due to the larger cylinder air mass. This larger amount of air in the diffusion mode increased oxidation rates and caused the particulate emissions to decrease.

**High Injection Pressure.** An increase in injection pressure in a direct injection diesel has the potential to decrease fuel droplet size and increase entrainment of air with the injected fuel. To evaluate this effect, the injection pressure for the single-cylinder engine was increased from 5500 psi to 12,000 psi at the operating condition of 1500 rpm and 87 psi IMEP. A fuel injection nozzle with four 0.15 mm diameter holes was used for these tests at both injection pressure levels. During this series of tests, the inlet boost pressure was maintained at 16 in. Hg. The baseline configuration of the single-cylinder engine used a Robert Bosch VE distributor fuel injection pump. To obtain the significantly higher injection pressure, a Lucas CAV Maximec in-line fuel injection pump with a significantly increased geometric rate of fuel displacement was used. The distributor fuel injection pump had a geometric fuel displacement rate of 17.3 mm<sup>3</sup>/pump degree whereas the in-line pump had a geometric fuel displacement rate of 39.6 mm<sup>3</sup>/pump degree.

Increased injection pressure provided moderate reductions in particulate emissions while the NO<sub>x</sub> emissions increased significantly, as shown in Fig. 10. Again, the emissions projected from the model agreed closely with the experimental test results.

The changes in the combustion process parameters which explained the observed trends in emissions are shown in Fig. 11. The earlier end of combustion resulted from the faster fuel injection rates at higher pressures. The increase in injection pressure also increased the premixed combustion fraction since more fuel was injected during the ignition delay period. The increased premixed combustion fraction caused the increase in NO<sub>x</sub> emissions. Likewise, the decrease in particulate

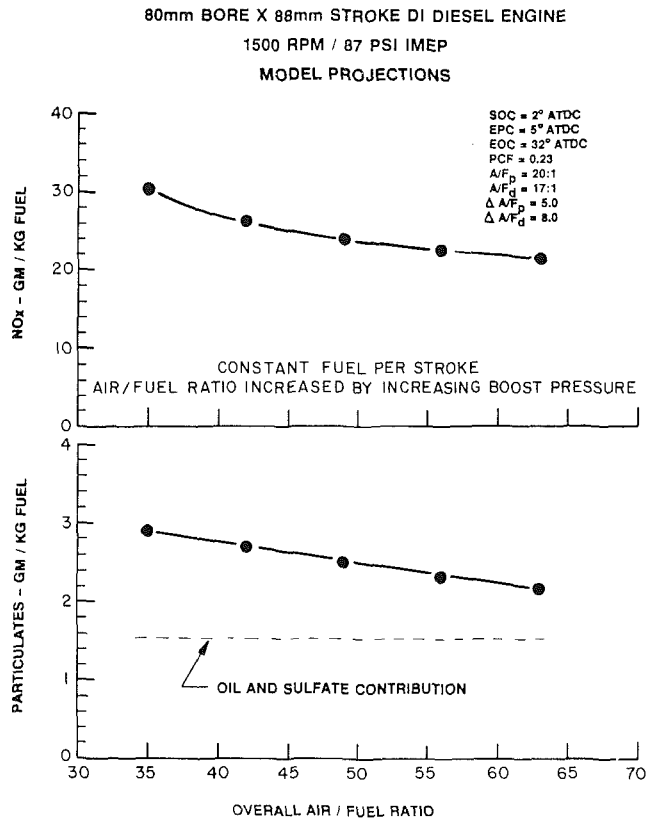


Fig. 12 Effects of overall air-fuel ratio on projected  $\text{NO}_x$  and particulate emissions

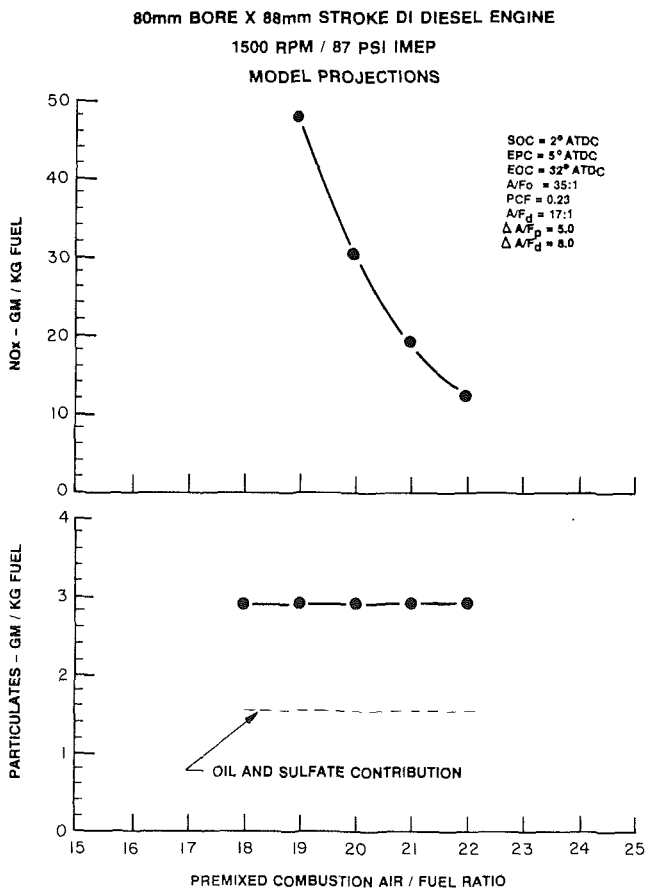


Fig. 13 Effects of premixed combustion mode air-fuel ratio on projected  $\text{NO}_x$  and particulate emissions

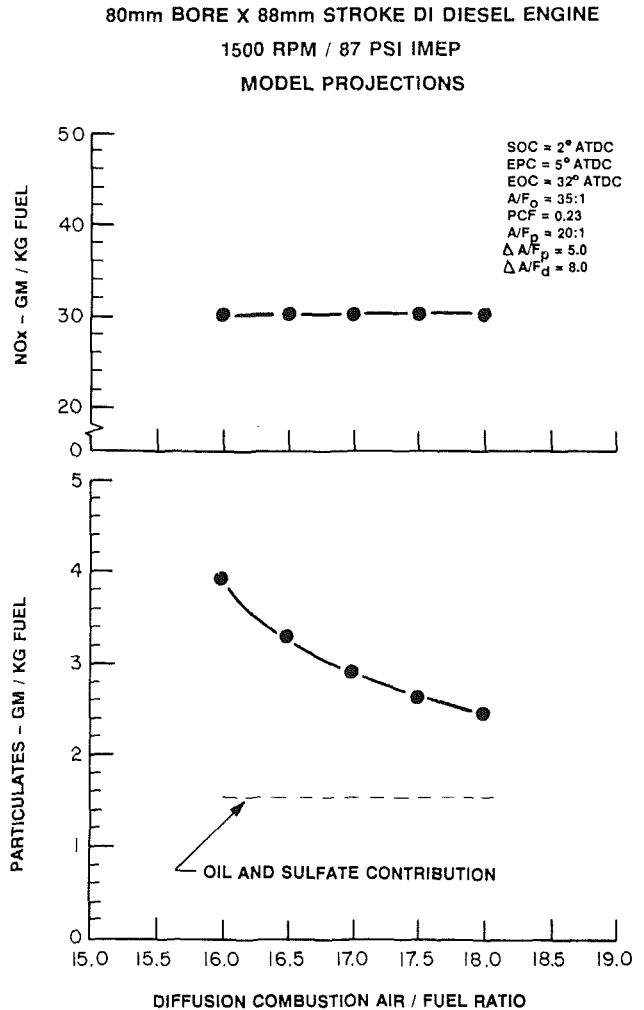


Fig. 14 Effects of diffusion combustion mode air-fuel ratio on projected  $\text{NO}_x$  and particulate emissions

emissions resulted from the increase in the premixed combustion fraction since less fuel was burned in the diffusion combustion mode where particulate formation occurred.

### Generalized Effects of Combustion Process Parameters

The preceding applications of the model showed that the projected emissions correlated well with the experimentally measured emissions when appropriate combustion process parameters were selected. Having obtained this good correlation, the generalized effects of the combustion process parameters on the particulate and  $\text{NO}_x$  emissions were calculated to provide guidelines for making additional modifications to the combustion system for further reductions in emissions. The results of these generalized calculations are presented in this section. For these calculations, the combustion process parameter of interest was varied, while in most cases, all of the other parameters were held constant. However, in several cases, other parameters were changed since they were directly affected by the primary parameter of interest.

**Overall Air-Fuel Ratio.** The effects of overall air-fuel ratio on  $\text{NO}_x$  and particulate emissions are shown in Fig. 12. The increase in overall air-fuel ratio was accompanied by a corresponding increase in intake manifold pressure to simulate the effect of turbocharging. Intercooling was assumed to provide a constant intake charge temperature. The premixed and diffusion combustion mode air-fuel ratios were assumed to be

80mm BORE X 88mm STROKE DI DIESEL ENGINE  
1500 RPM / 87 PSI IMEP  
MODEL PROJECTIONS

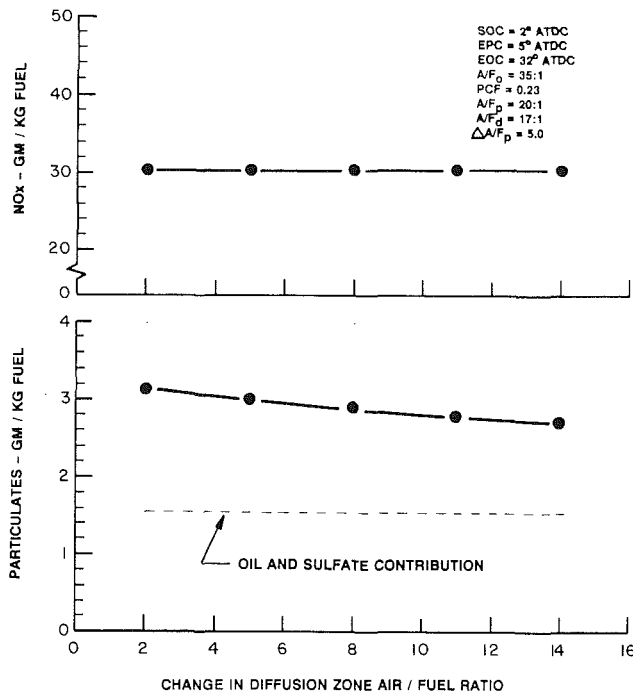


Fig. 15 Effects of increases in diffusion combustion zone air-fuel ratio after end of fuel injection event on projected NO<sub>x</sub> and particulate emissions

constant as the overall air-fuel ratio was increased. The projections from the model indicated that both NO<sub>x</sub> and particulate emissions were reduced at the leaner overall air-fuel ratios accompanying higher boost pressures. This was due to the lower overall temperatures which occurred as a result of the increased air dilution.

**Premixed Mode Air-Fuel Ratio.** The effects of changes in the premixed combustion mode air-fuel ratio on emissions are shown in Fig. 13. A leaner premixed combustion mode provided significant reductions in NO<sub>x</sub> emissions but did not affect the particulate emissions. The reduction in NO<sub>x</sub> emissions resulted from the lower temperatures in the leaner premixed combustion mode. Particulates were not affected since the premixed mode was not assumed to contribute to the particulate formation process.

**Diffusion Mode Air-Fuel Ratio.** The effects of changes in the diffusion combustion mode air-fuel ratio on emissions are shown in Fig. 14. A leaner diffusion combustion mode provided significant reductions in particulate emissions without affecting the NO<sub>x</sub> emissions. However, a leaner diffusion combustion mode would be very difficult to obtain since diffusion combustion tends to occur in the vapor-air interface surrounding the fuel droplet at air-fuel ratios ranging from 14.7:1 to 20:1 [10].

**Diffusion Mode Post Mixing.** Mixing of the diffusion combustion products with air after the end of the combustion process was described by the increase in the air-fuel ratio associated with the diffusion combustion products. The effects of the increase in the diffusion zone air-fuel ratio on emissions are shown in Fig. 15. Increased mixing of the diffusion combustion products was projected to provide moderate reductions in particulate emissions without affecting the NO<sub>x</sub> emissions.

80mm BORE X 88mm STROKE DI DIESEL ENGINE  
1500 RPM / 87 PSI IMEP  
MODEL PROJECTIONS

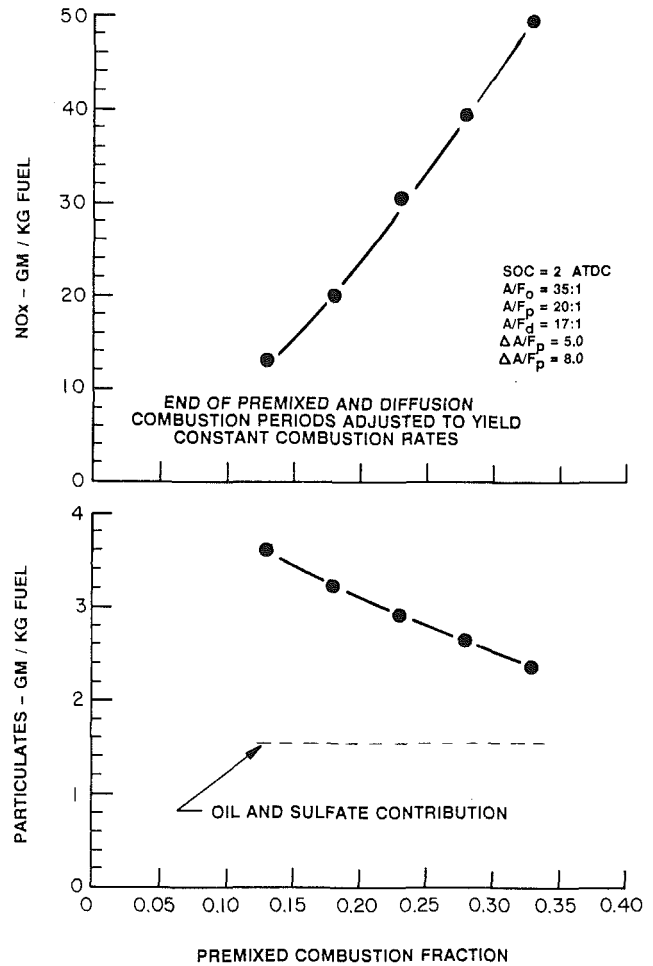


Fig. 16 Effects of premixed combustion fraction on projected NO<sub>x</sub> and particulate emissions

**Premixed Combustion Fraction.** The effects of the fraction of the fuel which burns in the premixed combustion mode on emissions are shown in Fig. 16. Constant combustion rates in both the premixed and diffusion combustion modes were assumed as changes were made to the premixed combustion fraction. Therefore, changes in combustion duration accompanied changes in the premixed combustion fraction. As shown in the figure, increases in the premixed combustion fraction provided significant reductions in particulate emissions and significant increases in NO<sub>x</sub> emissions. Changes in this parameter, therefore, are not capable of providing simultaneous reductions in NO<sub>x</sub> and particulate emissions.

### Techniques for Future Reductions in Emissions

After examining the generalized effects of the combustion process parameters on emissions, the diesel combustion model was used to evaluate the magnitude of the changes in the combustion process parameters which would be required to approach the objectives assumed for the 1991 Federal NO<sub>x</sub> and particulate emission regulations for heavy-duty diesel engines. The results of this analysis are shown in Fig. 17.

The reductions in NO<sub>x</sub> emissions were obtained with retarded start of combustion timing, a leaner overall air-fuel ratio obtained with boost pressure and a leaner premixed combustion mode air-fuel ratio. Reductions in particulate emis-



80mm BORE X 88mm STROKE DI DIESEL ENGINE  
1500 RPM / 87 PSI IMEP  
MODEL PROJECTIONS

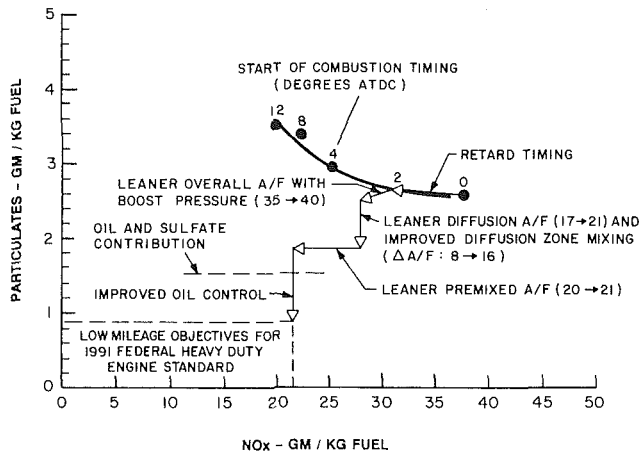


Fig. 17 Changes in combustion process parameters projected to be required to approach the 1991 Federal  $\text{NO}_x$  and particulate objectives for heavy-duty diesel engines

sions were obtained with a leaner overall air-fuel ratio, a leaner diffusion combustion mode air-fuel ratio and improved diffusion zone mixing.

As illustrated in the figure, the projected changes in the combustion process parameters were not adequate to approach the objectives assumed for the 1991 regulations. Therefore, to approach these objectives, a reduction in oil consumption was projected to be required. As shown in Fig. 5, 50 percent of the total particulates of the baseline engine, or 1.33 g/kg of fuel, consisted of lubricating oil. A 70 percent reduction in the contribution of the oil to the particulate emissions was projected to be required to approach the total particulate emission levels required by the 1991 Federal regulations. Smaller reductions would be required for other engines in which the oil contribution to the particulate emissions may be lower.

The results presented in Fig. 17 are for only one steady-state operating condition, whereas the 1991 requirements must be achieved over a wide range of operating conditions on a transient test. The effects of these modifications on engine durability and the emission deterioration factors, which are key considerations for meeting the emission regulations, were not evaluated in this study.

## Conclusions

1. A simplified model was formulated to project the  $\text{NO}_x$  and particulate emissions in a DI diesel engine. By selecting appropriate values of combustion process parameters, the emission values projected by the model agreed closely with ex-

perimentally measured values for a range of start of combustion timings.

2. Increased boost pressure and increased fuel injection pressures were shown to be effective in reducing particulate emissions. When rational changes to the combustion process parameters were selected, the emission values projected by the model agreed closely with the experimentally measured values.

3. The diesel combustion model was used to evaluate the generalized effects of changes in the combustion process parameters on emissions. Reductions in  $\text{NO}_x$  emissions were projected with a leaner overall air-fuel ratio, a leaner premixed combustion mode air-fuel ratio and a decrease in the premixed combustion fraction. Reductions in particulate emissions were projected with a leaner overall air-fuel ratio, a leaner diffusion combustion mode air-fuel ratio, an increase in the diffusion zone mixing, and an increase in the premixed combustion fraction.

4. The changes to the key combustion process parameters that might be used to approach the objectives assumed for the 1991 Federal  $\text{NO}_x$  and particulate emission regulations for heavy-duty diesel engines were projected for one steady-state operating condition encountered in the transient test specified by the regulations. The required changes in the combustion process parameters included retarded start of combustion timing, a leaner overall air-fuel ratio obtained with boost pressure, a leaner diffusion mode air-fuel ratio, a leaner premixed mode air-fuel ratio and improved diffusion zone mixing. A reduction in the lubricating oil contribution to the particulate emissions was also projected to be required to approach the 1991 objectives.

## References

- 1 "Federal Heavy Duty Engine 5.0 gm/bhp-hr  $\text{NO}_x$ , .25 gm/bhp-hr Particulate Standard," 50 Federal Register 10653, 40 CFR, 86.091-11, Mar. 15, 1985.
- 2 Hiroyasu, H., "Diesel Engine Combustion and Its Modeling," *Proceedings of International Symposium on Diagnostics and Modeling of Combustion in Reciprocating Engines*, Tokyo, Japan, Sept. 1985, pp. 53-75.
- 3 Shahed, S. M., Flynn, P. F., and Lyn, W. T., "A Model for the Formation of Emissions in a Direct-Injected Diesel Engine," in: *Combustion Modeling in Reciprocating Engines*, J. N. Mattavi and C. A. Amann, eds., GMRL, Plenum Press, 1980, p. 345.
- 4 Kono, S., Nagao, A., and Matooka, H., "Prediction of In-Cylinder Flow and Spray Formation Effects on Combustion in Direct Injection Diesel Engines," SAE Paper No. 850108, 1985.
- 5 Hiroyasu, H., Kadota, T., and Arai, M., "Development and Use of a Spray Combustion Modeling to Predict Diesel Engine Efficiency and Pollutant Emissions (Part 1)," *Trans. of JSME*, 42-432B, 1606.
- 6 Wade, W. R., Hunter, C. E., Trinker, F. H., and Hansen, S. P., "Future Diesel Engine Combustion Systems for Low Emissions and High Fuel Economy," XXI FISITA Congress, Belgrade, Yugoslavia, 1986, Paper No. 865012.
- 7 Harris, M. E., Rowe, V. R., Cook, E. B., and Grumer, J., "Reduction of Air Pollutants From Gas Burner Flames, Including Related Reaction Kinetics," U.S. Bureau of Mines Bulletin No. 653, 1970.
- 8 Wade, W. R., White, J. E., Jones, C. M., Hunter, C. E., and Hansen, S. P., "Combustion, Friction and Fuel Tolerance Improvements for the IDI Diesel Engine," SAE Paper No. 840515, 1984.
- 9 Hiroyasu, H., Arai, M., and Nakanishi, K., "Soot Formation and Oxidation in Diesel Engines," SAE Paper No. 800250, 1980.
- 10 Aoyagi, Y., Kamimoto, T., Matsui, Y., and Matsuoka, S., "A Gas Sampling Study on the Formation Processes of Soot and  $\text{NO}_x$  in a DI Diesel Engine," SAE Paper No. 800254, 1980.

L. E. Gettel

G. C. Perry

J. Boisvert

British Columbia Research,  
Vancouver, British Columbia, Canada

P. J. O'Sullivan

Natural Energy Research Ltd.,  
Vancouver, British Columbia, Canada

# Dual Fuel Engine Control Systems for Transportation Applications

*Microprocessor control systems have been developed for dual fuel diesel engines intended for transportation applications. Control system requirements for transportation engines are more demanding than for stationary engines, as the system must be able to cope with variable speed and load. Detailed fuel maps were determined for both normally aspirated and turbocharged diesel engines based on the criterion that the engine did not operate in the regimes where knock or incomplete combustion occurred. The control system was developed so that the engine would follow the detailed fuel map. The input variables to the control system are engine speed and load. Based on this, the system then controls the amount of natural gas and diesel fuel supplied to the engine. The performance of the system will be briefly summarized.*

## Introduction

Mechanical control systems have been used for more than forty years [1] in stationary dual fuel engines, which operate at a limited number of speed and load conditions. These engines typically operate with less than 10 percent diesel fuel ("pilot") which is used to initiate ignition of the natural gas. For transportation applications, however, dual fuel control systems must be able to allow the engine to operate continuously over a wide range of different speeds and loads. Due to this and the requirement of similar transient response, the average level of substitution of diesel for transportation applications will not be nearly as high as in stationary engines.

There are a number of commercially available mechanical dual fuel conversion systems which have been used for a number of years. However, it is not clear that they maximize efficiency and substitution of diesel fuel, while preventing the engine from operating in regimes where knock could occur or peak cylinder pressures are greater than on diesel. It has been widely reported [2-5] that to maximize the efficiency of a dual fuel engine it is necessary to vary the amount of pilot fuel as a function of engine speed and load especially for light load operation. In 1982 Karim [4] pointed out that to accomplish this, an electronic control system utilizing computer control would be necessary due to the nonlinear diesel/natural gas fuel map.

A control system for a dual fuel mobile engine must maximize engine efficiency and diesel substitution and at the same time ensure that the engine does not operate in a regime where durability will be reduced. Durability can be severely reduced by the presence of combustion knock as well as increased cylinder peak pressures and rate of pressure rise. Therefore, it is essential that the engine operate on dual fuel to the same specifications (i.e., peak cylinder pressure and rate of pressure rise, absence of knock) as for diesel operation at peak loads.

This criterion had priority over all others in the design of the system, even the efficiency of the engine.

The efficiency of a dual fuel engine at peak loads is comparable or might even be greater than that for diesel operation [6, 7]. The efficiency at light loads, however, is generally inferior to diesel operation. The design criteria chosen for the systems described in this paper were to maximize efficiency and diesel substitution levels on dual fuel under all conditions while retaining the same peak pressure levels as for diesel operation.

## Fuel Maps for Dual Fuel Mobile Engines

Based on the criteria mentioned in Section 1, dual fuel engine maps have been determined for two commercially available engines, a John Deere 6466T (turbocharged 165 hp) and a Caterpillar 3208 (normally aspirated 210 hp). Typical results showing the substitution of diesel fuel as a function of engine load are shown in Fig. 1. These results were obtained from dynamometer tests where the amount of natural gas admitted to the engine upstream of the inlet manifold or turbocharger was controlled manually. Piezoelectric pressure transducers were mounted in the combustion chamber of one cylinder for each engine to monitor cylinder pressure waveforms.

The maximum amount of natural gas for peak loads was determined by comparing the pressure waveforms with respect to peak pressure and rate of pressure rise on natural gas with those for diesel. In addition FFT (Fast Fourier Transform) analysis was performed to ensure that the frequency spectrum on natural gas was comparable to that for diesel.

Typical results showing engine efficiency are given in Fig. 2. From these results it is clear that for peak engine loads the efficiency on dual fuel is comparable to that for diesel operation, while for part load the dual fuel efficiency is less than for diesel. It should be pointed out that no alterations were made to the fuel injection timing for dual fuel operation. It has been shown in earlier work [8] that injection timing can have a

Contributed by the Internal Combustion Engine Division and presented at the Energy-Sources Technology Conference and Exhibition, Dallas, Texas, February 15-20, 1987. Manuscript received at ASME Headquarters November 26, 1986. Paper No. 87-ICE-12.

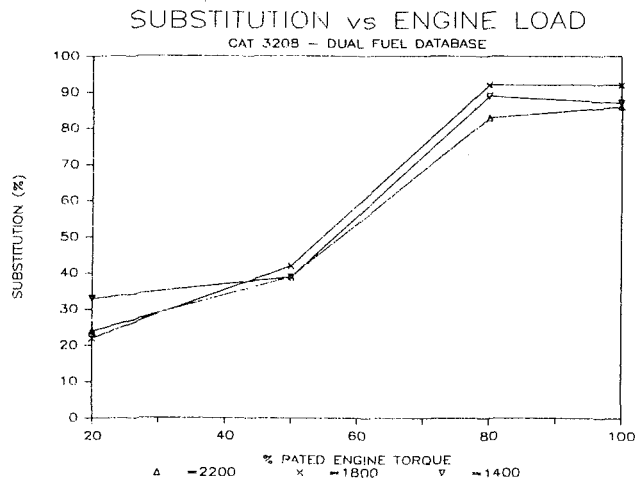


Fig. 1 Diesel substitution versus engine load: 1400, 1800, and 2200 rpm

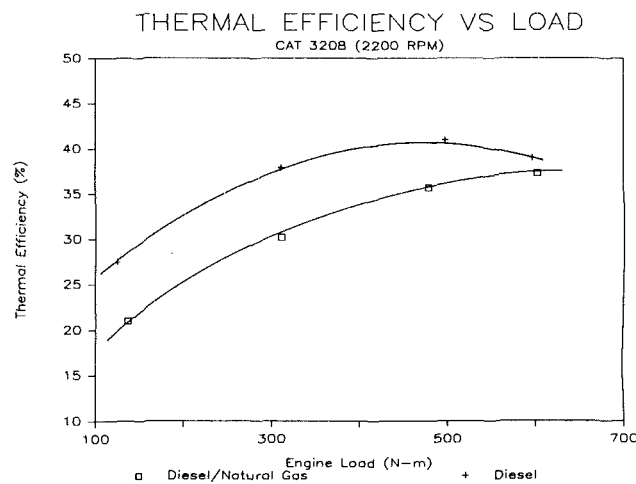


Fig. 2 Thermal efficiency versus engine load for diesel and diesel/natural gas at 1800 rpm

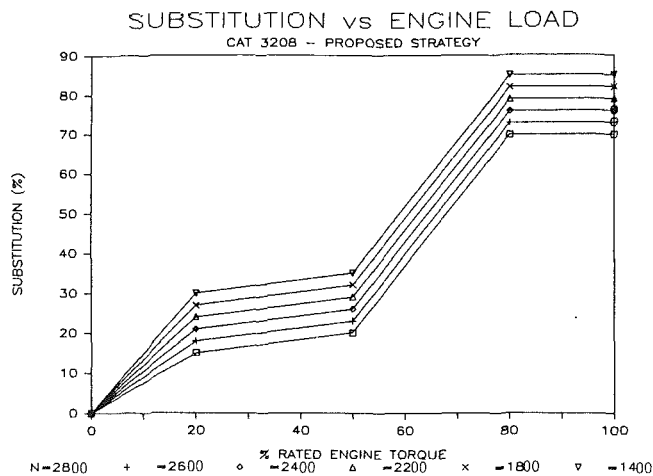


Fig. 3 Dual fueling strategy

significant effect on diesel substitution, peak pressures, and efficiency. Thus it could be possible to increase dual fuel engine performance by changing the fuel injection timing.

### Requirement for Electronic Control Systems

The typical results shown in Fig. 1 (i.e., substitution versus load) point out the nonlinear nature of the diesel/natural gas

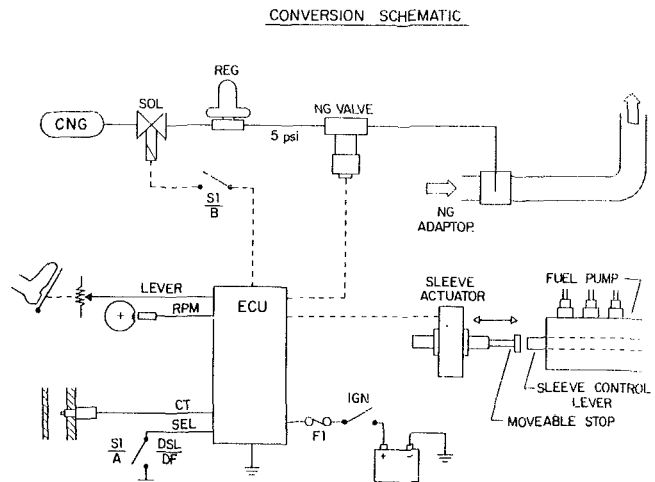


Fig. 4 Conversion system schematic

fuel maps that resulted from the design criteria given above. The dual fuel control system must be capable of following the fuel map given in Fig. 1. There are two possibilities for a basic control system, either a mechanically or electrically based system. Due to the inherent nonlinearity of the fuel map, it was decided that an electronically based control system was preferable, since it would be very difficult for any mechanical system to emulate fully the required fuel maps.

A digital microprocessor-based control system was chosen over analog systems due to the flexibility to alter the system fuel map easily as well as the ease with which the basic system could be modified for different engines.

A typical fuel map that the control system would follow is shown in Fig. 3. The diesel substitution versus torque curves have their common origin at diesel only conditions (i.e., zero substitution). This fueling profile piecewise linearizes the results obtained from the engine mapping results.

### Control System Design

**Design Criteria.** Prior to the start of the system design criteria were established for the development of a microprocessor-based diesel/natural gas system that would produce satisfactory results when installed in mobile transportation applications. These design criteria are summarized below:

- 1 Peak cylinder pressures shall be limited to peak values observed on diesel, and the rate of pressure rise shall be kept within manufacturer's specifications.
- 2 The torque curve should be as close as possible to the diesel torque curve.
- 3 No major engine modifications shall be required.
- 4 Diesel idle and overspeed governing shall still be functioning when the engine is operated on dual fuel.
- 5 Diesel only operation should still be possible.

**System Development.** As shown in Section 2 from the engine map test results, it is necessary to vary the quantity of both diesel and natural gas to the engine as a function of speed and load to optimize performance. The dual fuel conversion system developed for these two engines consists of three major components: an electronic control unit, a natural gas metering system, and a system to vary the diesel fuel.

A typical schematic of the conversion system for the Caterpillar 3208 is shown in Fig. 4. The system for the turbocharged John Deere 6466T is similar in layout, and hence the discussion of the system will be limited to the Caterpillar engine.

Natural gas stored in high-pressure cylinders passes first

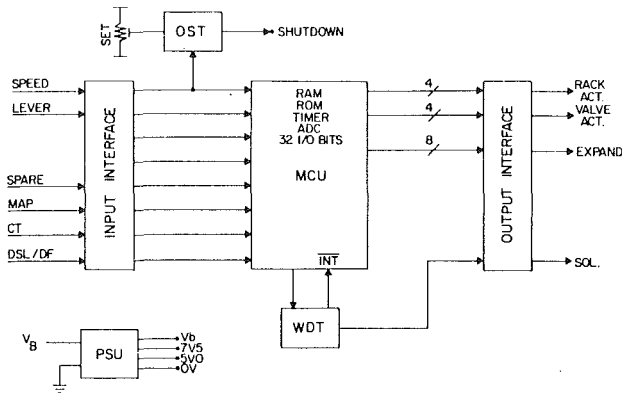


Fig. 5 Schematic of the ECU hardware

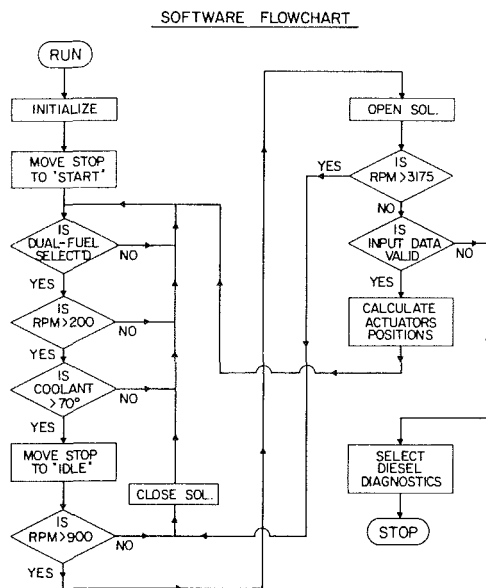


Fig. 6 System software flowchart

through a solenoid shut-off valve before being reduced and regulated to approximately 136 kPa. A valve controls the flow of natural gas entering the air-intake stream through an intake adaptor. An actuator controls the position of the fuel pump control lever, and hence the diesel fuel flow. A microprocessor-based electronic control unit (ECU) measures several engine parameters from which it calculates the correct amounts of diesel and natural gas from a fueling profile stored in the computer memory, which was determined from the engine map.

Variation of the diesel flow was accomplished by an automotive grade stepping motor which controlled the fuel injection pump sleeve position. The fuel injection pump was calibrated as a function of sleeve position and pump speed. It was found that accurate and repeatable control of diesel flow rate could be accomplished by control of the sleeve position. Hence, sleeve position was used to control diesel flow rate. It should be pointed out that this approach to controlling diesel flow rates did not involve any internal modifications to the fuel pump.

Metering of natural gas to the engine was done using a stepping motor controlled gas valve which was designed specifically for this application. It was of the cone-in-orifice type where gas flow varies according to the cone position. The cone is positioned using a linear stepping motor, similar to that used for the diesel fuel control. The actuator has a maximum travel of 9.5 mm and can be positioned to an accuracy of 0.04 mm.

This provides a wide dynamic range of flow control. The response time of the valve is typically 750 ms between fully open and closed.

The ECU controls the positioning of both the fuel injection pump sleeve and natural gas valve under all engine operating conditions. There are a number of control signals that are input to the ECU, which is processed, and then determines the relative amounts of each fuel to be supplied to the engine. The input signals include: fuel pump engine speed control lever position, engine speed, diesel/dual-fuel selection mode, and engine coolant temperature. The fuel pump lever position is measured using a throttle position sensor, which consists of a linear potentiometer that is mounted on the engine with a specially fabricated assembly. The output resistance varies as a function of fuel pump lever position. Since the characteristics of the fuel pump are known, then the engine torque can be deduced from a knowledge of the lever position and the engine speed. A magnetic pickup mounted on the starter ring gear teeth was used to determine engine speed. This sensor generated a series of pulses whose frequency is a function of engine speed. The coolant temperature sensor is a limit switch which indicates when the engine temperature is above or below 70°C.

A schematic of the ECU is shown in Fig. 5. The input interface conditions the signals from the various engine sensors. The microprocessor used is a Motorola 68705 which features 128 bytes of RAM, 3.8 K bytes of erasable programmable read only memory (EPROM), a timer/counter, an analog-to-digital converter, and several input/output ports. The maximum clock frequency for the microprocessor is 5 MHz, which allows up to 625 K of simple arithmetic instructions to be performed per second. The output interface provides the necessary signal conversion logic from the MCU to the output devices. Also included in the system is an expansion feature, which consists of a bidirectional input/output port which could be used for full diagnostic capability.

The ECU also includes an overspeed trip (OST) and a watchdog timer (WDT). The purpose of the latter is to detect microprocessor failures, which can be either of a software or hardware nature. If a failure is detected the main natural gas solenoid is closed and then a diagnostic routine is started, followed by a possible system restart.

A schematic of the system software is shown in Fig. 6 and consists of two main modules. The first, driven by an interrupt routine, positions the actuators, performs the analog-to-digital conversion and averaging of the input signals, and manages the routines for communicating outside of the controller. The second module calculates the position of the diesel and natural gas actuators.

The engine fueling profile is stored in two lookup tables. The main table is three dimensional and features sleeve position (diesel flow rate) as a function of speed and torque. Three-dimensional linear interpolation is used to calculate table values not specifically referenced. The second table is similar to the first except that natural gas valve position (natural gas flow rate) is now a function of speed and load.

The ECU system also includes software that allows complete engine simulation testing and on-screen display of the lookup table data. Since the values of the input signals for engine torque and speed are known, then engine operation could be simulated by applying suitable input signals to the ECU. The simulation software allowed on-screen display of the important system variables such as engine speed, lever position, and gas valve position.

## System Performance

Following completion of the design and construction of the ECU, extensive testing was performed. The first series of tests involved engine simulation analysis of the system. For these

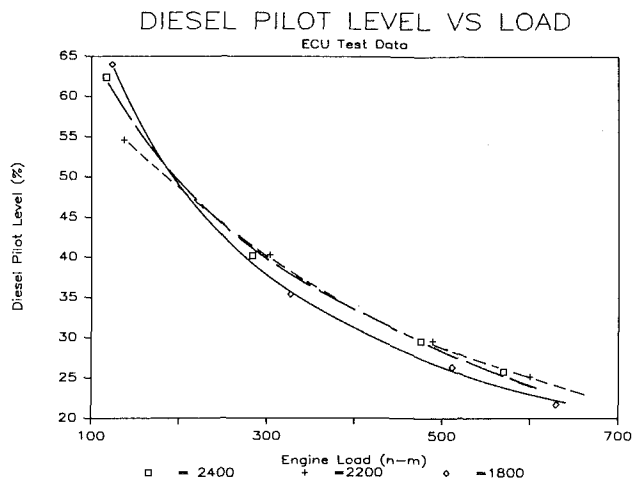


Fig. 7 Diesel pilot level versus engine load: 1800, 2200, and 2400 rpm

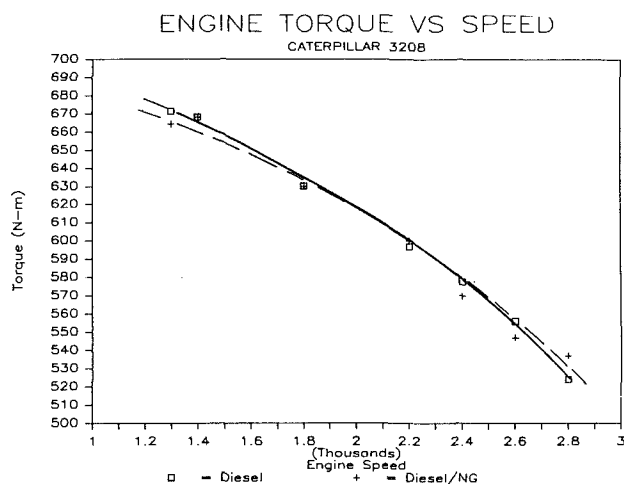


Fig. 8 Engine performance on diesel and diesel/natural gas

tests electrical inputs from a signal generator were applied to the input interface and the resulting control signals from the output interface were examined to ensure that the system was functioning properly.

After completion of these tests the control system was installed on the engine. All the operating points examined in the earlier database were repeated and the torque, level of substitution, and efficiency were determined using the ECU to control the amount of natural gas inducted, and diesel fuel injected into the engine. Typical results of the engine test pro-

gram are shown in Fig. 7. For the Caterpillar 3208 the maximum level of substitution of diesel was approximately 85 percent at 1400 rpm (full load) and falls to 75 percent at 2800 rpm.

Figure 8 shows the maximum engine torque as a function of speed for both diesel and dual fuel operation. The latter data were obtained with the ECU controlling the relative amounts of diesel and natural gas supplied to the engine, unlike the earlier results (Fig. 1), which were obtained by manually controlling the amount of natural gas and diesel admitted to the engine. It is clear from these results that the torque curve on dual fuel is virtually the same as for 100 percent diesel fuel.

## Conclusions

Advanced microprocessor-based dual fuel control systems have been developed for a normally aspirated Caterpillar 3208 and turbocharged John Deere 6466T diesel engines. The system continuously varies the amount of diesel and natural gas dependent on engine speed and load. The performance of the engine on dual fuel is comparable to diesel (i.e., the same torque curve and similar efficiencies at peak load). Light load efficiency is significantly lower on dual fuel for both engines. This could possibly be improved by optimizing the fuel injection timing for dual fuel operation.

## Acknowledgments

This work was supported under Contract No. 23SQ. 23216-3-6994A-1 with Energy, Mines and Resources Canada. We wish to thank the Finning Tractor Company for supplying the Caterpillar 3208 for this work.

## References

- 1 Karim, G. A., "A Review of Combustion Processes in the Dual Fuel Engine—The Gas Diesel Engine," *Prog. Energy Combust. Sci.*, Vol. 6, 1980, pp. 277-285.
- 2 Moore, N. P. W., and Lewis, J. D., "An Investigation of Combustion in Dual-Fuel Engines," IV Congr International du Chauffage Industriel, Mar. 10, 1952.
- 3 Karim, G. A., Klat, S. R., and Moore, N. P. W., "Knock in Dual Fuel Engines," *Proc. I. Mech. E.*, Vol. 181, Pt. 1, No. 20, 1966/1967.
- 4 Karim, G. A., "Methane and Diesel Engines," in: *Methane Fuel for the Future*, Plenum Press, New York, 1982, pp. 113-129.
- 5 Karim, G. A., "Some Considerations of the Use of Natural Gas in Diesel Engines," presented at Nonpetroleum Vehicular Fuels III, sponsored by IGT, Arlington, VA, 1982.
- 6 Moore, N. P. W., and Mitchell, R. W. S., "Comparative Study of Methane and Propane as Engine Fuels," *Proc. I. Mech. E.*, Vol. 170, No. 40, 1955, pp. 1157-1172.
- 7 Karim, G. A., "Dual Fuel Engine of the Compression Ignition Type—Prospects, Problems, and Solutions—A Review," SAE Paper No. 830173, 1983.
- 8 Song, S., "Performance of a Dual Fuel Prechamber Diesel Engine With Natural Gas," Report No. AFL 84-01, Department of Mechanical Engineering, University of B.C., Canada, 1984.

# A Correlation for the Burning Velocity of Methane-Air Mixtures at High Pressures and Temperatures

T. J. Al-Himyary  
G. A. Karim

Department of Mechanical Engineering,  
The University of Calgary,  
Calgary, Alberta, Canada

*A formulation for the burning velocity of methane-air mixtures was developed over a range of equivalence ratios at temperatures and pressures high enough to cover conditions encountered in a typical operating spark ignition engine using the experimental data of Babkin and Kozachenko [1]. An example involving the use of such data in a diagnostic program to yield information about the characteristics of flame propagation in an engine fueled with methane is shown.*

## Introduction

The burning velocity of any premixed fuel-air mixture is a parameter often found to be of significance in many predictive and diagnostic procedures for the performance of common combustion devices in general and the progress of the combustion process in particular. Accordingly, its value is needed for a very wide range of operating conditions, whenever such mixtures are employed. Currently, the prediction of the burning velocity, purely from analytical considerations, even for the relatively simple system of methane-air mixtures, is insufficiently reliable. This remains so, despite some recent advances, particularly when a very wide range of values of mixture temperature, pressure, and equivalence ratios is involved. Hence resort is usually made to experimental methods for determining the value of the laminar burning velocity. Data from such studies, when published in the open literature, tend to be in the form of graphs and only occasionally in the form of correlations that tend to be applicable over only a very limited range of operating conditions.

Recently, the authors have been involved in the development of a diagnostic approach to analyze the combustion process of a spark ignition engine fueled with methane based on the corresponding experimentally derived cylinder pressure time data [2]. Such a procedure can provide information about the characteristics of the propagating flame if the laminar burning velocity is known at the local instantaneous pressure and unburnt mixture temperature. Accordingly, a generalized formulation for the burning velocity of methane-air mixtures was required over a very wide range of methane-air mixtures and at temperatures and pressures high enough to cover conditions encountered in most operating engines. No such generalized correlation, suitable for incorporation in the diagnostic program, appeared to be readily

available from reference to the literature. The development of a relatively simple yet reliable correlation for the laminar burning velocity, based on a consistent set of reliable data, was judged to be the most effective approach at present. The paper presents such a correlation of the experimental data of Babkin and Kozachenko [1] involving methane-air mixtures in terms of equivalence ratio, temperature, and pressure. It is then shown that the incorporation of such a correlation in a diagnostic program of the combustion process, in a spark ignition CFR engine fueled with methane, can yield valuable information about the apparent flame propagation rates and the effective rates of change of the flame area.

There have been many attempts to establish the burning velocity of methane-air mixtures at high temperatures and pressures, when employing a variety of apparatus of the constant-volume bomb type. A very wide range of experimental techniques, associated theory, and operating conditions were employed. The differences in the reported results, not surprisingly, tend to be often large. In most of these cases, the burning velocity was determined under conditions that were limited by the apparatus employed [3]. In fact, reviews have shown that there is still a lack of consensus as to the reliability of published data for even the relatively simple fuel, methane, even at ambient temperature and pressure conditions [4].

Flame speed data, available in the literature, cannot be simply grouped to produce a useful set of data that can be employed in the production of a satisfactory correlation. Such a correlation needs to be based on comprehensive results obtained consistently from the same apparatus using the same approach. Furthermore, the experimental data need to cover the range of pressure, temperature, and equivalence ratio typical of the conditions encountered during combustion within the spark ignition engine. Many of the data and associated correlations, when available, were invariably limited to a narrow range of temperature, pressure, or equivalence ratio.

Contributed by the Internal Combustion Engine Division and presented at the Energy-Sources Technology Conference and Exhibition, Dallas, Texas, February 15-20, 1987. Manuscript received at ASME Headquarters November 18, 1986. Paper No. 87-ICE-6.

The diagnostic model, developed by the authors for analyzing the combustion process in a spark-ignited engine running on methane, was based on the measured cylinder pressure-time history [2], and considers the cylinder charge, at any instant during combustion, to be made up of two zones: unburned reactants and burned products. These two systems are considered to undergo distinctly different polytropic processes with continuously varying polytropic indices. The two systems exchange mass across moving flame front as well as exchanging heat with the adjacent cylinder walls at a rate determined by their respective temperatures and masses. Each system was assumed to be at a uniform temperature that varied throughout the combustion process. The model yielded a set of equations that allowed the calculation of the temperature and polytropic index histories for each of the systems. Those, in turn, allowed the calculation of the mass burning rates of the cylinder charge.

One of the main advantages of the model is its simple energy release analysis of the combustion process within the spark-ignited engine. The model could be extended to provide information about the characteristics of the flame propagation and its geometry. The turbulent flame propagating front can be viewed as having a wrinkled surface of known overall geometry, propagating at the local burning velocity as determined by the properties of the unburnt reactants at each instant during combustion

$$\frac{dm_b}{dt} = \rho_u A_f S_T = \rho_u A_1 S_u \quad (1)$$

where  $dm_b/dt$  is the mass burning rate of the charge,  $\rho_u$  is the density of the charge yet to be burned,  $A_f$  is the area of the flame front,  $S_T$  is the turbulent flame speed,  $A_1$  is the total area of the wrinkled flame surface, and  $S_u$  is the laminar burning velocity. Information derived about the turbulent flame speed or the changes in  $A_1$  is useful in assessing important factors such as the turbulence scale and intensity for a specific engine during the combustion process. Accordingly, the laminar burning velocity was needed to be calculated for any equivalence ratio at each interval of the combustion process, on the basis of the calculated temperature of the mixture just ahead of the flame as provided by the model and the corresponding instantaneous measured cylinder pressure. The present contribution describes such a correlation that was developed with a typical application to the gas-fueled spark ignition engine.

## Data and Method

A reasonably comprehensive and consistent set of data for the burning velocity of methane-air mixtures over a wide range of pressures, temperatures, and equivalence ratio is found in Babkin and Kozachenko [1]. Their results were available as published in the form of a number of figures each containing a set of curves of the burning velocity values versus equivalence ratio. Such a representation is very difficult to work with, especially when computer applications are involved. Hence, a suitable overall correlation for the flame speed data was derived and used for this purpose.

The burning velocity data were reported for pressures of 1, 8, 23, and 70 atm; temperatures of 50, 100, 150, and 200°C, as well as eight equivalence ratios spanning either side of the stoichiometric ratio, from 0.62 to 1.35. The method employed was based on the examination of the initial phase of flame propagation following spark ignition inside a constant-volume bomb, when significant changes in the elevated mixture pressure, due to energy release, can be neglected. The apparent flame velocity was determined experimentally using an optical Schlieren system.

The following trends were noted:

1 For any equivalence ratio and mixture temperature,  $S_u$  is proportional to  $p^n$ , where  $n$  is in the range of  $-0.66$  to  $-0.3$ . The effect of  $n$  was found to be weakest for mixtures near the stoichiometric ratio and strongest for lean and rich mixtures.

2 For any equivalence ratio and mixture pressure,  $S_u$  is proportional to  $T^m$ , where  $m$  is in the range of 1.78 to 3.01. The exponent  $m$  was found to be more influential (high values) for rich and lean mixtures but weakest (low values) for near the stoichiometric ratio.

The index  $n$  is a function of pressure, temperature, and equivalence ratio. However, the trends of the experimental results indicated that, in the pressure range of 8 to 70 atm, the value of  $n$  was almost constant with only a slight dependence on temperature. It was further concluded that  $m$  is a function of both pressure and equivalence ratio. The correlation that we developed took into account these reported trends, especially when considering the effects of the pressure and temperature.

## Results

The final form of the equation developed to describe the burning velocity,  $S_u$ , of methane in air, in terms of temperature, pressure, and equivalence ratio is as follows:

$$S_u = A + (F_1 \cdot F_2) \cdot (F_3 + F_4 \cdot f + F_5 \cdot f^2) \quad (2)$$

where

$S_u$  is the normal burning velocity

$$A = P^{-0.457} \cdot e^{(-746/T) + 6.193}$$

$$F_1 = a_1 + b_1 \cdot f + c_1 \cdot f^2 + d_1 \cdot f^3$$

$$F_2 = P^{(a_2 + b_2 \cdot f + c_2 \cdot f^2 + d_2 \cdot f^3)}$$

$$F_3 = a_3 + b_3 \cdot T + c_3 \cdot T^2$$

$$F_4 = a_4 + b_4 \cdot T + c_4 \cdot T^2$$

$$F_5 = a_5 + b_5 \cdot T + c_5 \cdot T^2$$

and where  $T$  = temperature of the reactants K;  $P$  = pressure in atmosphere;  $f$  = (equivalence ratio - 1.036).

The values for  $a$ ,  $b$ ,  $c$ , and  $d$  are listed below:

	$a$	$b$	$c$	$d$
$F_1$	0.27956	1.7608	10.829	5.9001
$F_2$	-0.29093	-0.69393	-2.1308	1.0085
$F_3$	-98.559	0.52495	-5.3456E-4	
$F_4$	3.8766	-0.04286	1.2538E-4	
$F_5$	260.89	-1.1259	2.4974E-3	

The correlation was designed to predict more closely the values of burning velocity for mixtures away from the stoichiometric region and for conditions of high temperature and pressure that are typical of the conditions normally encountered in the unburned mixture zone within an internal combustion engine.

Calculated values of  $S_u$ , from the correlation, are plotted against the corresponding experimental values in Figs. 1 and 2. Figure 1 shows that, for the majority of the points, the correlation underestimated the burning velocity. Predicted velocities were within a maximum deviation of 9 percent from the experimental values.

The pressures in the CFR spark-ignition engine range typically from 8 to 40 atm, while the temperature of the unburned mixture is 200°C and higher during the progress of the combustion process. Under such conditions, the pressure exponent tends to be fairly constant. Andrews and Bradley [5] have shown that, at pressures of 1 atm, the value of the pressure exponent deviates significantly from that constant value. Considering the restraints placed on our correlation, it is not surprising, as shown in Fig. 2, that the correlation pro-

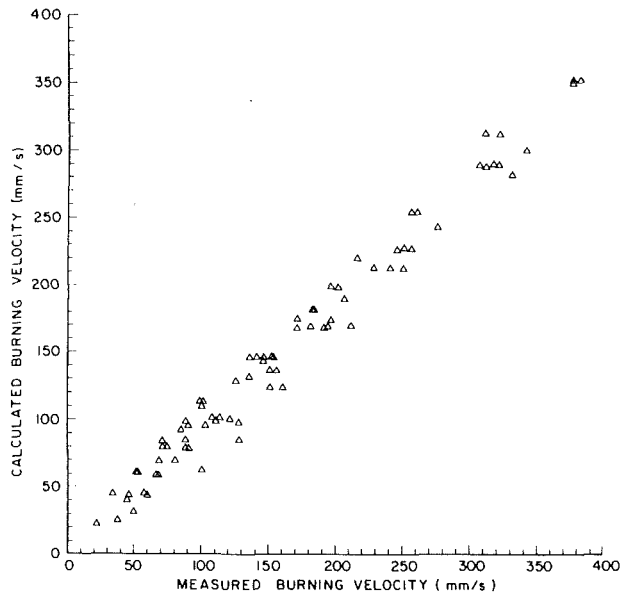


Fig. 1 Calculated values of the burning velocity of methane-air mixtures in accordance with the correlation of equation (2) versus measured values, primarily involving high pressure and temperature values

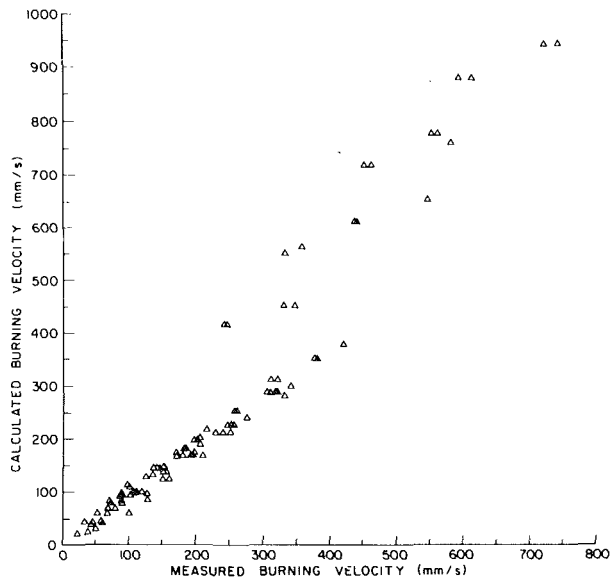


Fig. 2 Calculated values of the burning velocity of methane-air mixtures in accordance with the correlation of equation (2) versus measured values, including values at 1 atm

duces poor agreement with the experimental values at atmospheric pressure. Figure 3 shows a typical comparison between the computed and experimental flame speeds, for a range of equivalence ratios and temperatures at a pressure of 8 atm.

The correlation was deemed both convenient and satisfactory for use in the diagnostic modeling of the combustion process in a spark-ignition engine fueled with methane. The model provided the average temperature of the unburned reactants at every instant during the combustion process. This coupled with the corresponding, experimentally derived, cylinder pressure allowed the calculation of the burning velocity at each point, throughout the duration of the combustion process. Using equation (1), an estimate of the wrinkled area of the flame could then be made using the mass burning rate, provided by this diagnostic model or any alternate method.

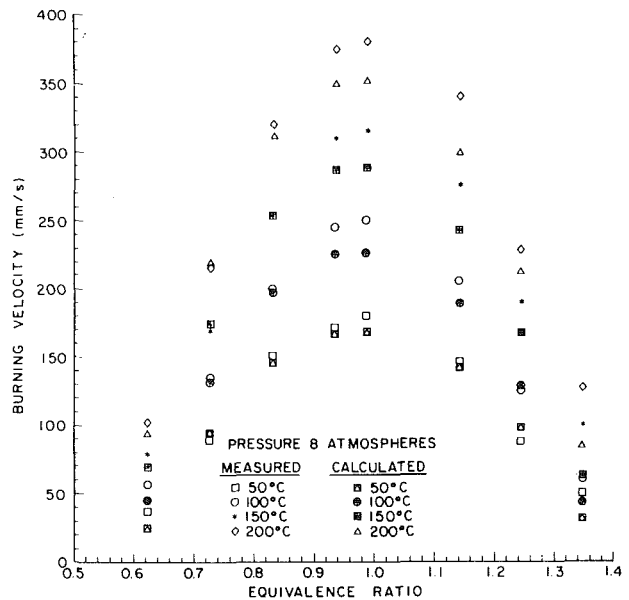


Fig. 3 Calculated and measured burning velocities for methane-air mixtures at a pressure of 8 atm for temperatures of 50, 100, 150, and 200°C

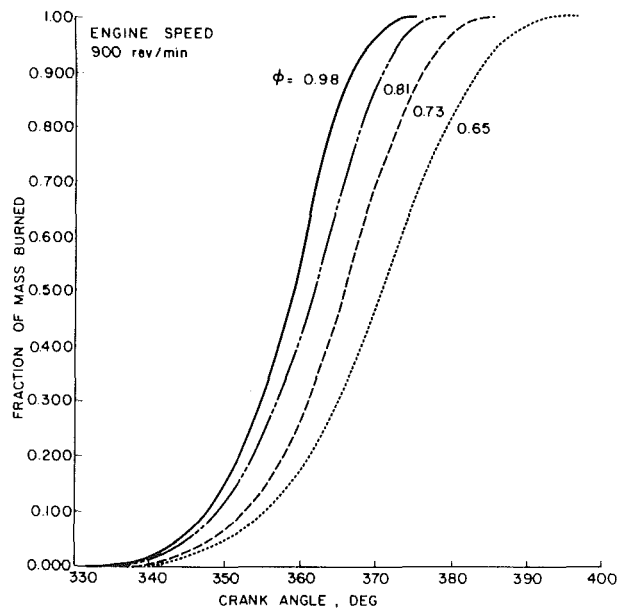


Fig. 4 Calculated fraction of mass burned versus crank angle, for four typical equivalence ratios as produced by the diagnostic model [2] involving methane as a fuel in a CFR engine

## Discussion

The CFR engine provided the opportunity to illustrate the use of the correlation of equation (2). Pressure-time records obtained from this engine, when fueled with methane, were used by the diagnostic model [2] to produce the mass burned history as well as the average temperature history for the yet-to-be-burned reactants and burned products. These are shown in Figs. 4 and 5 respectively, for four different equivalence ratios. The correlation made possible the calculation of the laminar burning speeds for these conditions (Fig. 6). It can be clearly seen that, for any equivalence ratio, the change in the pressure and temperature of the reactants brings about a general reduction of the burning velocity, during the period of combustion and flame propagation. This reduction is mainly



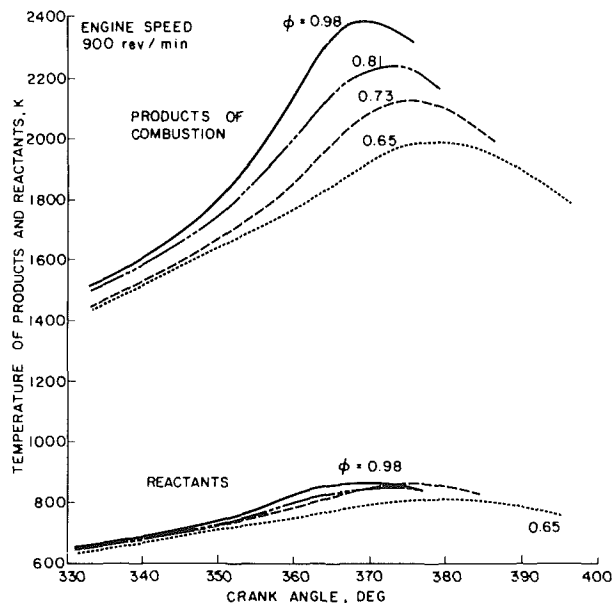


Fig. 5 Temperature history of the burned products and unburned reactants during the combustion process for four typical equivalence ratios, as produced by the diagnostic model [2] for a CFR engine fueled with methane

due to increasing the pressure of the cylinder, tempered by the effect of increasing the temperature of the reactants.

Using equation (1) and the calculated flame speeds, an area for the turbulent flame front can be established on the assumption that the flame front is highly wrinkled, but at the same time is traveling locally at the laminar flame speed dictated by the conditions of the unburned mixture ahead of the flame. Figure 7 shows the results of these calculations. It can be seen that the magnitude and the rate of change of the area of the propagating flame, at the initial stages of combustion, are nearly identical for the four equivalence ratios. This is so despite the widely differing values of the calculated burning velocities for these mixtures. This is an interesting indication that, for these conditions and at constant spark timing and engine speed, the flame development and propagation in the early stages of combustion are most probably governed by the fluid motion and its characteristics within the cylinder. At the latter stages of combustion, the rate of change of the flame area appears to be very similar for all four mixture strengths. The similarity stems from the fact that, in the latter stages of combustion, both the mass burned history and temperature of the unburned mixture are similar. However, the results for the four equivalence ratios are displaced in time with the leaner mixtures reaching a higher maximum flame area at a later time. This is explained by the longer combustion durations for the leaner mixtures, resulting from their associated slower flame speeds. The flame, for leaner mixtures can be considered to undergo a significant degree of stretch due to the movement of the piston resulting in higher cylinder volumes before combustion is completed. The correlation, as such, is very helpful in studying such trends. More work is obviously needed before flame propagation characteristics are fully understood and predicted reliably.

### Acknowledgments

The financial assistance of the Natural Sciences and Engineering Research Council of Canada (NSERC) is gratefully acknowledged.

### References

- 1 Babkin, V. S., and Kozachenko, L. S., "Study of Normal Burning

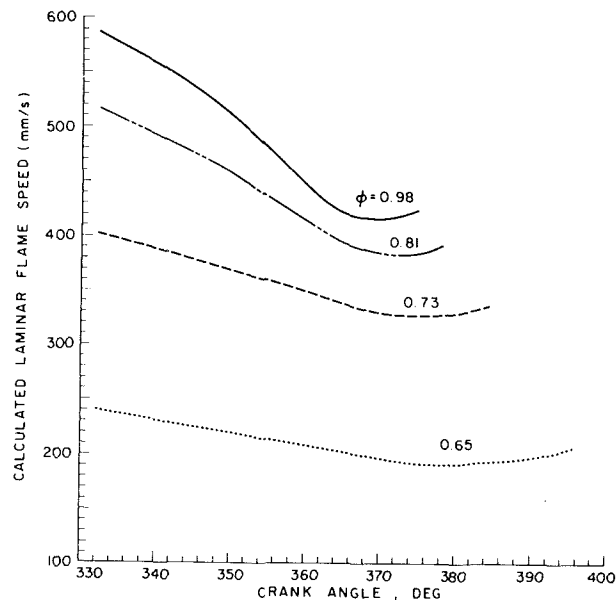


Fig. 6 Calculated laminar flame velocities of the unburned reactants from equation (2), during the combustion period for four typical equivalence ratios in a CFR engine fueled with methane

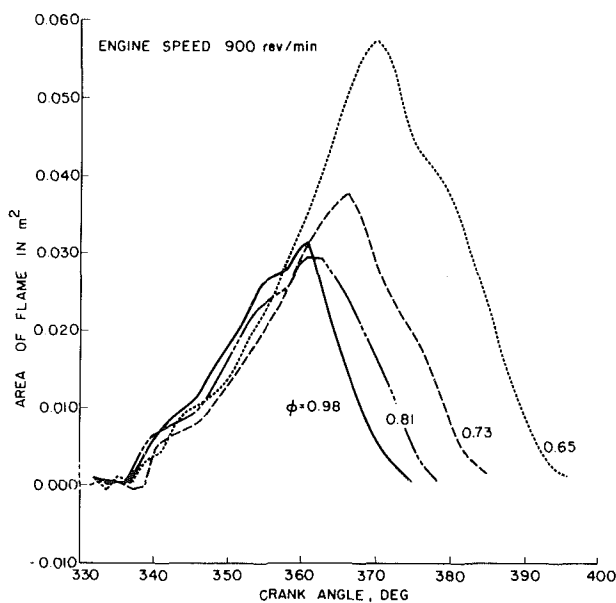


Fig. 7 Calculated values of the wrinkled area of the propagating flame versus crank angle for four typical equivalence ratios, as produced by the diagnostic model [2] for a CFR engine fueled with methane

Velocities in Methane/Air Mixtures at High Pressures" [English translation], *Combustion, Explosion and Shock Waves*, Vol. 2, 1966, pp. 46-52.

2 Al-Himyary, T. J., and Karim, G. A., "Analysis of the Combustion Process in Spark Ignition Engines Based on Cylinder Pressures," Technical Report, The Combustion Institute, Canadian and Western States Sections, Banff, Alberta, Canada, 1986.

3 Andrews, G. E., and Bradley, D., "Determination of Laminar Burning Velocity: A Critical Review," *Combustion and Flame*, Vol. 18, 1972, pp. 133-153.

4 Rallis, C. J., and Garforth, A. M., "The Determination of Laminar Burning Velocity," *Prog. Energy, Combustion Science*, Vol. 16, 1980, pp. 303-329.

5 Andrews, G. E., and Bradley, D., "The Burning Velocity of Methane-Air Mixtures," *Combustion and Flame*, Vol. 19, 1972, pp. 275-288.

6 Gaydon, X. Y., and Wolfhard, Y. Y., *Flames, Their Structures, Radiation and Temperatures*, 4th ed., Chapman and Hall, New York, 1979.

7 Strehlow, R., *Fundamentals of Combustion*, 2nd ed., International Textbook Co., New York, 1985.

8 Chigier, N., *Energy, Combustion and the Environment*, McGraw-Hill, New York, 1981.

# Operation of a Caterpillar 3516 Spark-Ignited Engine on Low-Btu Fuel

**N. C. Macari**

Test Engineer,  
Test & Evaluation,  
Engineering General Offices.

**R. D. Richardson**

Senior Design Engineer,  
Engine Division Engineering.

Caterpillar, Inc.,  
Peoria, IL

*The use of an engine-generator package, fueled by landfill gas, to produce usable electrical power has generated considerable interest among both landfill operators and engine manufacturers. Landfill gas operation presents some unusual technical challenges that require preparation of the gas prior to engine consumption as well as modifications to the spark-ignited engine. The primary obstacles to landfill gas operation are the low-Btu content of the gas, its poor combustion characteristics, and fluctuations in the heating value of the gas. Even so, the engine was not derated from the standard natural gas generator set rating of 762 kW net electrical output. In addition, the engine performance was optimized to meet the EPA site laws for stationary gas engines while still maintaining very low brake specific fuel consumption (BSFC). Finally, 90 days of continuous operation demonstrated engine durability.*

## Landfill Operation

Landfill gas is produced by the decomposition of organic material by anaerobic organisms and it is primarily composed of methane and carbon dioxide. The proportions can vary but are typically 60 percent methane and 40 percent carbon dioxide by volume. This yields a gas with a lower heating value (LHV) of about 500 Btu/sqft and a specific gravity of 0.90, which compares to pipeline quality natural gas with a LHV of 905 Btu/sqft and a specific gravity of 0.60. Since the LHV is approximately half that of natural gas, the carburetor must flow almost twice as much landfill gas as natural gas to maintain the same power. In addition, the high concentration of CO<sub>2</sub> results in very poor combustion because it tends to act as an inert gas and quenches combustion.

A typical landfill will begin to generate gas within 6 months after the area has been covered and an older site can produce a significant quantity of gas. For instance, one 200 acre landfill produces over 5 million cu ft of gas per day. The uncontrolled migration of this gas through the top of the fill would prevent the growth of vegetation and would present a severe odor control problem. Since most large landfills are located near urban areas, appearance and odor control are critical factors for good public relations. To encourage foliage growth and to promote odor control the gas must be prevented from escaping through the top of the fill. To accomplish this, a series of wells are installed throughout the landfill. The wells are connected to an underground gas collection system which leads into an underground storage tank. From the tank, the gas then typically flows to a flare where it is burned off. A separate gas engine is used to maintain the entire gas collection system at a

vacuum. If a centralized collection system is not utilized, the gas is flared off at the individual well heads.

Economic and environmental issues are the prime factors behind the rapid expansion of the spark-ignited landfill engine market. When natural gas is used for electrical power generation, the fuel cost is a major expense item; however, this is not the case for landfill gas operation. In this instance, the gas is readily available as a byproduct from the landfill. The only expense is the addition of a centralized gas collection system, which often already exists. The fuel is then essentially free. While natural gas is one of the most economical fuel sources, it can be the single largest expense for an operator. For example, assume an operator wants to generate 750 kW electrical power continuously. With natural gas at \$0.50 per therm and 95 percent generator availability, the annual fuel bill would be about \$365,000. In contrast, with landfill gas the fuel expense would be essentially zero. In addition, the use of landfill gas for electrical power generation is very good from a public relations viewpoint and tends to promote the "good neighbor" concept.

Even though methane is the natural byproduct of most landfills, this does not mean that all sites are good candidates for the centralized gas collection systems necessary for electrical power generation. To determine whether power generation is feasible on a long-term basis, the quantity of gas per cubic yard of waste must be estimated and the gas chemistry identified. If power generation is feasible, this information is also used as a basis for selecting the engine-generator package. The history and design of the landfill have a major impact on the methane generating potential for the site. For example, household waste has a much greater potential than demolition waste. High concentrations of liquids or sludges make a centralized gas collection system more difficult to design and maintain. In addition, the liquids must be removed prior to

Contributed by the Internal Combustion Engine Division and presented at the Energy-Sources Technology Conference and Exhibition, Dallas, Texas, February 15-20, 1987. Manuscript received at ASME Headquarters November 26, 1986. Paper No. 87-ICE-13.

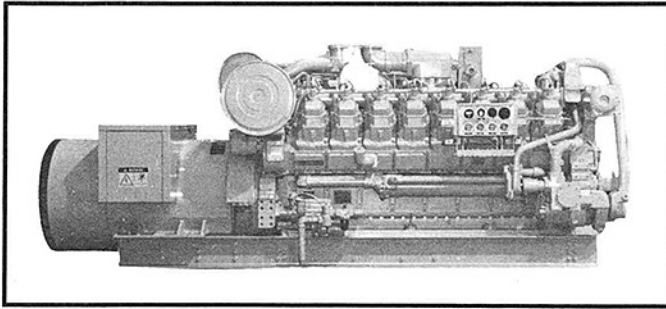


Fig. 1 3516 spark-ignited generator package

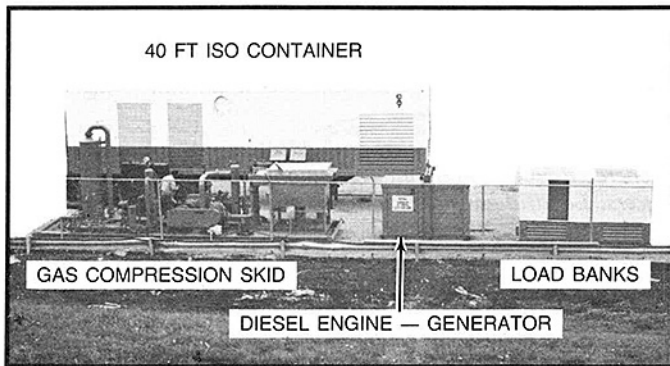


Fig. 2 Test site at waste management's CID landfill

engine combustion. Furthermore, high concentrations of industrial waste such as halogenated hydrocarbons may present a potentially corrosive environment for an engine.

Variations in the LHV also affect the power generation potential of a site. In natural gas pipeline operation the LHV does not fluctuate; however, in landfill operation the LHV constantly varies requiring a landfill engine to have a very broad operating range. The methane production varies based on the activity of the anaerobic organisms. For example, methane production increases after a rain because the rain seals the top of the fill and prevents air infiltration. Methane production decreases in hot weather, particularly in hot, *dry* weather. Methane production also decreases as air infiltration increases. Interaction of the gas collection system also affects the LHV. If the vacuum on the collection system is reduced, then the amount of air infiltration into the system is also reduced and the BTU content of the gas increases. If a well is damaged, a very real hazard at an active landfill, the gas collection system ingests a large amount of air, which dramatically reduces the LHV. Variations in the LHV can cause random engine shutdowns, especially in the case of a damaged well. They can also cause an engine to drop load or cause a change in the maximum power capability of an engine. The fluctuating LHV causes this application to be much more labor intensive than a typical natural gas pipeline installation.

### Engine Design Modifications

A Caterpillar 3516 spark-ignited, turbocharged, separate circuit, aftercooled engine was selected for use in the initial development program. This engine is the largest reciprocating spark-ignited engine currently offered by Caterpillar Inc. It has 16 cylinders, a displacement of 4211 cubic inches, and a 10:1 compression ratio and is rated at 1200 rpm. The basic engine (Fig. 1) is the same as described in [1]. Also available are the 3508 and 3512, the respective eight and twelve-cylinder versions of the engine.

A minimum LHV of 450 Btu/sqft was established for this program, and the LHV never exceeded 530 Btu/sqft. This meant that for the same power, the engine required almost

twice as much landfill gas than natural gas. The following design changes were required to operate on the landfill gas:

- 1 a larger, higher flow capacity, fuel shutoff valve
- 2 a high flow capacity pressure regulator
- 3 larger fuel piping between the pressure regulator and the carburetor
- 4 a carburetor with metering valves sized to operate on the low-Btu fuel

### Engine Instrumentation

The engine was instrumented to monitor various temperatures including fuel, turbocharger air discharge, exhaust stack, etc. Pressure ports were also provided to allow monitoring of boost pressure from each turbocharger, exhaust pressure, fuel pressure, etc. Ports to allow sampling of free oxygen in the exhaust were also provided. A cylinder pressure sensor was installed to monitor combustion pressures. In addition, special hardware was constructed to allow measurement of the secondary spark plug voltages. The secondary voltages were documented to evaluate the capacity of the ignition system and to predict spark plug life.

### Test Site

The entire development program was conducted at Waste Management's CID landfill in Calumet City, IL. The site was selected because of its location and its existing gas collection system. Since this was only a temporary installation, the engine was installed in a 40 ft. ISO sea container which was mounted on a triaxle semi-trailer (Fig. 2). The specially modified container made a complete, self-contained electrical power generation module. It included a 480-V, 60-Hz, 944 KVA generator; the generator switch gear; controls and motor starters for the gas compressor skid; a folded core jacket water radiator; and a horizontally mounted air-to-water heat exchanger for the separate circuit aftercooler.

In order to minimize changes to the standard 3516 spark-ignited engine configuration, the landfill gas had to be pressurized to overcome the turbocharger boost pressure. An electric motor driven compressor skid was constructed to accomplish this (Figs. 3 and 4). Besides pressurizing the fuel, the skid also removed particulates and condensate from the gas. The skid was built according to specifications that did not necessarily coincide with the engine's requirements. The skid was purchased ready-built and was not tested prior to installation.

The landfill gas was supplied to the skid from an existing underground collection tank which also supplied gas to a nearby flare. As the gas entered the skid it passed through a "Y" strainer where large particulates and a significant quantity of liquid were removed. The gas then passed through a water scrubber which removed particulates down to 10 microns in size. The scrubber was also promoted as a means to remove halogenated hydrocarbons; however, a gas analysis proved that the scrubber had minimal effect on the gas composition. The water makeup and discharge systems for the scrubber were also very unreliable and caused a great deal of down time. In addition, one of the functions of the skid was to supply dry gas to the engine and the scrubber was actually adding liquid to the gas. For these reasons, the water supply to the scrubber was disconnected. The engine has accumulated over 500 h since then with no adverse effects and, in fact, the reliability of the skid has improved dramatically. The water scrubber will be replaced with a coalescing type filter for future development.

After the water scrubber, the gas flowed through two compression stages. Two rotary lobe blowers were mounted in series. Each was belt driven by its own 50 hp electric motor. The first stage compressed the gas from about 6 in. Hg

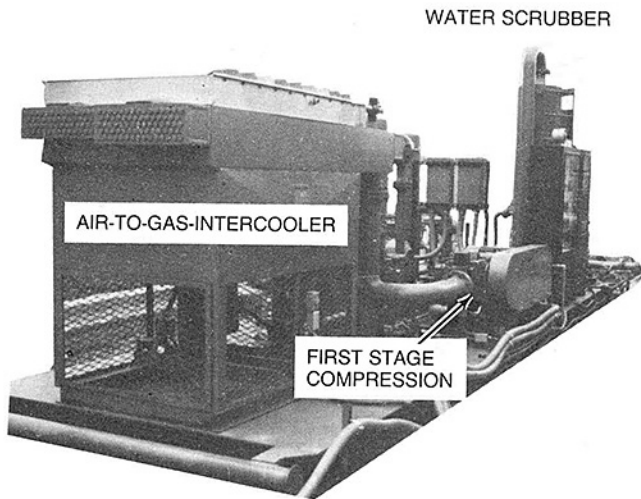


Fig. 3 Gas compressor skid

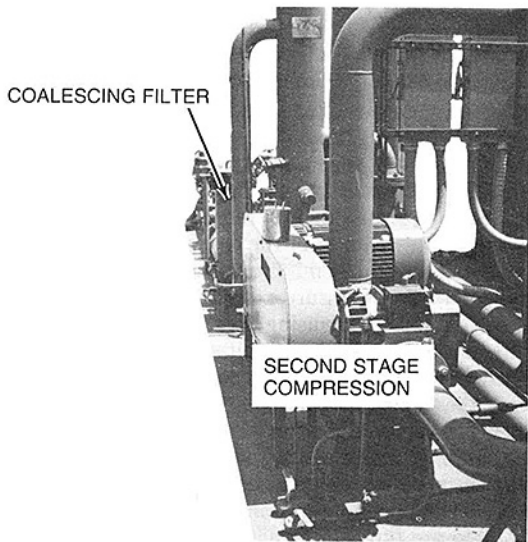


Fig. 4 Gas compressor skid

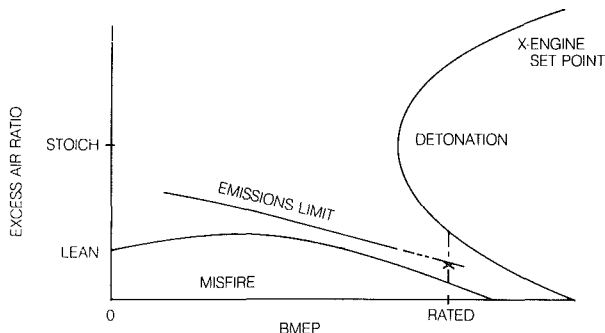


Fig. 5 Lean burn natural gas engine operation

vacuum to 6 psig and the second stage compressed the gas to 28 psig. At the outlet of each compression stage, an air-to-gas intercooler reduced the gas temperature while a vertical scrubber removed the excess condensate. Just prior to exiting the skid, the gas flowed through a four-element coalescing type filter which removed very fine particulates down to 2 microns in size as well as condensate. Once the gas exited the compressor skid, it flowed through a 250-gal tank that removed additional condensate and acted as an accumulator for

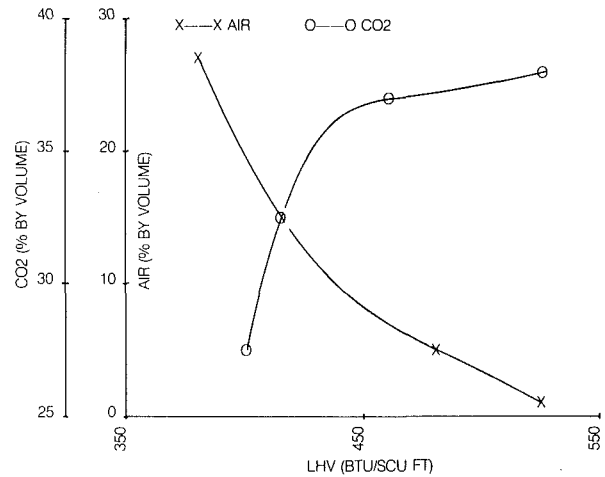


Fig. 6 LHV versus air and CO<sub>2</sub> content

pressure surges. To ensure that the remaining moisture in the gas was above the dew point, a jacket water heat exchanger was used to reheat the gas just prior to delivery to the engine. Condensate removed from the gas was collected and stored in an underground tank for final disposal.

A 120-kW diesel engine powered generator enabled the compressor skid to be started and brought up to pressure. The 3516 engine could be started once pressurized fuel was available. The two generators were then manually synchronized, which transferred the power source for the compressor skid from the diesel generator to the 3516 generator. Since it was not economically feasible to temporarily connect into the local utility power grid, a stepable 800-kW resistance load bank was used for additional load capability.

### Performance Development

To meet low emission levels, a spark-ignited engine must operate much closer to lean limit misfire conditions than a standard (near stoichiometric) engine (Fig. 5). This is especially true at higher loads. To add to the problem, the 3516 spark-ignited landfill engine had to be capable of operating very close to a lean limit misfire condition on a fuel which did not have a constant LHV. The fluctuations in LHV caused random engine shutdowns, caused the engine to drop load, and even affected the maximum power capability of the engine. Initially, the development program concentrated on quantifying the fluctuations in the gas LHV on an on-line basis. NDIR (non-dispersive infrared) analyzers were used to sample the fuel for methane and CO<sub>2</sub> with the amount of air then calculated assuming a 21 percent O<sub>2</sub> content by volume. As the amount of air infiltration increased, the LHV of the gas decreased (Fig. 6). LHV fluctuations in excess of 30 percent were recorded. The time span for these fluctuations varied from minutes to as long as several hours. As indicated in Fig. 6, the amount of CO<sub>2</sub> also varied in conjunction with the amount of air infiltration.

Once the variations in LHV were quantified, the focus then shifted to expanding the operating range of the engine. First modifications to the fuel pressure regulator to reduce the restriction in the registration line improved the transient response and load acceptance of the engine. A specially instrumented carburetor was used to size the gas orifices very quickly and shape the gas metering valves for landfill operation (Fig. 7). The gas orifice size was critical for good startability. The shape of the metering valves affected both part load emissions and stability. Both mixing bodies in the carburetor were equipped with a stepper motor, which controlled the position of the gas valves. The unit was also equipped with



Fig. 7 Specially instrumented carburetor

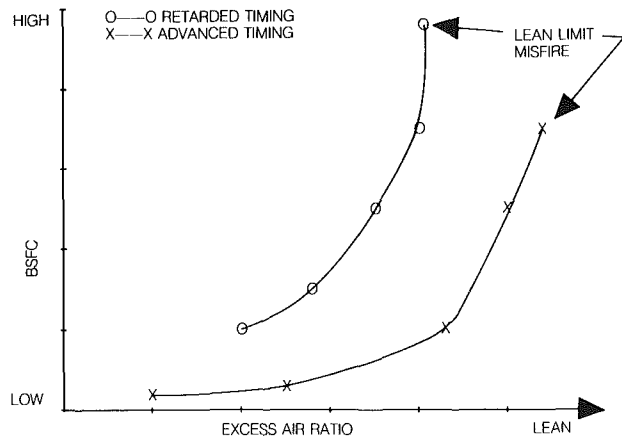


Fig. 8 BSFC and engine timing comparison

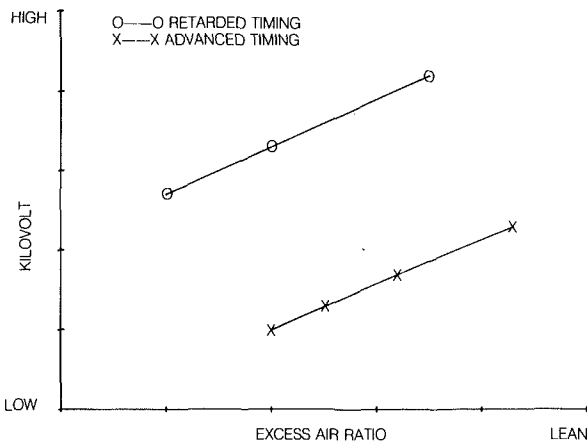


Fig. 9 Excess air ratio versus secondary voltage

a position readout for the gas and air valves. Once the gas orifices were sized to provide acceptable startability, the contour of the gas metering valves could be optimized in one iteration. Sizing the metering valves without the instrumented carburetor is an art and usually proceeds on a slow trial and error basis. The instrumented carburetor will also be a very valuable field tool because it will be possible quickly to optimize the orifice size and valve profile for any given gas.

Both the standard Caterpillar 3516 spark-ignited natural gas engine and the landfill gas engine have been developed for lean excess air fuel ratio (EAR) operation. This was necessary in order to meet the EPA site laws for stationary gas engines. The regulations specify maximum quantities of  $\text{NO}_x$  and CO that can be emitted from any one particular site on an annual

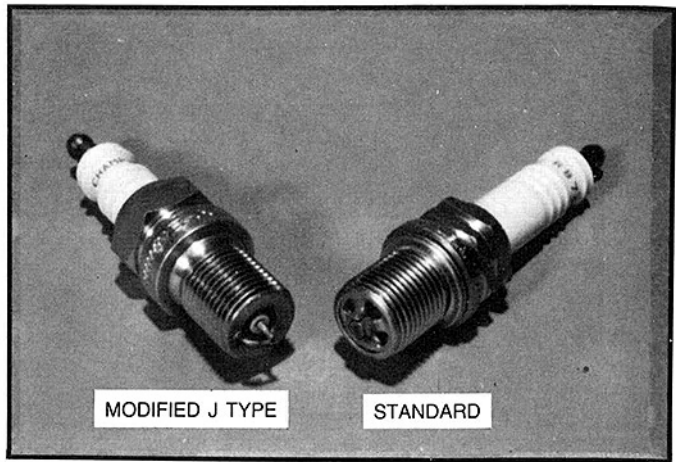


Fig. 10 Spark plug comparison

basis. If the site is located in an attainment area then the  $\text{NO}_x$  and CO levels are each limited to 250 tons per year. If the landfill is in a nonattainment area where one or both of the pollutants has exceeded a critical level established by the EPA, then that constituent is limited to 100 tons per year.

The 3516 spark-ignited landfill engine is capable of operating in the 2-4 g/hp-h  $\text{NO}_x$  emissions range at a gas supply pressures of 28 psig; however, the lean misfire margin is significantly increased by raising the gas supply pressure. Since the compressor skid was rated at 28 psig maximum, the gas supply pressure and not the combustible limit of the mixture determined the lean misfire point. At very lean EAR's the turbocharger boost pressure exceeded the gas supply pressure at the carburetor thus causing the engine to die. A higher gas pressure compressor skid is required and is now under design.

Advancing the timing expanded the operating range by allowing the engine to function at a leaner EAR before experiencing lean limit misfire (Fig. 8). In addition, the advanced timing significantly improved fuel consumption resulting in excellent bsfc values which ranged from 7300 to 8000 btu/hp-h depending upon the EAR and engine timing. While these are typical characteristics for natural gas spark-ignited engines, they are even more dramatic on landfill gas because of its slow combustion characteristics. When comparing landfill gas performance at 37 deg BTDC timing to natural gas performance at 22 deg BTDC timing, the ignition delay was 50 percent longer on landfill gas even when compared at the same exhaust  $\text{O}_2$  and power level. Thus, the start of combustion occurred much later in the cycle and at a much higher cylinder pressure with landfill gas. Although the advanced timing did expand the operating range and improve fuel consumption it also caused the exhaust  $\text{NO}_x$  level to increase for a given EAR. The optimum 37 deg BTDC timing was selected because more advanced timings did not improve fuel consumption but continued to increase exhaust  $\text{NO}_x$  levels.

The advanced timing also extended the life of the ignition system by reducing the spark plug voltages (Fig. 9). The voltages were reduced because as the timing was advanced the ignition voltage occurred earlier in the cycle. Less voltage was required since the gap was ionized at a lower cylinder pressure. The current standard production spark plug life meets or exceeds the standards of the landfill industry today. Preliminary results with a modified J-type plug with a precious metal electrode have been very promising. This plug has a much more exposed gap than the standard plug (Fig. 10), which enhances the initiation of combustion. This further extended the lean limit EAR and also improved the startability. The precious metal electrode should also extend the life of the plug. The new spark plug is part of a continuing development program.

Engine oil life was another aspect of the development program. The objective was to maintain the same 1000-h oil change period as the standard natural gas engine. A spark-ignited engine has extremely different oil requirements from a diesel engine and landfill gas even further complicates these requirements. In order to prevent the formation of combustion chamber deposits and to prevent fouling the spark plugs, standard spark-ignited engine oil has an ash content less than 0.5 percent by volume. The low ash content of the oil also means that it has a very low total base number (TBN). In a spark-ignited engine the water from combustion and other combustion byproducts tend to find their way into the engine oil where they react with the oil additives to form acids. Since the oil has such a low initial TBN, it can become highly acidic very quickly. The acidic oil then attacks the bronze and copper components in the engine causing a sharp increase in the Cu level of the oil with no significant increase in the wear metals. The typical solution for a standard spark-ignited engine is to maintain a very high oil temperature so that the water is in effect boiled off, preventing the formation of condensate.

Initially, only this method was used for the landfill engine. Even though the oil temperature was maintained at 190°F, after only 400 h of operation the standard spark-ignited engine oil had an unacceptably high Cu level. The high moisture content of the landfill gas accelerated the rate at which the engine oil became acidic. The relatively high concentration of ketones in the landfill gas (over 150 ppm by weight) also accelerated this phenomenon. At this point, it was decided that the landfill gas temperature as well as the oil temperature should be regulated. A jacket water heat exchanger was installed in the gas line just prior to the engine. The heat exchanger was used to reheat the gas to insure that any remaining moisture was above the dew point. A second, higher TBN oil with a relatively low ash content (less than 1 percent by volume) was also

selected for evaluation. The oil quality is still acceptable after over 600 h of operation. Extrapolation of the data indicates that this oil should meet the 1000-h change period goal; however, the oil quality will continue to be monitored during the endurance portion of the program.

### Conclusion

The 3516 spark-ignited engine has been successfully developed to operate on landfill gas ranging from 450 to 550 Btu/sqft without any derating from the standard natural gas rating. The engine performance has been optimized to meet the EPA site laws for stationary gas engines while still maintaining excellent bsfc values within the broad operating range of the engine. In addition, the instrumented carburetor has been identified as an important field development tool will make it very easy to configure a carburetor on site for any given gas. Once the endurance portion of the development program has been completed at CID, the engine will be returned to Caterpillar for inspection to assure that it will meet the required life expectancy. It will then be permanently installed at Waste Management's County Land landfill just outside of Denver, CO. The Denver site as well as another site in New Jersey will be part of a very close field follow-up program.

### Acknowledgments

The assistance of Mr. James Greenwell of Waste Management Corp. was much appreciated.

### References

- 1 McClung, C. L., "Design and Development of the Caterpillar 3500 Series Spark-Ignited Engine Family," in: *New Developments in Large Bore Engines*, Vol. 88, ASME, New York, 1985, p. i11.

# Progress Toward Life Modeling of Thermal Barrier Coatings for Aircraft Gas Turbine Engines

R. A. Miller

NASA Lewis Research Center,  
Cleveland, OH 44135

*Progress toward developing life models for simulating the behavior of thermal barrier coatings in aircraft gas turbine engines is discussed. A preliminary laboratory model is described as are current efforts to develop engine-capable models. Current understanding into failure mechanisms is also summarized.*

## Introduction

Current thermal barrier coatings research is focused primarily toward developing coatings for protecting air-cooled turbine blades and vanes in aircraft gas turbine engines. The engine environment which must be tolerated by these coatings is characterized by high temperatures, relatively high heat fluxes, and high partial pressures of oxygen. Early engine tests [1, 2] demonstrated that two-layer coating systems consisting of a layer of zirconia-yttria ceramic over a layer of an MCrAlY alloy had the potential to survive in the engine environment. The MCrAlY alloy layer, which is often called the bond coat, is typically applied by either low-pressure plasma spraying or by air plasma spraying, while the zirconia-yttria layer is typically applied by air plasma spraying. Typical coating thicknesses for aircraft gas turbine applications are 0.13 mm bond coat thickness and 0.25 mm ceramic layer thickness.

The benefits of thermal barrier coatings arise from the insulation provided by the ceramic layer. The insulation can allow higher gas temperatures, lower metal temperatures, reduced cooling air requirements, moderation of thermal transients, and a decrease in the severity of hot spots. This results in improvements in performance, efficiency, and/or component durability.

The greatest improvements in performance and efficiency would result from using thermal barrier coatings in the so-called "prime reliant" mode. In this mode gas turbine engines would be operated at temperatures high enough to heat uncoated metallic components to beyond their temperature capabilities. The risk inherent in such an approach is that loss of the coating would quickly lead to loss of the component. Because of this risk, engine designers must be able to predict how a given coating system would stand up in any given application. Therefore, life prediction models are essential to take full advantage of a given thermal barrier coating.

As a result of the vital role that life models are expected to take in enabling the benefits of thermal barrier coatings to be fully exploited, major efforts in this area are being sponsored

by the NASA Lewis Research Center. These efforts consisted initially of in-house programs designed to improve the understanding of coating failure mechanisms and to develop a model for treating laboratory data. These efforts were then extended to include three major contractual efforts sponsored through the NASA Hot Section Technology Program (HOST) [3-5]. These efforts are devised first to examine coating failure mechanisms through three approaches—literature searches, examination of prior engine and laboratory experience, and experimentation. The programs were also structured to determine materials properties and to analyze the stresses and strains imposed on the coating system by laboratory burner rig and engine environments. Finally they were devised to initially develop preliminary and then engine-capable life prediction models. All the contracts are now in the third and final year of the first phase which is aimed at developing the preliminary models. An optional second phase will then be devoted to developing models which are fully engine-capable.

## Coating Failure Mechanisms

A basic understanding of coating failure mechanisms is a prerequisite to the development of life models. Coating failure mechanisms in gas turbine engines and in laboratory simulations have been discussed in detail in several sources [3-9]. There is now general agreement that ceramic coatings in gas turbine engines fail primarily as a result of stresses induced by differential thermal expansion between the metallic and ceramic layers, and that these stresses are greatly influenced by the effects of time-at-temperature processes. One of the most important of these effects is bond coat oxidation. Other factors which may play a role include bond coat plasticity [5, 6], ceramic creep [3, 10], and ceramic sintering shrinkage [4]. Stresses resulting from heating transients in the engine may also contribute to failure but the experimental results suggest that heating stresses are not the primary source of coating failure [11].

The stress state in the ceramic layer which leads to delamination cracking and eventual spalling is one of biaxial compression in the plane of the coating and radial tension. This stress state is further complicated by the wavy and irregular bond coat/ceramic interface. Figure 1 shows

Contributed by the Internal Combustion Engine Division and presented at the Energy-Sources Technology Conference and Exhibition, Dallas, Texas, February 15-20, 1987. Manuscript received at ASME Headquarters December 1, 1986. Paper No. 87-ICE-18.

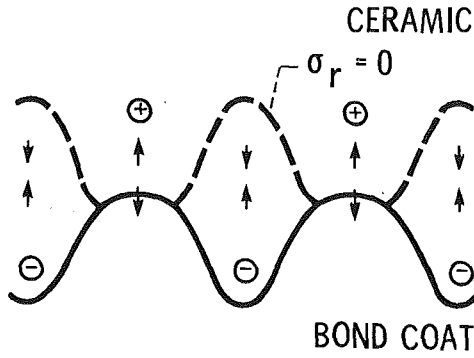


Fig. 1 Schematic representation of radial thermal expansion mismatch stress above a wavy interface as calculated by finite element analyses [12]

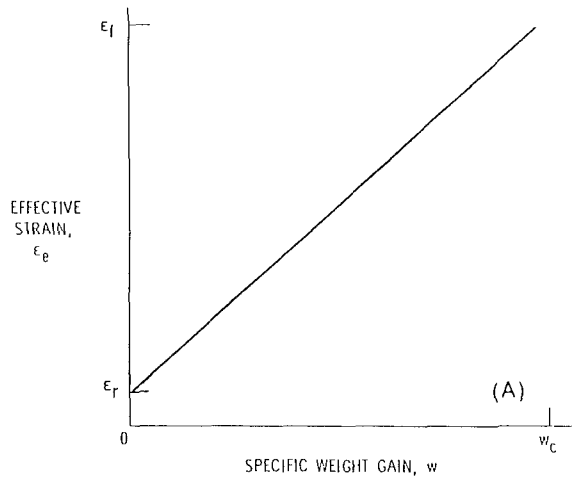


Fig. 2(a) Proposed relationship between effective strain and specific weight gain

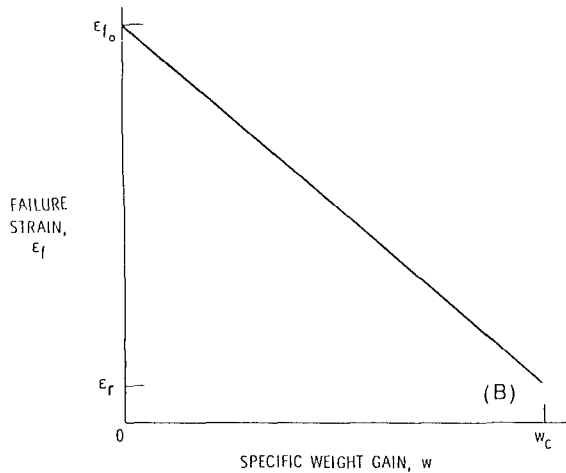


Fig. 2(b) Proposed alternative relationship between failure strain and specific weight gain

schematically the nature of the radial stress above a wavy interface based on HOST-sponsored finite element calculations [12]. The cracking leading to coating failure tends to take place mostly within the ceramic layer near to the interface with the bond coat. Reference [3] has documented how small microcracks increase in length and number upon cycling and eventually line up to form delamination cracks.

## Preliminary Laboratory Model Development

A preliminary life prediction model was discussed in [8, 9, 13, 14]. This model assumed that the complex states of stress and strain imposed on the coating system by the thermal loads could be adequately expressed in terms of a single parameter. The parameter chosen for discussion was labeled  $\epsilon_r$ , which was taken to be the radial component of the thermal expansion mismatch strain. Next it was assumed that time-at-temperature effects could be described in terms of oxidation alone and that oxidation could be expressed in terms of the specific weight gain  $\omega_N$ . Finally, weight gain and strain were related using either of two alternative approaches. In the first case depicted in Fig. 2(a) it was assumed that an oxidized coating behaves as if an effective strain  $\epsilon_e$  is increasing. At zero weight gain this effective strain would take on the value of  $\epsilon_r$ . At a critical weight gain  $\omega_c$ —defined as the weight gain required to fail the coating in a single cycle—the effective strain would equal a failure strain  $\epsilon_f$ . This leads to the expression

$$\epsilon_e = (\epsilon_f - \epsilon_r) \left( \frac{\omega}{\omega_c} \right)^m + \epsilon_r \quad (1)$$

where the exponent  $m$  has been added to allow the curve in Fig. 2(a) to be nonlinear. An alternative assumption [8, 9] is to assume that the failure strain of a coating falls from an initial value  $\epsilon_{fo}$  at zero weight gain to a final value of  $\epsilon_r$  at the critical weight gain. This case is illustrated in Fig. 2(b), and it leads to the expression

$$\frac{\epsilon_f}{\epsilon_r} = \left( 1 - \frac{\epsilon_{fo}}{\epsilon_r} \right) \left( \frac{\omega}{\omega_c} \right)^m + \frac{\epsilon_{fo}}{\epsilon_r} \quad (2)$$

Delamination cracking was assumed to occur in the ceramic layer according to a crack growth law of the form

$$\frac{da}{dN} = A \epsilon_e^b a^d \quad (3)$$

where  $da/dN$  is the incremental crack growth per cycle,  $A$  is a constant,  $b$  and  $d$  are exponents, and  $a$  is the crack length. An alternative starting point, given in [14], is to use the familiar expression

$$N_f = \left( \frac{\epsilon_e}{\epsilon_f} \right)^b \quad (4)$$

In either case the model resulting from equation (1) is

$$\sum_{N=1}^{N_f} \left[ \left( 1 - \frac{\epsilon_r}{\epsilon_f} \right) \left( \frac{\omega_N}{\omega_c} \right)^m + \frac{\epsilon_r}{\epsilon_f} \right]^b = 1 \quad (5)$$

and the alternative model resulting from equation (2) is

$$\sum_{N=1}^{N_f} \left[ \left( 1 - \frac{\epsilon_{fo}}{\epsilon_r} \right) \left( \frac{\omega_N}{\omega_c} \right)^m + \frac{\epsilon_{fo}}{\epsilon_r} \right]^{-b} = 1 \quad (6)$$

Figure 3 illustrates the fit obtained using equation (5) as applied to life data collected at 1100°C for three different cycle lengths. It should be mentioned that the set of parameters given in the figure is not unique. Numerous other sets are possible. For example, raising the value of  $b$  while lowering the strain ratio produces an equally good fit.

## Preliminary Engine Capable Life Modeling

A preliminary life model is discussed in [3]. While this model is similar to equation (6), there are several differences. First of all oxidation is expressed in terms of oxide layer thickness  $\delta$  rather than weight gain  $\omega$ . Second, two exponents labeled  $c$  and  $d$  are used in place of the single exponent  $m$ . Practically speaking this is a minor difference because these



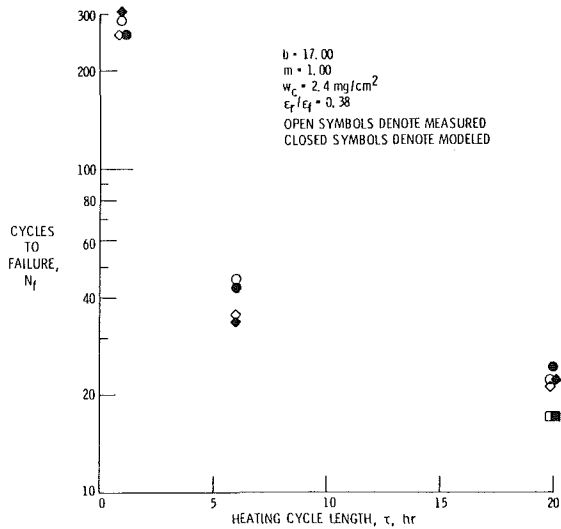


Fig. 3 Comparison of calculated and modeled cycles to failure as a function of heating cycle duration [14]

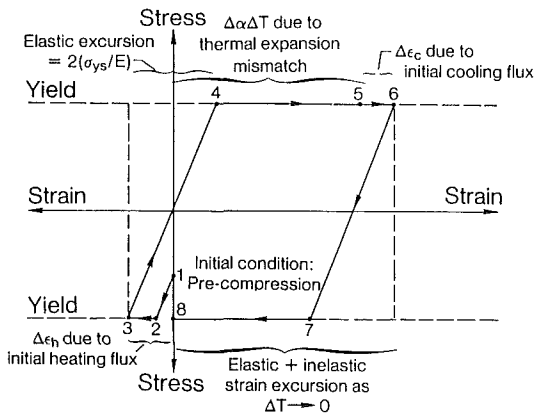


Fig. 4 Conceptual model of a thermally driven ceramic stress strain cycle [3]

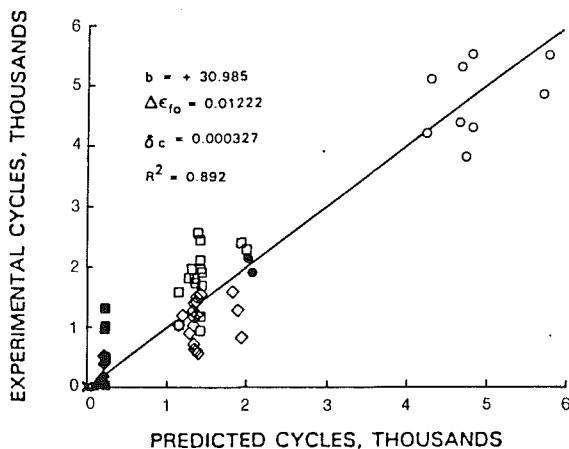


Fig. 5 Correlation between measured and modeled coating lives; plotting symbols refer to various test conditions discussed in [3]

exponents are typically set equal to unity. Third, the strain term is determined analytically assuming perfectly plastic behavior.

The term  $\Delta\epsilon_i$  is considered to be the inelastic strain range, and it is defined by

$$\Delta\epsilon_i = \Delta(\alpha \Delta T) + \Delta\epsilon_h + \Delta\epsilon_c - 2 \frac{\sigma_{ys}}{E} \quad (7)$$

- TBC DEGRADATION RATE =
- $F_1$  (MECHANICAL)
    - COATING STRESSES
    - TEMPERATURE
    - MATERIAL SYSTEM
      - $K_{IC}$
      - FLAW SIZE
      - ELASTIC MODULUS
      - SPALLING STRAIN
  - $F_2$  (OXIDATION)
    - TEMPERATURE
    - TIME
    - MATERIALS SYSTEM
  - $F_3$  (SALT DEPOSITION)
    - ALTITUDE (SALT INGESTION)
    - TURBINE PRESSURE
    - SALT EVAPORATION
    - SALT SOLIDIFICATION
    - TEMPERATURE
    - GAS VELOCITY
    - AIRCRAFT LOCATION
    - MATERIALS SYSTEM

Fig. 6 Engine, mission, and materials system parameters affecting coating life according to [4]

where  $\Delta(\alpha \Delta T)$  is the thermal expansion mismatch strain (expressed as  $\epsilon_r$  in the previous section),  $\Delta\epsilon_h$  is the inelastic strain resulting from the heating transient, and  $\epsilon_c$  is the strain resulting from the cooling transient. The term  $\sigma_{ys}/E$  is the yield strength divided by the elastic modulus. Equation (7) is depicted schematically in Fig. 5 from [3]. The expression corresponding to equation (2) in the previous section is

$$\Delta\epsilon_f = \Delta\epsilon_{fo} \left(1 - \frac{\delta}{\delta_c}\right)^c + \Delta\epsilon_i \left(\frac{\delta}{\delta_c}\right)^d \quad (8)$$

An example of how this model was used to fit experimental data is shown in Fig. 5. The accurate calculation of strains coupled with the measurement of materials properties needed for expressions (7) and (8) has proven to be very challenging.

For modeling data collected at differing temperatures it is necessary to use an Arrhenius expression to describe the dependence of  $\delta$  (or  $\omega$ ) on temperature and to redetermine the strain for the temperature of interest. The present author also believes that the critical thickness  $\delta_c$  or weight gain  $\omega_c$  would have to be adjusted upward for lower temperatures. Also, the present author agrees that a term such as the yield strength term in equation (7) would be required to model life successfully as a function of temperature. Finally, [3] also states that future versions of the model should include a temperature-dependent creep term.

Reference [4] gives a modeling strategy which differs somewhat from the above models. They propose to model according to the expression

$$\text{Life} = \left[ \text{Life}_{\text{oxide}}^{-1} + \text{Life}_{\text{salt}}^{-1} + \text{Life}_{\text{stress}}^{-1} \right]^{-1} \quad (9)$$

The various factors which may enter into the oxidation life, the hot salt life, and the cyclic stress life are listed in Fig. 7 from [4].

With the third contract, a modeling approach had not been specifically formulated at the time of publication of [5]. However, experiments, property measurements, and analytical efforts which will lead up to the modeling efforts are underway.

### Concluding Remarks

As a result of NASA in-house and HOST-sponsored contractual efforts several publicly available computer codes for

thermal barrier coating life modeling are being developed. The anticipated benefit of these models is that the technology may be advanced as designers learn how to exploit thermal barrier coatings fully.

The approach being used to develop these life models for thermal barrier coatings on gas turbine engine components may be applied to the development of life prediction models for coatings on diesel or other heat engine components. This approach involves understanding failure mechanisms, measuring material properties, formulating the failure mechanisms in terms of mathematical models, and verifying the models with test experience. Diesel engine coatings will differ from gas turbine coatings in that the maximum temperatures will be lower and coating thicknesses may be much greater. The current level of understanding and of property measurements on diesel engine coatings is at a very early stage and much more fundamental work in these areas is clearly required.

## References

- 1 Liebert, C. H., Jacobs, R. E., Stecura, S., and Morse, C. R., "Durability of Zirconia Thermal-Barrier Ceramic Coatings on Air-Cooled Turbine Blades in Cyclic Jet Engine Operation," NASA TM X-3410, 1976.
- 2 Stecura, S., "Two-Layer Thermal Barrier Coating for High Temperature Components," *Amer. Ceram. Soc. Bull.*, Vol. 56, 1977, pp. 1082-1086.
- 3 DeMasi, J. T., and Sheffler, K. D., "Thermal Barrier Coating Life Prediction Model Development Second Annual Report," NASA CR-179508, Pratt & Whitney Aircraft, 1986.
- 4 Strangman, T. E., Neumann, J., and Liu, A., "Thermal Barrier Coating Life-Prediction Model Development Second Annual Report," NASA CR-179507, Garrett Turbine Engine Company, 1986.
- 5 Hillery, R. V., and Pilsner, B. H., "Thermal Barrier Coating Life Prediction Model Second Annual Report," NASA CR-179504, General Electric Company, 1986.
- 6 Miller, R. A., and Lowell, C. E., "Failure Mechanisms of Thermal Barrier Coatings Exposed to Elevated Temperatures," *Thin Solid Films*, Vol. 95, 1983, pp. 265-273.
- 7 Liebert, C. H., and Miller, R. A., 1984, "Ceramic Thermal Barrier Coatings," *Ind. Eng. Chem. Prod. Res. and Dev.*, 1984, pp. 344-349.
- 8 Miller, R. A., "Current Status of Thermal Barrier Coatings—An Overview," *Surface and Coatings Technology*, in press.
- 9 Miller, R. A., "Ceramic Thermal Barrier Coatings," in: *High Temperature Corrosion-Resistant Coatings*, R. Streiff, ed., in preparation.
- 10 Padovan, J., Dougherty, D., Hendricks, R. C., Braun, M. J., and Chung, B. T. F., "High Temperature Thermomechanical Analysis of Ceramic Coatings," *J. Thermal Stress*, Vol. 7, 1984, pp. 51-74.
- 11 Miller, R. A., and Berndt, C. C., "Performance of Thermal Barrier Coatings in High Heat Flux Environments," *Thin Solid Films*, Vol. 119, 1984, pp. 195-202.
- 12 Chang, G. C., Phucharoen, W., and Miller, R. A., "Behavior of Thermal Barrier Coatings for Advanced Gas Turbine Blades," *Surface and Coatings Technology*, in press.
- 13 Miller, R. A., "Oxidation Based Model for Thermal Barrier Coatings Life," Vol. 67, 1984, pp. 517-521.
- 14 Miller, R. A., Agarwal, P., and Duderstadt, E. C., "Life Modeling of Atmospheric and Low Pressure Plasma Sprayed Thermal Barrier Coatings," *Ceram. Eng. Sci. Proc.*, Vol. 5, 1984, pp. 470-478.

# Study of the Flow Pattern in Compact Manifold Type Junctions by LDA

R. Sierens

P. Snauwaert

Laboratory for Machines and Construction of  
Machines,  
University of Gent,  
Gent, Belgium

*In this paper pressure and velocity measurements on two theoretical compact manifold type junctions (compact pulse converters) under steady-state conditions are described. The velocity measurements are done with Laser-Doppler anemometry (LDA). The pressure distributions and the velocity profiles for different flow configurations and different mass flow rates are presented. These results are used for calculation of loss coefficients and for comparison with a numerical algorithm for simulating the three dimensional turbulent quasi-steady flow in compact manifold type junctions.*

## Introduction

Turbocharging is generally used to increase the power output of diesel engines. This has the additional advantage of increasing the engine efficiency, creating a smoother combustion and an engine which is less sensitive to the fuel cetane number.

The basic turbocharging systems, namely the constant pressure system and the pulse system, are widely used in a variety of applications. The introduction of pulse converter systems has the aim to combine the advantages of both basic systems: simplicity of arrangement of the exhaust pipes, better efficiency in the turbine, and a higher energy recuperation at low load conditions.

This paper gives a description of measurements which are necessary for the development of pulse converter systems. Two theoretical compact manifold type junctions (converters) under steady-state conditions were examined. Two kinds of measurements were taken:

- pressure measurements: these results will be used as input data for a numerical simulation model of the gas exchange process of the engine (method of characteristics) [1, 2]. The shape and dimensions of the converter are chosen to provide the gas to flow preferentially in one direction, from the engine cylinder to the turbine; and to increase the resistance to flow in adverse direction. The resistance to this flow can be defined by means of pressure loss coefficients derived from experiments
- velocity measurements: these results will give an insight into the flow pattern inside the converter and will be used for comparison with a numerical algorithm for simulating the three-dimensional turbulent quasi-steady flow in the compact manifold junction (together with the pressure measurements) [3, 4].

Especially for the comparison with the numerical algorithm,

Contributed by the Internal Combustion Division and presented at the Energy-Sources Technology Conference and Exhibition, Dallas, Texas, February 15-20, 1987. Manuscript received at ASME Headquarters December 1, 1986. Paper No. 87-ICE-25.

simplified basic models of the manifold junctions were examined.

## Theoretical Considerations

**Simulation of Gas Exchange Process.** The method of characteristics has been extensively used to study the non-steady flow in the inlet and exhaust pipes of IC engines. The inlet and exhaust system is divided into a number of ducts. At the beginning and end of each duct, the flow in the duct interacts with boundaries. Such boundaries are the inlet or exhaust manifold, the inlet to the turbine, a junction of two pipes, etc. The interaction between the flow and these boundaries is described in so-called boundary conditions. The method of characteristics itself and the different boundary conditions have been described extensively in the literature [5-8].

The converter can be considered as a junction of three ducts with an adiabatic pressure loss at the junction for each of the possible flow directions. The loss coefficients are obtained under stationary flow conditions. Depending on the converter shape (symmetric or not) four or six flow geometries are possible.

The flow is then characterized by non-dimensional parameters.

*Mach Number  $M$*

$$M = \frac{u}{a}$$

where  $a = \sqrt{\kappa RT}$  = the velocity of sound (m/s);  $\kappa$  = ratio of specific heats;  $R$  = universal gas constant (J/Mol K);  $T$  = temperature of the gas (K).  $u$  stands for the mean velocity in a cross section  $A$ , and can be calculated from

$$u = \frac{m}{\rho A}$$

where  $m$  = mass flow (kg/s);  $\rho$  = density (kg/m<sup>3</sup>);  $A$  = cross-sectional area (m<sup>2</sup>).

**Pressure Loss Coefficient  $L$**

$$L_i = \frac{\Delta p_{s,i}}{p_T} = \frac{p_i - p_T}{p_T} \quad (i = 1, 2, 3)$$

The static pressure loss  $\Delta p_s$  is the difference of two static (mean) pressure readings in sections at equal distance of the junction. The subscript  $T$  indicates the pipe (branch) with the total mass flow.

**Resistance Coefficient  $K$**

$$K_i = f_{c,i} \frac{\kappa}{2}$$

where

$$f_{c,i} = \frac{\Delta p_{s,i}}{\rho_T u_T^2} = 2 \frac{p_i - p_T}{\rho_T u_T^2} \quad (i = 1, 2, 3)$$

or

$$K_i = \frac{\Delta p_{s,i} \kappa}{\rho_T u_T^2} \quad (i = 1, 2, 3)$$

The pressure loss coefficient  $L_i$  and the resistance coefficient  $K_i$  are functions of the Mach number  $M_T$  and the mass flow ratio  $m_i/m_T$

$$L_i = f(M_T, m_i/m_T)$$

$$K_i = f(M_T, m_i/m_T)$$

These coefficients are then used as input data for the boundaries of the compact manifold type junction. Although the pressure loss and resistance coefficients are obtained under steady-state flow conditions, these coefficients are used in the simulation model of the gas exchange process (quasi-steady-state calculations). The full theoretical discussion of this method is beyond the scope of this paper and is described elsewhere [1, 5, 8].

**Simulation of Three-Dimensional Turbulent Flow in the Compact Manifold Junction Under Steady-State Conditions.** At the University of Manchester Institute of Science and Technology (UMIST) a finite-volume-based computational algorithm has been written that is designed to simulate the three-dimensional flow in manifold junctions [3, 4].

Again, the description of the computational procedure is beyond the scope of this paper, but the experimental results given here are indispensable for the updating and the validation of the algorithm. The comparison will be made with velocity profiles in different planes of the junction and with pressure distributions along the walls of the junction.

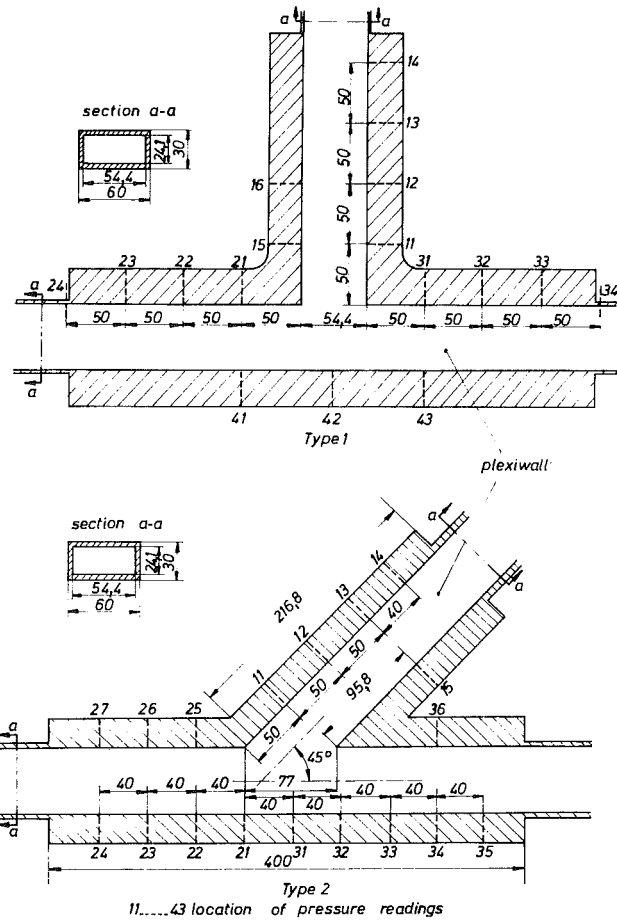


Fig. 1 Theoretical compact manifold junctions

**Experimental Setup**

**Test Bed Description.** Two theoretical compact manifold type junctions are examined, both consisting of a main duct and a side branch which form an angle of either 90 or 45 deg. In both junctions the branches have a rectangular section (Fig. 1).

Two flow coefficients are examined, configurations which are considered as the most important ones for compact manifold type converters (Fig. 2). Considering branch 1 as the connection pipe from a cylinder to the junction and branches 2 and 3 as a part of the main exhaust pipe, configuration A then represents the normal flow situation (joining flow). Configuration B is an unwanted but possible back flow situation

**Nomenclature**

- |  |   |   |
|--|---|---|
| $a$ = velocity of sound                                  |   |   |
| $A$ = cross-sectional area                               | ability-density distribution  | ability-density distribution  |
| $c$ = flatness (of the probability-density distribution) | $T$ = temperature   | $\rho$ = density  |
| $d$ = turbulent fluctuation                              | $u$ = mean velocity (general flow)  | $\sigma$ = standard deviation (of the probability-density distribution) |
| $K$ = resistance coefficient                             | $v$ = mean velocity   | $\phi$ = probability-density distribution                               |
| $L$ = pressure loss coefficient                          | $v_1$ = axial velocity component  |   |
| $m$ = mass flow  | $v_2$ = velocity component perpendicular to $v_1$ and parallel to the plexi walls |   |
| $M$ = Mach number  | $\kappa$ = ratio of specific heats  |   |
| $\Delta p_s$ = static pressure loss                      | $\mu$ = mean value (of the probability-density distribution)                      |   |
| $p$ = pressure   |   |   |
| $R$ = universal gas constant                             |   |   |
| $s$ = skewness (of the probability-density distribution) |   |   |
- Subscripts**  
 1, 2, 3,  $i$  = number of branch  
 $T$  = total (common branch)

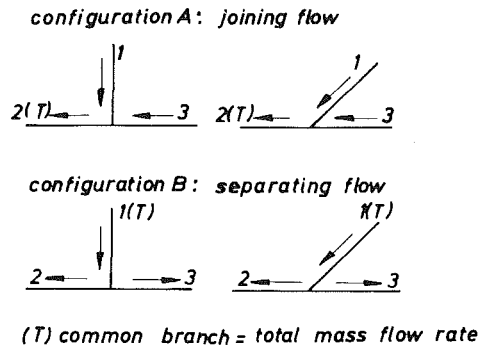


Fig. 2 Flow configurations

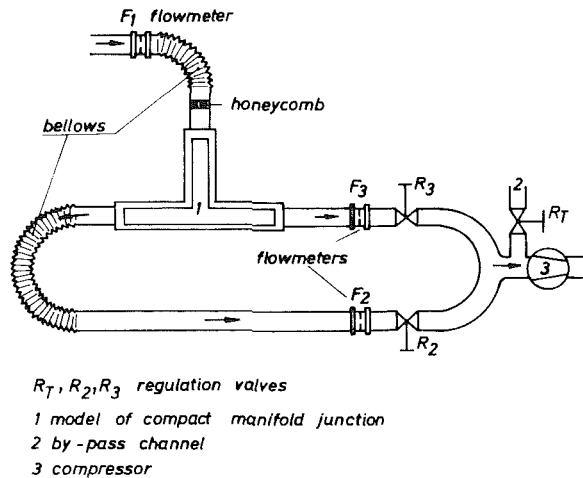


Fig. 3 Arrangements of the flow pipes

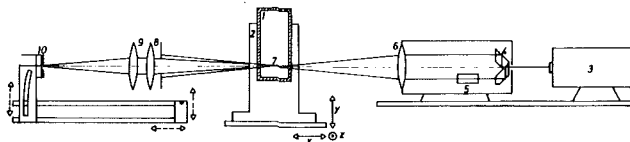


Fig. 4 LDA system: (1) model of the compact manifold junction; (2) plexi walls; (3) laser; (4) beam splitter; (5) Bragg cell; (6) focusing lens; (7) LDA measuring volume; (8) receiving lens; (9) focusing lens; (10) photomultiplier

(separating flow). For joining flow (configuration A) the total mass flow is going through branch 2 ( $m_T = m_2 = m_1 + m_3$ ). For separating flow (configuration B) the total mass flow is going through branch 1 ( $m_T = m_1 = m_2 + m_3$ ). The measurements are taken at a constant total mass flow through the junction (presented by the Mach number  $M_T$  of the common branch), but at different mass flow ratios in different branches ( $m_i/m_T$ ).

Figure 3 shows the test setup for separating flow. The junction is placed at the suction side of a rotary compressor. Valve  $R_T$  regulates the total mass flow; valves  $R_2$  and  $R_3$  regulate the mass flow ratios in branches 2 and 3. Flow meter  $F_1$  is used as a check of the measurements by the diaphragm type flow meters  $F_2$  and  $F_3$ . For joining flow a similar setup is realized.

**LDA System.** The LDA setup is a dual beam system operating in forward-scatter mode. The characteristics of the LDA system are given in Table 1.

The counter is connected to a data acquisition system for subsequent data processing. Seeding of the flow is obtained by atomization of oil at the entrance of the pipes.

The setup of the LDA is shown in Fig. 4. The transparent

Table 1 LDA system characteristics

He-Ne laser	power 12 mW
Beam splitter	beam separation 50 mm
Bragg cell	frequency shift 40 MHz
Focusing lens	beam intersection angle 11 deg
Photomultiplier	pinhole 0.2 mm quantum efficiency 13 percent
Signal processor	counter type maximum frequency 100 MHz resolution 2 ns
Measuring volume	$1.7 \times 0.17 \times 0.17 \text{ mm}^3$

walls of the junction allow velocity measurements in each point within the model. To reach the different positions, the table whereon the model of the junction is fixed allows translations in three orthogonal directions (accuracy 0.1 mm). The laser (with beam splitter, frequency shift, and focusing lens) is mounted on a solid table. The photomultiplier and receiving optics can be adjusted to obtain the correct alignment. The relative position of the junction to the LDA is corrected for refraction by the plexi walls.

**Data Acquisition System.** A counter type signal processor gives a discrete sample of the velocity each time a particle crosses the beam intersection area. Therefore a statistical evaluation of the data is necessary. One measurement consists of a series of  $n$  individual samples. All statistical information of the measurement is contained in a probability-density distribution  $\phi(v)$ .

By definition  $\phi(v)dv$  gives the probability to obtain a velocity value within the range  $(v, v + dv)$ .

A first approximation of the probability-density distribution can be obtained by dividing the velocity range into small classes and reconstructing a histogram which gives the relative number of samples for each class (Fig. 5). To store this statistical information, the moments of the probability-density distribution are calculated:

- first-order moment

$$m_1 = \frac{1}{n} \sum v_i$$

- second-order moment

$$m_2 = \frac{1}{n} \sum v_i^2$$

- third-order moment

$$m_3 = \frac{1}{n} \sum v_i^3$$

- fourth-order moment

$$m_4 = \frac{1}{n} \sum v_i^4$$

With these four values one can calculate:

- the mean value  $\mu = m_1$
- the standard deviation  $\sigma = (m_2 - m_1^2)^{1/2}$
- the skewness  $s = (m_3 - 3m_1 m_2 + 2m_1^3)/\sigma^3$
- the flatness  $c = (m_4 - 4m_1 m_3 + 6m_1^2 m_2 - 3m_1^4)/\sigma^4$

To reconstruct the velocity profiles,  $\mu$  is used as a measure for the mean velocity  $v$  and the standard deviation  $\sigma$  is used as a measure for the turbulent fluctuation  $d$ . By taking only  $\mu$  and  $\sigma$  into account, the probability-density distribution is approached by the best-fitting normal distribution (Fig. 5).

All the information extracted from one measurement is shown in Fig. 5. Besides the "useful" information about mean velocity  $\mu$  and turbulence  $\sigma$ , the shape of the distribution ( $s$ ,  $c$ , and the histogram) is also taken into account. For a normal

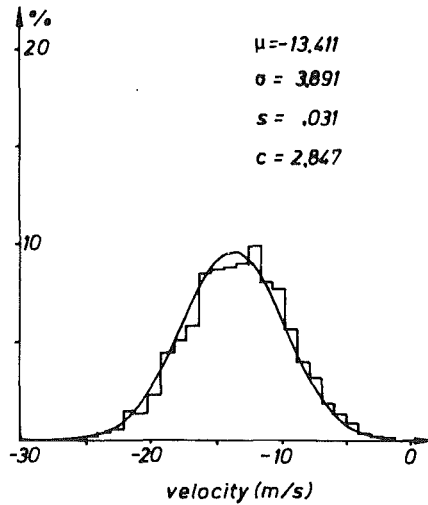


Fig. 5 Histogram (probability-density distribution)

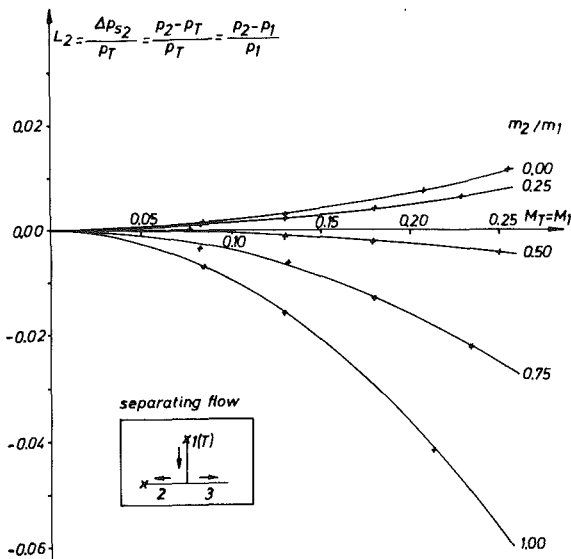


Fig. 6 Pressure loss coefficients as a function of the total mass flow ( $M_T = M_1$ )

distribution the skewness  $s$  should be equal to zero, and the flatness  $c$  equal to three. This results in a better control of the experiments and an improved accuracy of the tests.

Reference [9] gives a detailed error analysis of the LDA system, which is briefly repeated in [10, 11].

The most important error sources are the beam crossing angle uncertainty and the statistical uncertainty due to the turbulence and the limited number of samples. For a series of 1500 individual samples and a 20 percent turbulence intensity, a 2 percent error for the mean velocity and a 3.7 percent for the standard deviation are obtained.

The influences of the probe dimensions and the velocity gradients are negligible on the mean value and are below the statistical uncertainty for the standard deviation.

## Experimental Results

**Pressure Loss Coefficients.** The static pressure losses  $\Delta p_{s,i}$  across the junction are measured for the two basic flow configurations and for different total mass flow rates ( $M_T$ ) and different mass flow ratios ( $m_i/m_T$ ). The total mass flow rate is presented by the Mach number  $M_T$  of the common branch ( $x$

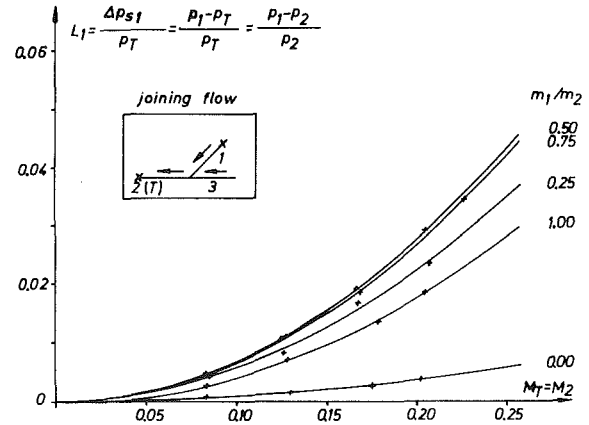


Fig. 7 Pressure loss coefficient as a function of the total mass flow ( $M_T = M_2$ )

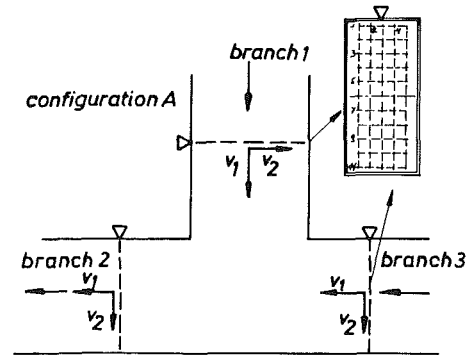


Fig. 8 Velocity components

axis of Figs. 6 and 7). From these the pressure loss coefficients  $L_i$  and resistance coefficients  $K_i$  are calculated.

As an example, the pressure loss coefficient  $L_2$  for separating flow of the 90 deg junction is given in Fig. 6 and the pressure loss coefficient  $L_1$  for joining flow of the 45 deg junction in Fig. 7. The results ( $\Delta p_{s,i}$ ,  $L_i$ , and  $K_i$  values) for all flow situations are presented in [12].

Looking at Figs. 6 and 7, of course the pressure losses (in absolute terms) increase by increasing Mach number  $M_T$  (total mass flow). To analyze the relative positions of the curves against each other, one has to keep in mind that only static pressure readings were taken. The smaller the mass flow rate through a particular branch, the more the static pressure will approach the total pressure. For example, in Fig. 6 by separating flow, when there is no flow in branch 2 ( $m_2/m_1 = 0$ ), the pressure reading 2 is a total pressure, and  $L_2$  can be positive. By increasing mass flow rate through branch 2 (limit  $m_2/m_1 = 1$ ), of course the static pressure in branch 2 has to be lower than in branch 1 ( $L_2$  negative).

Again for joining flow for the 45 deg junction (Fig. 7), to verify the relative position of the different curves, total pressures and pressure losses have to be considered, especially the influence of the mass flow rate in branch 3 on the flow behavior. The pressure in branch 1 has to be greater than in branch 2 ( $L_1$  always positive).

For the same joining flow configuration as in Fig. 7 but for the 90 deg junction (which is not presented in the paper) the pressure losses are always greater than for the 45 deg junction. As could be expected the 90 deg junction is not favorable for a streamlined flow situation. This can also be seen in Figs. 6 and 7 for the conditions where there is no flow in branch 3

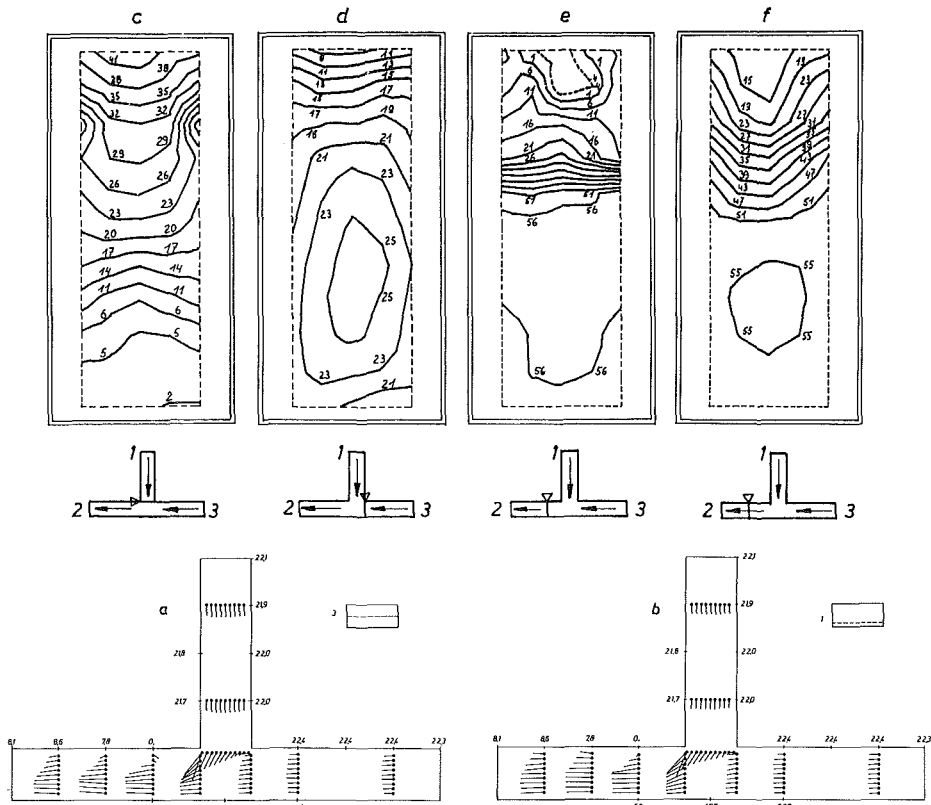


Fig. 9 Two-dimensional flow pattern (a, b) and axial velocity profiles (c, d, e, f);  $m_1/m_2 = 0.50$ ;  $m_T = 0.063$  kg/s;  $M_T = 0.122$ ;  $p_a = 0.997$  bar;  $\Delta p = 35.7$  mbar;  $-40$  m/s

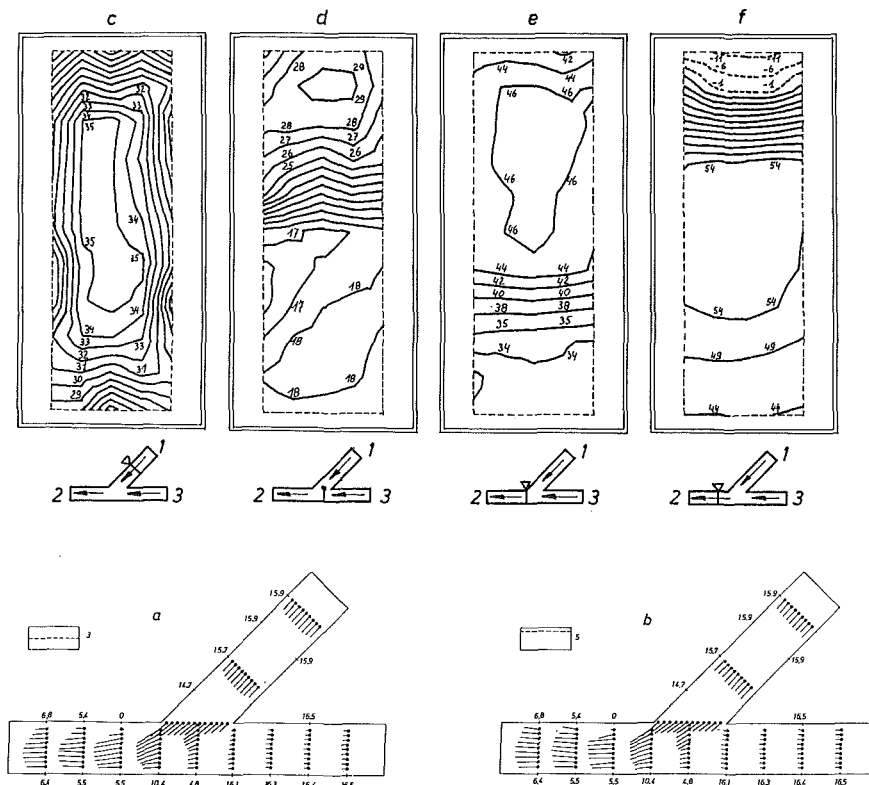


Fig. 10 Two-dimensional flow pattern (a, b) and axial velocity profiles (c, d, e, f);  $m_1/m_2 = 0.75$ ;  $m_T = 0.063$  kg/s;  $M_T = 0.122$ ;  $p_a = 0.988$  bar;  $p = 43.8$  mbar;  $-40$  m/s

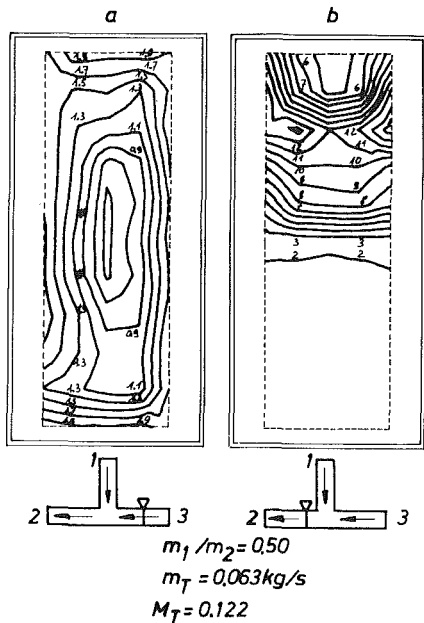


Fig. 11 Axial turbulence

( $m_2/m_1 = m_1/m_2 = 1$ ): The absolute value of the pressure loss coefficient for the 90 deg junction (at  $M_T = 0.25$ ) is about 0.06, where the pressure loss coefficient for the 45 deg junction is approximate 0.03.

The obtained results are similar to previous studies; for example see [5] for comparison with the 90 deg junction and [1] for comparison with the 45 deg junction. In [1] an ideal pulse converter with ejector nozzle and diffuser sections is tested. A general similarity is seen in both results; the differences are due to the shape of the cross-sectional areas and the inclination of the branches. The ejector and diffuser sections are responsible for a difference in the succession of the curves (as a function of the mass ratio).

**Presentation of the Flow Pattern.** The velocity measurements are carried out in planes perpendicular to the symmetry axis of each branch. Each plane is divided in 55 ( $5 \times 11$  grid) mesh points ( $\Delta X = 5$  mm,  $\Delta Y = 4$  mm) and in each mesh point two velocity components are measured (Fig. 8) with:  $v_1$  = axial velocity component; perpendicular to the measurement plane and positive in the direction of the general flow;  $v_2$  = velocity component perpendicular to  $v_1$  and parallel to the plexi walls.

Due to the construction and the geometry of the model, the flow pattern is merely two-dimensional, so the third component is neglected.

The experimental results are presented as follows:

**1 Axial velocity profiles (Figs. 9 and 10c, d, e, and f).** For a chosen plane and from interpolation of the axial velocity components ( $v_1$ ) in each of the 55 mesh points lines of equal velocity are drawn. On the figures the position of the measuring plane is indicated (small figure), the orientation of the planes follows the indication in Fig. 8(∇). Full lines represent positive flow (direction of the general flow), dotted lines backflow. The mass flow ratio, total mass flow rate, and Mach number (in the common branch) are also mentioned.

On the figures the outer rectangle (double line) presents the contour of the measurement plane. Because no measurements were possible close to the walls the inner rectangle (dotted line) presents the section of the measurements.

**2 Axial turbulence profiles (Fig. 11).** The axial turbulence is derived from the standard deviation of the prob-

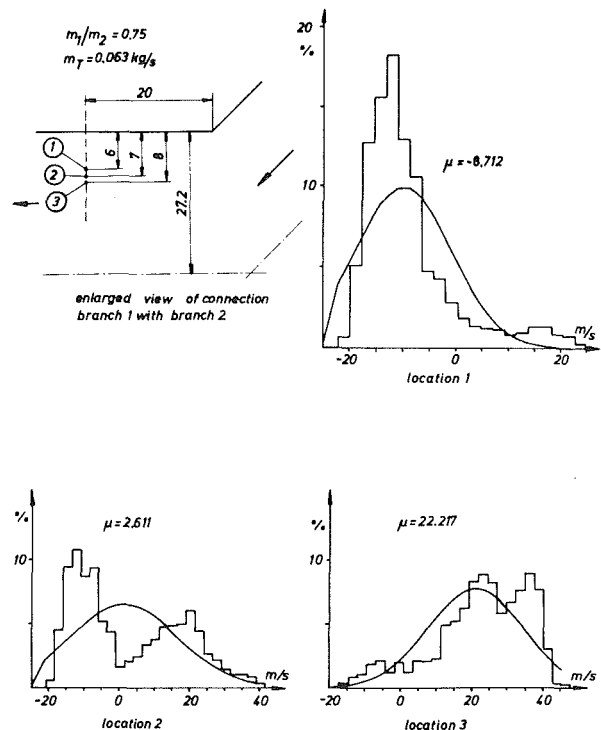


Fig. 12 Histograms at boundary of main and backflow

ability-density distribution function and is presented in the same way as for the axial velocity profiles.

**3 Two-dimensional flow pattern (Figs. 9 and 10a, b).** Adding the two mean velocity components  $v_1$  and  $v_2$ , a two-dimensional flow pattern can be obtained in a longitudinal plane of the junction.

On the figures the point of measurement is indicated by a dot, the length of the line is proportional to the velocity. The position of the longitudinal plane is mentioned as well. On the figures the static pressure reading at each of the pressure locations is given. These numbers (in mbar) are relative to a reference pressure (position of the lowest pressure is set equal to 0). The value of the reference pressure is given as the pressure ( $\Delta p$  in mbar) below the atmospheric pressure ( $p_{atm}$  in bar).

**Velocity Measurements.** The velocity measurements (LDA results) are taken for the two junctions for joining and separating flow and for two mass flow ratios ( $m_i/m_T = 0.50$  and  $m_i/m_T = 0.75$ ) at a constant total mass flow rate ( $m_T = 0.063$  kg/s).

Again these results are given in detail in [12, 13]. Two particular flow situations are presented hereafter. Each time four axial velocity profiles (out of 10 or 12) and two longitudinal flow patterns (out of five) are shown.

In Fig. 9 (90 deg junction) joining flow is represented for a mass flow ratio of 0.5. Figure 10 (45 deg junction) represents the joining flow situation at a mass flow ratio of 0.75. Joining flow is the normal flow condition in the junction.

When we compare Figs. 9(a) with 9(b) and 10(a) with 10(b), nearly no differences are found in the flow pattern of two longitudinal planes. This confirms that the objective to create a two-dimensional flow pattern is fulfilled.

The axial velocity profiles show:

- for the flow configuration of Figs. 9 the flow is regular and symmetric in branches 1 and 3. At the end plane of these branches the influence of the other branch is clearly visible. In Fig. 9(c) in the top part of channel 1, the velocity is increased



(connection area of branches 1 and 2); in the bottom part the velocity is drastically reduced (connection area of branches 1 and 3). For branch 2 (Fig. 9d) the velocity is decreased in the top part (connection area of branches 1 and 3). This results in a higher velocity in the bottom part of the entrance plane of branch 2, a situation which is going on further down branch 2 (Fig. 9e). At that moment backflow can occur in the top part of the section (Fig. 9e). At the end of branch 2 the higher velocities in the bottom half of the branch still exist; the backflow region has disappeared (Fig. 9f)

- for the flow configuration of Figs. 10 again the flow is regular and symmetric in branches 1 and 3. For example see the section of Fig. 10(c). In this situation, due to the direction of the inclined branch (branch 1) and also due to the higher mass ratio of branch 1, a higher velocity is detected at the connection of the branches (Figs. 10d and 10e). But even in this case backflow is detected in the top part of branch 2, just away from the connection area (Fig. 10f). This region of backflow, on the top part in the beginning of branch 2, is clearly seen in the longitudinal profiles. The region of backflow takes a much greater area for branch 2 of the 90 deg junction than of the 45 deg junction (comparing Fig. 9a and 10a).

In this region the axial turbulence velocity increases significantly. For example in branch 3 an axial turbulence velocity level of 0.9 to 1.9 m/s is measured (Fig. 11a). In branch 2 the turbulence level increases to 13 m/s at the boundary of main and backflow (Fig. 11b).

Looking more in detail at the measurements in this boundary, even under stationary state conditions, a periodic fluctuation can be observed. Figure 12 gives an enlarged view of the connection area of branch 1 with branch 2. The histograms at three different locations are shown, 20 mm downstream of the corner of the branches. The mean value of the velocity is negative at location 1, and positive at location 3. At location 2 the histogram shows two distinct peaks; neither the mean value of the velocity nor the standard deviation have any meaning. At location 2, within the size of the LDA measuring volume, positive and negative flow have been measured. It is clear that location 1 is situated in the backflow region, location 3 in the mainflow region, and that the results at location 2, just at the boundary of main and backflow, have to be interpreted with extreme care and cannot be used in the representation of the velocity profiles.

As a control on the laser measurements, the total mass flow through each section is calculated by integration of the measured axial velocities. These values are then compared with the measured mass flow (with flowmeters) in each branch. An error of less than 5 percent is obtained, proving the accuracy of the laser measurements.

## Conclusions

This paper describes the results of pressure and velocity

measurements on two theoretical compact manifold type junctions.

As far as the authors are aware, it is the first time that such detailed experiments have been carried out on compact manifold type junctions. The velocity measurements give a detailed and quantitative picture of the flow pattern in the junction for different flow configurations and different mass flow ratios.

Pressure measurements similar to previous investigations are used to calculate pressure loss coefficients. The pressure and velocity measurements are used to update a numerical algorithm for simulating the turbulent quasi-steady flow in these junctions. All these measurements are necessary for the development of compact manifold type junctions.

Finally, attention is drawn to the fact that at certain locations (boundary of main and back flow regions) the results have to be interpreted with extreme care.

## References

- 1 Benson, R. S., "The Application of Pulse Convertors to Automotive Four Stroke Cycle Engines," SAE Paper No. 770034, 1977.
- 2 Alexander, G. I., Nichols, J. R., Winterbone, D. E., and Sinha, S. K., "Optimization of the Design of an Exhaust Manifold System for Improved Turbocharger Performance," *J. Mech. Eng. C*, Vol. 48, 1982.
- 3 Dimitriadis, C., and Leschziner, M. A., "Computation of Three-Dimensional Flow in Duct Junctions by a Zonal Approach," *Proceedings 4th Int. Conference on Numerical Methods in Laminar and Turbulent Flow*, Swansea, July 1985, pp. 306-317.
- 4 Dimitriadis, C., Leschziner, M. A., Winterbone, D. E., Alexander, G. I., and Sierens, R., "Computation of Three-Dimensional Flow in Manifold Type Junctions," *ASME Third Int. Symposium on Flow and Flow Related Phenomena in Reciprocating Combustion Engines*, SED Vol. 28, Nov. 1985, pp. 57-62.
- 5 Benson, R. S., *The Thermodynamics and Gas Dynamics of Internal Combustion Engines*, Vol. I, Clarendon Press, 1982.
- 6 Shapiro, A. H., *The Dynamics and Thermodynamics of Compressible Fluid Flow*, Vol. II, The Ronald Press, 1954.
- 7 Benson, R. S., Garg, R. D., and Woolatt, D. A., "A Numerical Solution of Unsteady Flow Problems," *Int. J. Mech. Sci.*, Vol. 6, No. 1, 1964, pp. 117-144.
- 8 Baruah, P. C., "A Generalised Computer Program for Internal Combustion Engines Including Gas Exchange Systems," Ph.D. Thesis, University of Manchester, 1973.
- 9 Snauwaert, P., "Studie van de swirlbeweging bij directe injectie dieselmotoren door middel van Laser Doppler Anemometrie," Ph.D. Thesis, Rijksuniversiteit Gent, 1984.
- 10 Snauwaert, P., and Sierens, R., "Experimental Study of the Swirl Motion in Direct Injection Diesel Engines Under Steady-State Flow Conditions (by LDA)," SAE Paper No. 860026, 1986.
- 11 Snauwaert, P., and Sierens, R., "A Study of the Swirl Motion in Direct Injection Diesel Engines by Laser Doppler Anemometry," *Fisita Paper No. 865007*, 1986.
- 12 De Corte, D., and Deprez, M., "Studie van de stroming in een pulse convertor," *Eindejaarswerk Rijkuniversiteit Gent*, 1984.
- 13 Denecker, L., and Flamang, P., "Experimentele studie van de stroming in kompakt- en multipuls uitlaatsystemen van dieselmotoren," *Eindejaarswerk RUG*, 1985.

# An Analysis of the Engine Blowdown Process Using Multidimensional Computations

T. Uzkan

General Motors Corporation,  
Electro-Motive Division,  
La Grange, IL

*The details of the blowdown period were studied for the EMD-710 diesel engine by using a multidimensional computational code for in-cylinder flows. Computed results are presented describing both global and detailed features of the flow field during the blowdown period. Global features include variations of cylinder pressure, mass, angular momentum, turbulence kinetic energy, and the exhaust mass. A parametric analysis has shown that the percent pressure drop and the percent mass exhausted are almost invariable with the initial cylinder pressure or mass. Details of the mass convection process within the cylinder are investigated through development of the line separating the downward and upward flowing gas regions. The location and speed of propagation of this separation line are also found to be independent of initial cylinder pressure and mass. The results show that the speed of the separation line is about twice the piston speed for an initial period of 15 deg crank angle. Then it starts to decrease and becomes equal to the piston speed at about 26 deg after the exhaust valve opening. Beyond this time the separation line is slower than the piston speed.*

## Introduction

The period from the exhaust valve opening to the inlet port opening is called the blowdown period of reciprocating two-stroke I.C. engines. The timing for the beginning and the end of this period are important because they both affect the engine performance. On the one hand the beginning of blowdown is timed by the opening of the exhaust valve. If it starts early, possible performance gains due to further expansion of the combustion gases are lost. If it starts late, there may not be enough time to discharge the combustion gases through the exhaust valves before the fresh air enters the cylinder, leading to an increase in the cylinder residual gas and a possible increase in the power required for the gas exchange process. Moreover the increase in cylinder residual gases is known to decrease the volumetric and scavenging efficiencies, as well as the trapped air/fuel ratio. On the other hand, the end of the blowdown period is greatly influenced by the opening of the exhaust valves or ports. Early opening will cause increased backflow of chamber gases to the airbox due to the chamber pressure being higher than the airbox pressure. Late opening will not leave enough time to scavenge the combustion gases to the exhaust. These trends are all known to decrease engine efficiency.

Studies of the blowdown process are not new. There are several instructive papers and reviews available even in the classical I.C. engine textbooks [1, 2]. However, all of these studies treat the blowdown process from a global control

volume approach and do not give the details of the processes occurring in the cylinder. Benson and Whitehouse [2] give an analysis of an isentropic blowdown process as well as the maximum available energy to drive a turbine during a somewhat ideal blowdown period.

Recent advances in the multidimensional modeling techniques enables one to study the details of the in-cylinder processes [3, 4]. These methods have been used somewhat fruitfully for the study of complex processes, such as fluid motion [4-11], fuel spray development [12-14], heat transfer calculations [15, 16], ignition processes [17], and even the engine combustion process itself [18]. Although the blowdown process is a relatively simple process in comparison to these, multidimensional calculations were not applied to the study of the blowdown process itself. Using these techniques for the study of the blowdown process one may expect to gain further understanding of the physical details and hope to develop practical correlations linking the valve and port timing events to these details for possible engine improvements. Such a study is reported here.

## Model Assumptions

The objective of this work is to study the details of the blowdown process, in general, and to investigate the details of the flow processes within the cylinder of the EMD 710 engine in particular. Essential features of this engine are available in [19]. It is a 16-cylinder medium speed, two-stroke, uniflow scavenging type diesel engine. Simulation of the blowdown process of this engine at the full load and speed operation condition is the main application considered in this paper. The initial thermodynamic states of the working fluid at the begin-

Contributed by the Internal Combustion Engine Division and presented at the Energy-Sources Technology Conference and Exhibition, Dallas, Texas, February 15-20, 1987. Manuscript received at ASME Headquarters December 1, 1986. Paper No. 87-ICE-17.

ning of the blowdown period (exhaust valve opening), in the airbox, exhaust manifold, and in the cylinder are predicted through a two-zone, engine system simulation model as outlined in [8]. They are given below for the reference case.

Intake manifold pressure	261.04 kPa
Exhaust manifold pressure	239.04 kPa
Intake manifold temperature	379.0 K
Initial cylinder pressure	898.4 kPa
Initial cylinder temperature	1198.9 K

Major features of the engine and the operation conditions considered are as follows:

Bore	0.2302 m
Stroke	0.2794 m
Con. Rod L	0.5842 m
Engine speed	900 rpm

The analysis is performed by using the CONCHAS-SPRAY code as modified by El-Tahry [4] for k-E turbulence model and previously used by Diwakar [5], Uzkan [6], Plee [7], and others. The modeling of the flows by the inlet port and exhaust valves is done by Diwakar [5] and described in [5, 6, 8] in detail. In review, the valves are treated as an annular slot on the head. Valve opening process simulated through variation of the flow coefficients of this slot in a manner to account for the changes in the valve flow area and also its flow coefficient. Inlet ports are simulated as a circular opening on the liner with effective area controlled by the piston motion. The compressible flow equations with constant flow coefficients are used to calculate the flow rates to and from the cylinder. Backflow is not permitted at the exhaust valves. The details of the turbulence modeling and the boundary conditions are essentially the same as described in [5, 6, 8] and will not be elaborated further.

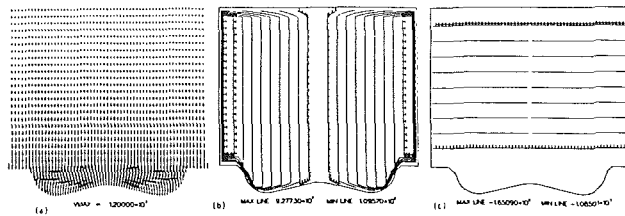


Fig. 1 Initial conditions at exhaust valve open: (a) velocity; (b) swirl; (c) vertical velocity

The details of the initial velocity field in the cylinder are assumed as follows, which can be seen on Fig. 1:

- Radial velocities: zero
- Axial velocities: axially downward, from the engine head toward the piston. Zero on the head, equal to the piston velocity on the piston and changing linearly in between.
- Swirl: Zero at the center and on the liner. Triangular velocity profile in between.

To simulate the mixing process in the cylinder, the residual gases are assumed to have the composition of air and the fresh charge composition is assumed to be NO at the above-mentioned thermodynamic states as in [6]. The intake port angle is held constant at 20 deg, computations are started at the exhaust valve opening (256 deg BTDC) and continued to a little after the inlet port opening (225 deg BTDC). The available VAX-11 computer system together with the FPS-164 vector processor are utilized. The computational mesh size used is  $(31 \times 32)$  in the half plane.

In [6], the effects of the inlet port angle on the flow field within the cylinder are reported for several inlet port angles and from EVO to TDC. The case for 20 deg inlet port angle is studied further during the blowdown period and the results are presented in this paper. The trends beyond the crank angles covered here are available in [6].

## Results and Discussion

(A) **Global Features of the Flow Field.** The global features of the flow field during the blowdown period are given in (Figs. 2a-f) in terms of:

- Cylinder pressure
- Cumulative exhaust mass
- Total cylinder mass
- Total angular momentum
- Turbulence kinetic energy
- Turbulence of mean kinetic energy ratio as a function of crank angle covering a span from  $-256$  to  $-225$  deg CA. Three different cases are shown on these figures. First is the reference case. The second and third cases have 150 and 200 percent more initial air in the cylinder with initial pressures 1.365 and 1.821 MPa, respectively, while all other conditions remain the same. During the blowdown period the following changes in the cylinder properties are observable on Fig. 2.

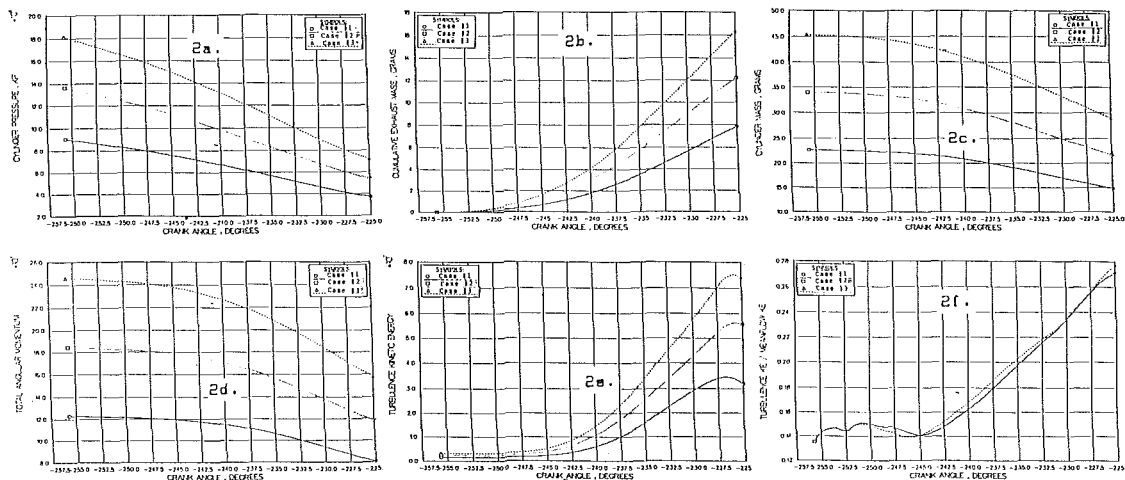


Fig. 2 Global properties of cylinder contents during blowdown: (a) cylinder pressure; (b) exhaust mass; (c) cylinder mass; (d) total angular momentum; (e) turbulence kinetic energy; (f) ratio of turbulence to mean kinetic energy

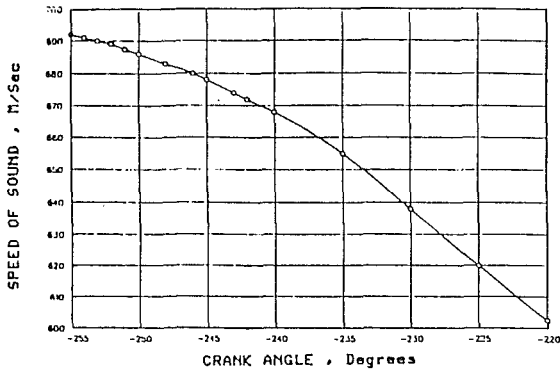


Fig. 3 Speed of sound versus engine crank angle

	Case 1	Case 2	Case 3
Cylinder pressure, MPa			
Initial	0.908	1.365	1.821
Final	0.369	0.538	0.718
Percent change	59.4	60.1	60.6
Cylinder mass, grams			
Initial	22.6	33.94	45.25
Final	14.78	21.70	28.93
Percent change	34.7	36.1	36.1

In Fig. 2(a) the slope of the pressure-crack angle curve is almost constant during the blowdown period and is about 0.0174 MPa/CA for the reference case 0.0277 for case 2 and 0.0356 for case 3. About 35 percent of the chamber gases are exhausted during this period and the chamber pressure dropped about 40 percent of the initial value.

In Fig. 2(b) the cumulative mass of gases going through the exhaust valves is shown. The slope of this curve increases at the beginning stays constant between  $-238$  and  $-223$  CA and then decreases after  $-223$  CA (not shown). The inlet ports open when the flowrate at the exhaust valve is almost maximum. The total angular momentum of cylinder contents (Fig. 2d) shows about 33 percent decrease in the angular momentum for all three cases. Comparing this to the perfect mass change in the cylinder (35 percent) indicates that a large portion of the angular momentum change is due to the loss of the cylinder mass rather than friction.

The turbulence kinetic energy curves (Fig. 2e) indicate a small increase in the turbulence level up to about  $-245$  CA but a large increase to a peak at about  $-228$  CA and then decreasing. Although the turbulence levels are different for the three cases, the ratio of the turbulence to mean kinetic energy is almost constant for all cases. Moreover the slope on this curve is almost constant with a value of about 0.007 per CA during  $-245$  to  $-225$  CA (Fig. 2f).

In comparing the three different cases presented on Fig. 2 the trends are very similar to each other, suggesting the presence of a similarity transformation to bring these curves together. Clearly the presence of such a similarity transformation enables one to reduce the results in terms of these similarity variables with application potential to a larger class of problems.

The effects of the valve opening on the blowdown processes are relatively small up to about  $-245$  CA. The increase in the exhaust mass, the decrease in the cylinder mass and momentum, and the turbulence production effectively starts about 10 CA after the valve opening. This is particularly observable in the plot of turbulence to mean kinetic energy ratio. One may identify this less important blowdown period as the "blowdown delay" period. Obviously the exhaust valve size, flow coefficient and its lift schedule are expected to influence this delay period. From the figure it is apparent that the ratio of turbulence to mean kinetic energy may be a good quantitative measure of this blowdown delay period because it is

approximately constant when blowdown is small, initially, and shows an abrupt increase when blowdown increases. With this definition the delay period is about 11 CA. This corresponds to a small exhaust flow in Fig. 2(b) (about 6 percent) but a large drop in cylinder pressure in Fig. 2(a) (15 percent).

**(B) Detailed Features of the Flow Field.** The details of the blowdown process are usually expressed in terms of the mass flow rate through the valves, and/or the time variation of the chamber pressure and its mass. Although these properties are important to quantify the blowdown process, they do not improve our basic understanding of the processes within the cylinder. Therefore, a physical model description that would improve our understanding as well as quantify the important details of the blowdown process would be very helpful. Such a model is described next before presenting results.

There are two essential physical factors affecting the flowfield during the blowdown period. First is the downward motion of the piston expanding the gases and generating a downward motion on the gases. Second is the pressure difference between the cylinder and the exhaust passages generating the outflow of gases and an upward motion on the fluid. Both of these factors are reducing the chamber pressure (so their effects are cumulative) but they have opposing effects on the flow velocity field. As the blowdown process develops, a portion of the fluid, from the downward flowing region, changes its flow direction and is convected to the upward flowing region. Development of this convection process is an essential part of the blowdown. One may identify the fluid region with upward velocity as the "valve-dominated region" (VDR) and the region with the downward velocity as the "piston-dominated region" (PDR). The "separation line" distinguishes these two regions clearly. The details of the fluid convection process in the cylinder can be observed by the motion of this separation line as a function of crank angle. This method will be used to study the blowdown process. When the inlet ports open, the pressure difference between the airbox and the cylinder becomes a third factor with major influence on the flowfield and the utility of this separation line (surface in three dimensions) concept becomes more complicated.

When the exhaust valve opens, the pressure difference between the cylinder and the exhaust manifold would generate a rarefaction wave traveling toward the piston in the cylinder at about the speed of sound. For the cylinder pressure and temperatures (of Case 1) this speed is estimated to be about 692 and 638 m/s at the beginning and at the end of the blowdown period (Fig. 3). Under the present conditions this rarefaction wave is estimated to travel from the engine head to the piston in about 0.67 deg CA. As the time step used in the calculations was about 0.06 CA, it is theoretically possible to identify the development of this wave with this code. However the strength of this wave was so low that we could not distinguish it from numerically generated pressure noise in the solution. As this pressure wave is not expected to play an important or even a significant role on the global blowdown process, more refined signal analysis methods are not utilized and the matter is not pursued further. On the other hand, these considerations have shown again that, for phenomenological modeling purposes and for one deg CA step size calculation intervals, the chamber pressure can be approximated reasonably well by assuming it constant throughout the combustion chamber, at least during the blowdown period.

The detailed features of the flowfield are shown in Figs. 4 and 5 in terms of the vertical velocity vector plots and the constant vertical velocity contour plots at selected crank angles. The velocity vector fields (radial and axial velocity components) are plotted for nine different crank angles during the blowdown period. At the beginning ( $-256$  CA) the gases in the cylinder are moving downward as shown in Fig. 1(a). When the valves open, the pressure difference between the

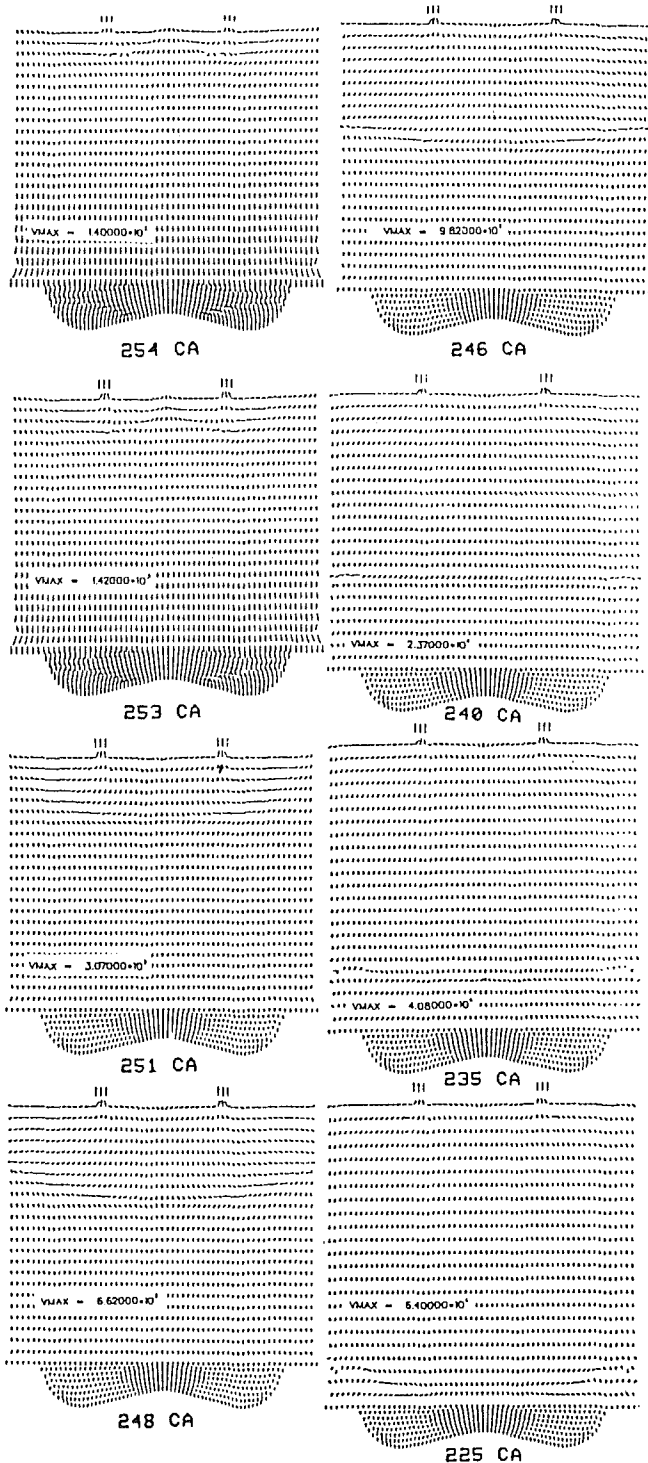


Fig. 4 Velocity vector plots at selected crank angles during blowdown period

chamber and the exhaust generates the flow through the valve. This creates a small domain around the valve with upward vertical velocity. This region develops into the cylinder by time. Its development can be observed in Fig. 4. In Fig. 5 the constant vertical velocity contours are shown at selected crank angles. On this figure the "maxline" (H) and "minline" (L) velocity values indicate the 90 and 10 percent of the difference between the maximum and minimum velocities with constant vertical velocity contours plotted at 10 percent increments. The values of vertical velocities are also given with positive direction indicating upward flows.

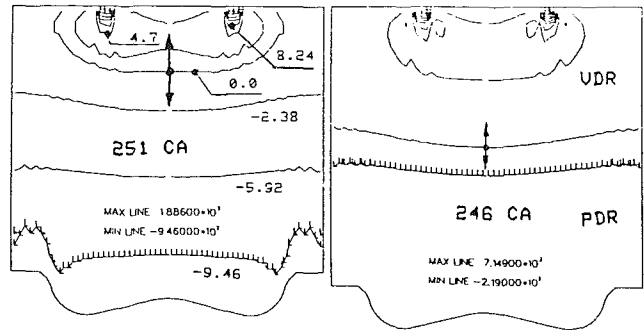


Fig. 5 Constant vertical velocity contours

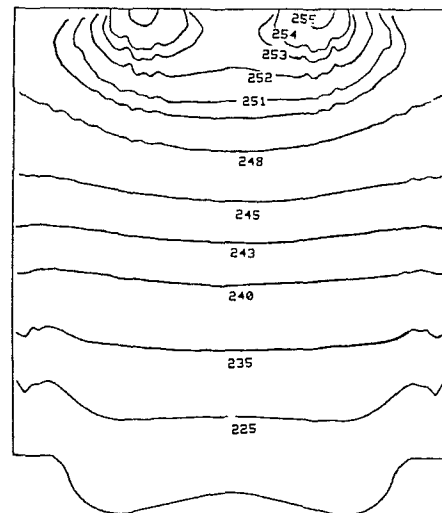


Fig. 6 Development of separation line during blowdown period

In Fig. 6 the position of only the separation line is considered and plotted at several selected crank angles. The piston position shown in Fig. 6 corresponds to that of  $-225$  CA but is not at this position for all these crank angles. This figure clearly shows the development of the separation line as a function of time. Two main points are observable on this plot. First, the valves are simulated as a slot on the head, the separation line develops around this slot like a pressure wave developing from the slot center. The presence of an actual valve is expected to modify this considerably. Second, from these plots it seems to be simpler to quantify the developing wave properties along a vertical line passing through the centerline of the slot rather than the line passing through any other vertical line.

The details of the blowdown can now be studied from Figs. 4, 5, and 6. At the exhaust valve opening a very small region is influenced (one on each valve or slot section). Up to  $-253$  CA these two sections stay separated but they combine and continue to grow together after  $-252$  CA. At about  $-249$  CA the outer portion of the separation line reaches the liner wall. Thereafter the separation line moves downward toward the piston like a spherical wavefront ( $-248$  CA). With further increase in crank angle the radius of curvature of this separation line increases ( $-245$  CA), leading to a somewhat straight form at about  $-240$  CA. Thereafter the wavefront seems to be under the influence of and begin to conform to the shape of the piston bowl rim with some boundary layer type influence near the liner walls ( $-235$  to  $-225$  CA). These trends continue until the opening of the inlet ports ( $-225$  CA). With the opening of the inlet ports the shape of the separation line changes and it moves somewhat upward with some modification in its shape due to inflow (not shown).

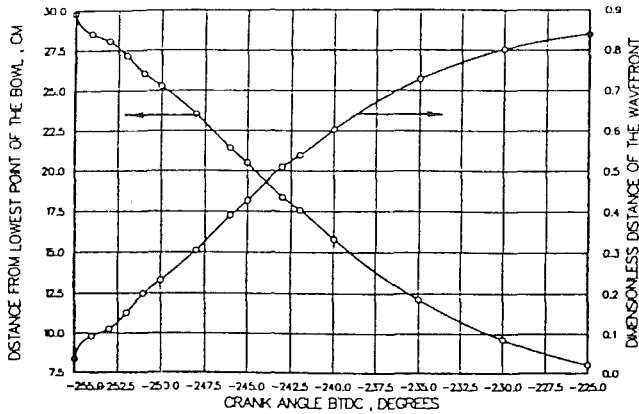


Fig. 7 Location of separation line as a function of crank angle

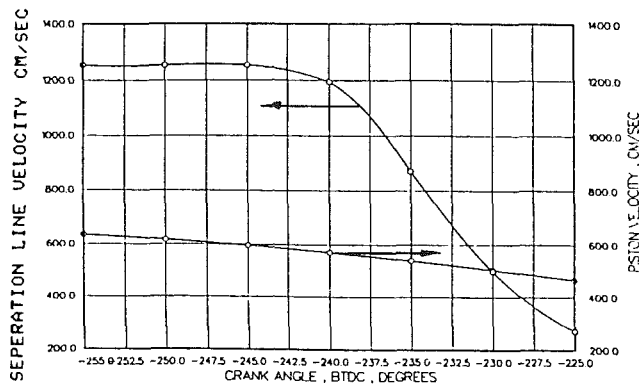


Fig. 8 Separation line and piston velocity during blowdown period

To quantify the development of this separation line in Fig. 7 the distance of the separation line from the lowest point of the bowl is shown as a function of crank angle. This figure indicates that the separation line approaches the bowl from a distance of about 30 cm at  $-255$  CA to about 7.9 cm at  $-225$  CA. The velocity of this wavefront is directly related to and can be considered as a measure of the strength of the blowdown process. In Fig. 8 the instantaneous wavefront velocity and the piston velocity are given during the blowdown period. This curve shows that the separation line velocity is almost constant initially, up to  $-243$  CA, decreases almost linearly up to  $-230$  CA, and then slows down. The piston velocity also decreases, almost linearly during the blowdown period, with a comparatively smaller slope throughout this time. It is also interesting that the separation line is faster than the piston before  $-230$  CA and slower thereafter. The implications of the location with piston velocity being equal to the separation line velocity requires some further study.

In Figs. 9(a, b) the ratios of the separation line convection velocity over the piston velocity, or the speed of sound, are given respectively. Figure 9(a) shows that the separation front velocity is about twice the piston speed initially, increases to a peak at about  $-240$  CA, and then start to decrease. At  $-230$  CA the piston and separation line velocities becomes equal and then decreases. Figure 9(b) shows that the separation line velocity is about 1.8 percent of the speed of sound at the beginning and about 0.4 percent at the end of the blowdown period.

The selection of a particular value of the vertical velocity contour to follow the development of the separation line from one crank angle to the next is somewhat arbitrary. For this purpose several alternative velocities at several locations are considered. In Fig. 10 the vertical velocity on a vertical line passing through the center of the slot center is shown (on the

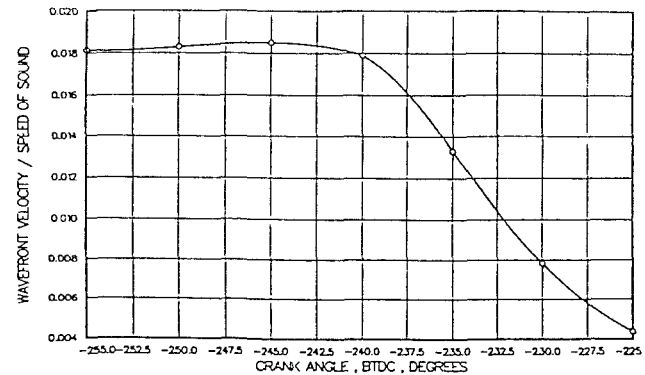
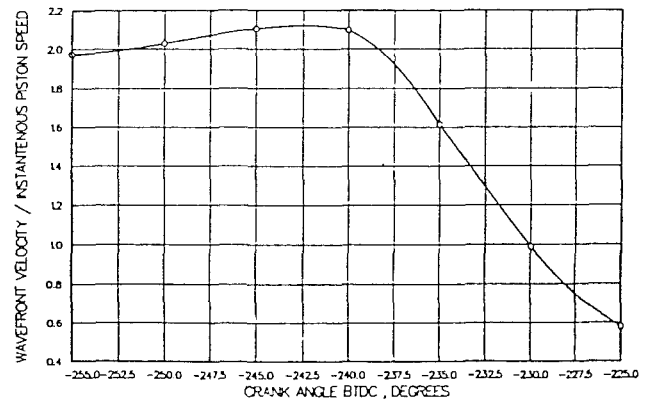


Fig. 9 Normalized separation line velocity: (a) by piston speed; (b) by speed of sound

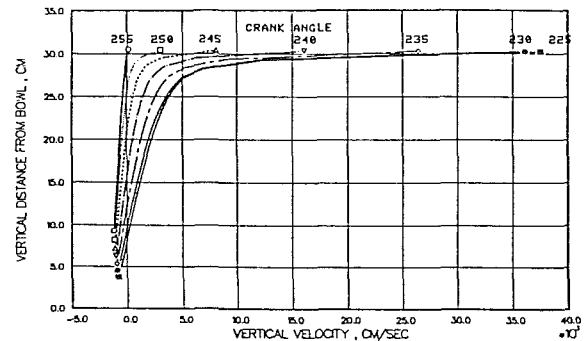


Fig. 10 Vertical velocity profiles at selected crank angles

abscissa) as a function of vertical distance (on the ordinate) for several crank angles. This curve shows that if one chooses to study a velocity contour (i.e., 5 cm/s) the variation is limited to a small region in the space (i.e., between 30 and 27 cm from the bowl). Choosing a velocity with a negative value has the same limitation. The figure shows that the zero velocity line gives a much larger development region.

The effects of the initial cylinder conditions on the details of the blowdown process are investigated and presented by comparing the solutions for cases 2 and 3. In Fig. 11(a) the position of the separation line (measured from the bottom of the piston bowl) is shown as a function of crank angle for both of these cases. Almost all of the calculated points coincide. A detailed comparative study of Fig. 11(a) and Fig. 7 also shows that both the location and the velocity of the separation line are independent of the initial cylinder pressure or density for the same temperature.

The gas masses in the cylinder having an upward (or downward) velocity are also calculated and given on Fig. 11(b) as a function of crank angle for cases 2 and 3. This figure shows that the gas mass with downward velocity (PDR

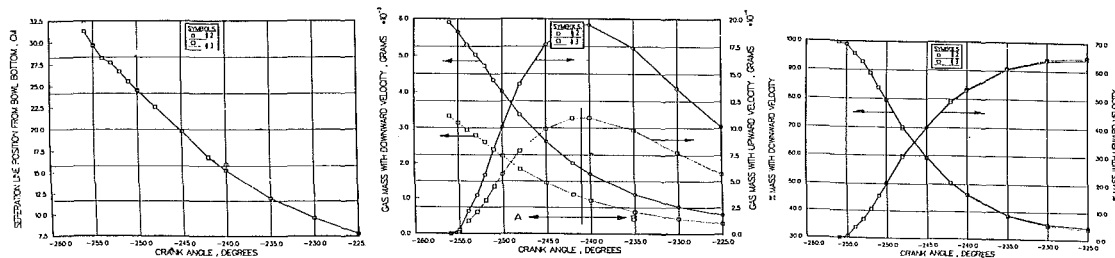


Fig. 11 Separation line position and masses of upward and downward flow regions

region) is decreasing continuously with crank angle. On the other hand, the gas mass with upward velocity (VDR region) starts from zero, increases to a peak at about  $-241$  CA (region A) then decreases from  $-241$  to  $-225$  (region B). In region A the increase in the mass means that the gas mass transferred from downward to upward velocity region is larger than the mass of the gas exhausted. For region B the reverse balance is true. This change in the mass balance and the location of the maximum point may be used to quantify some trends of the blowdown process.

The trends presented in Fig. 11(b) for cases 2 and 3 are very similar, although the cylinder masses are considerably different. In Fig. 11(c) the gas masses at PDR and VDR regions are plotted as a percentage of the instantaneous cylinder mass. This figure implies that the proper similarity variable to bring the trends together is the instantaneous cylinder mass.

**(C) Further Discussion on the Separation Line.** In a general physical sense, the development of the separation line toward the downward-moving velocity region may be considered as a property representing the convection of gas masses associated with the blowdown process. Generally speaking, any design or operational parameter variation that can increase its speed is expected to speed up the blowdown process and vice versa. In Fig. 11 it is shown that the location and the speed of the separation line are independent of the initial cylinder pressure or mass. The trends in Fig. 11(a, c) and best-fit correlations to these curves can be used to estimate the blowdown process details quickly during the design process. However these correlations should be treated as limited to the particular piston, cylinder, and valve arrangements they are calculated for, until their generality to other geometries are shown.

## Conclusions

An analysis of the blowdown processes for the EMD 710 engine, operating at maximum load and speed condition, is performed by using the CONCHAS-SPRAY code. The results are presented in several figures. Important conclusions are:

1 During the blowdown period the cylinder pressure drops about 40 percent while only 35 percent of the cylinder contents are exhausted.

2 The effects of the exhaust valve opening are not felt immediately. It takes some time to observe appreciable blowdown activity. The period between the opening of the exhaust valve and the observation of reasonable amount of outflow is named as the Blowdown Delay Period. It is easier to quantify this delay period from the turbulence to mean kinetic energy ratio plot.

3 Three instantaneous velocity scales are recognized as important during the blowdown period: the piston speed, the speed of sound, and the speed of mass convection within the cylinder. A physical model to describe the details of the processes in the cylinder is conceptualized. This model is based on the idea of separation line defined as the interface between up-

ward and downward-flowing gases in the cylinder. The motion of the separation line as a function of crank angle is given. It is shown that the separation line velocity is about twice the piston speed for about 16 deg CA, starts to decrease, and becomes equal to the piston speed in about 26 deg CA after the exhaust valve opening.

4 The location and the velocity of the separation line are found to be independent of the initial cylinder pressure and mass.

## References

- 1 Taylor, C. F., *The Internal Combustion Engine in Theory and Practice*, 2nd ed., MIT Press, Cambridge, MA, 1965.
- 2 Benson, R. S., and Whitehouse, N. D., *Internal Combustion Engines*, Pergamon Press, New York, 1979.
- 3 Cloutman, L. D., Dukowicz, J. K., Ramshaw, J. D., and Amsden, A. A., "Conchas-Spray: Computer Code for Reactive Flows With Fuel Sprays," Los Alamos National Lab Report LA-9294-MS, 1982.
- 4 El-Tahry, S. H., "A Numerical Study on the Effects of Fluid Motion at Inlet Valve Closure on Subsequent Fluid Motion in a Motored Engine," SAE Paper No. 820035, 1982.
- 5 Diwakar, R., "Multidimensional Modelling of the Gas Exchange Process in a Uniflow-Scavenged Two-Stroke Diesel Engine," *Third Int. Symposium on Flows in IC Engines*, FED-Vol. 28, ASME, New York, 19xx, pp. 107-115.
- 6 Uzman, T., and Hazelton, J. R., "The Influence of Swirl on the Fresh Charge Stratification in an IC Engine Combustion Chamber," SAE Paper No. 860466, 1986.
- 7 Plee, S. L., "A Computational Study of the Effects of Swirl Ratio, Squish Height and Bowl Geometry on the In-Cylinder Flow Field in Direct Injection Diesel Engine," *Third Int. Symposium on Flows in IC Engines*, FED-Vol. 28, ASME, New York, 19xx.
- 8 Uzman, T., Savage, T. J., and Hazelton, J. R., "The Effects of Piston Bowl Shape Modifications on the In-Cylinder Flow Characteristics of the EMD 710 Engine," ASME Paper No. 85-DGP-23, 1985.
- 9 Masatoshi, S., Masashi, S., and Shongo, T., "Effects of Combustion Chamber Configuration on In-Cylinder Air Motion of D.I. Diesel Engine," *Proc. Int. Symp. on Diagnostics and Modelling Combustion in Reciprocating Engines*, Tokyo, Japan, Sept. 4, 1985, p. 353.
- 10 Wakisaka, T., Shimamoto, Y., and Isshiki, Y., "Three Dimensional Numerical Analysis of In-Cylinder Flows in Reciprocating Engines," SAE Paper No. 860464, 1986.
- 11 Schapertons, H., and Thiele, F., "Three Dimensional Computations for Flowfields in DI Piston Bowls," SAE Paper No. 860463, 1986.
- 12 Bracco, F. V., "Modelling of Engine Sprays," SAE Paper No. 850394, 1985.
- 13 Watkins, A. P., Gosman, A. D., and Tabrizi, B. S., "Calculation of Three Dimensional Spray Motion in Engines," SAE Paper No. 860468, 1986.
- 14 Khaleghi, H., and Watkins, A. P., "Calculation of Three Dimensional Diesel Spray Into Curvilinear Piston Bowl and Comparison With Experiment," personal communication, May 1986.
- 15 Gosman, A. D., "Computer Modelling of Flow and Heat Transfer in Engines, Progress and Prospects," *Proc. Int. Symp. on Diagnostic and Modelling Combustion in Reciprocating Engines*, Tokyo, Japan, Sept. 4, 1985, p. 15.
- 16 Ikegami, M., Kidoguchi, Y., and Nishiwaki, K., "A Multidimensional Model Prediction of Heat Transfer in Non-fired Engines," SAE Paper No. 860467, 1986.
- 17 Theobald, M., and Cheng, W., "Study of the Diesel Ignition Processes Using Kiva Computer Program," personal communication, June 1986.
- 18 Bracco, F. V., "Modelling and Diagnostics of Combustion in Spark Ignition Engines," *Proc. Int. Symp. on Diagnostics and Modelling Combustion in Reciprocating Engines*, Tokyo, Japan, Sept. 4, 1985, p. 1.
- 19 Kotlin, J. J., Dunteman, N. R., Chen, J., and Heilenbach, J. W., "The General Motors EMD Model 710 Series Turbocharged Two-Stroke Cycle Diesel Engine," ASME Paper No. 85-DGP-22, 1985.

# Continued Development of a Coal/Water Slurry-Fired Slow-Speed Diesel Engine: a Review of Recent Test Results

S. E. Nydick

Thermo Electron Corporation,  
Waltham, MA

F. Porchet

H. A. Steiger

Sulzer Brothers Limited,  
Winterthur, Switzerland

*The results of tests performed on a slow-speed, two-stroke single-cylinder diesel engine show that thermal efficiency is approximately the same when fired with coal/water slurry fuels and diesel oil and that exhaust pollutant emissions, most notably  $NO_x$ , are lower with the coal/water slurry fuels. Engine wear, particularly at the piston ring/cylinder liner interface, is considerably greater than that which occurs with liquid fuels. However, it is concluded that by means of technological advances regarding piston ring/cylinder liner materials, new designs, and new concepts in lubrication, a reliable and economical coal/water slurry-fired slow-speed engine can be developed.*

## Introduction and Summary

This paper is a report on the continuation of an overall program to develop a high-efficiency industrial power system based on the use of coal-based fuels in a large, slow-speed (120 rpm), two-stroke crosshead type diesel engine. In the previous program, beginning in 1978, synthetic liquids (SCR II and COED) and coal/oil mixtures (containing 32 percent coal) were fired in a single-cylinder test engine, which had a power output of 1471 kW. These tests were performed at the Sulzer Brothers Ltd. test facility in Winterthur, Switzerland, and were done under contract to the Department of Energy, with very encouraging results. Engine efficiencies obtained with the three fuels came very close to those obtained with No. 2 fuel oil. Following these tests, a short engine run was performed at part load with a coal/water slurry containing 34 percent coal. The results of both the DOE sponsored program on synthetic coal liquids and coal/oil slurries and the additional testing on coal/water slurries were presented and discussed previously [1].

The next phase of the program, which is the subject of this paper, was initiated in Oct. 1982. This phase was concerned with coal/water slurries that contained beneficiated and micronized coal, in order to develop an industrial power system utilizing the lowest cost, coal-based fuel. The primary objective of this phase of the overall program was to demonstrate the feasibility of coal/water slurry combustion in slow-speed, two-stroke diesels. This included exhibiting economic power conversion efficiencies and power outputs, divulging engine and fuel related problems, and determining a range of slurry fuel specifications that would be technically and economically acceptable.

Contributed by the Internal Combustion Engine Division and presented at the Energy-Sources Technology Conference and Exhibition, Dallas, Texas, February 15-20, 1987. Manuscript received at ASME Headquarters November 24, 1986. Paper No. 87-ICE-10.

It was also decided to maximize the coal content of the slurry and use developing technologies to produce a de-ashed micronized coal product in order to minimize engine wear. After an extensive coal/water slurry technology evaluation program, four slurry formulations from three different sources were selected for engine testing. These slurry formulations had coal contents in the 46.5 to 53 percent range, with coal containing 0.5 to 1.10 percent ash, and having 5 to 16  $\mu\text{m}$  average particle size and 15 to 50  $\mu\text{m}$  top size. The coal content was limited to about 50 percent in order to obtain a rheologically acceptable micronized slurry. Our thermodynamic analysis showed that the power conversion efficiency is relatively insensitive to water content below approximately 60 percent water, and that coal particles of less than 30 to 60  $\mu\text{m}$  (top size) could be combusted within the allowable time duration in the slow-speed engine. Thus, it was decided that 46 to 50 percent coal was an acceptable range, although higher coal contents are obviously preferable.

Approximately 50 h of engine running time has been accumulated on the single-cylinder test engine utilizing the four selected coal/water slurry fuels at a variety of loads from 25 to 90 percent. The proprietary accumulator slurry injection system [1] has worked extremely well. Engine stability has been excellent, and cycle-to-cycle variations of engine parameters such as cylinder pressure have been about the same or less than those encountered with No. 2 fuel in the same engine, even with an unusually low quantity of pilot fuel amounting to approximately 1 percent of total fuel heating value for tests at 90 percent load. Initial hypotheses that the ignition process is governed by flame kernel ignition rather than by cycle temperature at ignition, and that engine parameters optimized for one slurry are valid for the other slurries, have been verified. Engine efficiencies for the four slurries were comparable to those obtained with No. 2 fuel oil, validating



**Table 1 Properties of slurries in single-cylinder tests (as tested in single-cylinder engine)**

Coal source	OTISCA	Resource	AMAX "F"	AMAX "C"
	E. Kentucky bituminous	Wentz Mine Wise County, Virginia	Indiana No. 7	Indiana No. 7
Coal (percent, dry)	48	46.5-48.5	50.1	54.2
Moisture (percent)	49.5	50.0-52.0	48.2	43.6
Additives (percent)	2.5	1.5	1.7	2.2
Particle size				
• 98 percent less than ( $\mu\text{m}$ )	19.5	14.5	32	47
• Average ( $\mu\text{m}$ )	6.9	4.8	10.2	16.3
Ash content (percent, dry)	0.65	0.78-1.1	0.53	0.52-0.60
Al <sub>2</sub> O <sub>3</sub> in ash (percent)	23.2	10.8	12.5	10.1
SiO <sub>2</sub> in ash (percent)	16.0	36.9	36.6	50.9
Sulfur (percent, dry)	0.74	0.84	0.78	0.98
Volatile matter (percent, dry)	41.2	38.0	38.2	40.5
Lower heating value, dry coal (Btu/lb)	13,500-13,860	14,236	13,900	13,900
Lower heating value, slurry (Btu/lb)	6350-6514	6200-6500	6500-6750	7300

our thermodynamic analysis that at 50 percent water content there is little loss in efficiency. There is little, if any, loss in efficiency compared to operation with diesel fuel oil because the amount of slurry water is still small and combustion efficiencies are comparable. The slurry engine can be thought of as a composite of two engines, one operating on diesel fuel with combustion gases as the working fluid, and the other deriving its heat from the combustion gases with water as the working fluid. Calculations indicate that the engine using water, for the range of water contents tested, has almost the same efficiency as the diesel fuel engine, resulting in an identical efficiency for the composite engine (i.e., slurry engine). In addition, work recently completed (but not reported on in the text of this paper) on obtaining definitive heat release diagrams indicates the combustion efficiency with diesel and slurry fuels to be comparable. The variation in the water content of the slurries tested, however, was not sufficient to demonstrate, experimentally, the expected decrease in efficiency above a water content of 60 percent. There appears to be a slight loss in efficiency with increasing coal particle size (above  $\sim 6 \mu\text{m}$ ).

NO<sub>x</sub>, HC, CO, and particulate emissions were measured as a function of load. These measurements show that NO<sub>x</sub> reductions, as compared to operation with No. 2 fuel oil, were about 50 percent or greater at all loads, and that there were significant additional reductions in the other gaseous emissions. The particulate emission measurements showed that virtually all the coal had combusted, leaving only ash in the gaseous exhaust stream.

Wear measurements were performed on the cylinder liner and piston rings after testing with the four slurry fuels. The cylinder liner and piston rings were both of conventional design and were made of a gray cast iron material utilized in Sulzer RND engines. Mineral oil (SAE 40) was used for cylinder lubrication. Cylinder liner wear for the four slurries was an average of 22 times greater, and piston ring wear 90 times greater, than would be expected if diesel fuel had been used.<sup>1</sup> However, it is expected that further developmental work and technological advances on piston ring and cylinder liner materials, as well as new piston ring designs and improved lubrication techniques, will enable successful commercial operation of the engine.

This program has demonstrated that the slow-speed two-stroke marine-type diesel is the ideal engine to be adapted for direct coal firing because of its inherent design advantages, such as complete freedom from crankcase contamination, low speed, and large bore.

<sup>1</sup>The range for cylinder liner wear was 13 to 42 and for top piston ring wear 56 to 160 times the wear expected with diesel fuel for operation with the coal/water slurry fuels.

### Selection of Coal/Water Slurries

Four coal/water slurries were selected for testing in the single-cylinder engine after approximately 15 different slurry samples from seven manufacturers were carefully evaluated.

Of particular importance in the specification of the coal/water slurry were: a minimum coal content of 50 percent, an ash content below 1 percent, pseudoplastic rheology at high shear rates, compatibility with No. 2 fuel oil, and stability and ease of remixing. A low ash content with a minimum amount of abrasives, such as silica and alumina, is necessary to minimize engine wear. Pseudoplastic rheology at high fluid shear rate is required to ensure that the slurry spray pattern from the high-pressure, accumulator-type injection system is optimal. Compatibility with No. 2 fuel oil is required because diesel engines need to be started and stopped on No. 2 fuel oil, a condition that results in a temporary slurry/fuel oil interface in the fuel delivery system. Storage stability was desired, particularly for these tests, because the slurry was shipped in 55-gal drums requiring remixing prior to testing in the single-cylinder test engine.

Coal ash content is dependent on the coal type and method of beneficiation. Slurry rheology, oil compatibility, and storage stability are primarily dependent on the water content and, to a lesser extent, on the size consist, particle size and distribution pattern, and the type of coal. The use of surfactants and other types of additives can dramatically alter the properties of the slurry resulting, for example, in a pseudoplastic and easily remixed slurry with a higher coal content. Typically, multimodal particle size distributions are utilized in larger diameter boiler-grade slurries to provide pseudoplasticity and storage stability. However, for micronized slurries, it is difficult to grind coal with even a bimodal distribution. It is also easier to disperse a larger size particle consist in a slurry that contains higher coal contents than in micronized slurries. Thus, boiler-grade slurries typically have particle size consists which are 85 percent passing 200 mesh (76  $\mu\text{m}$ ) and contain up to 70 percent coal, whereas a micronized coal with a 30  $\mu\text{m}$  top size can be loaded to a maximum of perhaps 50 percent coal.

Table 1 compares the properties of the four coal/water slurries tested. Table 1 shows that all four slurries met or exceeded all but the coal fraction specifications. The latter condition allowed engine tests to be performed with all slurries to a maximum of 90 percent load rather than the intended 100 percent. The Resource slurry had the smallest size consist, and the AMAX slurries had the largest. Thus, it was possible to load the AMAX "C" slurry with the highest coal content, whereas the Resource slurry with the smallest size consist had the lowest coal loading. When the Resource coal (used in the

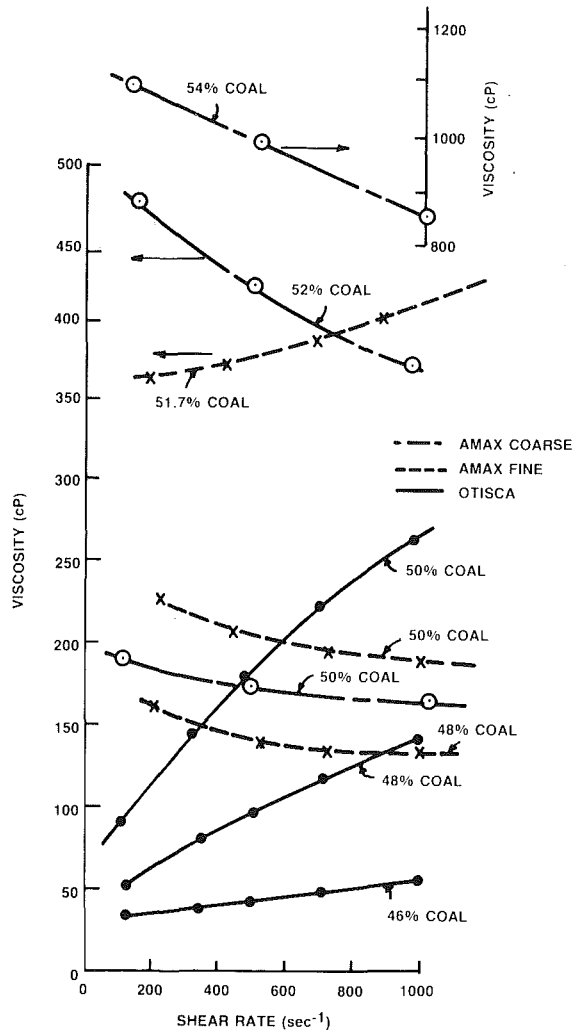


Fig. 1 Rheology of Otisca and AMAX coal/water slurries

single-cylinder test engine fuel system loop) was sampled, it was found to have a higher ash content than the other coals. The ash content of the Resource slurry was 0.40 to 0.69 percent upon analysis prior to shipment to Switzerland. Ash content doubled prior to use in the engine, either due to product inconsistency resulting from poor quality control, or in transit, handling, or during pumping. The volatile matter of all four slurries was also about equal and in the range of typical high volatile coals.

Figure 1 shows the effect of water content and shear rate on the slurry viscosity. From this figure, it is seen that the addition of a small amount of water and a larger particle size can change the absolute magnitude and the rheological characteristics (i.e., from dilatant to pseudoplastic) of the slurry. Similarly, No. 2 fuel oil mixed with the slurry affects the rheology. The addition of 10 percent No. 2 fuel oil tends to make the slurry pseudoplastic even for a highly dilatant slurry.

Slurries with different coal contents were also tested in a benchtop accumulator-type fuel delivery system where the slurry spray characteristics (at room temperature and atmospheric pressure) could be observed. Observations made on the basis of these tests as to whether the injection characteristics of a slurry were satisfactory were always correlated with whether a slurry was found to be pseudoplastic in the viscometric tests. The viscometric and injector testing both determined what levels of coal in the slurry were acceptable for testing in the single-cylinder engine.

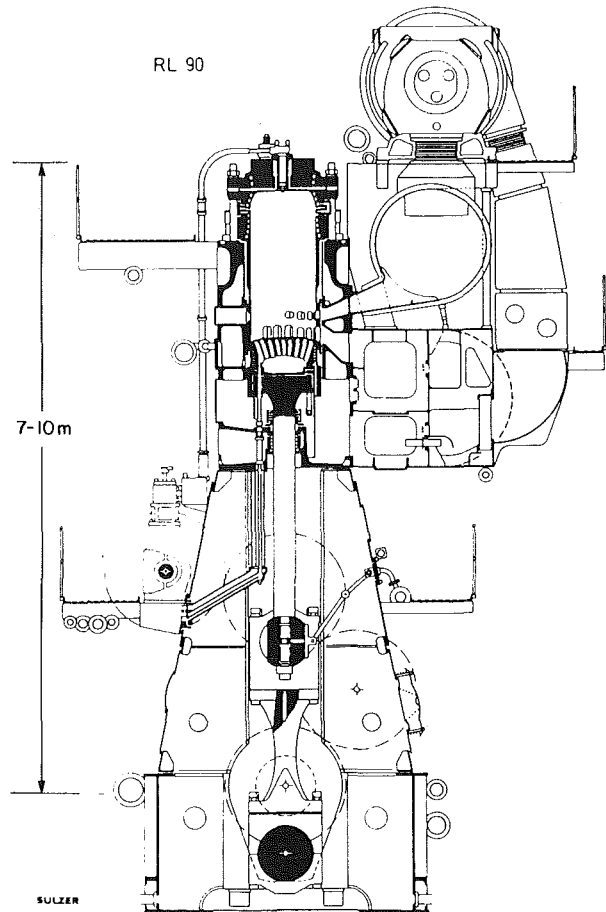


Fig. 2 Cross section of Sulzer slow-speed two-stroke cycle crosshead engine

The four slurries were produced by three different processes. Both the AMAX and Resource processes can be classified as chemical beneficiation, whereas the Otisca process is gravimetric. The AMAX [2] and Otisca [3] processes have been previously described in the literature. The details of the Resource process are proprietary to Resource Engineering. The principal advantages of a chemical process are that it is most likely applicable to a great variety of coals and that a greater reduction in ash content can be obtained. The chemical process, however, is likely to be more complex with less desirable waste material and, thus, possibly more expensive to produce than the gravimetric process.

### Slow-Speed Diesel Engine Characteristics

The slow-speed, two-stroke crosshead type diesel engine has some important, inherent characteristics which make it very attractive for the combustion of coal/water slurries. A cross section of the engine is shown in Fig. 2. The larger bore and stroke and slow speed result in a large combustion volume and long available combustion times. To obtain good efficiencies, burnout within about 60 crank angles is required. At a rotational speed of 120 rpm this equates to a combustion time of about 83 ms for a two-stroke engine, compared to about 17 ms for a four-stroke, 600 rpm engine. Also, because of the large dimensions of the engine, cylinder liner and piston ring wear of several millimeters are permissible. The slow rotational speed of the engine also results in low piston velocities compared to the medium-speed engines, tending to reduce wear as well. The valveless, ported design of the slow-speed engine does away with the erosion and corrosion problems of valves and valve seats associated with standard two-valved or

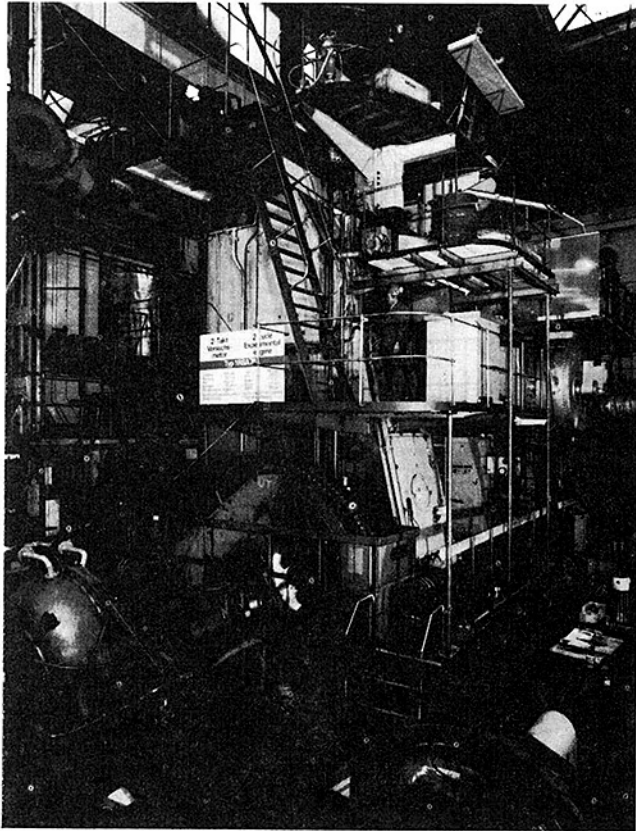


Fig. 3 1 RSA 76 experimental engine with water dynamometer

uniflow scavenged one-valved engines and eliminates the need for exotic valve materials. Loop-type scavenging also avoids the axial swirl that acts as a centrifuge for ash particles after combustion.

The crosshead design with the attendant linear motion of the connecting rod permits the inclusion of a seal between cylinder and crankcase. This design feature enables the use of two separate lube oil systems, which eliminates contamination of the oil lubricating the main engine bearings and crank shaft and allows optimization of the lube oil type for each application. These design features mean that the Sulzer types RND/RLB engines will require a minimum of design modifications for successful operation on coal/water slurries. The primary areas of modification from the standard Sulzer RND/RLB design are the injection system and the cylinder liner/piston ring/piston skirt area. A proprietary accumulator-type injection system design described below has worked well during the single cylinder tests described in this paper. The cylinder wear problem will require changes in material and lubrication design because of the wear caused by the coal ash.

The Sulzer RND and RLB engines are used extensively for stationary and marine power systems where the poorest grades of petroleum fuel are routinely burned. The engine exhibits high power conversion efficiencies over a wide range of load conditions. Production engines are typically designed for peak efficiency at about 75 percent of full load. High efficiencies are achieved from less than 50 percent load to 110 percent of full load. The engines are produced in multicylinder configurations covering a power range from 4000 to 28,000 kW.

### Description of Single-Cylinder Engine Test Facility

**Single-Cylinder Test Engine and Injection System.** The single-cylinder engine used for these tests is located at the

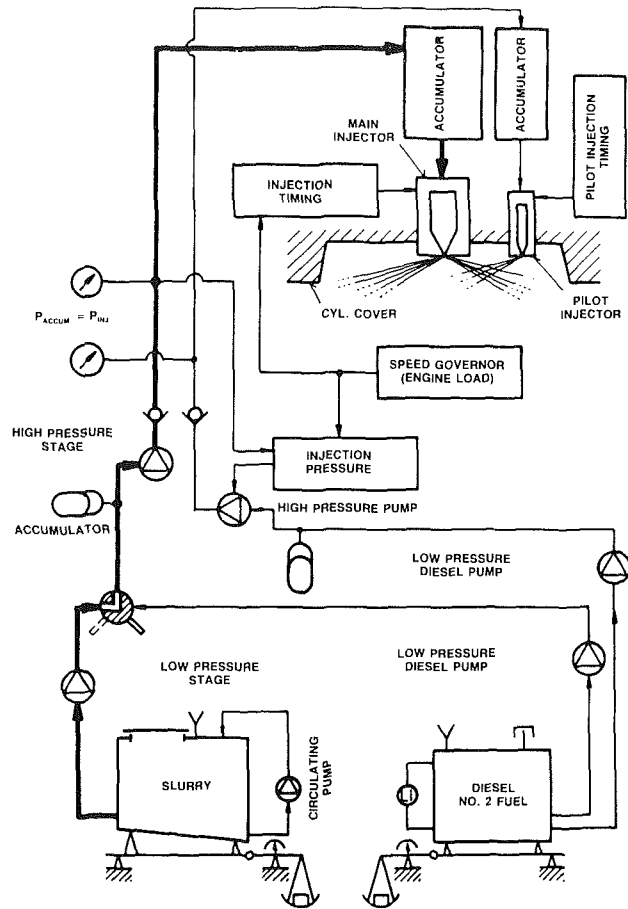


Fig. 4 Fuel system

Sulzer Brothers, Limited, test facility in Winterthur, Switzerland. A photograph of the engine and test facility is shown in Fig. 3. The research engine is a one-cylinder version of an older Sulzer large-bore, two-stroke, slow-speed diesel engine manufactured for both marine and stationary power applications. Power is absorbed by a water brake dynamometer. To allow rapid load changes and reduce the effect of cyclic irregularities, the mechanically controlled water brake was converted to a hydraulically controlled system. Details of the engine configuration are as follows:

Bore:	760 mm
Stroke:	1550 mm
Power (at 100% load):	1471 kW (1975 hp)
Rpm:	120
BMEP:	10.46 bar
Maximum combined power	84.3 bar (gauge)
Compression ratio:	10.63
Boost pressure:	2.03 bar (absolute)

To provide flexibility in testing, an externally powered air blower is used in place of the standard turbocharger. Air is filtered and pressurized in two stages with intermediate cooling. The airflow is controlled with bypass valves and is measured by a standard flow nozzle. The air temperature ahead of the engine is controlled by a heat exchanger. On the exhaust side, orifice plates are inserted to simulate the pressure conditions of the standard exhaust turbine.

The engine design was shown in Fig. 2. Piston cooling water is fully independent of the jacket cooling system. Loop scavenging is employed. Air enters through scavenging ports located at one side of the liner, near bottom dead center of the piston, while the exhaust leaves the cylinder through ports located higher up, but on the same side of the liner as the scavenging ports. Injection occurs directly into the combus-

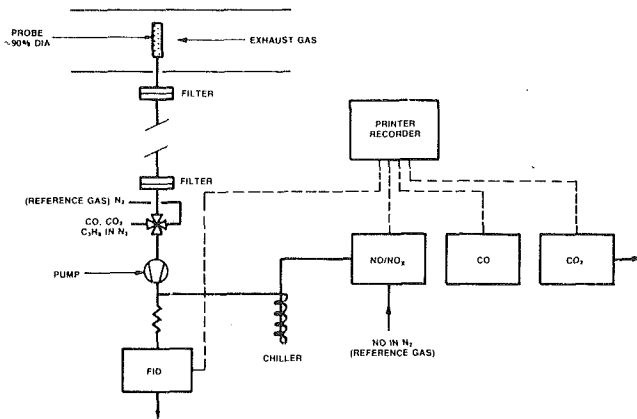


Fig. 5 Exhaust emission measuring schematic

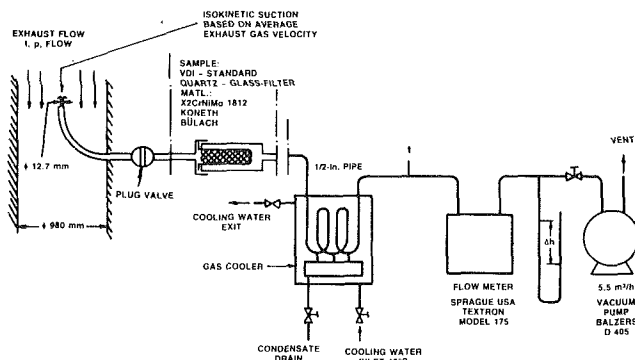


Fig. 6 Schematic of exhaust particle sampling system experimental plant at Sulzer Winterthur; 1 RSA 76 engine

tion space with a centrally located nozzle. A pilot fuel injector is located between the main injector and cylinder wall, with injection occurring in the direction of the main injector.

The fuel injection system is a newly developed proprietary system, which is of the accumulator type. It permits flexibility with regard to injection pressure (250 to 1000 bar) and timing. Both may be arbitrarily selected for any load and speed, and adjusted at any instant during operation. Pre-injection is also possible. A simplified fuel system schematic is shown in Fig. 4.

Both diesel No. 2 fuel and slurry are pumped into separate tanks installed on water scales. Fuel consumption measurements are calculated from the weight loss of fuel between two readings at constant engine power and speed. Diesel fuel is used for starting to warm up the engine, to ignite the slurry in the cylinder of the engine during operation by means of the pilot injector, and during stopping to flush slurry from the system. A low pressure Sulzer four-stage centrifugal pump supplies diesel fuel for operation to the engine via the fuel selection valve. The second low-pressure pump supplies fuel to the high-pressure reciprocating piston pump. The pilot injection timing unit controls the opening and closing of the needle valve in the pilot injector in relation to the crankshaft angle position. It is set manually from the operator's control panel. The timing for the main injection needle valve opening is also set manually from the control panel, and the duration of the injection (closing of the valve) is controlled by the speed (load) governor. When the engine has reached a stable operating condition on diesel fuel, the slurry low-pressure MOYNO-type progressive cavity pump, which has a rubber stator and steel rotor, is started. To avoid a bypass-type flow control (which has undesirable effects on slurry properties) the pump is driven with a variable speed motor controlled by the pressure in the high-pressure stage. The pump only supplies the amount

of fuel the engine actually consumes. With the fuel selection valve switched to slurry, the engine operates on slurry as soon as the diesel fuel in the high-pressure accumulator is consumed. At any time during operation the fuel can be switched back to the diesel fuel, which then pushes the slurry out of the system. The philosophy behind this system requires a slurry that is compatible with diesel No. 2 fuel.

An initial set of optimized performance data is obtained for the engine test configuration using conventional diesel fuel. These data establish a reference point for comparison with operation using the test fuel. After exchanging the injector with one optimized for slurry fuel and adding a pilot fuel injector, the engine is restarted on diesel fuel. The fuel is then switched to slurry fuel, and the test sequence proceeds. At the completion of the tests, a second set of reference performance data is taken using diesel fuel. The second diesel fuel tests verify the stability of the instrumentation and the various test engine components. All tests, independent of the fuel utilized, are adjusted to comparable thermodynamic parameters, maximum cylinder pressure, ratio of maximum to compression pressure, and scavenge air conditions.

**Engine Instrumentation.** Most of the important engine and system data can be observed and controlled from one central location. Performance measurements included engine configurational and operational parameters, brake specific fuel (including slurry, pilot oil and leakage oil) and air consumptions and exhaust particulate and gas pollutant emissions. Fuel consumption was measured two to three times per hour using a weighing tank. Air throughput was checked periodically.

Time varying pressures such as cylinder and injection pressures were recorded on an oscilloscope and stored on magnetic tape. Polaroid photos of the oscilloscopic traces were obtained over approximately ten cycles. Visicorder traces of five-ten cycles from the magnetic tape recordings were also obtained. Also shown on the visicorder traces was the time gradient of cylinder pressure. The oscilloscopic traces of cylinder and pilot and slurry fuel injection pressure were utilized to monitor instantaneous engine behavior and operational parameters, such as relative timing between pilot and slurry fuel, injection timing, and ignition delay. Comparison of the visicorder traces over ten consecutive cycles also gave an indication of cycle-to-cycle differences.

**Exhaust Gas Pollutant Instrumentation.** Both gaseous exhaust and particulate emissions were measured for performance load points. The gaseous exhaust emissions measured were  $\text{NO}_x$ ,  $\text{CO}$ ,  $\text{CO}_2$ ,  $\text{CH}_4$ , and  $\text{O}_2$ . Figure 5 shows a schematic of the measuring system for the gas exhaust emissions.

Exhaust particulate emissions were measured with the apparatus shown in Fig. 6. Measuring exhaust particulate emissions on a single-cylinder engine is very difficult. The fluctuating exhaust gas velocity prevents isokinetic sampling. In addition, the cross-sectional flow pattern across the exhaust duct probably changes with load, and the running time for a test run is not sufficiently long to maintain equilibrium between particles deposited on internal engine parts and those removed by flow-induced shear forces. The particulate emission measurements are most likely applicable for comparative purposes between fuels rather than to obtain absolute values.

## Engine Test Results

**Initial Optimization of Engine Parameters.** As mentioned earlier, four coal/water mixtures from three different manufacturers were selected for the testing. AMAX supplied a fine grade slurry with a mean particle size of  $10 \mu\text{m}$  and a coarse one with a mean particle size of  $16 \mu\text{m}$ . The first shipment of slurry was used to determine the optimum injection

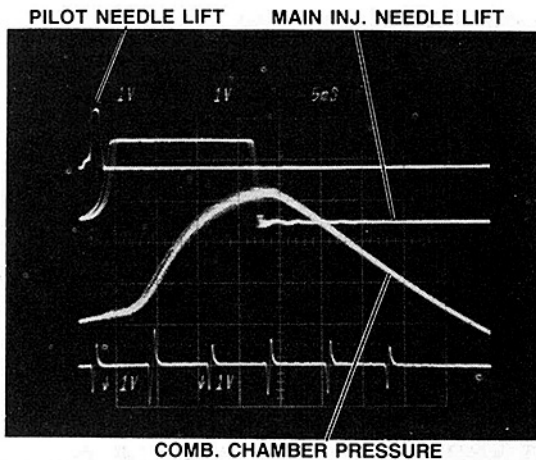


Fig. 7(a) Flame ignition hypothesis (test sequence No. 1/test No. M19)

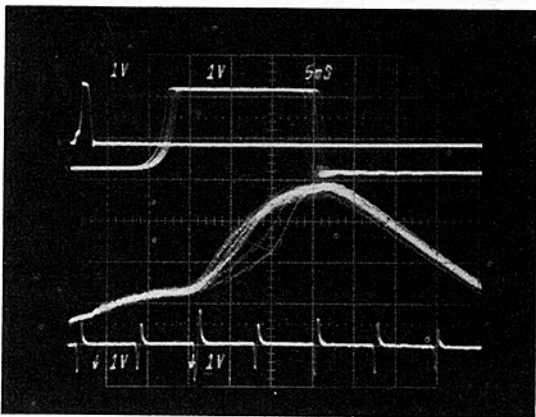


Fig. 7(b) Temperature rise hypothesis (test sequence No. 1/test No. M20)

Fig. 7 Polaroid photographs of cylinder pressure trace (over ten cycles)

nozzle configuration and mode of operation. The same nozzle design was then used with the three other slurries. It is necessary to maintain the same maximum cylinder pressure for both diesel and slurry fuel tests in order to have a thermodynamically correct basis for comparison, which in turn dictates the selection of main fuel injection timing. The optimum operating parameters were confirmed for each new slurry by performing additional tests with the parameters changed.

Two methods for the initiation of combustion were considered feasible: the flame ignition hypothesis, in which the slurry in the cylinder has to be ignited by a pilot flame, and the temperature rise hypothesis, in which an increase of the temperature in the cylinder leads to self-ignition of the slurry. The installation of the pilot injector easily allowed validation of either method by changing the relative timing between pilot and main fuel injection. To validate the temperature rise hypothesis, pilot fuel injection was advanced so that all the pilot fuel was combusted before the injection of the slurry started; whereas, to validate the flame ignition hypothesis, the relative timing was set so that slurry injection was initiated almost at the same moment that pilot injection ended. Thus, for the temperature rise hypothesis, the effect of the pilot fuel was to raise the temperature of the air charge, and for the flame ignition hypothesis, to provide sufficient activation energy to initiate combustion. Figure 7(a) shows the cylinder pressure rise over ten cycles, with the relative timing set according to the flame ignition hypothesis. Ignition and combus-

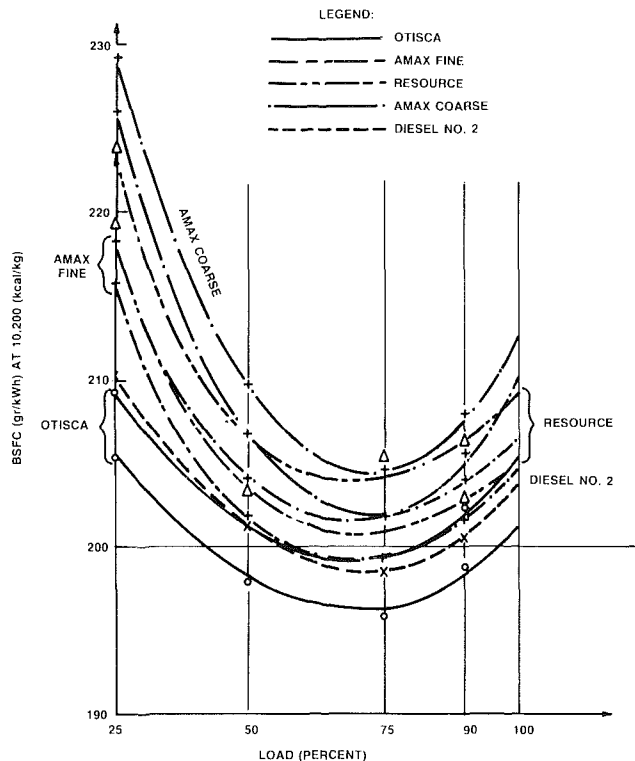


Fig. 8 1 RSA 76 engine fuel consumption measurements

tion were excellent. The cycle irregularities were very small and similar to those obtained with No. 2 fuel. Figure 7(b) shows the cylinder pressure rise with the relative timing set for the temperature rise hypothesis. Irregularities were much greater, and the engine behavior was poor. The specific fuel consumption also increased by 5 percent. In both cases the amount of pilot fuel was 3 to 4 percent (by a total heat input), and the engine load was 50 percent. Thus, the flame ignition hypothesis was shown to be valid within the range of scavenge air temperatures and pressures applicable to slow speed diesels. For all successive tests, relative timing was set according to the flame ignition hypothesis. The pilot fuel was subsequently reduced to 1 to 1.5 percent at 90 percent load.

**Fuel Consumption.** For each slurry, the engine was equipped with new piston rings and run in for approximately 20 h on No. 2 fuel. Figure 8 shows the specific fuel consumption for No. 2 fuel and the four different coal/water slurries. The reference measurements with No. 2 fuel shown in this figure were taken before the slurry runs. After engine operation with the Resource slurry, a new reference run on No. 2 fuel showed good agreement at 75, 90, and 100 percent load, while the consumption at 50 percent load was 3 g/kWh, and at 25 percent load 5 g/kWh higher. Both reference runs on No. 2 fuel were performed after running in the engine again to recondition the piston ring/cylinder liner interface. The specific fuel consumption values shown on the graph have been converted to a standard heating value of 10,200 kcal/kg (18,360 Btu/lb). Two curves are shown for each slurry. The lower curve represents the fuel consumption with the heating value of the slurry as determined by the Swiss Federal Institute for Materials Testing (EMPA), and the higher curve with the heating value measured by the Sulzer Laboratory. The differences in the heating values are due to the fact that the slurries are nonhomogeneous and more difficult to analyze than No. 2 fuel. The deviation was below 2 percent, and the EMPA measurement was always the lower value. Measurements were taken at 90, 75, 50, and 25 percent load at 120 rpm. Higher

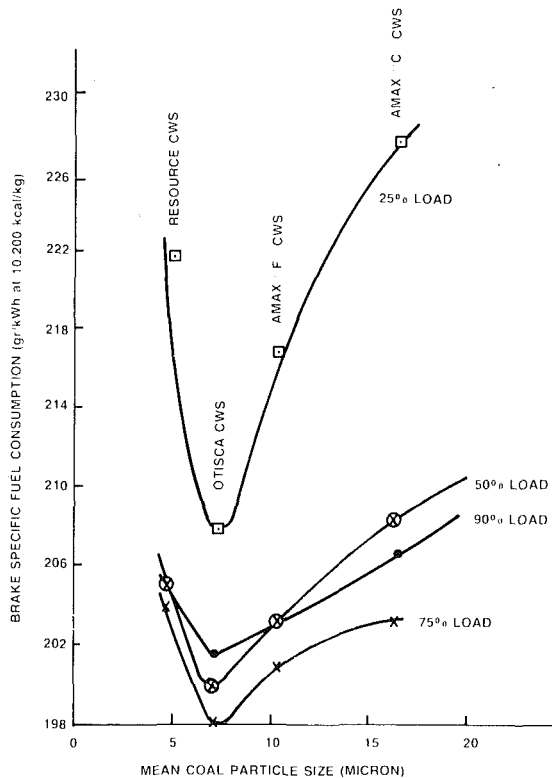


Fig. 9 Brake specific fuel consumption versus mean coal particle size for four coal/water slurries

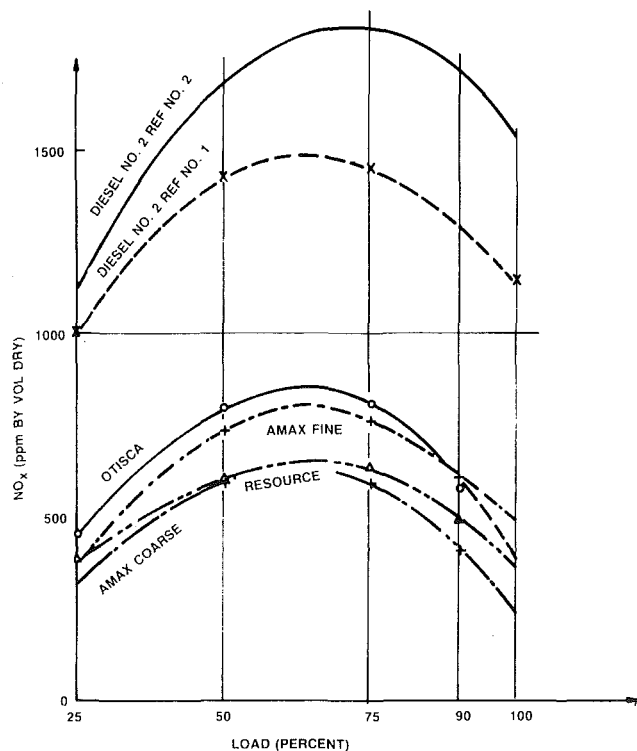


Fig. 10 1 RSA 76 engine  $NO_x$  measurements

loads could not be run because the heating value of the fuel was lower than the value used in the design of the injection system, which was based on a minimum heating value of 4000 kcal/kg (7200 Btu/lb). The specific fuel consumption values given in Fig. 8 include diesel pilot fuel and leakage oil. The leakage oil, amounting to 4 to 6.0 percent of total heat input at

50 to 90 percent loads, is a consequence of the design of the Sulzer proprietary fuel injection system utilized for these tests. It is important to realize that this small amount of leakage diesel fuel was not sufficient to induce ignition of the coal/water slurry. If the 1.0 to 1.5 percent pilot fuel oil was stopped, combustion became quite erratic. The oil leakage will be insignificant in the next generation design. In the present design, the leakage oil mixes with the injected slurry.

The Otisca slurry yielded a fuel consumption which was the same or lower than that of No. 2 fuel, followed, in ascending order, by AMAX "F", Resource, and AMAX "C". Fuel consumption for the AMAX "C" slurry was the highest relative to No. 2 fuel (approximately 3 to 8 percent, depending on load). It is interesting that Resource, with the smallest particle size, showed a high consumption, while Otisca, which underwent a physical beneficiation process, showed the lowest consumption.

Another set of reference measurements was also obtained using diesel No. 2 fuel oil immediately after the AMAX "C" tests, without a run-in period, in order to see the difference between an orderly run-in engine and an engine deteriorated by slurry operation when piston ring and cylinder liner surfaces are rough and friction losses are increased. The later tests showed 3 to 11 g/kWh higher fuel consumption, almost equivalent to the difference between the various slurries. This difference amounts to an additional friction loss of approximately 20 kW, which is equivalent to an increase in friction loss of nearly 20 percent compared to diesel fuel operation. It also may indicate that the BSFC of the slurries might be somewhat better than that reported in Fig. 8.

Specific fuel consumption is shown in Fig. 9, plotted versus mean coal particle size. Except for the Resource slurry, this figure shows an increase in fuel consumption with increasing particle size, with the increase more severe at 25 percent load than at higher loads. The AMAX slurries both contained more coal than either the Resource or Otisca slurries. Analysis indicates approximately a 0.7 g/kWh (0.35 percent) increase in fuel consumption per 1  $\mu\text{m}$  increase in particle size, excluding the Resource data.

**Pilot Oil Quantity.** As expected, smooth and controlled ignition with coal/water slurry fuel was not possible without pilot injection. Temporary omission of the pilot fuel resulted in erratic and very late ignition of the coal fuel. Customarily, 5 to 10 percent of the total heating value of the fuel must be in the form of pilot fuel in order to obtain satisfactory combustion of a low-cetane fuel. A totally new concept of pilot injection, previously developed by Sulzer, did however result in a reduction of the pilot-fuel requirement equivalent to about 1 percent at 100 percent load, while at the same time improving combustion and decreasing cyclic irregularities. Pilot fuel quantity was kept constant at all loads and for each slurry.

**Exhaust Emissions.** The amount of nitrogen oxide emissions from the slurries was found to be approximately half the amount found with the No. 2 fuel (Fig. 10), although the nitrogen content of the coals was 1.5 to 2 percent (by weight of dry coal) compared to nearly zero for diesel oil. Thus, the reduction in thermal  $NO_x$  was even greater. This is a significant result. A high-efficiency diesel engine utilizing a coal/water slurry fuel would be able to meet the proposed EPA standards of 600 ppm (corrected to 35 percent efficiency and 15 percent  $O_2$ ) without any degradation in performance. The lower  $NO_x$  value can largely be attributed to the fact that the high water content in the fuel reduces local flame front temperatures.

Figure 11 presents CO and HC emissions. The results are not conclusive, but generally speaking, they are within the same range or lower than No. 2 fuel.

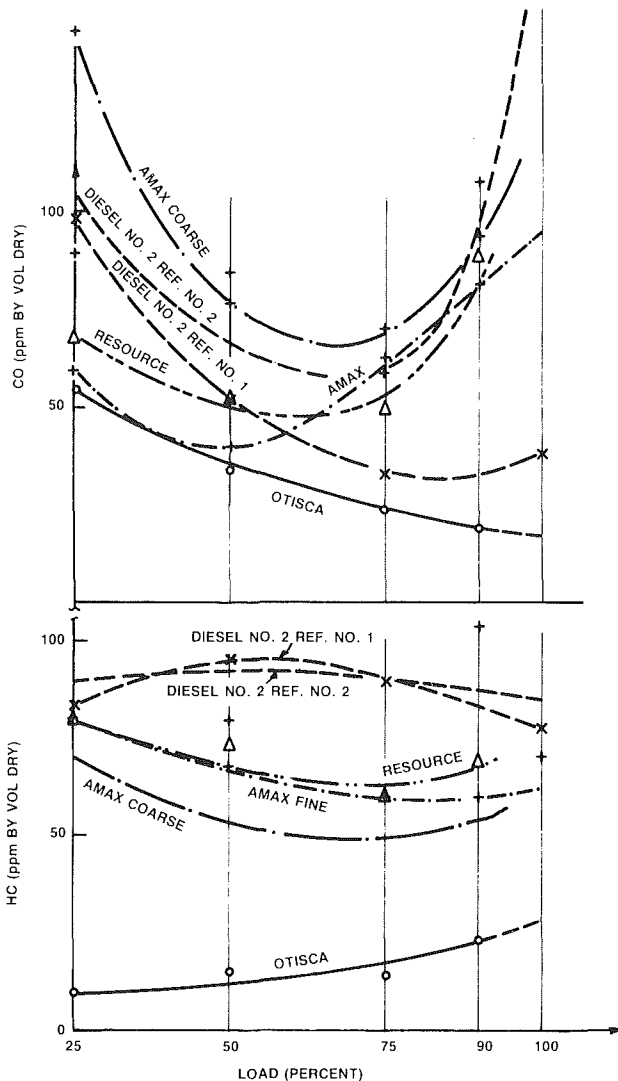


Fig. 11 1 RSA 76 engine CO and HC measurements

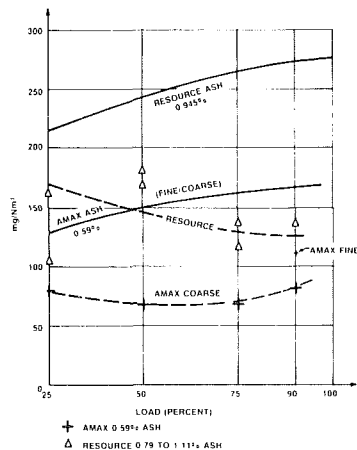


Fig. 12 1 RSA 76 engine exhaust particle measurements

**Exhaust Gas Particulates.** Exhaust gas particulate measurements could not be obtained for the Otisca slurry, and could only be observed at a 90 percent load point for the AMAX "F" slurry, because of the problems encountered when the filter collector fractured. Measurements were obtained, however, over the complete range of loads for the

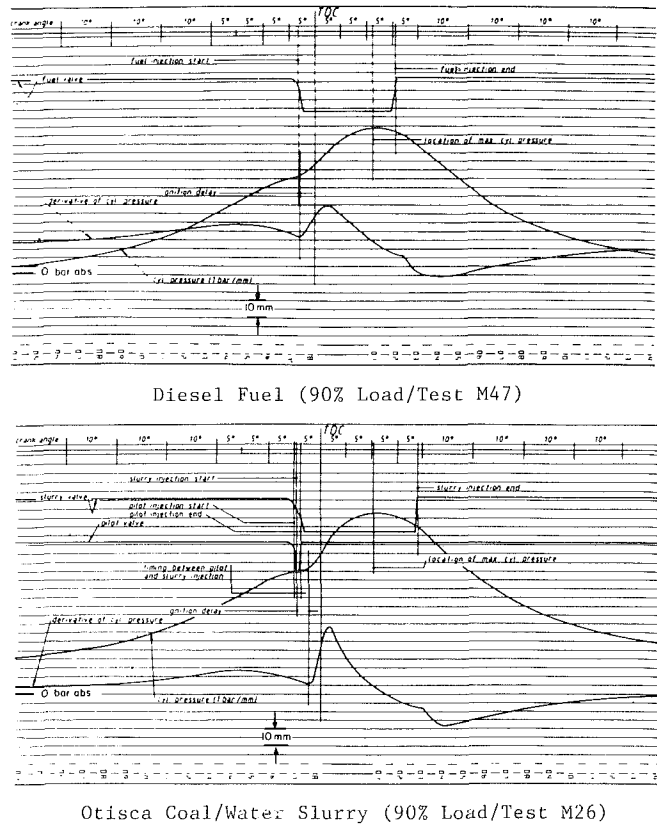


Fig. 13 Comparison of visicorder traces of cylinder pressure for diesel fuel and Otisca coal/water slurry

Resource and AMAX "C" slurries. The results of these tests are shown in Fig. 12. The 50 and 75 percent points with the Resource slurry were repeated at different times with good agreement. For comparison, Fig. 12 also shows curves for exhaust gas particulate loading based only on the ash present in the fuel. The actual particulate measurements are consistently below the ash-only values. The low particulate measurements could be a result of particulates sticking to engine parts and exhaust ducts or particulates carried out with the cylinder lubricating oil into the housing below the piston.

Alternatively, the lower readings could be due to the fact that the combustion temperatures in the diesel are higher than the 815°C at which coal is typically de-ashed in ASTM type tests. At the higher temperatures the oxides in the exhaust may lose their oxygen and become more metallic, or alkali metals may vaporize, forming fine particles which, upon condensing, pass through the collecting filter. The higher particulate loadings measured at 25 to 50 percent load, compared to 75 and 90 percent load, may be due, therefore, to the lower combustion temperatures occurring at the lower loads. The sampling point would also contribute to inaccuracies due to flow irregularities as it evidently does in the measurement of gaseous exhaust gas pollutants.

The Bosch Smoke Number was also measured for all performance tests. However, because the ash particles in the slurry exhaust are light gray and not black as they are in fuel oil consumption, measured particulate loadings in the exhaust were higher at a given Bosch Number for the slurry tests than those obtained typically on No. 2 fuel. In addition, because of the scatter in the data, it was not possible to correlate particulate emissions and Bosch Numbers for the slurry tests.

**Cylinder Pressure Traces and Cycle-to-Cycle Irregularities.** Figure 13 compares the visicorder traces over a single cycle obtained at 90 percent load for diesel fuel and the

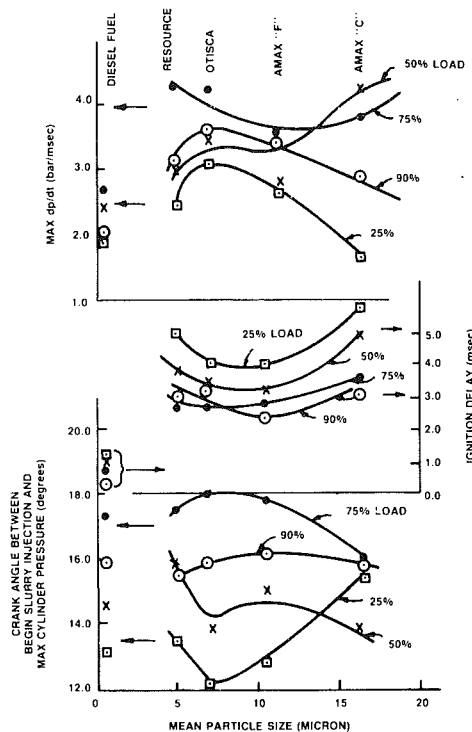
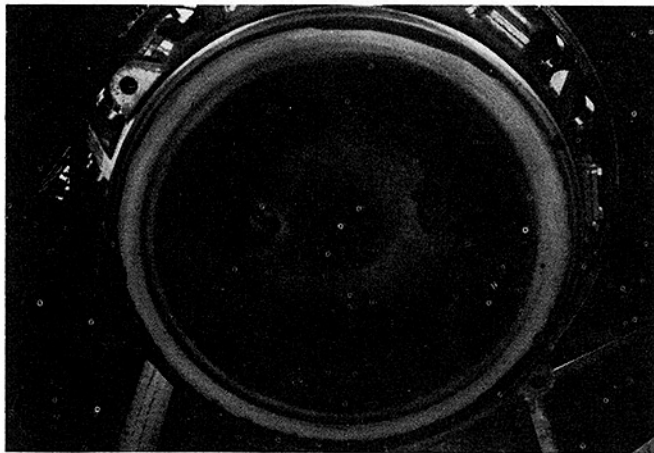


Fig. 14 Correlation of average cycle-to-cycle dynamic parameters versus coal particle size



Main injector in middle, pilot injector on right, starting air opening on left and piezoelectric quartz pressure pick-up on bottom. Note cleanliness of combustion space.

Fig. 15 Photograph of cylinder cover and insert after testing of Otisca coal/water slurry for 17.5 h

Otisca slurry. Three observations can be made from the comparison: (1) the ignition delay for the slurry is much greater than for diesel oil; (2) the  $dp/dt$  for the slurry rises more rapidly and to a higher value than the  $dp/dt$  for the diesel fuel (as a result of longer ignition delay), resulting in significantly different behavior during the initial kinetically controlled rapid combustion regime; but (3) the  $dp/dt$  curves for the two fuels are similar in slope after about 5 deg ATDC, indicating that the diffusion controlled combustion regimes are similar.

Attempts were made to correlate the maximum  $dp/dt$ , the crank angle difference between the beginning of slurry injection and the location of the maximum cylinder pressure, and ignition delay versus particle size. Only ignition delay versus particle size, plotted in Fig. 14, showed a consistent trend. The minimum ignition delay occurs for the Otisca ( $\sim 6.9 \mu\text{m}$ ) and the AMAX "F" ( $\sim 10.3 \mu\text{m}$ ) slurries, and increases as the coal particles get finer and coarser, respectively. There also is a definite increase in the ignition delay as the load decreases. The reason for the definitive correlation of particle size and load with ignition delay and the poor correlation of the maximum  $dp/dt$  with the crank angle difference may be due to the fact that the volatile matter of each of the coals was similar, but the surface reactivities are probably different (it is in the initial kinetically controlled rapid combustion regime after ignition where surface reactivities would become an important property).

**Engine Disassembly and Engine Wear.** Figure 15 shows a photograph of the cylinder cover and insert after 17.5 h of operation with the Otisca slurry. As seen in this photograph, the combustion space was very clean, with only a negligible layer of particulate matter on the cylinder cover. The cylinder cover, piston crown, and piston side at disassembly after operation with the other slurries showed similar light patterns of deposits. There is a clear indication that the usual deposits of combustion matter after comparable operating times and loads are less in the case of slurry operation than with No. 2 diesel fuel.

Previous tests performed with a 34 percent coal/oil slurry in 1978 and 1979 utilized a standard hardened tool steel injection nozzle tip [1]. Erosion of the nozzle tip was severe after 9.5 h of operation, and this prohibited use of this material in the present program. The present series of DOE tests was performed primarily with a sintered tungsten carbide (94 percent W, 6 percent Co) nozzle insert. This nozzle material represented an interim solution, allowing continuous operation of the engine for 5 to 10 h, sufficient to perform the required parametric and performance testing. Failures occurred after 3 to 12 h, either because of tip fatigue or enlargement of injection holes (although failure was not catastrophic, as it was for the tool steel inserts). Nozzle wear appears to be dependent on particle size rather than on coal ash content. This finding confirms expectations, since for erosion, in contrast to abrasion, impact and not hardness is the decisive factor.

Table 2 Wear rates for single-cylinder testing of Otisca, AMAX "F", Resource, and AMAX "C" coal/water slurries

	Running (h)	Top piston Ring radial wear (mm)	Top piston ring radial wear rates		Cylinder liner diameter wear (mm)	Cylinder liner diameter wear rates	
			(mm/hr)	Ratio slurry/No. 2		(mm/hr)	Ratio slurry/No. 2
Otisca	17.5	2.05	0.117	56	0.12	0.00686	16
AMAX "F"	11.0	1.575	0.143	68	0.06	0.00545	13
Resource	8.75	1.763	0.201	96	0.155	0.0177	42
AMAX "C"	5.25	1.78	0.339	161	0.04	0.0076	18
No. 2 diesel	—	—	0.0021*	—	—	0.00042*	—

\*Expected wear rates for first 20 h of operation on new liners.



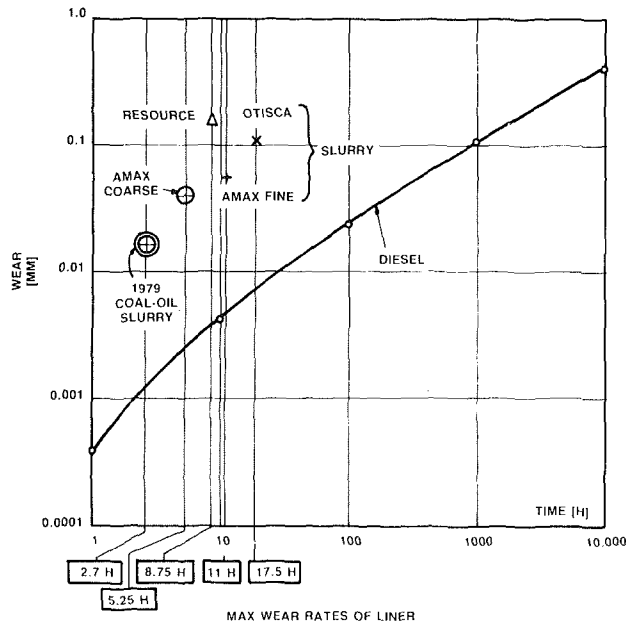


Fig. 16 Comparison of liner wear between diesel and "microslurry" operation (1 RSA 76 test engine)

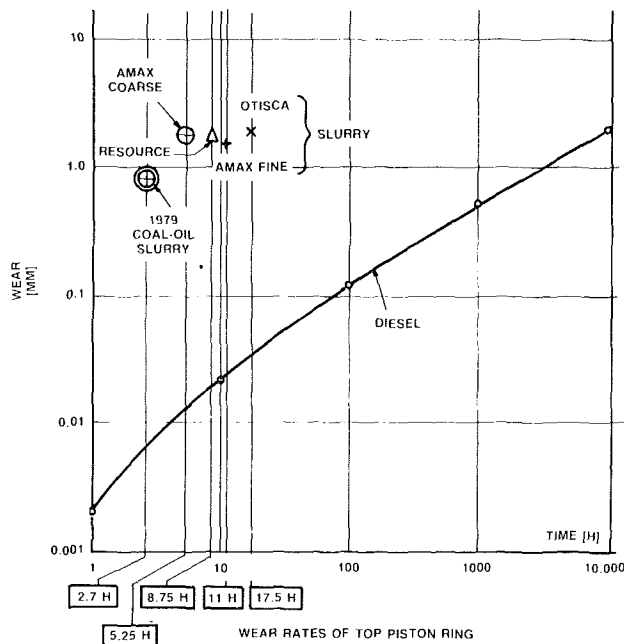


Fig. 17 Comparison of piston ring wear between diesel and "microslurry" operation (1 RSA 76 test engine)

Piston ring and cylinder liner dimensions were measured before and after a slurry run. Both piston rings and cylinder liners were fabricated from the standard gray cast iron GG25 spez utilized on all slow-speed Sulzer engines. A high-quality SAE 40 mineral oil with a high viscosity index was used for the cylinder lube oil. Oil consumption was adjusted to approximately 1 g/kWh, which is the normal rate for such engines.

Analysis of piston ring and cylinder liner wear with slurry fuels was conducted as follows:

- Comparisons were made of expected wear rates, using the No. 2 fuel, and using the slurries.
- Correlation of particle size and ash content.

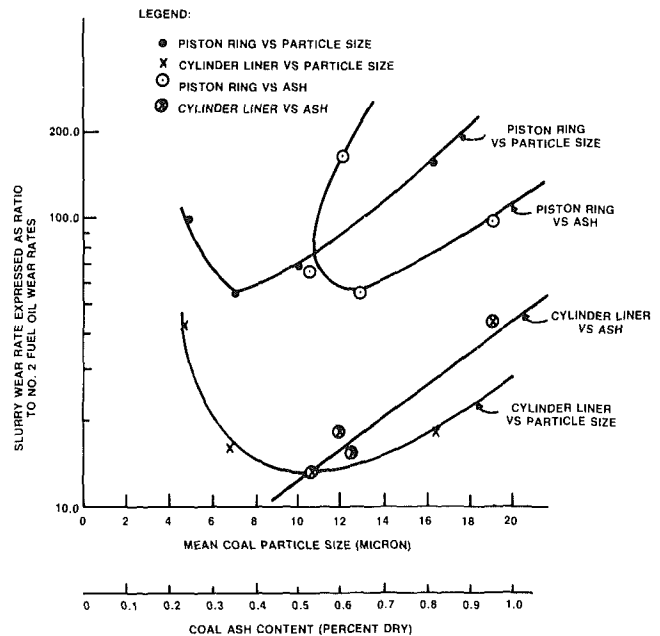


Fig. 18 Correlation of piston ring/cylinder liner wear rates versus mean coal particle size and coal ash content

- Calculation of "wear coefficients" and segmentation into wear regimes.
- Observation of wear component surface condition based on photomicrographs and comments relative to segmentation into wear regimes based on wear coefficients.

Table 2 summarizes the top piston ring and cylinder liner wear rates and compares these values to those found in operation with diesel oil. Figures 16 and 17 show the comparison graphically. It is seen from these figures that the cylinder liner wear rate is 11 to 29 percent of the piston ring wear rate. The cylinder liner and piston ring wear rates for the Otisca and AMAX "F" slurries are approximately the same, and are the lowest of the four slurries. The cylinder liner wear rate for the Resource slurry is the highest, while for the top piston ring it is the second highest. It is interesting to note that the top piston ring wear for the AMAX "C" slurry is almost three times the value measured for the Otisca and AMAX "F" slurries, whereas the cylinder liner wear is of the same order of magnitude as for these two slurries.

Figure 18 shows a correlation of wear rates obtained with the four slurries versus mean particle size and coal ash content. The data show a minimum in the wear/rate particle size correlation at 6 to 10  $\mu$ m for both the top piston ring and cylinder liner, a linear correlation of cylinder liner wear rate with ash content, but no correlation of piston ring wear rate with ash content. The shape of the curves in Fig. 18 could be affected by the fact that the Resource slurry has the smallest particle size and the largest amount of ash. The relationship between particle size and ash content for the other three slurries is random. If the Resource wear rate data are eliminated, a strong relationship between increasing piston ring wear rate and a weak relationship between cylinder liner wear rate with increasing particle size (Fig. 18) are suggested. The relationship of wear rates to ash content remains essentially unchanged with and without the Resource data.

Since silica and alumina were both present in the ash (see Table 1) and these oxides are among the hardest of substances, a correlation of wear rates was also attempted versus the content of these compounds. Figure 19 shows the plots versus silica content and the sum of the silica and alumina contents. The data of the plot versus silica content show a random variation for both cylinder liner and piston ring wear. However, the

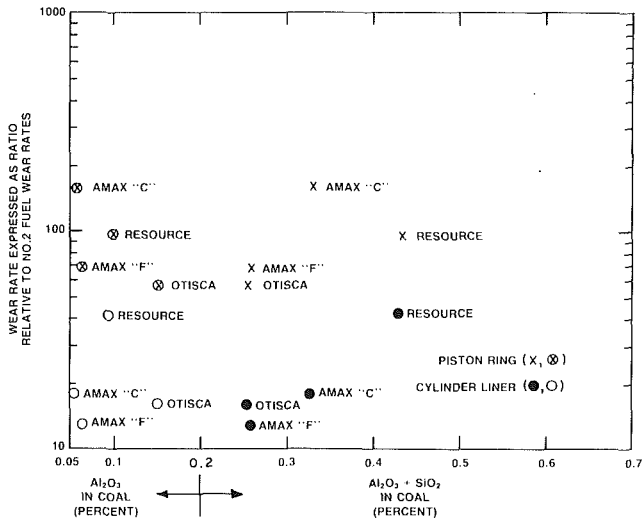


Fig. 19 Wear rates versus  $Al_2O_3$  and  $Al_2O_3 + SiO_2$  content in coal

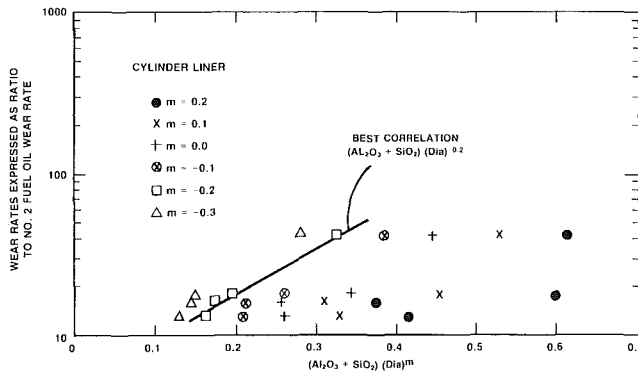
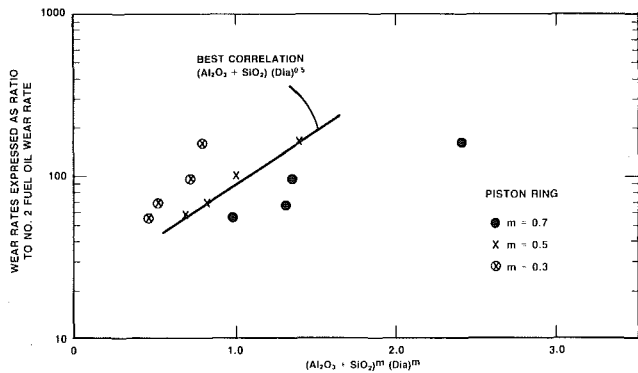
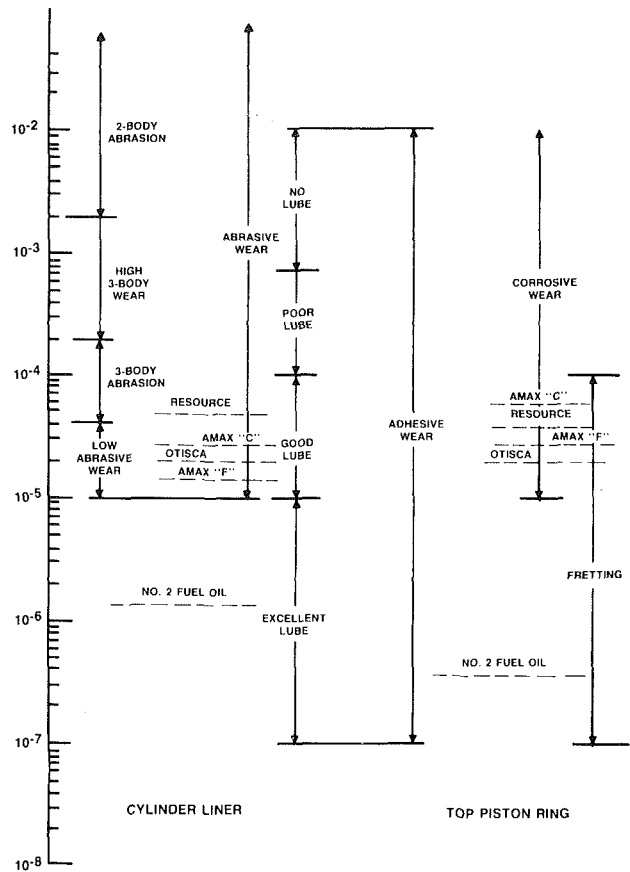


Fig. 20 Correlation of wear rates with alumina and silica content of coal and coal particle size (dia)

plot versus the sum of silica and alumina contents shows a strong relationship for cylinder liner wear (similar to the relationship for total ash content shown in Fig. 18) and a much better correlations for piston ring wear than Fig. 18. In fact, removal of the Resource data results in a strong increasing relationship of piston ring wear with the sum of silica and alumina contents. The randomness of the correlation with alumina and the better correlation with the sum of the alumina and silica contents suggest that the alumina and silica may be tied together in the ash in the form of alumina silicates which generally have hardness values less than alumina ( $2100 \text{ kg/mm}^2$ ) but greater than silica ( $800 \text{ kg/mm}^2$ ).

The relationship of wear with coal partical diameter is investigated further in Fig. 20 where wear is plotted versus the



Source: E. Rabinowicz, "Wear Coefficient Metals," West Control Handbook, ASME 1980

Fig. 21 Comparative analysis of slurry wear coefficients and typical values for same metal on metal sliding systems

parameter (silica + alumina)  $\times$  (dia)<sup>m</sup>. Figure 20 shows that the best relationship for cylinder liner wear is (alumina + silica)  $\times$  (dia)<sup>-0.2</sup> and (alumina + silica)  $\times$  (dia)<sup>0.5</sup> for piston ring wear. Analysis of Figs. 18–20 thus strongly suggests that cylinder liner wear is primarily dependent on the sum of silica and alumina contents in the coal, whereas piston ring wear is dependent on both the sum of the silica and alumina contents and the coal particle diameter. From this observation it can be hypothesized that the ash or coal particles adhere to the cylinder liner walls either because the coal particles are soft or because the oil film is sticky, and the particles abrade the piston ring rather than rolling between the liner and piston ring.

The wear rates tabulated in Table 2 can be used to assess roughly the type of wear mechanism through an order of magnitude calculation, by means of the wear equation [4, 5]

$$W = \frac{KLD}{H}$$

where

- $W$  = volume of water
- $L$  = applied load
- $D$  = sliding distance
- $H$  = penetration hardness
- $K$  = nondimensional wear coefficient

The idea is to compute the  $K$  values from the test data and the above equation and compare the resulting values with typical wear coefficients associated with different wear mechanisms.

A comparison between the calculated values and the range of wear coefficients characteristic of different categories of wear mechanisms is shown in Fig. 21 for both the cylinder

liner and piston ring. For the most part the calculated slurry wear coefficients are in the low abrasive wear region and good lubrication subregime of adhesive wear, whereas the calculated No. 2 fuel oil coefficients are all in the excellent lubrication subregime of adhesive wear. (There are no indications of either corrosive or fretting type wear. These wear mechanisms, therefore, were eliminated from consideration.) The analysis suggests that an improvement in lubrication that could decrease wear is possible.

Photomicrographs of the piston ring surface show evidence of both adhesive and abrasive wear. Clean straight furrows, which indicate abrasive wear, and rough torn surfaces, plastic deformation and metallic wear fragments, which indicate adhesive wear, are all visible in these photomicrographs. If adhesive wear is indeed an important contribution, it may be the result of the solid coal and ash particles adsorbing and absorbing the lubrication film on the cylinder walls, thereby leaving a poorly lubricated condition. On the other hand, if abrasion is the more important contributor to wear, the tips of the furrows on mating surfaces could be gouging each other as the piston ring rotates, causing the rough torn surfaces. If, as hypothesized above, the particles are adhering to the cylinder liner wall, the rough torn surface could be the result of a rolling effect. There is also strong evidence that the plastic flow pattern, indicative of adhesive wear, which is seen in at least one of the photomicrographs, occurs as an aftermath of ash-related abrasion as the liner surface degrades and destroys the liner lubrication film.

## Conclusions

The testing of four coal/water slurries in the Sulzer single-cylinder, slow-speed, diesel facility demonstrated that economic power conversion efficiencies can be obtained when firing coal/water slurries containing approximately 50 percent coal with mean coal particles up to 16  $\mu\text{m}$  in diameter. Thermal efficiencies were comparable to those obtained with No. 2 fuel oil. The previously developed proprietary accumulator injection system operated successfully, although wear of the nozzle insert with the materials available was excessive. Cylinder liner and piston ring wear were, respectively, 13 to 42 and 56 to 160 times those expected with No. 2 fuel, using the standard Sulzer cylinder liner/piston ring design and materials and operating with mineral oil as lubricant. There were fewer cyclic irregularities with the slurry fuels, and the engine ran smoother than when operated on No. 2 fuel.

Specific observations related to the slurries and the testing program are:

### Engine Thermal Performance

- Thermal efficiency with operation on the Otisca coal/water slurry fuel was slightly greater than that obtained with No. 2 diesel fuel. Thermal efficiency for the other slurries was slightly lower.

- It appears that thermal efficiency is a function of the coal particle size within the ranges tested. Specifically, thermal efficiency appears to decrease 0.4 percent (approximately 0.14 percentage points) for each 1.0  $\mu\text{m}$  increase in mean particle size (three of the four slurry data points support this trend). The change in efficiency is likely related to the rate the particle combusts (rather than to incomplete burnout) or the additional friction generated by the larger diameter coal particles at the piston ring/cylinder liner interface.

### Exhaust Emissions

- $\text{NO}_x$  emission measurements with slurry fuel firing were

30 to 50 percent of the values obtained in the same engine with No. 2 diesel fuel. CO emissions were generally equal to or slightly lower with slurry fuels and hydrocarbons were 25 to 60 percent of the values obtained with No. 2 fuel oil.

- Particulate exhaust emissions were measured during the performance tests on three of the slurries. Although the absolute value of measurements on a single-cylinder engine is difficult to evaluate, it is significant that the measured values were consistently less than what would be expected based on the coal ash contents, indicating complete burnout. Surprisingly, values obtained for the coarsest slurry were about 60 percent of those obtained with the finest particle size slurry.

- Upon disassembly, after firing with all four slurries, the combustion space was found to be equally clean and free of carbon buildup with each slurry.

### Coal Ignition Properties

- Coal ignition seems to occur, according to the flame ignition hypothesis, in a slow-speed diesel engine with stable engine operation attainable with about 1 percent (by total heat input) diesel oil utilized as a pilot.

- Ignition delays with the slurry fuels are in the 2.0 to 4.0 ms range, compared to 0.4 to 1.0 ms for diesel fuel for loads from 50 to 90 percent.

- The maximum time derivative of cylinder pressure was always greater for slurry fuels than for diesel fuel. Thus, the characteristics of the kinetically controlled rapid combustion regime differed significantly between the slurries and diesel fuel.

### Engine Wear

- Injection nozzle erosion appears to be related to particle size than to ash content for the sintered tungsten carbide insert utilized in most of the tests.

- Different analyses performed suggest that adhesive and abrasive wear could both be primary contributing factors and that they both could be significant. The wear data indicate that both the sum of the coal's alumina and silica content and the mean coal particle size are primary contributing variables to piston ring wear and that the sum of the coal's alumina and silica content is the primary contributing factor for cylinder liner wear.

### Acknowledgments

This work was performed under contract to the Industrial Program Office, Division of Conservation and Renewable Energy U.S. Department of Energy under Contract No. DE-AC02-82CE40539. Details of the work performed are reported in "Task 4.0 Topical Report—The Development of a Coal/Water Slurry Fueled Diesel Engine for Industrial Cogeneration," DOE Report No. DE-AC02-82CE40539-04, Apr. 1986 and in "Development of a Coal/Water Slurry Fueled Diesel Engine for Industrial Cogeneration," DOE Report No. DE-AC02-82CE40539-06, Feb. 1987.

### References

- 1 Dunlay, J. B., et al., "Slow Speed Two-Stroke Diesel Engine Tests Using Coal Based Fuels," ASME Paper No. 81-DGP-12.
- 2 Smit, F. J., et al., "Properties of Ultra-Clean Coal-Water Slurry Fuels for Direct Fired Gas Turbines," ASME Paper No. JPGC-GT-5.
- 3 Keller, D. V., Jr., "Coal Slurries With Less Than One Weight Percent Ash," Fifth International Symposium on Coal Slurry Combustion and Technology, Vol. 1, Tampa, Florida, Apr. 25-27, 1983.
- 4 Rabinowicz, E., "Wear Coefficient Metals," Wear Control Handbook, ASME, New York, 1980.
- 5 Rabinowicz, E., *Friction and Wear of Materials*, Wiley, New York, 1965.

# Calculation of Integral Compressor Misalignments From Measured Web Deflections

**R. W. James**

Assistant Professor,  
Texas A&M University,  
College Station, TX 77843-3136

**L. E. Bishop, Jr.**

Senior Staff Engineer,  
Exxon Co., USA,  
Corpus Christi, TX 78403-2528

*Exxon's South Texas Division operates approximately 100 engine/compressors ranging from 1000 to 3400 hp (746-2535 kW) each. Traditionally, engine frame realignment procedures for these units have been basically trial and error. This paper presents an analytical procedure that eliminates much of the trial and error associated with engine frame realignment efforts by converting crankshaft web deflection readings to a profile of the main bearing shells. The program output indicates both the magnitude and direction of corrections that are needed to reduce any excessive web deflection readings. Raw field data are mathematically smoothed by a curve-fitting routine to provide insight on possible errors which could be easily overlooked in a visual examination of a web deflection survey. This paper addresses the key aspects of applying this approach in both routine evaluation and in major realignment work. Several examples are presented, including one case history showing how computer modeling of a 3400 hp (2535 kW) engine/compressor crankshaft profile permitted new chocks to be custom made before shutdown of the unit for realignment. This reduced downtime for the complete rechocking and realignment from 4 days to 14 h.*

## Introduction

Integral gas compressors are reciprocating natural gas compressors driven by gas-fired reciprocating engines integral to the same crankcase. These compressors operate at low speeds and high torques typically generating over 1000 hp (746 kW). Main bearing alignment in such relatively long crankcases is a critical factor in bearing and crankshaft maintenance. Main bearing misalignments are detected in practice by web deflection measurements. When the manufacturer's maximum allowable web deflection values are exceeded, the engine frame must be realigned. Realignment of misaligned integral compressors is presently an art, accomplished by experienced technicians based on intuition and trial and error using the web deflection measurements. The procedure described here allows a rational evaluation of measured web deflection data, resulting in calculated mean bearing alignment profiles. Such profiles are a valuable tool in the realignment process. In addition to reducing the dependence on the skill and experience of the individual technician, the method leads to significant reductions in downtime associated with realignment.

The literature does not include many recent reports of studies of integral gas compressor alignment or maintenance problems. Alignment and realignment of compressors was a topic of significant interest at the 41st Conference of the Diesel and Gas Engine Power Division of the ASME [1, 2]. Since that 1969 conference, interest has primarily been fo-

cused on the high technology problems associated with the rapidly developing field of gas turbine engines, with occasional reports of integral gas compressor problems surfacing [3-5]. The present economic demands on the gas processing and transmission industry, however, are renewing interest in innovative maintenance techniques.

## Web Deflection Measurements

Crankshaft web deflection measurements are measurements of the opening and closing of the space between the webs on either side of a crankshaft throw at various positions of crankshaft rotation. Figure 1, showing a portion of an ideal-

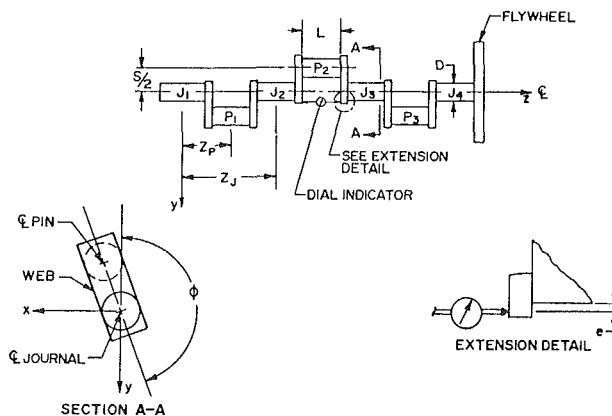


Fig. 1 Web deflection measurement procedure and notation

Contributed by the Internal Combustion Engine Division and presented at the Energy-Sources Technology Conference and Exhibition, Dallas, Texas, February 15-20, 1987. Manuscript received at ASME Headquarters November 12, 1986. Paper No. 87-ICE-3.

ized crankshaft, illustrates the method of measuring web deflections and introduces terminology used in the calculations presented here. A deflection dial indicator, usually with 0.001 in. (0.0254 mm) resolution, is installed in punched marks between crankshaft webs across a crank pin, diametrically opposite the journal axis from the crank pin. The indicator is zeroed at an arbitrary reference point, usually with the crank pin near bottom dead center (BDC), and the crankshaft is rotated manually. Rotation is halted at intervals of approximately 45 deg and the dial indicator extension  $\delta_e$  is read, usually estimating to the nearest 1/4 mil (0.00025 in. = 0.0635 mm) and recorded along with the estimated angular position of the indicator  $\phi$ . Typically, data can be obtained over an angular range of only 140 to 180 deg due to difficult access and interference from the connecting rod. The observed dial indicator reading  $\delta_e$  is corrected for the extension  $e$ , using the formula

$$\delta = \left( \frac{S+D}{S+D+2e} \right) \delta_e \quad (1)$$

### Method of Analysis

Assuming an initially straight crankshaft rotating in close-fitting misaligned bearing journals, the data  $\delta$  will be a harmonic function of the angular position  $\phi$ , of the general form

$$\delta(\phi) = A \sin \phi + B \cos \phi + C \quad (2)$$

The coefficients  $A$ ,  $B$ , and  $C$  that best fit the data can be determined by defining a residual  $r$

$$r = \sum_{i=1}^n [A \sin \phi_i + B \cos \phi_i + C - \delta_i]^2 \quad (3)$$

and writing the three linearly independent equations in  $A$ ,  $B$ , and  $C$ , to minimize the residual  $r$ ,

$$\frac{\partial r}{\partial A} = \frac{\partial r}{\partial B} = \frac{\partial r}{\partial C} = 0 \quad (4)$$

In matrix form, these equations become

$$\begin{bmatrix} \sum \sin^2 \phi_i & \sum \sin \phi_i \cos \phi_i & \sum \sin \phi_i \\ \sum \sin \phi_i \cos \phi_i & \sum \cos^2 \phi_i & \sum \cos \phi_i \\ \sum \sin \phi_i & \sum \cos \phi_i & n \end{bmatrix} \begin{Bmatrix} A \\ B \\ C \end{Bmatrix} = \begin{Bmatrix} \sum \delta_i \sin \phi_i \\ \sum \delta_i \cos \phi_i \\ \sum \delta_i \end{Bmatrix} \quad (5)$$

A solution  $A$ ,  $B$ , and  $C$  of the three linear algebraic equations is obtained and the maximum measured deflection  $d$  is the double amplitude of the harmonic function, given by

$$d = 2\sqrt{A^2 + B^2} \quad (6)$$

This system of algebraic equations is written and solved at each throw where web deflection data are available. Solutions  $A$ ,  $B$ , and  $C$  are obtained for each throw.

The parameters  $A$  and  $B$  can be related to the curvature at each throw assuming Euler beam behavior. The curvature in the horizontal plane is given by

$$\kappa_x = \frac{2A}{\left(\frac{D+S}{2}\right)L} = \frac{4A}{(D+S)L} \quad (7)$$

and the curvature in the vertical plane is given by

$$\kappa_y = \frac{4B}{(D+S)L} \quad (8)$$

Positive curvatures  $\kappa_x$  and  $\kappa_y$  imply that the deformed crankshaft is bowing to the right and upward, respectively, at that throw. Given curvatures at discrete points, here taken to be the centers of each of the crank pins, an equation for the elastic curve can be calculated. If there are web deflection data at  $m$  crank pins, then the resulting  $m$  discrete curvatures can be fit exactly to an  $(m-1)$  order polynomial in the axial coordinate  $z$ , or fit approximately to a polynomial of order less than  $(m-1)$ . Since the curvature is the second derivative of the deflection of the elastic curve, a curvature of order  $(m-1)$  corresponds to an  $(m+1)$  order elastic curve. The two additional coefficients in the  $(m+1)$  order polynomial elastic curve are arbitrary and can be chosen so that deflections are measured relative to a straight line between centers of end main bearings.

Here a fourth-order polynomial is fit to the discrete curvature data in both the horizontal and vertical planes. The determined fourth-order curve does not reflect any reduction in flexural stiffness due to the presence of the crankshaft webs. To correct for the effect of web flexibility requires a reduction in the calculated deflection of the elastic curve. Measured web deflections include some contribution from web flexure as well as from shaft flexure; therefore the actual curvature of the shaft centroidal axis will be less than the curvature calculated from the measured web deflection data. At present, an empirical correction factor for GMWA-8 crankshafts, and other geometrically similar crankshafts, has been determined. This factor is equivalent to multiplication of the calculated elastic curve deflection by 0.22 to yield an elastic curve corrected for web flexure. Data to obtain such empirical correction factors are scarce; however, numerical stress analysis methods may yield correction factors for other crankshaft geometries, and such an effort is in progress.

### Case Histories

As an example of the described procedure, consider the web

## Nomenclature

$D$  = main bearing diameter, in.  
 $S$  = stroke, in.  
 $L$  = length of pin, in.  
 $e$  = extension of dial indicator past extreme fiber of journal, in.  
 $J_i$  = throw number, numbered from end opposite flywheel

$P_i$  = throw number, numbered from end opposite flywheel  
 $Z_j, Z_p$  = distance from reference at center of  $J_1$  to center of main bearing or pin, respectively, in.  
 $\delta$  = extension of dial indicator, corrected for extension  $e$

(mil), i.e., corrected web deflection  
 $\delta_e$  = observed extension of dial indicator with respect to arbitrary zero (mil), i.e., web deflection  
 $\phi$  = angular position of dial indicator, clockwise from top as viewed from flywheel end, deg

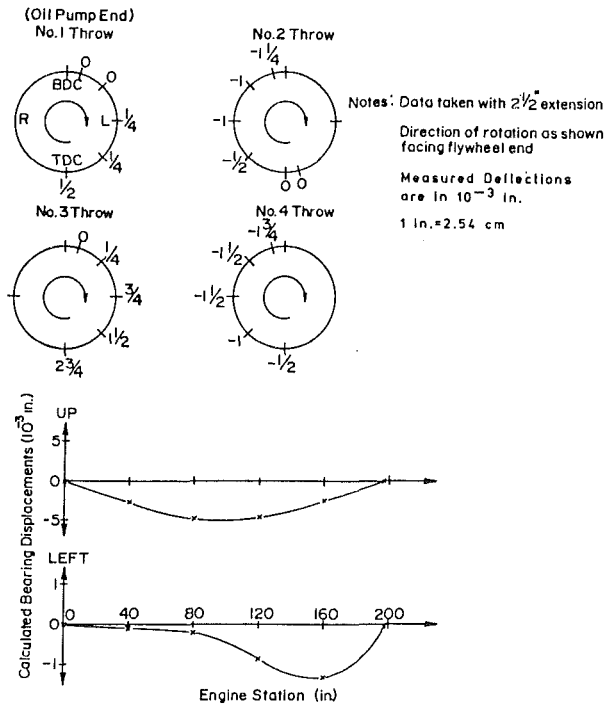


Fig. 2 Example 1: GMWA-8 web deflection data and bearing alignment properties

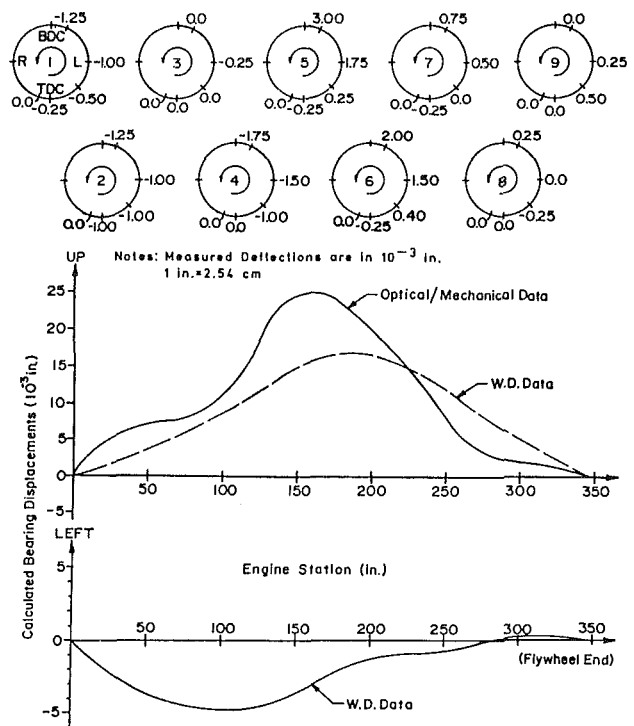


Fig. 4 Example 3: 410KVR web deflection data and bearing alignment profiles

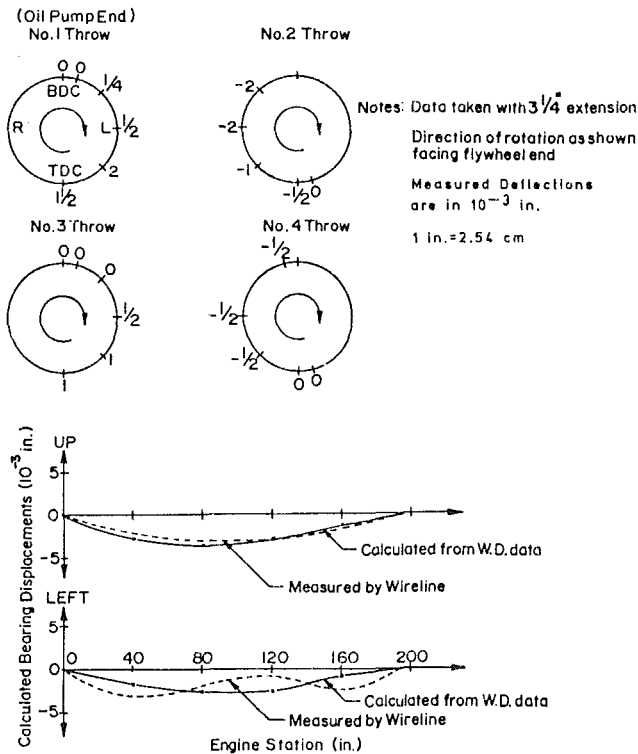


Fig. 3 Example 2: GMWA-8 web deflection data and bearing alignment profiles

deflection data shown in Fig. 2 from a 2000 hp (1491 kW) Cooper-Bessemer GMWA-8 compressor. The data of Fig. 2, when fit to equations of the form of (2), yield the intermediate results shown in Table 1.

The parameter  $C$  is not necessary for determining the curvatures, which depend only on  $A$  and  $B$ . The calculated main bearing displacement profiles are also shown in Fig. 2. The calculated bearing profiles indicate a "sagging" condition of

Table 1 Intermediate results for example 1

Throw No.	$A$ ( $10^{-3}$ in.)*	$B$ ( $10^{-3}$ in.)*	$d$ ( $10^{-3}$ in.)*	Phase angles (deg)
1	0.06499	0.19573	0.41	18
2	0.30842	-0.44869	1.09	146
3	-0.65281	-1.02030	2.42	213
4	0.50254	-0.50418	1.42	135

\* $10^{-3}$  in. = 0.254 mm.

approximately 5 mils (0.005 in. = 0.127 mm) relative to the two end main bearings and a smaller horizontal bowing to the right of approximately 1 mil (0.001 in. = 0.0254 mm). The vertical bearing misalignment could be corrected by replacement of chocks at interior anchor bolts by thicker chocks to counteract the sag shown in Fig. 2.

A second example involving a companion GMWA-8 compressor is described in Fig. 3. Shown for comparison are the horizontal and vertical main bearing alignment profiles as measured by wireline after removal of the crankshaft. The calculated main bearing alignment profile shows good agreement with the measured data from the wireline survey. The quantitative comparison is of course affected by the choice of the empirical correction factor, which was taken to be 0.22 for the GMWA-8 engine.

For a third example, a 3400 hp (2535 kW) Ingersoll-Rand 410KVR compressor is studied. Figure 4 summarizes the measured web deflection data and presents calculated main bearing profiles. For comparison, a measured vertical bearing profile is presented also. This was obtained by optical and mechanical measurements of the profile of the rail and of the base of the engine, which was milled plane and parallel to the centerline of the main bearings at the time of manufacture. The web deflection data were obtained during a preventive maintenance brief shutdown of the engine, and subsequently analyzed. After a decision to realign, the optical survey

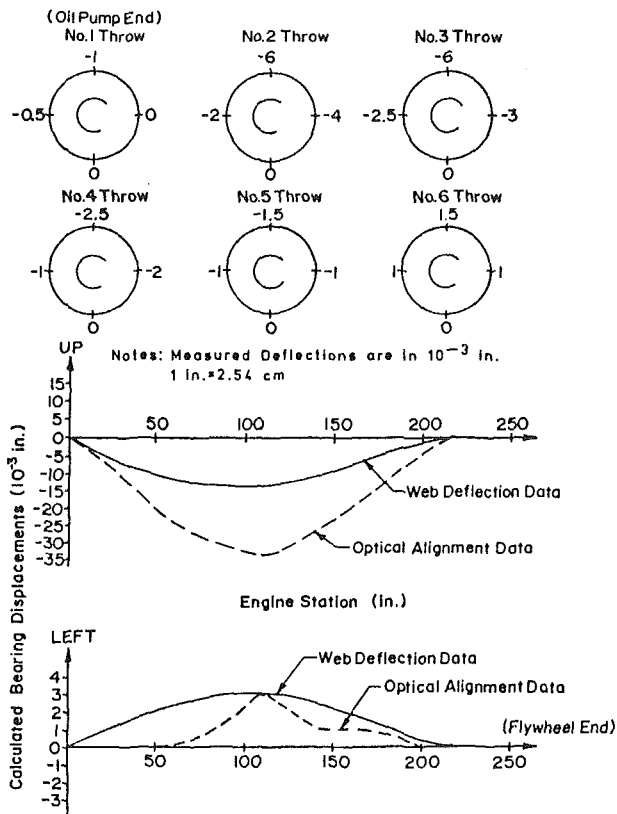


Fig. 5 Example 4: 412KVS web deflection data and bearing alignment profiles

measurements were made during engine operation to confirm the profile derived from the earlier web deflection measurements and to aid in determining the required thicknesses for new chocks. The new chocks were fabricated, and the engine was shut down for their installation. After replacement of the chocks, web deflection measurements were recorded, and the engine was put back into service. This procedure reduced downtime for realignment from an estimated 85 h to 14.5 h.

As a final example, an Ingersoll-Rand 412KVS engine is studied. Figure 5 shows the measured web deflection data and the predicted main bearing profile. Shown for comparison are the horizontal and vertical profiles as obtained by precision optical survey techniques using a K&E alignment telescope. The predicted main bearing profiles are generally less than the actual main bearing profiles as determined by the precision optical survey. The deviation is thought to be due to the use of the correction factor developed empirically for engines similar to the GMWA-8. Based on the comparison in this example, the correction factor for the 412KVS engine should be less than that for the GMWA-8 engine. Since the correction is a measure of the crankshaft curvature due to web flexure rather than shaft flexure, this result is not unexpected. The 11-in. (279 mm) diameter 412KVS shaft is likely to be more flexible relative to the webs than the 14-in. (356 mm) shaft of the GMWA-8 engine.

The validity of the correction factor discussed above and the contention that the correction factor is due to a greater degree of flexure in the webs than in the cylindrical sections of the shaft have been verified by an alternative mathematical model. Approaching the problem from the opposite perspective, one can assume that all flexure is in the webs. Such a separate analysis, assuming that all web deflection is due to flexure of the webs and including certain other geometric simplifying assumptions, generally confirmed the analysis in the example of the 410KVR engine. This separate analysis con-

firms the conclusion that most of the web deflection in the 410KVR crankshaft is due to web flexure rather than shaft flexure. Application of this geometrically simplified approach has been successful in a number of other field studies similar to those documented in this study.

## Summary and Conclusions

An analytical procedure has been developed to process web deflection data for reciprocating internal combustion engines, which yields calculated profiles of main bearing centerlines. This procedure will be of value to the responsible engineer by allowing observation of changes or trends in misalignment and by reducing downtime during realignment. Four case histories describing successful application of the method are presented, illustrating the measured web deflection data and the calculated compressor misalignment profile. The calculated profiles are compared with independent measurements. In one case history discussed, downtime for realignment has been reduced more than 80 percent, resulting in significant savings in lost production. With the use of the described procedure, the required alignment corrections can be determined from hot web deflection measurements prior to tearing down the engine. Corrective measures can be planned quantitatively in advance of teardown to reduce downtime. It should be pointed out that some alignment devices, such as metal chocks with shim packs, are more easily adjusted than other devices. Advance knowledge of required magnitudes of alignment corrections may not reduce downtime so dramatically for some designs.

It should be emphasized that the actual measurement of web deflections requires patience and expertise. Erroneous readings often result from measurements made under difficult conditions. Electronic displacement transducers are becoming more widely used for this task, which should improve the overall accuracy of the measurements. Whatever the method used, the readings should be repeatable. The method presented offers a partial check of the results in that a correlation coefficient is calculated that indicates the degree to which the data are fit by a sinusoidal function. If this coefficient indicates a poor fit, the analyst is forewarned that the data are erroneous.

## Acknowledgments

The work reported was sponsored by Exxon Company, U.S.A. South Texas Division, whose support is gratefully acknowledged. The authors are also grateful to El Paso Natural Gas Co., particularly Mr. David Ackerman, for certain data used to evaluate the procedure discussed in the paper.

## References

- 1 Bemiller, C. C., "Advances in Setting and Grouting Large Compressor Units," *Proceedings of the Diesel and Gas Engine Power Division of the American Society of Mechanical Engineers*, 41st Conference, Kansas City, MO, Apr. 1969, Paper No. 69-DGP-3.
- 2 Kauffman, W. M. (Moderator), "Panel Discussion: Engine Foundation and Mounting," *Proceedings of the Diesel and Gas Engine Power Division of the American Society of Mechanical Engineers*, 41st Conference, Kansas City, MO, Apr. 1969.
- 3 James, R. W., and Winston, W. G., "Predicting Creep Lifetimes for Epoxy Grouts Under Integral Gas Compressors," *ASME International Conference on Advances in Life Prediction Methods*, Albany, NY, Apr. 1983, pp. 217-222.
- 4 Charron, J. L., "Experimental Study of Oil Film Thickness, Journal Paths, Angular Misalignment and Clearance Variation in Diesel Engine Main Bearings," *ASME Paper No. 84-DGP-6*, 1984.
- 5 Tripp, H. A., and Drosjack, M. J., "Analysis of Reciprocating Compressor Piston Rod Failures," *ASME Paper No. 84-Pet-30*, 1984.

# Reciprocating Compressor Frame Distortion During a Cold Start

**A. J. Smalley**

Institute Engineer,  
Applied Physics Division,  
Southwest Research Institute,  
San Antonio, TX 78284

*This paper presents measurements of vertical and horizontal distortions of a compressor frame during the days following a cold start. The distortions are measured using a laser beam directed along the back of the compressor at the level of the bearings. Laser targets attached to the frame generate voltages proportional to the vertical and horizontal displacement of the targets relative to the laser beam. Data are acquired by a microcomputer and high-speed A-to-D converter. Coherent averaging techniques reduce the influence of vibration on these readings to a tolerable level. Frame distortion readings are supplemented by temperatures measured at a number of points on the compressor frame and foundation block. Averaged signals from laser targets and thermocouples are logged by the computer every 2 min. Two sets of results are presented: one for a compressor mounted on a concrete block with a sand-cement full bed grout, the other for a compressor mounted on epoxy chocks. Data for the full bed grout unit cover a 53-h period. Data for the chock-mounted unit cover a 96-h period. Both units show some unexpected distortion transients during the first 24 h, and the magnitude of these is significantly greater for the full bed grout unit. Both units exhibit pronounced swings in frame distortion as ambient temperature changes from day to night. This daily cycling with ambient temperature, in particular, shows the need for careful interpretation of isolated readings of frame or crankshaft bearing alignment. The frame distortion and temperature data are supplemented by predictions of nominal crankshaft bending stress resulting from the observed misalignment.*

## Introduction

In May 1983, a project was initiated at Southwest Research Institute (SwRI), under sponsorship of the Pipeline Research Committee (PRC) of the American Gas Association (A.G.A.), to investigate crankshaft misalignment. The title established for this program is "Crankshaft Stress Reduction through Improved Alignment Practice."

The PRC has set challenging goals for this program. In essence it is to develop scientific methods of measurement and analysis, bringing them to bear on the time-honored art of crankshaft alignment. The program is being carefully executed and monitored, with initial results helping to guide future planning.

During the first year of the project laboratory test and analysis techniques were developed for characterizing crankshafts; results gave relationships between stresses and web deflections and showed that existing criteria (Caldwell, 1951) were safely conservative, but not unreasonably so.

Some subsequent effort has been directed at developing and applying methods for continuously monitoring changes in alignment following startup of a large engine/compressor. This work forms the subject of the paper which follows.

Contributed by the Internal Combustion Engine Division and presented at the Energy-Sources Technology Conference and Exhibition, Dallas, Texas, February 15-20, 1987. Manuscript received at ASME Headquarters November 12, 1986. Paper No. 87-ICE-4.

## Background

Users of large reciprocating engine/compressors are concerned about alignment of such units and the influence of misalignment on crankshaft stresses. Probably the most widely employed method of monitoring the state of alignment of an engine is to measure crankshaft web deflections. These are the peak-to-peak change in separation of web faces for each throw of the crankshaft measured with dial indicators as the engine is barred over. A criterion exists (Caldwell, 1951) for allowable web deflections as a function of engine stroke. Periodic optical measurement of changes in compressor frame alignment is also quite widespread. However, it is not clear that a similar criterion for changes in frame alignment is available.

It has long been recognized that the heat generated by the engine, bearings, and sump can influence distortion of the foundation and frame when the unit is running. It is believed that there is a tendency for foundations to develop a hump at their center, particularly in the case of very long engines. In one example (Stenberg, 1963), crankshaft failures were quite convincingly associated with thermal distortions.

The use of chock mounting is increasing in popularity, and one reason is the belief that this approach to engine mounting causes less distortion of the frame, foundation, and crankshaft.

There are considerable difficulties in making measurements that truly reflect the hot state of engine alignment. Clearly, dial indicator readings of web deflections can only be made



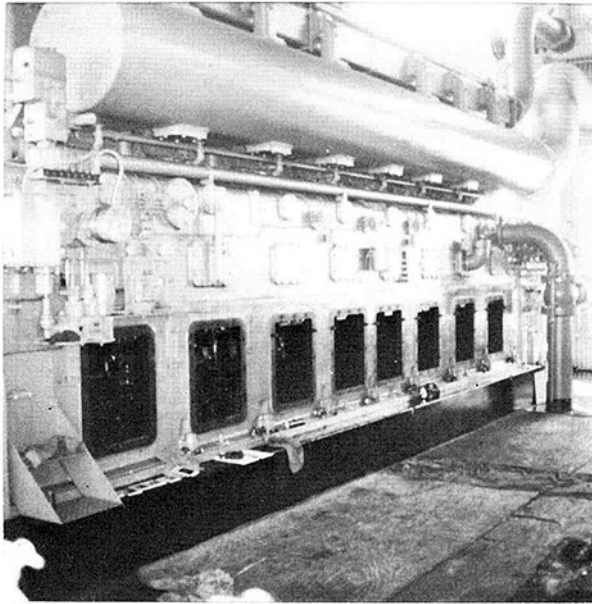


Fig. 1 Full bed grouted HBA-8 prior to test

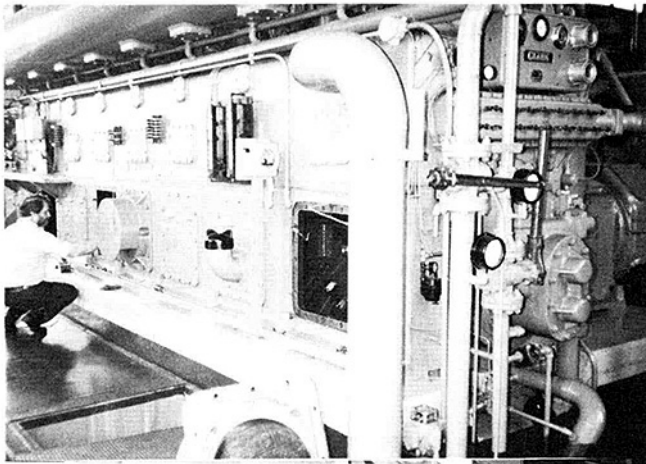


Fig. 2 Photo of chock-mounted unit prior to test

when the engine is stopped, and it is difficult to install dial indicators immediately after shutting down a unit. An added complication is that the dial indicator cannot be maintained in position for a complete revolution of any crank throw (unless the connecting rods are removed!). Optical measurements of frame misalignment do not require access to a hot crank case, but normally require the engine to be stopped for reliable readings to be obtained. A set of optical readings at each bearing takes about 30 min, so it is difficult to use optical methods for continuous monitoring of an engine over a period of hours or days.

The studies described in this paper were undertaken for a number of reasons:

- 1 To help understand the nature of compressor frame and bearing thermal misalignments.
- 2 To gain some information on short-term misalignment transients and variability in thermal misalignment.
- 3 To compare similar units mounted on a full bed grout and on chocks.
- 4 To evaluate the use of a laser system for continuously monitoring the alignment of an engine.

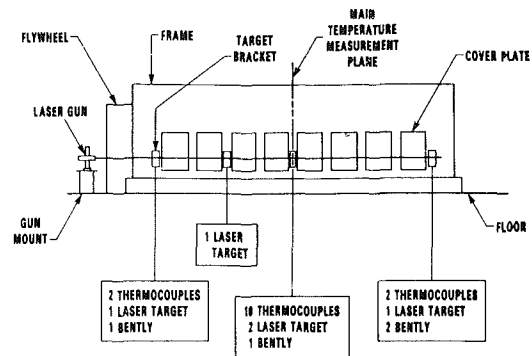


Fig. 3 Overview of external measurement (full bed test)

Two different tests are described, each involving the startup of an initially cold unit. In each case, frame distortions were measured by targets, attached to the frame, through which a laser beam was fired. Temperature measurements were recorded on the frame, at various points within the crank case, and on the foundation block. Data were acquired and averaged by a computer at approximately 2-min intervals. One test lasted about 50 h; the other test lasted about 100 h.

The first unit tested was mounted on its concrete block by a sand-cement full bed grout. The block and grout appeared in good condition though they had been installed more than 20 years earlier. The concrete block was more than 10 ft (3 m) tall and extended from the floor of a basement; thus the sides of the block were exposed and accessible.

The second unit tested was mounted on a series of epoxy chocks, about 1.5 in. (38 mm) thick and 8 in. (200 mm) wide, one under each bearing. These chocks separated the unit from a 12 to 14-in. (300 to 350 mm) thick layer of epoxy material, below which was the original concrete block. There were about eight expansion joints running the width and depth of the epoxy layer. The concrete block was about 6 ft (2 m) tall and, in this case, there was no basement from which the block could be accessed. The unit was separated from the foundation by air space in all locations but the sole plates. The unit's previous full bed grout had been replaced with this arrangement about a year earlier.

As will be seen, the most severe distortion transients occurred during the first 24 h of testing. The chock-mounted unit generally exhibited less severe distortion transients. Significant variations in distortion would occur apparently as a function of variations in ambient temperature, including day to night variations. Encouraging agreement was obtained between sets of optical data and the laser measurements.

### Test Description

A full bed grouted unit in Refugio, TX was tested in Apr. 1984 and a chock-mounted unit in Marietta, Pennsylvania was tested in Aug. 1985. In both cases, the unit was a Clark HBA-8 with four double-acting, horizontal, compressor cylinders, eight in-line, vertical, power cylinders, and two scavenge cylinders. Nominal speed of the unit is 300 rpm. Nominal horsepower is 1760 (1340 kW). There is a single bearing between each pair of crankshaft throws, a bearing at each end of the shaft, and an extra bearing (No. 10) beside the flywheel. Figure 1 is a photo of the full bed grout unit. Figure 2 is a photo of the chock-mounted unit. The individual chocks at each tie-down point may be seen between frame and foundation of the chock-mounted unit. These epoxy chocks provide the only points of support for the compressor frame. The remainder of the frame, sump, and oil pan are freely suspended.

Figure 3 is a test schematic for the full bed unit, which shows the laser gun mounted off the floor at bearing level, firing a beam horizontally down the back of the unit. The beam

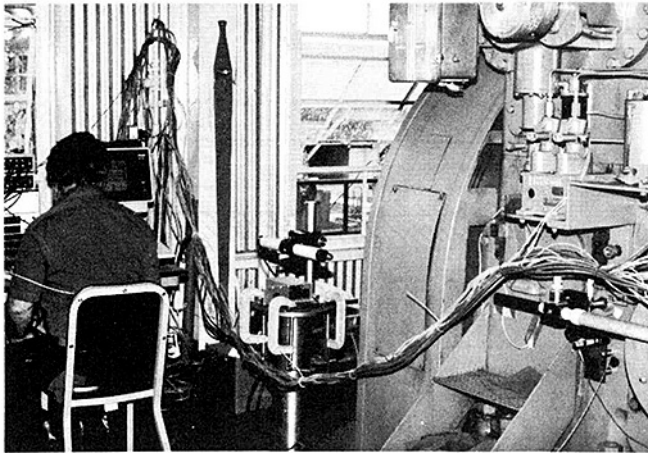


Fig. 4 Photo showing laser gun and Bearing 9 target (full bed test)

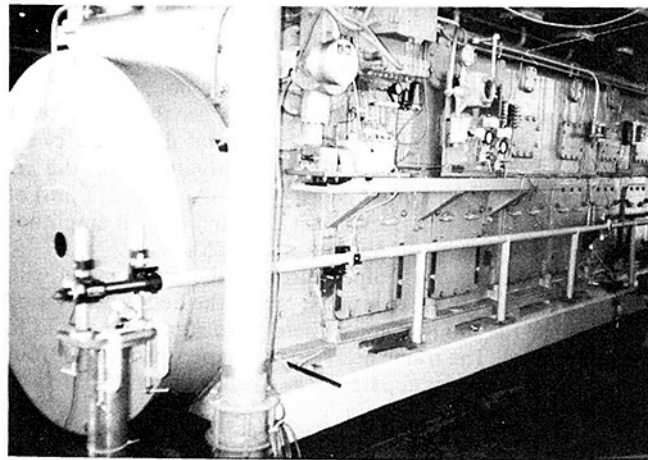


Fig. 5 Laser gun and target with shield tubes (chock mount test)

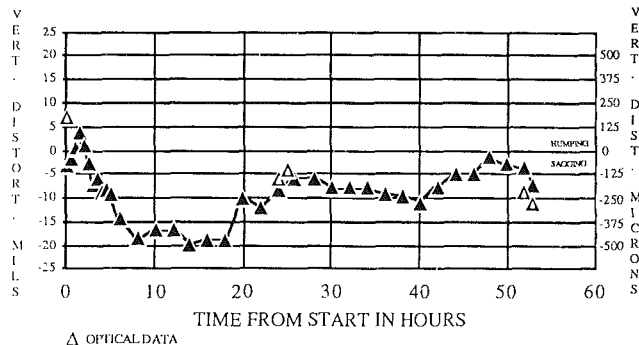


Fig. 6 Vertical distortion of Bearing 5 relative to a line joining Bearings 1 and 9 as a function of time (full bed grouted unit)

passes through four targets attached to the frame at Bearings 1, 5, 7, and 9 (counting toward the flywheel). All targets except that farthest from the gun contain a beam splitter, which reflects approximately 30 percent of the incident light onto a four-quadrant photo cell. Voltage outputs proportional to horizontal and vertical displacement of laser beam relative to the center of the target are obtained. In the target farthest from the laser gun all incident light falls directly on the photo cell; otherwise this target provides a similar pair of outputs proportional to horizontal and vertical displacements. For the chock mount test only three targets, at Bearings 1, 5, and 9, were used. During the full bed test, several sets of optical alignment data were taken for comparison with the laser measurements.

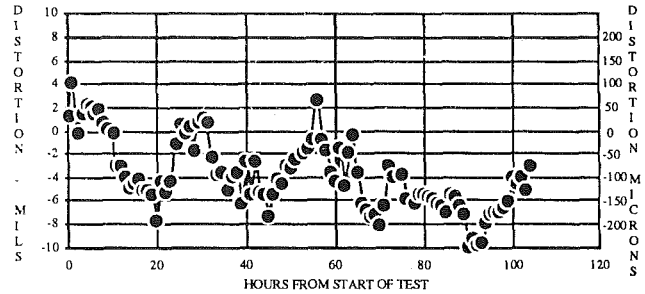


Fig. 7(a) Vertical distortion of Bearing 5 relative to a line joining Bearings 1 and 9 (chock mount test)

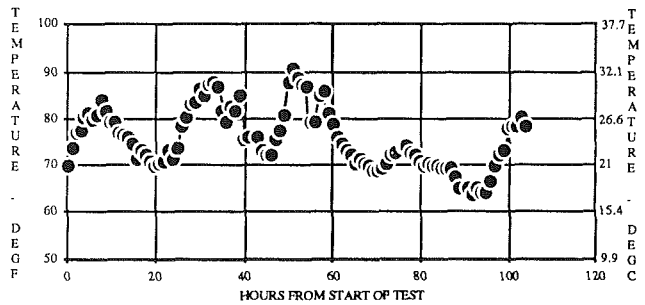


Fig. 7(b) Variation of ambient temperature (chock mount test)

Figure 4 shows the laser gun and targets at Bearing 9 for the full bed test. Figure 5 shows an overview of the test for the chock-mounted unit. Clearly visible in this figure are the shield tubes suspended between the laser targets, which ensured that the laser beam was not disturbed by changes in ambient light, dust particles, camera flashes, etc.

In addition to the laser measurements, 15 or 16 thermocouples were deployed at various points including the housings of Bearings 1, 5, and 9, the compressor frame level with Bearings 1, 5, and 9, the water jacket, the base of the compressor frame, the top of the block, and several points lower down in the block. During the full bed test, several sets of optical distortion data were taken for comparison with the laser measurements.

## Test Results

Figure 6 shows the variation in vertical distortion of the full bed grout unit during the 53-h test. Vertical distortion is calculated as the vertical displacement of the target at Bearing 5 relative to a straight line joining the targets at Bearings 1 and 9. Positive distortion in Fig. 6 means that Bearing 5 has moved up relative to the end bearings. Negative distortion means that Bearing 5 has moved down. Initial distortion is positive for a short period of perhaps 2 h, but a sustained period of negative distortion follows. About 8 h into the test the distortion reaches about 18 mils (460  $\mu\text{m}$ ) negative and maintains a similar level for another 10 h from 10:00 p.m. to 8:00 a.m. the following day. After the first 18 h of the test, the distortion starts to increase from its extreme negative value and, over the last half of the test, cycles between about  $-11$  mils ( $-280 \mu\text{m}$ ) and  $-2$  mils ( $-50 \mu\text{m}$ ). The distortion has its most strongly negative values during the cold hours of the night, and its least negative values during the warm of the day.

Several optical measurements were taken, when the unit was not running; just before the test; just after the test; and during a 1-h shutdown in the middle of the test. These optical readings are superimposed on Fig. 6 and, while not agreeing precisely with the laser data, they clearly confirm the trend that, relative to the start of the test, the unit develops a sagging condition during the elapsed 53 h of the test.

Vertical distortion for the chock-mounted unit over the 96 h of the test is shown in Fig. 7. Included for direct comparison is

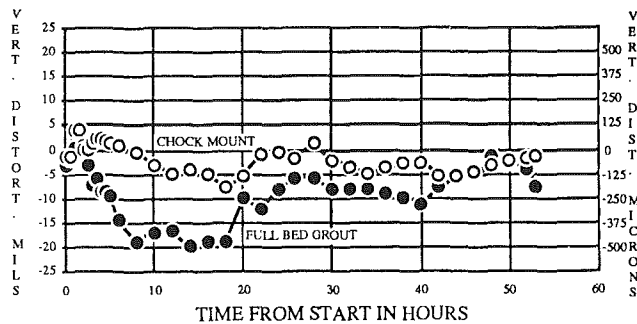


Fig. 8 Comparison of vertical distortion for sole plate and full bed grout units over first 53 h of test

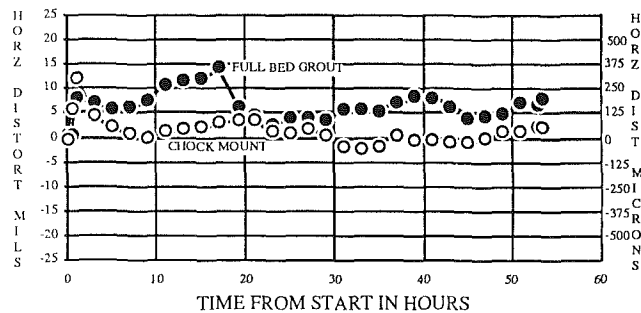


Fig. 9 Comparison of horizontal distortion for chock mount and full bed grout units over first 53 h of test

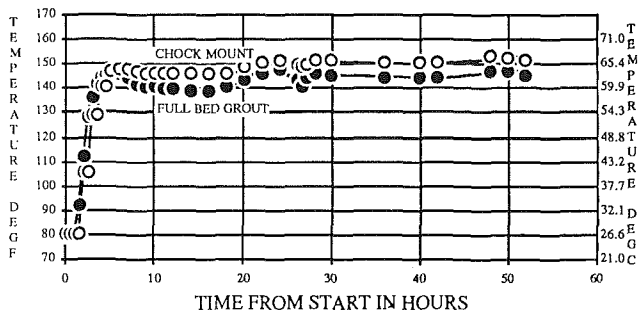


Fig. 10 Comparison of temperatures on frame at Bearing 5 for chock mount and full bed grout units over first 53 h of test

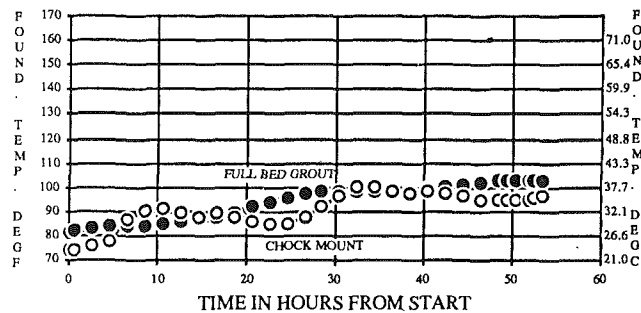
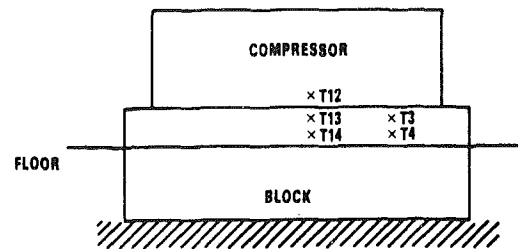


Fig. 11 Comparison of temperatures near top of block at Bearing 5 for chock mount and full bed grout units over first 53 h of test

a plot of ambient temperature as a function of time. There is almost 10 h of mild positive distortion (2 to 4 mils) (50 to 100  $\mu\text{m}$ ) followed by about 10 h of 4 to 6 mils (100 to 150  $\mu\text{m}$ ) negative distortion. Apart from the first 10 h, when the unit is heating up internally, the distortion rather closely follows the ambient temperature. This apparent correlation with ambient temperature means that vertical distortions can vary over a 24-h day by 10 mils (250  $\mu\text{m}$ ) or more.

Figure 8 directly compares the chock mount and full bed grout vertical distortion over 53 h from the cold start. Trends



DATE	UNIT NO.	MOUNT	T2	T4	T12	T13	T14
8/28	2	CHOCK	98.3/36.7	97.7/36.4	134.1/56.6	97.1/36.1	94.3/34.5
8/28	5	FULL BED	99.737.5	101.0/38.2	136.6/58.0	98.5/36.8	97.4/36.2
8/30	2	CHOCK	93.6/34.1	96.835.9	129.0/53.8	95.0/34.9	94.2/34.4
8/30	5	FULL BED	95.1/34.9	99.337.3	131.7/55.3	95.9/35.4	95.6/35.2

Fig. 12 Comparison of temperatures on Units 2 and 5

are qualitatively similar but the chock-mounted distortions are less severe.

Figure 9 compares horizontal distortion for the two units. Most significant here is the transient positive distortion (bowing outward) of about 14 mils (360  $\mu\text{m}$ ) for both units. This occurs within the first 2 h for the chock-mounted unit and after about 18 h for the full bed unit. After this initial transient, the chock-mounted unit's horizontal distortion cycles with 5 mils (125  $\mu\text{m}$ ) peak-to-peak amplitude for the remainder of the test, but stays within about 3 mils (75  $\mu\text{m}$ ) of zero. The full bed unit cycles with a 5 mil (125  $\mu\text{m}$ ) amplitude and an average value of about 5 mils (125  $\mu\text{m}$ ).

Figure 10 compares temperatures on the frame, level with Bearing No. 5, for the two units. While the detailed variation is different for the two units, there is no significant trend to the difference. The frame heats up over a period of about four hours and then cycles apparently as a result of variation in ambient temperature.

Figure 11 shows distinct differences in behavior of temperature at the top of the block near Bearing 5 for the two units. The full bed grout unit exhibits very slow response to changes in temperature of the compressor and ambient. It appears to be undergoing very slow heating from the compressor, which is modulated by the day to night variations in temperature, but remains monotonically increasing. The chock-mounted unit, on the other hand, seems to heat up faster at the top of the block and to exhibit distinct cyclic reversals in temperature variation as a result of day to night ambient temperature variations.

Figure 12 presents temperature data taken at the site of the chock mount test. At this station, there were a number of units identical in every way except for the fact that some were chock mounted and some were full bed grouted. Using a hand-held temperature measurement device, temperatures were recorded on the base of the frame and at four points on the block corresponding to similar points on the unit being tested with thermocouples. These measurements cannot be viewed as having the same absolute accuracy as the thermocouples, which were imbedded in the block, but a consistent procedure was followed and it is reasonable to compare the two sets of data obtained with the hand-held device. The measurements were repeated on two different days and show the full bed grout to be consistently hotter than the chock-mounted unit by 1° to 4°F (0.5 to 2°C).

Thermocouple data taken at the end of the full bed test show a temperature of 143°F (61.5°C) at the compressor base and 103°F (39.3°C) at the top of the block, a difference of 40°F (4.3°C). At the end of the chock-mounted test, temperature at the top of the block is 96°F (35.4°C) and at the base of the unit is 138°F (58.8°C), a temperature difference of 42°F (5.4°C).

Figure 13 shows measurements obtained with noncontact displacement probes cantilevered from the inside of the com-

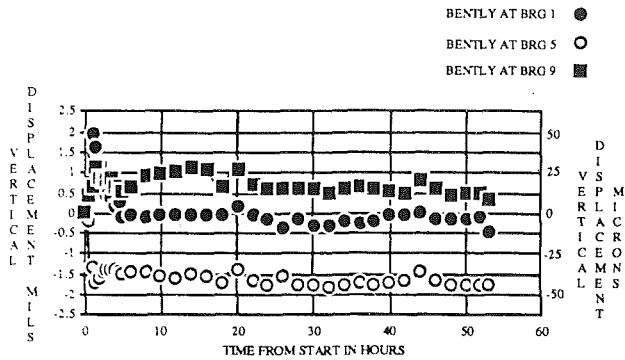


Fig. 13 Variation in vertical deflection of bearings relative to case at Bearings 1, 5, and 9—full bed grouted unit

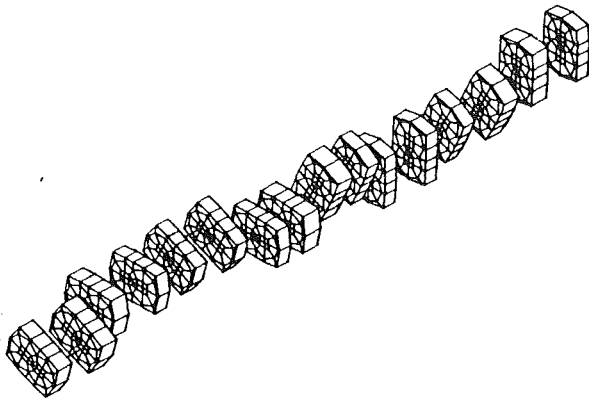


Fig. 14 Three-dimensional isometric model check plot

pressor frame looking at the bearing housings. These were check measurements designed to verify that the displacements of the bearings would follow closely those of the frame. The data were taken during the full bed grout test, and it may be seen that maximum deviations which occur at Bearing 5 are less than 2 mils ( $50 \mu\text{m}$ ). This small difference provides justification for relying on external frame measurements.

### Analytical Results

A finite element model of the crankshaft was used to calculate stresses in the crankshaft when made to rotate in a set of bearings offset from each other by the amounts indicated by the frame distortion. The finite element model, which has been previously documented and verified (Smalley and Palazzolo, 1984) is shown in Fig. 14. Crankshaft webs were modeled as solid elements. The crank pins and main journals were modeled as beams connected to the solid webs by arrays of rigid links.

Figure 15 shows the horizontal and vertical displacements imposed on the chock-mounted shaft. A corresponding set of displacements was imposed for the full bed grout unit and differed mainly in that the displacements were larger and predominantly vertical. It was necessary to infer displacements at each bearing from available data at a smaller number of bearings. This inference was guided by the availability of the fourth laser target at Bearing 7 in the full bed grout test.

Figure 16 shows the predicted nominal stresses at main journal, web, and crank pin of the crankshaft for both units. The highest stress for the full bed unit is predicted to be approximately 3000 psi (21 MPa), and for the chock-mounted unit approximately 1800 psi (12.5 MPa). The highest predicted stress occurs in the crank pin. Based on material data for the crankshaft, its ultimate tensile strength is estimated at approximately 85,000 psi (590 MPa), and from Wilson (1965) the safe

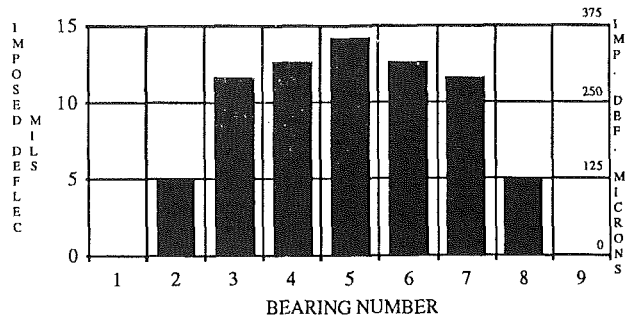


Fig. 15(a) Imposed horizontal deflections at each bearing as input for stress prediction analysis—chock-mounted unit

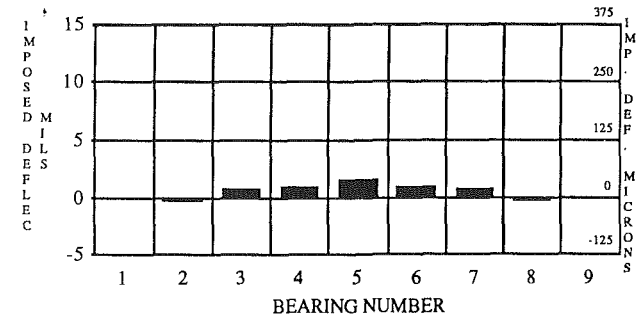


Fig. 15(b) Imposed vertical distortions at each bearing as input for crankshaft stress prediction analysis—chock-mounted unit

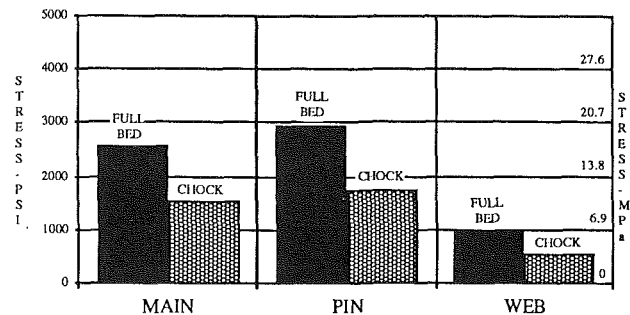


Fig. 16 Comparison of stresses at main journal, crank pin, and web for full bed and chock-mounted units

working stress for combined bending and torsion is about 8000 psi (55 MPa) peak-to-peak. Thus, the stresses induced by misalignment are significant, but should normally be safe relative to working stress levels for the shaft material, provided no other causes of excessive stress are present.

### Technical Discussion

The tendency to develop a sagging condition of the engine frame during these tests was not an expected result; however, it was confirmed by optical data in one test and, upon careful review, does not appear strongly to contradict other sources, particularly the data of Stenberg for a 4200 hp (3200 kW) diesel engine of length similar to the engine tested here. Stenberg's data show, for a rail-mounted unit, after 34 days running, that the foundation block developed more than 25 mils ( $635 \mu\text{m}$ ) elevation at its center relative to the end bearing locations. However, the engine frame at the level of the crankshaft developed no perceptible distortion up or down; it was still level in spite of foundation block distortions.

At the end of the four-day chock-mounted test reported in this paper there was about 8 mils ( $200 \mu\text{m}$ ) sag, which actually differs from zero by less than the observed 10 mils ( $250 \mu\text{m}$ ) range of day-to-day cycling. Indeed near the end of the second

and third days of the chock-mounted test Fig. 7(a) shows the existence of a momentary hump in the engine frame at crankshaft centerline.

Thus the longer term tendencies of the engines involved in these tests may differ only in degree from other engines.

The emphasis in these results has, however, been on short term trends which do raise some concerns. The first concern is that the early hours following a cold start are the most severe. Although the stresses predicted for the full bed grout unit were not excessive, the high distortion condition lasted for eight to ten hours during which close to 200,000 cycles of stress reversal would have been imposed on the crankshaft. To reduce the severity of cold start transients there may be merit to maintaining warm sump oil even when a unit is stopped.

A second concern is that the practice of setting the center of a unit down in order to compensate for anticipated "humping" of the block and frame when it gets hot can be expected to compound the misalignment stresses resulting from short-term transient "sagging" of the frame, if such sagging is present in other units.

It is also clear that the daily cycling of frame distortion is a significant factor to be dealt with in periodic assessment of the state of alignment of a reciprocating compressor. If, for example, a set of optical readings on targets attached to fixed points on the frame is taken every three months on a unit, the measurements of this paper suggest that the results obtained by this periodic monitoring will be significantly influenced by the ambient temperature conditions and the time of day; there could easily be a 10 mil (250  $\mu\text{m}$ ) band of uncertainty in the results for the vertical position of the center of the unit relative to its ends. Any monitoring program should be set up to account for this potential uncertainty. Some approaches which might be beneficial are to ensure that readings are taken at about the same time each day on a particular unit, and that the unit has been running for several days when a set of readings is taken. Desirably, ambient temperature and block temperature should be documented at the same time.

The results for chock-mounted and full bed grouted units, when compared, provide some positive evidence for the benefits of chock mounting. Transient vertical distortion appears to be significantly less than for the full bed grout unit. Probable contributory reasons are the reduced heat transfer to the block resulting from the air space between the base of the unit and the grout, and a reduced tendency of the block to distort because of expansion joints which lie in a plane, perpendicular to the crankshaft centerline, in the grouted top 12 in. (300 mm).

The fact that the relative displacement between frame and bearings as measured by a cantilevered displacement probe was less than 2 mils (50  $\mu\text{m}$ ) throughout the test provides some encouragement for inferring bearing misalignment information from frame misalignment measurements.

The field measurement method has demonstrated its ability to provide a continuous readout of change in vertical and horizontal alignment. The method does, however, require careful planning for each application and close monitoring throughout the tests to ensure continually satisfactory data.

## Summary and Conclusions

Based on the measured and predicted results, the following conclusions are drawn:

1 The laser measurement system and computerized data acquisition have proven their ability to monitor the continuous variations in alignment of a reciprocating compressor frame.

2 Both the full bed grouted unit and the chock-mounted unit showed a tendency to develop a "sagging" condition at the center during the period of the test.

3 Both units showed the most extreme distortions in the first 24 h of the test.

4 The magnitude of vertical distortions in the first 24 h was distinctly less for the chock-mounted unit than for the full bed grouted unit (7 mils versus 20 mils) (180  $\mu\text{m}$  versus 500  $\mu\text{m}$ ).

5 Both units showed a daily cycling in the vertical distortions.

6 Transient extremes of horizontal distortion were similar for both units (14 mils) (360  $\mu\text{m}$ ).

7 Frame and bearing temperatures followed similar trends for both units:

- Operating temperature was reached in 3 to 4 h.
- Bearing 5 temperature was cooler than those of 1 or 9.
- Temperature showed 5 to 10°F (2.5 to 6°C) daily cycling.

8 Temperature at the top of the block for the chock-mounted unit responded more rapidly to changes in compressor and ambient temperature than the full bed grout and showed a more distinct day-night cycle.

9 One-for-one comparison on two other units at the test site, one chock mounted and one full bed grouted, showed the chock mount unit's block to be cooler near its top by 1° to 3°F (0.5 to 2°C).

10 Using the largest measured distortions from each test as input, misalignment severity analysis showed the chock mount maximum crankshaft stress to be 1800 psi (12.4 MPa) peak-to-peak, compared to over 3000 psi (21 MPa) peak-to-peak for the full bed grouted unit.

## Acknowledgments

The author wishes to thank the Pipeline Research Committee of the American Gas Association for permission to publish this material; the Compressor Research Supervisory Committee for their active support, advice, and encouragement both as a body and through their representative Ad-Hoc Committee; PRC member companies for the loan of crankshafts for evaluation; Mr. David Hatch whose painstaking efforts in testing and data acquisition contributed to the success of this project; and to Ms. Linda Bauer for editorial contribution.

## References

- Caldwell, J. H., 1951, "Practical Preventive Maintenance for Gas Engines," Cooper Bessemer Corp.
- Smalley, A. J., and Palazzolo, A. B., 1984, "Crankshaft Stress and Deflection Relationships for Large Reciprocating Compressors," *American Gas Association Operating Section Proceedings*, pp. 351-357.
- Stenberg, R. A., 1963, "Alignment of Large Diesel Engines," Engineering Institute of Canada, Paper No. EIC-63-MECH 14.
- Wilson, W. K., 1965, *Practical Solution of Torsional Vibration Problems*, Vol. 3, 3rd ed., Chapman and Hall Ltd., London, pp. 26-27.

**D. W. Eckard**  
Development Engineer.

**J. V. Servé**  
Manager, New Engine Development.

Cooper Industries—Superior,  
Springfield, OH 45503

# Maintaining Low Exhaust Emissions With Turbocharged Gas Engines Using a Feedback Air-Fuel Ratio Control System

*Maintaining low exhaust emissions on a turbocharged, natural gas engine through the speed and load range requires precise control of the air-fuel ratio. Changes in ambient conditions or fuel heating value will cause the air-fuel ratio to change substantially. By combining air-gas pressure with preturbine temperature control, the air-fuel ratio can be maintained regardless of changes in the ambient conditions or the fuel's heating value. Design conditions and operating results are presented for an air-fuel controller for a turbocharged engine.*

## Introduction

Low exhaust emissions can be maintained on a turbocharged engine by controlling the engine's air-fuel ratio. To control the air-fuel ratio, many variables must be considered. These variables include ambient temperature, barometric pressure, air manifold pressure and temperature, fuel heating value, ignition timing, and engine speed. Proper control of these parameters is a key element to maintaining low exhaust emissions throughout the engine speed and load range.

Precise air-fuel ratio control is beyond the capability of a simple carburetor. The carbureted air-fuel ratio can be set at a single point with the help of an oxygen meter or a CO meter, but a change in load or speed will require resetting. The design of carburetors is such that the air-to-fuel ratio will change significantly as the engine moves from a high flow condition to a low flow. Also a carbureted system is insensitive to fuel heating value, fuel or air temperatures, or ambient pressures. It is a volume flow device which merely uses air pressure drop to determine the quantity of fuel added.

To maintain exhaust emissions requires a feedback controller. A pneumatic controller, which adjusts air manifold pressure based on gas manifold pressure and engine speed, was developed with the introduction of Superior's CleanBurn engines in 1981. The pneumatic controller was able to control the air-fuel ratio throughout the engine's load and speed range as was demonstrated in over 35 on-site tests. Many of these tests were performed by independent agencies.

The pneumatic controller has some limitations though. It requires external controls to maintain air and gas manifold temperatures. Also, it could not adjust for fuel heating value changes. Individual air-fuel curves were supplied for each engine which accounted for site elevation and fuel heating

value. When a change in the heating value occurred, a new air-fuel curve had to be developed and the pneumatic controller adjusted for this new curve.

To be able to compensate for changes in ambient conditions and fuel heating value another engine parameter had to be monitored. During the early development period, direct measurement of oxygen in the exhaust was considered as a potential control variable. Eventually, it was determined that a thermocouple based control system could provide equivalent or superior control. In addition, cost and system complexity were reduced.

Preturbine temperature is a reliable indication of the engine air-fuel ratio. For a given fuel heating value, air manifold pressure and engine load, the preturbine temperature is repeatable. If the heating value changes and the load remains constant, the air-fuel ratio and preturbine temperature will change. If the air manifold pressure is adjusted to return the preturbine temperature to its original value, the air-fuel ratio will also return to the correct ratio to maintain exhaust emissions. Thus by including the preturbine temperature in the control scheme, the controller will be able to compensate for heating value changes.

## Controller Specifications

The basic design considerations such as long life, minimum operator interface, and high accuracy were specified. Besides the basic considerations, the controller had to be field programmable and self-compensating for ambient conditions and fuel heating value. It also had to be able to be installed on any Superior CleanBurn engine with a minimum of changes.

Many engines operate unattended for long periods and in critical applications. Safety systems had to be incorporated into the controller to insure safe engine operation in the event of a failure.

Contributed by the Internal Combustion Engine Division and presented at the Energy-Sources Technology Conference and Exhibition, Dallas, Texas, February 15-20, 1987. Manuscript received at ASME Headquarters November 14, 1986. Paper No. 87-ICE-2.

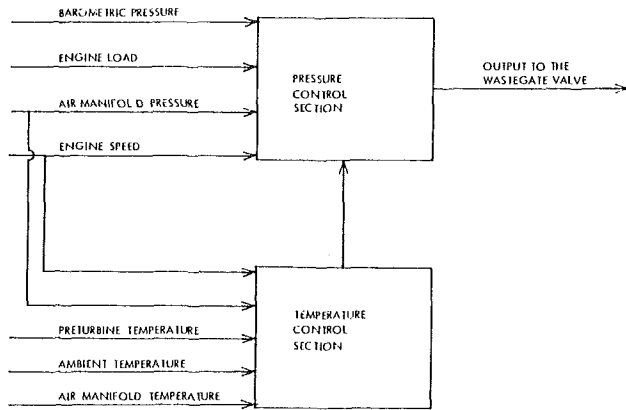


Fig. 1 Controller block diagram

### Controller Description

The controller is a self-powered, microprocessor based, two-level cascaded system. The purpose of the controller is to adjust the air-fuel ratio by positioning a wastegate valve, which bypasses exhaust gas around the turbocharger, based on the input data. Figure 1 is a block diagram of the controller.

The controller has two control sections—pressure and temperature—that were designed to work together to control the air-fuel ratio. The controller analyzes the input data, compares the data to the calculated set point, and makes a correction if necessary.

Since the controller is self-compensating, air-fuel curves that were supplied with the pneumatic panel are no longer required. These curves were based on site elevation and fuel heating value to insure that the engine operated on the correct air-fuel ratio to maintain low exhaust emissions regardless of engine speed or load. The air-fuel data sheet with the correct constants for each engine model is now supplied. Figures 2 and 3 are samples of an air-fuel ratio data sheet and the pneumatic curve. The constants have been developed by mapping each engine for various loads and speeds. If the constants are the same as the air-fuel data sheet, the engine is operating at the correct air-fuel ratio.

The controller can display various engine parameters. Desired (set point) as well as actual air manifold pressure and preturbine temperature can be viewed. The other engine parameters that may be displayed are gas manifold pressure, engine speed, and site barometric pressure.

The controller is mounted on a panel that also has the pneumatic starting logic. The panel has the same dimensions as the pneumatic panel, which makes field retrofits easy.

### Development Program

A long and thorough test program, which included both laboratory and field evaluation, was conducted to insure the controller would work correctly. The pressure control section had already been proven based on the pneumatic panel, but the temperature section had to be thoroughly tested to insure the controller could compensate for fuel heating value changes and ambient temperature changes.

The engine used in the laboratory development was a six-cylinder, turbocharged, four-cycle, spark ignited gas engine rated at 1106 kW (825 brake horsepower). It utilizes the lean combustion, prechamber concept for emissions control.

Both digital and analog approaches were evaluated for a controller. The digital system was chosen because of the complexity required to use pressure and temperature control. A special microprocessor using ROM was designed and built and contains two circuit boards.

AFR DATA SHEET NO: \_\_\_\_\_

Recommended Air Fuel Ratio Data for:

ENGINE MODEL: \_\_\_\_\_ IMEP: \_\_\_\_\_

SERIAL NO: \_\_\_\_\_ SITE: \_\_\_\_\_

AIR MANIFOLD TEMPERATURE: \_\_\_\_\_ ELEVATION: \_\_\_\_\_

AIR FUEL RATIO CONSTANTS

PRESSURE: PX \_\_\_\_\_ PY \_\_\_\_\_ C1 \_\_\_\_\_ K2 \_\_\_\_\_

TEMPERATURE: PB \_\_\_\_\_ TA \_\_\_\_\_ K3 \_\_\_\_\_ K4 \_\_\_\_\_

K5 \_\_\_\_\_ TON \_\_\_\_\_ TC \_\_\_\_\_

ENGINE IGNITION TIMING VS. SPEED

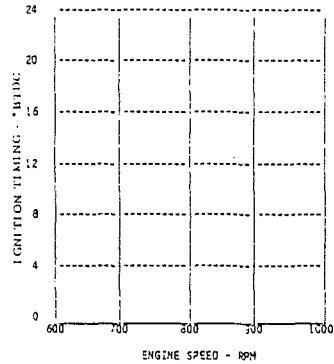


Fig. 2

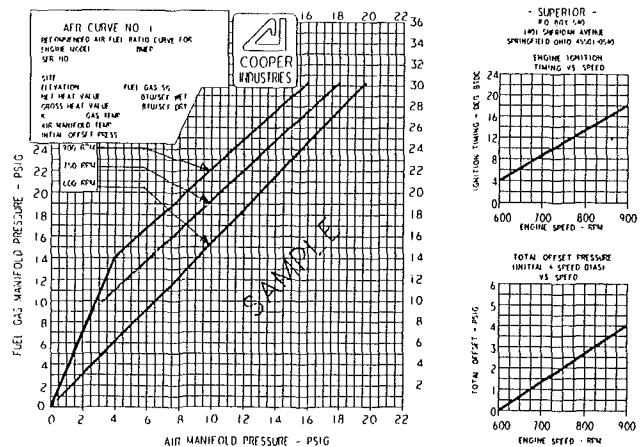


Fig. 3

The controller power source is two magnetic pickups mounted at the rear of the engine over the flywheel ring gear. This approach eliminates the need for an external power source and is considered “intrinsically safe.” The ring gear teeth cut the magnetic lines of flux producing an electrical output. The pickup’s outlet is inversely proportional to the air gap between the magnetic pole piece and the ring gear teeth. The magnetic pickups were selected because no moving parts and no additional gears are required and also because of enhanced retrofit possibilities. Only a bracket to hold both pickups and to insure the pickups are perpendicular to the ring gear is required. Testing was conducted to determine the air gap required to operate the controller at minimum engine speed. This gap is 0.51 mm (0.020 in.).

The controller output has a digital-to-analog (D/A) converter to change the controller’s output to a 1 to 5 mA signal for a current-to-pressure (I-to-P) transducer. The I-to-P transducer controls the wastegate valve which in turn controls the engine

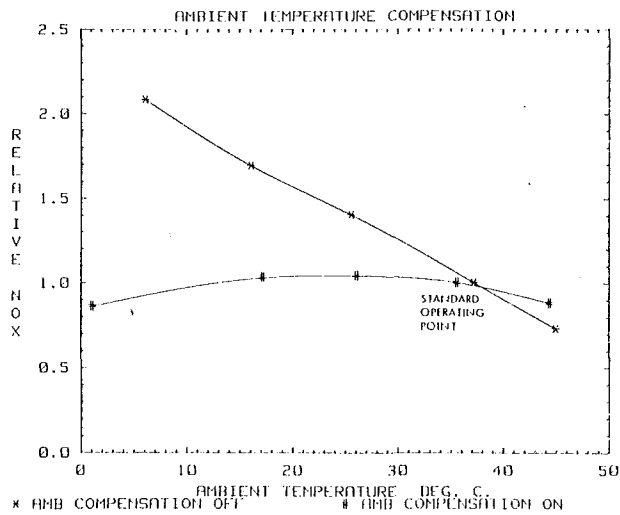


Fig. 4

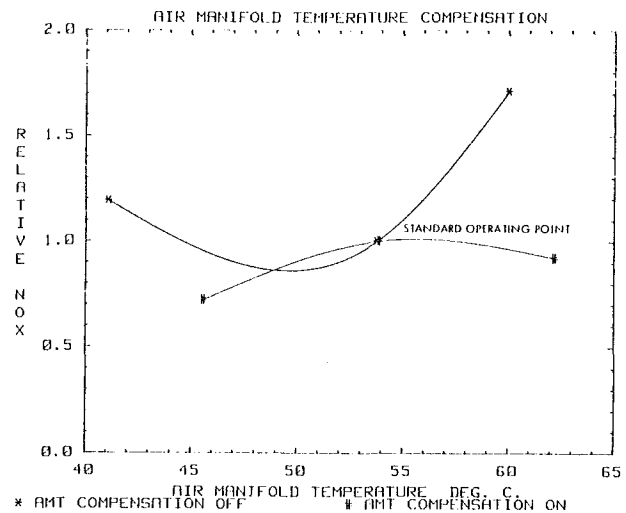


Fig. 6

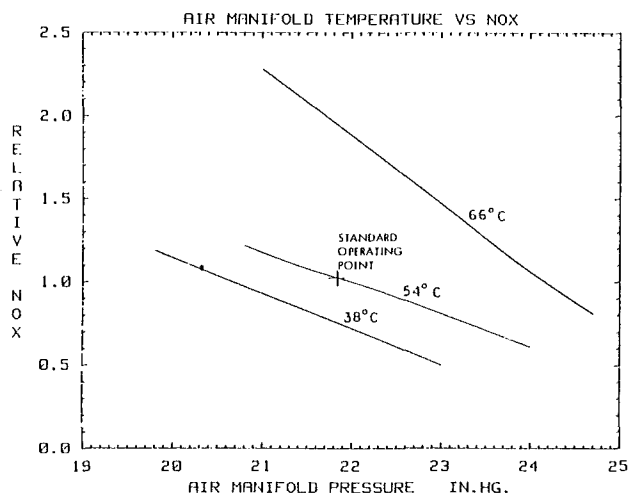


Fig. 5

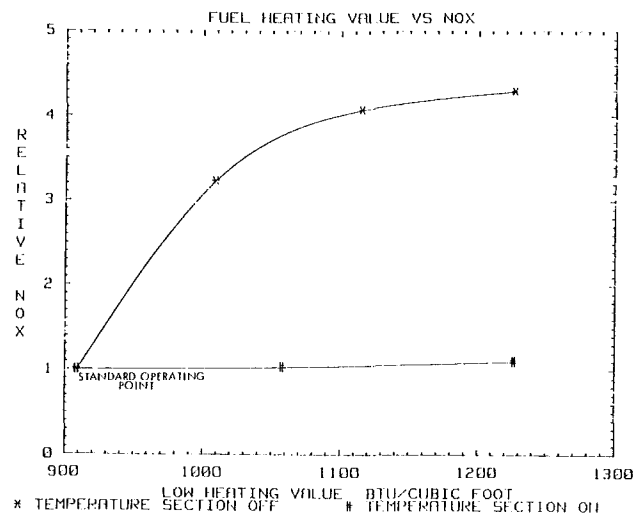


Fig. 7

air manifold pressure (AMP). Initially an eight-bit D/A converter was used. During the early testing, it was observed that the AMP was fluctuating even though the engine speed and load were not changing. It was determined the controller's output was too coarse, causing an overcorrection. To improve the system dynamics the D/A converter was changed to a 16-bit output. This change made the AMP steady.

Use of the preturbine temperature as a control set point requires some compensation for ambient temperatures. The temperature rise across a turbocharged engine is basically constant for a given air pressure, speed, and load and is a function of the ambient and air manifold temperatures. The use of preturbine temperature as a control setpoint without any ambient temperature compensation causes the air-fuel ratio to drift and the exhaust emissions could increase. Figure 4 is a comparison of  $\text{NO}_x$  exhaust emissions with and without ambient temperature compensation. With ambient temperature compensation, the  $\text{NO}_x$  level will remain at a low level.

A turbocharged gas engine uses an intercooler to cool the charge air. A simple system would use a thermostat to control the coolant temperature, while a complex system would monitor the charge air temperature and adjust the system to maintain a particular temperature. This charge air temperature has an effect on exhaust emissions, preturbine temperature, and air-fuel ratio. Figure 5 shows this effect on  $\text{NO}_x$  emissions. As the temperature increases,  $\text{NO}_x$  level and preturbine temperature will also increase.

Use of the preturbine temperature as a control point also requires some air manifold temperature compensation. Figure 6 is a plot of  $\text{NO}_x$  emissions with and without air manifold temperature compensation. With the compensation, the  $\text{NO}_x$  levels remained low as the air manifold temperature varied.

In a gas gathering application, the fuel heating value can vary from station to station or well to well. At a given site, it is common to experience significant changes in the heating value as wells are switched on and off. At a stripping plant, an upset may occur that will cause a heating value change from processed to unprocessed fuel. To insure the controller could maintain the exhaust emissions, propane was blended with pipeline quality natural gas to increase the heating value. The results of these tests are plotted in Fig. 7. With a simple pressure control system, the air manifold pressure would decrease as the heating value increased, exhaust emissions would increase and the engine's knock limit margin would decrease. Within the range of fuel blends tested, the controller was able to maintain stable emissions as the fuel heating value increased.

Before the controller could be field tested, the control constants had to be developed. The constants are unique to each engine model. With these unique constants, air-fuel ratio curves for each site are not required. For most applications, the constants will be the same regardless of where the engine is installed. Data maps of gas manifold pressure (GMP), AMP,



and preturbine temperature were developed for various engine speeds and loads. The controller constants were then calculated based on the data maps and entered into the controller. The engine was then operated on the controller to insure that exhaust emissions were maintained throughout the engine speed and load range.

### Field Development

Two controllers were installed at different sites. The first controller was installed July 1985 and the second unit in Aug. 1985. Each engine is a Superior CleanBurn 8GTLA. One engine is driving a refrigeration compressor for a process plant. This engine is in an enclosure with three other 8GTLA engines and the controller was exposed to extremely high ambient temperatures. The fuel at this location is process natural gas, but if the plant has an upset, the fuel for the engines becomes the incoming gas. The other engine is compressing well gas. The engine operates on the well gas and the wells are switched periodically. The engine and controller are not enclosed and are subjected to extremes in ambient conditions, which could be expected at any location. Both controllers were mounted near the engine on the skid. They were subjected to engine vibration as well as ignition noise.

The controller installation required 8 hr and was easily accomplished. The pneumatic panel was removed and the new panel installed in its place. The new panel required a small amount of tubing installation since the panel connections are not in the same location as the pneumatic panel. The three controller thermocouples were installed in existing adaptors and the magnetic pickup bracket used existing bolts.

The engine was started and the panel constants checked. The engine was then loaded and controller operation was checked throughout the engine's speed range. To determine

whether the engine was operating at the correct air-fuel ratio, the GMP and AMP were compared to the values on the air-fuel curve supplied with the pneumatic panel. The values were within 0.2 psig.

The field test was an unqualified success. Both controllers have been in operation for over 1 year. During this time, the panel constants have not changed after being set and sealed. The engine operators have developed confidence in the system; consequently control panel complaints have become virtually nonexistent. These early successes have led to the installation of numerous additional retrofit units.

A significant problem was thermocouple failures. The thermocouple had a large head for the extension wire connections. Due to engine vibration, the thermocouples would break at the connection. New thermocouples that do not use this head were installed and have operated trouble free.

### Summary

Many features must be controlled to insure an engine is operating at the desired air-fuel ratio for low exhaust emissions and good fuel economy. The electronic controller has proven it can control the air-fuel ratio regardless of varying ambient conditions and fuel heating values throughout the engine load and speed range.

The electronic controller is now standard with Superior CleanBurn engines and has improved performance.

### Acknowledgments

The authors wish to express appreciation to all the Superior R & D personnel who worked to the successful completion of this project. Special acknowledgment goes to Dudley D. Nye, Jr. of TRW Dynalco Controls Division who designed the electronic circuits.

# Induction System Effects on Small-Scale Turbulence in a High-Speed Diesel Engine

A. E. Catania

A. Mittica

Dipartimento di Energetica,  
Politecnico di Torino,  
Turin, Italy

*The influence of the induction system on small-scale turbulence in a high-speed, automotive diesel engine was investigated under variable swirl conditions. The induction system was made up of two equiverse swirl tangential ducts, and valves of the same size and lift. Variable swirl conditions were obtained by keeping one of the inlet valves either closed or functioning, and by changing engine speed. The investigation was carried out for two induction system configurations: with both ducts operating and with only one of them operating. Two different engine speeds were considered, one relatively low (1600 rpm) and the other quite high (3000 rpm), the latter being the highest speed at which engine turbulence has been measured up to now. Cycle-resolved hot-wire anemometry measurements of air velocity were performed throughout the induction and compression strokes, under motored conditions, along a radial direction at an axial level that was virtually in the middle of the combustion chamber at top dead center. The velocity data were analyzed using the nonstationary time-averaging procedure previously developed by the authors. Correlation and spectral analysis of the small-scale turbulence so determined was also performed. The turbulence intensity and its degree of nonhomogeneity and anisotropy were sensibly influenced by the variable swirl conditions, depending on both the intake system configuration and engine speed; they generally showed an increase with increasing swirl intensity, at the end of the compression stroke. A similar trend was observed in the cyclic fluctuation of both the mean velocity and turbulence intensity. The micro time scale of turbulence was found to be almost uniform during induction and compression, showing a slight dependence on the measurement point and on the intake system configuration, but a more sensible dependence on the engine speed. No effect of the cylinder wall on turbulence was apparent.*

## Introduction

The performance and exhaust emissions of a reciprocating internal combustion engine can be strongly influenced by the in-cylinder turbulent flow, showing a rather complex dependence on the intake system and combustion chamber configuration, on other engine geometric parameters, as well as on engine operating conditions [1-10].

One way of enhancing fuel-air mixing in compression ignition engines and of promoting fast burn in lean mixtures, as well as in mixtures diluted with exhaust gas, is to increase the turbulence level by providing suitable swirl inducing ports for intake. This can be considered as a means of improving fuel economy, while lowering the formation of smoke and other pollutants, at specific engine operating conditions.

Different intake port designs yielding comparable swirl numbers, as obtained on the stationary flow test rig, can pro-

duce significantly different effects on the performance of the same engine under the same operating conditions.

Variable swirl and/or turbulence-producing intake systems can improve engine performance and emissions over a wide range of engine speeds.

These statements are based on the results reported, for example, in [1, 3, 4, 11-16].

Most of the investigations on the relationship between in-cylinder turbulent flow parameters and engine combustion process have been performed by correlating the flow data acquired under motored conditions to combustion data acquired in the firing engine, owing to the difficulties of making turbulence measurements in combusting flows. Although an interaction between engine turbulence and combustion may exist [17, 18], the validity of this approach is confirmed by two facts: firstly, similar turbulent flow patterns before combustion under motored and firing conditions, respectively, have been shown [19, 20]; secondly, the results of conditionally sampled measurements in a firing spark ignition engine [14] suggest that cyclic variation in burn duration may be caused by cyclic variation in the turbulence intensity, evaluated as

Contributed by the Internal Combustion Engine Division and presented at the Energy-Sources Technology Conference and Exhibition, Dallas, Texas, February 15-20, 1987. Manuscript received at ASME Headquarters December 10, 1986. Paper No. 87-ICE-38.

root-mean-square (rms) velocity fluctuation, ahead of the flame, and this is in agreement with the general finding that the burn rate increases with turbulence intensity.

Therefore it is important to correlate turbulent flow parameters to the engine geometric features in order better to understand the effects of engine shape on its performance. In addition, more experimental data on engine turbulence are needed to improve familiarity with its structure, the exact nature of its role, and its dependence on other engine variables, particularly in high-speed diesel engines, where few data exist at present. This need is further stressed by the fact that the fluid mechanical turbulence of internal combustion reciprocating engines is a very challenging field of research owing to unsteadiness and cyclic fluctuation of the in-cylinder "mean" flow. To give an example, it is shown in [21], with reference to a specific ported engine, that the question of whether the in-cylinder turbulence intensity without swirl is smaller or larger than with swirl could have different answers depending on the procedure used to extract turbulence intensity from the same velocity data, particularly for the no-swirl case.

In fact the definition of turbulence in an engine differs from author to author [22–29].

In this study a nonstationary time-averaging procedure [29] distinct from that proposed in [25], was used to obtain time-dependent mean velocity and turbulence intensity from cycle-resolved velocity data. Correlation and spectral analysis [30] of the engine turbulence was also performed.

The influence of induction system on small-scale turbulence quantities in a high-speed, automotive diesel engine was investigated under substantially different swirl level conditions, to provide information on the in-cylinder turbulent flow as produced by a variable intake swirl system at practical engine speeds.

The engine was an open-chamber single cylinder with a relatively wide and shallow piston bowl so as not to introduce relevant organized gas motion during compression. Thus the in-cylinder turbulent flow was due primarily to the intake process. The induction system had two equiverse swirl tangential ports, and valves of the same size and lift. Variable swirl conditions were obtained by keeping one of the inlet valves either closed or working, and by changing engine speed. The investigation was carried out for two induction system configurations: with both ducts operating and with only one of them operating. Two different engine speeds were considered, one relatively low (1600 rpm, that is 167.6 rad/s) and the other quite high (3000 rpm, that is 314.2 rad/s), the latter being the highest speed at which engine turbulence has been measured up to now.

A hot-wire anemometry technique was used to perform cycle-resolved measurements of air velocity during the induction and compression strokes, under motored conditions. The velocity data were acquired at different locations, along a radial direction, at an axial level that was virtually in the middle of the combustion chamber at top dead center (TDC).

Although the measurements are obviously specific to the engine considered, tangential intake ports have commonly been used in production engines. Furthermore, the effect of compression ratio on TDC turbulence intensity was generally found not to be strong [21, 25, 31]. So the results of this study can be expected to have more general and basic applications.

## Literature Review

Regarding the influence of the intake system, in its wider sense, on the in-cylinder turbulent flow and limiting our attention mainly to experimental investigation, many studies have been carried out under motored conditions using both hot wire anemometer (HWA) (e.g., [4, 25, 32–35]) and laser-Doppler velocimeter (LDV) (e.g., [21, 31, 36–39]).

Some researchers examined the effect of inlet port design on both mean flow and turbulence in valved engines at very low speeds (960 rpm [34], 200 rpm [36], and 916 rpm [38]) and at more practical speeds (1100–2400 rpm [4] and 1500 rpm [31]). Tangential and helical ports of different types, but with comparable swirl numbers (as obtained from steady flow rig tests), were considered in [4, 34] and it was found that in an open-chamber diesel engine with a standard-type toroidal combustion bowl the helical port produced higher swirl velocities than the tangential port at both lower and higher speeds [4, 34] and greater turbulence intensities at higher speeds [4], while at lower speeds no significant differences in turbulence between the ports were observed [4, 34].

A similar result was obtained at very low engine speeds in model and production type engines with disk-chamber and different swirl-inducing ports [36, 38], where axial turbulence levels as high as 0.3–0.4  $V_p$  ( $V_p$  being the mean piston speed), and nearly uniform in the midclearance plane, were observed at TDC of compression, independent of the type of induction system and engine speed. During compression the turbulence intensity was found to remain constant with magnitudes of 0.5  $V_p$  until 20 deg before TDC and then to decay suddenly to the abovementioned value at TDC.

In [31] two heads, both featuring a helical intake port, were used to vary the intake swirl level in an open-chamber diesel engine with a re-entrant bowl. The swirl ratios at inlet valve closing, as predicted using steady-flow swirl-rig results, were not largely different, being 2.9 for the high-swirl head and 2.3 for the low-swirl head. Turbulence was not found to be strongly influenced by the initial swirl for several bowl geometric parameters. Besides, levels of turbulence intensity as high as approximately equal to the mean piston speed were determined on compression with a slightly decreasing pattern from a crank-angle of 270 to 320 deg, that is, before turbulence generation due to squish became significant.

Other researchers studied the effects of swirl-producing shrouded valves (for example [25, 33]) as well as of throttling [25] on engine turbulence. A shrouded valve was shown to increase TDC turbulence intensity, with respect to an unshrouded valve, in a flat piston engine, depending on the shroud position and engine speed [25, 33]. A slightly higher turbulence was observed by increasing volumetric efficiency with a throttling valve at a given engine speed [25]. Furthermore, it was evidenced in [33] that the turbulence in the swirling flow at TDC of compression was in an unrelaxed state so that the turbulence generated during induction contributed considerably to the engine turbulence before combustion.

A ported engine with and without swirl, depending on the direction of intake side ports, with a combustion chamber of disk type was used in [21, 37] for turbulent flow studies near TDC of compression. The engine was motored at 1200, 1800, and 2400 rpm and fed by an air compressor supplying a mass flow rate which was increased linearly with engine speed. In the presence of swirl the turbulence intensity, evaluated as ensemble average of turbulence in 1 deg windows [28] along the tangential direction, was greater than without swirl. It was found to be nearly proportional to engine speed and to be approximately homogeneous in all cases. A relatively high degree of isotropy was observed in TDC turbulence in the absence of swirl. Finally, based on both experimental and computational results [40] a maximum value for the turbulence intensity at TDC for an open-chamber engine without swirl was suggested to be about equal to 1/2 of the average piston speed.

In [39] values of TDC turbulence intensity within a disk chamber, evaluated as spatial-averaged rms velocity fluctuation in the axial direction, were found to increase from 0.4 to 0.5 times the mean piston speed in the presence of a rather weak swirl level (a swirl ratio as low as  $\approx 1.2$  was obtained) and from 0.45 to 0.6 without swirl, in the speed range of 300

to 2000 rpm, keeping for the swirl case lower than for the no-swirl case throughout the speed interval. A tendency toward isotropy was observed in turbulence at TDC.

An almost linear dependence of TDC turbulence intensity on engine speed has been found by many other researchers at low and intermediate engine speeds with a slope of the curve that varied, sometimes considerably, from author to author, depending on engine geometry and speed, as well as on measurement and data reduction method (a summary of the main results is reported in [21, 39]). A tendency of the flow field to scale with engine speed was more recently found for open-chamber engines with rather shallow re-entrant bowls [31] and a quite deep cylindrical bowl [41], though at very low engine speeds (less than 600 rpm) in the latter case.

Furthermore, homogeneity and isotropy of TDC turbulence intensity in the absence of swirl have been found since the earliest turbulence measurements carried out in CFR engines [22, 23].

The influence of the induction system on the mean flow pattern in the cylinder of the automotive diesel engine referred to in the present work was examined in [32, 35] for the same variable swirl conditions here considered. It was inferred that keeping one of the two inlet valves closed could be a means of increasing the swirl level, without significantly affecting the volumetric efficiency at low speeds. At 167.6 rad/s the swirl ratio (SR)<sup>1</sup> at TDC of compression was 3.0 for both intake ducts operating and 4.4 for only one intake duct operating (being virtually the same no matter which of the two intake ducts was operating alone [32]). The corresponding values of volumetric efficiency were 0.82 and 0.86, respectively. At 314.2 rad/s SR was 2.9 for both ducts and 3.6 for only one duct, volumetric efficiency being 0.785 and 0.695, respectively. It appeared that the swirl level was, for both ducts,  $\approx 2/3$  as high as for only one, at 167.6 rad/s, and  $\approx 4/5$  at 314.2 rad/s. This was most likely due to the reciprocal stabilizing effect of the two swirling flows and to less energy dissipation caused by interference between the main flow and the secondary jet flow on induction for the two ducts, and to the sensibly decreased volumetric efficiency at the higher engine speed for only one duct. It also appeared that the swirl ratio was nearly constant for both ducts while for only one duct it decreased sensibly as the engine speed was increased, keeping virtually proportional to volumetric efficiency. In the literature an almost linear dependence of the swirl velocity on engine speed has been found for disk-type chambers at low and intermediate speeds (up to 2400 rpm) [4, 21, 39]. A more or less strong three dimensionality of the in-cylinder mean flow and a tendency of this to develop swirl with the main features of a solid-body vortex near TDC of compression are common results [4, 31, 32, 35, 39].

Some of the results on the in-cylinder turbulence quantities obtained for only one duct at 167.6 rad/s, including measurements taken very close to the cylinder wall, are reported in [30, 42], with the following main conclusions: A strong turbulence anisotropy and nonhomogeneity existed during the induction stroke while a tendency toward isotropy and homogeneity was observed on the compression stroke; a certain degree of anisotropy and nonhomogeneity was still apparent at TDC of compression. The spectral analysis results indicated that the structure of the in-cylinder small scale turbulence before combustion was practically the same as that on induction in the secondary jet flow as well as in the main flow. No effect of the wall appeared to be relevant.

<sup>1</sup> Swirl ratio is the ratio between the equivalent (same angular momentum) solid-body rotational speed of the air, obtained from the measured tangential velocity profile, and the engine speed.

## Ensemble-Averaging and Cycle-Resolved Data Reduction Procedures

Basically, all velocity data reduction procedures for turbulence analysis in reciprocating engines can be grouped into two main classes: ensemble-averaging procedures (or phase-averaging, as termed in [14, 26]) and cycle-by-cycle reduction procedures.

The periodic nature of the engine cycle suggests that phase averaging may be used, where the instantaneous velocity, or briefly the velocity, at a specific crank-angle position is averaged over many cycles, so as to obtain the mean velocity, and the turbulence intensity is taken to be equal to the rms fluctuation of the velocity about the ensemble-averaged velocity. The mean or bulk velocity defined in this way is identical from cycle to cycle. In an engine, however, it is generally accepted that the bulk velocity does change from cycle to cycle; therefore the turbulence intensity may be overestimated, owing to these variations [21, 43].

To remove cyclic variations from phase-averaged data, conditionally sampled velocity measurements were chosen for investigation [14], based on the time of flame arrival at the LDV probe volume. However, it is not specified in [14] how cyclic variations in turbulence intensity should be quantified (only trends for these are presented) and what the width (or resolution) of each segment forming a conditionally sampled data set should be, taking into account the resolving power of the instrument chosen to detect the condition under which to sample. Furthermore no indication is given in [14] of the way to remove the apparent turbulence in the phase average due to other cyclic variations in the selected conditioning process (e.g., variation of the flame surface geometry).

On the other hand, the combustion process in a reciprocating engine occurs within each individual cycle and so it is directly influenced by the in-cycle turbulent flow parameters. This suggests that the analysis of engine turbulence should be performed on a single-cycle basis first. To that end, in order to characterize the mean velocity and turbulence in each cycle, it is necessary to make cycle-resolved measurements. These enable one not only to separate the cyclic fluctuation of the mean velocity from turbulence, but also to evaluate the cycle-to-cycle variations in the engine turbulent flow. Furthermore ensemble-averaged turbulence quantities can be obtained from the cycle-resolved results as parameters characterizing the gas dynamics of a specific engine so that a correlation between the performance of the engine on average and these parameters can be established as well.

Several cycle-resolved data reduction procedures have been developed and applied to the analysis of turbulent flow in a reciprocating engine [25, 27–29]. HWA measurements were performed in [25, 29], while LDV was used in [27, 28]. Other investigators [24] have processed HWA data using a low-pass/high-pass filter instead.

The conventional procedure of time-averaging the velocity to obtain a steady mean velocity for specific intervals within each engine cycle includes as turbulence the time-varying component of the bulk motion, as shown in [25].

A nonstationary time-averaging procedure of data reduction was developed in [25], where eight successive 45 deg crank-angle intervals were considered throughout intake and compression. The ensemble-averaged velocity was first calculated from the measured velocities at each crank-angle degree and then an in-cycle unsteady mean velocity in each interval was evaluated as the sum of the ensemble-averaged velocity and a constant quantity (but not the same for each interval) given by the time average of the difference between the instantaneous velocity and the ensemble-averaged one in the specific interval. The in-cycle turbulence intensity in each interval was then obtained as time-averaged turbulence intensity

from the turbulent velocity component, considered as a stationary random fluctuation superimposed on the unsteady bulk motion. This procedure led to a cycle-resolved mean velocity curve with discontinuities at the boundaries of each interval and included in the turbulence a spurious contribution arising from the fact that the mean velocity pattern may be considerably different from cycle to cycle and so very dissimilar from the ensemble-averaged velocity pattern [27-29].

The two different, but similar in some aspects, cycle-resolved data reduction procedures proposed in [27, 28] are conditioned by the inherent limitation of LDV measurements that the in-cylinder velocities cannot be evaluated at a specific crank-angle location but must be evaluated over a crank-angle window usually centered on it. Characterization of the mean velocity in each engine cycle requires a data rate high enough to give a virtually continuous velocity trace in every cycle. While constituting no problem for HWA measurements, for LDV measurements this implies a small window size and hence the ability to acquire and store large amounts of data, depending on the probability of having at least one measurement in each window. The first step taken in [27] as well as in [28] for processing the data from a single cycle was to calculate a velocity for each window by arithmetically averaging the data in those windows with multiple measurements and by assigning linearly interpolated values to those windows with no measurements. Of course this sort of filtering reduces the frequency content of the original data, and the window size itself determines the highest frequency which could be included in the resulting average window data set. The discretionary choice of a 1-deg window size was made in both references. As for the next step, a mean-velocity curve was fitted to the average window values using a cubic-spline smoothing routine [27]. In [28] the frequency spectrum of the average window data was obtained using a fast Fourier transform; then all frequency components above a selected cutoff frequency were set to zero and the inverse transform was taken, yielding the mean-velocity curve. The in-cycle turbulence intensity was evaluated for each window as the absolute value of the difference between the average window velocity and the mean velocity from either the cubic-spline smoothing routine or the inverse fast Fourier transform. However there is no evidence of the results this turbulence definition will yield, nor of their exact meaning, when a window size greater than one degree is chosen.<sup>2</sup> Besides, the time separation of the data points in each window was not taken into account and so it is not clear how the time varying component of the mean velocity was separated from turbulence in each window. Finally, in [28], while an ensemble-averaged turbulence intensity was taken from the cycle-resolved values at each window, the cyclic fluctuations in the turbulence intensity were evaluated as cyclic fluctuations in the "time-averaged" turbulence intensity over the 60-deg interval.

### Present Cycle-Resolved Data Reduction Procedure

A new nonstationary time-averaging procedure of cycle-resolved data reduction was developed in [29]. It differs from the previous one [25] in the definition of the cycle-resolved mean velocity and consequently in the turbulent fluctuation about this. Details on the procedure and its application to the analysis of engine turbulence are reported in [29, 30]. A summarized description follows.

The instantaneous velocity in each engine cycle is split, as usual, into an unsteady mean velocity and a turbulent fluctuation about it. The latter is regarded as being a stationary random function, with time-averaged value equal to zero, for

<sup>2</sup>As stated in [27], the one-degree window size is not considered to be a limiting factor and could be removed if desired.

specific time intervals within the engine cycle. Evaluation of the in-cycle mean velocity is accomplished through the following steps. First, the time average of the instantaneous velocity is evaluated in each time interval into which the engine cycle or part of it is divided and the resulting averaged velocity values, taken in the middle of the respective intervals, constitute the first set of mean velocity values which are interpolated to obtain the initial mean velocity curve.<sup>3</sup> Then time-averaged velocity values in each interval are taken from this curve and compared to the values previously determined, so that if a difference among them exists, interval by interval, above an arbitrary small quantity,<sup>4</sup> then a new set of mean velocity values is obtained from the previous one by means of a factor, evaluated interval by interval from the abovementioned difference, and a new interpolating curve is determined. So an iterative process is started that terminates when the time-averaged velocity values from the final interpolating curve (that is the mean velocity curve) are equal<sup>5</sup> to those previously determined from the instantaneous velocity curve. The turbulent velocity component is given by the difference between the instantaneous velocity and the mean velocity at the same instant. The in-cycle turbulence intensity for each interval is then evaluated as time-averaged and a cycle-resolved turbulence intensity curve can be drawn therefrom by interpolation. Ensemble-averaged mean velocity and turbulence intensity values can be obtained from the cycle-resolved results for each interval as well, giving information on the gas dynamic behaviour of the engine on average and allowing evaluation of rms fluctuations in both the mean velocity and the turbulence intensity. The procedure includes, as limit cases, the conventional time-averaging data reduction method, ordinarily used for the analysis of steady-state turbulent flows, that is when the whole part of the engine cycle considered is taken as the time-averaging interval, and the standard ensemble-averaging procedure, that is when an averaging interval as small as zero<sup>6</sup> is chosen, in which case the time-averaged turbulence intensity tends to zero, while the ensemble-averaged turbulence intensity corresponds exactly to the rms velocity fluctuation. Furthermore the procedure was shown to be suitable for correlation and spectral analysis of reciprocating engine turbulence without presenting the limits exhibited by the ensemble-averaging procedure when this was used to obtain the autocorrelation coefficient in the analysis of the same data [30].<sup>7</sup>

Analytical expressions of turbulence quantities are given in the appendix.

### Experimental System

**Measuring Equipment and Procedure.** The test engine (Fig. 1) was a single-cylinder, derived from a production engine at Fiat Research Center, with a bore and stroke of 75.5 mm and 83.5 mm, respectively, and a nominal compression ratio of 16. Other engine specifications are reported in [35].

A schematic of the engine with the anemometric probe setup is shown in Fig. 2. A minor modification of the engine design was required to accommodate the probe at TDC.

Air velocity measurements were taken along a radial direction at five different locations, specified by the respective

<sup>3</sup>A cubic-spline was used for the interpolation; however, a linear interpolation could be used as well, without any significant difference.

<sup>4</sup>0.5 percent was chosen; however 1 percent is accurate as well.

<sup>5</sup>Within the above-mentioned difference (ordinarily convergence was reached in a few iterative steps).

<sup>6</sup>The choice of a 1-deg crank-angle interval is consistent with the procedures used for LDV measurements, where a window of 1 deg is usually chosen.

<sup>7</sup>More specifically, the two ways of evaluating the micro time scale of turbulence, one by intersecting the abscissa axis with the osculating parabola in the vertex of the autocorrelation curve and the other by means of the normalized energy spectral density function [44] were not shown to be univocally equivalent when a pure ensemble-averaging procedure was used to determine the autocorrelation coefficient.

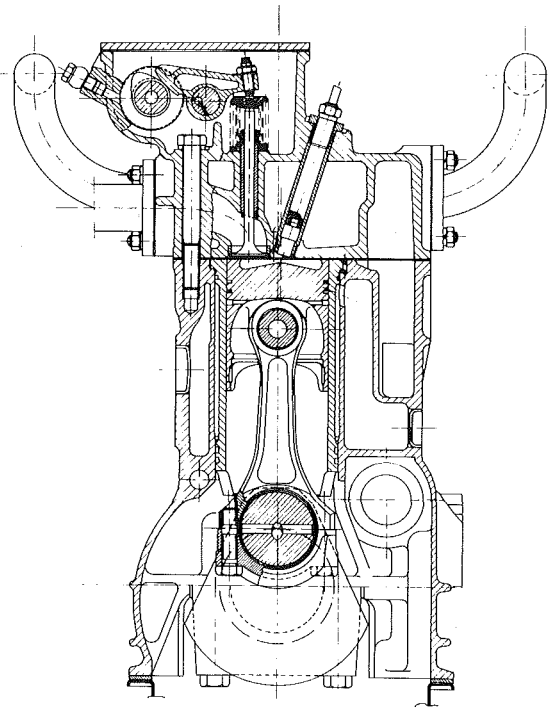


Fig. 1 Test engine

values of the radius  $r$  (from the cylinder axis): 6, 18, 28, 33, and 37 mm; the last was very close to the cylinder wall, that is  $0.75 \pm 0.25$  mm away from the wall. The probe axis was at a level of  $\approx 3.5$  mm underneath the flat cylinder head. It was almost in the middle of the relatively wide and shallow combustion bowl at TDC (the throat and the maximum depth of the bowl were  $\approx 60$  mm and  $\approx 8$  mm, respectively; the clearance height was 0.7 mm), so that the velocity measured within the bowl at the end of the compression stroke could be considered as representative of the motion of the whole charge at that stage. Measurements at the two locations close to the cylinder wall,  $r=33$  mm and 37 mm, were not performed at the higher engine speed due to difficulties arising from a reduced mean life of the sensing wire there. All the measurements were carried out in the crank-angle interval  $\vartheta=0-360$  deg, that is from the start of the induction stroke to the end of the compression stroke.

At each sensor location three data sets were acquired for the three different orientations of the sensing wire corresponding to the following values of the angle  $\alpha$  between the wire axis and the cylinder axis (Fig. 3):  $\alpha=0$ ,  $\alpha=\pi/4$ ,  $\alpha=\pi/2$ . Since the wire was most sensible to the velocity component in a plane normal to its axis, the turbulence intensities determined for each measurement set were correlated to the turbulence intensity components along the tangential ( $s$ ), radial ( $r$ ), and axial ( $z$ ) directions, by means of the correlations deduced in [29], so as to obtain information about the directional dependence of turbulence.

Between 30 and 50 cycles of data were recorded on analog tape for each measurement set and this was repeated once or, in some cases, twice. A 50 kHz low-pass filter was used in recording the analog data. The analog records of gas pressure and temperature, as well as of wire prong temperature data, were taken in addition to the analog records of velocity, since the anemometer output voltage depends on all of these quantities. The data were then digitized and stored in a computer file. The computation of gas velocity at each digitized point and also the analysis of the computed velocities (so as to obtain the cycle-resolved turbulent flow parameters and their ensemble average) were then performed by means of an in-

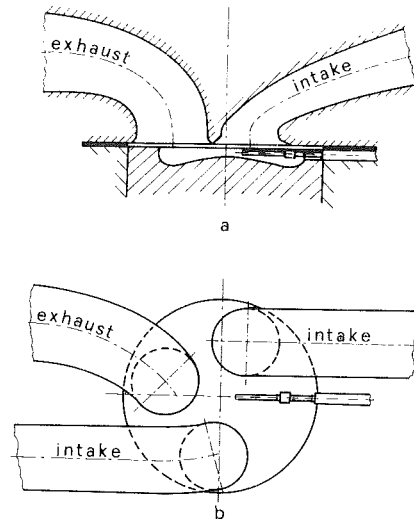


Fig. 2 Schematic of the engine and probe setup

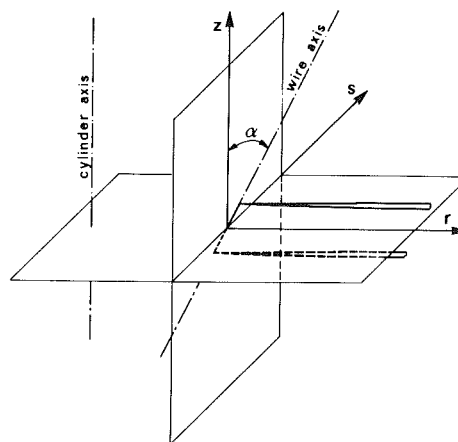


Fig. 3 Reference frame and wire orientation

teractive computer code developed ad hoc for an HP-1000, RTF-VI unit. A modified version of the algorithm developed in [45, 46] was used for the spectrum function estimation. An analytical method, based on heat balance equations for the anemometric and thermometric wires, was used to compute gas velocity from the anemometer output, taking into account all the influences on this, as well as the temperature probe lag. It is necessary to stress that this method is different from all of those considered in [47]. Since there is evidence that this paper has contributed to a general tendency toward shelving HWA in favor of LDV for analysis of reciprocating engine flows under motored conditions, the authors cannot avoid making at least the following observations. The paper only shows the discrepancies and limits in those semiempirical analytical models used to correct the anemometer signal, due to its dependence on the gas temperature and pressure, after calibration of the probe for velocity in air at room temperature. Furthermore, in [47] it was not demonstrated, but only assumed, that the velocity component measured with LDV and HWA was the same (though the radial component of the velocity could have been measured by LDV to check if it was negligible, as assumed, in all the phases of the engine cycle). This, in the authors' opinion, is not an assessment of the "validity of hot-wire measurements."

Details on the hot-wire anemometry technique used in the present study are reported in [32].

**Experimental Uncertainties.** As stated in previous papers (e.g., [29, 35]), the method used for computing gas velocity

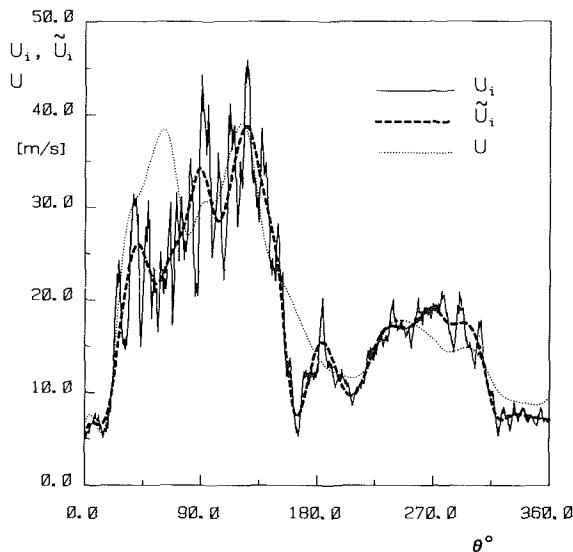


Fig. 4 Instantaneous velocity  $U_i$  and corresponding mean velocity  $\bar{U}_i$  for one cycle; ensemble-averaged mean velocity  $U$  within the proposed definition

from the experimental data was validated in nonstationary as well as stationary conditions, at different gas pressures and temperatures. The tests showed a standard deviation of less than  $\pm 5$  percent. The main sources of uncertainties in the gaseous engine environment are of different types and give rise to very complex effects which are difficult to evaluate separately. Many of them were reduced as far as possible (for example, the fouling effect was lowered by using a new wire for each set of measurements, etc.). Therefore, based on the previous findings and on the average deviations of repeated measurement sets, a maximum uncertainty of  $\pm 10$  percent could be ascribed to the computed velocities. However it can be expected that the implications of the results and the related conclusions are not influenced by the overall experimental uncertainty.

## Results and Discussion

Figure 4 shows the instantaneous velocity  $U_i$  in one cycle, as determined from the anemometer output (both intake ducts operating,  $r = 18$  mm,  $\omega = 167.6$  rad/s,  $\alpha = 0$ ) and the corresponding mean velocity  $\bar{U}_i$  on induction and compression. The figure also reports the ensemble-averaged mean velocity  $U$  (or briefly the mean velocity, as it will also be termed in what follows), obtained by interpolating the ensemble-averaged values, made up of in-cycle time-averaged velocity values in each interval. It is evident how much the cycle-resolved mean velocity can differ from the ensemble-averaged one. Figure 5 shows the turbulent velocity component  $u_i$  of the instantaneous velocity reported in Fig. 4, and the related turbulence intensity  $u'_i$ . It also shows the ensemble-averaged turbulence intensity  $u'$  (or briefly the turbulence intensity), as derived from the cycle-resolved turbulence intensity values, using the same data leading to the mean velocity  $U$  of Fig. 4.

The crank-angle interval  $\Theta = 12$  deg was used for the in-cycle time average, corresponding to the periods  $T = 1.25$  ms and  $T = 0.67$  ms at 167.6 rad/s and 314.2 rad/s, respectively. These were relatively large with respect to the dissipative time scales of turbulence determined. Regarding the choice of the averaging interval we must say first of all that every cycle-resolved data reduction procedure is conditioned by the rate of change of the bulk velocity during one cycle and so by the threshold of the filtering process used to separate mean velocity from turbulence. It is worthwhile to recall the following points which emerged in [29]. The ensemble-averaged mean

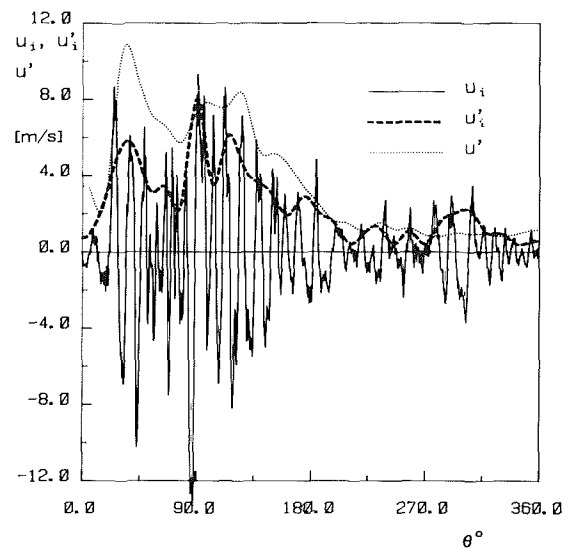


Fig. 5 Velocity fluctuation  $u_i$  and corresponding turbulence intensity  $u'_i$  for one cycle; ensemble-averaged turbulence intensity  $u'$  within the proposed definition

velocity was not strongly dependent on the length of the averaging interval,<sup>8</sup> while the turbulence intensity was shown to be more sensitive to this parameter. However, very short lengths yielded a strong decrease in turbulence intensity and increase in the frequency content of the mean flow. On the other hand excessively long intervals yielded a degree of filtering of the instantaneous velocity so high as to include in the turbulence a significant time-varying component of the bulk flow. Furthermore the upper frequency limit of the spectrum of the ensemble-averaged mean velocity, obtained using the fast Fourier transform, showed a broad minimum between  $\Theta = 10$  and 18 deg for the three orientations of the sensing wire, indicating that a proper selection of the averaging interval length could occur between these crank-angle intervals.  $\Theta = 12$  deg corresponded to a minimum upper frequency limit for  $\alpha = 0$  and  $\alpha = \pi/4$ . Values different from this and in some cases higher than 18 deg, up to 24 deg, were shown to be a reasonable choice as well, particularly near TDC of compression. This is evident in Figs. 6 and 7 where the ensemble-averaged turbulence intensities, normalized to the mean piston speed  $V_p$ , are shown for the values of  $\Theta$  indicated, and compared to the rms velocity fluctuation, that is to the turbulence intensity within a pure ensemble-averaging procedure ( $u'_E$ ). At TDC of compression values of  $u'$  sensibly less than  $u'_E$  (Fig. 7) or even slightly higher than  $u'_E$  (Fig. 6) can be found (more specifically,  $u'/V_p \approx 0.55$  in Fig. 6 and  $\approx 0.32$  in Fig. 7, while  $u'_E/V_p \approx 0.5$  in Fig. 6 and  $\approx 0.6$  in Fig. 7). It is also evident from these figures that in some cases, at least on some parts of the engine cycle, the turbulence intensity within the authors' definition can be considered as similar to rms velocity fluctuation, depending on the degree of approximation that one is inclined to accept in an engine.

In the figures, intake 1 (or briefly 1) refers to only one duct operating, that is the duct evidenced in Fig. 2(a). Intake 2 (or briefly 2) refers to both ducts operating.

Figures 8 and 9 show the turbulence intensity distributions versus crank angle obtained at 167.6 rad/s. A strong nonhomogeneity in turbulence is shown by Fig. 8, for only one duct operating, during induction and the early part of compression. In this case the probe sensed only the secondary jet flow due to its location close to the cylinder head and

<sup>8</sup>The authors' procedure and the standard ensemble-averaging one ( $\Theta = 1$  deg) led to almost the same result [29].

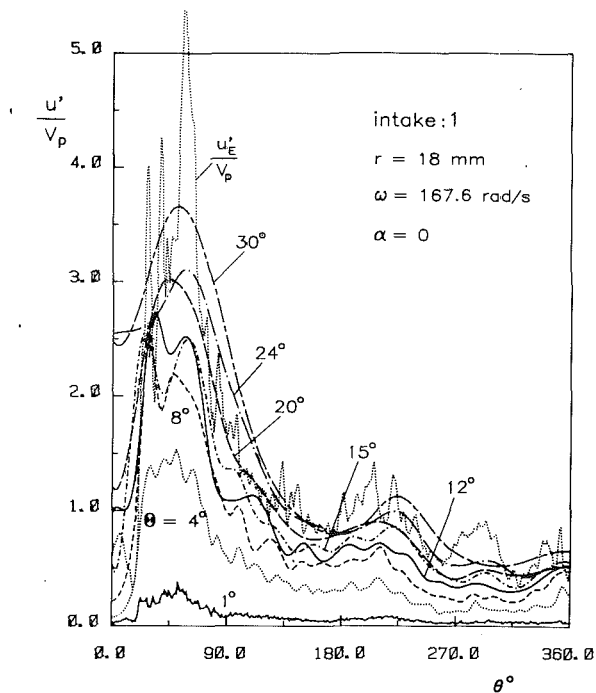


Fig. 6 Normalized turbulence intensity distributions obtained for different lengths of the averaging interval  $\theta$  and, for comparison, normalized rms velocity fluctuation ( $u_E/V_p$ )

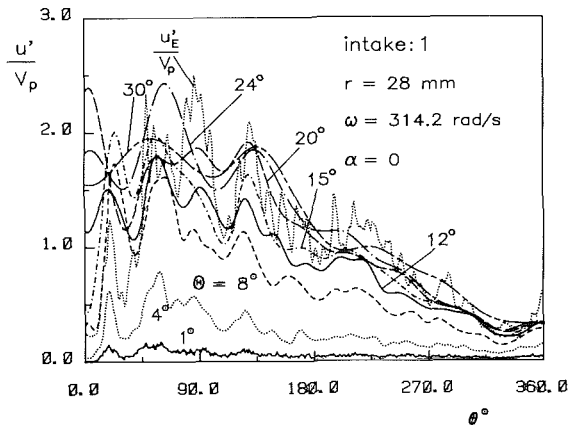


Fig. 7 Normalized turbulence intensity distributions obtained for different lengths of the averaging interval  $\theta$  and, for comparison, normalized rms velocity fluctuation ( $u_E/V_p$ )

upstream of the valve (Fig. 2b) and to the features of the bulk flow that enters the cylinder and spirals downward in a helix-like shape [32]. The same figure shows a tendency toward homogeneity in turbulence on compression after the inlet valve closure ( $\vartheta = 248$  deg) when the probe is reached by the swirling flow pressed against the cylinder top by the piston. Nonhomogeneity is still apparent at the end of compression. The sudden increase of  $u'$  just before TDC at  $r = 33$  mm and  $r = 37$  mm is probably due to the fact that from  $\vartheta = 340$  deg to  $\vartheta = 360$  deg the sensing wire fits into a small groove machined into the piston crown to avoid interference with the probe at TDC. Nevertheless a residual nonhomogeneity persisted within the bowl at TDC; a small effect of the squish flow on this may not be excluded, although no apparent squish effect on turbulence should be expected, owing to the geometric features and size of the bowl [31]. For the configuration with both ducts operating a strong nonhomogeneity in turbulence was observed mainly during the early part of induction and, to a lesser extent, soon after the full opening of the inlet valves ( $\vartheta \approx 105$  deg), when secondary jet flows were sensed at loca-

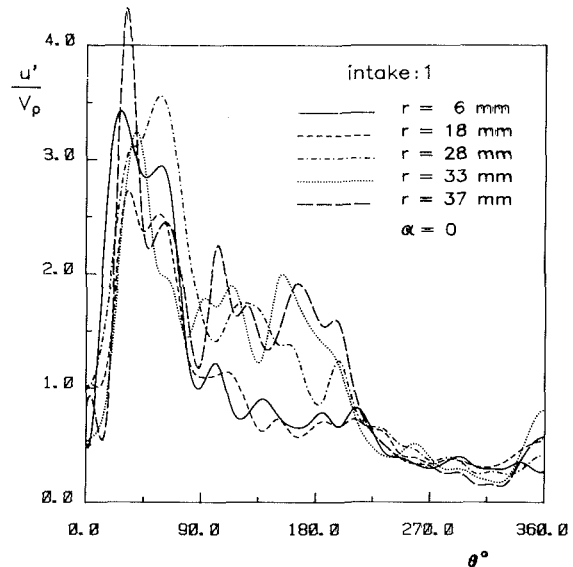


Fig. 8 Normalized turbulence intensity distributions

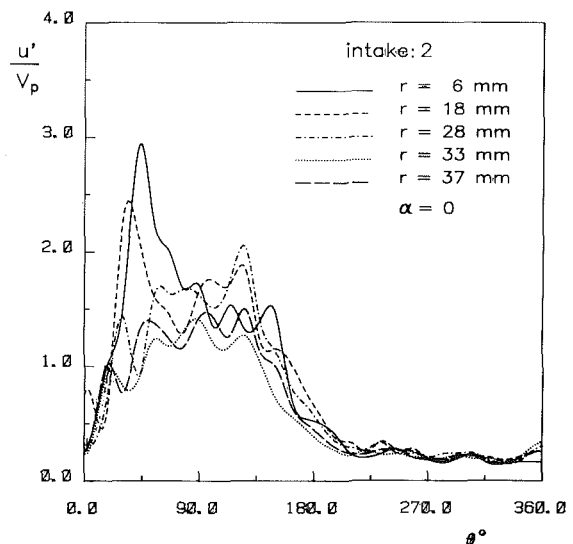


Fig. 9 Normalized turbulence intensity distributions

tions close to the cylinder axis [32]. In the last part of induction and during compression a lower degree of nonhomogeneity, as well as lower intensity in turbulence, was observed with respect to the other configuration. This could be explained by the lower values of velocity and velocity gradients for both ducts [32], leading to less energy dissipation due to interference between the main and secondary inlet flows and to less intense and more homogeneous turbulence production. The patterns of  $u'$  on induction and compression at  $r = 37$  mm in Figs. 8 and 9 do not show any apparent effect of the wall on the engine turbulence.

Figures 10 and 11 compare the turbulence intensity distributions for all the conditions considered, at two locations:  $r = 18$  mm, i.e., roughly half the bore radius, and  $r = 28$  mm, that is close to the wall of the piston bowl at TDC; both relatively far from the cylinder axis so that the mean velocity obtained for  $\alpha = 0$  could be considered as approximately equal to the tangential velocity component at the last stage of compression [35]. For only one intake duct operating, the turbulence intensity at that stage was higher than for both ducts operating, and this result was more sensible at the lower speed, showing a dependence on the measurement location. Therefore keeping one of the two inlet valves closed could be regarded as a means



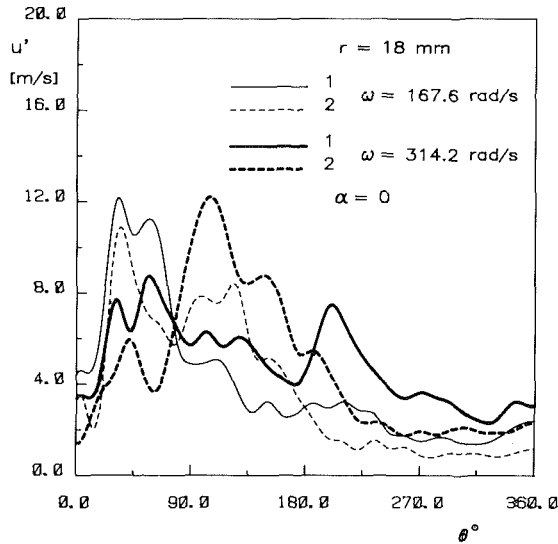


Fig. 10 Turbulence intensity distributions

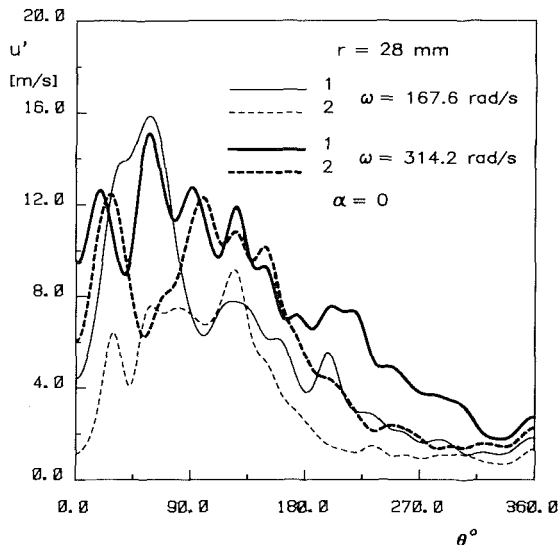


Fig. 11 Turbulence intensity distributions

of increasing, not only the swirl level, but also the turbulence intensity, without significantly affecting volumetric efficiency at the lower speed. Furthermore, for both ducts the turbulence intensity on the last part of compression increased almost proportionally with the engine speed, while for only one duct it kept less than proportional. These conclusions could not be easily drawn from the distributions of  $u'$  on the induction stroke, when the probe sensed the secondary jet flow for only one duct and part of the main flow for both ducts. This indicates that the turbulence at the end of compression is mainly due to that generated on induction in the bulk flow. In support of this deduction the distributions of  $k_1 = v_s'^2 - v_z'^2$  and  $k_3 \approx v_s'^2 + v_r'^2$  reported in Figs. 12 and 13 show a prevailing tangential turbulence component ( $v_s'$ ) at the full opening of the inlet valves, when the probe sensed induced main flow, for both ducts, as well as at the end of compression, when the probe was reached by the whole swirling charge, for both configurations. From these figures a strong turbulence anisotropy is evident on the induction stroke and a tendency toward isotropy can be observed on compression, particularly after the inlet valve closure. The degree of anisotropy at the end of compression increased with the engine speed for each configuration and with the swirl level at each speed. It should be pointed out that while the three components of the mean

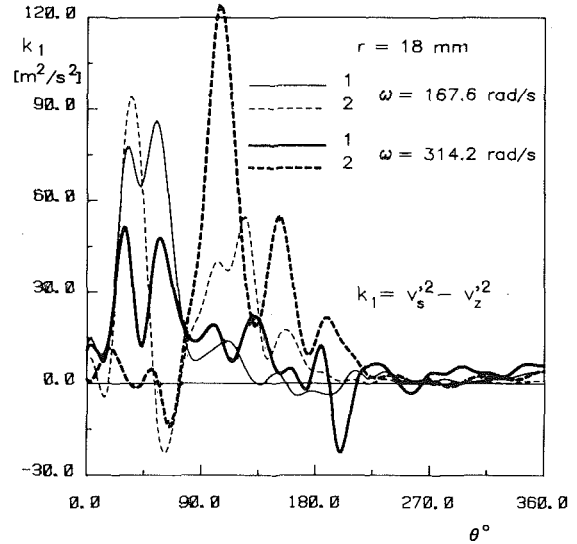


Fig. 12 Distributions of the difference ( $k_1$ ) between the squared turbulence intensity components along the tangential and axial directions

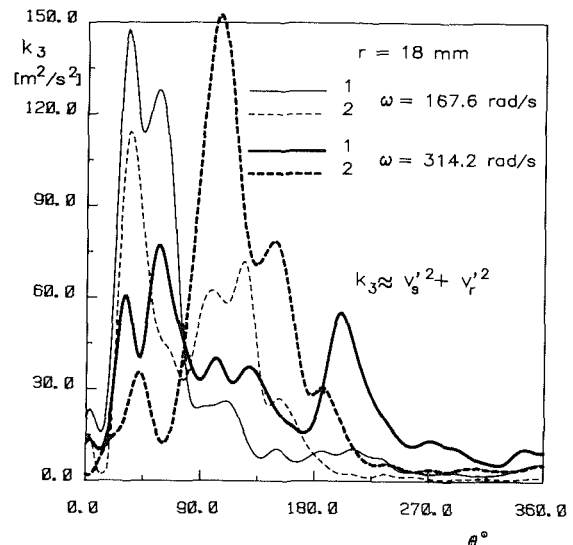


Fig. 13 Distributions of the sum ( $k_3$ ) of the squared turbulence intensity components along the tangential and the radial directions

velocity could be extracted from those sensed by the wire, using the correlations deduced in [48, 49], it was not possible to separate the three components of the turbulence intensity completely, unless measurements with different directions of the probe axis or with multiple wire probes were taken, owing to the presence of the shear stress [29].

Figures 14 and 15 plot turbulence intensity profiles versus the radial coordinate, normalized to the bore radius  $R$ , at  $\vartheta = 345$  deg and  $\vartheta = 360$  deg. A nonhomogeneity in turbulence is evident, which increases when passing from configuration 2 to 1 at both speeds and when increasing the engine speed (in particular for the configuration with both ducts operating). In the figures the mean piston speed is indicated as  $V_{pl}$  at 167.6 rad/s or as  $V_{pH}$  at 314.2 rad/s. Spatial-averaged turbulence intensities were determined over the radial direction. Their normalized values at TDC within the bowl were:  $(u'/V_{pl})_1 \approx 0.47$  for only one intake duct and  $(u'/V_{pl})_2 \approx 0.28$  for both ducts;  $(u'/V_{pH})_1 \approx 0.35$  and  $(u'/V_{pH})_2 \approx 0.27$ . It appears that the turbulence intensity is, for both ducts,  $\approx 3/5$  as high as for only one, at 167.6 rad/s, and  $\approx 3/4$  at 314.2 rad/s. When compared with the mean flow results recalled in the Literature Review section, these results show that deactivation of one in-

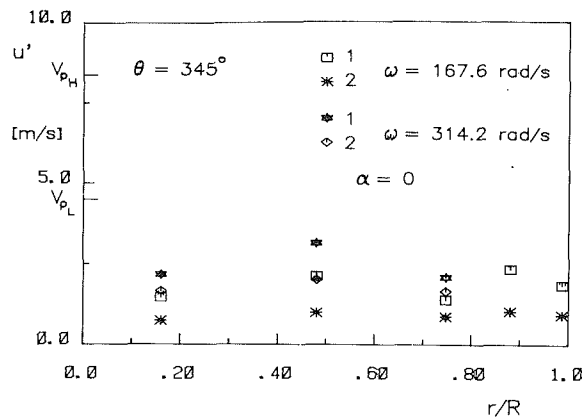


Fig. 14 Turbulence intensity profiles

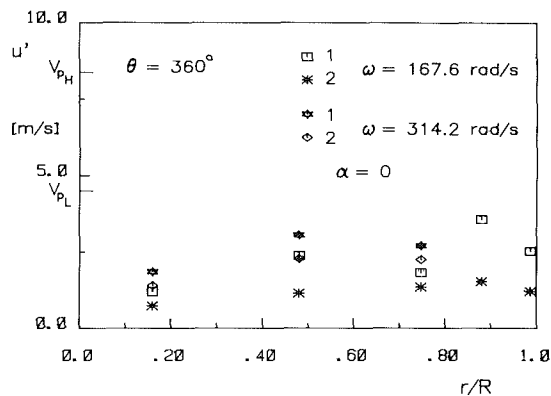


Fig. 15 Turbulence intensity profiles

take duct leads to an increase in turbulence higher than the increase in swirl, owing to both higher velocities and velocity gradients, and this effect is less sensible at the greater speed, due to the decreased volumetric efficiency for only one duct. Furthermore the turbulence intensity was nearly proportional to the engine speed for both ducts while for only one duct it was sensibly less than proportional, mainly due to the effect of volumetric efficiency.

Values of the relative turbulence intensity  $u'/U$  at the end of compression were found to be 15–18 percent at  $r=6$  mm, 12–15 percent at  $r=18$  mm, and 7–8 percent at  $r=28$  mm, for all conditions considered.

Figures 16 and 17 report the rms fluctuation of the in-cycle mean velocity ( $U_{rms}$ ) and turbulence intensity ( $u'_{rms}$ ) about the respective ensemble-averaged values, so as to give information about the cyclic variations in the engine turbulent flow and their dependence on intake system configuration and engine speed. The following deductions can be drawn from the results of Fig. 16, when compared to those of Fig. 10, and their relevance also resides in the fact that similar results hold for the turbulence intensity as determined within the standard ensemble-averaging procedure from the same data.

$U_{rms}$  at TDC is less sensitive to the intake system configuration, mainly at the lower speed. This is consistent with results obtained in the literature, either at very low speeds or for configurations leading to swirl levels not largely different [31, 34, 36, 38].  $U_{rms}$  at TDC is more sensitive to the engine speed, particularly for only one intake duct,<sup>9</sup> and this conforms to the results in [31, 39]. The relative rms fluctuation of the mean velocity  $U_{rms}/U$  at TDC was 18–24 percent at  $r=6$  mm, 15–20

<sup>9</sup>Though in the last part of compression, from  $\vartheta=310$  deg to  $\vartheta=345$  deg,  $U_{rms}$  showed a very small dependence on the speed at  $r=28$  mm, for only one duct.

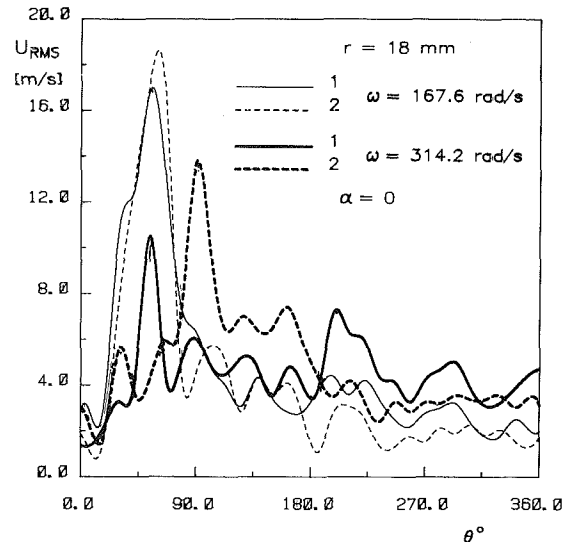


Fig. 16 Distributions of rms fluctuation of the mean velocity

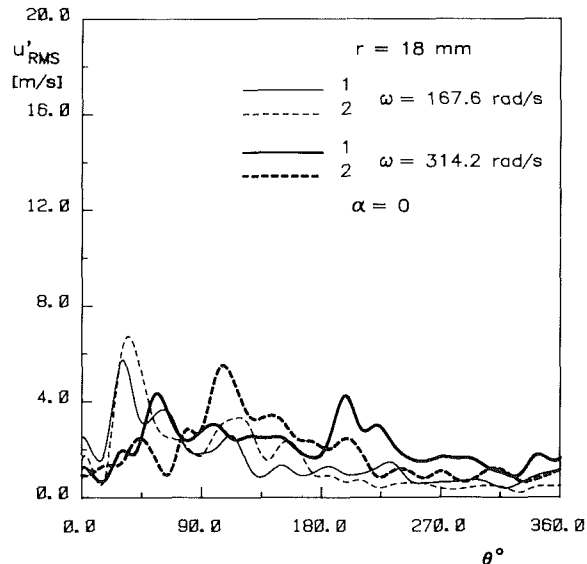


Fig. 17 Distributions of rms fluctuation of the turbulence intensity

percent at  $r=18$  mm, 8–10 percent at  $r=28$  mm, for all engine configurations and speeds.

The behavior of  $u'_{rms}$  (Fig. 17) at the last stage of compression was quite similar to that of turbulence intensity (Fig. 10), at all measurement locations. The relative rms fluctuation of the turbulence intensity  $u'_{rms}/u'$  at TDC was as high as  $\approx 40$ –50 percent.

Some representative results of the correlation and spectral analysis of the turbulent velocity component are given in Figs. 18–22. The crank angle  $\Phi=30$  deg was used as correlation interval in the power spectrum estimation. Figure 18 shows the autocorrelation coefficient  $R$  as a function of  $\vartheta-\vartheta_0$  obtained in the last 30 deg of compression at  $r=18$  mm, for all conditions. The normalized energy spectral density functions obtained from the autocorrelation coefficients of Fig. 18 are shown in Fig. 19. It can be inferred from both figures that the structure of the small scale turbulence is more sensitive to the engine speed than to the intake system configuration. This is also evident for all the correlation intervals during the induction and compression strokes, from the distributions of the dissipative or micro time scale of turbulence ( $\lambda_T$ ) reported in Figs. 20 and 21.

The patterns of  $\lambda_T$ , fluctuating about a constant value,

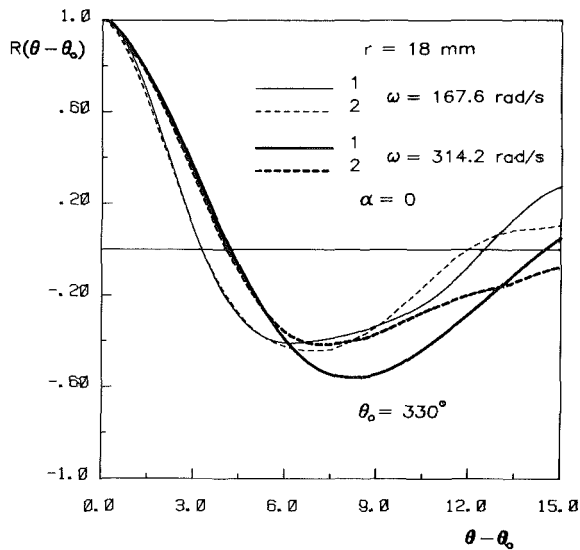


Fig. 18 Autocorrelation coefficient

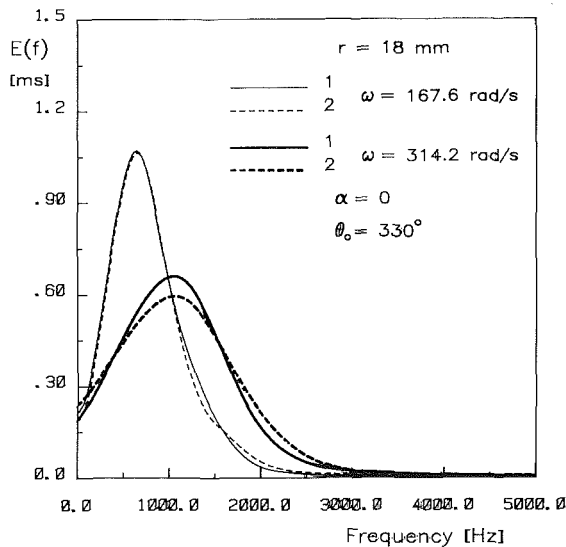


Fig. 19 Normalized energy spectral density function

$\approx 0.20$  ms at 167.5 rad/s and  $\approx 0.14$  at 314.2 rad/s, showed that the structure of the engine turbulence was virtually uniform in the secondary jet flow, as well as in the main flow, on the induction and compression strokes, for both speeds.

Figure 22 shows the distributions of the macro time scale of turbulence ( $\Lambda_T$ ) evaluated as the time interval corresponding to the crank angle  $\vartheta - \vartheta_0$  (Fig. 18) at which the autocorrelation coefficient is minimum [50]. This parameter was also shown to be mainly dependent on engine speed. Furthermore at 167.6 rad/s it was, at the end of compression, higher than on induction, as expected because smaller eddies decay more rapidly than larger ones, while it was more uniform on induction and compression at 314.2 rad/s keeping more than twice as high as the micro time scale of turbulence.

## Conclusions

Turbulence quantities were investigated in a high-speed, automotive diesel engine for different swirl flow conditions produced by an intake system with two tangential ducts, when both were operating and when one of them was deactivated, at two engine speeds, 167.6 rad/s and 314.2 rad/s, one representative of the lower speeds and the other of the higher speed range.

The following main conclusions were reached:

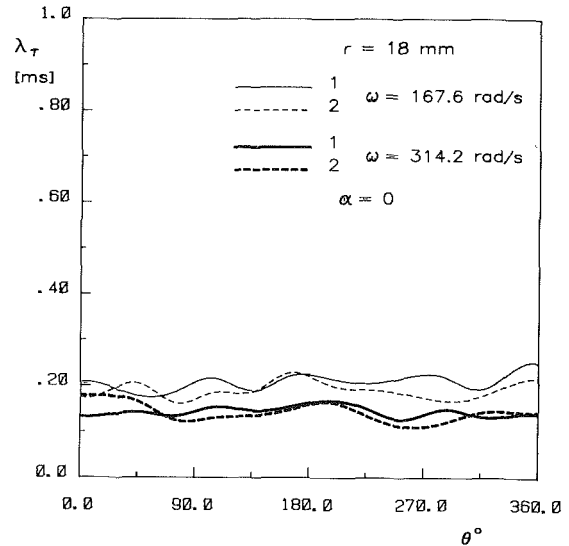


Fig. 20 Distributions of the micro time scale of turbulence

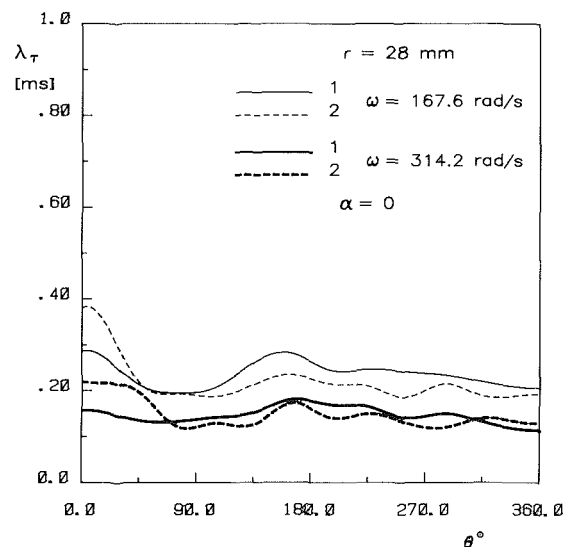


Fig. 21 Distributions of the micro time scale of turbulence

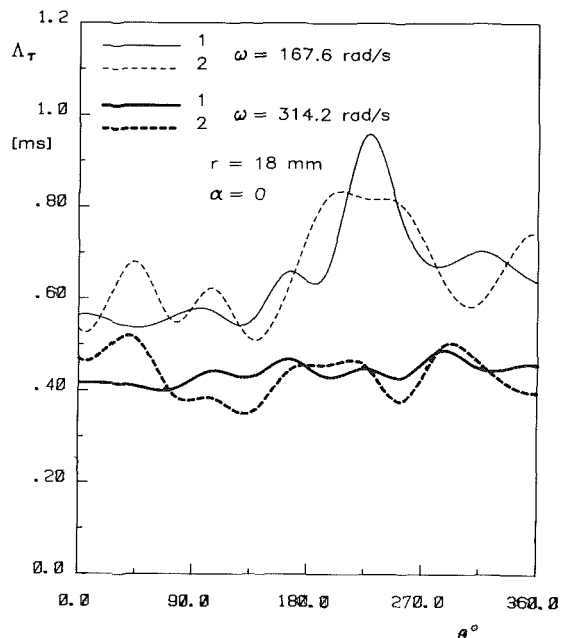


Fig. 22 Distributions of the integral time scale of turbulence

The turbulence intensity and its degree of nonhomogeneity and anisotropy were sensibly influenced by the variable swirl conditions, depending on the intake system configuration as well as on the engine speed, generally showing an increase with increasing swirl intensity at the end of the compression stroke. A similar trend was observed in the cyclic fluctuation of both the mean velocity and turbulence intensity, the fluctuation of the latter not being relatively low.

Keeping one inlet valve closed yielded an increase in both swirl level and turbulence intensity, without significantly affecting volumetric efficiency at the lower speed. The increase in turbulence was higher than the increase in swirl, owing to both higher velocities and velocity gradients, and this effect was less sensible at the greater speed, due to the reduced volumetric efficiency for only one duct.

For both ducts the turbulence intensity at the end of compression increased proportionally with the engine speed, while for only one duct it kept sensibly less than proportional, mainly due to the effect of volumetric efficiency. In fact, for the latter configuration the swirl ratio decreased sensibly when the engine speed was increased.

The rms fluctuation of the mean velocity at TDC was less sensitive to the intake system configuration, mainly at the lower speed, and was more sensitive to the engine speed, particularly for only one duct, with respect to the turbulence intensity. This is consistent with results obtained in the literature for rms velocity fluctuation.

The micro time scale of turbulence was found to be almost uniform during induction and compression indicating that the structure of turbulence before combustion was practically the same as that in the secondary jet flow as well as in the main swirling flow on induction. It did show a slight dependence on the measurement point and on the intake system configuration, but was more sensitive to the engine speed.

Finally, no apparent effect of the cylinder wall on small-scale turbulence quantities was found.

## Acknowledgments

Support for this work was provided by M.P.I. (Ministero Pubblica Istruzione) under 40 percent fund and partially by C.N.R.-P.F.T. (Consiglio Nazionale delle Ricerche - Progetto Finalizzato Trasporti) under Contract No. 84.00384.93.

## References

- Lancaster, D. R., Krieger, R. B., Sorenson, S. C., and Hull, W. L., "Effects of Turbulence on Spark-Ignition Engine Combustion," *Trans. SAE*, Paper No. 760160, 1976.
- Huber, F. W., "Influence of Mixture Formation on the Efficiency of a Diesel Engine With Direct Injection," *MTZ*, 1976.
- Nagayama, I., Araki, Y., and Iioka, Y., "Effects of Swirl and Squish on S.I. Engine Combustion and Emission," *Trans. SAE*, Paper No. 770217, 1977.
- Brandl, F., Reverencic, I., Cartellieri, W., and Dent, J. C., "Turbulent Air Flow in the Combustion Bowl of a D.I. Diesel Engine and Its Effect on Engine Performance," *Trans. SAE*, Paper No. 790040, 1979.
- Greeves, G., Wang, C. H. T., and Kyriazis, G. A., "Inlet Port Design and Fuel Injection Rate Requirements for Direct Injection Diesel Engines," *FISITA 80*, Paper No. 80.4.1.4, 1980.
- Inoue, T., Nakanishi, K., Noguchi, H., and Iguchi, S., "The Role of Swirl and Squish in Combustion of the S.I. Engine," *FISITA 80*, Paper No. 80.4.4.4, 1980.
- Monaghan, M. L., Pettifer, H. F., "Air Motion and Its Effect on Diesel Performance and Emissions," *Trans. SAE*, Paper No. 810255, 1981.
- Belaire, R. C., Davis, G. C., Kent, J. C., and Tabaczynski, R. J., "Combustion Chamber Effects on Burn Rates in a High Swirl Spark Ignition Engine," *Trans. SAE*, Paper No. 830335, 1983.
- Shimoda, M., Shigemori, M., and Tsuruoka, S., "Effect of Combustion Chamber Configuration on In-Cylinder Air Motion and Combustion Characteristics of D.I. Diesel Engine," *SAE Paper No. 850070*, 1985.
- Van Gerpen, J. H., Huang, C., and Borman, G. L., "The Effects of Swirl and Injection Parameters on Diesel Combustion and Heat Transfer," *SAE Paper No. 850265*, 1985.
- Stivender, D. L., "Intake Valve Throttling (IVT) - A Sonic Throttling Intake Valve Engine," *Trans. SAE*, Paper No. 680399, 1968.
- Mayo, J., "The Effects of Engine Design Parameters on Combustion Rate in Spark Ignition Engines," *SAE Paper No. 750355*, 1975.
- Davis, G. C., Tabaczynski, R. J., and Belaire, R. C., "The Effect of Intake Valve Lift on Turbulence Intensity and Burnrate in S.I. Engines-Model Versus Experiment," *Trans. SAE*, Paper No. 840030, 1984.
- Witze, P. O., Martin, J. K., and Borgnakke, C., "Conditionally-Sampled Velocity and Turbulence Measurements in a Spark Ignition Engine," *Combustion Science and Technology*, Vol. 36, 1984, pp. 301-317.
- Matsushita, S., Inoue, T., Nakanishi, K., Okumura, T., and Isogai, K., "Effects of Helical Port With Swirl Control Valve on the Combustion and Performance of S.I. Engine," *SAE Paper No. 850046*, 1985.
- Hashimoto, T., Okada, K., and Oikawa, T., "ISUZU New 9.8L Diesel Engine With Variable Geometry Turbocharger," *SAE Paper No. 860460*, 1986.
- Martin, J. K., Witze, P. O., and Borgnakke, C., "Combustion Effects on the Pre-flame Flow Field in a Research Engine," *SAE Paper No. 850122*, 1985.
- Hall, M. J., Bracco, F. V., and Santavicca, D. A., "Cycle-Resolved Velocity and Turbulence Measurements in an IC Engine With Combustion," *SAE Paper No. 860320*, 1986.
- Ohigashi, S., Hamamoto, Y., and Tanabe, S., "Swirl - Its Measurement and Effect on Combustion in a Diesel Engine," *Instn Mech Engrs*, Vol. 134, 1971.
- Rask, R. B., "Laser Doppler Anemometer Measurements in an Internal Combustion Engine," *Trans. SAE*, Paper No. 790094, 1979.
- Liou, T.-M., Santavicca, D. A., and Bracco, F. V., "Laser Doppler Velocimetry Measurements in Valved and Ported Engines," *Trans. SAE*, Paper No. 840375, 1984.
- Semenov, E. S., "Studies of Turbulent Gas Flow in Piston Engines," *Otdeliniye Technicheskikh Nauk*, No. 8, 1958 (NASA Technical Translation F97).
- Winsor, R. E., and Patterson, D. J., "Mixture Turbulence, A Key to Cyclic Variation," *SAE Paper No. 730086*, 1973.
- Dent, J. C., and Salama, N. S., "The Measurement of Turbulence Characteristics in an Internal Combustion Engine Cylinder," *SAE Paper No. 750886*, 1975.
- Lancaster, D. R., "Effects of Engine Variables on Turbulence in a Spark-Ignition Engine," *Trans. SAE*, Paper No. 760159, 1976.
- Witze, P. O., "Measurements of the Spatial Distribution and Engine Speed Dependence of Turbulent Air Motion in an I.C. Engine," *Trans. SAE*, Paper No. 770220, 1977.
- Rask, R. B., "Comparison of Window, Smoothed-Ensemble, and Cycle-by-Cycle Data Reduction Techniques for Laser Doppler Anemometer Measurements of In-Cylinder Velocity," in: *Fluid Mechanics of Combustion Systems*, T. Morel, R. P. Lohmann, and J. M. Rackley, eds., ASME, New York, 1981.
- Liou, T.-M., and Santavicca, D. A., "Cycle Resolved LDV Measurements in a Motored IC Engine," *ASME Journal of Fluids Engineering*, Vol. 107, 1985, pp. 232-240.
- Catania, A. E., and Mittica, A., "A Contribution to the Definition and Measurement of Turbulence in a Reciprocating I.C. Engine," in: *ASME Diesel & Gas Engines Symposium, ETCE*, 1985, Paper No. 85-DGP-12.
- Catania, A. E., and Mittica, A., "Cycle-by-Cycle, Correlation and Spectral Analysis of I.C. Engine Turbulence," in: *Flows in Internal Combustion Engines - III*, FED-Vol. 28, T. Uzman, W. G. Tiederman, and J. M. Novak, eds., ASME, New York, 1985.
- Rask, R. B., and Saxena, V., "Influence of Geometry on Flow in the Combustion Chamber of a Direct-Injection Diesel Engine," in: *Flows in Internal Combustion Engines - III*, FED-Vol. 28, T. Uzman, W. G. Tiederman, and J. M. Novak, eds., New York, 1985.
- Catania, A. E., "3-D Swirling Flows in an Open-Chamber Automotive Diesel Engine With Different Induction Systems," in: *Flows in I.C. Engines*, T. Uzman, ed., ASME, New York, 1982.
- Wakisaka, T., Hamamoto, Y., Shimamoto, Y., "Turbulence Structure of Air Swirl in Reciprocating Engine Cylinders," in: *Flows in I.C. Engines*, T. Uzman, ed., ASME, New York, 1982.
- Tindal, M. J., Williams, T. J., and Aldoory, M., "The Effect of Inlet Port Design on Cylinder Gas Motion in Direct Injection Diesel Engines," in: *Flows in I.C. Engines*, T. Uzman, ed., ASME, New York, 1982.
- Catania, A. E., "Induction System Effects on the Fluid-Dynamics of a D.I. Automotive Diesel Engine," *ASME Diesel & Gas Engines Symposium, ETCE*, 1985, Paper No. 85-DGP-11.
- Arcoumanis, C., Bicen, A. F., and Whitelaw, J. H., "Effect of Inlet Parameters on the Flow Characteristics in a Four-Stroke Model Engine," *SAE Paper No. 820750*, 1982.
- Liou, T.-M., and Santavicca, D. A., "Cycle Resolved Turbulence Measurements in a Ported Engine With and Without Swirl," *SAE Paper No. 830419*, 1983.
- Arcoumanis, C., Vafidis, C., and Whitelaw, J. H., "Valve and In-Cylinder Flow Generated by a Helical Port in a Production Diesel Engine," in: *Flows in Internal Combustion Engines - III*, FED-Vol. 28, T. Uzman, W. G. Tiederman, and J. M. Novak, eds., ASME, New York, 1985.
- Bopp, S., Vafidis, C., and Whitelaw, J. H., "The Effect of Engine Speed on the TDC Flowfield in a Motored Reciprocating Engine," *SAE Paper No. 860023*, 1986.
- Hayder, M. E., Varma, A. K., and Bracco, F. V., "A Limit to TDC Turbulence Intensity in Internal Combustion Engines," submitted for publication to *AIAA Journal*, 1984.
- Fansler, T. D., "Laser Velocimetry Measurements of Swirl and Squish

Flows in an Engine With a Cylindrical Piston Bowl," SAE paper No. 850124, 1985.

42 Catania, A. E., and Mittica, A., "Analysis of Turbulent Flow Parameters in a Motored Automotive Engine," *COMODIA 85*, JSME, Tokyo, 1985, pp. 96-106.

43 Reynolds, W. C., "Modeling of Fluid Motions in Engines - An Introductory Overview," *Combustion Modeling in Reciprocating Engines*, J. N. Mattavi and C. A. Amann, eds., Plenum Press, New York, 1980.

44 Hinze, J. O., *Turbulence*, McGraw-Hill, New York, 1975.

45 Rader, C. M., "An Improved Algorithm for High Speed Autocorrelation With Applications to Spectral Estimation," *IEEE Trans. Audio Electroacoustics*, Vol. AU-18, No. 4, 1970.

46 Rabiner, L. R., Schafer, R. W., and Dlugos, D., "Correlation Method for Power Spectrum Estimation," *IEEE Programs for Digital Signal Processing*, 1979.

47 Witze, P. O., "A Critical Comparison of Hot-Wire Anemometry and Laser Doppler Velocimetry for I.C. Engine Applications," SAE Paper No. 800132, 1980.

48 Huebner, K. H., and McDonald, A. T., "A Dynamic Model and Measurement Technique for Studying Induction Air Swirl in an Engine Cylinder," *ASME JOURNAL OF ENGINEERING FOR POWER*, Apr. 1970.

49 Catania, A. E., "Air Flow Investigation in the Open Combustion Chamber of a High-Speed, Four-Stroke Diesel Engine," ASME Paper 80-FE-5, 1980.

50 Tritton, D. J., *Physical Fluid Dynamics*, Van Nostrand Reinhold, United Kingdom, 1977.

## APPENDIX

The instantaneous velocity is split into a mean nonstationary component and a turbulent fluctuation about this, so that, with reference to the engine cycle  $i$

$$U_i(t) = \bar{U}_i(t) + u_i(t) \quad (1)$$

where  $\bar{U}_i(t)$  is the mean velocity at time  $t$  (corresponding to the crank angle  $\theta$ ) and  $u_i(t)$  is the velocity fluctuation about the mean. Using the symbol  $\bar{f}$  to represent the average of any variable  $f(t)$  (or  $f(\theta)$ ) in the time interval  $T$  (or in the crank angle interval  $\Theta$ )

$$\bar{f} = \frac{1}{T} \int_0^T f(t+\tau) d\tau = \frac{1}{\Theta} \int_0^\Theta f(\theta+\varphi) d\varphi \quad (2)$$

$\bar{U}_i(t)$  was determined so that

$$\bar{U}_i = \bar{\bar{U}}_i \quad (3)$$

and, from equation (1)

$$\bar{u}_i = 0 \quad (4)$$

as it should be in agreement with the conventional definition of turbulence for a steady flow. The average turbulence intensity in  $T$  is then given by

$$u'_i = \sqrt{(U_i - \bar{U}_i)^2} \quad (5)$$

The ensemble-averaged mean velocity  $U$  in the interval  $T$  is defined, for an ensemble of  $N$  records (or cycles), as

$$U = \frac{1}{N} \sum_{i=1}^N \bar{U}_i \quad (6)$$

and so the ensemble-averaged turbulence intensity in  $T$  is given by

$$u' = \sqrt{\frac{1}{N} \sum_{i=1}^N (U_i - \bar{U}_i)^2} \quad (7)$$

The rms fluctuation of the in-cycle mean velocity and turbulence intensity about the respective averaged values are (with reference to the time-averaged values in  $T$ )

$$U_{\text{rms}} = \sqrt{\frac{1}{N} \sum_{i=1}^N (\bar{U}_i - U)^2} \quad (8)$$

$$u'_{\text{rms}} = \sqrt{\frac{1}{N} \sum_{i=1}^N (u'_i - u')^2} \quad (9)$$

The Eulerian time autocorrelation coefficient in the period  $T$ , starting at time  $t_0$  (corresponding to the crank angle  $\theta_0$ ), is defined, in its ensemble-average form, as

$$R(\tau) = \frac{1}{u'^2} \frac{1}{N} \sum_{i=1}^N \left[ \frac{1}{T-\tau} \int_0^{T-\tau} u_i(t) u_i(t+\tau) dt \right] \quad (10)^{10}$$

where the time  $t$  is intended as relative to  $t_0$  and the time variable  $\tau$  in  $T$  ranges from 0 to  $\tau_{\text{max}} = T/2$ .

The normalized energy spectral density function in  $T$  is expressed, in terms of autocorrelation coefficient, as

$$E(f) = 4 \int_0^{\tau_{\text{max}}} R(\tau) w(\tau) \cos(2\pi f\tau) d\tau \quad (11)$$

where  $w(\tau)$  is a window function of rectangular or Hamming type. This expression of the energy density spectrum requires that  $u_i(t)$  be a stationary random function in  $T$ , which in fact it is within an approximation adequate for the purposes of the proposed method [30].

The micro (or dissipative) time scale of turbulence is then given by

$$\lambda_\tau = 1 / \sqrt{2\pi^2 \int_0^{f_{\text{max}}} f^2 E(f) df} \quad (12)$$

where  $f_{\text{max}}$  is the maximum frequency for which  $E(f)$  is still finite and significant.

The macro time scale of turbulence can be evaluated for example as

$$\Lambda_\tau = \int_0^{\tau_{\text{max}}} R(\tau) d\tau \quad (13)$$

or as the time interval ( $\tau$ ) in which  $R$  falls to  $1/e$ , or, if the curve has a negative region, the time at which  $R$  is a minimum [50].

It is worthwhile to observe that the standard ensemble-average definition of the mean velocity component  $U_E$  is given by the limit of equation (6) as the time-averaging interval length tends to zero

$$U_E = \lim_{T \rightarrow 0} U \quad (14)$$

The turbulence intensity  $u'_E$ , within a pure ensemble-averaging procedure, is then given by

$$u'_E = \lim_{T \rightarrow 0} U_{\text{rms}} \quad (15)$$

<sup>10</sup>The expression of the autocorrelation coefficient  $R_i(\tau)$  for cycle  $i$  is simply derived from equation (10) by omitting the ensemble-averaging summation and substituting  $u_i'^2$  for  $u'^2$ .

## Effects of Honeycomb-Shaped Walls on the Flow Regime Between a Rotating Disk and a Stationary Wall<sup>1</sup>

**J. M. Owen.**<sup>2</sup> To minimize the cooling air necessary to prevent the ingress of hot gas into a turbine wheel space, a peripheral seal is usually fitted between the turbine disk and the adjacent stationary casing. The authors have used an open rotor-stator system, and it would be interesting to see what effect the honeycomb stator has when it is used in a sealed system. Are there plans to do this?

<sup>1</sup>By T. Uzkan and N. J. Lipstein, published in the July 1986 issue of the JOURNAL OF ENGINEERING FOR GAS TURBINES AND POWER, Vol. 108, No. 3, pp. 553-561.

<sup>2</sup>School of Engineering & Applied Sciences, University of Sussex, Falmer, Brighton BN1 9QT, England.

Richardson and Saunders [14] noted that when the diameter of the stator was larger than that of the rotor, the flow leaving the rotor could snap on to the stator thereby altering the flow structure. Why did the authors make their stator larger than the rotor, and did they observe any strange flow behavior?

The following comments apply to errors and omissions on the figures. The gap ratio is variously referred to as  $s/a$ ,  $s/r_1$ , and  $\bar{S}$ , and in Fig. 3(b) the values for  $s/r_1 = 0.0166$  and  $0.0666$  appear to have been reversed. Similarly, some of the values of  $Q$  appear to have been reversed in Fig. 4. It would also be helpful to indicate the values of  $s/r_1$  and  $Q$  on the appropriate figures; there are many (e.g., Figs. 3 and 7-10) where the information is missing.

### References

- 14 Richardson, P. D., and Saunders, O. A., "Studies of Flow and Heat Transfer Associated With a Rotating Disc," *J. Mech. Engng. Sci.*, Vol. 5, 1963, p. 336.